AD-A266 817

3

AGARD-R-766 (Addendum)

AGARD-R-766 (Addendum)

AGARD

ADVISORY GROUP FOR AEROSPACE RESEARCH & DEVELOPMENT

7 RUE ANCELLE 92200 NEUILLY SUR SEINE FRANCE

AGARD REPORT 766 (Addendum)

AGARD Engine Disc Cooperative Test Programme

Rapport sur le Programme d'Essais Commun des Disques Moteur (supplément)

This publication was sponsored by the Structures and Materials Panel of AGARD.

NORTH ATLANTIC TREATY ORGANIZATION

Published April 1993

Distribution and Availability on Back Cover

AGARD-R-765 (Addendum)

AGARD

ADVISORY GROUP FOR AEROSPACE RESEARCH & DEVELOPMENT

7 RUE ANCELLE 92200 NEUILLY SUR SEINE FRANCE

AGARD REPORT 766 (Addendum)

AGARD Engine Disc Cooperative Test Programme

Rapport sur le Programme d'Essais Commun des Disques Moteur (supplément)

This publication was sponsored by the Structures and Materials Panel of AGARD.

North Atlantic Treaty Organization

Organisation du Traité de l'Atlantique Nord

The Mission of AGARD

According to its Charter, the mission of AGARD is to bring together the leading personalities of the NATO nations in the fields of science and technology relating to aerospace for the following purposes:

— Recommending effective ways for the member nations to use their research and development capabilities for the common benefit of the NATO community;

— Providing scientific and technical advice and assistance to the Military Committee in the field of aerospace research and development (with particular regard to its military application);

— Continuously stimulating advances in the aerospace sciences relevant to strengthening the common defence posture;

— Improving the co-operation among member nations in aerospace research and development;

— Exchange of scientific and technical information;

— Providing assistance to member nations for the purpose of increasing their scientific and technical potential;

— Rendering scientific and technical assistance, as requested, to other NATO bodies and to member nations in connection with research and development problems in the aerospace field.

The highest authority within AGARD is the National Delegates Board consisting of officially appointed senior representatives from each member nation. The mission of AGARD is carried out through the Panels which are composed of experts appointed by the National Delegates, the Consultant and Exchange Programme and the Aerospace Applications Studies Programme. The results of AGARD work are reported to the member nations and the NATO Authorities through the AGARD series of publications of which this is one.

Participation in AGARD activities is by invitation only and is normally limited to citizens of the NATO nations.

The content of this publication has been reproduced
directly from material supplied by AGARD or the authors.

Published April 1993

ISBN 92-835-0709-6

Printed by Specialised Printing Services Limited
40 Chigwell Lane, Loughton, Essex IG10 3TZ

Preface

The Structures and Materials Panel has been involved in studies of fatigue and fracture of critical jet engine components for many years. In 1982 a Sub-committee on "Damage Tolerance Concepts for Critical Engine Components" was formed to study the overall philosophy and the implications of introducing damage tolerance concepts (DTC) into the design and use of critical engine components.

The damage tolerance philosophy offers potential cost savings of considerable magnitude when compared with a "safe-life" approach provided such a concept can be implemented with an assurance that current safety standards will not be prejudiced. As an example of possible savings, it has been estimated that over 80% of engine discs have ten or more low cycle fatigue lives remaining when discarded under "safe-life" rules, and it is the useful remaining life that DTC aims to exploit in service. Apart from economic advantages, the DTC approach offers a practical method for using modern high-strength disc materials that could be rejected by the application of "safe-life" conditions of usage.

In 1983 the Sub-committee on Damage Tolerance Concepts of Critical Engine Components, under the chairmanship of D.A. Fanner (UK), organized a Cooperative Test Programme on Damage Tolerance in Titanium Alloy Engine Disc Materials. A separate Sub-committee on Engine Discs Cooperative Tests was formed to direct this activity. Over the years the following Panel members participated in the sub-committee:

A. Ankara (TU)	L. Kompotiatis (GR)
H.M. Burte (US)	R. Labourdette (FR)
H.J.G. Carvalhinhos (PO)	J.S.L. Leach (UK)
M.N. Clark (CA), Chairman 1983-85	Mrs. C.E.W. (Anita) Looije (NL)
D. Coutsouradis (BE)	B.F. Peters (CA)
J.J. De Luccia (US)	C.L. Petrin (US)
G.L. Denman (US)	R. Potter (UK)
A. Deruyttere (BE)	A. Salvetti (IT)
M. Doruk (TU)	R. Schmidt (US)
C.N. Economidis (GR)	H.P. van Leeuwen (NL)
W. Elber (US)	S.L. Venneri (US)
D.A. Fanner (UK)	A.P. Ward (UK)
H.F.N. Goncalo (PO)	J.J. Waldman (US)
L. Grabowski (UK)	W. Wallace (CA)
G. Grueninger (GE)	H. Zocher (GE)
J.J. Kacprzynski (CA) Chairman 1986-	

As a result of the very large size of the test programme, it appeared to be convenient from an administrative point of view to divide it into a Core Programme followed by Supplemental Programmes. In the Core Programme all the laboratories performed identical fatigue and fracture tests for one material, Ti-6Al-4V, at constant amplitude and at room temperature. The summary of these tests is included in AGARD Report 766.

For the Supplemental Programme, three materials were tested, Ti-6Al-4V, IMI 685 and Ti-17, under both constant amplitude and under variable amplitude TURBISTAN loading sequences. Tests were performed at room temperature; high temperature tests became a separate activity and will be reported in another report. Five crack growth models were evaluated and their predictions were verified by experimental data.

In the Supplemental Programme 13 laboratories participated and were represented by 23 participants from:

Europe:	CEAT, Toulouse France	T. Pardessus, E. Jany
	FFA, Stockholm, Sweden	A. Blom
	IABG, Ottobrunn, Germany	P. Heuler, W. Schütz
	NLR, Amsterdam, The Netherlands	C.E.W. (Anita) Looije, R.J.H. Wanhill
	RAE, Farnborough, UK	C. Gostelow, C. Wilkinson
	Rolls Royce, Derby, UK	R. Jeal, C. Howland, L. Grabowski, M. Walsh
	University of Pisa, Italy	A. Frediani
North America	AFML, Dayton, US	C. Harmsworth, J. Ruschau, A. Krawczyk
	NADC, Warminster, US	E.U. Lee
	IAR/NRCC, Ottawa, Canada	M.D. Raizenne
	NASA Langley	J. Newman
	QETE, Ottawa, Canada	M. Yanishevsky
	University of Toronto, Canada	D. McCammond, P. Sooley

T. Pardessus and E. Jany served as coordinators for Europe and M.D. Raizenne for North America.

The present Report, written by 11 authors, includes the summary of tests and analysis. All the test data from both the core and the supplemental programme are stored at the Institute for Aerospace Research at the National Research Council of Canada, and are available on request.

Finally it has to be emphasized that research of this size and complexity can be performed only as a collaborative programme, not only due to reasons of costs but also by the need to bring together experts from different areas and countries and by encouraging the exchange of ideas and expertise.

Many thanks to all participants for their valuable contribution in tests, analysis and in the preparation of this Report. Many thanks to the members of the Sub-committee who over the years patiently served with guidance. Thanks to AGARD for making it possible.

J.J. Kacprzynski
Chairman 1986-
Sub-committee on Engine Discs Materials
Collaborative Programme

Structures and Materials Panel

Chairman: Mr Roger Labourdette
Directeur Scientifique des Structures
ONERA
29 ave de la Division Leclerc
92322 Châtillon
France

Deputy Chairman: Dipl. Ing. O. Sensburg
Chief Engineer for Structures
MBB Flugzeuge/FEZ
Postfach 801160
W-8000, München 80
Germany

SUB-COMMITTEE

Chairman: Dr J.J. Kacprzynski
Structures and Materials Laboratory
Institute for Aerospace Research
Ottawa, Ontario K1A 0R6
Canada

Members (Fall 1991)

Dr H.J.G. Carvalhinhos — PO
Mr D. Coutsouradis — BE
Prof. A. Deruyttere — BE
Prof. M. Doruk — TU
Dr C.N. Economidis — GR
Dr W. Elber — US
Major H.F.N. Goncalo — PO
Dr L. Grabowski — UK
Prof. G. Grueninger — GE
Mr Z. Kompotiatis — GR
Mr R. Labourdette — FR
Mrs C.E.W. (Anita) Looije — NL
Dr B.F. Peters — CA
Mr C.L. Petrin — US
Mr R. Potter — UK
Prof. A. Salvetti — IT
Mr S.L. Venneri — US
Dr J.J. Waldman — US
Dr W. Wallace — CA
Mr A.P. Ward — UK
Mr H. Zocher — GE

Technical Coordinators

T. Pardessus, E. Jany — FR
M.D. Raizenne — CA

PANEL EXECUTIVE

Dr Jose M. Carballal, Spain

Mail from Europe:
AGARD—OTAN
Attn: SMP Executive
7, rue Ancelle
92200 Neuilly-sur-Seine
France

Mail from US and Canada:
AGARD—NATO
Attn: SMP Executive
Unit 21551
APO AE 09777

Tel: 33(1)47 38 57 90 & 57 92
Telex: 610176 (France)
Telefax: 33(1) 47 38 57 99

Abstract

The Report describes fatigue and crack growth tests of Ti-Al6-4V, IMI 685 and Ti-17 specimens under constant amplitude and under variable amplitude TURBISTAN loading sequences at room temperature. Five crack growth models are evaluated and compared against experimental data. Microstructure and fractography data for the tested materials are also presented.

Résumé

Ce rapport décrit les résultats d'essais de fatigue oligocyclique et de propagation des fissures de fatigue sous des sollicitations d'amplitude constante, ou sous chargement TURBISTAN à amplitude variable, pour des échantillons de Ti6Al4V, de IMI685 et de Ti17, à la température ambiante. Cinq modèles de croissance des fissures sont évalués en fonction des résultats expérimentaux. La microstructure des matériaux et les faciès de surface de rupture sont également présentés.

Contents

		Page
Preface		iii
Structures and Materials Panel		v
Abstract/Résumé		vi
Chapter 1	The AGARD SMP Engine Disc Cooperative Test Programme by M.D. Raizenne	1-1
Chapter 2		
Part I	Fractographic and Microstructural Analysis of Fatigue Crack Growth in Ti-6Al-4V Fan Disc Forgings by R.J.H. Wanhill and C.E.W. Looije	2-1
Part II	Fractographic Investigation of IMI 685 Crack Propagation Specimens for SMP SC33 by C. Wilkinson and P. Heuler	2-41
Part III	Material Characterization and Fractographic Examination of Ti-17 Fatigue Crack Growth Specimens for SMP SC33 by M. Yanishevsky, B. Cornwall and M. Roth	2-45
Chapter 3	Low Cycle Fatigue Behaviour of Titanium Disc Alloys by C.E.W. Looije	3-1
Chapter 4	Fatigue Crack Growth Results for Ti-6Al-4V, IMI 685 and Ti-17 by M.D. Raizenne	4-1
Chapter 5	Crack Growth Prediction Models by E. Jany and P. Heuler	5-1
Chapter 6	Crack Growth Prediction Results by E. Jany, O. Renne and P. Heuler	6-1
Chapter 7	Conclusions and Recommendations by P. Heuler, W. Schütz and E. Jany	7-1

The AGARD SMP Engine Disc Cooperative Test Programme

M.D. Raizenne
Institute for Aerospace Research
National Research Council of Canada
Ottawa, Ontario, K1A 0R6

Since the late 1970's there has been a concerted effort in the gas turbine engine industry to enhance the safe-life design of rotating engine components by including damage tolerant lifing methodologies in the design process. Damage tolerant lifing had been in place for airframe structures since MIL-A-83444 [1] was introduced in 1971. By safely adding damage tolerant lifing to the component design process substantial cost savings can be realized in the form of extended component lives.

In recognition of this emerging technology, the AGARD Structures and Materials Panel formed two sub-committees in 1982 to address the key issues in this area. The first sub-committee, designated SMP/SC.27, was formed to organize a specialists' meeting on 'Damage Tolerance Concepts for Critical Engine Components' which was held in San Antonio Texas in April 1985 [2]. A series of four follow-on workshops which addressed the key issues raised at the specialists' meeting were held in 1988 and 1989 [3,4,5,6].

The second sub-committee, designated SMP/SC.33, was formed in 1983 to organize a test programme between NATO countries to promote:

- familiarization of NATO laboratories with test techniques for damage tolerance properties of engine disc materials,
- standardization of test specimen geometries and test techniques for engine disc materials, and
- calibration of participating laboratories through a round robin test programme using low cycle fatigue and fatigue crack growth specimens.

The subcommittee was formally called the 'Engine Disc Material Cooperative Test Programme'.

Through the use of typical engine disc materials, Ti-6Al-4V, IMI 685 and Ti-17, and the use of realistic engine loading sequences the Engine Disc Material Cooperative Test Program was intended to establish a data base for evaluation of different modelling techniques in the prediction of fatigue crack growth lives.

The SMP/SC.33 subcommittee appointed a European and a North American coordinator to set the round robin test programme in motion.

The Engine Disc Material Cooperative Test Programme was carried out in two parts. The first part called the Core Programme was tightly controlled, limited to one material, Ti-6Al-4V, and a single constant amplitude loading sequence $R = 0.1$. There were 12 participating laboratories representing seven countries in the Core Programme. The round robin testing was completed in 1988 and was published as an AGARD report [7].

The second part of the programme called the Supplemental Programme expanded the titanium data base to include IMI 685 and Ti-17. The number of loading sequences was increased to include constant amplitude and variable amplitude loading. Five different crack growth models were evaluated. Thirteen laboratories, two of which had not participated in the Core Programme, NASA Langley and the FFA, participated in the Supplemental Programme.

The purpose of this report is to present the Supplemental Programme results. Chapters Two through Seven present the microstructure, fractography, low cycle fatigue, fatigue crack growth and fatigue crack growth modelling results respectively. Each chapter is authored by one of the Supplemental Programme participants.

OVERVIEW OF THE CORE PROGRAMME

The intent of the Core Programme was to familarize participants with state-of-the-art test techniques using a well behaved titanium alloy, Ti-6Al-4V. Detailed test procedures [8] were written. Four specimen geometries were selected, two investigating low cycle fatigue properties and two damage tolerance properties (See Chapters Three and Four). The Ti-6Al-4V material for the

programme was provided by Rolls Royce from RB211 fan disc forgings.

Tables 1 and 2 provide a list of the participating laboratories and an overview of the Core Programme test matrix. There were 216 tests carried out by the 12 participating laboratories. The final report concluded that:

- standardization of test specimens and procedures provided a basis for the comparison and calibration of the participating laboratories.
- statistical analysis of both the LCF and the fatigue crack growth data indicated no deviating test results.
- potential drop technique proved extremely accurate in measuring small flaw sizes for both initiation (LCF) and fatigue crack growth specimens, and
- a sufficiently large data base on Ti-6Al-4V was generated which could be used in the Supplemental Programme for life prediction modelling.

OVERVIEW OF THE SUPPLEMENTAL PROGRAMME

At the conclusion of the Core Programme the participants agreed that all of the original programme objectives had been achieved and that a Supplemental Programme should:

- expand the titanium data base to include coarser grained alloys such as β-processed IMI 685 and Ti-17. This would increase the confidence level in the potential drop system in detecting flaw initiation and growth.
- include loading sequences that would be typical of those experienced by engine compressor discs. The supplemental programme included two constant amplitude sequences and five variable amplitude sequences based on the Turbistan loading sequence [9].
- use the expanded fatigue crack growth data base to evaluate state-of-the-art fatigue crack growth modelling techniques.

An overview of the Supplemental Programme is provided in Tables 3 and 4. The disc materials for the Supplemental Programme were provided by Rolls Royce and General Electric. A second set of test procedures was written for the participants [10].

Before the modelling phase of the programme started, the constant amplitude crack growth data was collected from the participants, collated into a data base and forwarded to the modelling participants with 60 load cases to be modelled [11]. Six participants including one gas turbine engine manufacturer, Rolls Royce, participated in the modelling phase of the programme. The modellers did not have access to the experimentally generated data for the load cases they were predicting. The modelling results were collected and a comparison was carried out between the modelling results and the experimental data.

The contents of this report constitute a major effort by the participating NATO countries to determine if damage tolerant lifing methodologies are applicable to gas turbine engine disc materials.

REFERENCES

1. Military Specification MIL-A-83444, "Airplane Damage Tolerance Requirements (U.S.)", July 1971.

2. "Damage Tolerance Concepts for Critical Engine Components", AGARD Conference Proceedings 393, April 1985.

3. "AGARD/SMP Review - Damage Tolerance for Engine Structures: 1. Non-Destructive Evaluation", AGARD Report 768, November 1988.

4. "AGARD/SMP Review - Damage Tolerance for Engine Structures: 2. Defects and Quantitative Materials Behaviour", AGARD Report 769, August 1989.

5. "AGARD/SMP Review - Damage Tolerance for Engine Structures: 3. Component Behaviour and Life Management", AGARD Report 770, June 1990.

6. "AGARD/SMP Review - Damage Tolerance for Engine Structures: 4. Reliability and Quality Assurance", AGARD Report 773, December 1991.

7. Mom, A.J.A. and Raizenne, M.D., "AGARD Engine Disc Cooperative Test Programme", AGARD Report 766, August 1988.

8. Mom, A.J.A., "Working Document for the AGARD Cooperative Test Programme on Titanium Alloy Engine Disc Material", NLR TR 84022L, 1984.

9. Ten Have, A.A., "Cold Turbistan - Final Definition of a Standardized Fatigue Test Loading Sequence for Tactical Aircraft Cold Section Engine Discs", NLR TR 87054L, March 1987.

10. Raizenne, M.D., "AGARD TX114 Test Procedures for Supplemental Engine Disc Test Programme", IAR LTR-ST-1671, June 1988.

11. Raizenne, M.D., "AGARD/SMP Sub-Committee 33 Engine Disc Test Programme Fatigue Crack Growth Rate Data and Modelling Cases for Ti-6Al-4V, IMI 685 and Ti-17", IAR LTR-ST-1785, November 1990.

TABLE 1
CORE PROGRAMME
List of Participating Laboratories and Their Representatives

North America	AFML, Dayton, USA	C. Harmsworth
	NADC, Warminster, USA	E.U. Lee
	IAR/NRCC, Ottawa, Canada	M.D. Raizenne*
	NASA Lewis, Cleveland, USA	J. Telesman
	QETE, Ottawa, Canada	M. Yanishevsky
	University of Toronto, Canada	P. Sooley
Europe	CEAT, Toulouse, France	A. Liberge, T. Pardessus
	IABG, Ottobrunn, Germany	J. Foth, W. Schütz
	NLR, Amsterdam, Netherlands	A. Mom*
	RAE, Franborough, UK	C. Gostelow, C. Wilkinson
	Rolls Royce, Derby, UK	R. Jeal, N. McLeod, C. Howland
	University of Pisa, Italy	A. Frediani

* Programme Coordinators

TABLE 2
CORE PROGRAMME
Test Matrix

Type of Test	LCF Life / Crack Formation		Crack Propagation	
Test Specimen	Smooth Cylindrical	Flat Notched Kt ~ 2.2	Corner Crack	Compact Tension
Number of Specimens	6	6	3	3
Crack Detection Technique	—	potential drop (PD)	PD or optical	PD
Test Objective	total life	total life + initial crack formation	'short' crack range	total da/dN - ΔK curve

TABLE 3
SUPPLEMENTAL PROGRAMME
List of Participating Laboratories and Their Representatives

North America	AFML, Dayton, USA	C. Harmsworth, J. Ruschau, A. Krawczyk
	NADC, Warminster, USA	E.U. Lee
	IAR/NRCC, Ottawa, Canada	M.D. Raizenne*
	NASA Langley	J. Newman
	QETE, Ottawa, Canada	M. Yanishevsky
	University of Toronto, Canada	D. McCammond, P. Sooley
Europe	CEAT, Toulouse, France	T. Pardessus*, E. Jany*
	FFA, Stockholm, Sweden	A. Blom
	IABG, Ottobrunn, Germany	P. Heuler, W. Schütz
	NLR, Amsterdam, Netherlands	C.E.W. Looije
	RAE, Franborough, UK	C. Gostelow, C. Wilkinson
	Rolls Royce, Derby, UK	R. Jeal, C. Howland, L. Grabowski, M. Walsh
	University of Pisa, Italy	A. Frediani

* Programme Coordinators

TABLE 4
SUPPLEMENTAL PROGRAMME
Test Matrix

Material	Ti-6Al-4V				IMI 685				Ti-17			
Sequence Type	Core* RT	Simple Sequence	Complex Sequence	Total	Core RT	Simple Sequence	Complex Sequence	Total	Core RT	Simple Sequence	Complex Sequence	Total
LCF	C (6) O			6	18			18	6			6
Kt ~ 2.2	M P				18			18	6			6
Compact Tension	L E (2) T	16	24	42	9	16	32	57	4	10	10	24
Corner Crack	E D	8	16	24	9	16	32	57	4	10	10	24
Participating Laboratories	all (RR)	CEAT AFML	CEAT AFML PISA		IABG NLR RR	RAE RR	IABG RAE RR NLR		NADC U of T QETE	U of T QETE	U of T QETE	

* Additional data required for material verification.

FRACTOGRAPHIC AND MICROSTRUCTURAL ANALYSIS OF FATIGUE CRACK GROWTH IN Ti-6Al-4V FAN DISC FORGINGS

R.J.H. Wanhill and C.E.W. Looije,
National Aerospace Laboratory NLR,
P.O. Box 90502, 1006 BM Amsterdam
The Netherlands

SUMMARY

The constant amplitude and flight simulation (TURBISTAN) fatigue crack growth behaviour of Ti-6Al-4V fan disc forgings tested in the AGARD engine disc cooperative test programme was investigated by fractographic and microstructural analysis. The crack growth curve shapes and fractographic characteristics were similar. Transitions in the fatigue crack growth curves correlated with a change from structure-sensitive to continuum-mode crack growth, primarily in the transformed and aged β grains, and decreased fracture surface roughness. The transitions were most probably caused by the maximum plane strain cyclic plastic zone sizes becoming equal to and exceeding the average platelet α packet sizes. The significance of such transitions for prediction of fatigue crack growth and service failure analysis is discussed.

Key words: fatigue crack growth, Ti-6Al-4V titanium alloy, microstructure, fractography.

NOMENCLATURE

a	crack length
α	titanium alloy phase with hexagonal close packed crystal structure
β	titanium alloy phase with body centered cubic crystal structure
CORONA 5	titanium alloy containing nominally 4.5 weight % aluminium, 5 weight % molybdenum and 1.5 weight % chromium
d	grain size
da/dn	fatigue crack growth rate
G	crack driving force per unit thickness
γ	degree of clustering
K_{max}	maximum stress intensity factor
K_{op}	crack opening stress intensity factor
ΔK_{eff}	effective stress intensity factor range
ΔK_{rm}	root mean value of effective stress intensity factor range
m_b, m_a	hypotransitional and hypertransitional exponents of linear approximations to the fatigue crack growth curve
n	number of cycles or flights
p	packet size
P_{max}	maximum load
r_x, r_y, r_x^c, r_y^c	monotonic and cyclic plane strain plastic zone dimensions in x and y directions
R	stress ratio ($\sigma_{min}/\sigma_{max}$)
R_L, R_S	fracture surface roughness parameters
STA	solution treated and aged
$\sigma_{max}, \sigma_{min}$	maximum and minimum fatigue stresses
σ_y, σ_y^c	monotonic and cyclic yield stresses (0.2 % offset)
Ti-6Al-4V	titanium alloy containing nominally 6 weight % aluminium and 4 weight % vanadium
Ti-8Al-1Mo-1V	titanium alloy containing nominally 8 weight % aluminium, 1 weight % molybdenum and 1 weight % vanadium
TURBISTAN	TURBine loading STANdard
UTS	ultimate tensile strength

1 INTRODUCTION

As part of the NLR contribution to the AGARD engine disc cooperative test programme [1] the constant amplitude and flight simulation (TURBISTAN) fatigue crack growth properties of Ti-6Al-4V fan disc forgings were investigated using fractographic and microstructural analysis. This type of analysis is an essential background to selection and use of fatigue crack growth prediction methods and to interpretation of the prediction results.

2 MATERIALS, SPECIMENS AND TEST CONDITIONS

The materials were Ti-6Al-4V titanium alloy fan disc forgings supplied by Rolls-Royce for the AGARD programme. The forgings were in the conventional ($\alpha + \beta$) solution treated and aged condition. This STA heat treatment results in a duplex microstructure of primary α and platelet α in β.

An overview of the specimens and test conditions is given in table 1. Compact tension specimens conforming to ASTM Standard E399 were machined from disc rim locations by Rolls-Royce. All these specimens were oriented with the loading direction tangential and the crack growth direction radial. This is illustrated in figure 1, which also shows that the discs were textured. The texture was typically moderate, with hexagonal α {0002} planes parallel to the radial and axial directions of the discs [1].
Cylindrical axial fatigue test specimens, diameter 4.5 mm, were supplied by Rolls-Royce for the determination of monotonic and cyclic stress-strain curves. These specimens all came from disc bore locations.

3 MECHANICAL PROPERTIES

Average and minimum mechanical properties for disc rim locations, in the tangential direction, are given in table 2. This direction has been chosen because it corresponds with the loading axis of the compact tension fatigue crack growth specimens. The cyclic stress-strain curves for disc bore locations were determined by the multiple step strain method [3]. Results of the monotonic and cyclic tests are compared in figure 2. The cyclic yield stess was 93 % of the monotonic yield stress. This is in excellent agreement with the results of Borchert [4].

TABLE 1
Specimens and test conditions

SPECIMEN TYPE	DISC LOCATION	TEST CONDITIONS, TEST HOUSE, AND SPECIMEN CODE			
		FATIGUE CRACK GROWTH			MONOTONIC AND CYCLIC STRESS-STRAIN CURVES
		CONSTANT AMPLITUDE		TURBISTAN	
		R = 0.1	R = 0.7		
Compact tension	Rim	NLR:NLCT25	CEAT: CECT12	NLR: NLCT26 PISA: PICT18 PICT19	
Round bar	Bore				NLR

TABLE 2
Mechanical properties for disc rim locations, in the tangential direction [1, 2]

TYPES OF VALUES	0.2 % σ_y (MPa)	UTS (MPa)	ELONGATION (%)
Average	960	1046	12
Minimum	856	949	11

4 FATIGUE CRACK GROWTH

4.1 Constant Amplitude Tests

The constant amplitude fatigue crack growth tests were done in laboratory air at room temperature (293-295 K). There were two stress ratios. For R = 0.1 the stress waveform was trapezoidal with a nominal cycle frequency of 0.25 Hz. For R = 0.7 the stress waveform was triangular with a cycle frequency of 1.5 Hz [5]. Automated crack growth measurements were made using the DC potential drop technique. Full experimental details are given in reference [1].

Fatigue crack growth rates were calculated from incremental measurements of crack growth as follows:

$$da/dn = (a_{i+1}-a_i)/(n_{i+1}-n_i) \qquad (1)$$

and were correlated with ΔK values derived from the mean of the crack growth interval, i.e. $(a_{i+1}+a_i)/2$. The results are shown in figure 3. Similar results were obtained by other participants in the AGARD programme.

Figure 3 shows that the fatigue crack growth curves are approximately bilinear on a log-log plot, with transitions, ΔK_T, at 8.44 and 16.0 $MPa\sqrt{m}$. As will be shown, these transitions correlate with changes in fatigue fracture mechanisms and topography, and they occur when the cyclic plastic zone size becomes equal to characteristic microstructural dimensions [6-9].

Figure 4 shows the crack growth rate data plotted against ΔK_{eff}. The values of ΔK_{eff} were derived from the following formula:

$$\Delta K_{eff} = K_{max}-K_{op} = K_{max}\,(0.75-0.05R-1.13R^2+0.64R^3) \qquad (2)$$

which is an approximation derived from Newman's continuum mechanics crack opening model [10], assuming plane strain conditions. It is seen that the hypertransitional (upper) crack growth curves are well correlated by ΔK_{eff}, but the occurrence of transitions at widely different ΔK_T values and crack growth rates results in non-correlation by ΔK_{eff} in the hypotransitional regions.

4.2 TURBISTAN Tests

TURBISTAN is a spectrum load history for fighter aircraft engine discs [11]. The TURBISTAN sequence contains 15452 load reversals in a block of 100 different flights, whose average length is about 80 cycles [11]. A sample of TURBISTAN, comprising flights 66-69, is shown in figure 5. It is important to note that there are frequent load excursions from 0 to 100 % (once per flight) and less than 20 % to about 100 %. Owing to their frequent occurrence, these large load excursions may be expected to control the fatigue crack growth behaviour and to result in a more or less regular process of crack extension [12].

The TURBISTAN fatigue crack growth tests were done in laboratory air at room temperature (293-295 K). A constant loading rate was maintained, resulting in cycle frequencies ranging from 1 Hz for the largest load excursions to 20 Hz for the smallest load excursions. Automated crack growth measurements were made using the DC potential drop technique. The experimental details are given in references [1, 13].

Fatigue crack growth rates were calculated from incremental measurements of crack growth, see equation (1), and were correlated with K_{max} and ΔK_{rm} values derived for the mean of the crack growth interval specified in equation (1). The general expression for ΔK_{rm} is

$$\Delta K_{rm} = \sqrt[m]{\frac{\sum n_i (\Delta K_i)^m}{\sum n_i}} \qquad (3)$$

where n_i is the number of load excursions corresponding to ΔK_i; m is the slope of the constant amplitude log da/dn versus log ΔK_{eff} plot; and ΔK_i is obtained from $\Delta K_{eff,i} = K_{max,i} - K_{op,i}$.

Estimates of $\Delta K_{eff,1}$ were derived from equation (2), assuming no load interaction effects on K_{op}. This is a simplification, which in the first instance is defensible because most load excursions in TURBISTAN have similar high maxima, see figure 5.

Figure 6 shows the TURBISTAN crack growth rates plotted against K_{max}, together with bilinear approximations to the data below $K_{max} = 30\ MPa\sqrt{m}$. As in the case of the constant amplitude data, figure 3, these approximations indicate transitions in the crack growth curves. Figure 7 correlates the TURBISTAN and constant amplitude crack growth rate data with ΔK_{eff}, which for constant amplitude loading is ΔK_{eff}. An overall value of $n = 3$ has been used, which is clearly incorrect for the hypotransitional (n_1) parts of the TURBISTAN fatigue crack growth curves. However, the main point is that the hypertransitional (n_2) parts of the TURBISTAN and constant amplitude fatigue crack growth curves can be described by a single data envelope, which is linear on a log da/dn versus log ΔK_{eff} plot.

This collinearity is more clearly shown in figure 8, which fits so-called "Paris law" expressions to the TURBISTAN and constant amplitude hypertransitional fatigue crack growth rate data from the present investigation and reference [1]. These fits have obvious practical significance for prediction of fatigue crack growth. This is discussed later in this paper, in section 10.2.

5 MICROSTRUCTURAL ANALYSIS

The microstructures of all five compact tension fatigue crack growth specimens were examined on three orthogonal sections and quantified by semi-automated image analysis. Examples of the microstructures in the overall plane of fatigue crack growth are given in figure 9. These show considerable variation in the relative amounts and morphologies of primary α and transformed and aged β.

Table 3 lists values of the characteristic microstructural parameters. Most of these parameters are self-evident, but the degree of clustering, γ, requires explanation. The general expressions for the degree of clustering are

$$\text{grain size} \qquad \gamma = (d^{0.95} - \bar{d})^{-1} \tag{4}$$

$$\alpha \text{ packet size} \qquad \gamma = (p^{0.95} - \bar{p})^{-1} \tag{5}$$

where $d^{0.95}$, $p^{0.95}$, $\bar{d}$ and $\bar{p}$ are the 95th percentiles and averages of the grain and packet size distributions. Also, the most important parameters are plotted in figure 10.

The quantitative results confirm the wide variation in the relative amounts of primary α and transformed and aged β. On the other hand, the most consistent parameters are the average sizes of the primary α grains and platelet α packets.

6 FRACTOGRAPHIC ANALYSIS

In the first instance the fatigue fracture surfaces were examined by optical microscopy. Indications of "transitions" in the fracture surface appearances were seen, more or less corresponding to the crack growth rate transitions pointed out in figures 3 and 6. The fracture surface transitions proved very difficult to photograph. Figure 11 shows the clearest examples, which were for constant amplitude loading: in fact, only the transition on NLCT25 is really visible optically, and the transition on CECT12 is indicated by a dashed line derived mainly from scanning electron microscopy.

TABLE 3
Characteristic microstructural parameters for the compact tension specimens

MICROSTRUCTURAL PARAMETERS	CONSTANT AMPLITUDE		TURBISTAN		
	R = 0.1	R = 0.7			
	NLCT25	CECT12	NLCT26	PICT18	PICT19
• Primary α grains					
maximum diameter (μm)	17 ± 7	12 ± 5	12 ± 6	12 ± 5	12 ± 5
minimum diameter (μm)	10 ± 4	7 ± 3	6 ± 3	7 ± 3	7 ± 3
aspect ratio	1.9 ± 0.9	1.7 ± 0.04	2.1 ± 1.4	1.7 ± 0.5	1.8 ± 0.5
average diameter (μm)	13	10	9	9	10
degree of clustering about average diameter (μm^{-1})	0.117	0.093	0.071	0.092	0 079
volume %	42.5	26.9	46.4	29.5	24.7
• Transformed and aged β grains					
maximum diameter (μm)	23 ± 9	n.d.	19 ± 10	n.d.	41 ± 11
minimum diameter (μm)	14 ± 5	n.d.	10 ± 5	n.d.	23 ± 8
aspect ratio	1.8 ± 0.7	n.d.	2.2 ± 0.9	n.d.	1.9 ± 0.6
average diameter (μm)	18	n.d.	14	n.d.	32
degree of clustering about average diameter (μm^{-1})	0.103	n.d.	0.043	n.d.	0.040
volume %	57.5	73.1	53.6	70.5	75.3
• Platelet α packet size					
maximum diameter (μm)	18 ± 7	14 ± 7	13 ± 5	15 ± 9	16 ± 9
minimum diameter (μm)	11 ± 4	8 ± 5	7 ± 3	8 ± 5	9 ± 6
aspect ratio	1.7 ± 0.5	2.2 ± 2.2	2.0 ± 0.8	2.1 ± 1.1	2.1 ± 1.1
average diameter (μm)	14	11	10	12	12
degree of clustering about average diameter (μm^{-1})	0.093	0.059	0.075	0.050	0.050

Detailed fractographic analysis was done using scanning electron microscopy at an accelerating voltage of 12 kV. A comprehensive analysis was made of specimen NLCT25, as reported previously [14], and this analysis is presented in detail in section 6.1. The main features of this analysis were checked for the other specimens, which are discussed in section 6.2.

6.1 Specimen NLCT25 (Constant Amplitude, R = 0.1)

Particular attention was paid to the pre- and post-transition fractographic characteristics. A summary of the results is given in table 4.

Pre-transition fractographic characteristics

Representative views at intermediate magnification are given in figure 12. The fatigue fractures were microscopically very rough and consisted of

(1) Cyclic cleavage facets, both in primary α and transformed and aged β, figures 13 and 14.

(2) Specific features associated with cyclic cleavage facets, figure 15. These features have been termed pseudofluting [15] and furrows [16] or terraces [17]. Note that the furrowed terraces in figure 15b were already indicated in figure 12.

(3) A complex mixture of structure-sensitive fractures, figure 16, without resolvable fatigue striations. The highly geometrical nature of these fractures indicates that they result from cracking along slip bands and the intersections of slip bands. A typical area of complex structure-sensitive fracture is also indicated in figure 12.

Post-transition fractographic characteristics

Representative views of immediately post-transition fatigue fractures at intermediate magnification are given in figure 17. The fractures were microscopically less rough than before the transition, compare figures 12 and 17. Characteristic features of the immediately post-transition fatigue fracture were

(1) Cyclic cleavage facets, both in primary α and transformed and aged β, figures 18a-18d. Both types of cleavage were covered with microserrated ridges, unlike pre-transition α cleavage (see figure 13).

(2) Ill-defined pseudofluting and furrowed terraces, figures 18b, 18d.

(3) Smooth and irregular continuum-mode fractures, figures 18c, 18e, 18f.

(4) Fatigue striations always resolvable on smooth and irregular continuum-mode fractures, figures 19a-19c, and occasionally resolvable on cyclic cleavage facets, figure 19d. Striation spacings were larger than the macroscopically determined crack growth increments per cycle, as was also found in reference [1].

TABLE 4

Summary of fractographic observations for specimen NLCT25 (constant amplitude, R = 0.1)

CRACK GROWTH REGIME	ΔK (MPa√m)	FATIGUE FRACTURE CHARACTERISTICS	FIGURE NUMBERS
pre-transition	10-14	• cyclic cleavage - primary α: flat fracture with feathery markings - transformed and aged β: flat fracture with microserrated ridges, often accompanied by parallel slip lines (β-lines) [7] • features specifically associated with cyclic cleavage facets - pseudofluting [15] - furrowed terraces [16, 17] • geometrical fractures along slip bands and intersections of slip bands - blocky fracture - smooth fracture - fissured fracture	12,13 14 15 15 16 16 16
immediate post-transition	14-18	• cyclic cleavage - primary α: rough fracture with microserrated ridges - transformed and aged β: rough fracture with microserrated ridges, often accompanied by parallel slip lines • features specifically associated with cyclic cleavage facets - ill-defined pseudofluting - ill-defined furrowed terraces • continuum-mode fractures covered with fatigue striations - smooth continuum-mode fracture - irregular continuum-mode fracture • fatigue striations - always resolvable on continuum-mode fractures - occasionally resolvable on cyclic cleavage facets	17 18 18 18 18 18 18 19 19
post-transition	20	• rough cyclic cleavage with microserrated ridges and occasionally resolvable fatigue striations • continuum-mode fractures covered with fatigue striations	20 20
	30	• continuum-mode fractures covered with fatigue striations • isolated rough cyclic cleavage with microserrated ridges	21 21
	40	• continuum-mode fractures covered with fatigue striations • very occasional rough cyclic cleavage with microserrated ridges	22 22
	50	• continuum-mode fractures (fatigue striations) and microvoid coalescence	23

Representative and detailed views of post-transition fatigue fractures at ΔK values of 20, 30, 40 and 50 $MPa\sqrt{m}$ are given in figures 20-23. Up to $\Delta K = 40$ $MPa\sqrt{m}$ the main characteristics were continuum-mode fractures and isolated rough cyclic cleavage facets. At $\Delta K = 50$ $MPa\sqrt{m}$ the continuum-mode fatigue striations were interspersed with microvoid coalescence, figure 23: no cyclic cleavage facets were observed

6.2 Specimens CECT12, NLCT26, PICT18 and PICT19

General pre- and post-transition fractographic characteristics

Representative views at intermediate magnifications are given in figures 24-26. In general, the pre- and post-transition fractographic characteristics were the same as those of specimen NLCT25, see section 6.1. However, there was one notable exception. For specimen NLCT26 both the pre- and post-transition fracture surfaces showed occasional smooth continuum-mode fractures (SCF) with resolvable fatigue striations. These types of fracture are indicated in figure 25, and detailed views are given in figure 27.

TURBISTAN fatigue striation patterns

Figure 27 also shows the pattern of fatigue striations produced by TURBISTAN loading at low K_{max} values. The pattern is indistinguishable from that produced by constant amplitude loading, for example figures 19a and 21a. At higher stress intensities the TURBISTAN fatigue striation patterns became more complicated. Examples are given in figure 28. These show that the striations form block patterns, which are most probably demarcated by the large load excursions that occur at the beginning and end of each flight, see figure 5.

7 FRACTOGRAPHIC AND MICROSTRUCTURAL CORRELATIONS

Specimen NLCT25 (constant amplitude, $R = 0.1$) was precision sectioned normal to the fatigue crack growth direction at ΔK values of 10 and 18 $MPa\sqrt{m}$, i.e. before and after the transition in the fatigue crack growth rate curve, see figure 3. The fracture surfaces were protected by Technovit two-component resin (Kulzer GmbH, Friedrichsdorf, FRG) while the sections were polished and then etched in Kroll's reagent. The resin was subsequently dissolved away in acetone.

The precision sections enabled simultaneous viewing of the fracture surfaces and the underlying microstructural features, using scanning electron microscopy. Important examples of the relations between fractographic and microstructural features are shown in figures 29 and 30. Primary α cyclic cleavage facets are visible, and it is evident that irregular structure-sensitive and continuum-mode fractures are associated with the transformed and aged β grains, and hence the platelet α packets.

In view of the fractographic results, discussed in section 6, and the fractographic and microstructural correlations illustrated by figures 29 and 30, it may be concluded that the fatigue crack growth curve transitions observed for all specimens are primarily associated with a change from structure-sensitive to continuum-mode fractures, which in turn are mainly associated with the transformed and aged β grains. However, it must be noted that these associations are not rigorous, as mentioned in section 6.2, specimen NLCT26 showed occasional smooth continuum mode fractures both before and after the fatigue crack growth curve transition.

8 FRACTURE SURFACE ROUGHNESS

The NLCT25 precision section fracture profiles at ΔK values of 10 and 18 $MPa\sqrt{m}$ were examined by optical metallography at magnifications up to 800X. The linear roughness parameter R_L was used to characterize the fracture profiles. R_L is the ratio of the true length of profile to the projected length along a selected reference direction [18]. The linear roughness parameter occupies a central position in characterizing fracture profiles, and for three-dimensionally similar fracture topographies is simply related to the surface area roughness R_s according to [19]:

$$R_s = [4(R_L-1)/\pi] + 1. \tag{6}$$

Examples of the fracture profiles before and after the transition in the fatigue crack growth curve for specimen NLCT25 are given in figure 31. The pre-transition fracture surface roughness was significantly greater than the post-transition roughness.

9 ANALYSIS OF THE FATIGUE CRACK GROWTH CURVE TRANSITIONS

The fatigue crack growth curve transitions like those in figures 3 and 6 may be analysed in two respects [6-9]:

(1) Correlation of the crack tip plastic zone sizes with microstructural features (grain sizes and platelet α packet sizes).

(2) The relation between the sharpness of the transition, i.e. the change in slope of the fatigue crack growth curve, and the degree of clustering of the distribution of grain sizes and platelet α packet sizes about their mean values.

9.1 Crack Tip Plastic Zone Sizes

A proper description of crack tip plastic zone sizes and shapes is difficult to obtain. This is especially true for plane strain and cyclic loading conditions. Hahn et al. [20, 21] used an etching technique to reveal plane strain monotonic and cyclic plastic zones in the interiors of thick specimens of Fe-3Si steel. They proposed the following dimensions of the monotonic and cyclic plastic zones in the x and y directions:

monotonic plane strain
$$\begin{cases} r_x = 0.03 \quad (K_{max}/\sigma_y)^2 & (7) \\ r_y = 0.13 \quad (K_{max}/\sigma_y)^2 & (8) \end{cases}$$

cyclic plane strain, $R = 0.1$
$$\begin{cases} r_x^c = 0.0075 \quad (\Delta K/\sigma_y^c)^2 & (9) \\ r_y^c = 0.033 \quad (\Delta K/\sigma_y^c)^2 & (10) \end{cases}$$

where σ_y^c is the cyclic yield stress.

Newman's continuum mechanics crack opening model [10], specifically the formula in equation (2), enables substituting ΔK_{eff} for ΔK in equations (9) and (10). The results are

cyclic plane strain
$$\begin{cases} r_x^c = 0.011 \, (\Delta K_{eff}/\sigma_y^c)^2 & (11) \\ r_y^c = 0.050 \, (\Delta K_{eff}/\sigma_y^c)^2 & (12) \end{cases}$$

Relations for r_y and r_y^c are particularly important because they determine the maximum extent of the plastic zones. This is illustrated in figure 32, which gives schematic drawings of the plane strain

monotonic and cyclic plastic zone sizes, with r_x, r_y, r_x^c and r_y^c determined by equations (7) - (12) and the assumption that $\sigma_y^c = 0.93\ \sigma_y$, see section 3.

9.2 Correlation of Plastic Zone Sizes with Microstructural Parameters

Monotonic and cyclic plane strain plastic zone dimensions at the fatigue crack growth curve transitions shown in figures 3 and 6 were calculated using equations (7), (8), (11) and (12). For TURBISTAN loading two values of ΔK_{eff} were selected: ΔK_{rm}, representing an average for the entire spectrum, and ΔK_{eff} for the once-per-flight maximum load excursion with R = 0. The results are listed in tables 5 and 6, and compared with the primary α grain sizes and platelet α packet sizes in figure 33.

Figure 33 shows that at the fatigue crack growth transitions the values of r_x and r_y^c correlate best with the primary α grain sizes and platelet α packet sizes: note, however, that for TURBISTAN loading the correlation of r_y^c with these microstructural parameters is good only when the ΔK_{eff} values for the maximum load excursion are substituted into equation (12). In view of previous work [6-9] it is most likely that r_y^c, the maximum extent of the plane strain cyclic plastic zone, is the fracture mechanics parameter of most significance for the crack growth curve transitions. But the similarity of primary α grain sizes and platelet α packet sizes does not permit direct determination of which microstructural parameter is important for the transitions.

From the fractographic results in section 6 it appears that the change from a complex mixture of structure-sensitive fractures to continuum-mode fractures is the most significant feature of material behaviour associated with the fatigue crack growth curve transitions. In turn, the fractographic and microstructural correlations in section 7 showed that these types of fractures were primarily associated with the transformed and aged β, and hence the platelet α packets.

It is therefore concluded, especially in view of previous work [6, 7, 22], that the fatigue crack growth curve transitions most probably occurred as a consequence of the maximum plane strain cyclic plastic zone sizes, r_y^c, becoming equal to and exceeding the platelet α packet sizes.

9.3 Sharpness of the Crack Growth Curve Transitions

The sharpness of the fatigue crack growth curve transitions may be quantified by the ratios of the hypotransitional exponents to hypertransitional exponents, m_b/m_a, of the linear approximations to the fatigue crack growth curves shown in figures 3 and 6. Yoder et al. [22] related the transition sharpness for β annealed titanium alloys to the degree of clustering of the distribution of platelet α packet sizes about their mean values, see equation (5).The m_b/m_a values for Yoder's and

TABLE 5
Estimates of plane strain monotonic plastic zone sizes at fatigue crack growth curve transitions

FATIGUE LOAD HISTORY		SPECIMEN NUMBER	K_{max_T} (MPa$\sqrt{m}$)	0.2 % σ_y (MPa)	r_x (μm)	r_y (μm)
Constant Amplitude	R = 0.1	NLCT25	17.8	Average: 960 Minimum: 856	10.3 12.9	44.6 56.1
	R = 0.7	CECT12	28.1	Average: 960 Minimum: 856	25.8 32.4	112 140
TURBISTAN		NLCT26	14.2	Average: 960 Minimum: 856	6.56 8.26	28.4 35.8
		PICT18 PICT19	16.0	Average: 960 Minimum: 856	8.33 10.5	36.1 45.4

TABLE 6
Estimates of plane strain cyclic plastic zone sizes at fatigue crack growth curve transitions

FATIGUE LOAD HISTORY		SPECIMEN NUMBER	CHARACTERISTIC ΔK (MPa$\sqrt{m}$)	$\sigma_y^c = 0.093\ \sigma_y$ (MPa)	r_x^c (μm)	r_y^c (μm)
Constant Amplitude	R = 0.1	NLCT25	ΔK_{eff_T}: 13.0	Average: 893 Minimum: 796	2.34 2.95	10.6 13.4
	R = 0.7	CECT12	ΔK_{eff_T}: 5.44	Average: 893 Minimum: 796	0.98 1.24	4.47 5.62
TURBISTAN		NLCT26	ΔK_{rm_T}: 3.99	Average: 893 Minimum: 796	0.22 0.28	1.00 1.26
			ΔK_{eff_T} (R=0): 10.7	Average: 893 Minimum: 796	1.58 1.99	7.18 9.03
		PICT18 PICT19	ΔK_{rm_T}: 4.50	Average: 893 Minimum: 796	0.28 0.35	1.27 1.60
			ΔK_{eff_T} (R=0): 12.0	Average: 893 Minimum: 796	1.99 2.50	9.03 11.4

our materials are plotted against the degrees of clustering, γ, in the upper diagram of figure 34. Values of m_a versus γ are plotted in the lower diagram. The results show the following:

(1) Although Yoder's results indicate an increase in transition sharpness, m_b/m_a, with the degree of clustering of the platelet α packet size, there is no consistent trend from the present investigation.

(2) Hypertransitional exponents, m_a, decrease to a value of about 3 with increased degree of clustering of the platelet α packet size. Yoder et al. [22] attributed this effect to remnants of structure-sensitive fractures in the nominally continuum-mode hypertransitional region. the significance of such remnants would decrease with increased degree of clustering because there would be fewer platelet α packets larger than the current plastic zone size.

The lack of a correlation between transition sharpness, m_b/m_a, and the degree of clustering of the platelet α packet size for the Ti-6Al-4V fan disc forgings is most probably a consequence of microstructure. The materials tested by Yoder et al. [22] consisted entirely of transformed and aged β and hence platelet α packets, while the Ti-6Al-4V STA materials from the present investigation contained significant amounts of primary α that also contributed to the fatigue crack growth process.

10 DISCUSSION

10.1 Fatigue Crack Growth Curve Transitions

The present results have shown that the fatigue crack growth process in conventionally $(\alpha+\beta)$ solution treated and aged Ti-6Al-4V fan disc forging materials is highly complex, especially in the hypotransitional region of the fatigue crack growth curve. Previous investigators [23, 24] did not fully recognise this, nor did they notice fatigue crack growth curve transitions that correlated with changes in the fracture process. However, the transitions can be observed in figures 3-5 from both investigations. Also, it is worth noting that fatigue crack growth curve transitions generally occur. They have been reported for aluminium alloys [25-27], high strength steels [28] and an iron-base superalloy [29]

An overview of the hypotransitional and hypertransitional fatigue crack growth characteristics of the Ti-6Al-4V STA fan disc forging materials is given in figure 35. This overview is useful for discussing the fatigue crack growth curve transitions. The transitions evidently result in changes in crack growth rate dependence on the characterizing stress intensity factor (ΔK, K_{max}, ΔK_{eff}, ΔK_{rm}), and these changes are quantified by the exponents m_b and m_a of linear approximations to the fatigue crack growth curves. On a more fundamental level, these changes must involve changes in fatigue crack driving force and fatigue crack growth resistance.

Several factors may contribute to the fatigue crack driving force and fatigue crack growth resistance.

(1) *Crack driving force* is provided by the effective ΔK. Structure-sensitive crack paths that are the result of inhomogeneous plastic deformation result in crack deflection, crack branching, and roughness-induced enhanced crack closure, all of which reduce the effective ΔK [6, 7, 9, 30-32). Microstructural barriers such as dislocation substructures and grain boundaries, and also crystallographic texture, play an indirect role by affecting the homogeneity of plastic deformation. Finally, crystallographic texture directly affects the actual crack driving force, G, through its effect on the elastic modulus: a higher elastic modulus decreases G.

(2) *Crack growth resistance* is, in the first instance, provided by a material's intrinsic resistance to dislocation motion (lattice friction stress and microstructural barriers) and the efficiency with which crack tip plasticity, i.e. dislocation movement, is converted into crack extension. Crack tip plasticity in structure-sensitive fractures tends to be highly directional and more concentrated at the actual crack tip [33]. This means on the one hand that slip should be used more effectively for crack extension than crack tip plasticity in continuum-mode fractures, and on the other hand that slip reversibility may be more efficient [29]. Crystallographic texture plays an indirect role by affecting the homogeneity of plastic deformation and hence the crack growth resistance.

Besides these *intrinsic* factors, many of which are interrelated and can influence both the crack driving force and crack growth resistance, an important *extrinsic* factor is the fatigue environment. Aggressive environments can greatly reduce the fatigue crack growth resistance. For titanium alloys the crack growth resistance can be reduced in at least two ways. Firstly, an aggressive environment promotes cyclic cleavage [16, 34, 35]. This has an accelerating effect on fatigue crack growth, especially in highly textured materials where {0002} are in the macroscopic plane of fracture, since the cyclic cleavage occurs on or near the hexagonal α {0002} planes [16, 35-38]. Secondly, environmental interaction with emergent slip steps can reduce slip reversibility during structure-sensitive fatigue fracture [39]. Note also that the fatigue environment can indirectly affect the crack driving force by inducing changes in crack tip plasticity, crack deflection, crack branching, and roughness-induced crack closure.

From figure 35 it may be deduced that apart from texture and environmental changes, the fatigue crack growth curve transitions for the Ti-6Al-4V STA fan disc forging materials in the present investigation involved most - if not all - of the foregoing factors. This is also the case for transitions in other materials, e.g. [27]. Thus in general the shape of a fatigue crack growth curve transition and the values of m_b and m_a will depend on a balance of several competing and reinforcing factors. This is illustrated schematically in figure 36, which also shows that for titanium alloys there are at least three types of fatigue crack growth curve transition involving changes from structure-sensitive to continuum-mode crack growth, and that a change of environment can reverse the transition inflection.

10.2 Fatigue Crack Growth Prediction

Figures 7 and 8 show that it is possible to correlate the hypertransitional constant amplitude and TURBISTAN fatigue crack growth rate data using ΔK_{rm}, the root mean value of the effective stress intensity factor range. The incentives for attempting such correlations are the efficient estimation of spectrum loading fatigue crack growth lives using constant amplitude data banks and the

possibility of simply accounting for spectrum variations by recalculating ΔK_{rm}.

A necessary, but not sufficient, condition for such *characteristic-K* correlations is that fatigue crack growth be a regular, quasi-stationary process [12, 42]. This is typically the case when the fatigue load history contains peak loads with short recurrence periods, as does TURBISTAN. However, as can be seen from figures 7 and 8, the correlations fail in the hypotransitional fatigue crack growth regime. There are two reasons for this:

(1) Variations in alloy microstructure influence the locations of the fatigue crack growth curve transitions, which most probably depend on r_y^c becoming equal to and exceeding the platelet α packet sizes.

(2) For spectrum loading like TURBISTAN, which contains frequent (once per flight) maximum load excursions, the value of r_y^c which controls the fatigue crack growth curve transition is the maximum value, and not the root mean value. Thus a correlation of fatigue crack growth rates by ΔK_{rm} will always fail if there is a crack growth curve transition. This has already been *predicted* for simple spectrum loading of landing gear steels [43]. Supporting evidence that the maximum value of r_y^c controls the fatigue crack growth curve transitions is provided by the TURBISTAN fatigue striation patterns. Close to the transitions the striation pattern is indistinguishable from that produced by constant amplitude loading, see figure 27 and section 6.2. This means that fatigue crack growth in the transitional region is controlled by the maximum load excursions.

Despite the inability of the characteristic-K (ΔK_{rm}) approach to account for fatigue crack growth curve transitions, figure 8 shows that "Paris law" expressions based on the hypertransitional data provide a best fit and upper bound that are reasonably conservative for TURBISTAN loading. Hence these expressions can be used to predict fatigue crack growth - *for "long" cracks* - even if the transition point is unknown. Such predictions may be deterministic or probabilistic. The advantage of the more difficult probabilistic approach is that it avoids excessive conservatism [44, 45].

A more serious problem for fatigue crack growth prediction is the behaviour of "short" cracks. As pointed out by Koul et al. [45], short crack behaviour differs considerably from that of long cracks, and the prediction of fatigue crack growth lives based only on long crack data can be unconservative [46]. This problem can be solved only by experiments to obtain short fatigue crack growth data and the development of analytical modelling techniques for short cracks. One of us (RJHW) has recently shown that short fatigue crack growth should be modelled probabilistically to avoid excessive conservatism [47].

10.3 Service Failure Analysis

It may be anticipated that structure-sensitive to continuum-mode fracture transitions will occur in Ti-6Al-4V STA discs that experience fatigue cracking in service. This is because the service load histories will likely resemble TURBISTAN in that they will include many maximum load excursions with short (once per flight) recurrence periods. If the transitions are readily definable on service fatigue fractures, they could act as benchmarks for checking the analysis of local stress and stress intensity conditions and fatigue crack growth rates, thereby assisting in the overall analysis of service problems. However, this requires detailed microstructural analysis as well as fractographic analysis, and there is obviously room for uncertainty in determining the transition point ΔK_{eff} for the maximum load excursion from the assumed equivalence of the platelet α packet size and the maximum plane strain cyclic plastic zone size.

11 CONCLUSIONS

Fractographic and microstructural analysis of constant amplitude and flight simulation (TURBISTAN) fatigue crack growth in conventionally (α+β) solution treated and aged Ti-6Al-4V fan disc forging materials showed that:

(1) The fatigue crack growth process was highly complex with many interrelated fracture features.

(2) Transitions in the fatigue crack growth rate curves correlated with changes in the fatigue fracture process: specifically, a change from structure-sensitive to continuum-mode crack growth and a reduction in the roughness of the overall fracture topography.

(3) The change from structure-sensitive to continuum-mode fatigue crack growth was primarily associated with the transformed and aged β grains, and hence the platelet α packets.

(4) Close to the fatigue crack growth transitions the TURBISTAN fatigue striation patterns were indistinguishable from that of constant amplitude loading. At higher stress intensities the TURBISTAN fatigue striations formed block patterns, which were most probably demarcated by the large load excursions that occurred at the beginning and end of each flight.

(5) The hypertransitional fatigue crack growth rates were correlated by ΔK_{rm}, the root mean value of the effective stress intensity factor range. However, the correlations failed in the hypotransitional fatigue crack growth regime.

(6) The fatigue crack growth curve transitions most probably occurred as a consequence of the maximum plane strain cyclic plastic zone sizes, r_y^c, becoming equal to and exceeding the platelet α packet sizes.

(7) The overall shapes of fatigue crack growth curve transitions depend on several competing and reinforcing factors that contribute to the fatigue crack driving force and fatigue crack growth resistance.

(8) "Paris law" expressions based on the hypertransitional fatigue crack growth rate data correlated by ΔK_{rm} provide a best fit and upper bound that are reasonably conservative for predicting long fatigue crack growth under realistic (TURBISTAN) load histories.

(9) Structure-sensitive to continuum-mode fracture transitions may be definable on the fracture surfaces of Ti-6Al-4V discs that experience fatigue cracking in service. These transitions could assist in the overall analysis of such service problems.

12 REFERENCES

1. A.J.A. Mom and M.D. Raizenne, "AGARD engine disc cooperative test programme", AGARD Report No. 766, Advisory Group for Aerospace Research and Development, Neuilly sur Seine, France (August 1988).

2. L. Grabowski, Personal Communication, Rolls-Royce plc, Derby, England.

3. R.W. Landgraf, JoDean Morrow and T. Endo, "Determination of the cyclic stress-strain curve", Journal of Materials, Vol. 4, pp. 176-188 (1969).

4. B. Borchert, "Low cycle fatigue and service life of engine rotor discs", High Temperature Alloys for Gas Turbines, Applied Science Publishers Ltd., pp. 573-598 (1978): London.

5. E. Jany, Personal Communication, CEAT, Toulouse, France.

6. G.R. Yoder, L.A. Cooley and T.W. Crooker, "Fatigue crack propagation resistance of beta-annealed Ti-6Al-4V alloys of differing interstitial oxygen contents", Metallurgical Transitions A, Vol. 9A, pp. 1413-1420 (1978).

7. G.R. Yoder, L.A. Cooley and T.W. Crooker, "Observations on microstructurally sensitive fatigue crack growth in a Widmanstätten Ti-6Al-4V alloy", Metallurgical Transactions A, Vol. 8A, pp. 1737-1743 (1977).

8. G.R. Yoder, L.A. Cooley and T.W. Crooker, "50-fold difference in Region-II fatigue crack propagation resistance of titanium alloys: a grain-size effect", Journal of Engineering Materials and Technology, Vol. 101, pp.. 86-90 (1979).

9. G.R. Yoder, L.A. Cooley and T.W. Crooker, "Observations on the generality of the grain-size effect on fatigue crack growth in $\alpha + \beta$ titanium alloys", Titanium '80 Science and Technology, The Metallurgical Society of AIME, pp. 1865-1873 (1980): Warrendale, Pennsylvania.

10. J.C. Newman, Jr., "A crack-closure model for predicting fatigue crack growth under aircraft spectrum loading", Methods and Models for Predicting Fatigue Crack Growth Under Random Loading, ASTM STP 748, American Society for Testing and Materials, pp. 53-84 (1981): Philadelphia, Pennsylvania

11. A.J.A. Mom, W.J. Evans and A.A. ten Have, "TURBISTAN, a standard load sequence for aircraft engine discs", AGARD Conference Proceedings No. 393, Damage Tolerance Concepts for Critical Engine Components, Advisory Group for Aerospace Research and Development, pp. 20-1–20-11 (1985): Neuilly sur Seine, France.

12. H.L. Ewalds and R.J.H. Wanhill, Fracture Mechanics, Edward Arnold and Delftse Uitgevers Maatschappij, Third Imprint, p. 155 (1986), London and Delft.

13. M.D. Raizenne, "AGARD TX114 test procedures for supplemental engine disc test programme", Laboratory Technical Report LTR ST-1671, National Aeronautical Establishment, Ottawa, Canada (June 1988).

14. R.J.H. Wanhill, R. Galatolo and C.E.W. Looije, "Fractographic and microstructural analysis of fatigue crack growth in a Ti-6Al-4V fan disc forging", International Journal of Fatigue, Vol. 11, pp. 407-416 (1989).

15. D.A. Meyn and E.J. Brooks, "Microstructural origin of flutes and their use in distinguishing striationless fatigue cleavage from stress-corrosion cracking in titanium alloys", Fractography and Materials Science, ASTM STP 733, American Society for Testing and Materials, pp. 5-31 (1981), Philadelphia, Pennsylvania.

16. C.M. Ward-Close and C.J. Beevers, "The influence of grain orientation on the mode and rate of fatigue crack growth in α-titanium", Metallurgical Transactions A, Vol. 11A, pp 1007-1017 (1980).

17. J.C. Chesnutt and J.C. Williams, "Comments on the electron fractography of α-titanium", Metallurgical Transactions A, Vol. 8A, pp. 514-515 (1977).

18. E.E. Underwood, "Practical solutions to stereological problems", Practical Applications of Quantitative Metallography, ASTM STP 839, American Society for Testing and Materials, pp. 160-179 (1984): Philadelphia, Pennsylvania.

19. E.E. Underwood and K. Banerji, "Fractals in fractography", Materials Science and Engineering, Vol. 80, pp. 1-14 (1986).

20. G.T. Hahn, M. Sarrate and A.R Rosenfield, "Plastic zones in Fe-3Si steel double-cantilever-beam specimens", International Journal of Fracture Mechanics, Vol. 7, pp. 435-446 (1971).

21. G.T. Hahn, R.G. Hoagland and A.R. Rosenfield, "Local yielding attending fatigue crack growth", Metallurgical Transactions, Vol.3, pp. 1189-1202 (1972).

22. G.R. Yoder, L.A. Cooley and T.W. Crooker, "Quantitative analysis of microstructural effects on fatigue crack growth in Widmanstätten Ti-6Al-4V and Ti-8Al-1Mo-1V" Engineering Fracture Mechanics, Vol. 11, pp 805-816 (1979).

23. A. Yuen, S.W. Hopkins, G.R. Leverant and C.A. Rau, "Correlations between fracture surface appearance and fracture mechanics parameters for Stage II fatigue crack propagation in Ti-6Al-4V", Metallurgical Transactions, Vol 5, pp. 1833-1842 (1974).

24. B.E. Powell and T.V. Duggan, "Crack growth in Ti-6Al-4V under conjoint action of high and low cycle fatigue", International Journal of Fatigue, Vol. 9, pp. 195-202 (1987).

25. G.R. Yoder, L.A. Cooley and T.W. Crooker, "On microstructural control of near-threshold fatigue crack growth in 7000-series aluminium alloys", Scripta Metallurgica, Vol. 16, pp. 1021-1025 (1982).

26. R.J. Stofanak, R.W. Hertzberg, J. Leupp and R. Jaccard, "On the cyclic behaviour of cast and extruded aluminium alloys. Part B: fractography", Engineering Fracture Mechanics, Vol. 17, pp 541-554 (1983).

27. R.J.H. Wanhill, "Low stress intensity fatigue crack growth in 2024-T3 and T351", Engineering Fracture Mechanics, Vol. 30, pp. 233-260 (1988).

28. G.R. Yoder, L.A. Cooley and T.W. Crooker, "A critical analysis of grain-size and yield-strength dependence of near-threshold fatigue-crack growth in steels", NRL Memorandum Report 4576, Naval Research Laboratory, Washington, DC (July 1981).

29. E. Hornbogen and K.H. Zum Gahr, "Microstructure and fatigue crack growth in a γ-Fe-Ni-Al alloy", Acta Metallurgica, Vol. 24, pp. 581-592 (1976).

30. S. Suresh and R.O. Ritchie, "A geometrical model for fatigue crack closure induced by fracture surface morphology", Metallurgical Transactions A, Vol. 13A, pp. 1627-1631 (1982).

31. S. Suresh, "Crack deflection: implications for the growth of long and short fatigue cracks", Metallurgical Transactions A, Vol. 14A, pp. 2375-2385 (1983).

32. S. Suresh, "Fatigue crack deflection and fracture surface contact: micromechanical models", Metallurgical Transactions A, Vol. 16A, pp. 249-259 (1985).

33. D.L. Davidson and J. Lankford, "The breakdown of crack tip microstructure during fatigue crack extension in aluminium alloys", High Strength Powder Metallurgy Aluminium Alloys II, The Metallurgical Society of AIME, pp. 47-59 (1986): Warrendale, Pennsylvania.

34. R.J.H. Wanhill, "A fractographic analysis of environmental fatigue crack propagation in Ti-6Al-4V sheet", Corrosion, Vol. 32, pp. 163-172 (1976).

35. R.J.H. Wanhill, "Environmental fatigue crack propagation in Ti-6Al-4V sheet", Metallurgical Transactions A, Vol. 7A, pp. 1365-1373 (1976).

36. R.J.H. Wanhill, "The influence of texture on environmental fatigue crack propagation in titanium alloys", Textures of Materials, The Metals Society, pp. 529-537 (1978): London.

37. D.A. Meyn, "An analysis of frequency and amplitude effects on corrosion fatigue crack propagation in Ti-8Al-1Mo-1V", Metallurgical Transactions, Vol. 2, pp. 853-865 (1971).

38. R.J.H. Wanhill and H. Döker, "Vacuum fatigue fracture in titanium alloy plate", TMS-AIME 107th Annual Meeting, February/March 1978, Denver. Also NLR Miscellaneous Publication 78002 U, National Aerospace Laboratory NLR, Amsterdam (December 1977).

39. C. Fong and D. Tromans, "Stage I corrosion fatigue crack crystallography in austenitic stainless steel (316L)", Metallurgical Transactions A, Vol. 19A, pp. 2765-2773 (1988).

40. R.J.H. Wanhill, "Environmental effects on fatigue of aluminium and titanium alloys", AGARD Report No. 659, Corrosion Fatigue of Aircraft Materials, Advisory Group for Aerospace Research and Development, pp. 2-1–2-37 (1977): Neuilly sur Seine, France.

41. G.R. Yoder, F.H. Froes and D. Eylon, "Effect of microstructure, strength, and oxygen content on fatigue crack growth rate of Ti-4.5Al-5.0Mo-1.5Cr (CORONA 5)", Metallurgical Transitions A, Vol. 15A, pp. 183-197 (1984).

42. R.J.H. Wanhill, "Engineering application of fracture mechanics to flight simulation fatigue crack propagation", Fracture Mechanics in Engineering Application, Sijthoff and Noordhoff International Publishers, pp. 241-250 (1979): Alphen aan den Rijn, The Netherlands.

43. R.J.H. Wanhill, "Fatigue fracture in landing gear steels", ICAS Proceedings 1986, 15th Congress of the International Council of the Aeronautical Sciences, American Institute of Aeronautics and Astronautics, Vol. 2, pp. 1347-1355 (1986): New York.

44. A.K. Koul, N.C. Bellinger and A. Fahr, "Damage-tolerance-based life prediction of aeroengine compressor discs: I. A deterministic fracture mechanics approach", International Journal of Fatigue, Vol. 12, pp. 379-387 (1990).

45. A.K. Koul, N.C. Bellinger and G. Gould, "Damage-tolerance-based life prediction of aeroengine compressor discs: II. A probabilistic fracture mechanics approach", International Journal of Fatigue, Vol. 12, pp. 388-396 (1990).

46. J. Lankford and S.J. Hudak, Jr., "Relevance of the small crack problem to lifetime prediction in gas turbines", International Journal of Fatigue, Vol. 9, pp. 87-93 (1987).

47. R.J.H. Wanhill, "Durability analysis using short and long fatigue crack growth data", Paper presented at the International Conference on Aircraft Damage Assessment and Repair, Melbourne, Australia, August 1991. Also NLR Technical Publication TP 91120 L, National Aerospace Laboratory NLR, Amsterdam (March 1991).

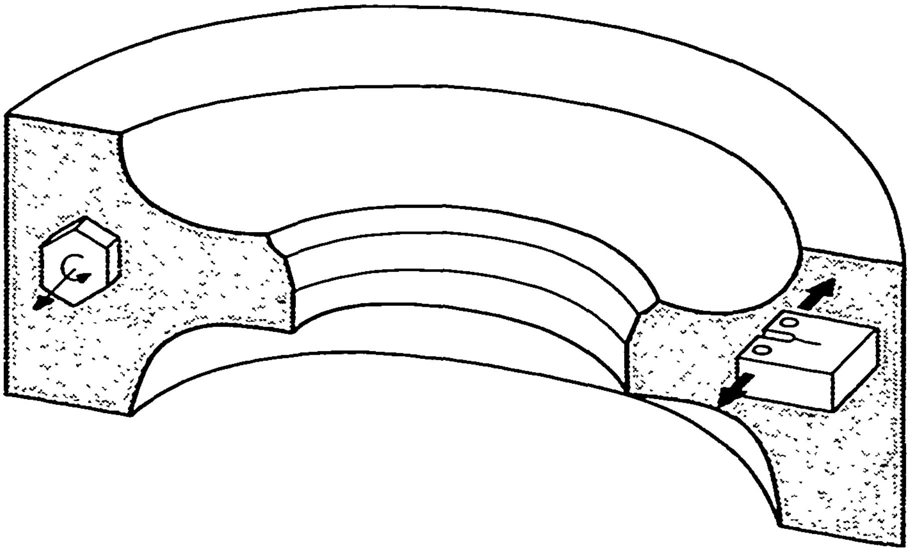

Fig. 1 Compact tension specimen orientation in the fan disc forgings and the hexagonal α {0002} texture [1]

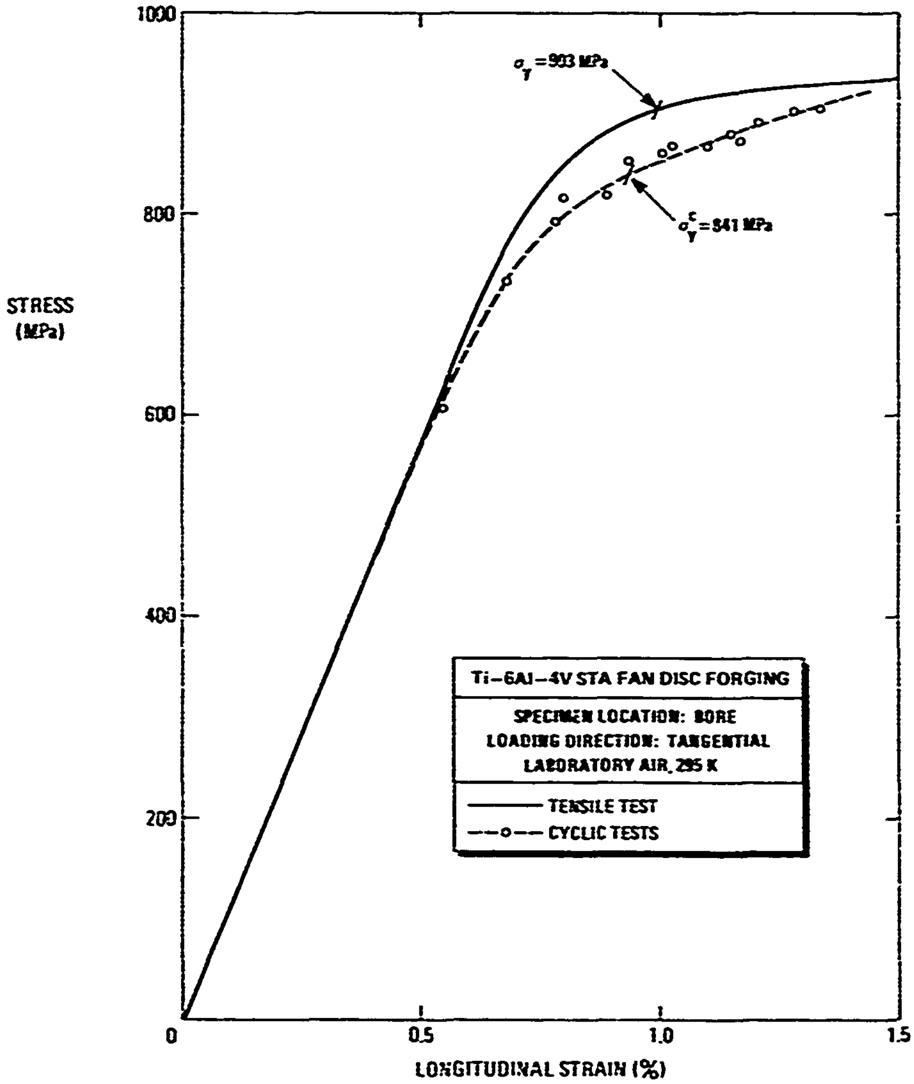

Fig. 2 Comparison of monotonic and cyclic stress-strain curves

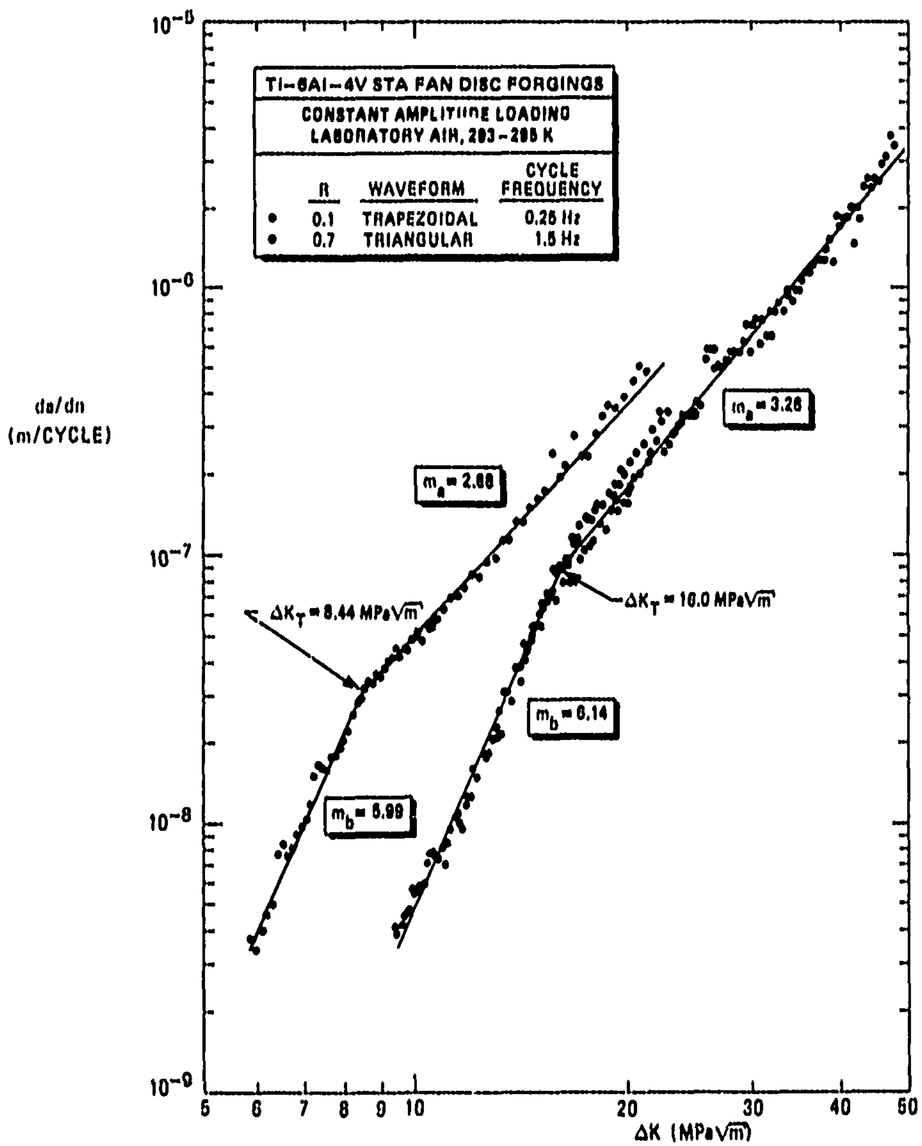

Fig. 3 Constant amplitude fatigue crack growth rate data: m_a and m_b are the exponents of bilinear approximations to the data

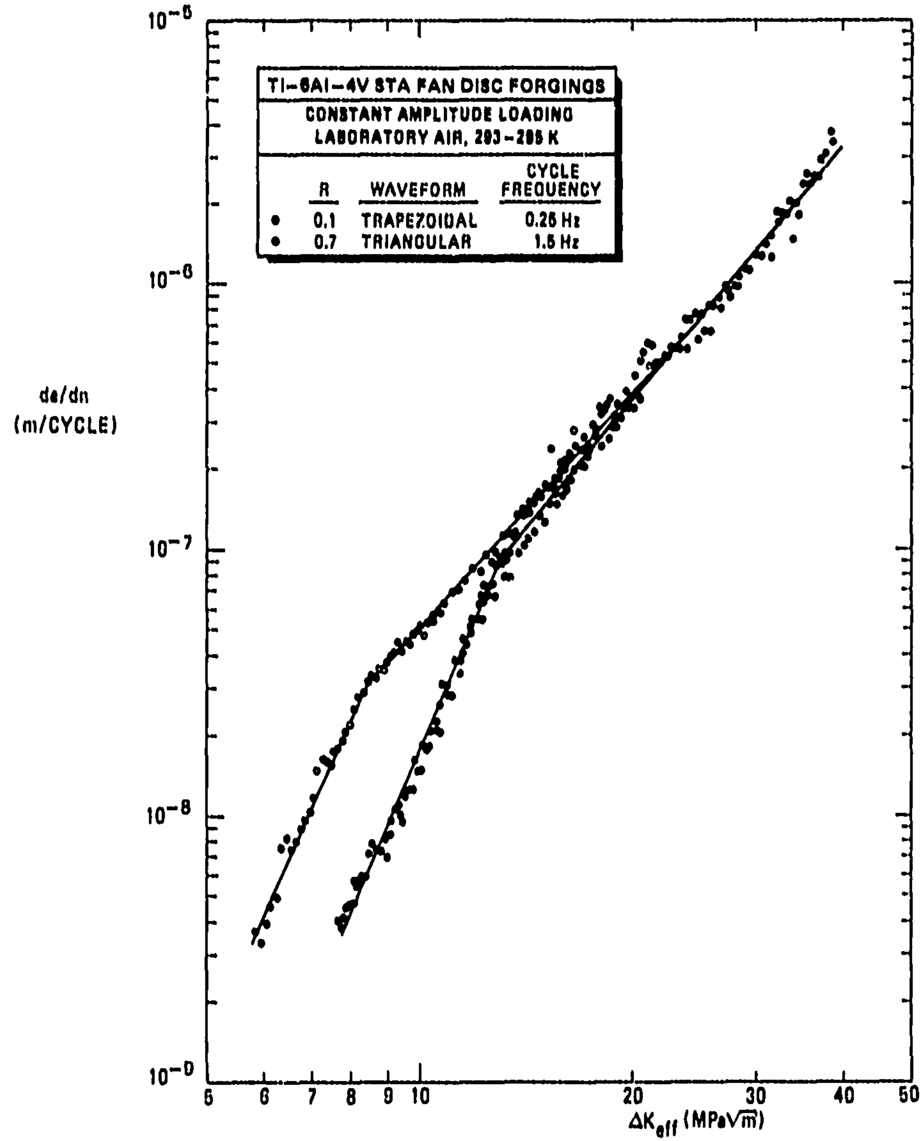

Fig. 4 Constant amplitude fatigue crack growth rate data versus ΔK_{eff}

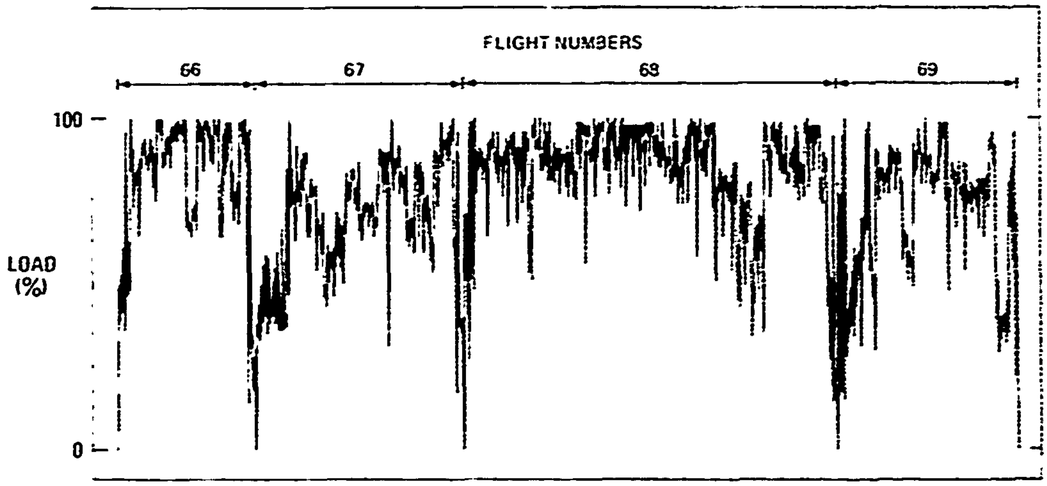

Fig. 5 Sample of TURBISTAN, flights 66 - 69

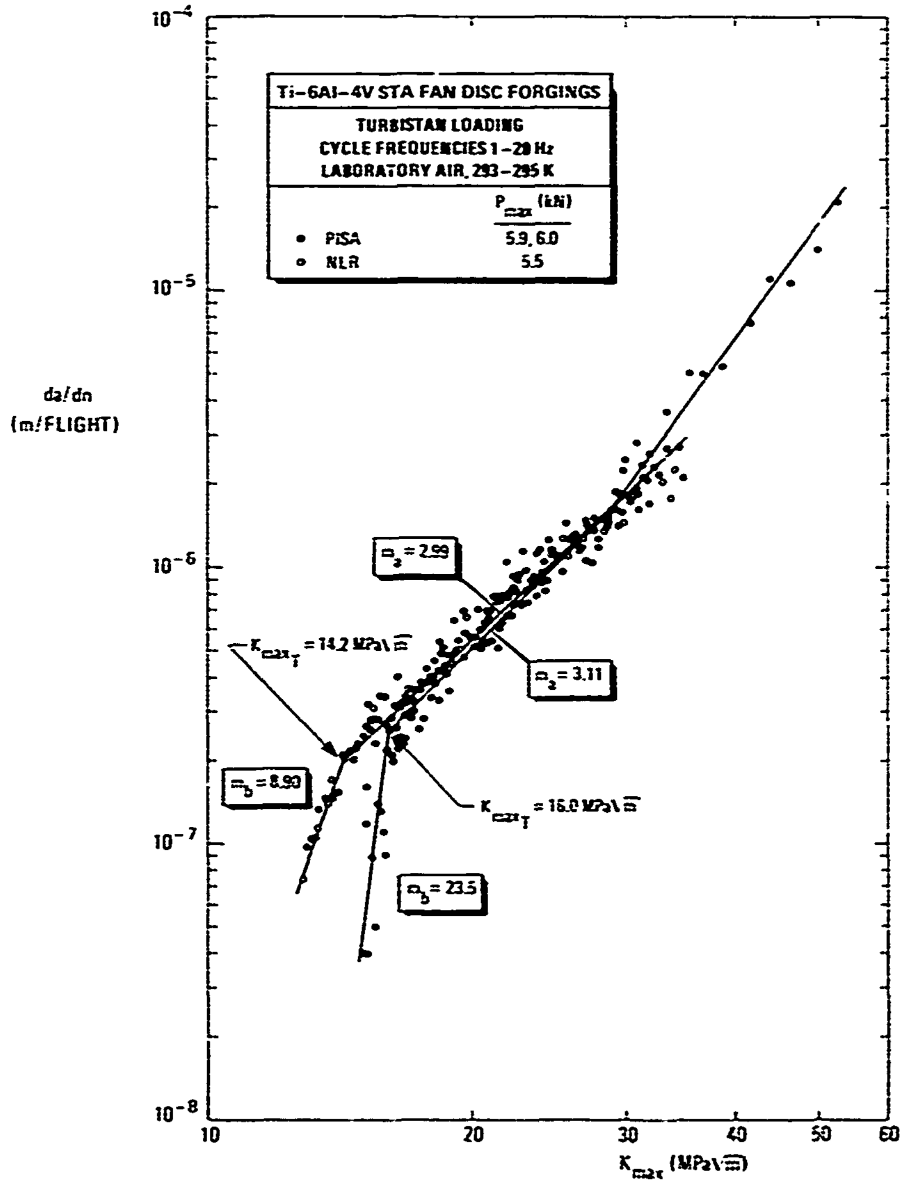

Fig. 6 TURBISTAN fatigue crack growth rate data. m_a and m_b are the exponents of linear approximations to the data below K_{max} = 30 MPa$\sqrt{m}$

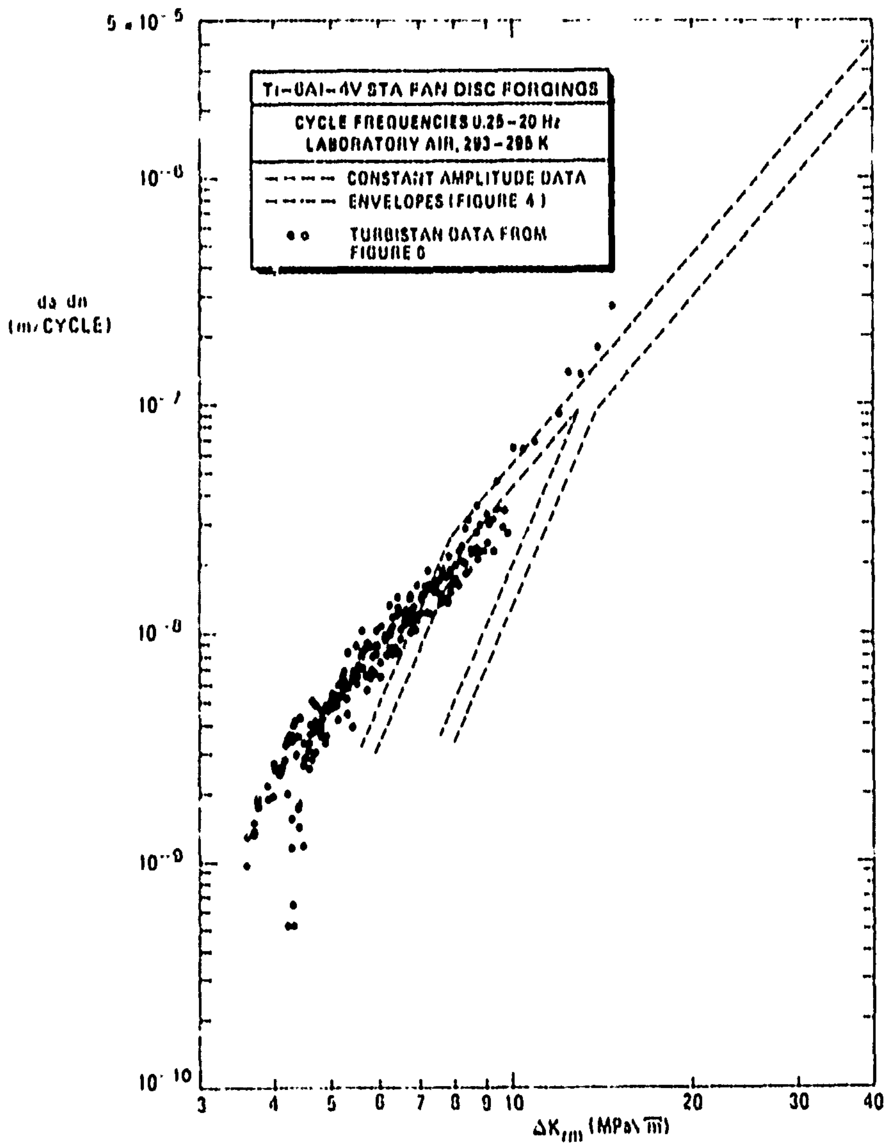

Fig. 7 Constant amplitude and TURBISTAN fatigue crack growth rate data versus ΔK_{rm}

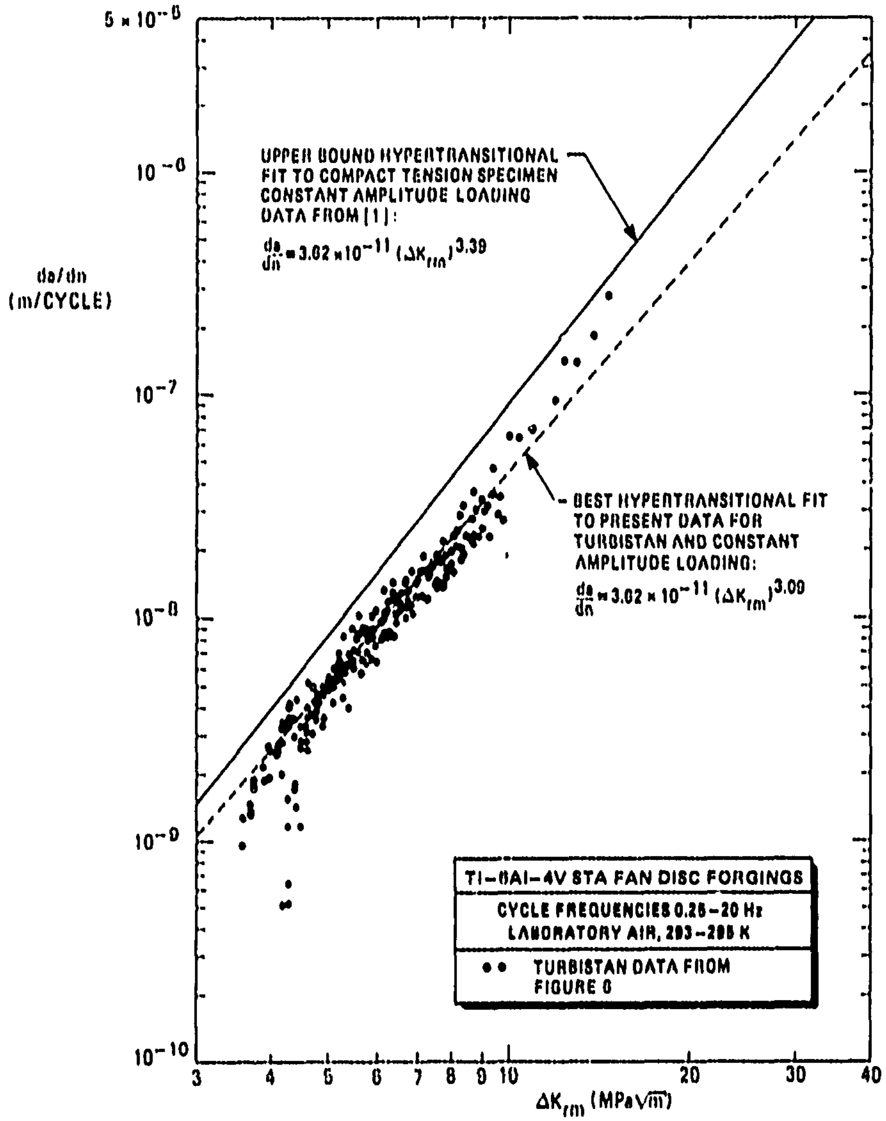

Fig. 8 "Paris law" fits to constant amplitude and TURBISTAN fatigue crack growth rate data versus ΔK_{rm}

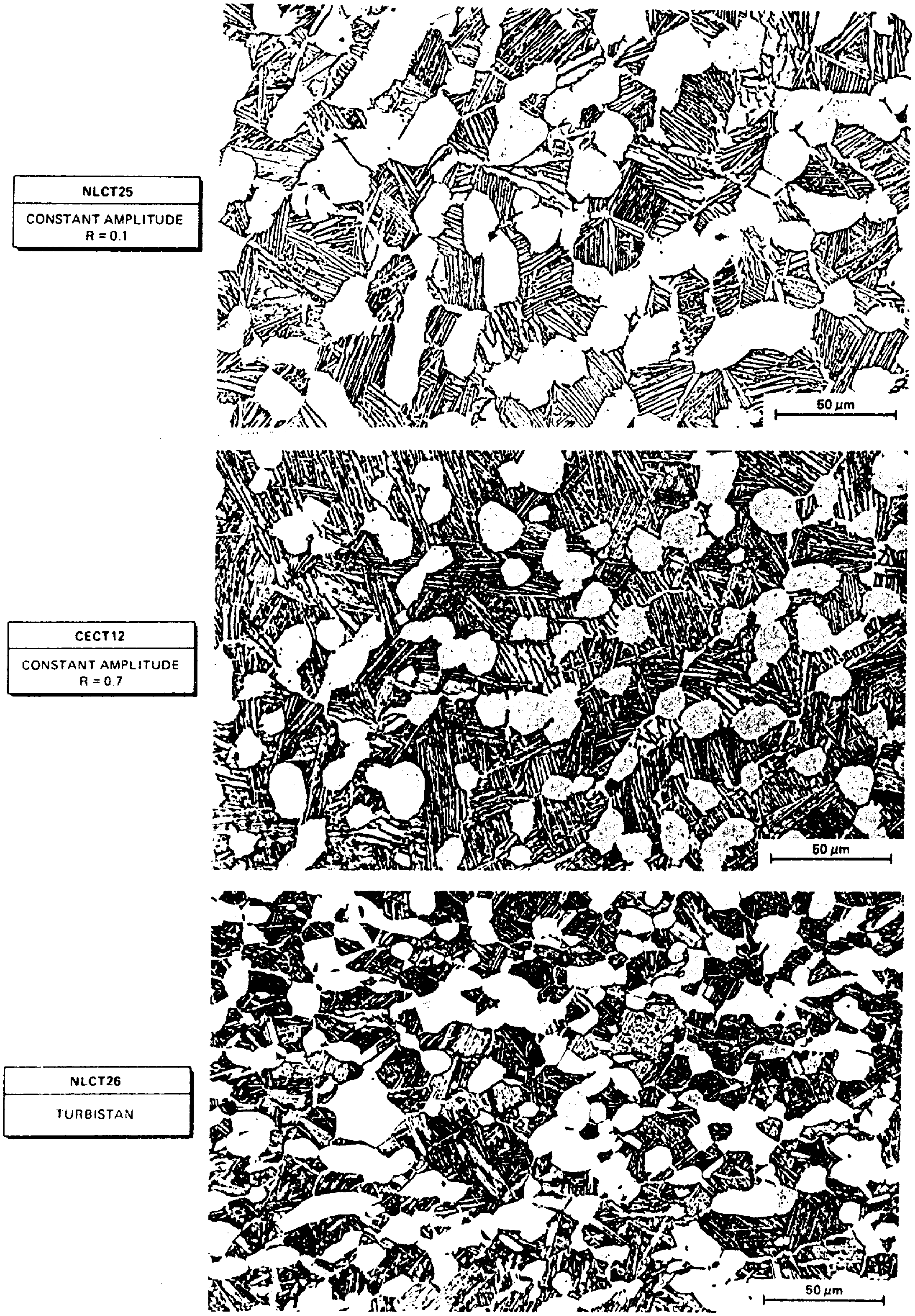

Fig. 9 Examples of microstructures in the overall plane of fatigue crack growth
(to be continued on the next page)

PICT18

TURBISTAN

PICT19

TURBISTAN

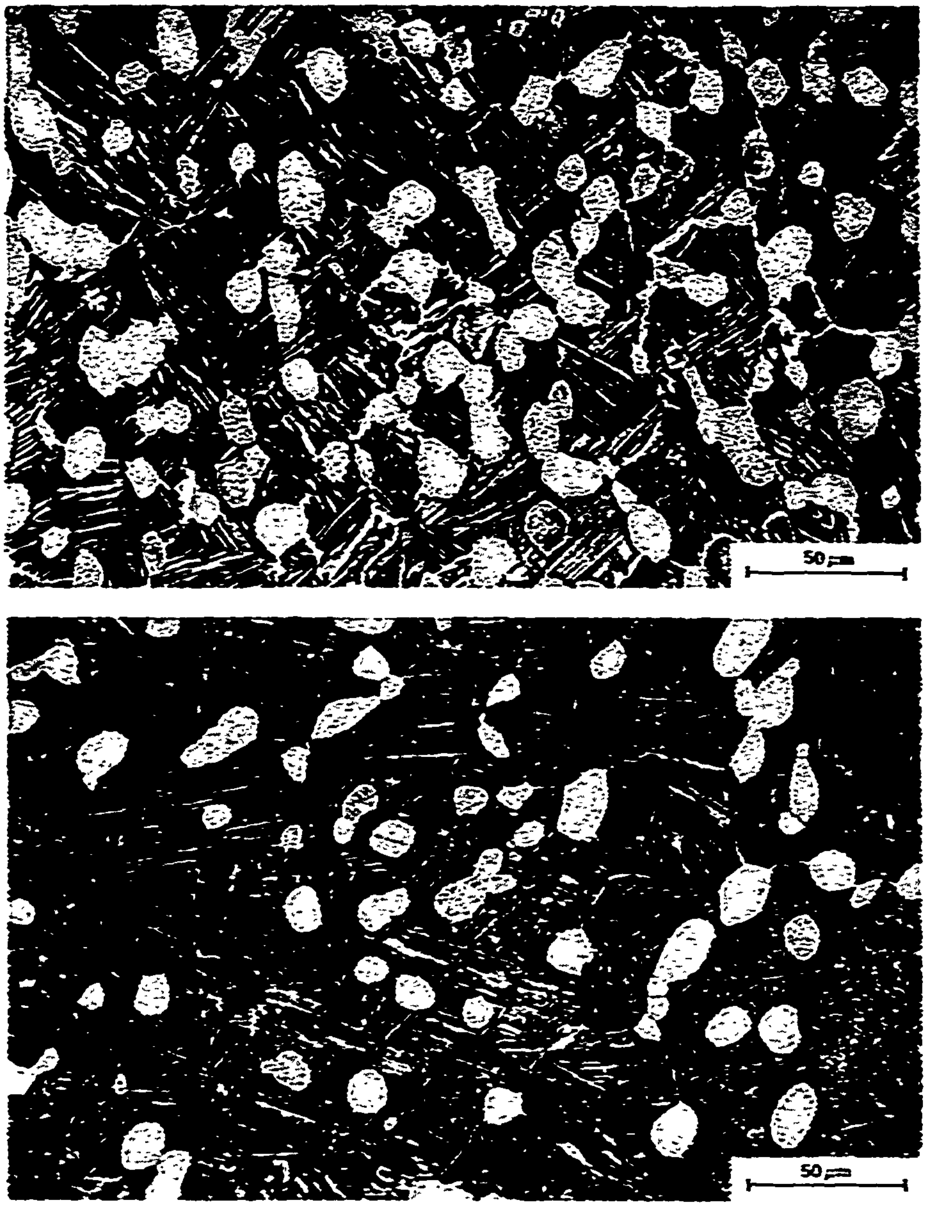

Fig. 9 Examples of microstructures in the overall plane of fatigue crack growth (concluded)

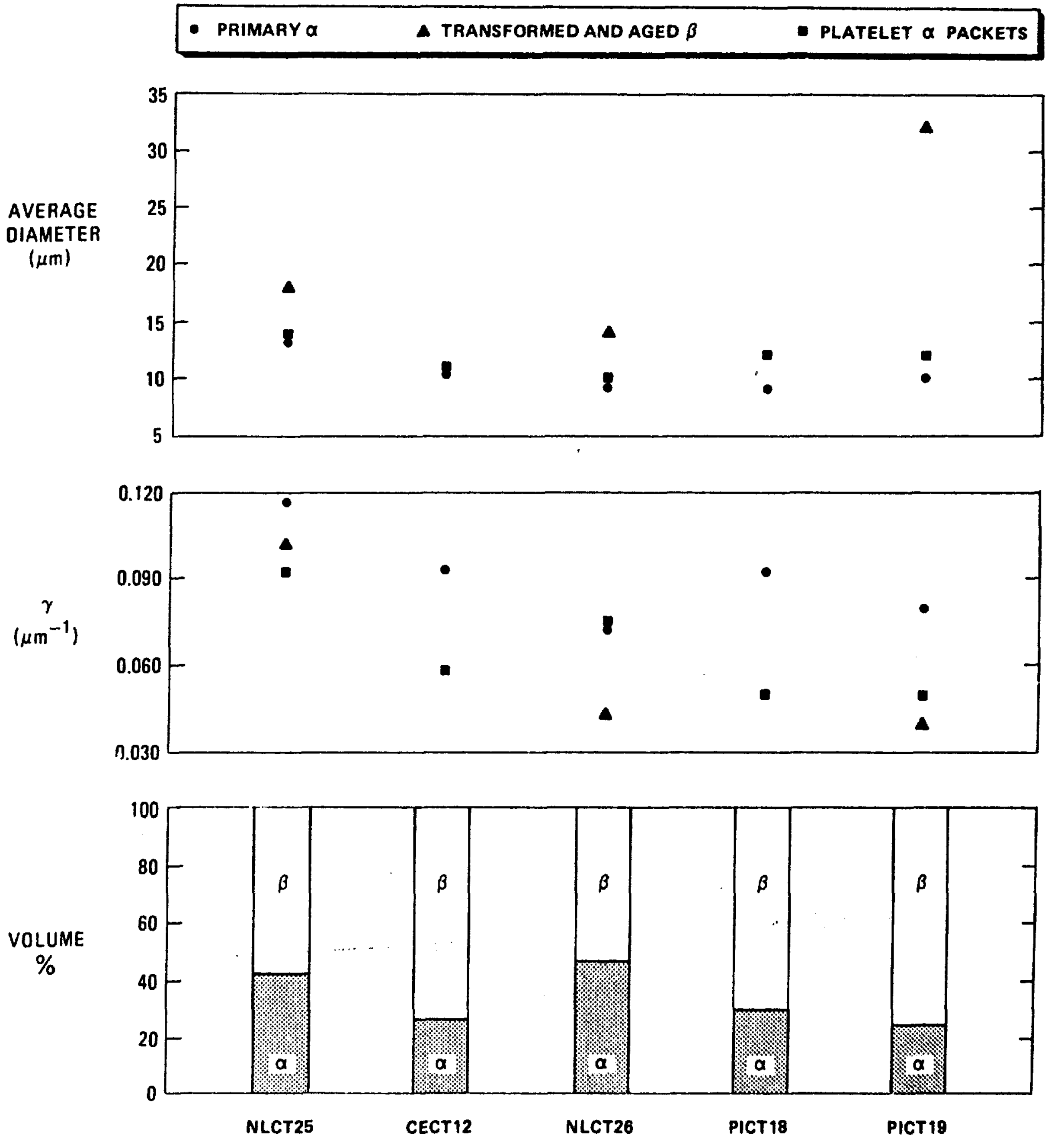

Fig. 10 Principal microstructural parameters for the compact tension specimens

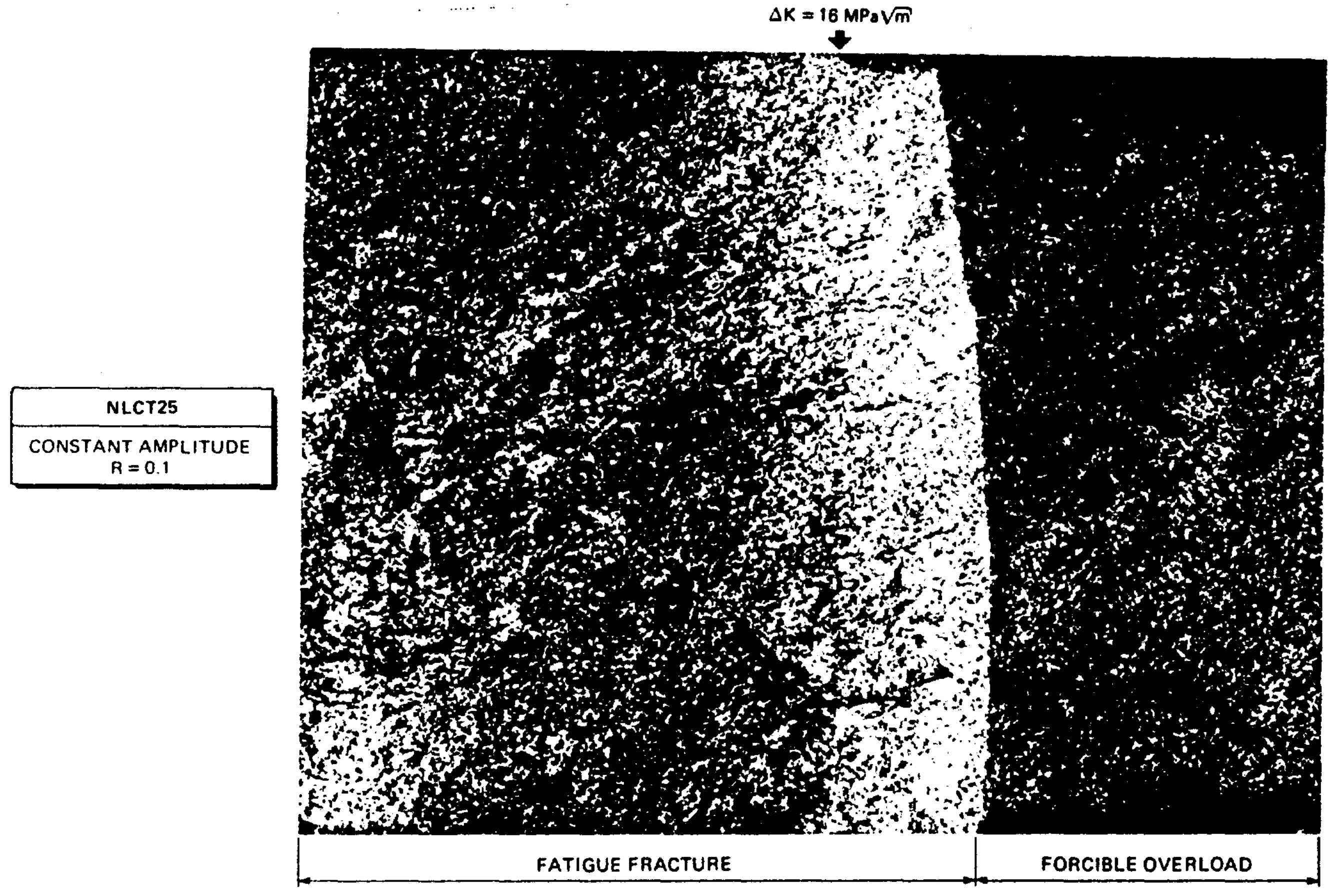

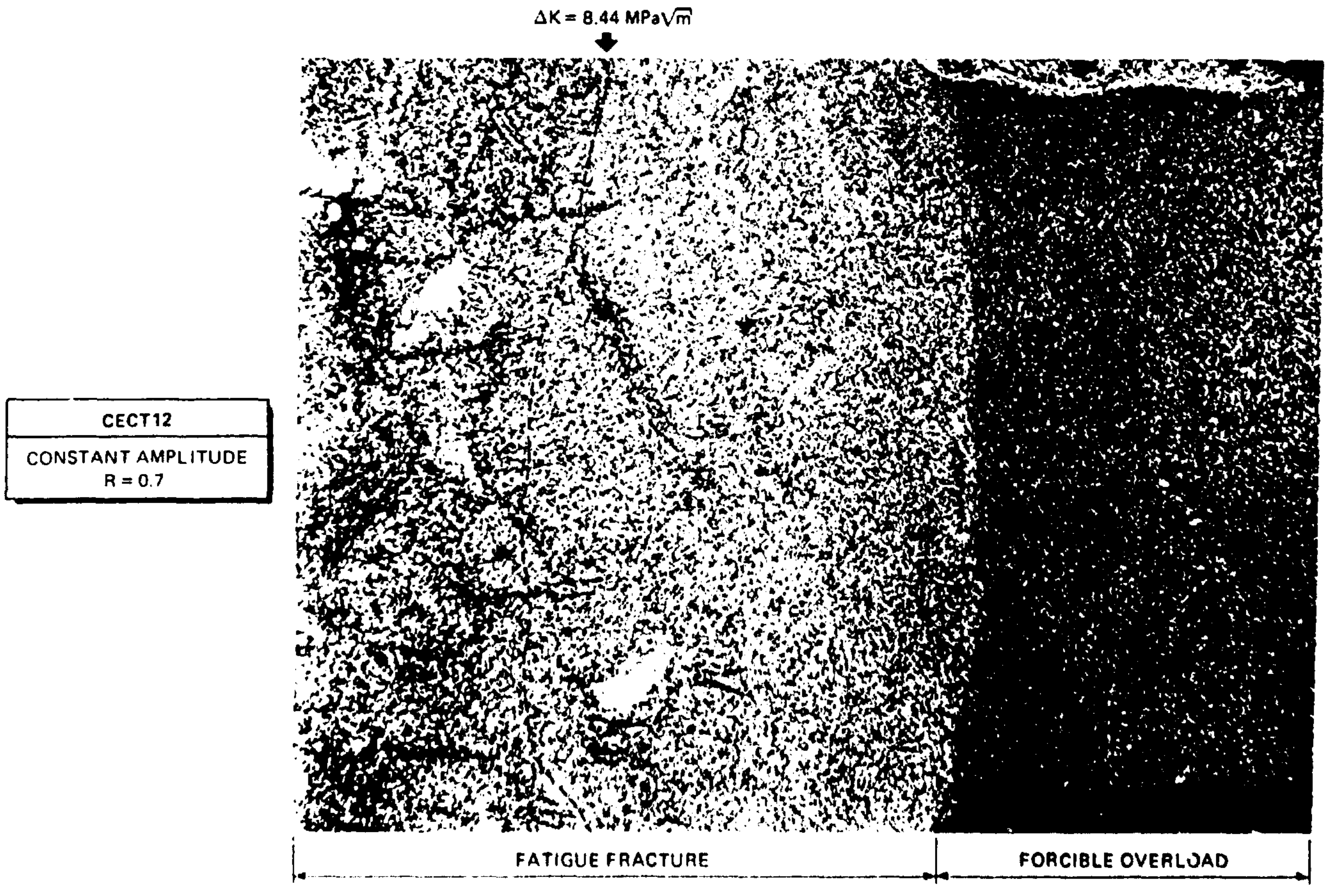

Fig. 11 Macrofractographs of the compact tension specimens tested under constant amplitude loading

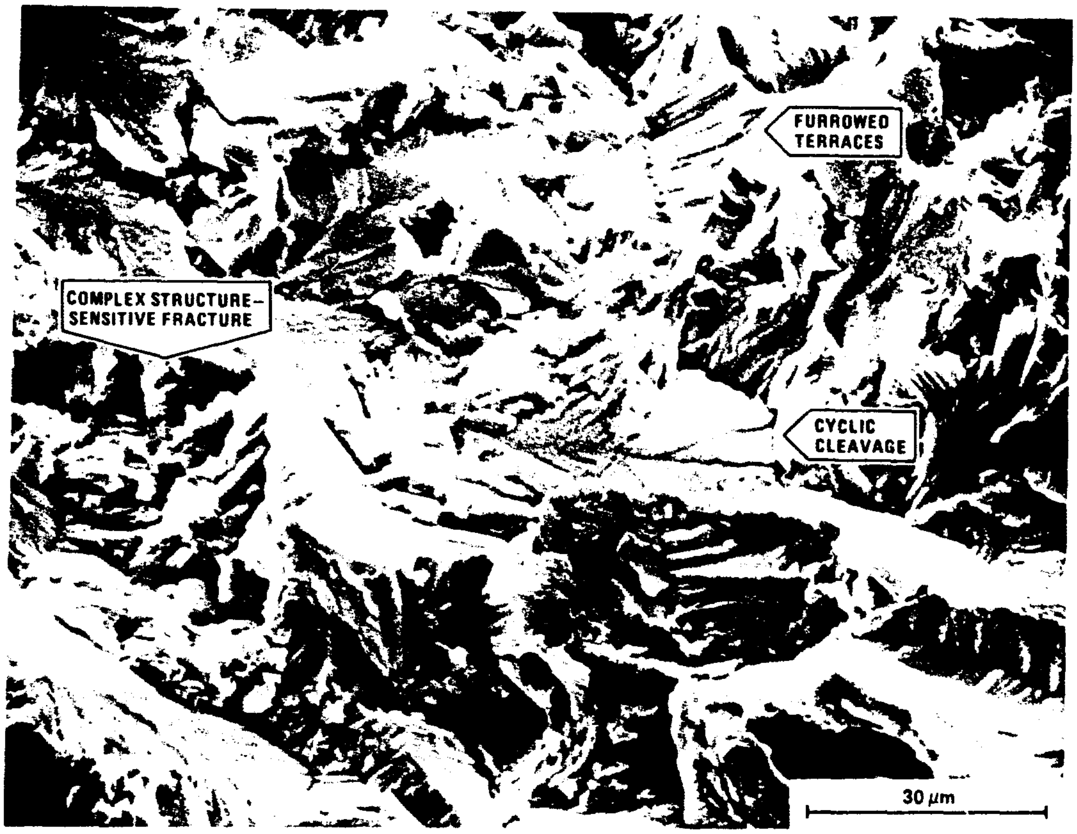

a | $\Delta K = 10\ MPa\sqrt{m}$

b | $\Delta K = 14\ MPa\sqrt{m}$

Fig. 12 Characteristic features of pre-transition fatigue fracture for constant amplitude fatigue, R = 0.1

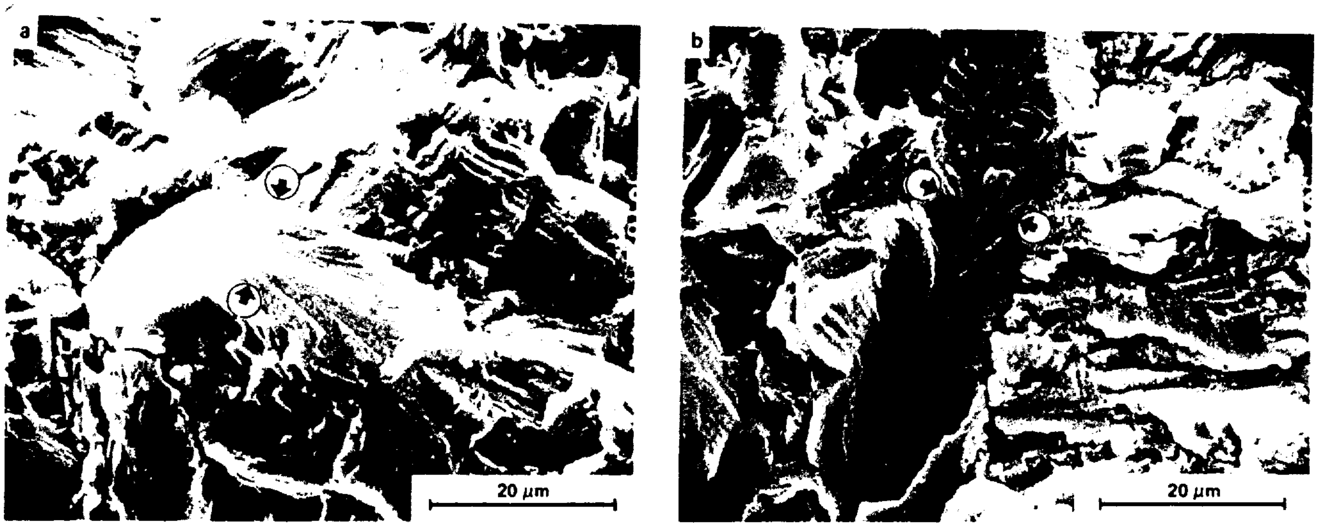

- FLAT FRACTURE WITH MAINLY CONVEX GRAIN BOUNDARIES
- FEATHERY MARKINGS
- OCCASIONAL INTERSECTING SLIP MARKINGS

Fig. 13 Characteristics of cyclic cleavage in primary α for $R = 0.1$ and $\Delta K = 10$ MPa$\sqrt{m}$. Arrows indicate (a) a high angle grain boundary and (b) a low angle grain boundary

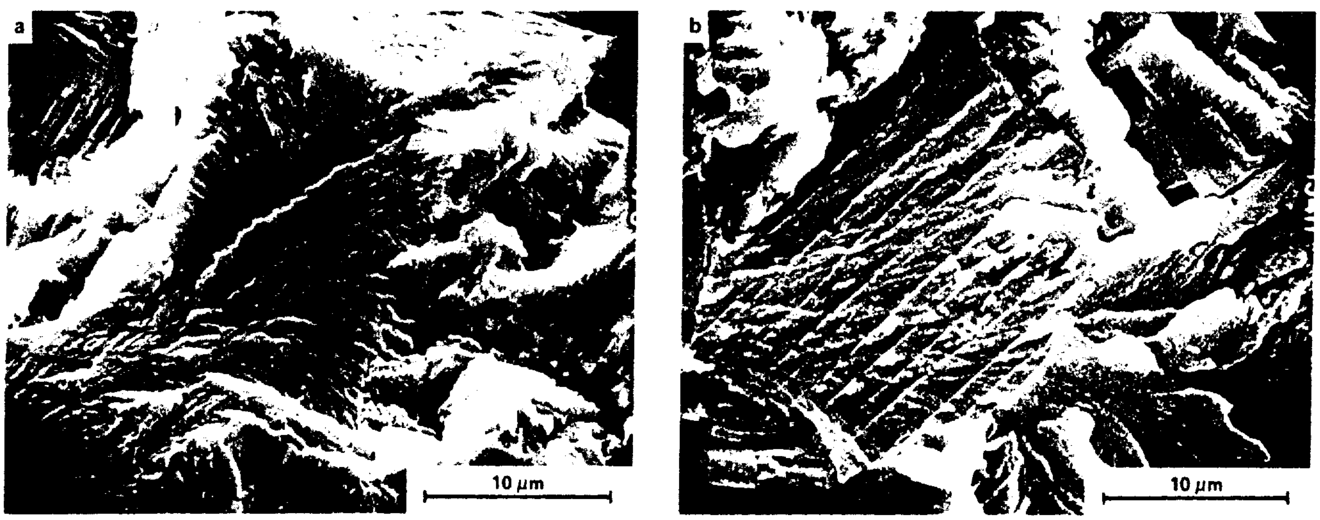

- FLAT FRACTURE WITH FREQUENT CONCAVE GRAIN BOUNDARIES
- MICROSERRATED RIDGES
- OFTEN WITH PARALLEL SLIP LINES (W–LINES) [7]

Fig. 14 Characteristics of cyclic cleavage in transformed and aged β for $R = 0.1$ and $\Delta K = 10$ MPa$\sqrt{m}$

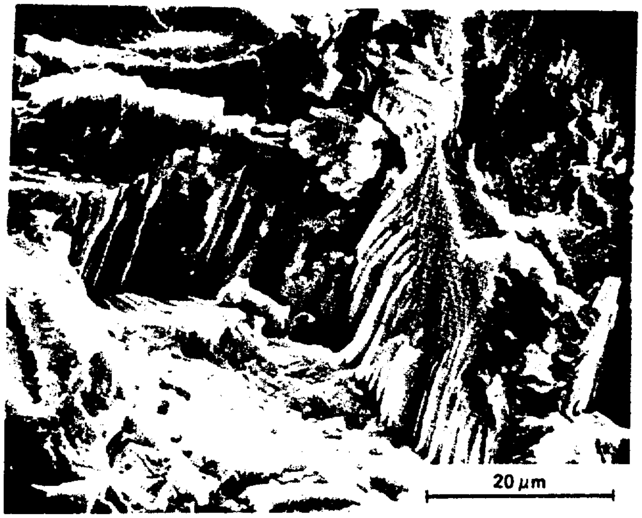

a	PSEUDOFLUTING [15] ● FAIRLY STRAIGHT RIDGES ● COMPLEMENTARY ON MATCHING FRACTURE SURFACES

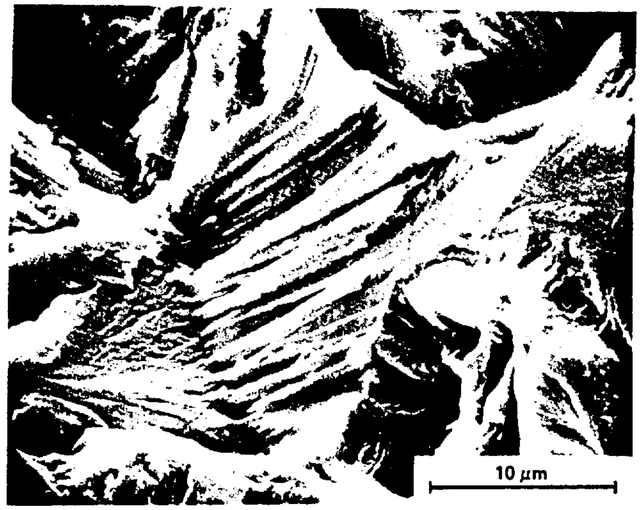

b	FURROWED TERRACES [16, 17] ● FINE LINES AT $\sim 30^\circ$ TO FURROWS ● COMPLEMENTARY ON MATCHING FRACTURE SURFACES

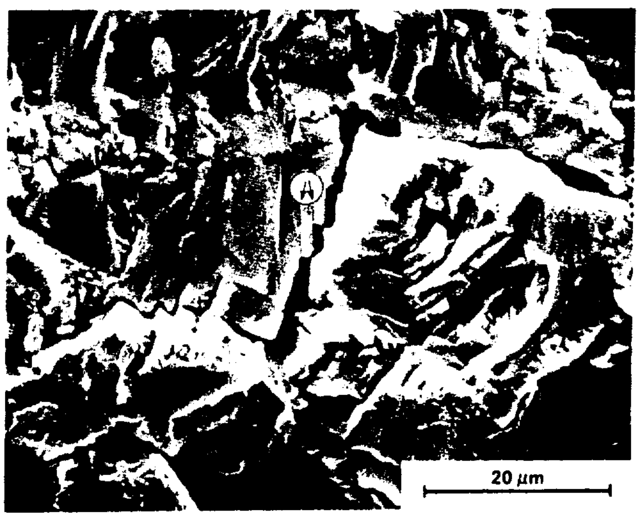

c	COMPLEMENTARY FRACTURE SURFACES ● PSEUDOFLUTING AND FURROWED TERRACES ● ARROWED SLIP TRACES PROBABLY $\{10\bar{1}0\}<11\bar{2}0>$

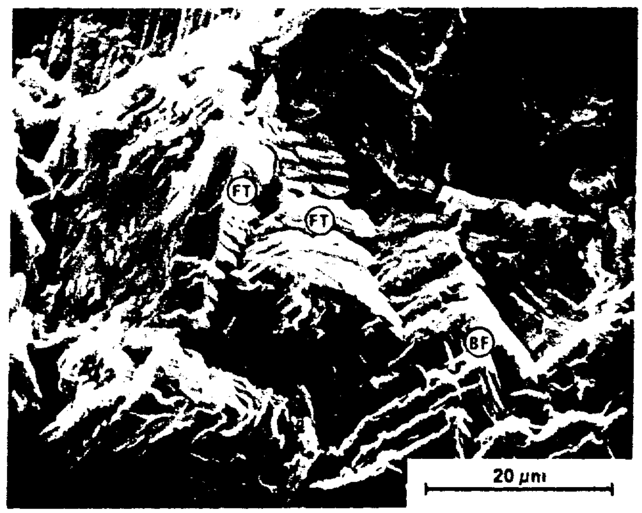

d	FURROWED TERRACES (FT) → BLOCKY FRACTURE (BF)

Fig. 15 Characteristic features associated with cyclic cleavage fracture for R = 0.1 and $\Delta K = 10$ MPa$\sqrt{m}$

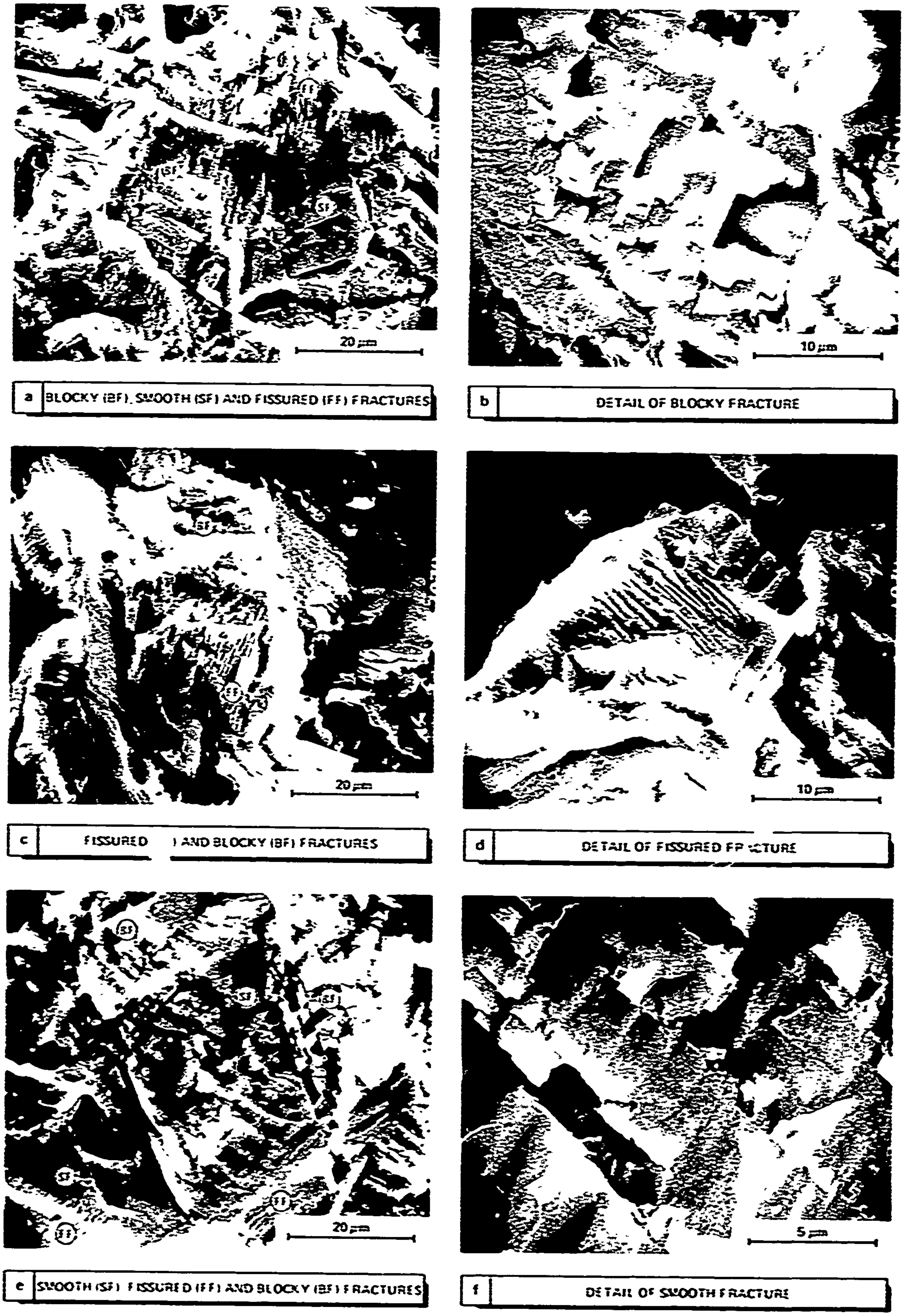

Fig. 16 Characteristic features of blocky, fissured and "smooth" fractures for R = 0.1 and ΔK = 10 MPa$\sqrt{m}$. Smooth and fissured fractures are less common and tend to be broken up into blocks.

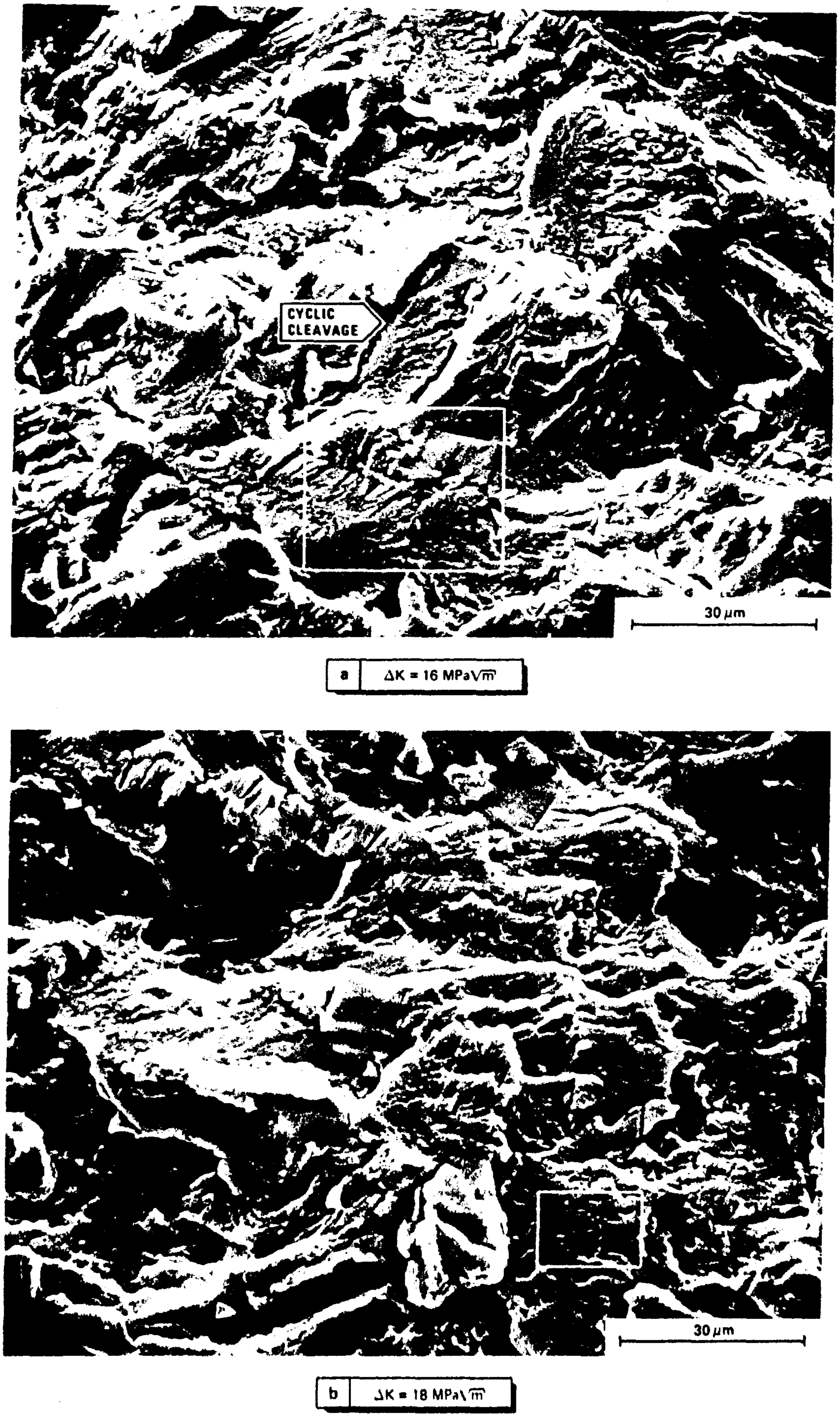

Fig. 17 Characteristic features of immediately post-transition fatigue fracture for constant amplitude fatigue, R = 0.1. Insets are shown in detail in figures 18c and 19d respectively

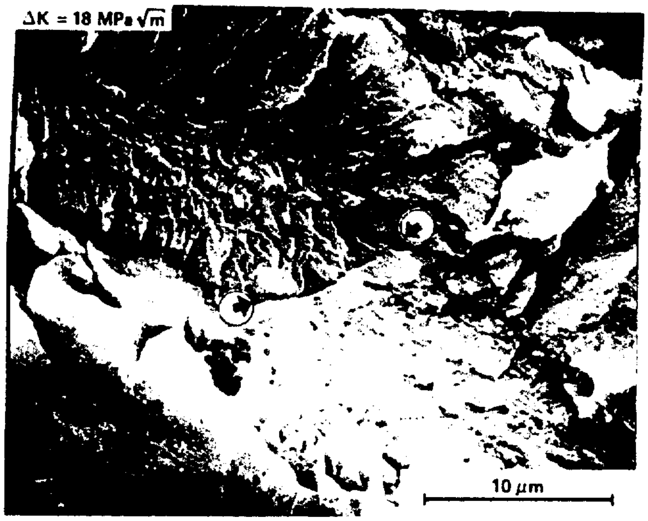

a	α CLEAVAGE WITH MICROSERRATED RIDGES AND FISSURE AT A GRAIN BOUNDARY (ARROWED).

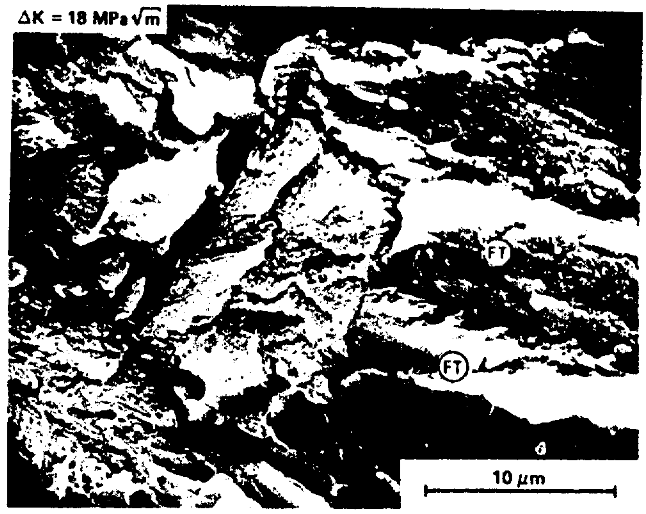

b	TRANSFORMED AND AGED β CLEAVAGE AND ILL–DEFINED FURROWED TERRACES (FT)

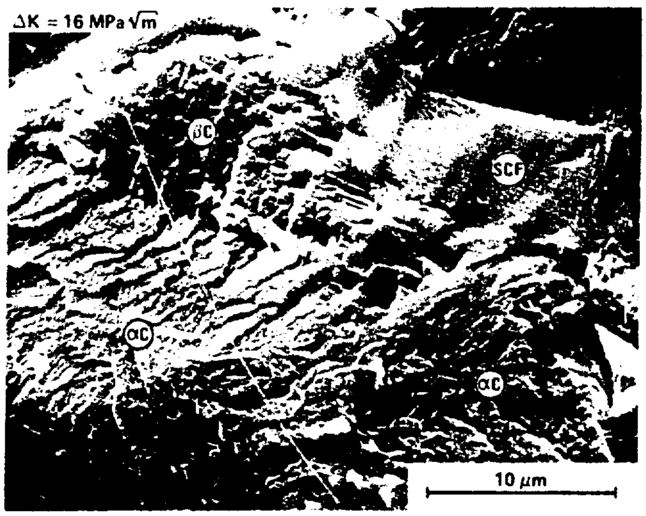

c	α CLEAVAGE (αC), β CLEAVAGE WITH W–LINES (βC) AND SMOOTH CONTINUUM–MODE FRACTURE (SCF)

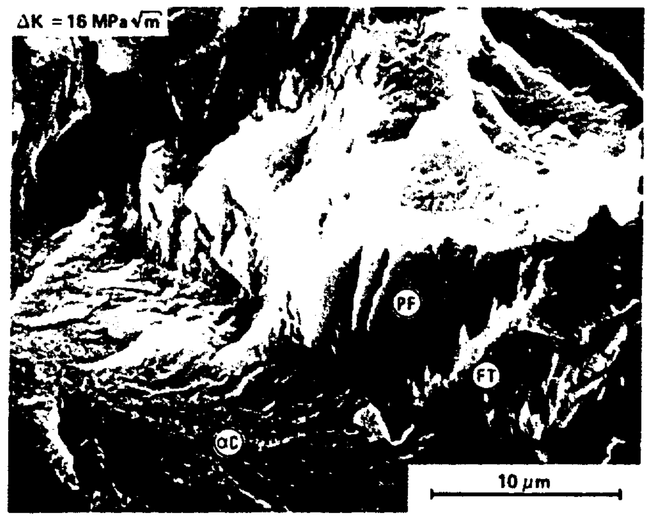

d	α CLEAVAGE (αC) AND ILL–DEFINED PSEUDOFLUTING (PF) AND FURROWED TERRACES (FT)

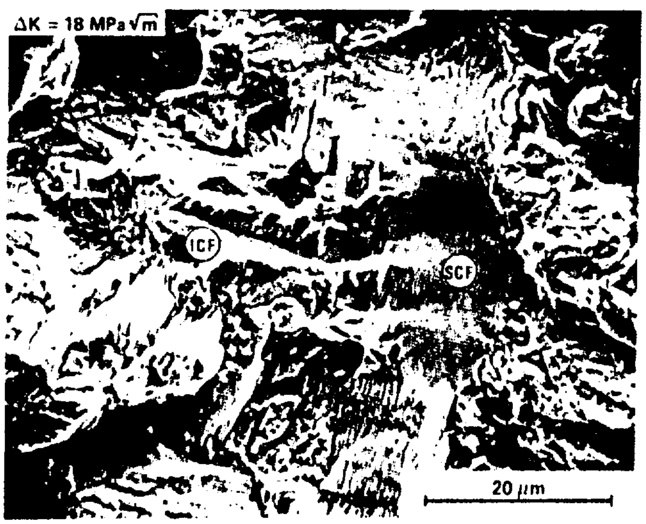

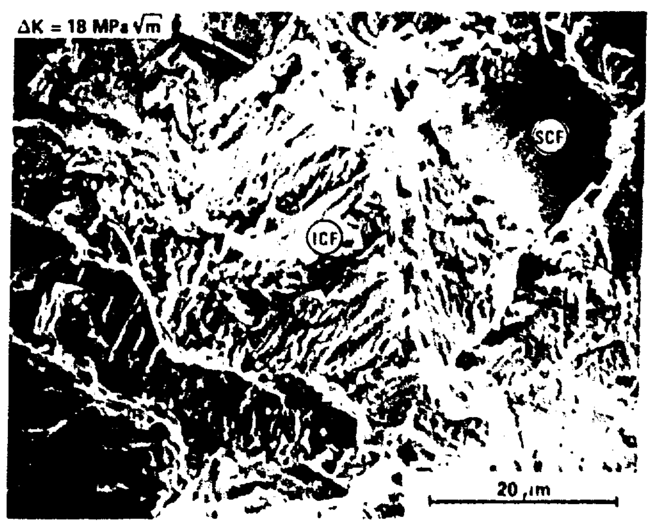

e AND f	SMOOTH (SCF) AND IRREGULAR (ICF) CONTINUUM MODE FRACTURES. SECONDARY CRACKS ON IRREGULAR CONTINUUM MODE FRACTURES ARE PARALLEL TO FATIGUE STRIATIONS

Fig. 18 Details of characteristic features of immediately post-transition fatigue fracture for R = 0.1

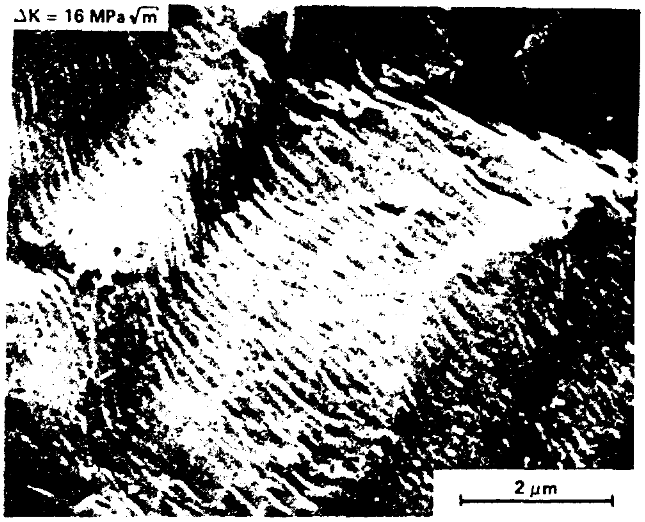

a	DETAIL OF FIGURE 18c: FATIGUE STRIATIONS ON SMOOTH CONTINUUM-MODE FRACTURE. STRIATION SPACING ~0.14 μm. MACROSCOPIC CRACK GROWTH RATE ~0.09 μm/CYCLE

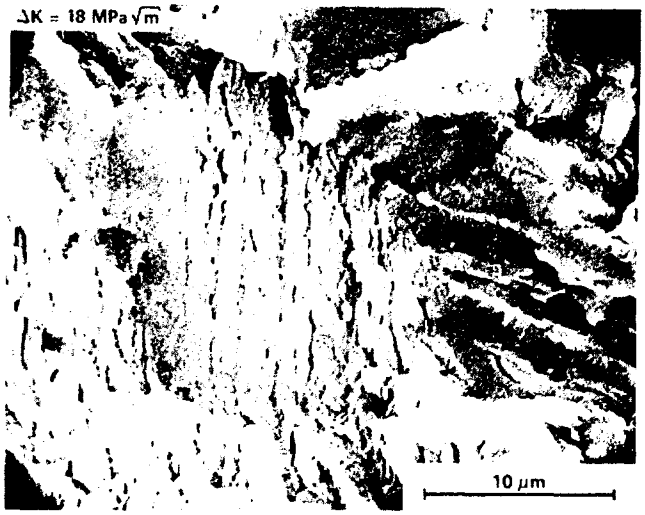

b	IRREGULAR CONTINUUM-MODE FRACTURE ACROSS A PLATELET α PACKET. SECONDARY CRACKS ARE PARALLEL TO FATIGUE STRIATIONS AND ALSO OCCUR AT α/β INTERFACES

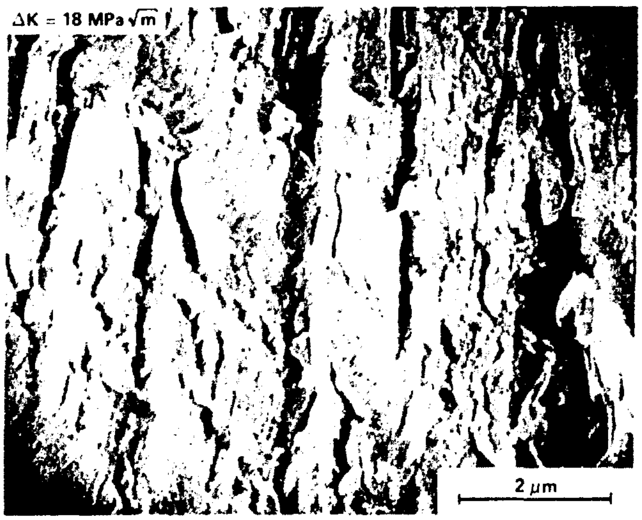

c	DETAIL OF FIGURE 19b: FATIGUE STRIATIONS ON IRREGULAR CONTINUUM-MODE FRACTURE. STRIATION SPACING ~0.23 μm. MACROSCOPIC CRACK GROWTH RATE ~0.13 μm/CYCLE

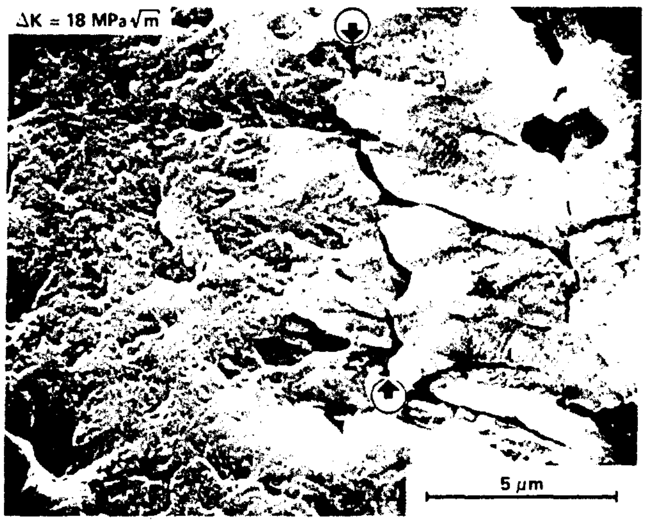

d	FATIGUE STRIATIONS ON A CLEAVAGE FACET. STRIATION SPACING ~0.17 μm. MACROSCOPIC CRACK GROWTH RATE ~0.13 μm/CYCLE. ARROWS POINT TO FISSURE AT A GRAIN BOUNDARY

Fig. 19 Characteristics of fatigue striations on immediately post-transition fatigue fractures for R = 0.1

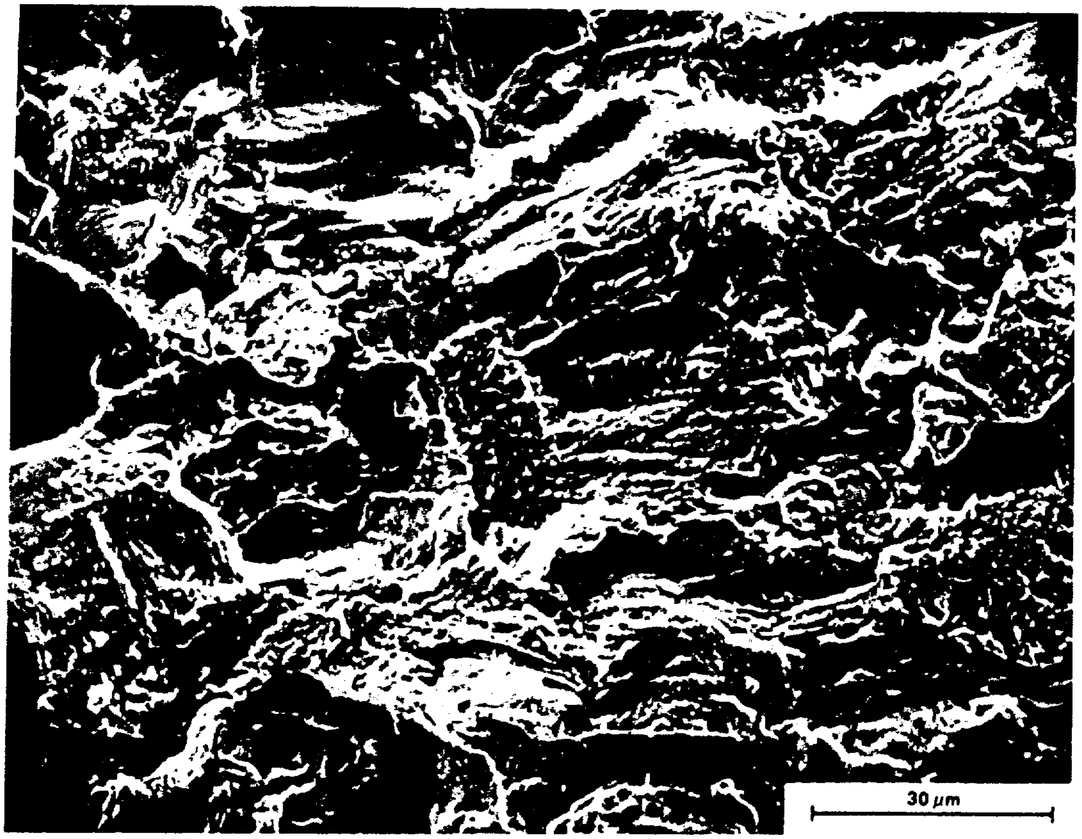

a REPRESENTATIVE VIEW AT INTERMEDIATE MAGNIFICATION

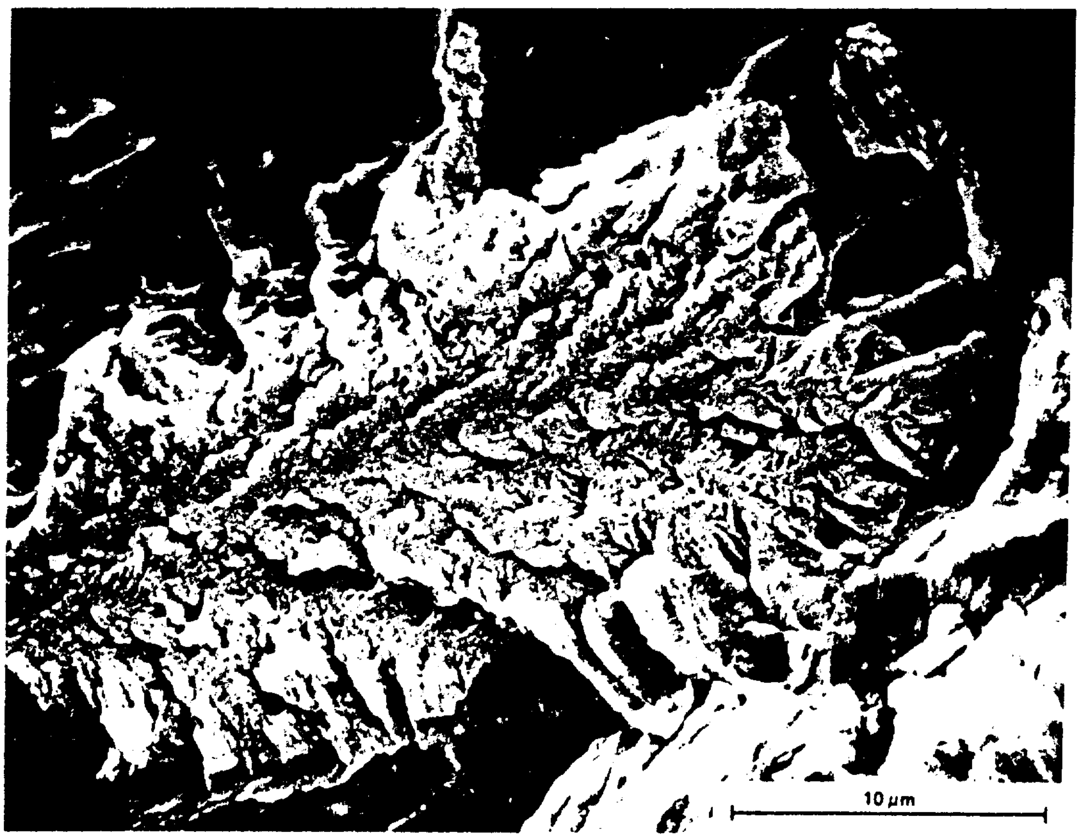

b ROUGH CLEAVAGE FACET WITH MICROSERRATED RIDGES

Fig. 20 Characteristic features of fatigue fracture at $\Delta K = 20\ MPa\sqrt{m}$ for $R = 0.1$

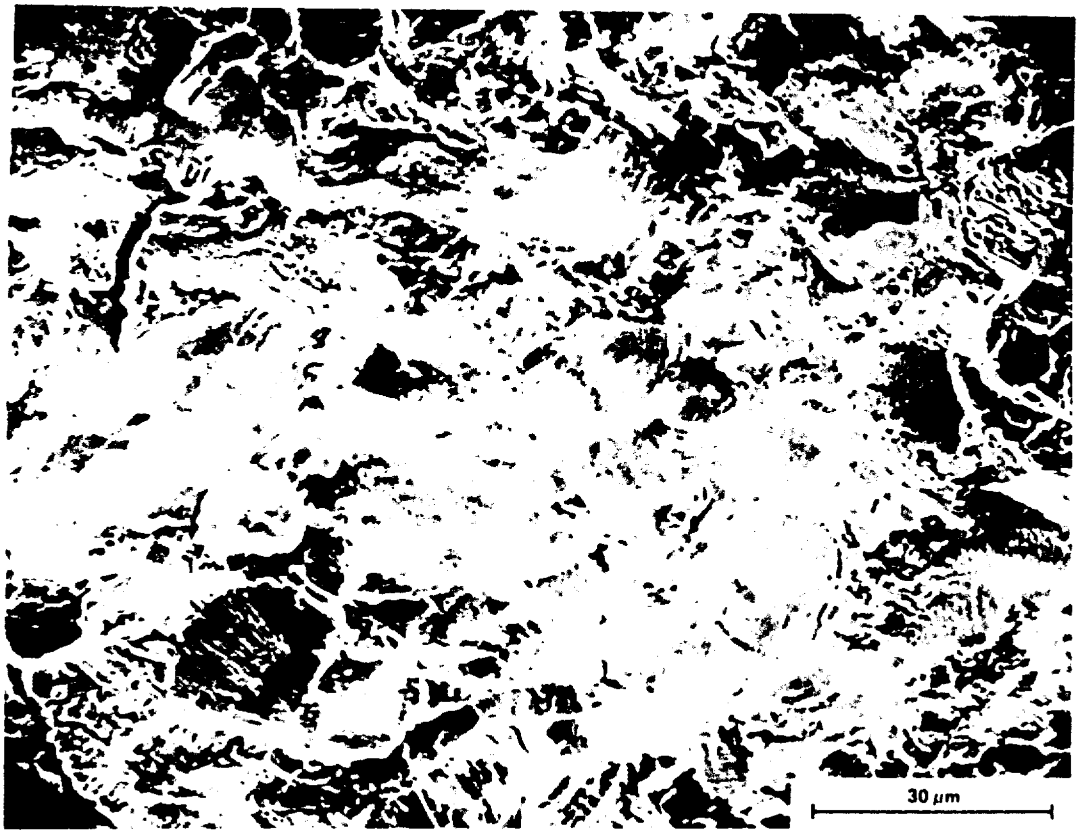

a REPRESENTATIVE VIEW AT INTERMEDIATE MAGNIFICATION

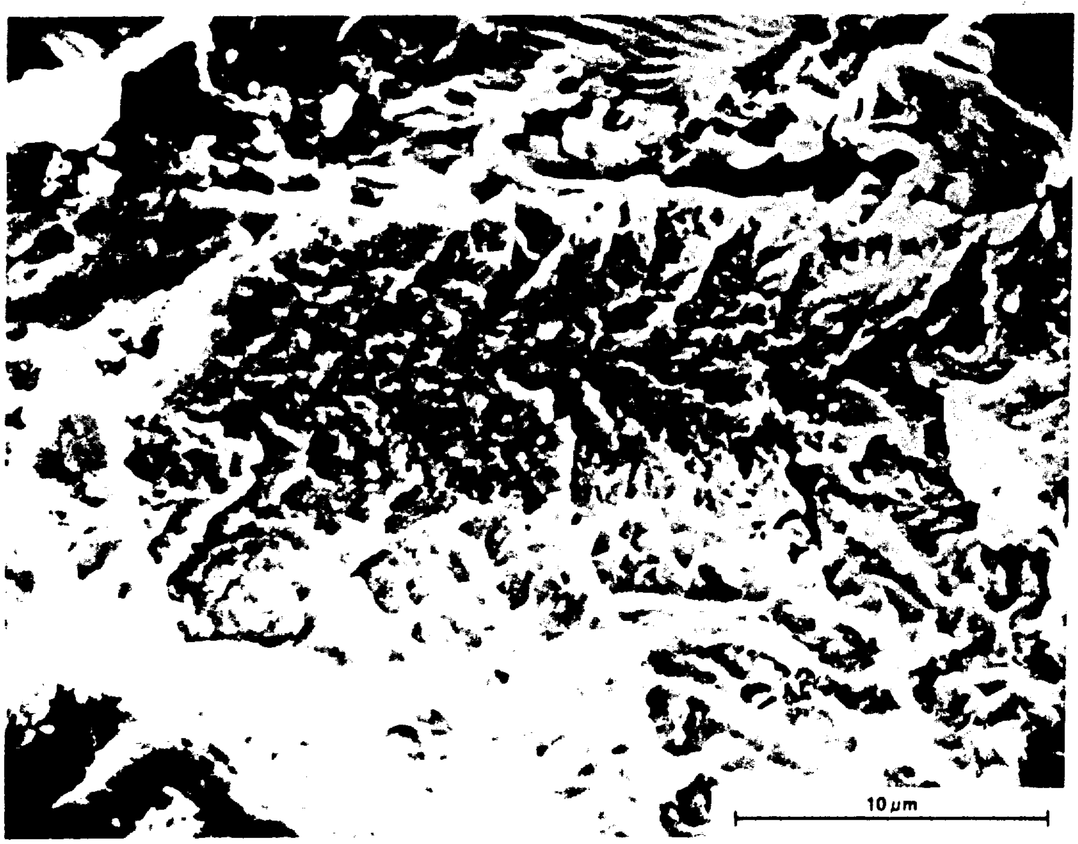

b ROUGH CLEAVAGE FACET WITH MICROSERRATED RIDGES

Fig. 21 Characteristic features of fatigue fracture at $\Delta K = 30\ MPa\sqrt{m}$ for $R = 0.1$

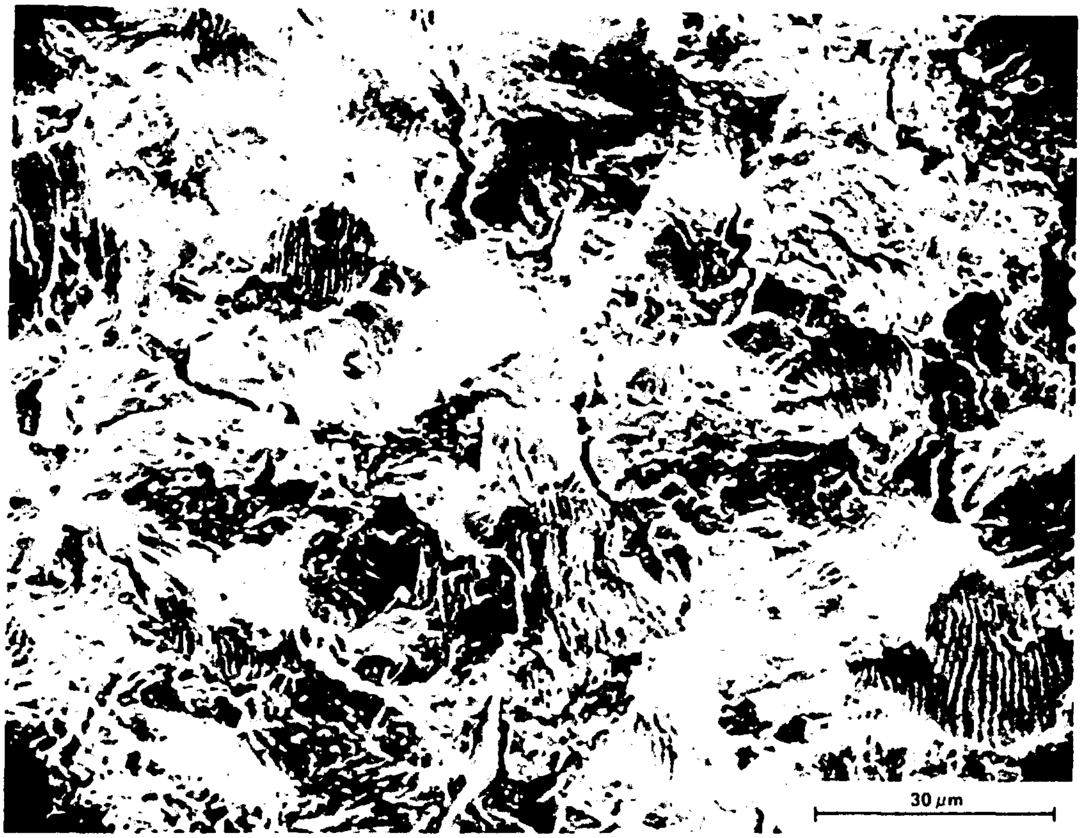

a REPRESENTATIVE VIEW AT INTERMEDIATE MAGNIFICATION

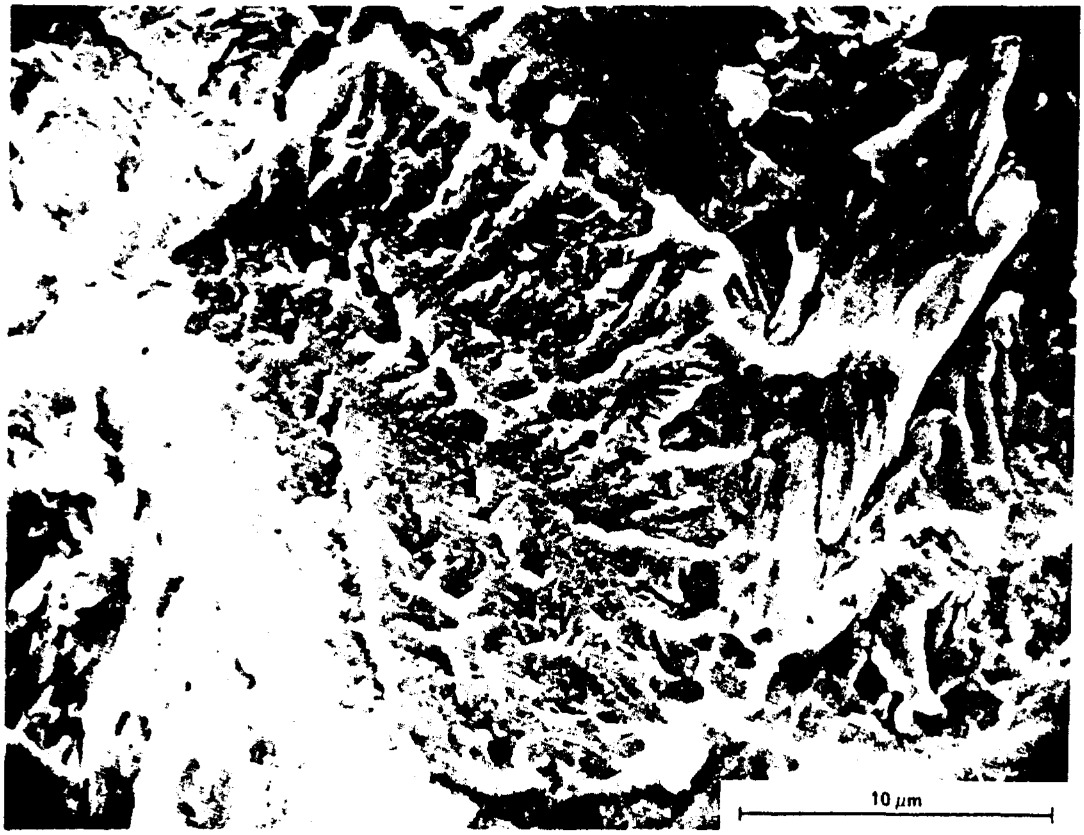

b ROUGH CLEAVAGE FACET WITH MICROSERRATED RIDGES

Fig. 22 Characteristic features of fatigue fracture at $\Delta K = 40$ MPa$\sqrt{m}$ for $R = 0.1$

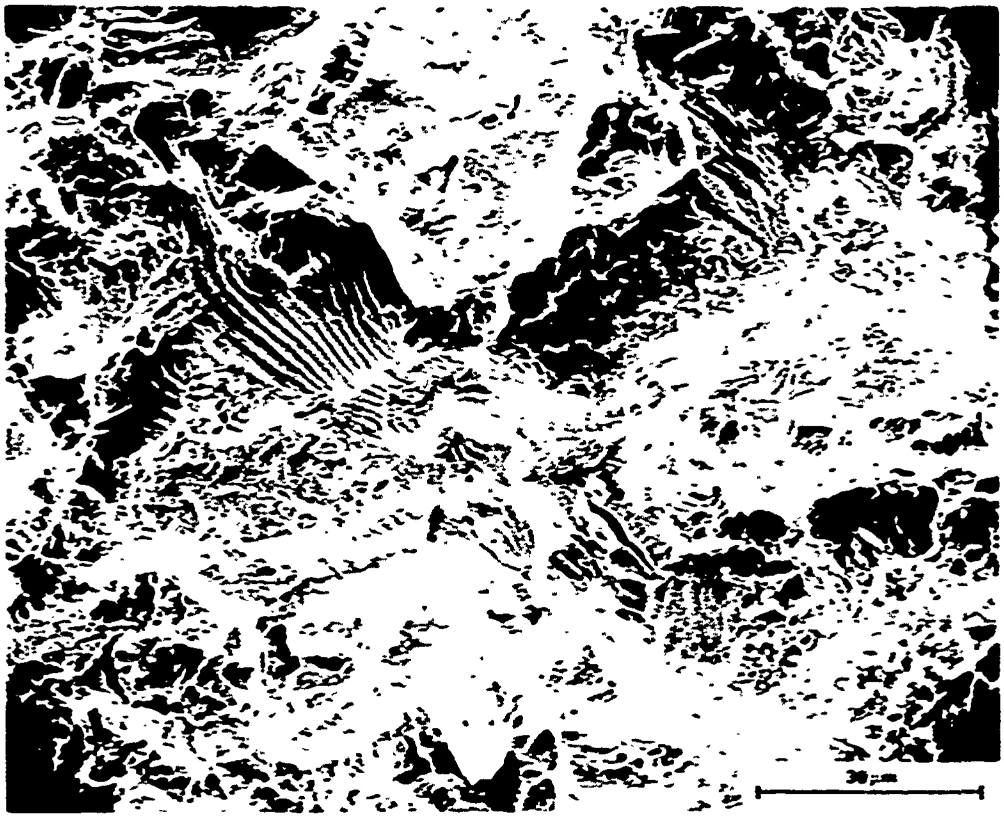

a | REPRESENTATIVE VIEW AT INTERMEDIATE MAGNIFICATION

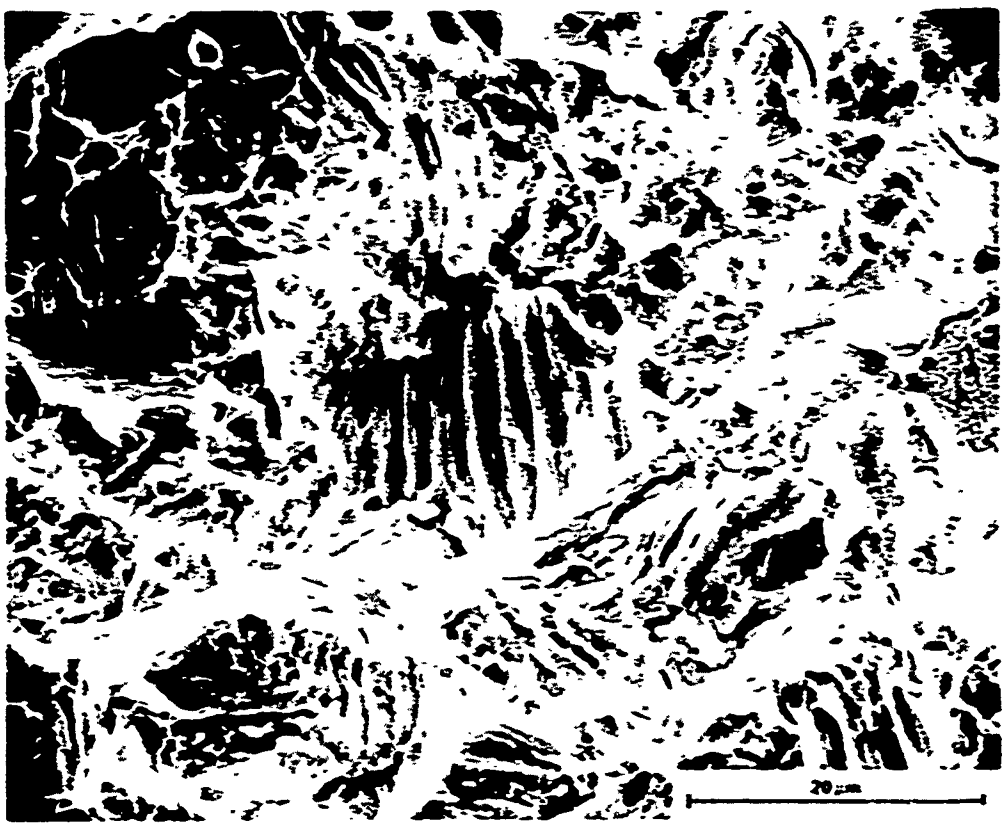

b | DETAIL OF STRIATIONS AND MICROVOID COALESCENCE

Fig. 11 Characteristic features of fatigue fracture at ΔK 30 MPa$\sqrt{m}$ for R = 0.1

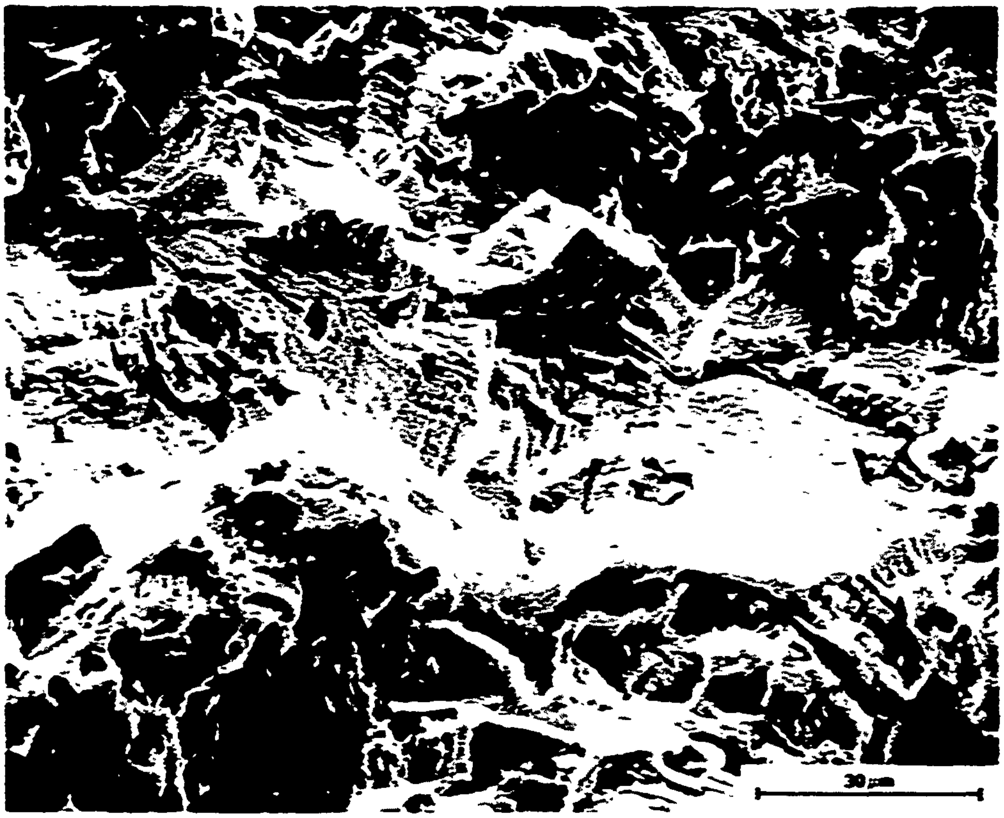

a PRE TRANSITION

b POST TRANSITION

Fig. 22 Characteristic features of immediately pre- and post transition fatigue fracture for constant amplitude fatigue, R = 0.2

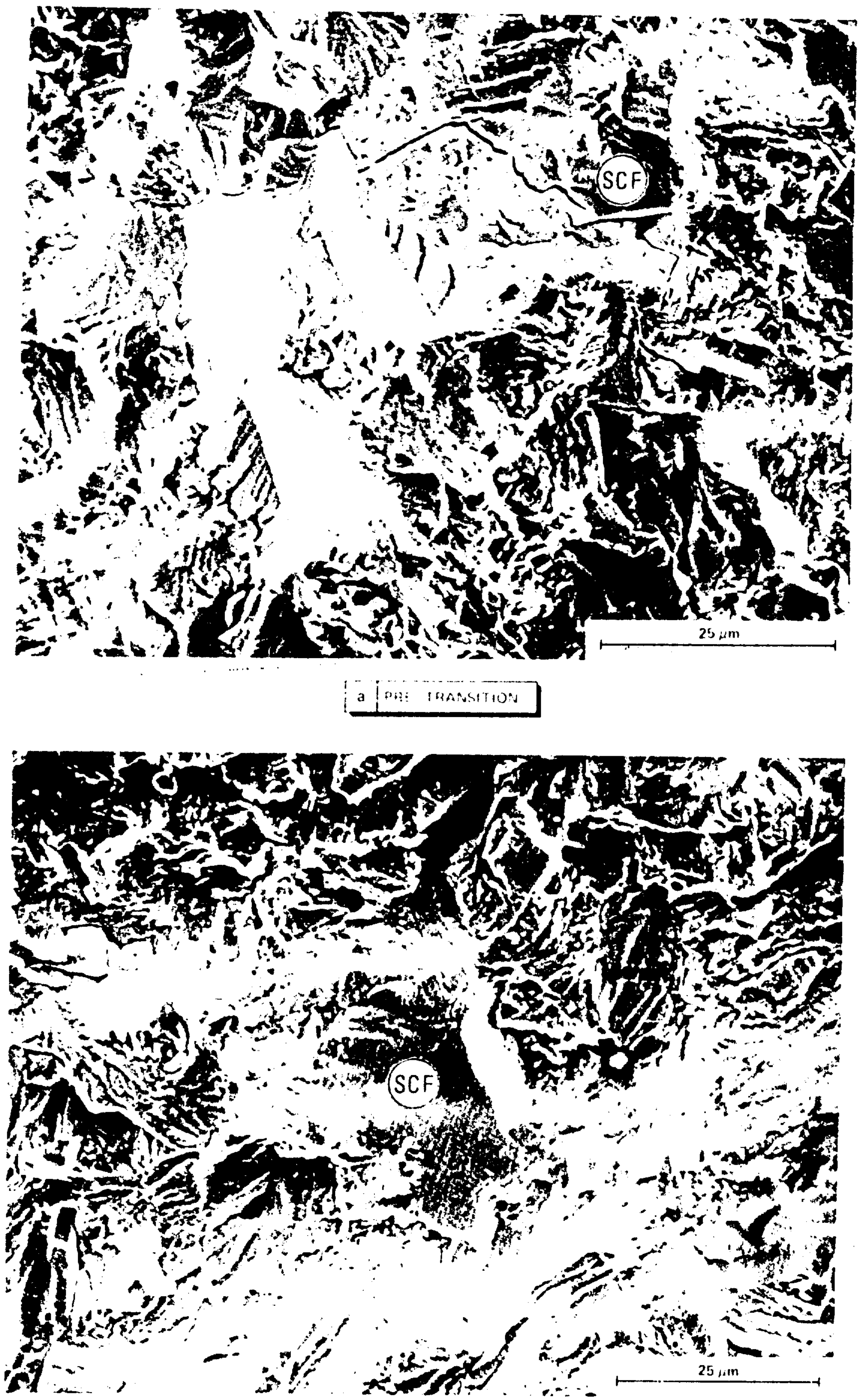

Fig. [illegible] Characteristic features of immediately pre- and post-transition fatigue fracture for specimen NLCT26 tested with TURBISTAN

a PRE TRANSITION

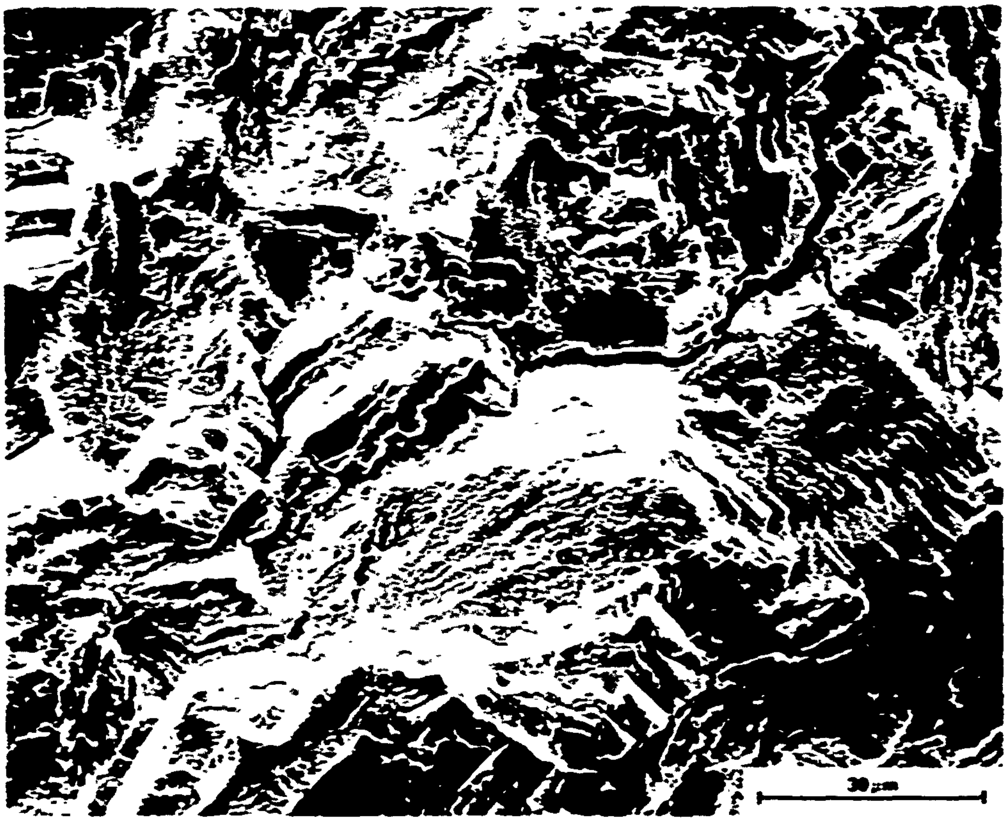

b POST TRANSITION

Fig. 26 Characteristic features of immediately pre- and post transition fatigue fracture for specimens PICT18 and PICT19 tested with TERBISTAN

a PRE TRANSITION

b POST TRANSITION

Fig. 27 Details of the smooth continuum-mode fractures (SCF) indicated in figure 25

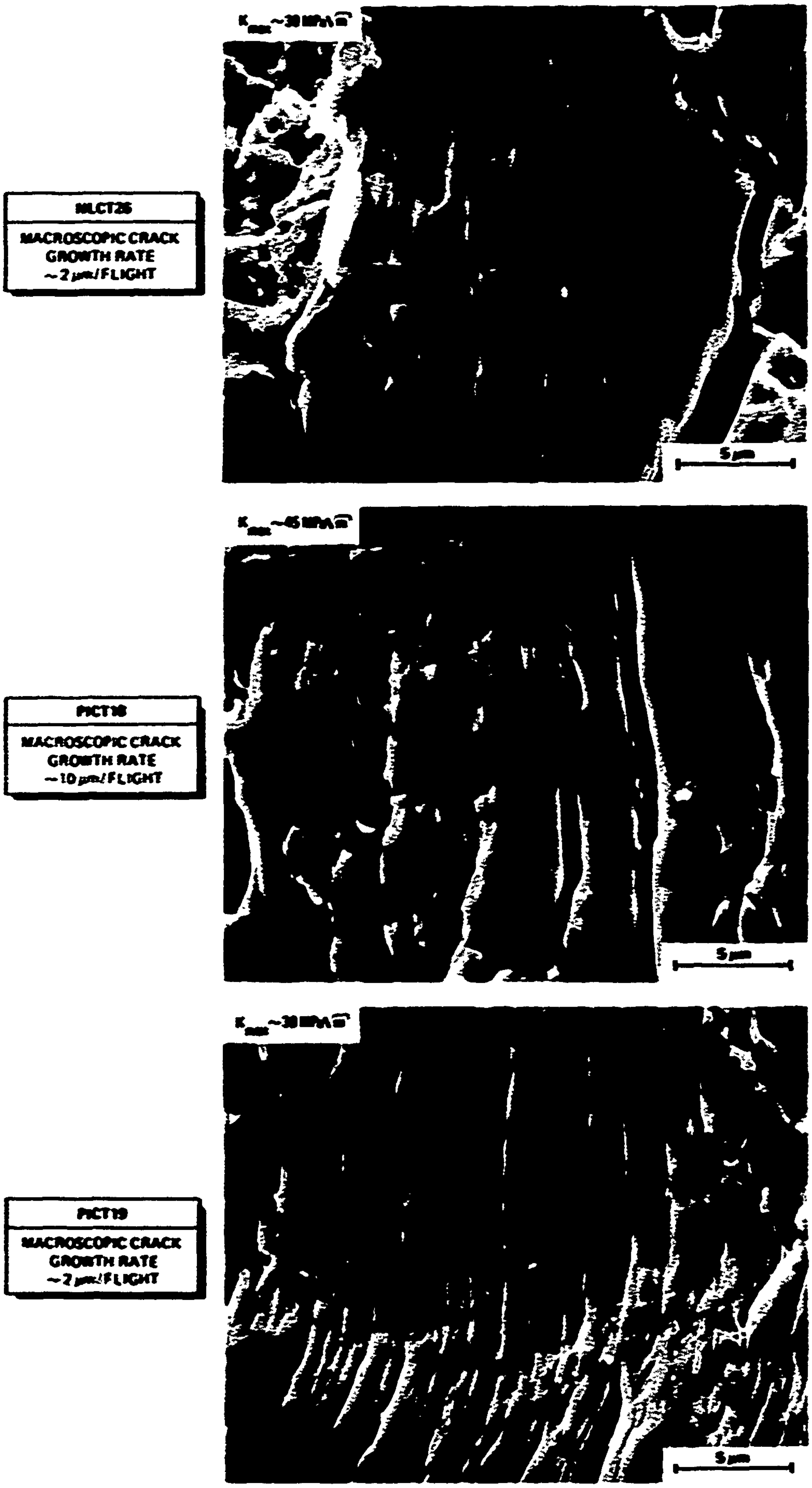

Fig. 28 TURBISTAN fatigue striation patterns at high K_{max} values

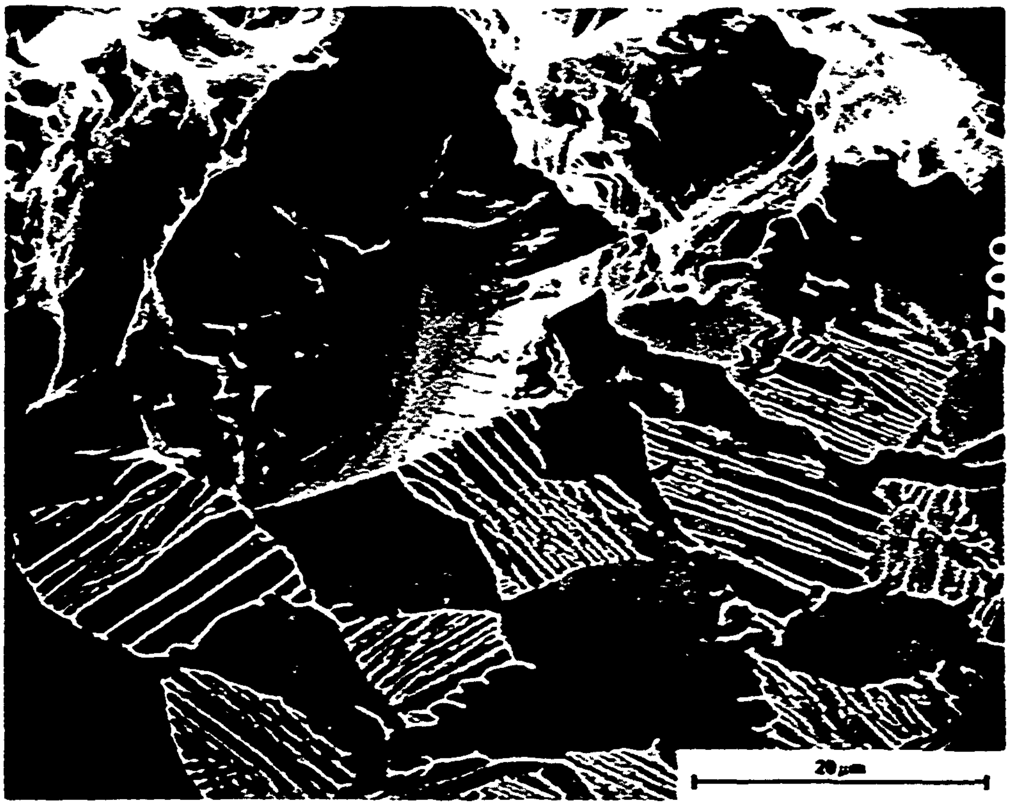

a | PRIMARY α CLEAVAGE AND STRUCTURE-SENSITIVE FRACTURES IN TRANSFORMED AND AGED β

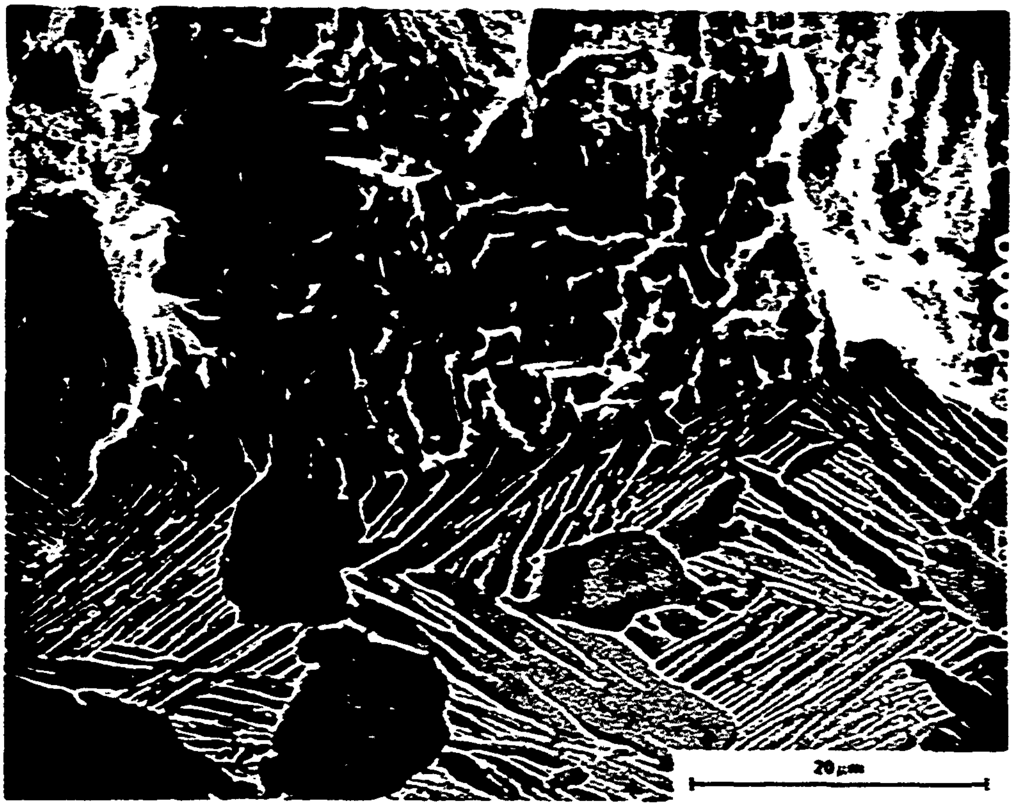

b | BLOCKY STRUCTURE SENSITIVE FRACTURE IN TRANSFORMED AND AGED β

Fig. 29 Significant fractographic and microstructural correlations for pre-transition constant amplitude fatigue, R = 0.1, at ΔK = 10 $MPa\sqrt{m}$

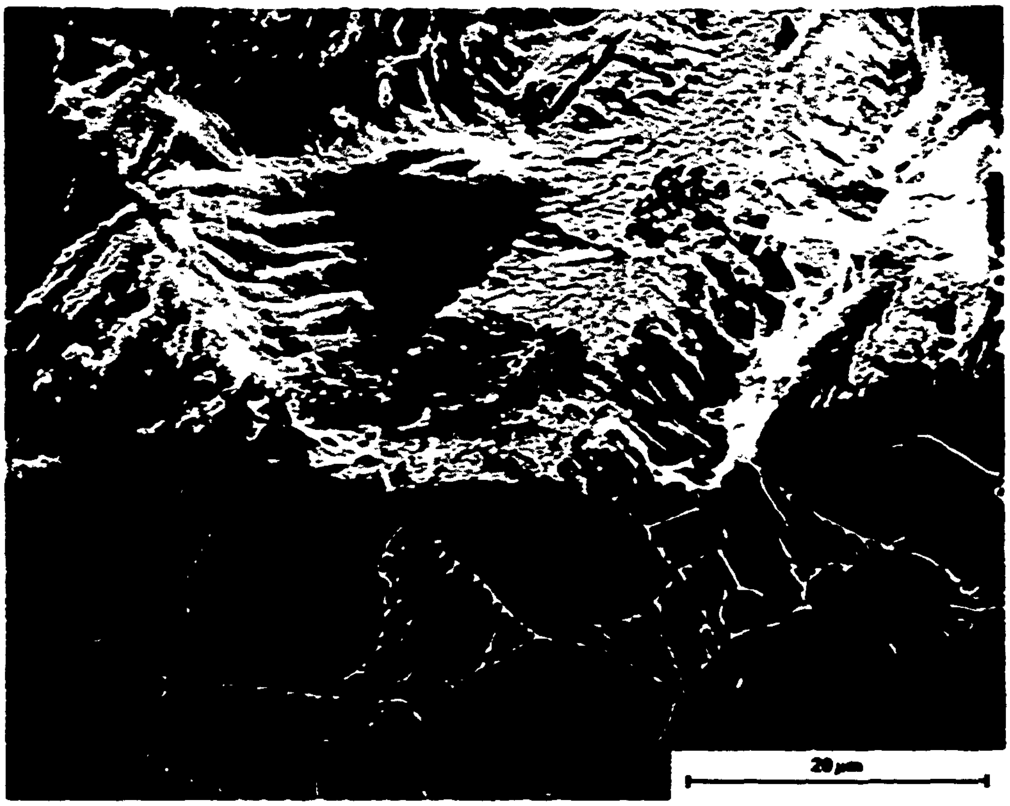

a	PRIMARY α CLEAVAGE AND STRUCTURE-SENSITIVE FRACTURES IN TRANSFORMED AND AGED β

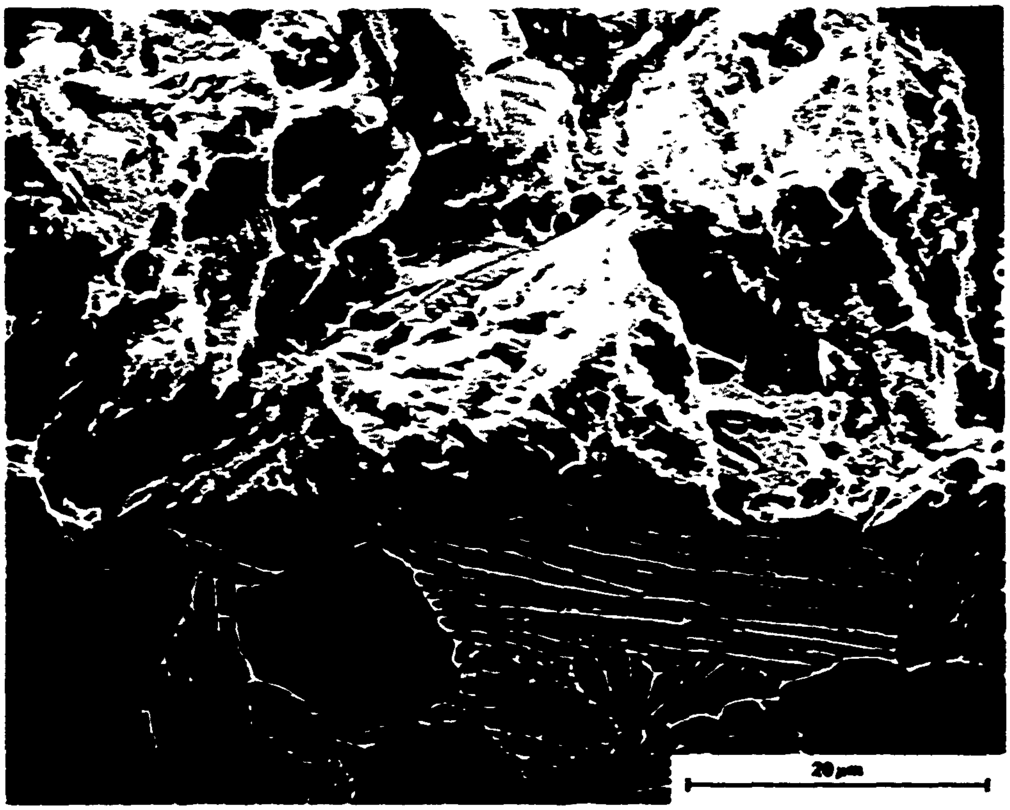

b	PRIMARY α CLEAVAGE AND IRREGULAR CONTINUUM-MODE FRACTURES IN TRANSFORMED AND AGED β

Fig. 30 Significant fractographic and microstructural correlations for post-transition constant amplitude fatigue, $R = 0.1$, at $\Delta K = 18$ $MPa\sqrt{m}$

Fig. 31 Pre- and post-transition fracture profiles for constant amplitude fatigue, R = 0.1

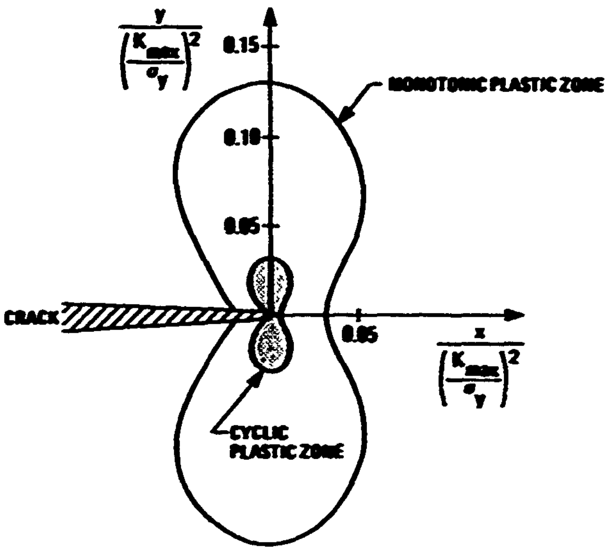

Fig. 32 Plane strain plastic zone size estimates for fatigue crack growth in the Ti-6Al-4V fan disc forgings under constant amplitude loading at R = 0.1

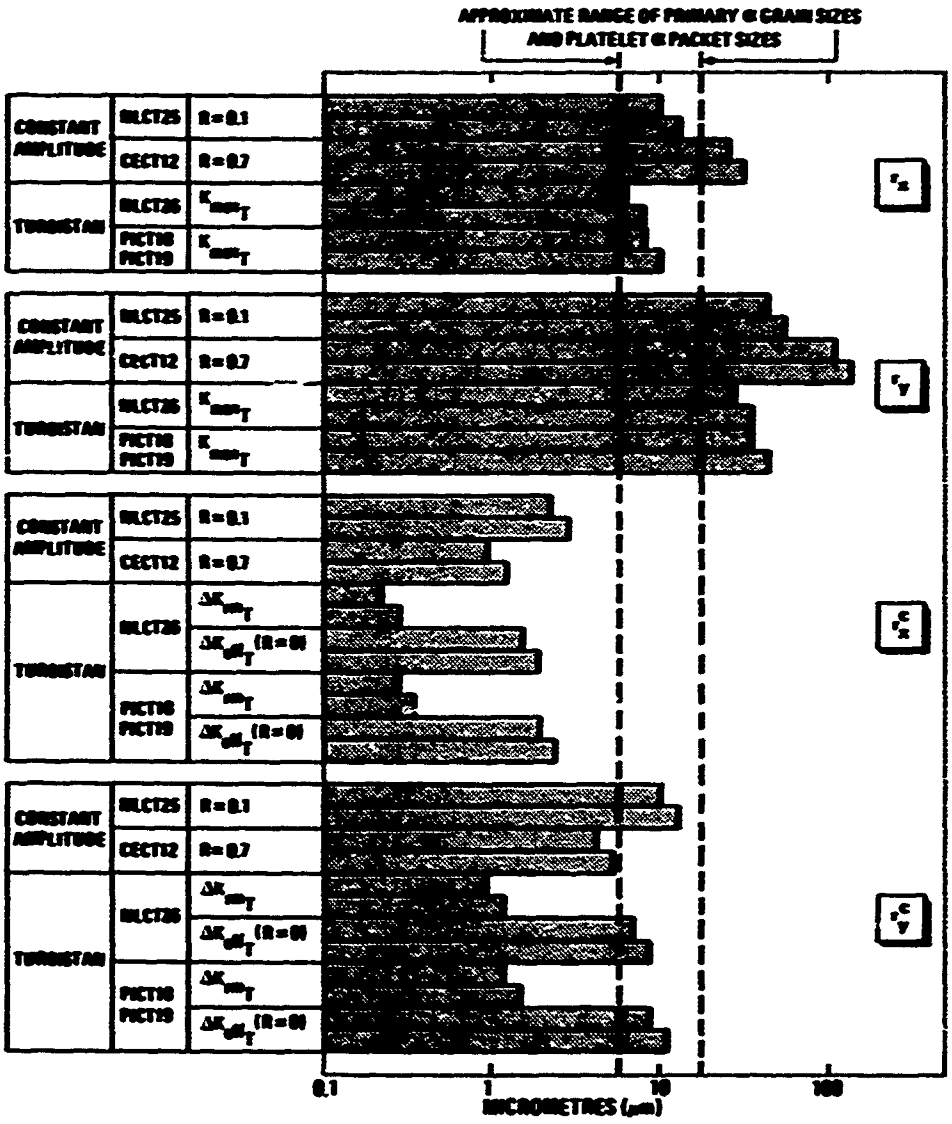

Fig. 33 Comparisons of monotonic and cyclic plane strain plastic zone dimensions at fatigue crack growth curve transitions with the primary α grain sizes and platelet α packet sizes

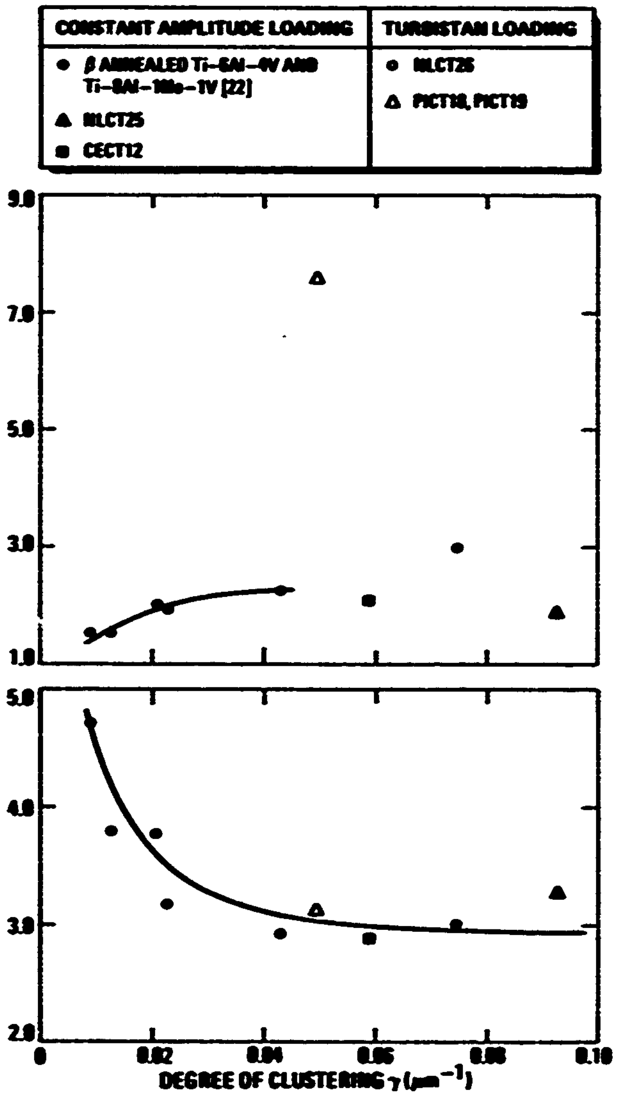

Fig. 34 Transition sharpness (m_1/m_2) and hypertransitional exponent (m_2) of the fatigue crack growth curves as functions of the degree of clustering of the platelet α packet size

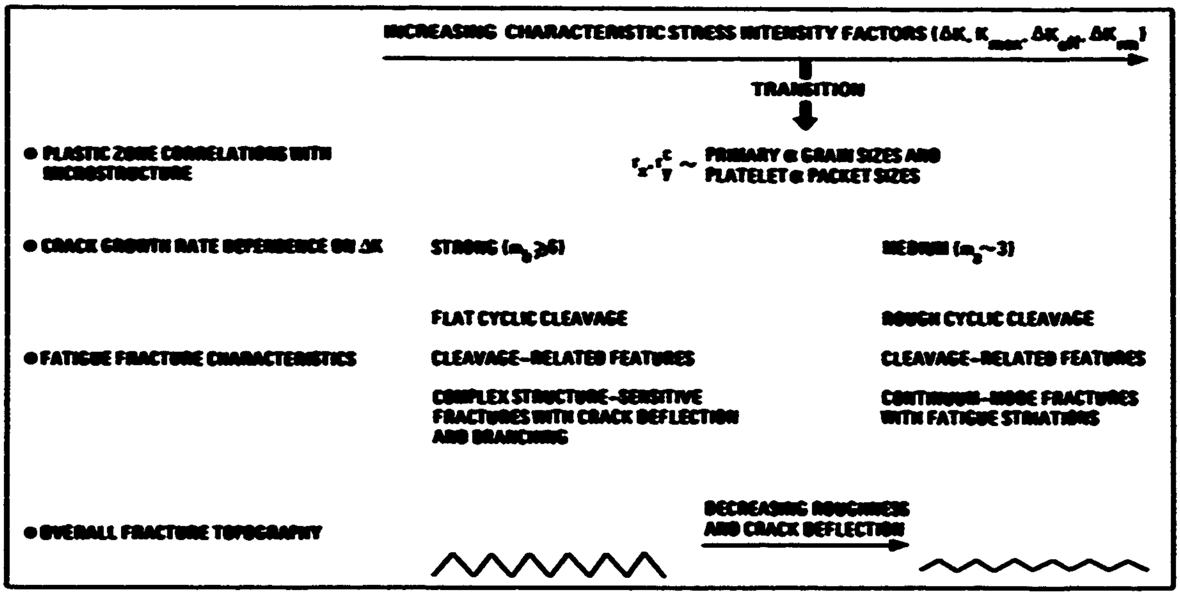

Fig. 35 Hypotransitional and hypertransitional fatigue crack growth characteristics of the Ti-6Al-4V STA fan disc forging materials

I

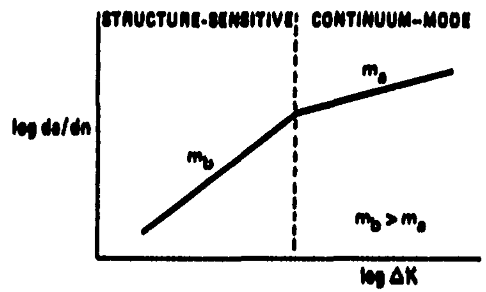

EXAMPLES: Ti–6Al–4V, Ti–8Al–1Mo–1V IN AIR (6–9,22–24,40)

II

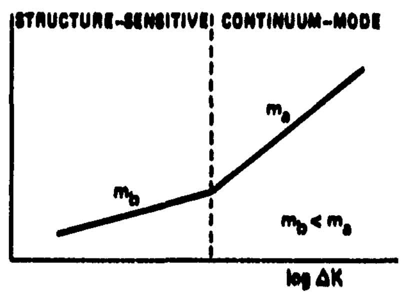

EXAMPLES: Ti–6Al–4V, Ti–8Al–1Mo–1V IN VACUO AND Ti–6Al–4V AND COMMERCIALLY PURE Ti IN DRY ARGON (40)

III

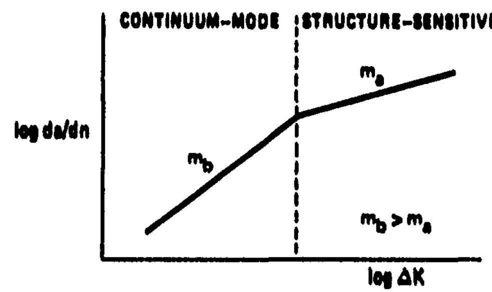

EXAMPLE: Ti–4.5Al–5.0Mo–1.5Cr (CORONA 5) IN AIR (41)

HYPOTRANSITIONAL REGION		HYPERTRANSITIONAL REGION	
FACTORS AFFECTING FATIGUE CRACK GROWTH	EFFECTS RELATIVE TO HYPERTRANSITIONAL REGION	FACTORS AFFECTING FATIGUE CRACK GROWTH	EFFECTS RELATIVE TO HYPOTRANSITIONAL REGION
● STRUCTURE-SENSITIVE CRACK PATH AND CRACK DEFLECTION	CDF ↓ da/dn ↓	● CONTINUUM-MODE CRACK PATH	↑ CDF ↑ da/dn
● DIRECTIONAL CRACK TIP PLASTICITY	CGR ↓ ↑ da/dn	● HOMOGENEOUS CRACK TIP PLASTICITY	↑ CGR da/dn ↓
● STRONG MICROSTRUCTURAL BARRIER	↑ CGR da/dn ↓	● WEAK MICROSTRUCTURAL BARRIER	CGR ↓ ↑ da/dn

HYPOTRANSITIONAL REGION		HYPERTRANSITIONAL REGION	
FACTORS AFFECTING FATIGUE CRACK GROWTH	EFFECTS RELATIVE TO HYPERTRANSITIONAL REGION	FACTORS AFFECTING FATIGUE CRACK GROWTH	EFFECTS RELATIVE TO HYPOTRANSITIONAL REGION
● CONTINUUM-MODE CRACK PATH	↑ CDF ↑ da/dn	● STRUCTURE-SENSITIVE CRACK PATH AND CRACK DEFLECTION	CDF ↓ da/dn ↓
● HOMOGENEOUS CRACK TIP PLASTICITY	↑ CGR da/dn ↓	● DIRECTIONAL CRACK TIP PLASTICITY	CGR ↓ ↑ da/dn
● STRONG MICROSTRUCTURAL BARRIER	↑ CGR da/dn ↓	● WEAK MICROSTRUCTURAL BARRIER	CGR ↓ ↑ da/dn

Fig. 36 Types of fatigue crack growth curve transitions observed for titanium alloys and the factors that affect crack growth rates and hence the values of m_b and m_a, the exponents of linear approximations to the crack growth curves: CDF = Crack Driving Force; CGR = Crack Growth Resistance

FRACTOGRAPHIC INVESTIGATION OF IMI685 CRACK PROPAGATION SPECIMENS FOR SMP SC33.

by

Chris Wilkinson
Defence Research Agency
Pyestock, Farnborough
Hants. GU14 OLS. UK

and

Paul Heuler
Industrieanlagen-Betriebsgesellschaft mbH
Einsteinstrasse 20, D-8012 Ottobrunn
Germany

Summary

Fracture surfaces from compact tension and corner crack specimens have been examined for various complex waveforms. Features have been related to the various stages of crack growth, as well as to the known response of the material.

1. Introduction

IMI685 is a beta processed titanium alloy. Al is added as an alpha stabiliser, Zr as an alpha /beta strengthener, Mo as a beta stabiliser whilst Si is added to improve tensile and creep properties. The alloy is heat treated at about 1050°C followed by an oil quench, which results in a martensitic transformation of the beta to alpha/beta lathes. If slower cooling rates are employed, filmy alpha occurs at the grain boundaries prior to the transformation tc a more coarse alpha/beta structure. Ageing at 550°C re-distributes the dislocation structure.

2. Heat Treatment

Five engine discs in IMI 685 were allocated to the programme[1]. The heat treatment was:-

Solution Treat	1050°C	1\2H	O.Q.
Age	550°C	24H	A.C.

From the limited micrographs available the grain size was estimated as ASTM 3.7

3. Fractography

Specimens discussed here represent the extremes of the test conditions used i.e Type 1, Type 4, Turb10, Turb50 and Full Turbistan.

3.1 Compact Tension Specimens

The first specimen to be examined had been subjected to a Type 1 waveform in which the minor cycle R ratio = 0.9. Early stages of crack growth contained areas of angular fracture as well as quasi-cleavage fractures, Fig.1: facets containing very fine ductile dimpling which indicated that a mixed mode of trans and inter granular growth was occurring.

Away from the notch, areas were found where irregular lines were observed on angular features, Fig.2. As the lines are often parallel to the growth direction it is unlikely that they are striations. NLR have observed similar features which they call "W" lines. These probably correspond to underlying microstructural features such as alpha/beta lathes and should not be confused with striations.

Specimens tested with the Type 4 waveform (minor cycle R=0.1) exhibited highly faceted fracture with plenty of evidence cf striated crack growth, Fig.3. This was in marked contrast to the previous specimens where the Type 1 waveform produced few signs of striated crack growth.

With the complex Turbistan cycles it was more difficult to identify uniform striated regions from any portion of the fracture surface.

The fracture surface of the specimen subjected to the Turb10 waveform contained a number of areas where "W" lines perpendicular to the growth axis existed. In addition, it was possible to find a

few isolated regions containing faint striations, Fig.4.

The Turb50 waveform should have been more likely to produce a well defined striated structure, however little or no evidence was observed of well defined striations. The fracture surface contained faceted regions and areas of angular fracture, indicating a mixture of trans and inter granular failure.

3.2 Corner Crack Specimens

In stark contrast, the corner crack specimens showed more regular striated growth than the corresponding compact tension specimen.

The specimen subjected to the Type 1 waveform showed evidence of striated crack growth of regular spacing throughout the fracture surface. There was evidence of significantly different crack growth rates in adjacent grains, Fig.5. For a material with a grain size of approximately 1mm, short crack growth effects would be evident up to crack depths of 2 or 3mm.

The fracture surface of the specimen subjected to the Type 4 waveform was expected to show clearly the overload cycle in contrast to the minor cycles. The striations that were observed were not as well defined as in the previous specimen and were more widely spaced, Fig.6. It is believed that the overload cycle is the only one that is forming a resolvable striation.

Testing with the Turb10 waveform produced faint striations on facets close to the notch. Evidence of well defined striated growth was also observed close to the final fracture, Fig.7. It is difficult to decide whether the area was originally all striated and subsequently damaged or the visible striations occurred in lathes oriented parallel to the growth direction.

The only corner crack specimen not to show appreciable amounts of striated growth was that subjected to the Turb50 waveform. As with the corresponding CT specimen the fracture surface contained faceted areas and inter-granular fracture but no where were there any well defined striations.

The most interesting fracture surface was a corner crack specimen that had been subjected to the Full Turbistan cycle. The crack growth data showed a significant increase and a later retardation of crack growth rate for a crack length from 0.6 to 1.8 mm. Examination of the fracture surface showed that this corresponded to a large facet containing well defined striations, Fig.8. From the striated regions it was possible to estimate the crack growth rates and these corresponded well with the bulk results.

In contrast to the good agreement for a large facet close to the notch, striated regions close to the overload did not correlate with the bulk crack growth rates. If the crack is longer than about two or three grain diameters then the short crack effect is unlikely and continuum mechanics will apply.

4. Conclusions

Deformation of the material is by intense planar slip on planes close to the basal plane. Dislocation pile-up occurs in the beta lathes until shearing of the alpha lathes occurs. This may be mistaken for irregular striation. Some early cracking may be inter-granular in appearance. Fractures are typically faceted combined with significant amounts of secondary cracking. Some facets may appear featureless however at high magnifications it is possible to resolve ductile dimpling on a very fine scale. This is termed quasi-cleavage fracture. Some of the facets exhibit striated growth which may appear regular or irregular, depending on the packet orientation that the crack is passing through. Final fracture is of a ductile nature.

Due to the large grain size of IMI685 it is difficult to draw any firm conclusions as to the effect of various waveforms on the mode of fracture.

Reference

(1) AGARD: Co-operative Programme on Aircraft Engine Discs - Supplementary Programme Material Evaluation. C. Howland; Rolls Royce Internal Report MEG030360 Nov 1987.

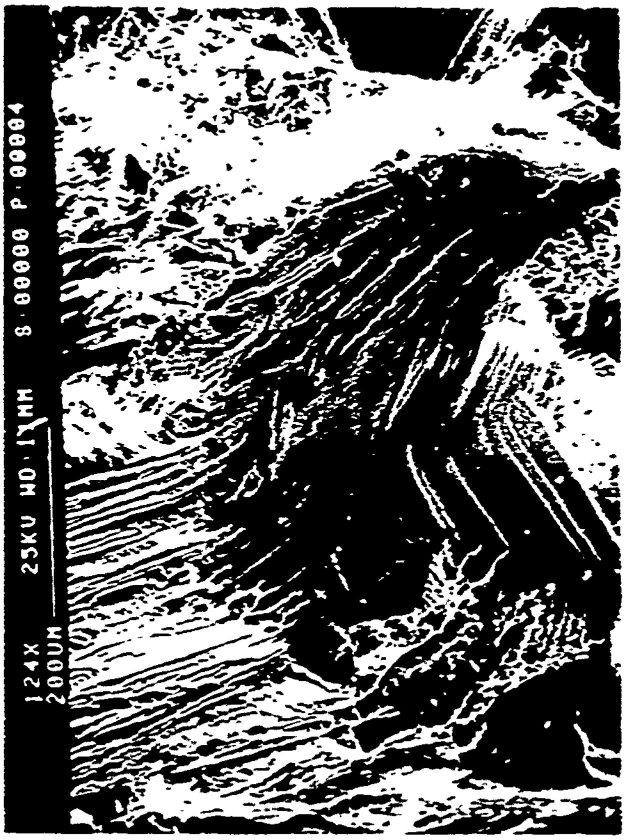

Fig.1 Quasi-cleavage fracture

Fig.3 Striated growth on all facets

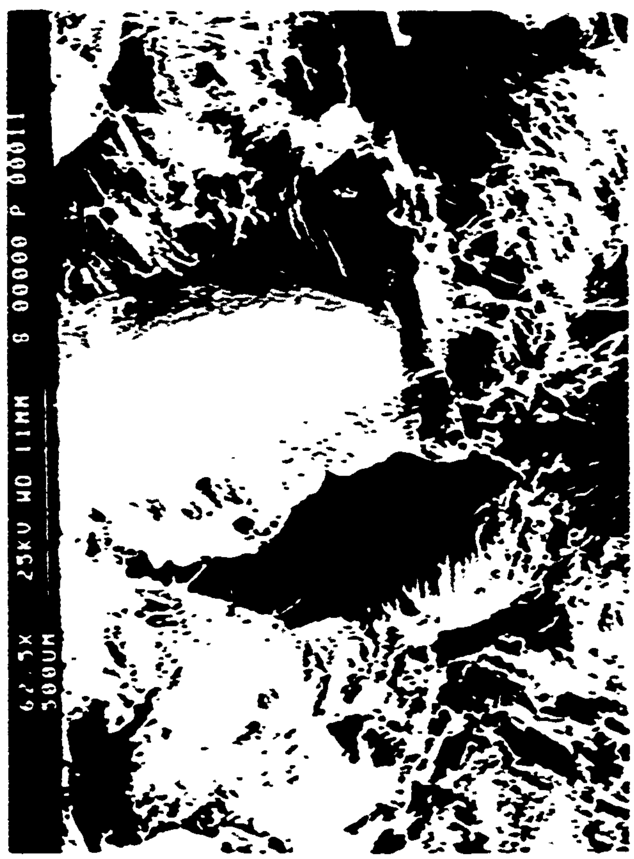

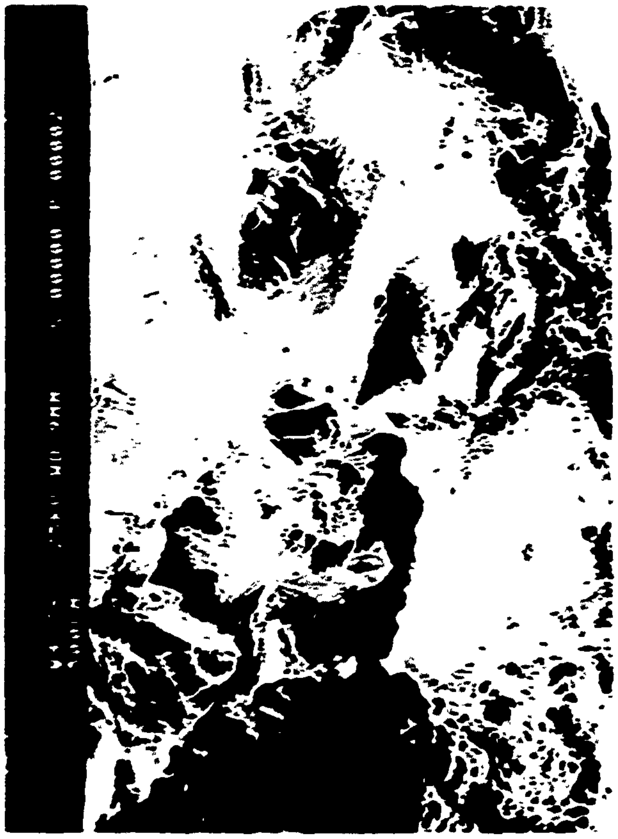

Fig.5 Large variation in striations

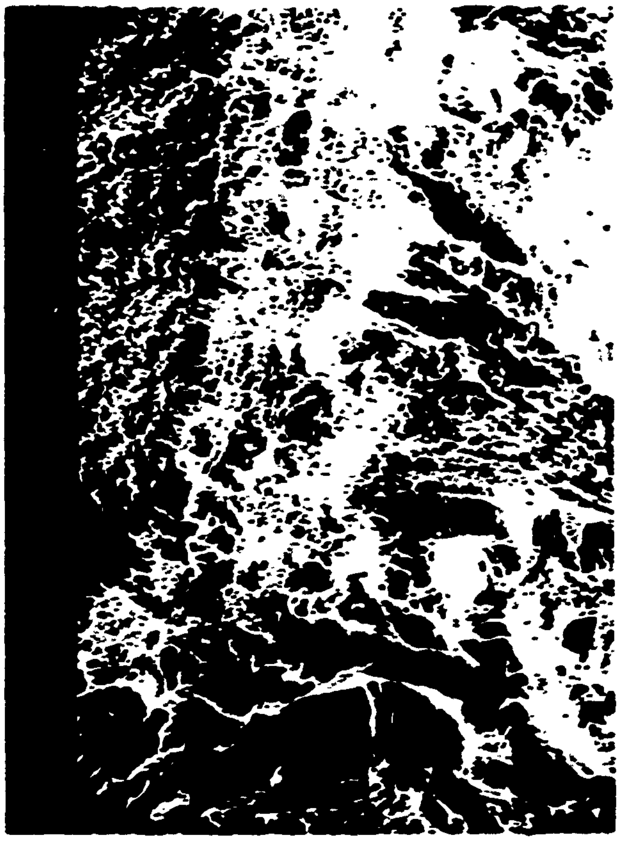

Fig.7 Localised striations.

Fig.6 Wide spaced striation

Fig.8 Large facet 0.6-1.8mm

MATERIAL CHARACTERIZATION AND FRACTOGRAPHIC EXAMINATION OF Ti-17 FATIGUE CRACK GROWTH SPECIMENS FOR SMP SC33

Marko Yanishevsky
Bryan Cornwall*
Martin Roth
Quality Engineering Test Establishment
Department of National Defence
Ottawa, Ontario, K1A 0K2
Canada

Summary

This annex contains material characterization and metallographic examination of the Ti-17 material tested as part of the Supplemental Programme for Engine Disc Damage Tolerance Testing AGARD SC33 (Refs 1 and 2). As well, a complete fractographic examination is provided for the compact tension specimens tested under the six types of simple spectra load conditions and the four levels of load excursion damage level omission of the complex spectrum TURBISTAN, this latter spectrum representing NATO gas turbine engine missions used in fighter aircraft applications (Ref 3).

1. Description of the Disc

The Ti-17 (Ti-5Al-2Sn-2Zr-4Mo-4Cr) forged and machined disc utilized in this study was received from General Electric Inc. and had undergone the full processing and heat treatment cycle for the stage 1 and 2 compressor rotor disc employed in F404 gas turbine engines powering CF188 aircraft. The compact tension (CT) specimens tested at QETE were removed from the upper, lower and vertical web sections of the disc in C-R, C-T, R-C and T-C orientations, where C is the circumferential, R is the radial and T is the thickness direction.

2. Material Characterization

A chemical analysis of the Ti-17 disc material tested was conducted and the results are presented in Table 1. The aluminium, tin, molybdenum, chromium and iron elements were analyzed using atomic absorption. Carbon was analyzed using a high frequency induction furnace, where the products of combustion were passed through a catalyst converting any carbon monoxide present to carbon dioxide, and the carbon content was measured in the carbon infrared cell. The zirconium content was determined using the Mandelic Acid Method. The elements oxygen, nitrogen and hydrogen were analyzed at CANMET/MTL. Oxygen and nitrogen content was determined using the Inert Gas Fusion technique; hydrogen was measured using the Hot Extraction Method.

A metallographic investigation was conducted in the three areas of the disc where the CT fatigue crack propagation specimens were extracted, i.e., the thin sections of the upper and lower discs and the vertical web. In each case the microstructure was examined in three orthogonal planes (perpendicular to the radial, circumferential and thickness directions). In addition, a section of the lower web was also investigated in a plane perpendicular to the circumferential direction.

The microstructure of the Ti-17 alloy was characteristic of beta processed, beta rich alpha-beta titanium alloys, where the alpha phase was present along a large portion of the former high temperature beta grains and where the grain interiors consisted of alpha Widmanstätten plates within the beta matrix (Photos 1 and 2). High

* Presently at Queen's University, Dept. of Mechanical Engineering, Kingston, Ontario, K7L 3N6, Canada.

Table 1. Chemical Composition of the Ti-17 Disc Material

Alloying Element	Weight % of Alloy Nominal	Range	Actual
Aluminium	5.0	4.5 - 5.5	4.82
Tin	2.0	1.5 - 2.5	1.87
Zirconium	2.0	1.5 - 2.5	1.92
Molybdenum	4.0	3.5 - 4.5	3.94
Chromium	4.0	3.5 - 4.5	4.23
Carbon	-	-	0.011
Oxygen	0.10	0.08-0.13	0.09
Nitrogen	-	0.04 max	0.005
Hydrogen	-	0.0125 max	0.0015
Iron	-	0.30 max	0.0015

Table 2. Ti-17 Grain Size Based Upon the Linear Intercept Method (Ref 4)

LOCATION	RADIAL DIR'N (mm)	CIRCUMFERENTIAL DIR'N (mm)	THICKNESS DIR'N (mm)
Upper web	0.33 / 0.36	0.33 / 0.36	0.17 / 0.16
Lower web	0.36 / 0.34	0.40 / 0.35	0.17 / 0.16
Vertical web	0.25 / 0.21	0.31 / 0.34	0.44 / 0.28

Note 1. The radial and thickness direction measurements carried out on the vertical web were offset approximately 30 degrees to obtain the maximum and minimum ranges of these grain sizes.

Note 2. Difficulties in differentiating grains in the thickness direction of the vertical web affected the accuracy of these measurements.

TABLE 3. FRACTOGRAPHY SUMMARY

SPECIMEN NUMBER	LOAD SEQUENCE	δK or Kmax (6 MPa√m)	δK or Kmax (10 MPa√m)	δK or Kmax (20 MPa√m)	δK or Kmax (35 MPa√m)
	SIMPLE				
CT5A	0, R=0.1		Photo 17	Photo 18	Photo 19
CT6B	0, R=0.7	Photo 20	Photo 21		
CT1	1 (10%)		Photo 22	Photo 23	Photo 24
CT12	2 (30%)		Photo 25	Photo 26	Photo 27
CT7	3 (50%)		Photo 28	Photo 29	Photo 30
CT2	4 (170%)		Photo 31	Photo 32	Photo 33
	TURBISTAN				
CT10A	0 (Full)		Photo 34	Photo 35	Photo 36
CT24	1 (10%)		Photo 37	Photo 38	Photo 39
CT13	2 (30%)		Photo 40	Photo 41	Photo 42
CT5B	3 (50%)		Photo 43	Photo 44	Photo 45

magnification scanning electron microscopic (SEM) examination of the microstructure (Photo 3) revealed the presence of fine needle-like alpha plates in the beta phase indicative of material ageing (N.B. the SEM micrograph contrast is opposite to that in the optical micrographs). The grain boundary alpha phase width appeared to be typically 1 to 2 μm in thickness, slightly thicker than the Widmanstätten alpha plates.

The fairly large grain size of this material was revealed best under polarized light, as shown in Photo 4. Some grain flow and grain flattening were apparent in the planes of the upper, lower and vertical webs due to forging of the disc blank. The grain sizes were measured by the linear intercept method in three orthogonal directions (radial, circumferential and thickness) in areas typical of the fatigue crack propagation in the CT specimens. The grain sizes, given in Table 2, are the average intercept distance, Heyn intercept value, or mean free path in accordance with the ASTM E112 method (Ref 4), where two different specimens were used for grain size measurements in each direction.

Energy dispersive X-ray analyses of the alpha and beta phases revealed differences in the distribution of some of the alloying elements. Mo and Cr, known beta stabilizers, were found to be higher in the beta phase. Al, an alpha stabilizer and solid solution strengthener, was found to be slightly higher in the alpha phase. Sn and Zr, solid solution strengtheners, were found to be evenly distributed in both phases.

3. Fractographic Observations

Scanning electron microscope (SEM) examination was performed on samples selected to cover the ten different loading conditions investigated in this study.

3.1 General Observations

Under all loading conditions, the fatigue fractographic features were influenced by the microstructure, mainly the orientation of the alpha plates which varied from one prior beta grain to another. Under conditions corresponding to a low K_{max} value, typically 10 MPa√m, the prior beta grains were clearly recognizable because of changes in surface roughness and degree of facetting from grain to grain. Facetting occurred when fatigue cracking followed favourably orientated alpha plates at an angle to the macroscopic crack plane (Photo 5). In some grains there was secondary cracking along the set of alpha plates with its orientation most closely approaching that of the macroscopic crack front. Occasionally, fatigue striations were present on some of the facets associated with propagation along a suitably orientated alpha plate (Photo 6). At intermediate K_{max}, typically around 20 MPa√m, the macroscopic differences from one prior beta grain to another were less pronounced. Secondary cracking increased in severity (Photo 7) and sometimes occurred along two sets of alpha plates (Photo 8). Fatigue striations were also observed along alpha plates (Photo 8). At K_{max} approximately 35 MPa√m and higher, the fatigue surface became rougher and the differences between the grains less pronounced. These could still be distinguished by the change of orientation of the secondary cracking from grain to grain (Photo 9). Occasionally, the crack path followed the alpha phase along a prior beta grain boundary. The more readily observable fatigue striations were no longer restricted to favourably oriented alpha plates (Photo 10).

The local rate of crack advance per cycle was estimated from the spacing of the striations such as shown in Photos 6 and 8. Even within one grain, there appeared to be local variations. In Photo 8, the striation spacing was 0.5 μm (5E-7 m/cycle). Similar features in close proximity of to this site indicated striation spacings of 0.3 μm (3E-7 m/cycle). The corresponding macroscopic crack growth rate obtained by the potential drop technique was 0.2 μm (2E-7 m/cycle).

The influence of the microstructure on fatigue crack propagation was clearly illustrated when the polished side of a cracked specimen was investigated in the SEM using the back scattered imaging mode revealing the microstructure (Photos 11 to 13). Generally, the cracking occurred across alpha plates (Photo 11); occasionally, the crack path followed a suitably oriented alpha plate (Photo 12). As K_{max} increased, cracking could occur along the alpha phase outlining the prior beta grains (Photo 13). Further insight into the cracking process is provided when the crack surface is viewed along with the microstructure in a plane perpendicular to the crack (Photo 14).

The overload failure in this material was characterized by coarse tearing along the prior beta grain boundaries at the macroscopic level (Photo 15) and ductile dimples at the microscopic level (Photo 16).

3.2 Detailed Observations

Detailed SEM fractographic examination was performed on samples selected to cover the ten different loading cases investigated in this study. A summary of the photos taken are presented in Table 3. Whenever possible, the fatigue features were scrutinized in areas corresponding to stress intensity ranges, δK, of 10, 20 and 35 $MPa\sqrt{m}$ for Simple Sequences Types 0 (R=0.1), 1, 2, 3 and 4, and corresponding K_{max} values for all four of the TURBISTAN load sequences. For the load sequence Type 0 with R=0.7, fatigue features were examined corresponding to δK values of 6 and 10 $MPa\sqrt{m}$. This approach facilitated comparison of the cracking behaviour between the various specimens. To portray typical features at each δK or K_{max} level, four photos were taken: a low magnification photo to show the entire width of the sample, a X200 magnification photo with back-scattered detector turned half on to illustrate differences between grains with different orientations, and two higher magnification photos (typically at X1000) to illustrate the fatigue features in more detail. In all photos the direction of crack propagation is from the bottom of the photo to the top.

3.2.1 Simple Sequence Type 0, R=0.1, Specimen CT5A

At the low δK value of 10 $MPa\sqrt{m}$, the fatigue fractographic features were very dependent on the microstructure, specifically the orientation of the alpha plates, which varies from one prior beta grain to another. At low to intermediate magnifications, the prior beta grains were clearly recognizable because of changes in surface roughness and degree of facetting (Photos 17a and 17b). In some of these grains, the microscopic plane of cracking coincided with the macroscopic one and the fatigue crack surface was relatively smooth (Photos 17b and 17c). In some other grains, crack propagation occurred in part along favourably oriented alpha plates at an angle to the macroscopic crack plane leading to a rough facetted surface (Photo 17d). High magnification examination revealed the existence of secondary cracking along the set of alpha plates with its orientation most closely approaching that of the macroscopic crack front.

At intermediate δK values (approximately 20 $MPa\sqrt{m}$), the fatigue features were still dependent on the microstructure, but the macroscopic differences from one prior beta grain to another were less pronounced (Photos 18a and 18b). Secondary cracking was more severe than at the lower δK level and in some cases the cracking occurred along two sets of alpha plates (Photos 18c and 18d).

At high δK levels near 35 $MPa\sqrt{m}$, the fatigue surface became rougher and the differences between grains less pronounced (Photos 19a and 19b). These could still be distinguished by the changes in the orientation of the secondary cracking from grain to grain (Photo 19b). In some grains, the secondary cracking was very pronounced (Photo 19c). Indicative of crack propagation at higher δK in some grains was quasi-overload characterized by dimple-like features, combined with other fatigue cracking features (Photo 19d).

3.2.2 Simple Sequence Type 0, R=0.7, Specimen CT6B

At high R values, K_{max} will approach the fracture toughness K_{IC} of the material at much lower δK values than in the case of low R values. As such, K_{max} is approximately the same at δK=6 MPa√m with R=0.7 and at δK=20 MPa√m when R=0.1, and δK=10 MPa√m with R=0.7 and at δK=35 MPa√m when R=0.1.

At δK=6 MPa√m, the roughness and extent of facetting were very grain dependent (Photos 20a and 20b), and quite similar to the features of Photos 17a and 17b. At higher magnification, there was evidence of secondary cracking along favourably oriented alpha plates (Photos 20c and 20d). At δK=10 MPa√m, where K_{max} approached K_{IC}, the crack surface was quite rough and at low magnification, it was not possible to recognize the prior beta grains (Photos 21a, 21b and 21c). Occasional significant local deviation of the crack from the macroscopic crack plane, possibly along the alpha phase outlining the prior beta grain boundaries, could be observed among areas with fatigue features typical of this material (Photo 21d).

Comparing the fractographic features at R=0.1 and 0.7 revealed similar features in situations corresponding approximately to the same K_{max} rather than δK.

3.2.3 Simple Sequence Type 1, 10% Minor Cycles, Specimen CT1

The fatigue fractographic features were quite similar to those observed under Type 0 loading with R=0.1. At low δK, the variations in surface roughness and facetting from prior beta grain to grain were also quite noticeable (Photos 22a and 22b). The facetting was associated with local crack propagation along alpha plates (Photos 22c and 22d). As δK increased, so did the extent of secondary cracking (Photos 23b to 23d). At the same time, the macroscopic fractographic differences between former beta grains diminished as can be seen when Photos 22a (δK=10 MPa√m), 23a (δK=20 MPa√m) and 24a (δK=35 MPa√m), in addition to the severe secondary cracking usually along more than one set of alpha plates, some coarse striations were observed (Photos 24c and 24d). The average striation spacing was about 1 µm (1E-6 m/cycle), while the macroscopic growth rate was 1.9 µm (1.9E-6 m/cycle). There were local variations in the direction of crack growth as indicated by the orientation of some of the striations (Photos 24d).

3.2.4 Simple Sequence Type 2, 30% Minor Cycles, Specimen CT12

There were no marked fractographic differences compared to the previous loading sequence. Some of the photos, illustrate well cases of facetting from preferential cracking along alpha plates (Photos 25d, 26c, 26d and 27c). At high δK, well defined coarse fatigue striations were observed when cracking occurred along suitably oriented alpha plates, while there were no visible striations when the crack path was across the alpha plates. The fatigue striation spacing along the Photo 27c alpha plate was about 1.2E-6 m/cycle compared to a macroscopic crack growth rate per cycle of 1.7E-6 m/cycle.

3.2.5 Simple Sequence Type 3, 50% Minor Cycles, Specimen CT7

At low and intermediate magnifications, the fatigue features were similar to those for Type 0 trapezoidal waveforms and load sequences 1 and 2. At higher magnification, fatigue striations along suitably oriented alpha plates could be observed at δK as low as 10 MPa√m (Photo 28c). As δK increased, the fatigue striation spacings increased from 0.6 µm (6E-7 m/cycle) at δK=20 MPa√m (Photo 29d) to 1.6 µm (1.6E-6 m/cycle) at δK=35 MPa√m (Photo 30c): the corresponding macroscopic crack advances per cycle were 0.46 µm (4.6E-7 m/cycle) and 4.2 µm (4.2E-6 m/cycle respectively. As K_{max} approached K_{IC}, areas with ductile dimples were present (Photos 30d).

3.2.6 Simple Sequence Type 4, 170% Overload, Specimen CT2

The 170% spike overload every 1000 cycles induced well defined beach marks which indicated clearly the location of the crack front as the crack propagated (Photos 31b, 31c, 32a and 33a). There was significant crack front curvature and the local crack growth direction was occasionally quite different from the macroscopic direction (Photos 31b and 31d). The crack growth was faster in some grains than in the adjacent ones (Photos 32b). At higher δK, the beach marks were in fact a narrow band with overload features (Photos 33b and 33d); between these marks, typical fatigue features were observed.

3.2.7 Full TURBISTAN, Specimen CT10A

At low and intermediate magnification, the fatigue fractographic features were very similar to those under constant amplitude Type 0 loading with R=0.1. At K_{max}=10 MPa$\sqrt{m}$, the crack path followed favourably oriented alpha plates in some grains (Photo 34c); the extent of secondary cracking varied from grain to grain. As K_{max} increased, so did the secondary cracking (Photo 35d). At K_{max}=20 MPa$\sqrt{m}$ some faint striations were observed when the crack followed alpha plates (Photo 35d). At higher K_{max}, the fatigue striations, where observable, showed variable spacing typical of spectrum loading (Photo 36d).

3.2.8 TURBISTAN 10% Damage Omission, Specimen CT24

Compared to the Full TURBISTAN, there were no noticeable differences in the fatigue fractographic features. Resolvable fatigue striations were observed along some of the alpha plates at K_{max} around 20 MPa$\sqrt{m}$ (Photo 38d). As K_{max} increased with crack depth, the striations became coarser (Photos 39c and 39d).

3.2.9 TURBISTAN 30% Damage Omission, Specimen CT13

Omission of a greater proportion of the load cycles did not change the fractographic features compared to the Full TURBISTAN case. Some areas in this specimen illustrated clearly the geometric relationship between the alpha plates where crack propagation occurred along one set of plates and secondary cracking occurred along another set (Photo 40d). As in the previous case, fatigue striations were first observed along alpha plates at intermediate K_{max} (Photo 41d) and then more uniformly as K_{max} increased (Photos 42c and 42d).

3.2.10 TURBISTAN 50% Damage Omission, Specimen CT5B

In the final TURBISTAN sequence, the vast majority of cycles were of very large amplitude and low R ratio, and the fractographic features were very similar to those under constant amplitude loading at low R ratio at equivalent K_{max} values. As before, fatigue striations were first observed along alpha plates at intermediate K_{max} (Photo 44d) and these were more readily apparent and uniform in the K_{max}=35 MPa$\sqrt{m}$ case (Photos 45c and 45d).

4. Conclusions

Scanning electron microscope (SEM) fractography indicated that:

a. Under all loading conditions, the fatigue fractographic features were influenced by the microstructure, mainly the orientation of the alpha plates which varied from one prior beta grain to another.

b. At low levels of δK, the prior beta grains were clearly recognizable because of changes in surface roughness and degree of facetting from grain to grain, with the facetting occurring primarily when fatigue cracking followed favourably oriented alpha plates at an angle to the macroscopic crack plane. Secondary cracking was found to occur along alpha plates with the orientation most closely approaching that of the macroscopic crack front. Fatigue striations were present on some of the facets associated with crack propagation along a suitably oriented alpha plate.

c. At intermediate levels of δK around 20 MPa√m, the macroscopic differences from one prior beta grain to another were less pronounced. Secondary cracking increased in severity. Fatigue striations were also observed along alpha plates.

d. At δK approximately 35 MPa√m and higher, the fatigue surface became rougher and the differences between the grains less pronounced, with the grains being distinguished by the change of orientation of the secondary cracking from grain to grain. Occasionally, the crack path followed the alpha phase along a prior beta grain boundary. The more readily observable fatigue striations were no longer restricted to favourably oriented alpha plates.

e. The overload failure in this material was characterized by coarse tearing along the prior beta grain boundaries at the macroscopic level and ductile dimples at the microscopic level.

5. References

1. A.J.A. Mom and M.D. Raizenne, "AGARD Engine Disc Cooperative Test Programme", AGARD Report No. 766, August 1988.

2. M.D. Raizenne, "AGARD TX114 Test Procedures for Supplemental Engine Disc Test Programme, NAE/NRCC LTR-ST-1671, June 1988.

3. A.A. ten Have, "Cold Turbistan - Final Definition of a Standardized Fatigue Test Loading Sequence for Tactical Aircraft Cold Section Engine Discs", NLR TR 87054L, 31 March 1987.

4. American Society for Testing and Materials, "E112-88 Standard Test Methods for Determining Average Grain Size", 1990 Annual Book of ASTM Standards, Volume 3.01, pp. 282-307.

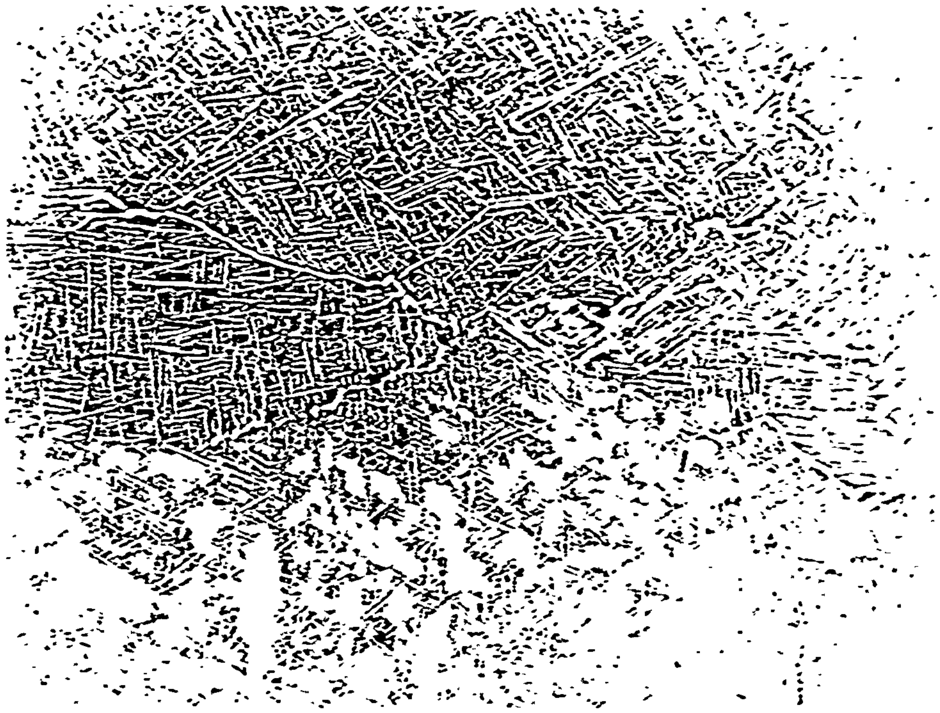

Keller's Etch PHOTO 1 X 400

Microstructure of the Ti-17 disc forging in the upper web in the first stage compressor.

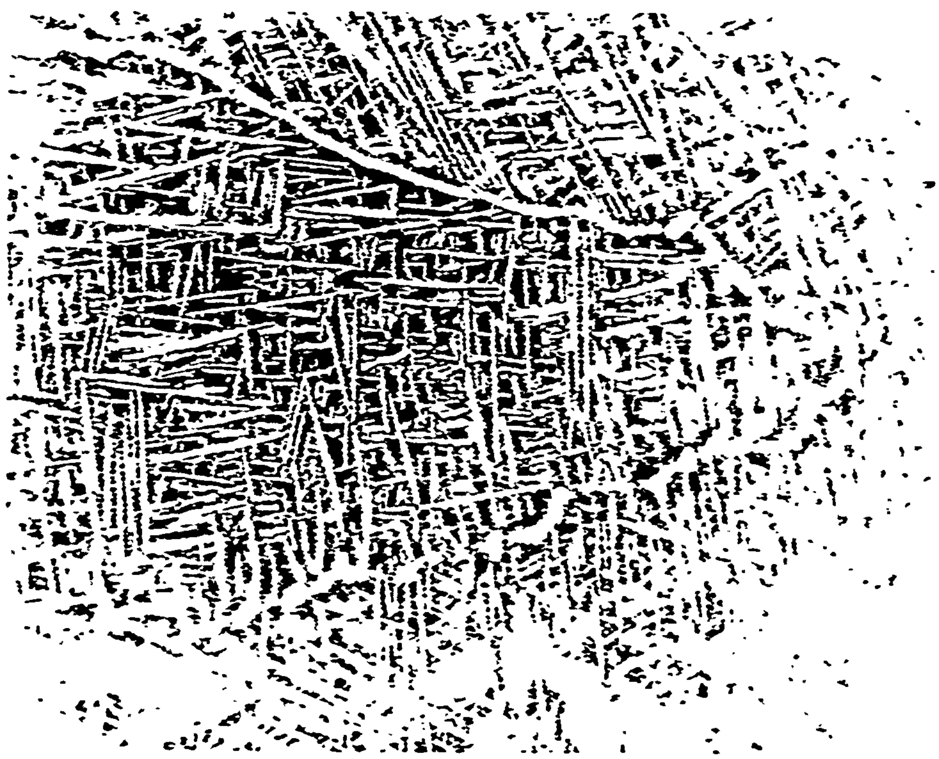

Keller's Etch PHOTO 2 X 1000

Details of the Ti-17 microstructure consisting of Widmanstätten alpha plates within a beta matrix and alpha phase outlining the prior beta grain boundaries.

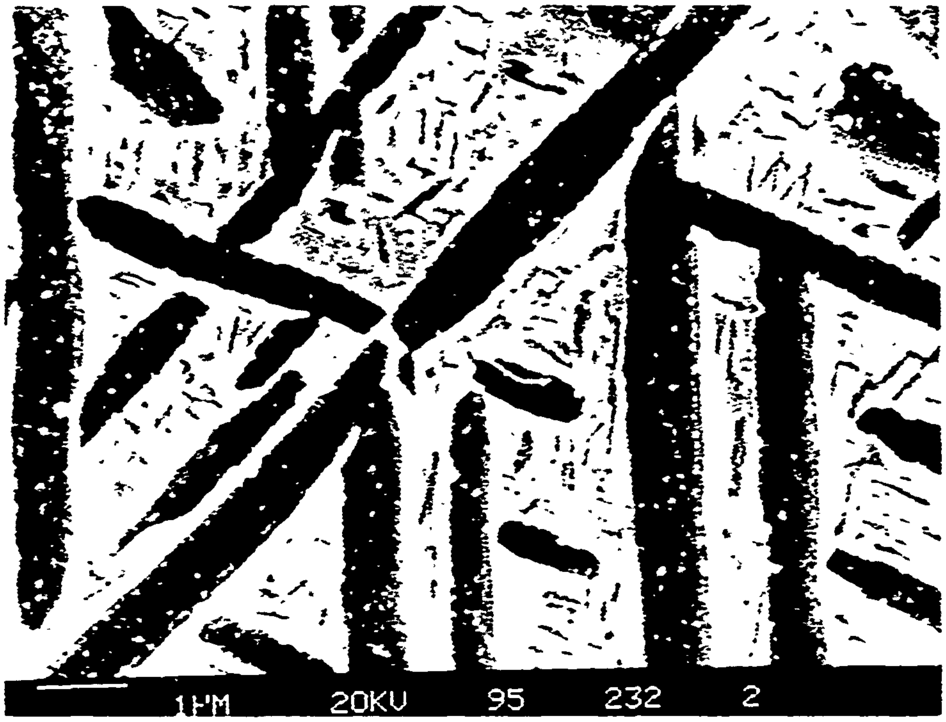

Keller's Etch PHOTO 3 X 10,000

SEM back-scattered electron imaging of the Ti-17 microstructure showing the Widmanstätten alpha plates (dark) and fine needle-like alpha phase within the beta phase indicative of ageing.

Keller's Etch PHOTO 4 X 100

Polarized light examination revealing the fairly large grain size of the Ti-17 alloy.

SEM PHOTO 5 X 500

Fatigue features with facetting and secondary cracking (Simple Sequence Type 0, R=0.1 loading, δK = 12 MPa√m, specimen 6A.

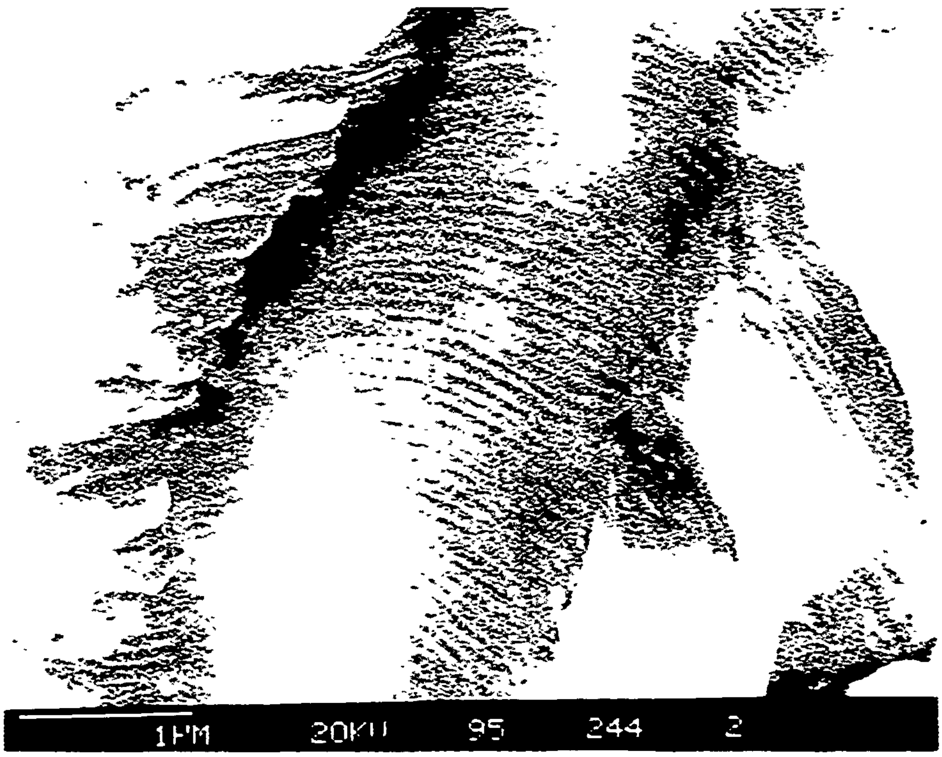

SEM PHOTO 6 X 20,000

Fatigue striations along an alpha plate in the field of Photo 5. The striation spacing is approximately 0.08 µm.

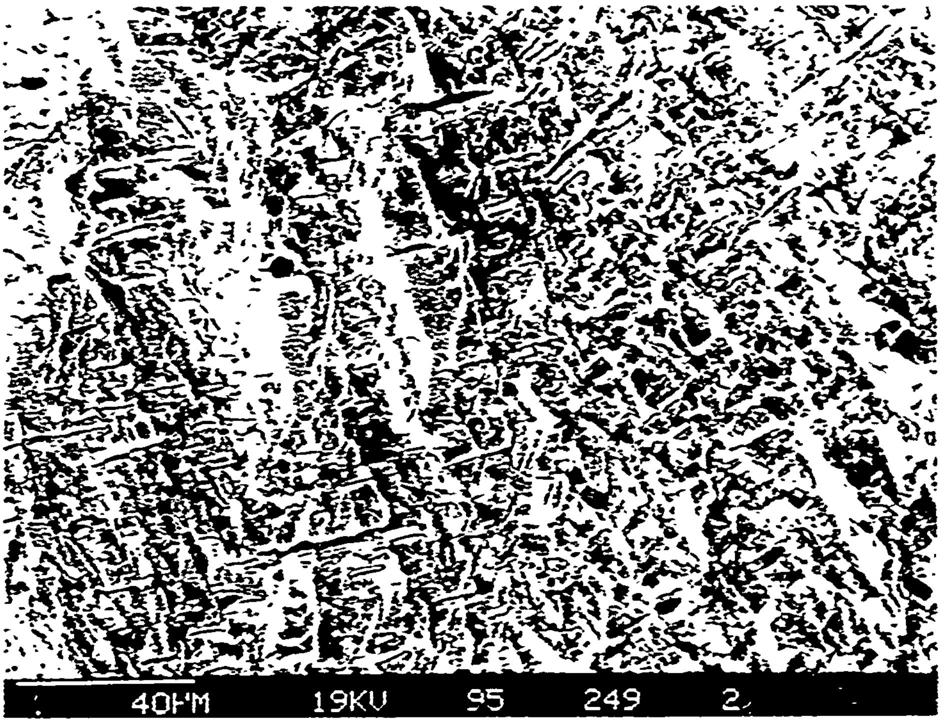

SEM PHOTO 7 X 500

Fatigue features with secondary cracking and some facetting (Simple Sequence Type 0, R=0.1 loading, δK = 20 MPa√m, specimen 6A).

SEM PHOTO 8 X 2000

Fatigue striations along an alpha plate in the field of Photo 7. The striation spacing is approximately 0.5 µm.

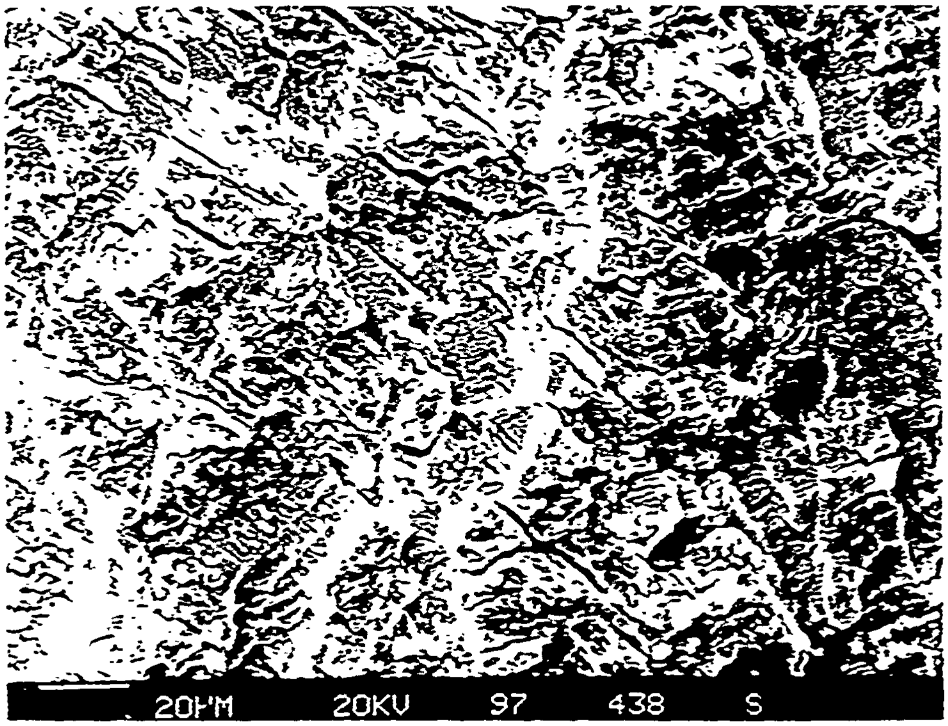

SEM PHOTO 9 X 500

Fatigue features as K_{max} approaches K_{Ic} of the material, (trapezoidal loading, R=0.1, δK = 34 MPa√m, specimen CT21).

SEM [illegible] X [illegible]

Fa[illegible]

SEM PHOTO 11 X 500

Back-scattered electron imaging of the side of specimen 16 showing the crack cutting across alpha plates (K_{max} = 18.5 MPa√m).

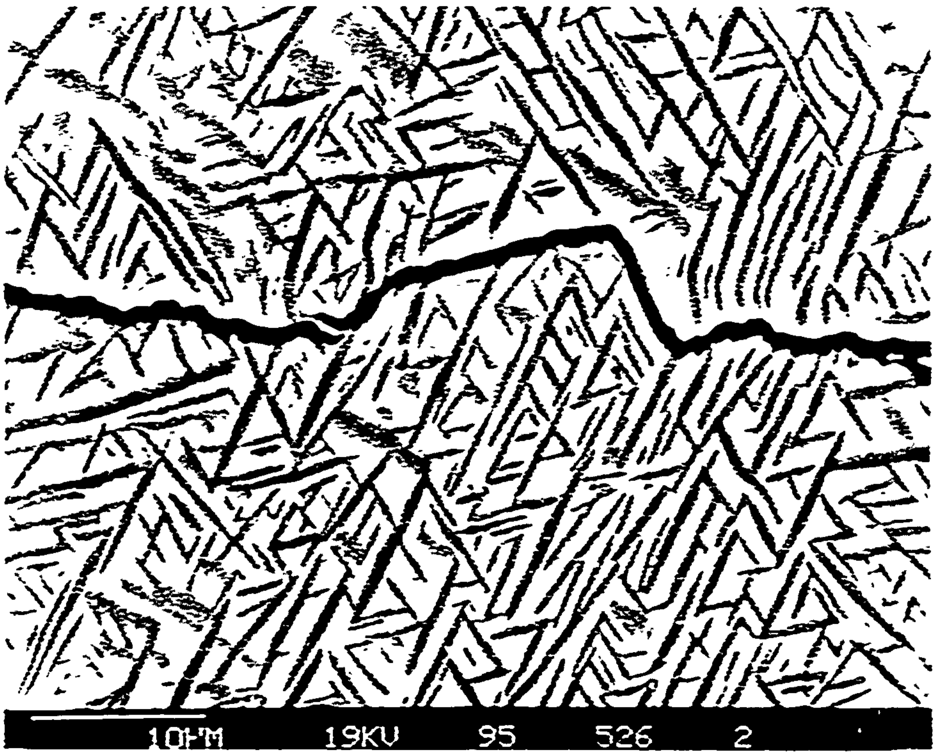

SEM PHOTO 12 X 2000

Back-scattered electron imaging of the side of specimen 16 showing the crack following a favourably oriented alpha plate (K_{max} = [illegible] MPa√m).

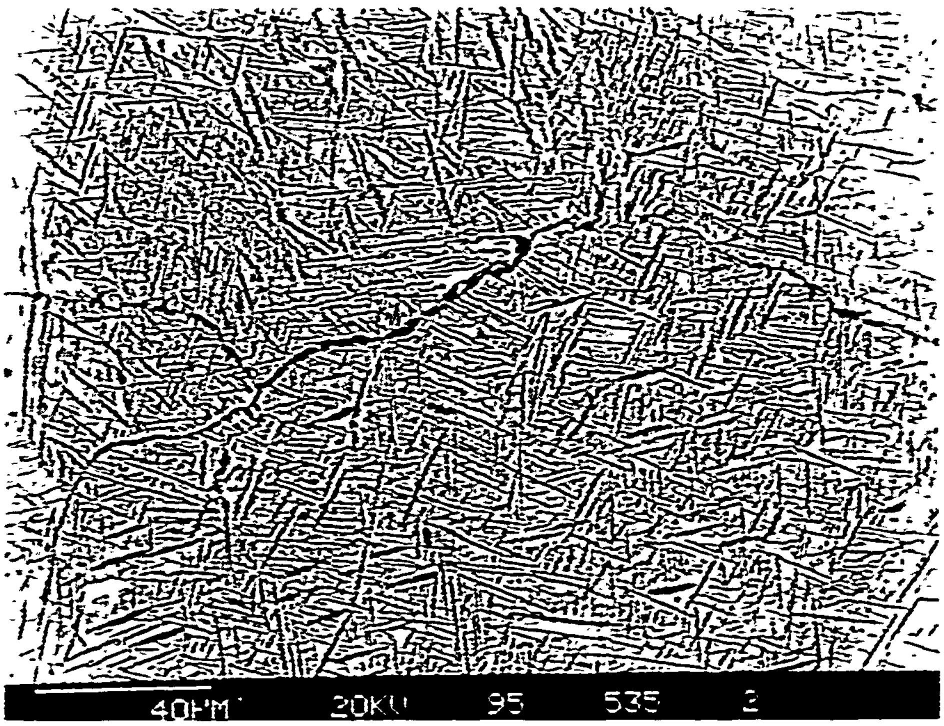

SEM PHOTO 13 X 500

Back-scattered electron imaging of the side of specimen 16 showing the crack following the alpha phase along the prior beta grain boundaries as K_{max} approaches K_{IC}.

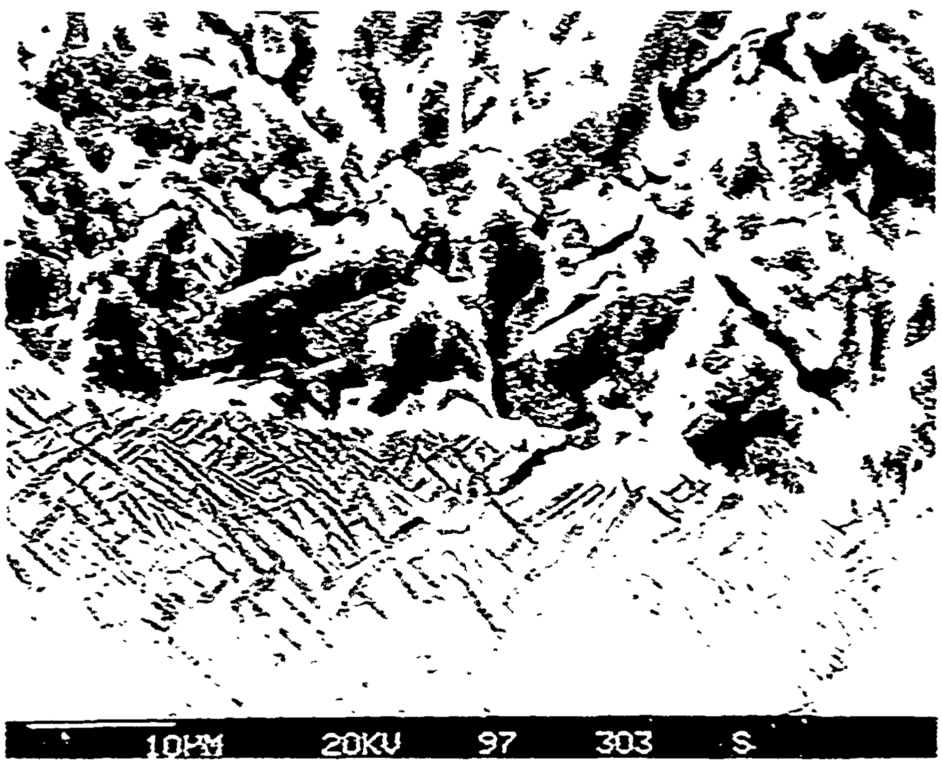

SEM PHOTO 14 X 1500

Fatigue crack features and microstructure in a plane perpendicular to the crack growth direction indicated by the arrow

SEM PHOTO 15 X 60

Overload coarse tearing along prior beta grain boundaries.

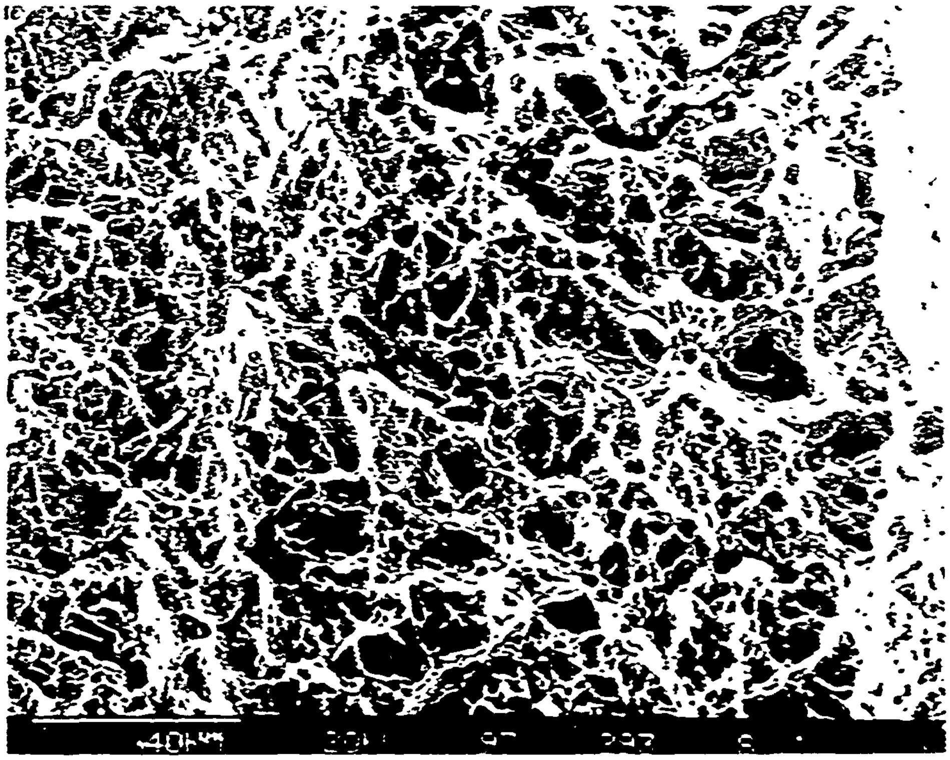

SEM PHOTO 16 X 600

Overload ductile dimples.

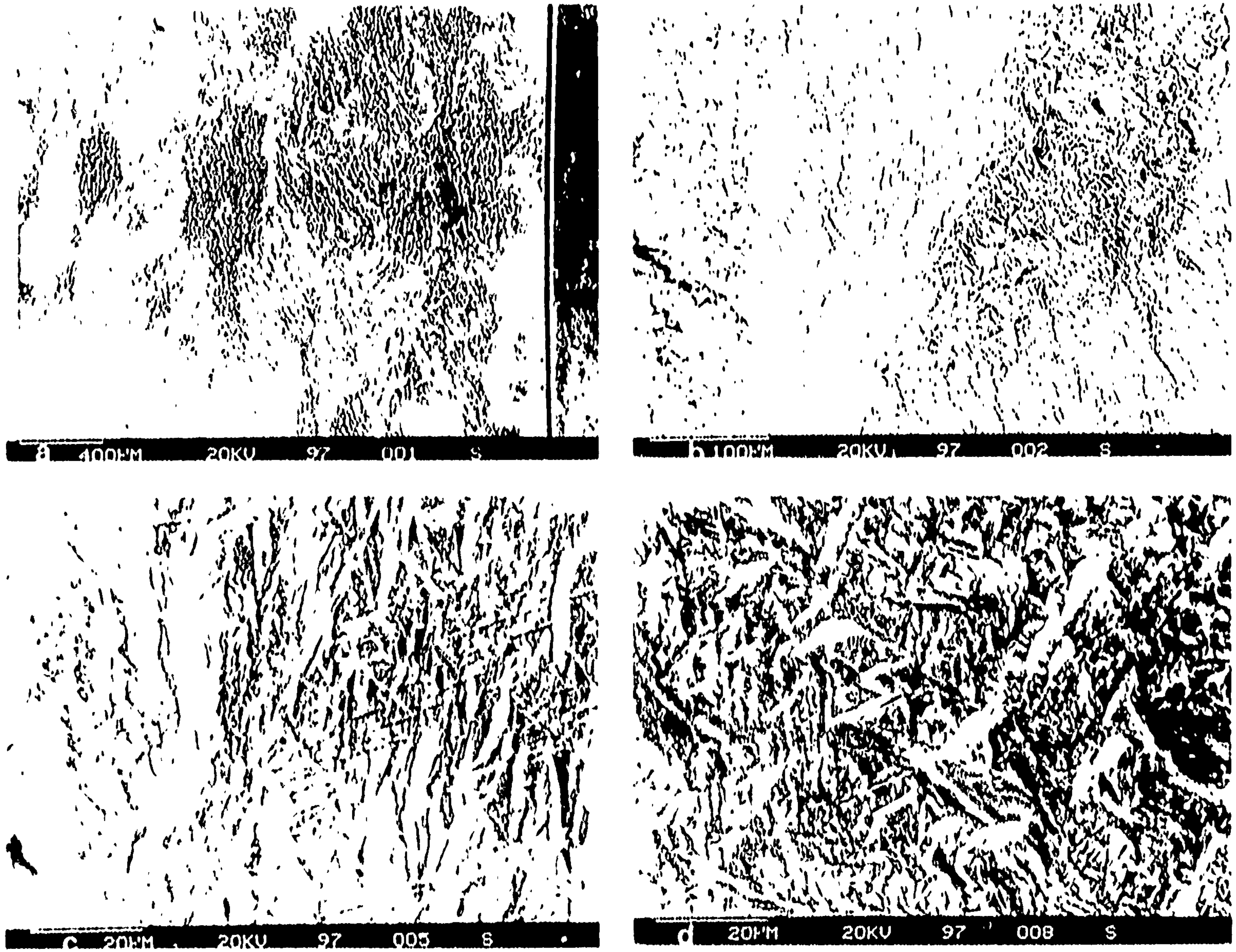

PHOTO 17 Fatigue fractographic features in specimen CT5A under Simple Spectrum Type 0 R 0.1 and ΔK 10 MPa√m. (a: 37X; b: 200X; c: 1000X; and d: 1000X).

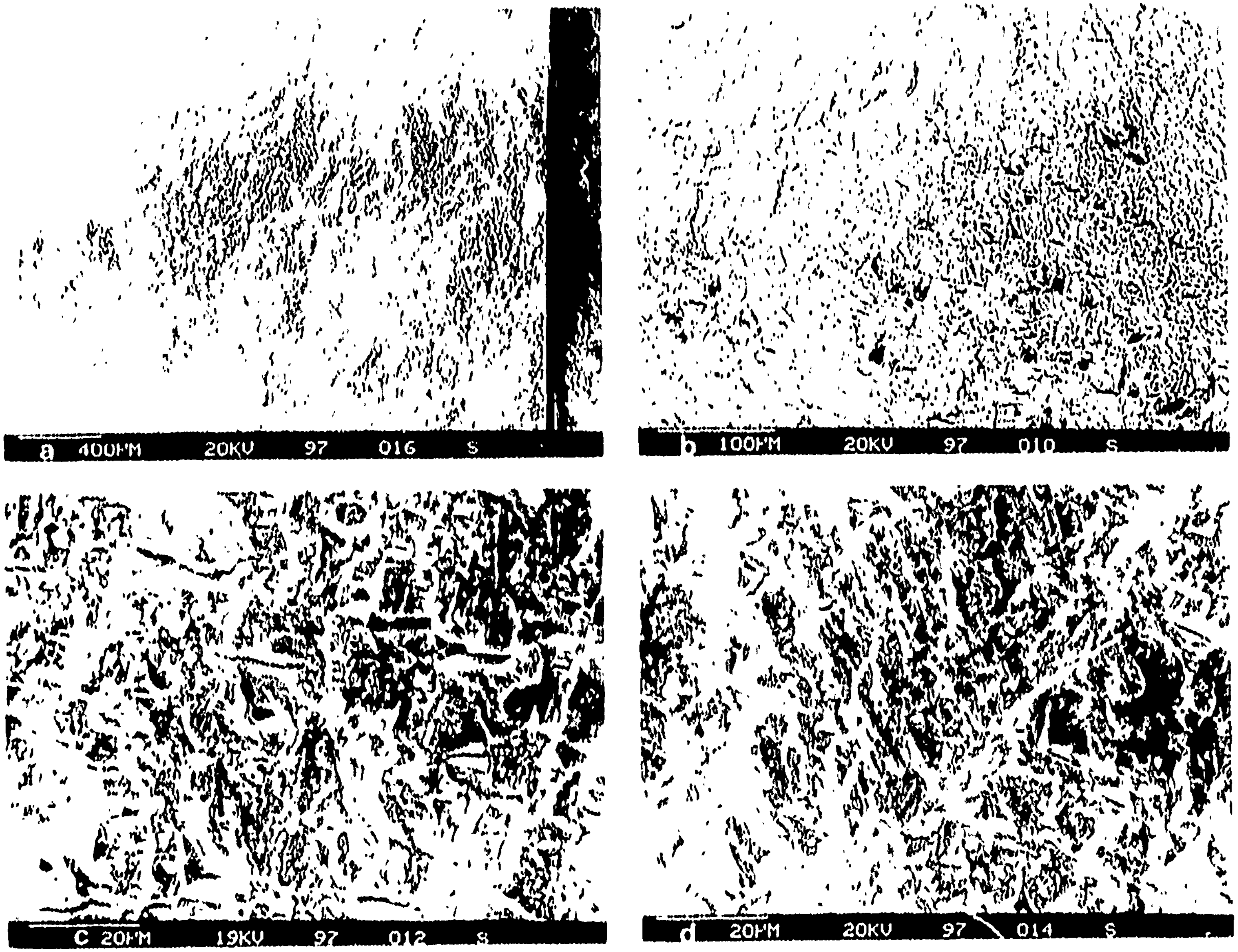

PHOTO 18 Fatigue fractographic features in specimen CT6A under Simple Spectrum Type 0, R 0.1 and ΔK 20 MPa√m. (a: 17X; b: 200X; c: 1000X; and d: 1000X)

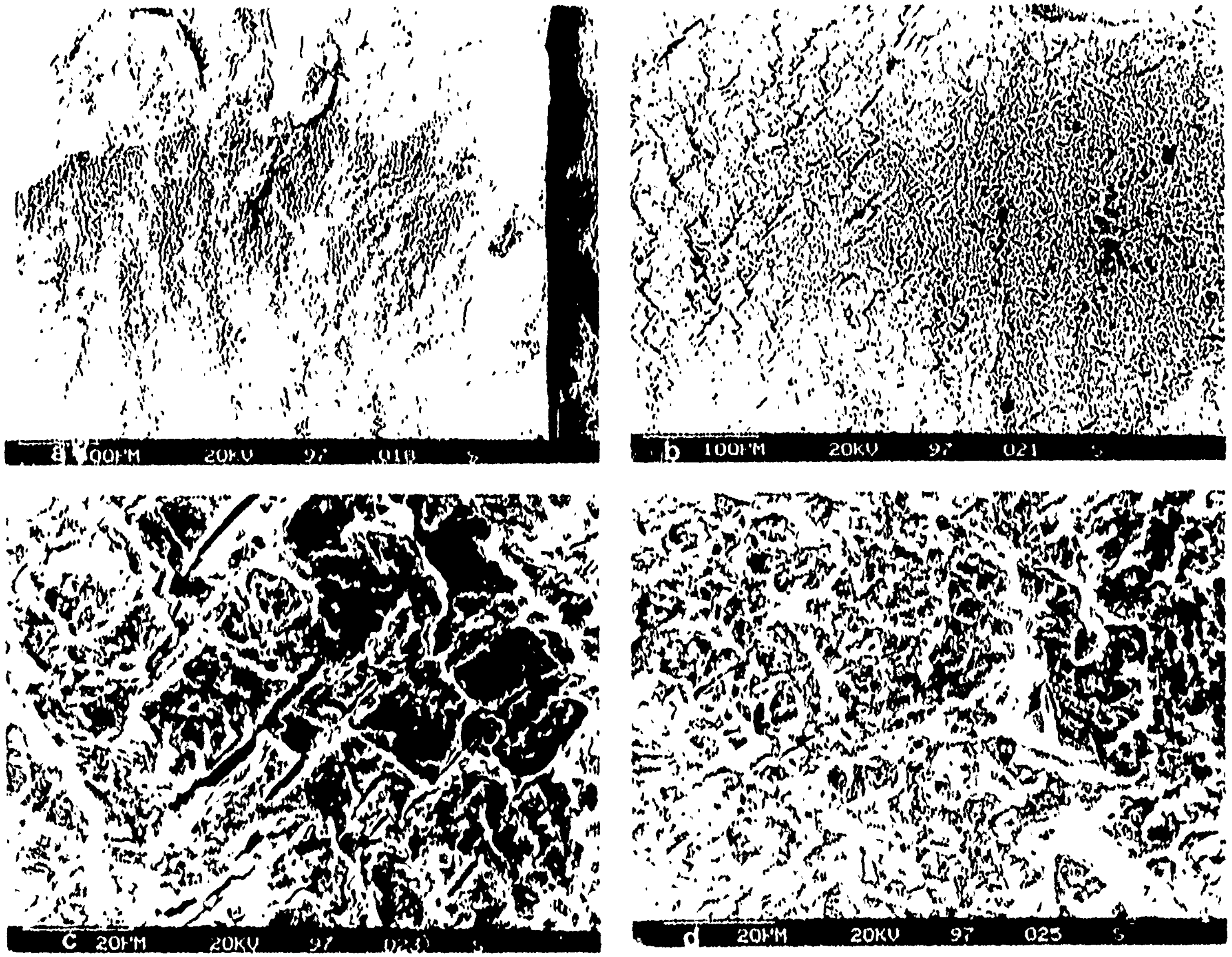

PHOTO 19 Fatigue fractographic features in specimen CT5A under Simple Spectrum Type 0, $R = 0.1$ and $\Delta K = 35$ MPa$\sqrt{m}$. (a: 37X; b: 200X; c: 1000X; and d: 1000X).

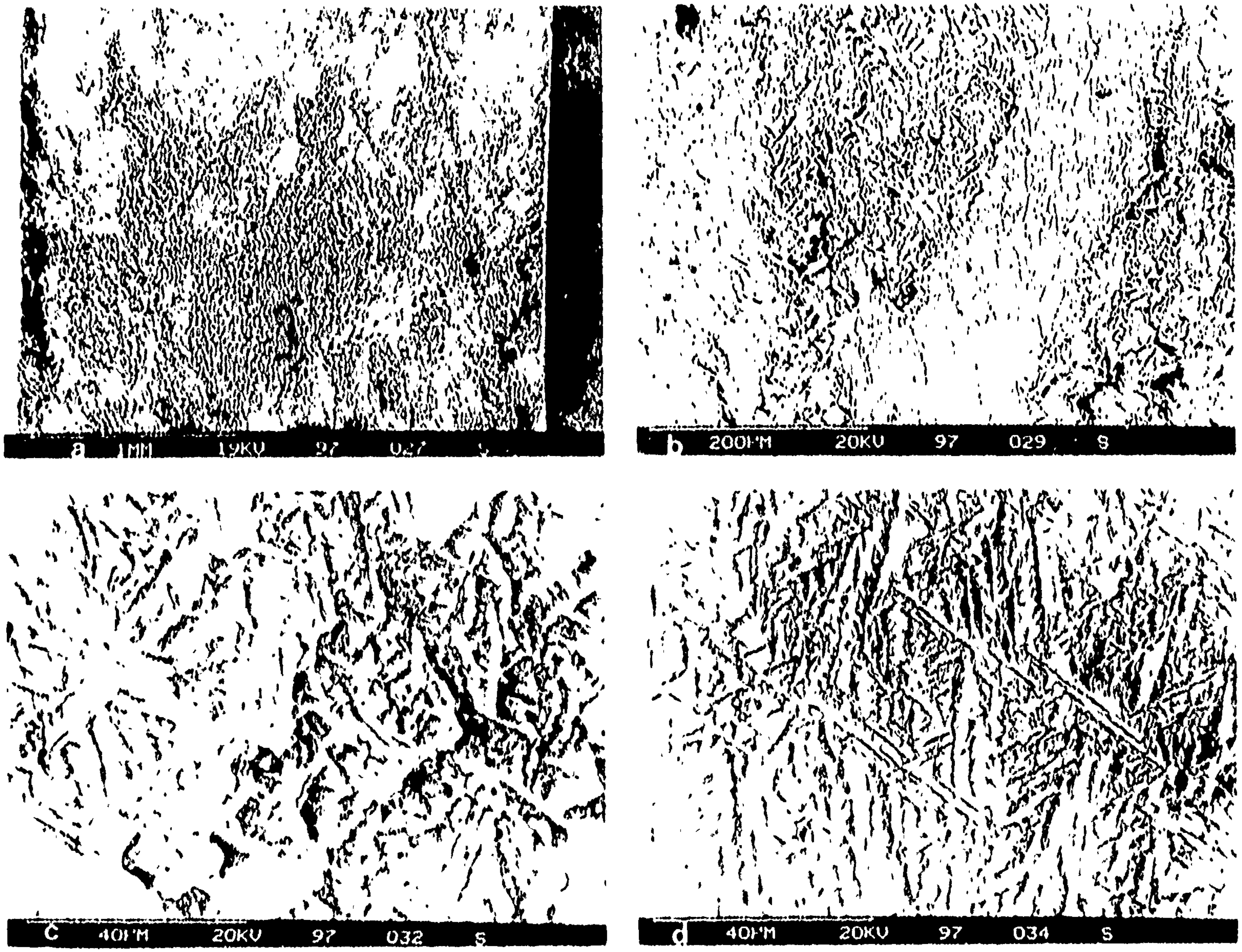

PHOTO 20 Fatigue fractographic features in specimen CT6B under Simple Spectrum Type 0, R=0.7 and ΔK = 6 MPa√m. (a: 37X; b: 200X; c: 1000X; and d: 1000X).

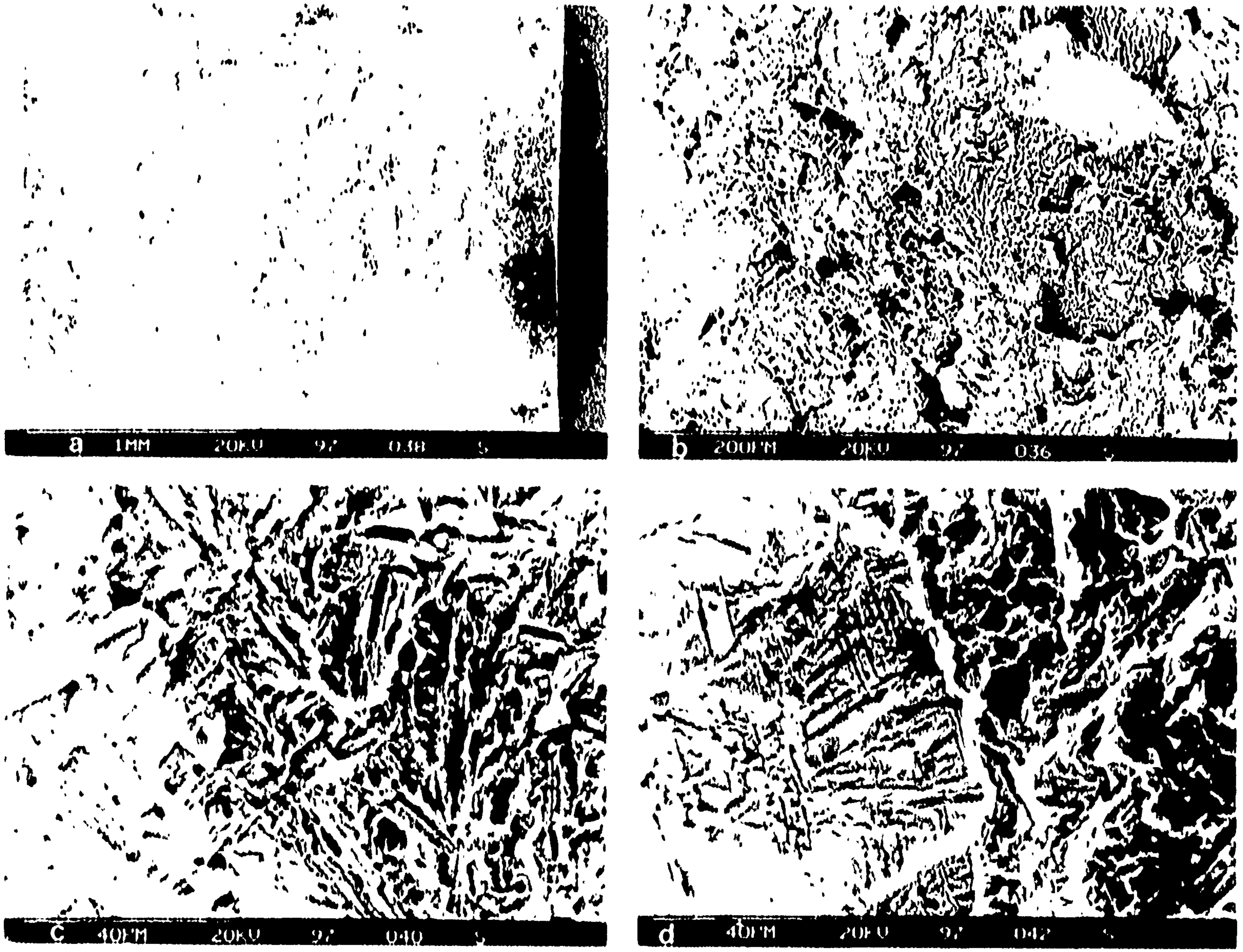

PHOTO 21 Fatigue fractographic features in specimen CT6B under Simple Spectrum Type 0, R=0.7 and ΔK = 10 MPa√m. (a: 37X; b: 200X; c: 1000X; and d: 1000X).

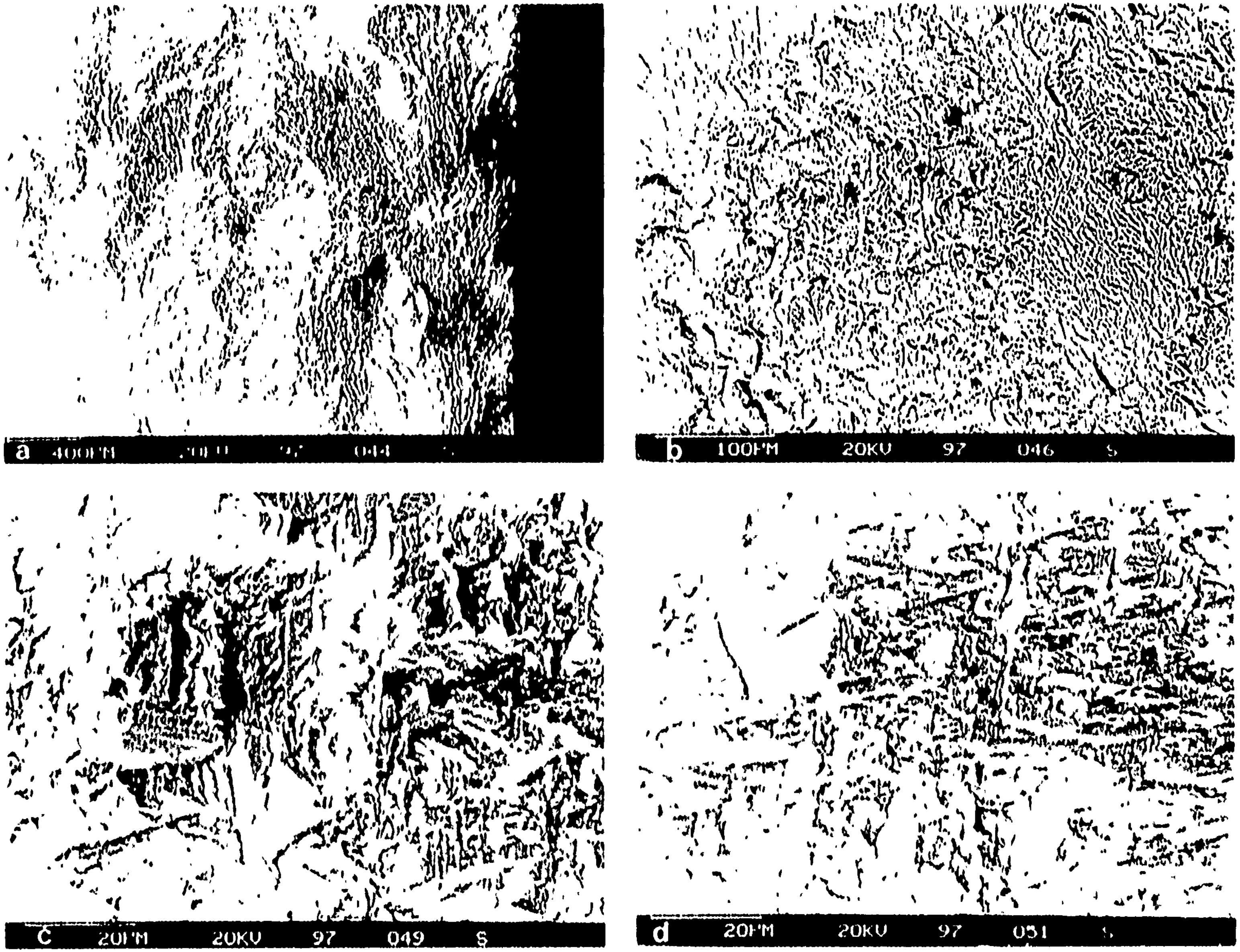

PHOTO 22 Fatigue fractographic features in specimen CT1 under Simple Spectrum Type I, and ΔK - 10 MPa√m. (a: 40X; b: 200X; c: 1000X; and d: 1000X).

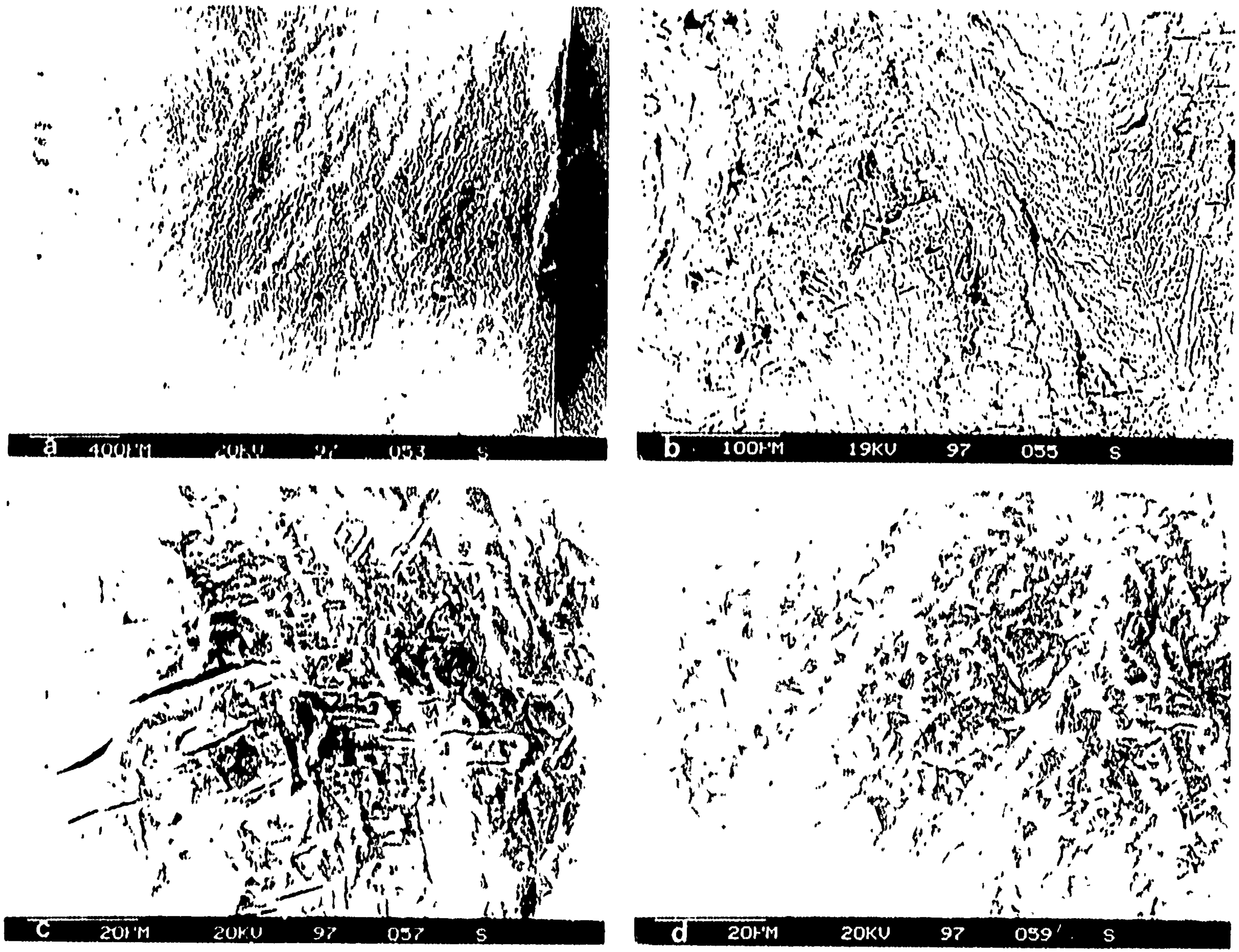

PHOTO 23 Fatigue fractographic features in specimen CT1 under Simple Spectrum Type 1, and ΔK = 20 MPa$\sqrt{m}$. (a: 40X; b: 200X; c: 1000X; and d: 1000X).

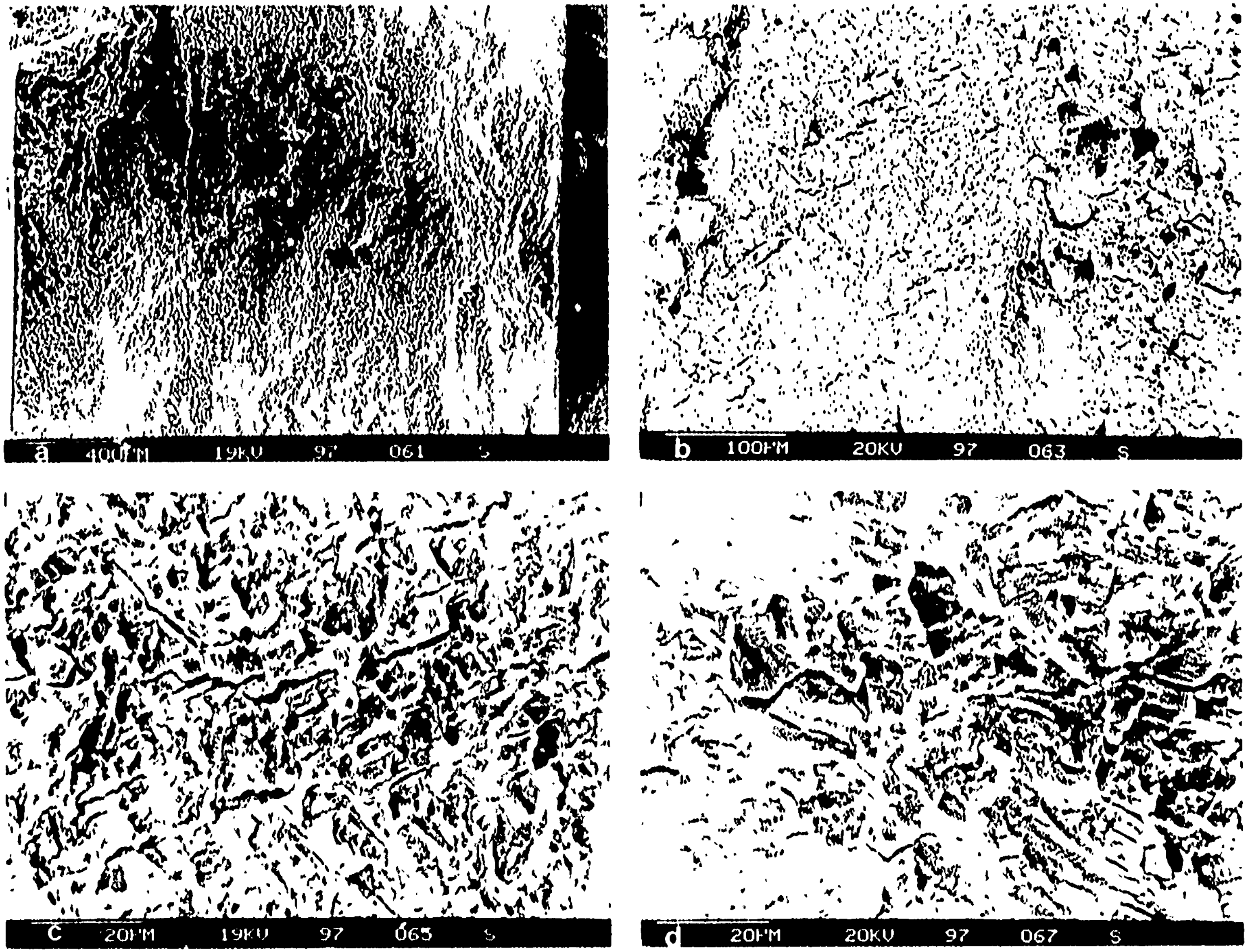

PHOTO 24 Fatigue fractographic features in specimen CT1 under Simple Spectrum Type 1, and ΔK = 35 MPa$\sqrt{m}$. (a: 40X; b: 200X; c: 1000X; and d: 1000X).

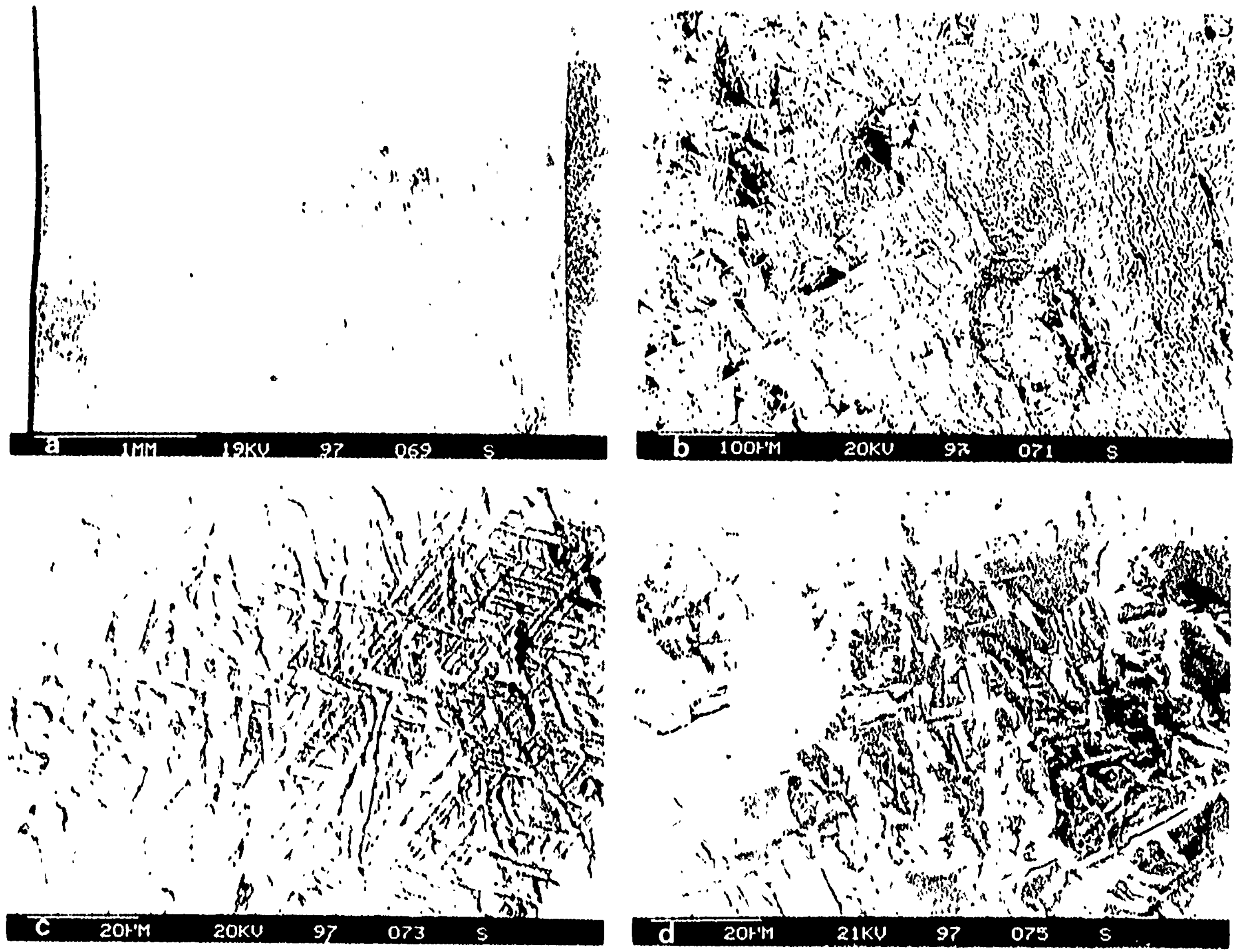

PHOTO 25 Fatigue fractographic features in specimen CT12 under Simple Spectrum Type 2, and $\Delta K = 10$ MPa$\sqrt{m}$. (a: 28X; b: 200X; c: 1000X; and d: 1000X).

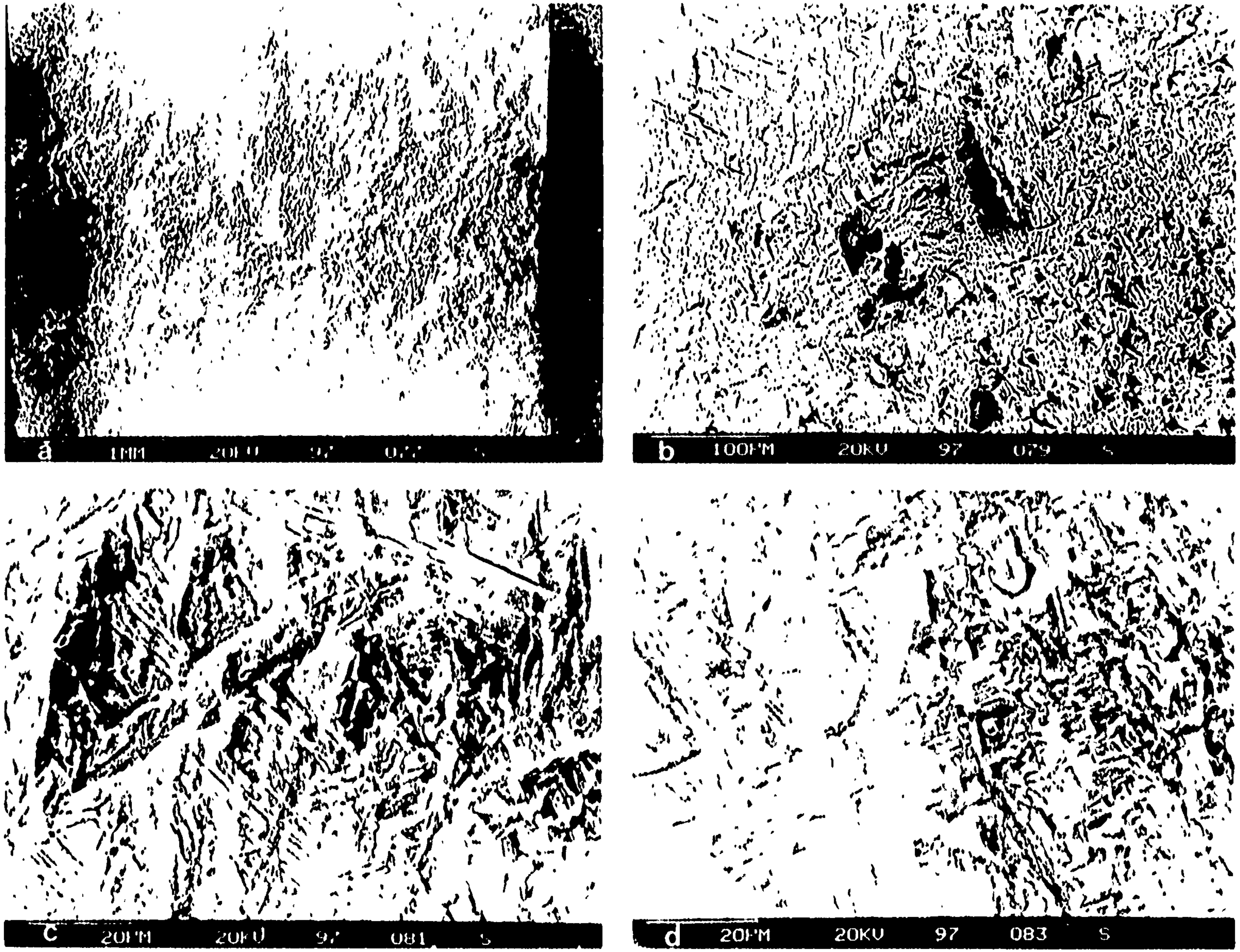

PHOTO 26 Fatigue fractographic features in specimen CT12 under Simple Spectrum Type 2, and ΔK = 20 MPa$\sqrt{m}$. (a: 28X; b: 200X; c: 1000X; and d: 1000X).

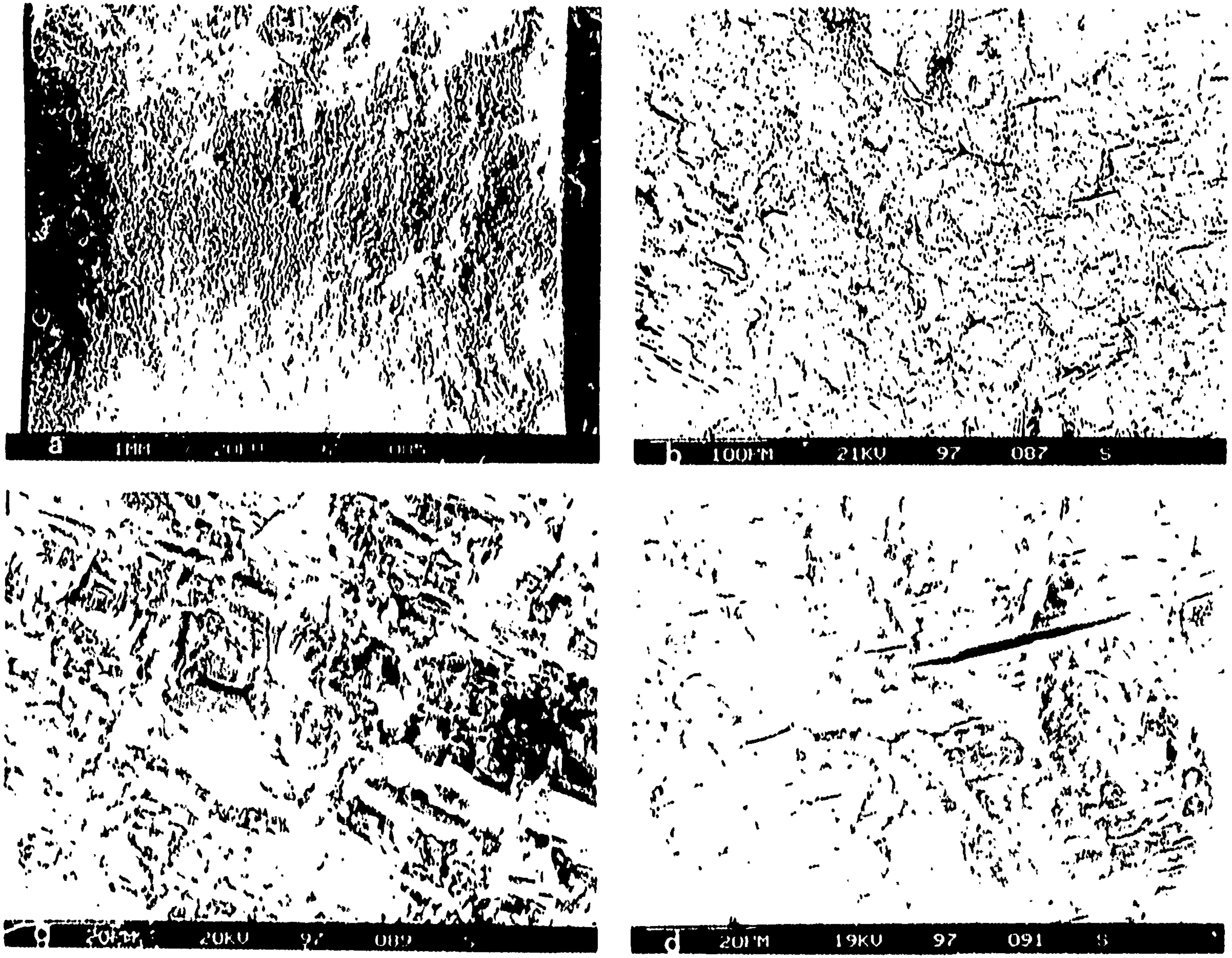

PHOTO 27 Fatigue fractographic features in specimen CT12 under Simple Spectrum Type 2, and ΔK = 35 MPa$\sqrt{m}$. (a: 28X; b: 200X; c: 1000X; and d: 1000X).

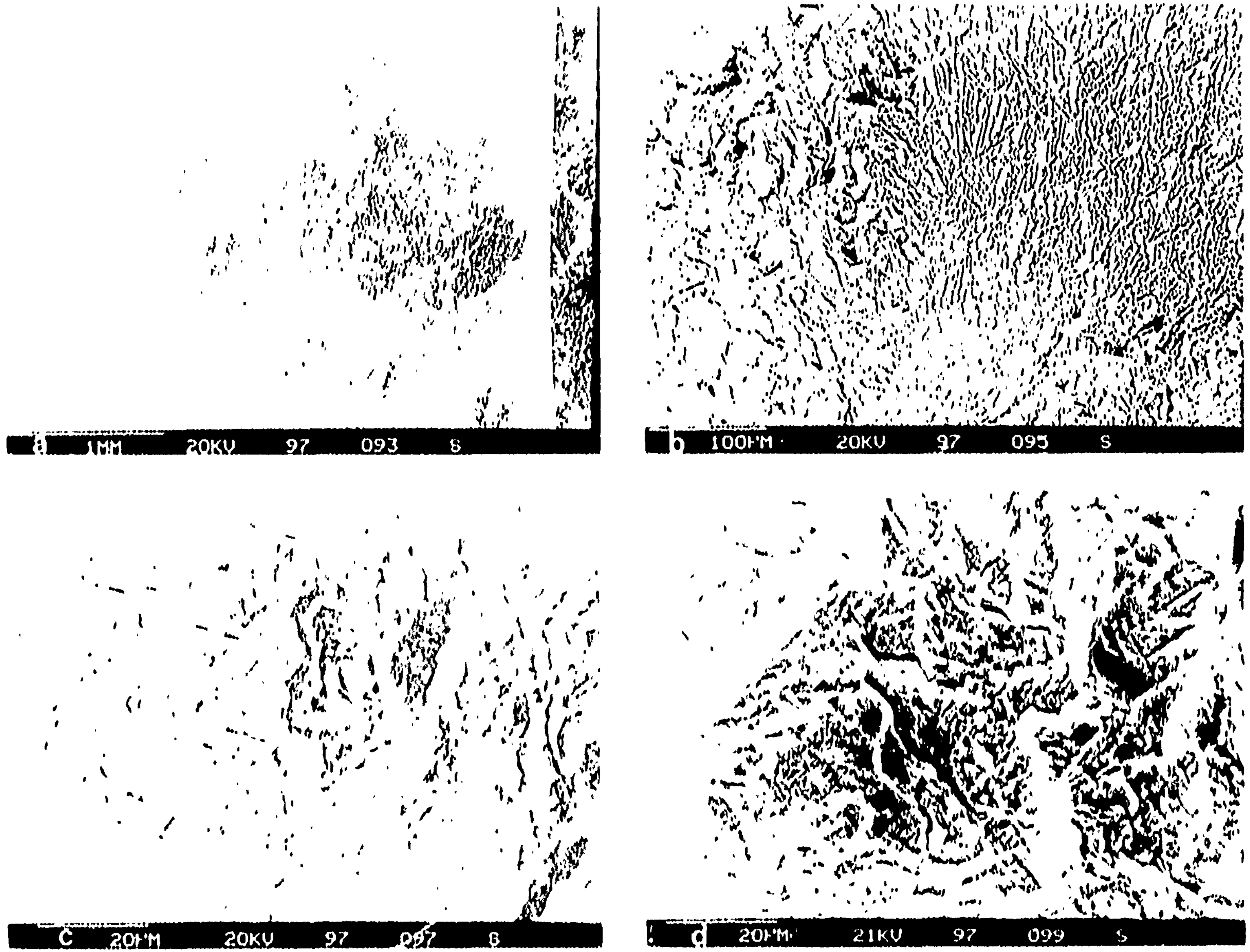

PHOTO 28 Fatigue fractographic features in specimen CT7 under Simple Spectrum Type 3, and $\Delta K = 10$ MPa$\sqrt{m}$. (a: 29X; b: 200X; c: 1000X; and d: 1000X).

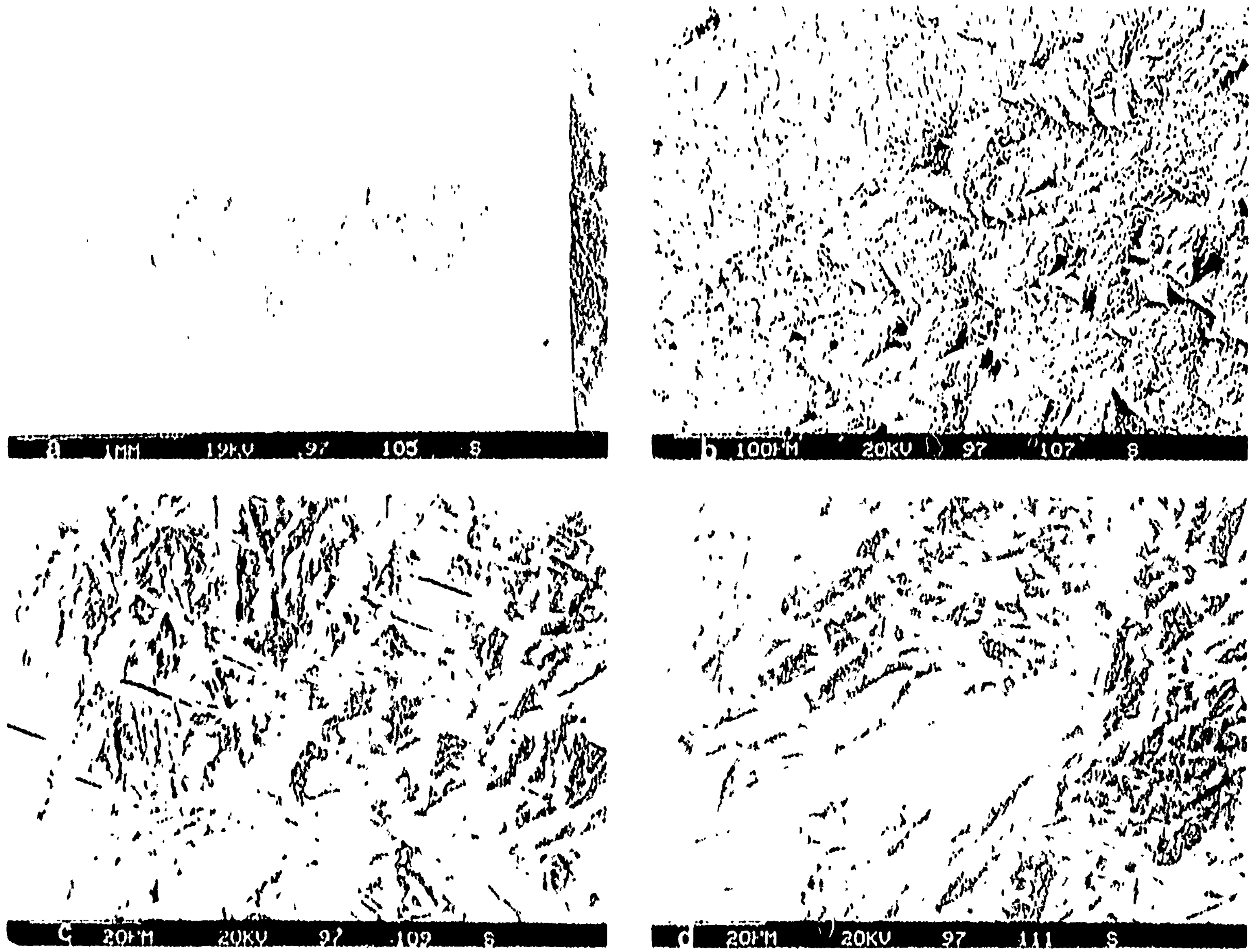

PHOTO 29 Fatigue fractographic features in specimen CT7 under Simple Spectrum Type 3, and $\Delta K = 20$ MPa$\sqrt{m}$. (a: 29X; b: 200X; c: 1000X; and d: 1000X).

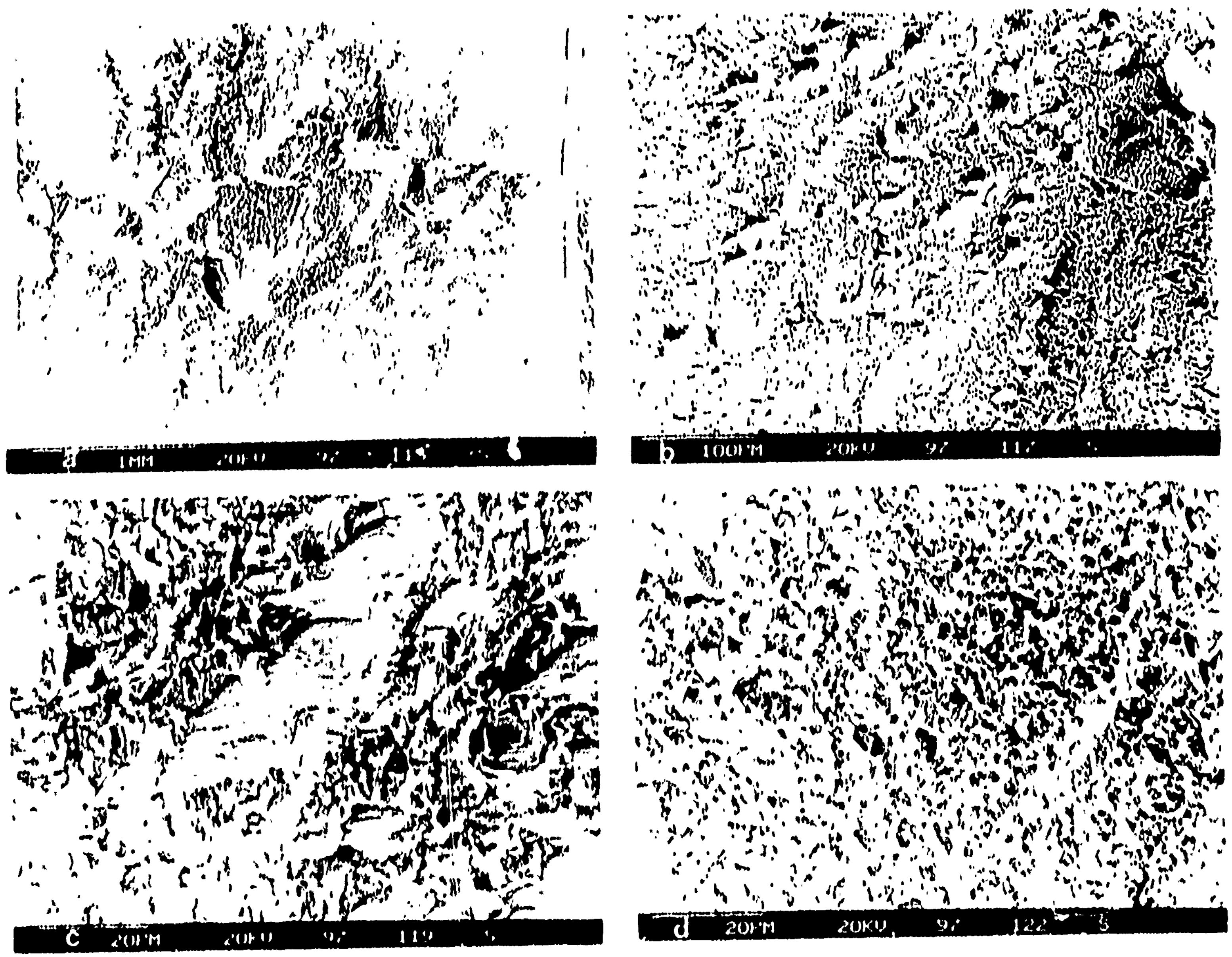

PHOTO 30 Fatigue fractographic features in specimen CT7 under Simple Spectrum Type 3, and ΔK - 35 MPa√m. (a: 29X; b: 200X; c: 1000X; and d: 1000X).

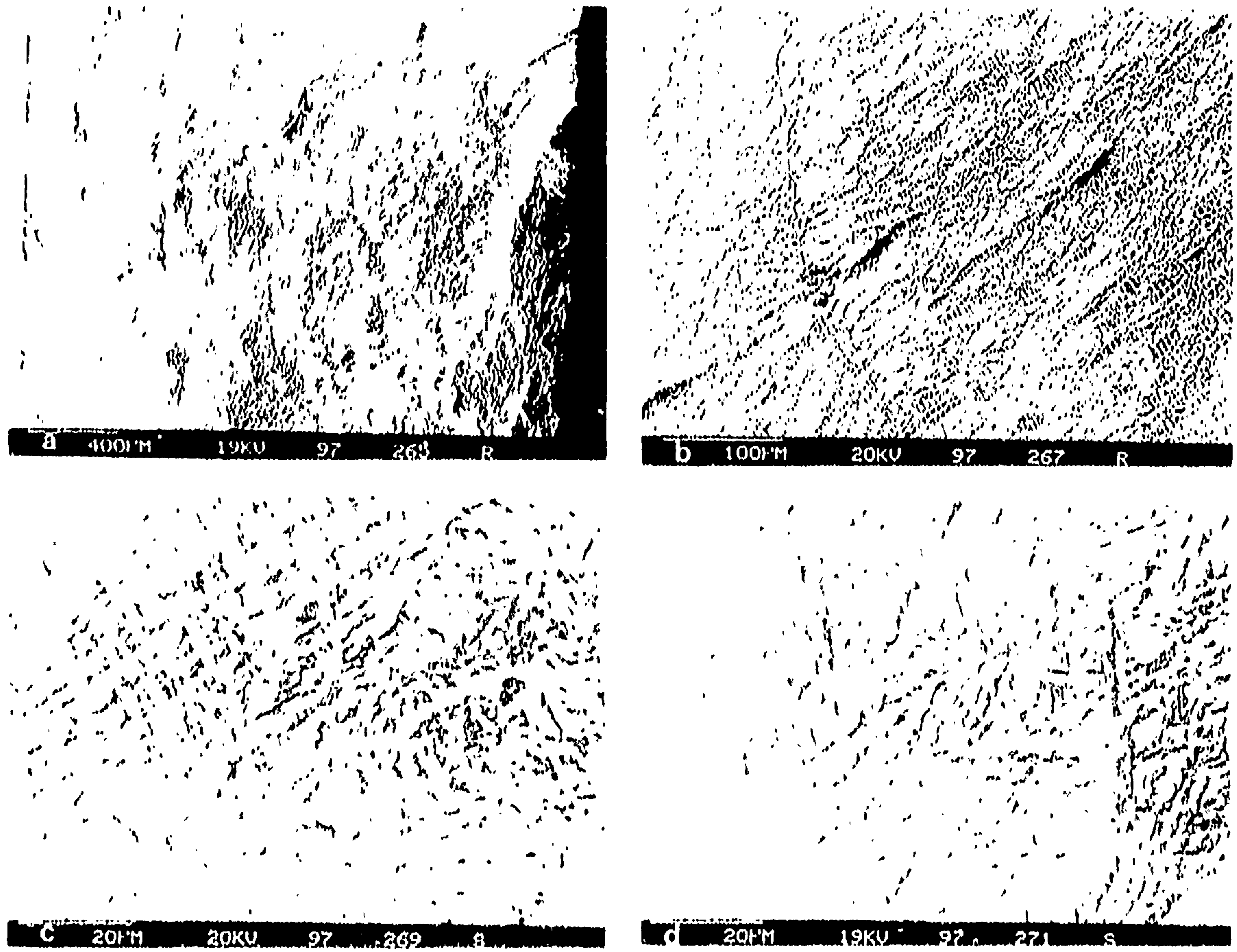

PHOTO 31 Fatigue fractographic features in specimen CT2 under Simple Spectrum Type 4, and $\Delta K = 10$ MPa$\sqrt{m}$. (a: 40X; b: 200X; c: 1000X; and d: 1000X).

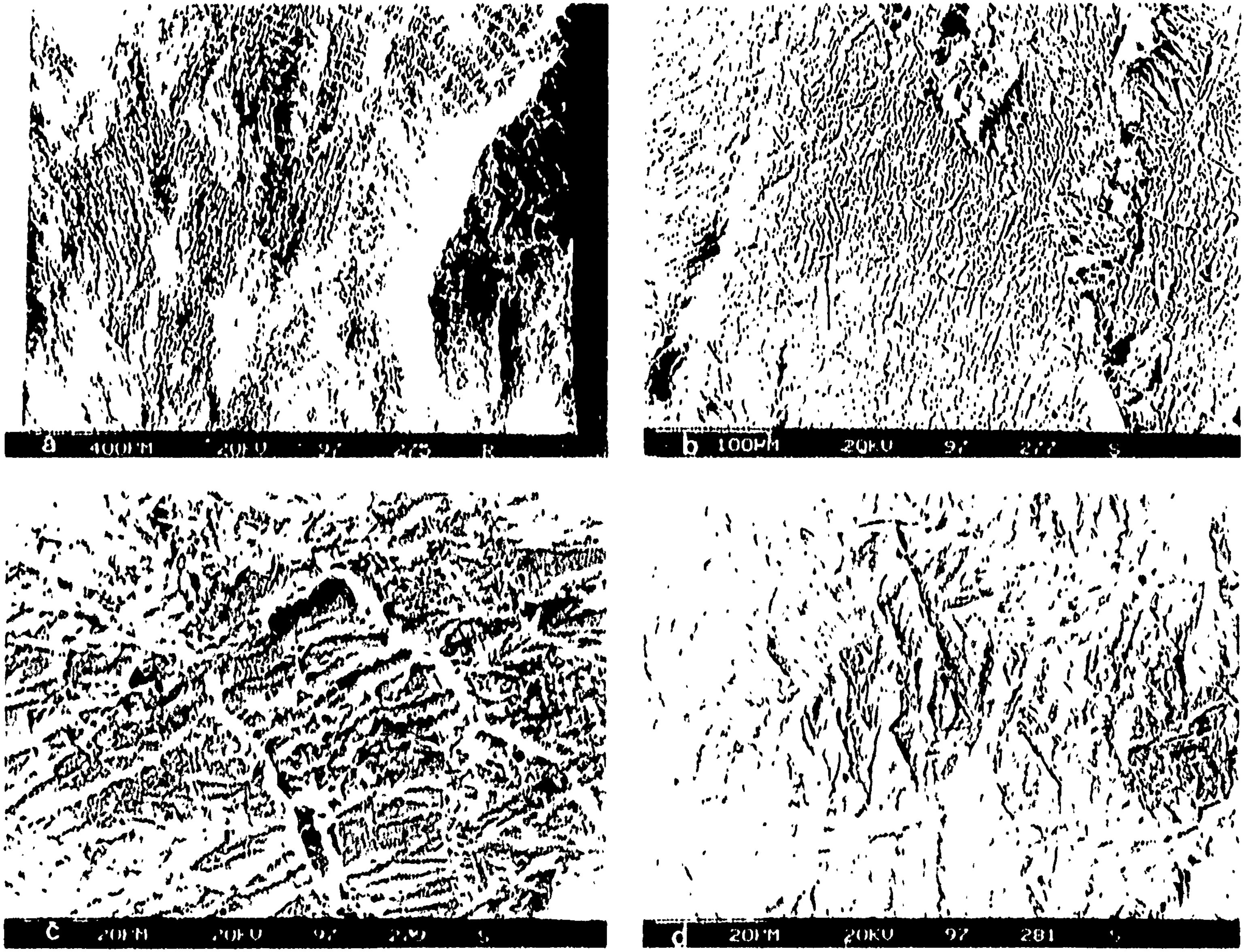

PHOTO 32 Fatigue fractographic features in specimen CT2 under Simple Spectrum Type 4, and ΔK - 20 MPa√m. (a: 40X; b: 200X; c: 1000X; and d: 1000X).

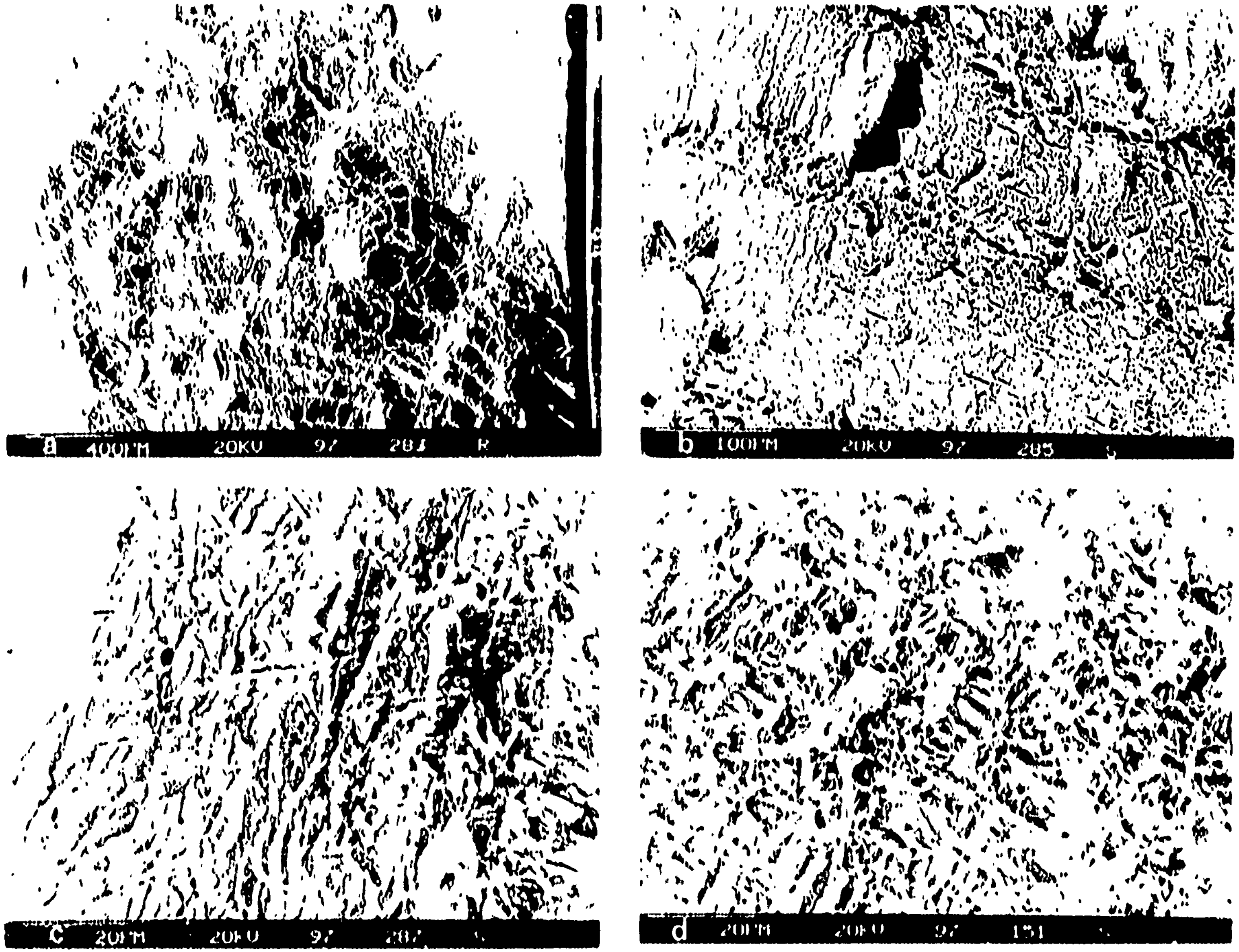

PHOTO 33 Fatigue fractographic features in specimen CT2 under Simple Spectrum Type 4, and ΔK - 35 MPa$\sqrt{m}$. (a: 40X; b: 200X; c: 1000X; and d: 1000X).

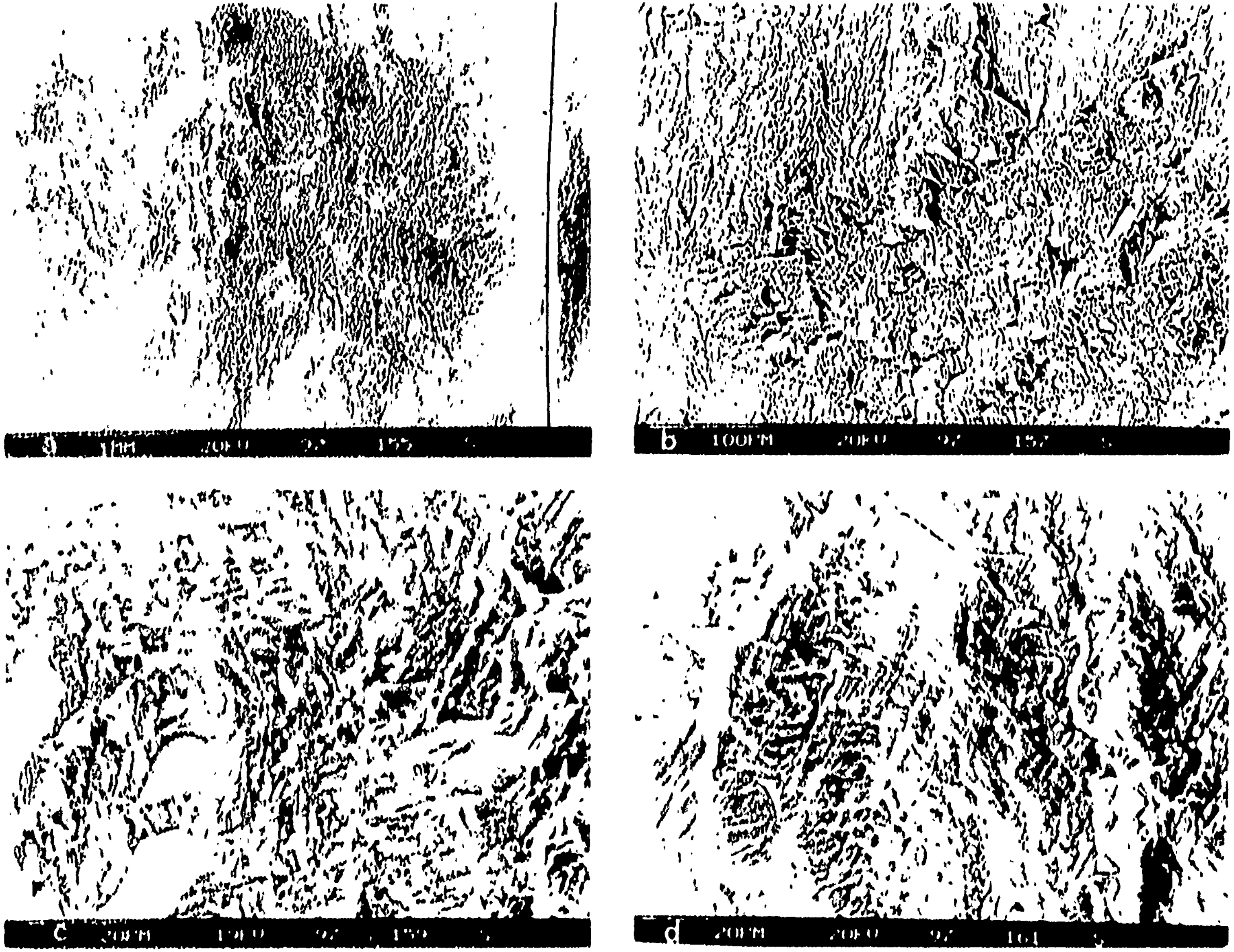

PHOTO 34 Fatigue fractographic features in specimen CT10A under FULL TURBISTAN, and K_{max} = 10 MPa√m. (a: 30X; b: 200X; c: 1000X; and d: 1000X).

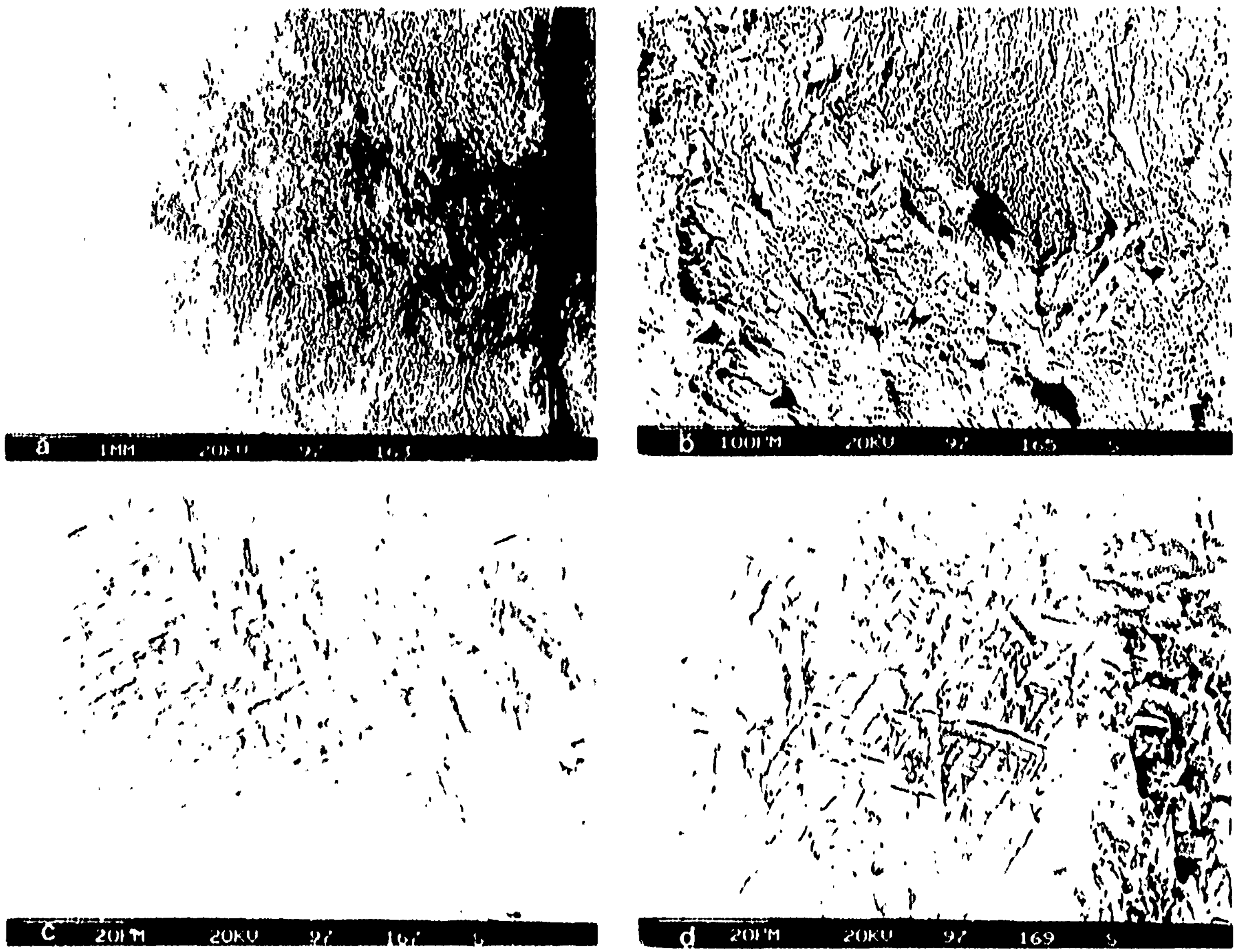

PHOTO 35 Fatigue fractographic features in specimen CT10A under FULL TURBISTAN, and K_{MAX} = 20 MPa$\sqrt{m}$. (a: 30X; b: 200X; c: 1000X; and d: 1000X).

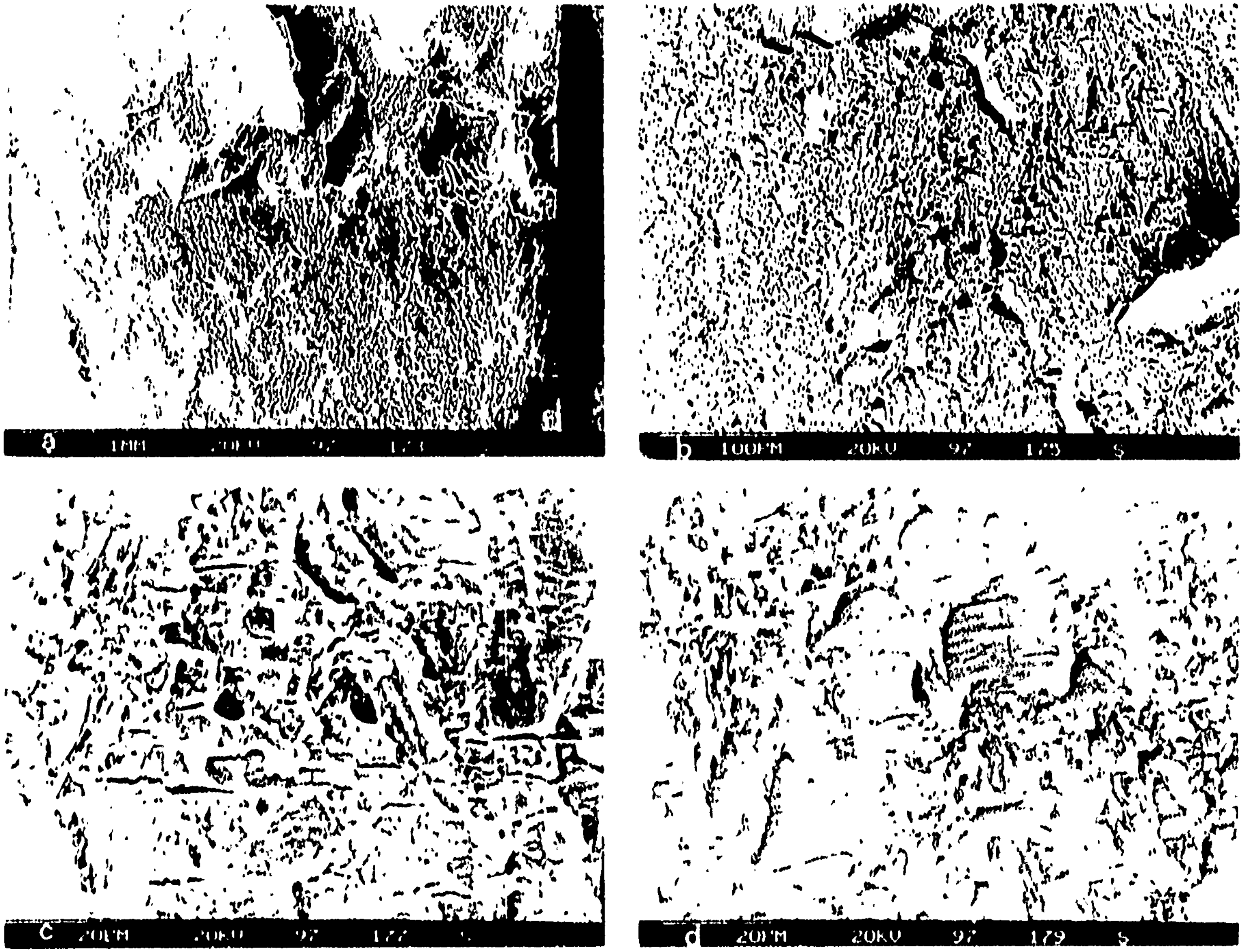

PHOTO 36 Fatigue fractographic features in specimen CT10A under FULL TURBISTAN, and K_{MAX} = 35 MPa$\sqrt{m}$. (a: 30X; b: 200X; c: 1000X; and d: 1000X).

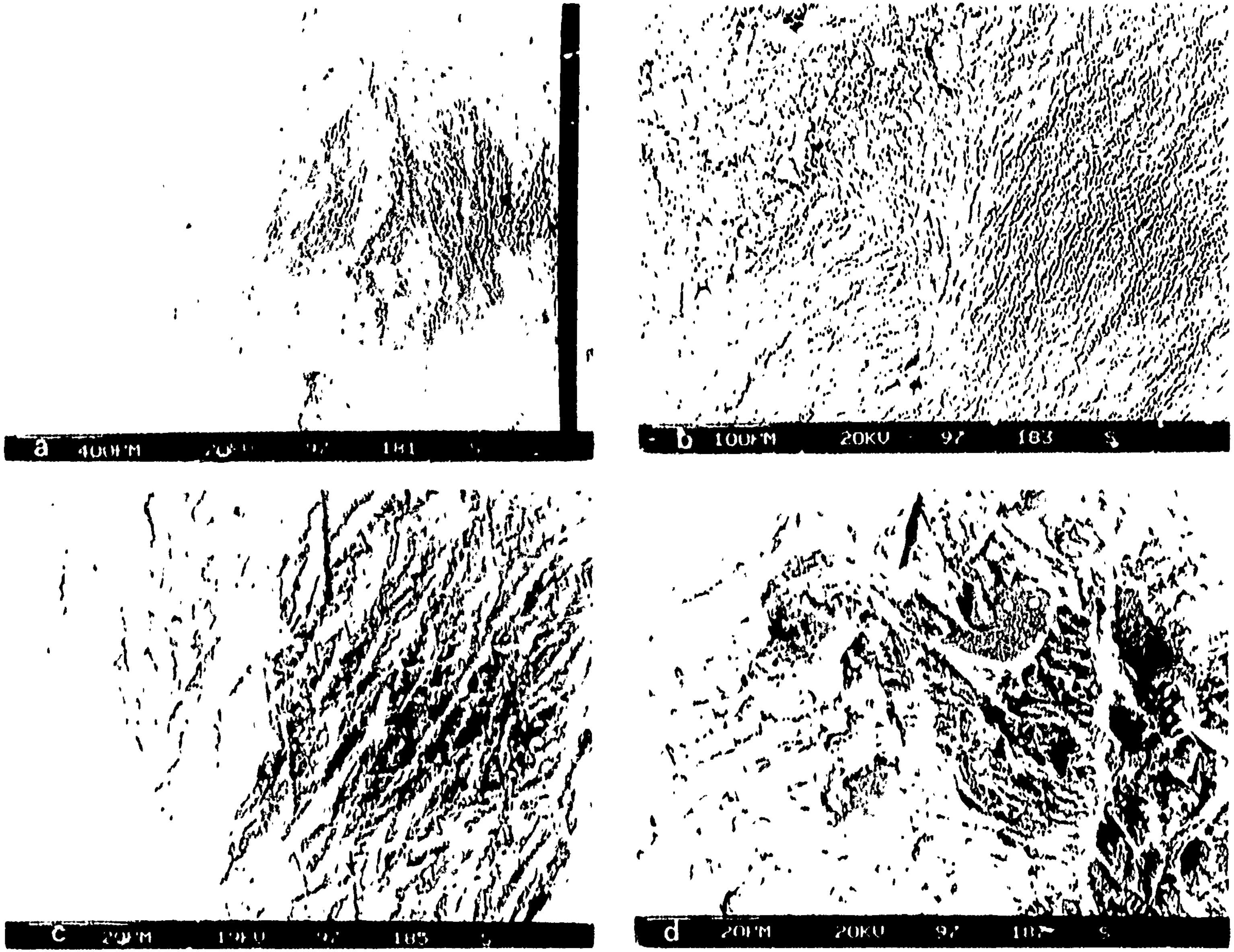

PHOTO 37 Fatigue fractographic features in specimen CT24 under 10% Omission TURBISTAN, and K_{MAX} = 10 MPa$\sqrt{m}$. (a: 37X; b: 200X; c: 1000X; and d: 1000X).

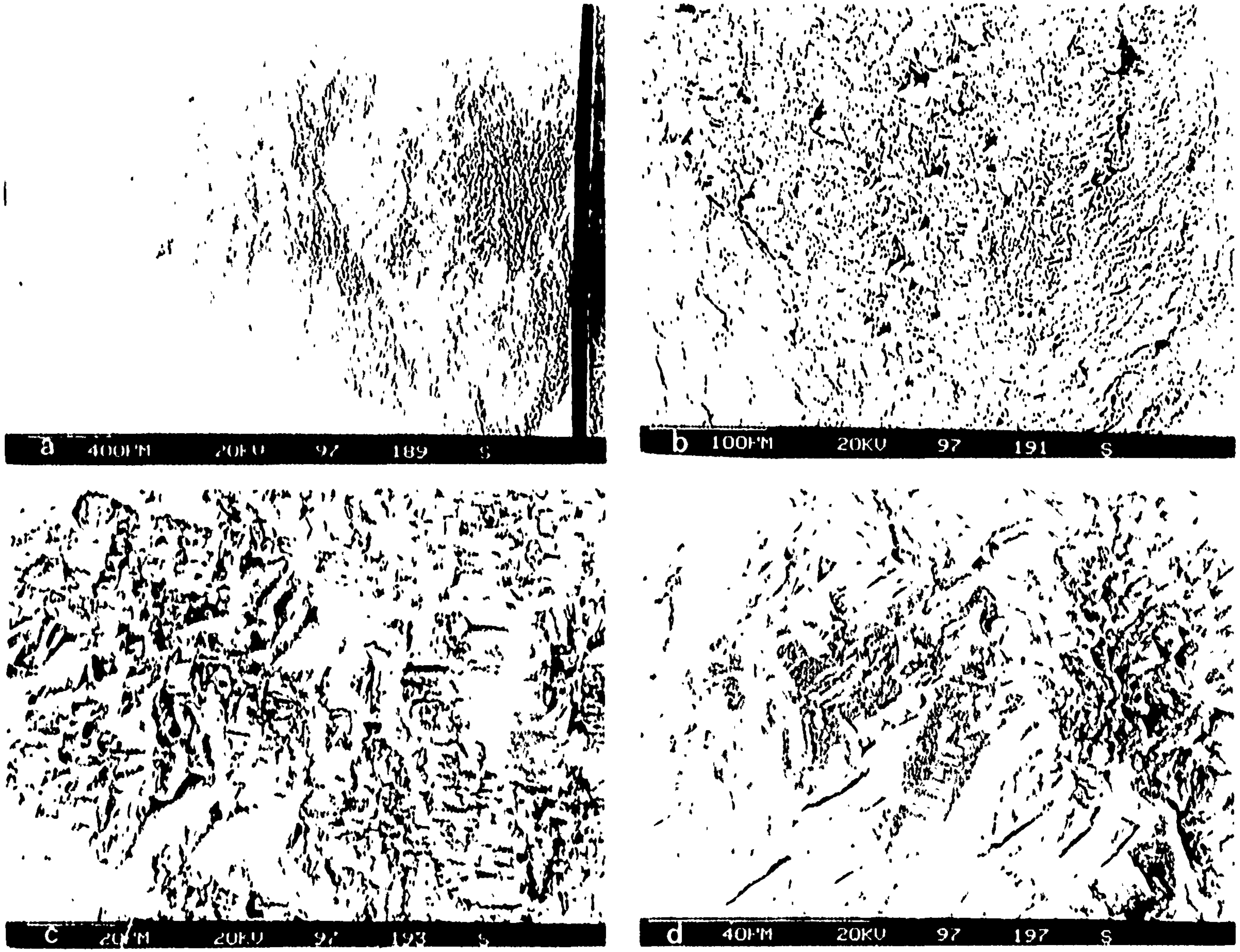

PHOTO 38 Fatigue fractographic features in specimen CT24 under 10% Omission TURBISTAN, and K_{MAX} = 20 MPa√m. (a: 37X; b: 200X; c: 1000X; and d: 1000X).

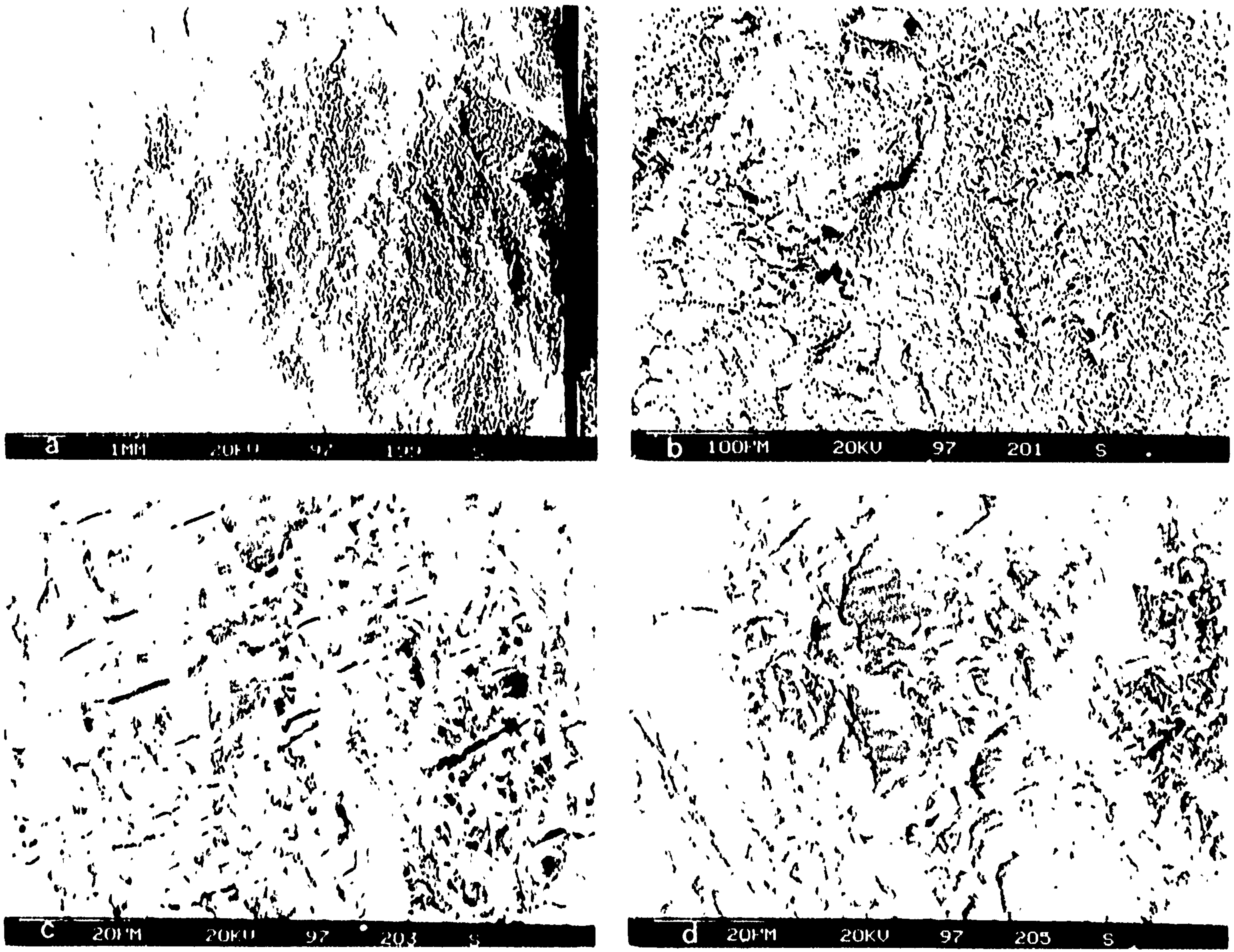

PHOTO 39 Fatigue fractographic features in specimen CT24 under 10% Omission TURBISTAN, and K_{MAX} = 35 MPa√m. (a: 37X; b: 200X; c: 1000X; and d: 1000X).

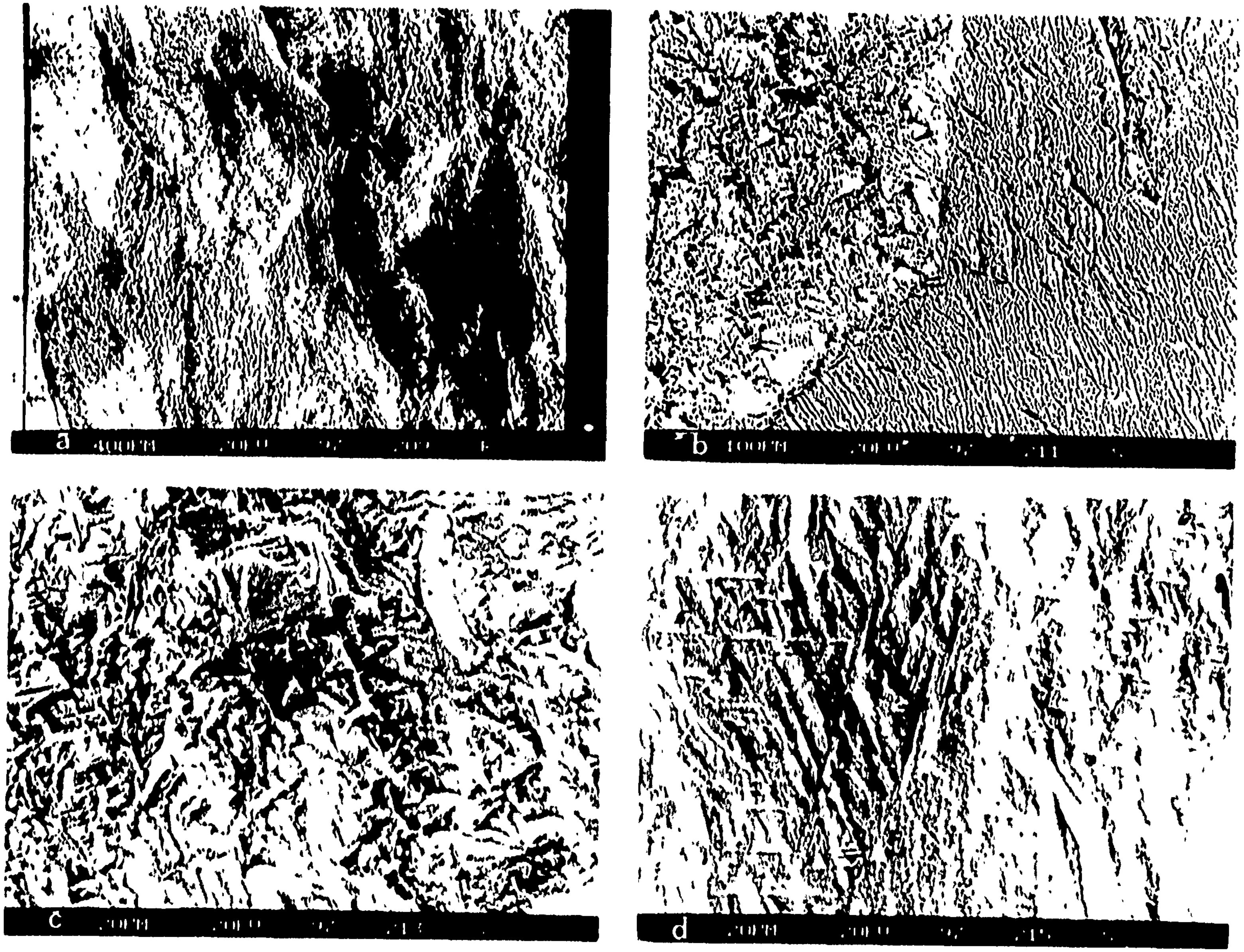

PHOTO 40 Fatigue fractographic features in specimen CT13 under 30% Omission TURBISTAN, and K_{MAX} = 10 MPa$\sqrt{m}$. (a: 36X; b: 200X; c: 1000X; and d: 1000X).

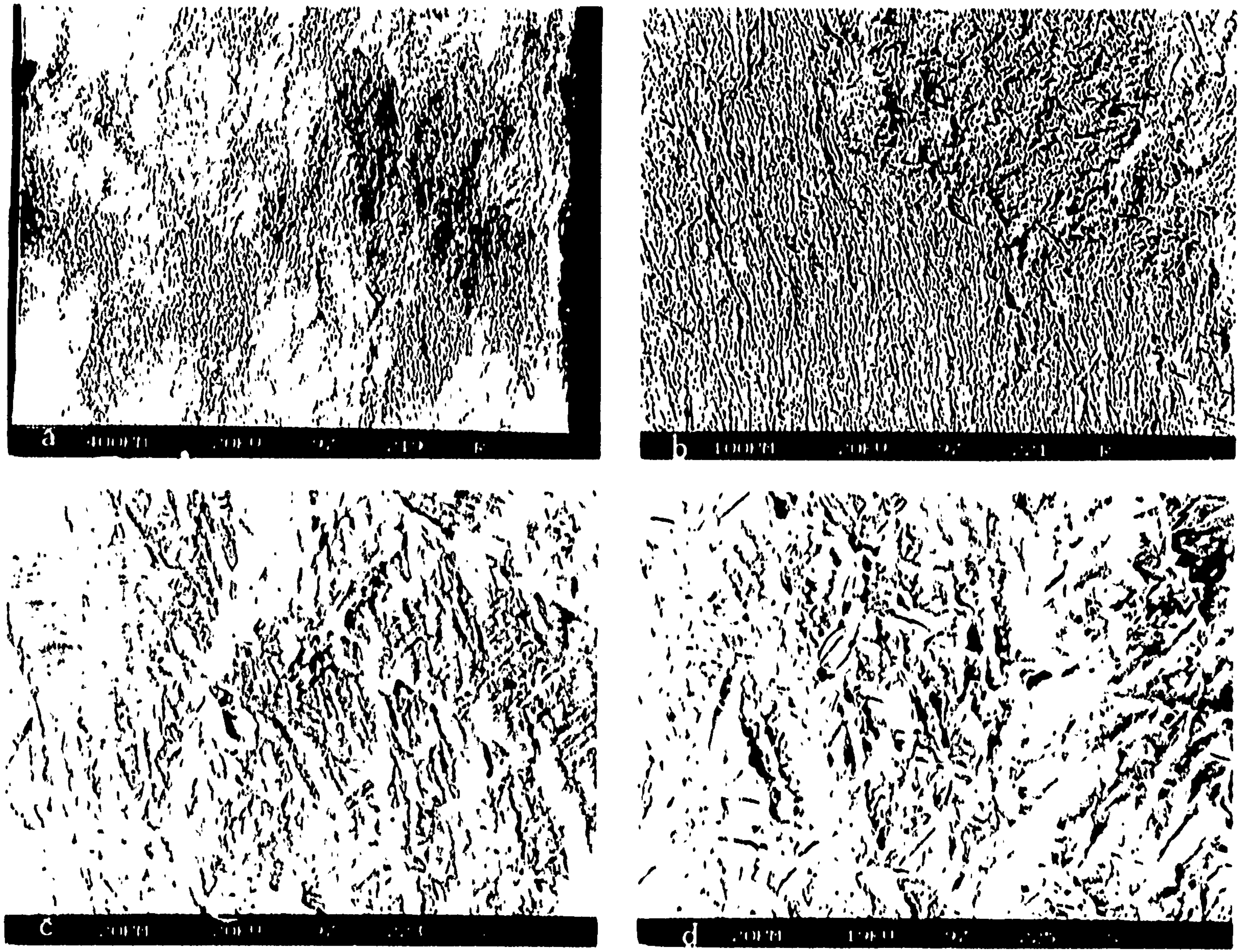

PHOTO 41 Fatigue fractographic features in specimen CT13 under 30% Omission TURBISTAN, and K_{MAX} = 20 MPa$\sqrt{m}$. (a: 36X; b: 200X; c: 1000X; and d: 1000X).

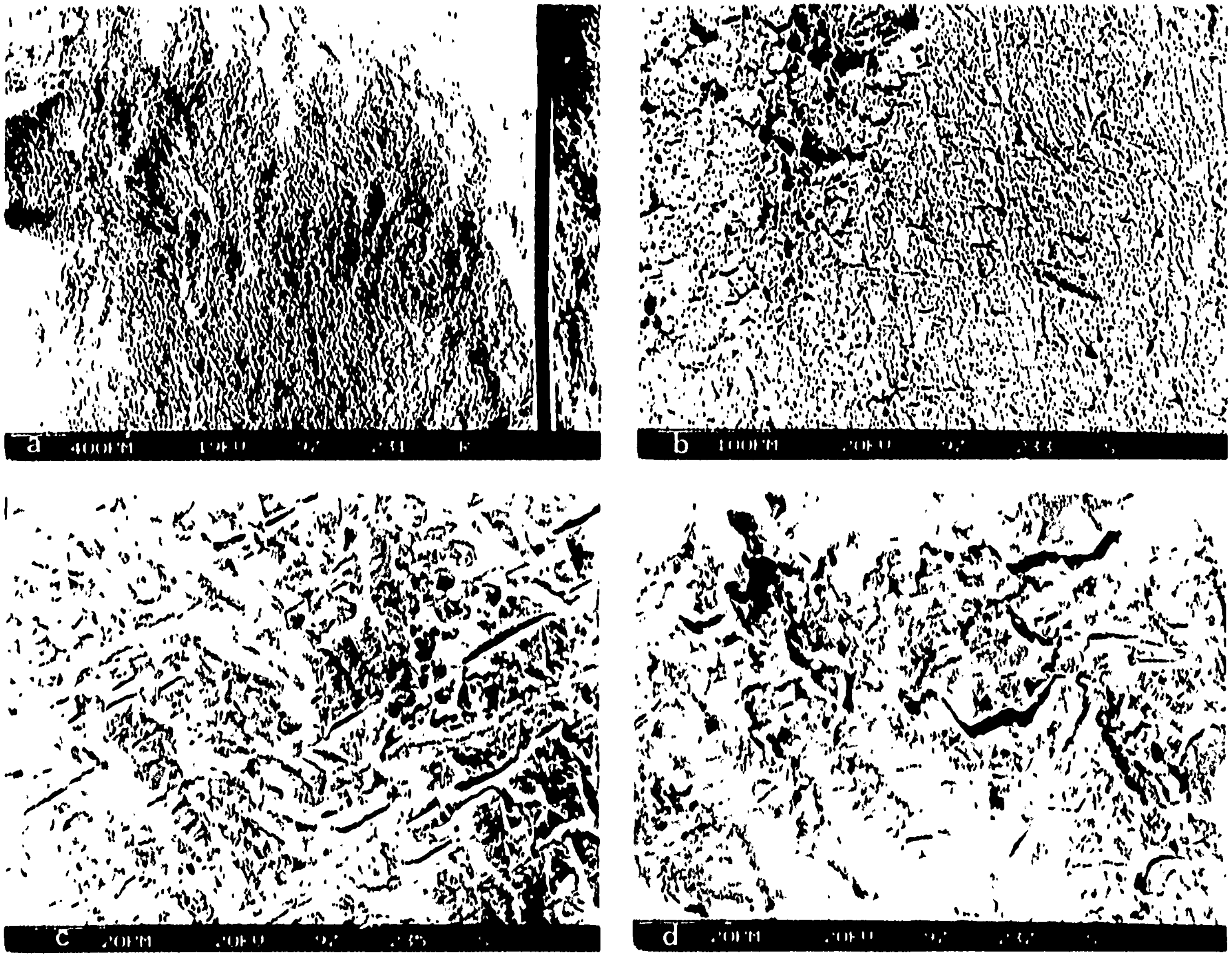

PHOTO 42 Fatigue fractographic features in specimen CT13 under 30% Omission TURBISTAN, and K_{MAX} = 35 MPa$\sqrt{m}$. (a: 36X; b: 200X; c: 1000X; and d: 1000X).

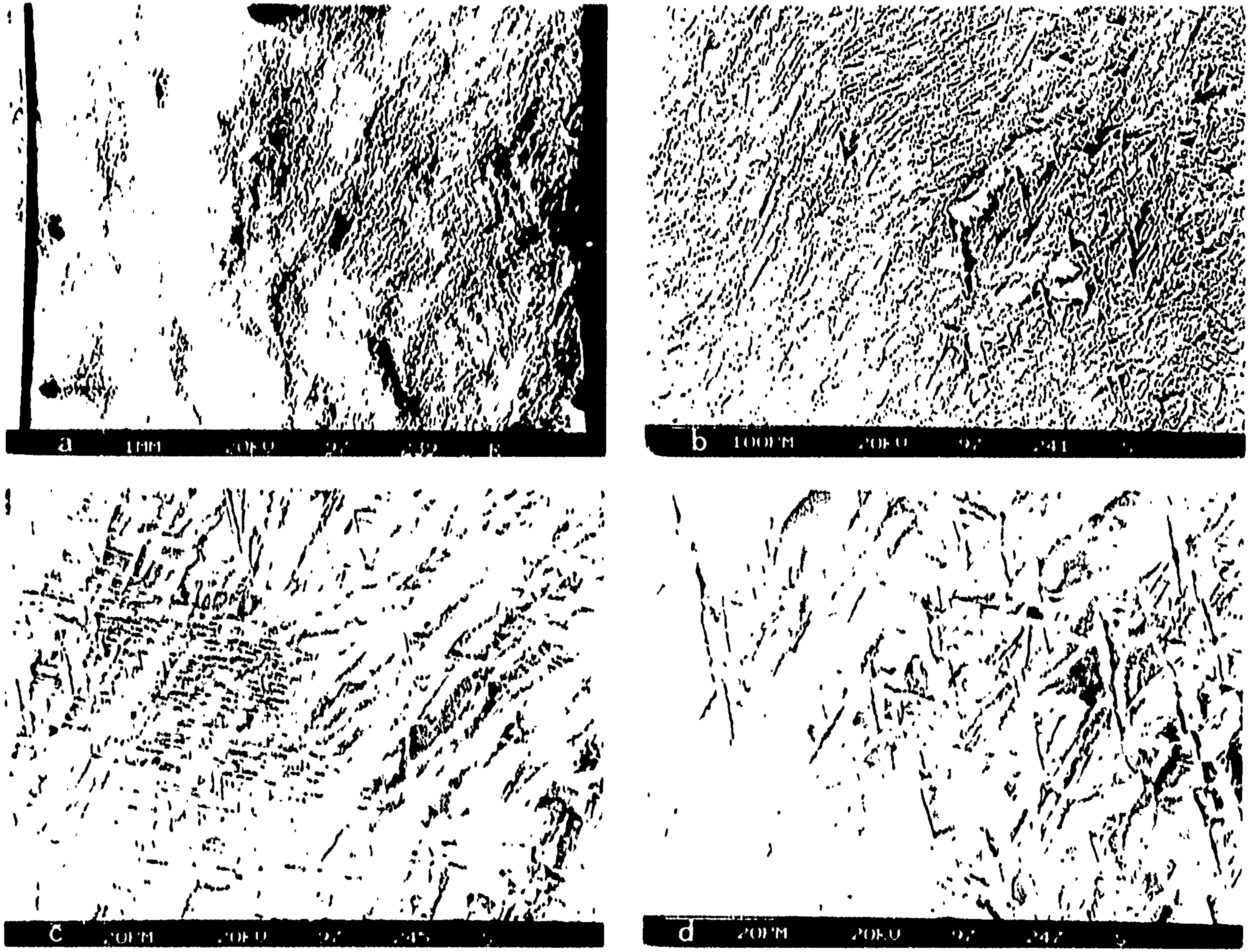

PHOTO 43 Fatigue fractographic features in specimen CT5B under 50% Omission TURBISTAN, and K_{MAX} = 10 MPa$\sqrt{m}$. (a: 22X; b: 200X; c: 1000X; and d: 1000X).

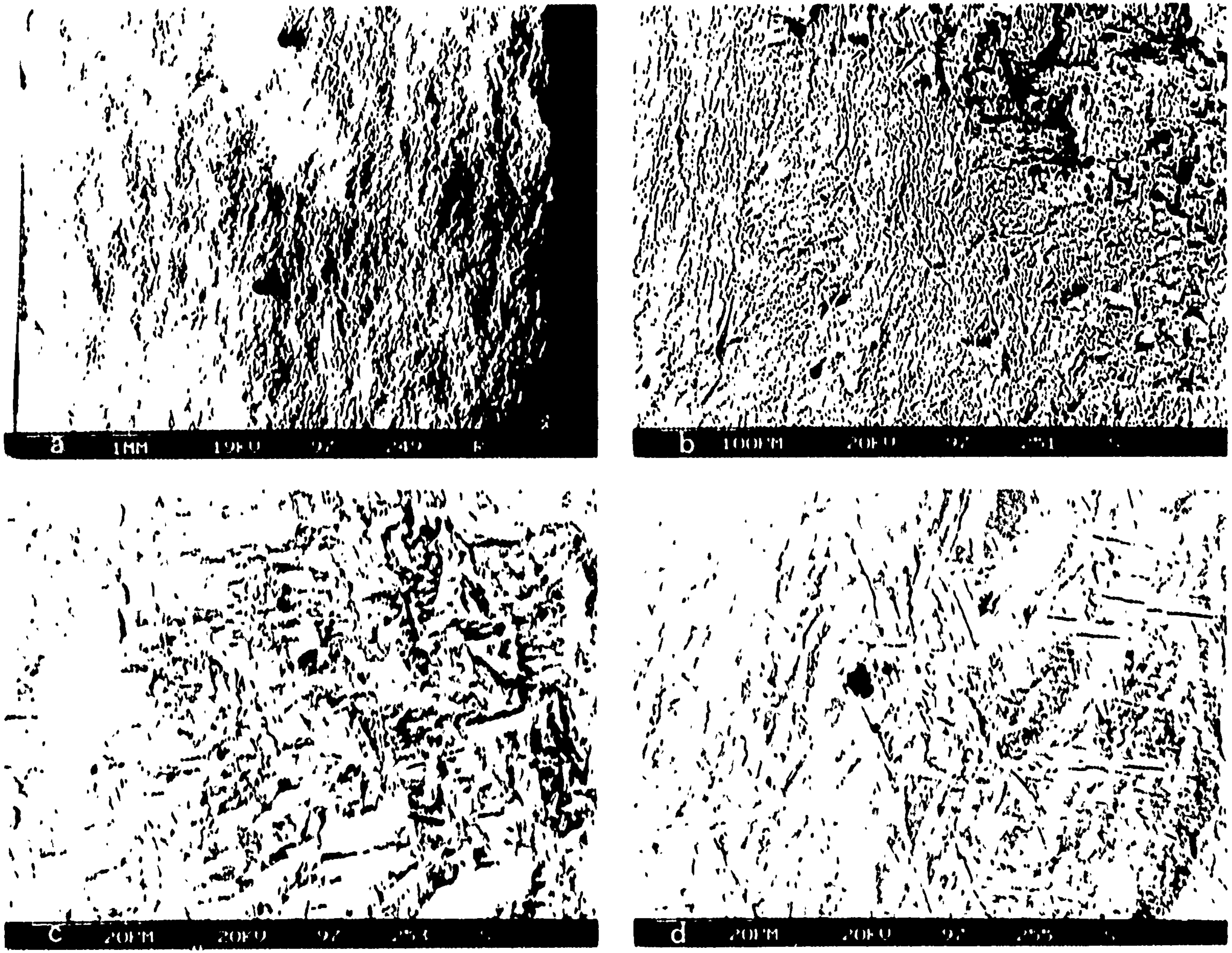

PHOTO 44 Fatigue fractographic features in specimen CT5B under 50% Omission TURBISTAN, and K_{MAX} = 20 MPa$\sqrt{m}$. (a: 22X; b: 200X; c: 1000X; and d: 1000X).

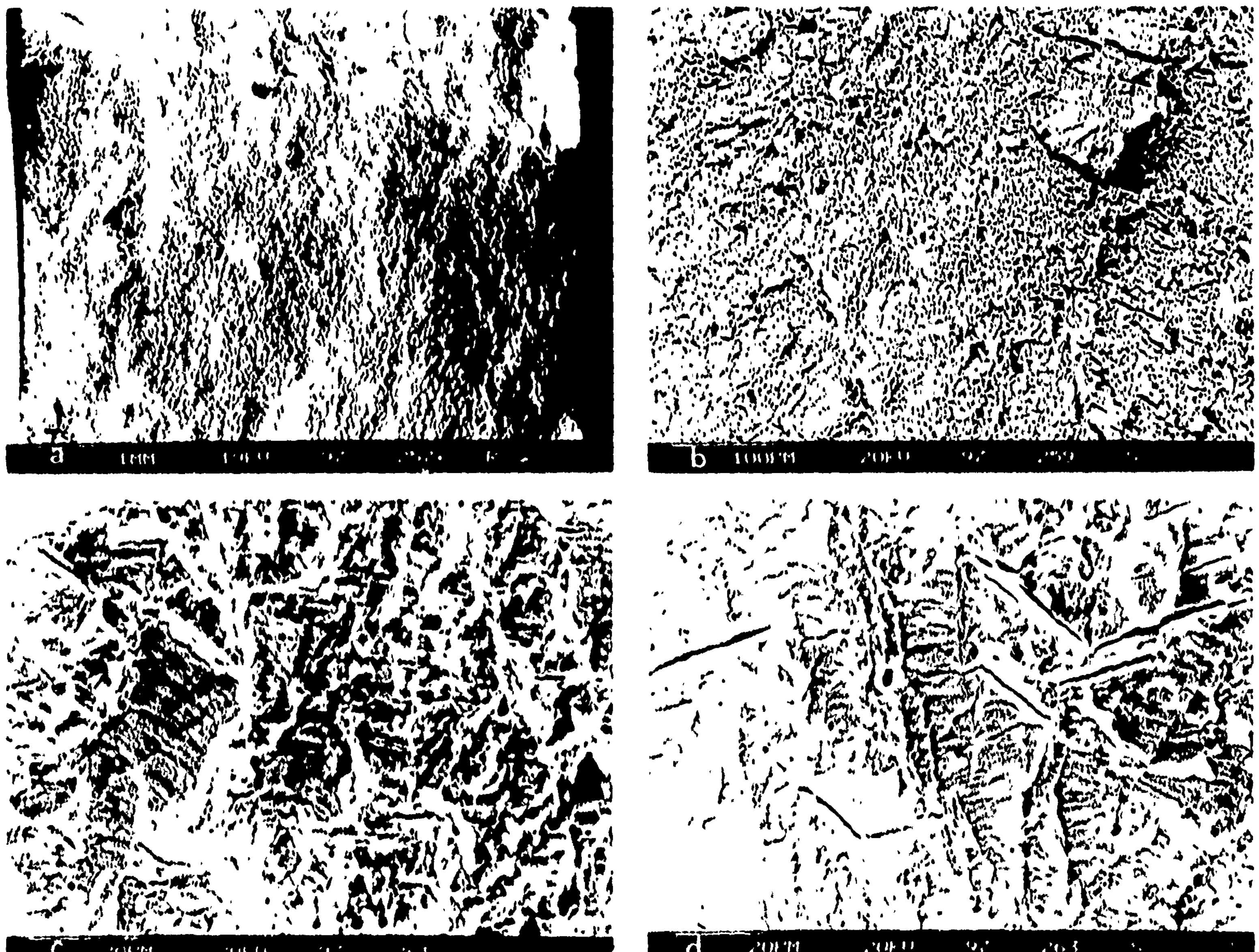

PHOTO 45 Fatigue fractographic features in specimen CT5B under 50% Omission TURBISTAN, and K_{MAX} = 35 MPa$\sqrt{m}$. (a: 22X; b: 200X; c: 1000X; and d: 1000X).

LOW CYCLE FATIGUE BEHAVIOUR OF TITANIUM DISC ALLOYS

C.E.W. Looije
National Aerospace Laboratory NLR,
P.O. Box 90502, 1006 BM Amsterdam
The Netherlands

SUMMARY

This paper describes the low cycle fatigue behaviour of the titanium alloys IMI 685, Ti-17 and Ti-6Al-4V tested in the AGARD Engine Disc Cooperative Test Programme. Load controlled low cycle fatigue tests were carried out on smooth cylindrical and flat double edge notched specimens at room temperature. The test results were statistically analysed and discussed. The tests showed that the differences in low cycle fatigue behaviour between IMI 685 and Ti-6Al-4V are negligible and that Ti-17 has superior low cycle fatigue properties.

PARTICIPANTS

- AF Air Force Materials Laboratory (AFML), WPAFB, Dayton, Ohio, USA
- CE Centre d'Essais Aéronautique de Toulouse, France
- IA Industrieanlagen-Betriebsgesellschaft (IABG), Ottobrunn, Germany
- ND Naval Air Development Center (NADC), Warminster, Pennsylvania, USA
- NL National Aerospace Laboratory NLR, Amsterdam, The Netherlands
- NR National Research Council, Institute for Aerospace Research (IAR), Ottawa, Canada
- NS National Aeronautics and Space Administration (NASA), Cleveland, Ohio, USA
- PI University of Pisa, Pisa, Italy
- QE Quality Engineering Test Establishment (QETE), Ottawa, Canada
- RA Royal Aerospace Establishment (RAE), Farnborough, United Kingdom
- RR Rolls Royce (RR), Derby, United Kingdom
- UT University of Toronto, Toronto, Canada

1 INTRODUCTION

Three titanium alloys were investigated in the AGARD Engine Disc Cooperative Test Programme. In the core programme [1] a large amount of Ti-6Al-4V data was generated, while in the supplemental programme IMI 685, Ti-17 and a few Ti-6Al-4V data were generated.

In this paper the low cycle fatigue results of the supplemental programme are presented and compared with the Ti-6Al-4V results generated in the core programme.

2 MATERIALS, SPECIMENS AND TEST PROCEDURES

The titanium alloys IMI 685, Ti-17 and Ti-6Al-4V were investigated. The specimens were extracted from fan disc forgings provided by Rolls-Royce and General Electric. The forgings were in the solution treated and aged conditions. Ti-6Al-4V was conventionally ($\alpha+\beta$) processed while IMI 685 and Ti-17 were β processed. The mechanical properties are given in table 1.
Two different types of specimens were selected for the low cycle fatigue tests. A smooth cylindrical specimen (designated as LCF specimen) and a flat double edge notched specimen with K_t=2.2 (designated as K_t2.2 specimen) were used in the core programme as well as in the supplemental programme. Rolls-Royce used their own smooth cylindrical specimen (designated as RLH 8001 specimen) for the additional Ti-6Al-4V tests in the supplemental programme. The specimens are shown in figure 1. The surface finish of the specimens was identical to that specified in the core programme.

Load controlled low cycle fatigue tests were carried out in laboratory air at room temperature, using a trapezoidal waveform with stress ratio R=0.1 and a nominal frequency of 0.25 Hz. However, the Ti-6Al-4V tests and some IMI 685 tests, performed by Rolls-Royce, were done with stress ratio R=0. The notched specimen was used to measure the number of cycles to "initiate" a certain crack size as well as the number of cycles to failure. Crack initiation was determined by using the DC potential drop (PD) technique; i.e. the number of cycles at which a 1% increase in PD level was obtained. The actual crack size for a 1% PD increment has been estimated in the core programme [1]. The crack shape was semi-elliptical and had a maximum crack depth of about 0.6 mm, with a surface length of 1.6 mm. More details are given in reference [2]. An overview of the low cycle fatigue tests performed in the core and supplemental programme is shown in table 2.

TABLE 1
Typical material properties

	UTS (MPa)	0.2% yield strength (MPa)	elongation (%)	reduction in area (%)
IMI 685	1029	903	6*	15*
Ti-17	1175	1035	10	19
Ti-6Al-4V	970	870	11	27

* minimum specified

TABLE 2
Low cycle fatigue test matrix

	number of test specimens		participating laboratories
	smooth cylindrical	flat notched K_t=2.2	
Core programme: • Ti-6Al-4V	72	72	AF, CE, IA, ND, NL, NR, NS, PI, QE, RA, RR, UT
Supplemental programme:			
• IMI 685	18	18	IA, NL, RR
• Ti-17	6	6	ND
• Ti-6Al-4V	6	-	RR

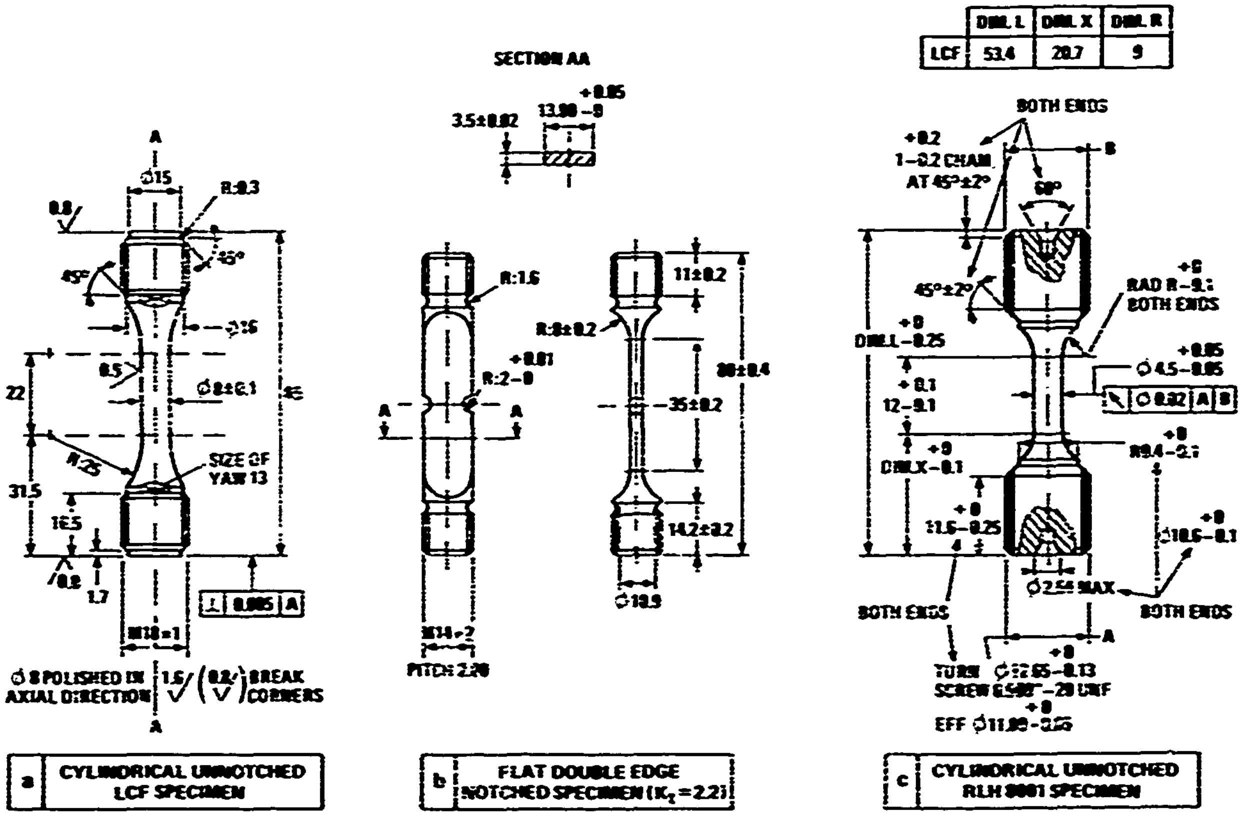

Fig. 1 Specimens used in the programme

3 STATISTICAL ANALYSIS

A statistical analysis of the results was performed to detect differences or deviating trends in the results from individual laboratories. The test results were analysed according to the procedures described in ASTM Standard Practice E 739-80 [3]. A short summary is given in Appendix A. The analysis involved the establishment of linear relationships between stress and life based on a log-normal distribution, and the establishment of confidence intervals for these curves. For these purposes, it is assumed that the fatigue life is log-normally distributed, and that the variance of log life is constant over the entire range of the independent variable (the stress parameter).
The linear expression used in the statistical analysis was:

$$Y = A + BX \qquad (1)$$

in which:
- Y = $\log N$
- N = number of cycles to failure
- X = stress range

The variance, the 95% confidence intervals for parameters A and B and a 95% confidence band for the entire median S-N curve were computed. These parameters are described in Appendix A. The meaning of the confidence band is that, based on the analysis of a series of independent data sets, one may expect that 95% of the computed hyperbolic bands will include the mean curve. Or, in other words, the statement "the mean curve (of the total distribution) lies within the computed interval" has a 95% probability of being correct.

4 RESULTS

An overview of the low cycle fatigue test results of the core programme is shown in Appendix B. In the next subsections the results of the supplemental programme are presented.

4.1 Smooth cylindrical LCF specimens

The test results are presented in table 3. The applied stress levels at a stress ratio R=0 have been converted to comparable stress levels at a stress ratio R=0.1. The ratio $\sigma_{alt,\ R=0}$ / $\sigma_{alt,\ R=0.1}$ at a given number of cycles to failure is determined by linear interpolation in figure 2 [4]. The stress range belonging to stress ratio R=0.1 for this number of cycles to failure can be calculated now. It should be noticed that the constant life lines plotted in figure 2 have been derived for unnotched IMI 685 specimens at room temperature. Because there were no Ti-6Al-4V data available, figure 2 was also used to convert the Ti-6Al-4V stress ranges. The test results are shown graphically in figures 3-6. Note that, unlike engineering convention, the stress range as the independent variable is plotted on the horizontal axis and the cycles to failure on the vertical axis. This is for commonality with the statistical analyses of the results.

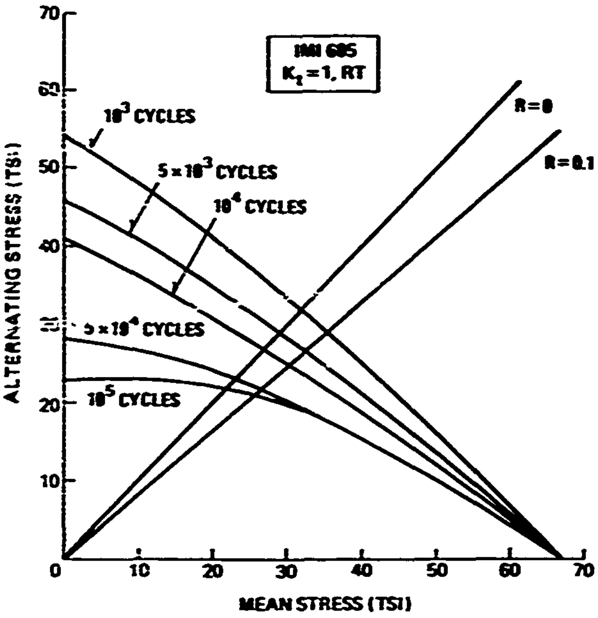

Fig. 2 Constant life diagram [4]

TABLE 3
Fatigue life test results on smooth cylindrical LCF specimens

laboratory	disc no.	specimen no.	stress ratio R	stress range (MPa)	converted stress range (MPa)	cycles to failure N_f
IMI 685						
IA	2	1	0.1	797		6160
		2		797		3820
		3		747		14190
		4		∮		∮
		5		842		2080
		6		850		1720
NL	1	1	0.1	775		15847
		2		850		2210
		3		730		24782
		4		775		14830
		5		850		3886
		6		730		23552
RR	3	1	0	820	763	22553
		2		900	825	4642
		3		780	729	33083
		4		740	687	15609
		5		700	667	94669
		6		720	677	50819
Ti-17						
ND	GL567	1	0.1	750		1851300
		2		750		1460560
		3		850		377240
		4		950		14450
		5		850		472885
		6		950		12410
Ti-6Al-4V						
RR	∮	1	0	860		18558*
		2		860		19564*
		3		860	796	10290*
		4		800	742	15493
		5		740	694	43541
		6		700		65968*

* thread failure
∮ data not available

Figure 3 shows the test results and associated median curve and confidence intervals for IMI 685. The individual fitted curves of the three laboratories which tested IMI 685 are plotted in figure 4. The overall median curve and confidence interval are also plotted in figure 4. The individual laboratory curves fall within the 95% confidence interval. There is no indication of deviating results for individual laboratories.

Figures 5 and 6 show the test results and associated median curves and confidence intervals for Ti-17 and Ti-6Al-4V respectively. Owing to the very few data, the confidence interval of the Ti-6Al-4V curve has been omitted.

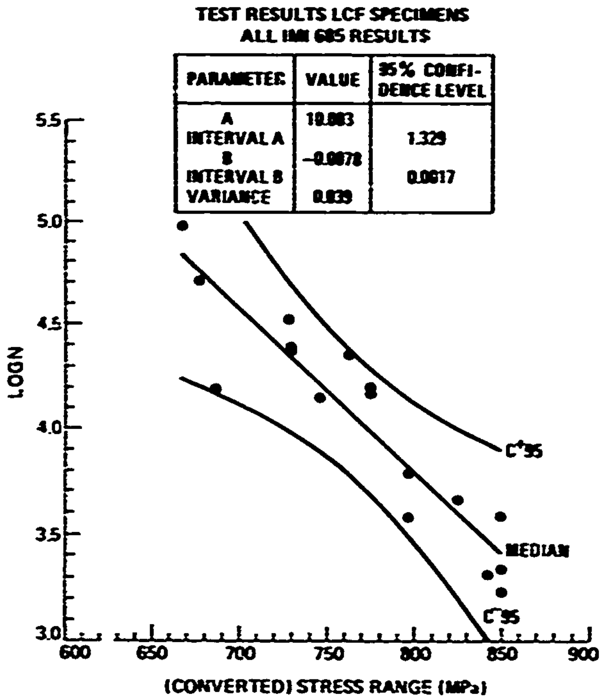

Fig. 3 Fitted relationship between fatigue life and stress range for all IMI 685 LCF data. The 95% confidence interval is also indicated

Fig. 4 Comparison between the overall median curve and the individual laboratories. The 95% confidence interval relates to the overall curve

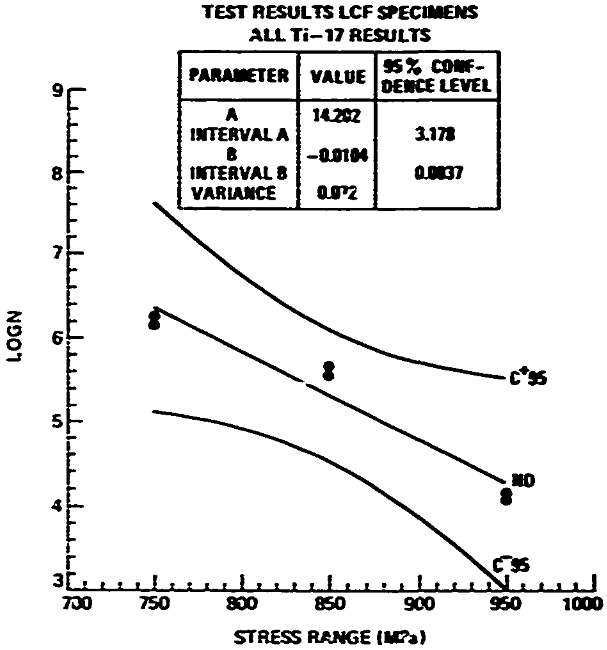

Fig. 5 Fitted relationship between fatigue life and stress range for all Ti-17 LCF data. The 95% confidence interval is also indicated

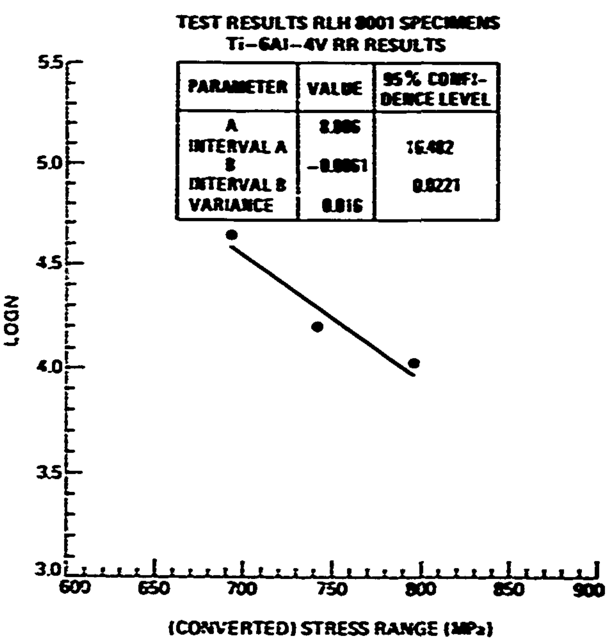

Fig. 6 Fitted relationship between life and stress range for the Ti-6Al-4V data generated in the supplemental programme

4.2 Flat double edge notched K_t=2.2 specimens

For the K_t2.2 specimens both the life to crack initiation and the life to failure were determined. Owing to the size of the specimen, the larger part (78-95%) of the total number of cycles consists of the cycles to crack initiation. This is shown in table 4. No significant difference in crack initiation versus total life between the titanium alloys was observed. The life to failure results

are shown graphically in figures 7-9. Again, the stress range is plotted on the horizontal axis whereas the cycles to failure are plotted on the vertical axis.
Figure 7 shows the test data and fitted relationship including the 95% confidence intervals for IMI 685. A comparison between the overall median curve of IMI 685 with the individual laboratory curves is made in figure 8. This figure shows that the individual laboratory curves lie close to the overall median curve and are all well within the 95% confidence interval.
Figure 9 shows the test results and fitted relationship including the 95% confidence intervals for Ti-17.

5 DISCUSSION

The monotonic and cyclic stress-strain curves for Ti-6Al-4V and IMI 685 are shown in figures 10 and 11 [5] respectively. Figure 12 shows the cyclic stress-strain curve for Ti-17 [6]. The monotonic stress-strain curve for Ti-17 is missing because there were no data available.
Figures 10-12 and table 1 show that there are no marked differences in cyclic behaviour of the three titanium alloys: mild softening takes place at room temperature. However, there are differences in mechanical properties between the titanium alloys. Especially the 0.2% yield strength of Ti-17 is superior. Keeping this in mind, the test results

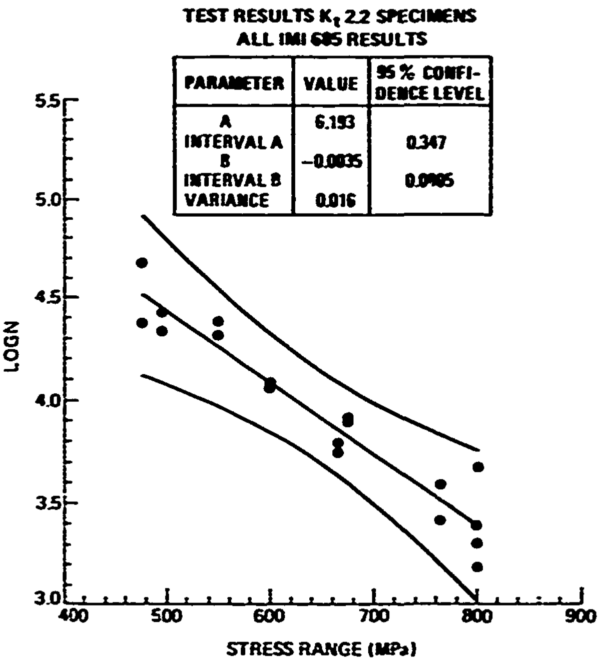

Fig. 7 Fitted relationship between fatigue life and stress range for all IMI 685 K_t2.2 data. The 95% confidence interval is also indicated

TABLE 4
Fatigue life test results on K_t=2.2 specimens (R=0.1)

laboratory	disc no.	specimen no.	stress range (MPa)	cycles to "1% crack initiation" N_i	cycles to failure N_f	N_i/N_f (%)
IMI 685						
IA	2	1	675	7150	8160	88
		2	549	18850	20700	91
		3	675	7420	7840	95
		4	801	1520	1520*	100
		5	549	21800	23900	91
		6	801	4050	4680	87
NL	1	1	600	10100	11422	88
		2	800	1650	2017	82
		3	475	44450	47290	94
		4	600	11075	12044	92
		5	800	2140	2450	87
		6	475	18900	23852	79
RR	3	1	765	3060	3860	79
		2	666	4605	5560	83
		3	495	18500	21601	86
		4	495	24820	26939	92
		5	666	5425	6166	88
		6	765	2070	2577	80
Ti-17						
ND	GL567	1	475	-#	30088	-#
		2	475	18500	23643	78
		3	625	-#	10456	-#
		4	625	13100	16738	78
		5	775	5700	6212	92
		6	775	7200	7566	95

* sudden rupture
\# data not available

have been plotted in two different ways: the fatigue life as function of the stress range and as function of the ratio of stress range to 0.2% yield strength.
Figures 13 and 14 show the median curves of the LCF and K_t2.2 test results generated in the core and

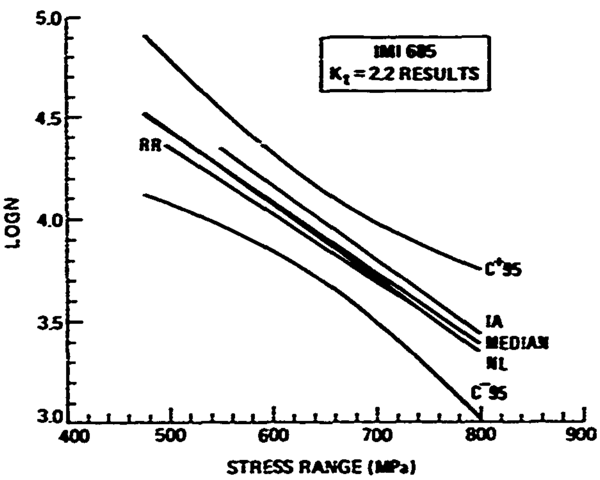

Fig. 8 Comparison between the overall median curve and the individual laboratories. The 95% confidence interval relates to the overall curve

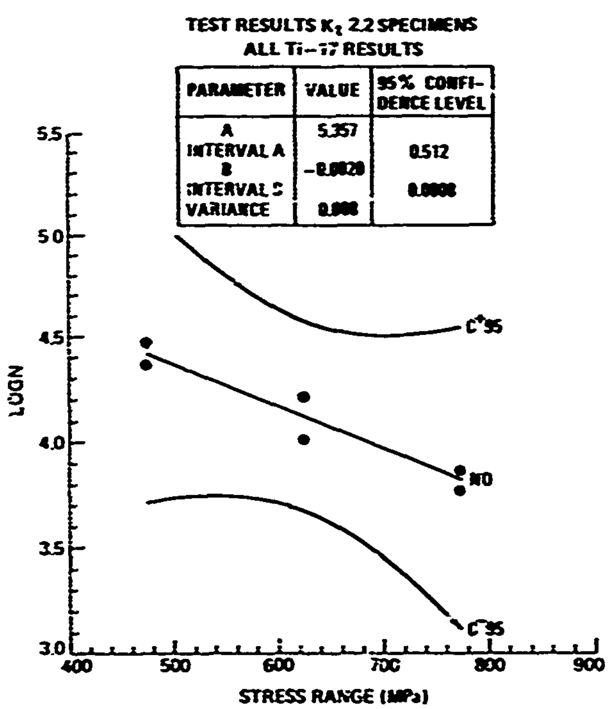

Fig. 9 Fitted relationship between fatigue life and stress range for all Ti-17 K_t2.2 data. The 95% confidence interval is also indicated

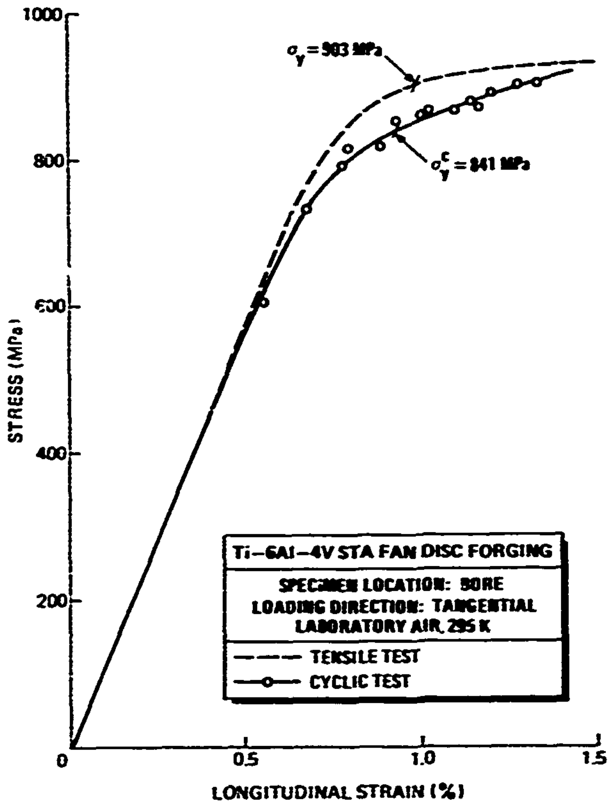

Fig. 10 Stress-strain behaviour of Ti-6Al-4V at room temperature

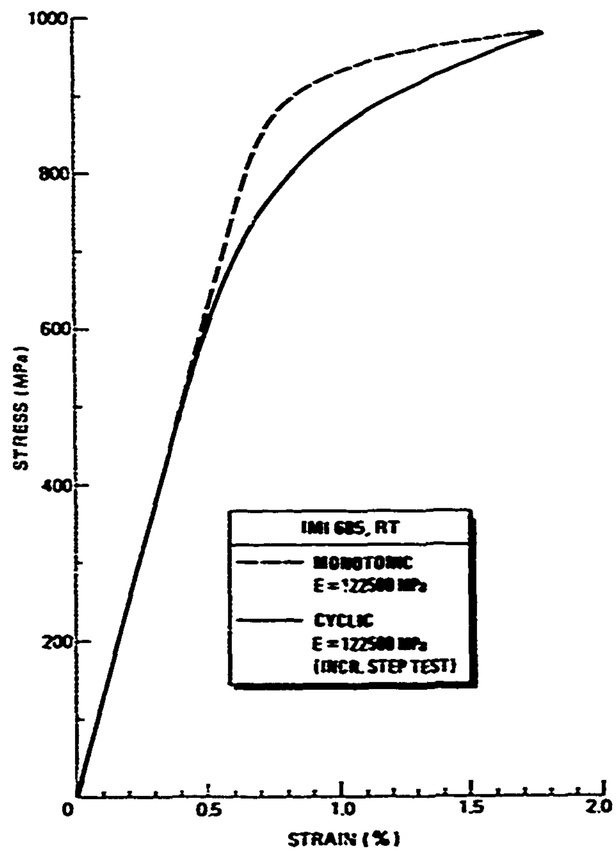

Fig. 11 Stress-strain behaviour of IMI 685 at room temperature [5]

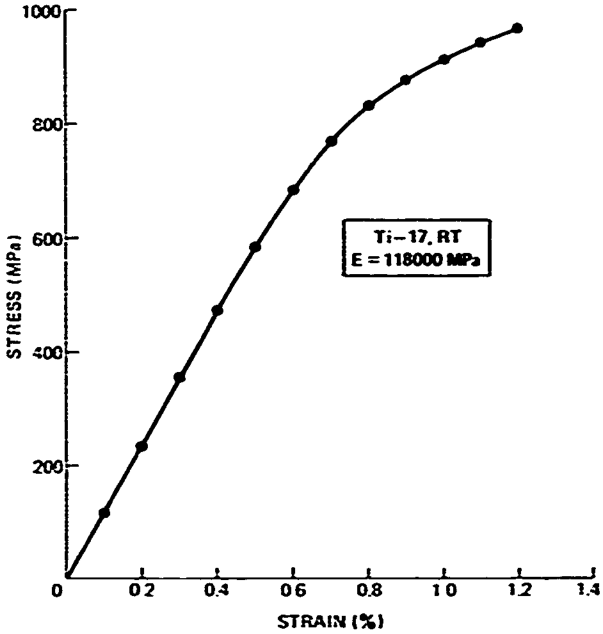

Fig. 12 Cyclic stress-strain behaviour of Ti-17 at room temperature [6]

supplemental programme. Almost no differences in smooth as well as notched low cycle fatigue behaviour between Ti-6Al-4V and IMI 685 were observed: both sets of Ti-6Al-4V and IMI 685 curves lie close to each other. Furthermore figures 13 and 14 show that Ti-17 has very good smooth but less pronounced notched low cycle fatigue behaviour compared with Ti-6Al-4V and IMI 685. In fact, the K_t2.2 curve of Ti-17 crosses the IMI 685 and Ti-6Al-4V curves, with Ti-17 showing better notched low cycle fatigue behaviour at higher stress ranges. The good low cycle fatigue properties of Ti-17 at higher stress ranges have also been reported in the literature [7] alloy. Ti-17 was developed to provide an grade suitable for use in aircraft engines as a fan and compressor disc material. This alloy possesses improved properties compared to commercial titanium alloys like Ti-6Al-4V [7]. However, the reduction in fatigue life due to the double edge notches is greater in Ti-17 than in Ti-6Al-4V and IMI 685. This is illustrated by the fatigue notch factor K_f, which is defined as the ratio of the stress range of the unnotched specimen to that of the notched specimen at a specified number of fatigue loading cycles. The K_f value at 25000 fatigue loading cycles of both Ti-6Al-4V and IMI 685 is 1.4, whereas that of Ti-17 is 1.9.

When taking the 0.2% yield strength into account the smooth low cycle fatigue behaviour of Ti-17 is

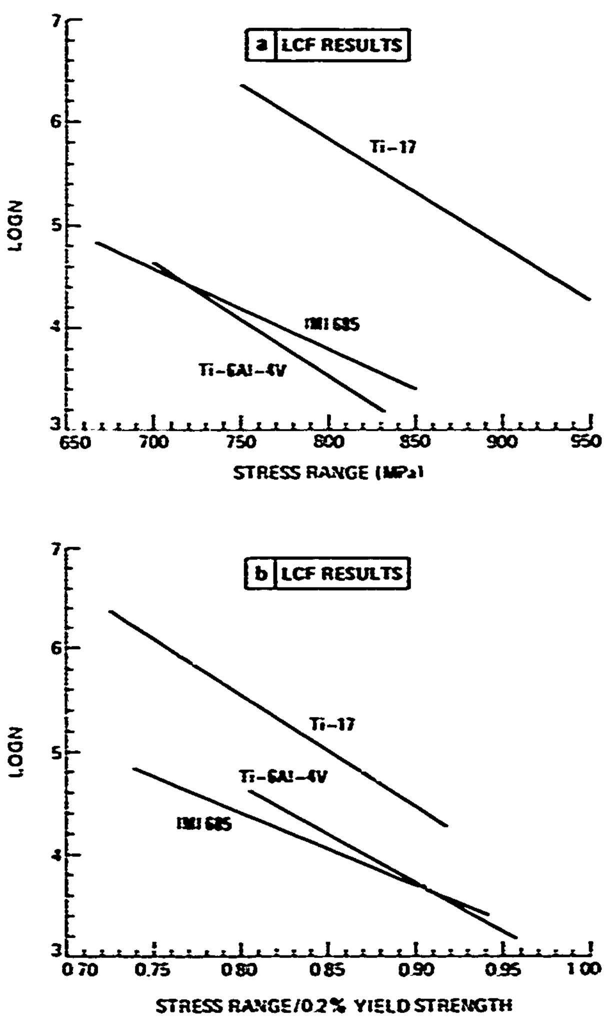

Fig. 13 Comparison of the smooth LCF specimen results generated in the core and supplemental programme

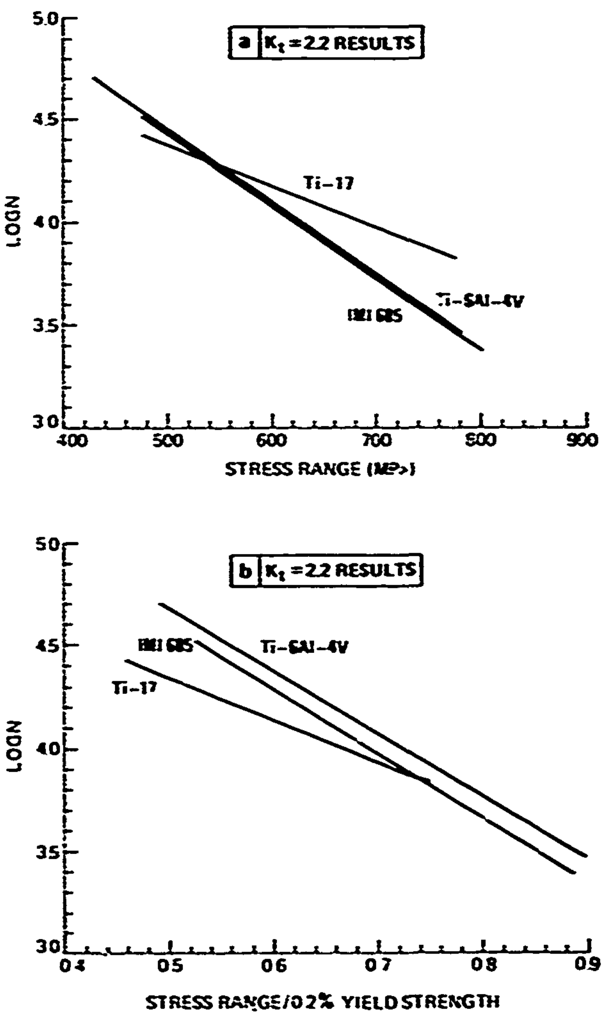

Fig. 14 Comparison of the K_t2.2 results generated in the core and supplemental programme

still superior but the Ti-17 K_t2.2 curve now lies below the Ti-6Al-4V and IMI 685 curves. More test results will be necessary to describe the notched low cycle fatigue behaviour of Ti-17, especially at high stress ranges, because it is not allowed to extrapolate the Ti-17 curve [3].

6 CONCLUSIONS

1. The results of the statistical analysis indicated no deviating test outcome for individual laboratories.
2. The larger part (78-95%) of the total life of the K_t=2.2 specimens consisted of cycles to crack initiation, as defined in section 2.
3. Ti-6Al-4V and IMI 685 showed similarity in low cycle fatigue behaviour.
4. Ti-17 has superior smooth low cycle fatigue properties as compared with Ti-6Al-4V and IMI 685.
5. The good notched low cycle behaviour of Ti-17, which is present at higher stress ranges, is neutralized by taking the 0.2% yield strength into account.

7 REFERENCES

1. A.J.A. Mom and M.D. Raizenne, "AGARD engine disc cooperative test programme", AGARD Report No. 766, Advisory Group for Aerospace Research and Development, Neuilly sur Seine, France, 1988.
2. A.J.A. Mom, "Revised working document for the AGARD cooperative test programme on titanium alloy engine disc material", NLR TR 86019 L, 1986.
3. ASTM E 739-80 "Standard practice for statistical analysis of linear and linearized stress-life (S-N) and strain-life (ε-N) fatigue data".
4. L. Grabowski, Personal communication from Rolls-Royce plc., Derby, United Kingdom.
5. P. Heuler, "LCF and notch fatigue data of Ti alloys for constant amplitude loading", IABG TFB-T-23/90, 1990.
6. J. Waldman, Personal communication from Naval Air Development Center, Warminster, USA.
7. M.J. Donachie, "Titanium and titanium alloys Source book", American Society for Metals, USA, pp. 10-14, 1982.

APPENDIX A

The statistical analysis of the LCF and K_t=2.2 data is based on the procedures described in ASTM E739 "Standard practice for statistical analysis of linear or linearized stress-life (S-N) and strain-life (ϵ-N) fatigue data".
A short summary of the procedure applied in the current AGARD programme is presented below.

Line equation

The statistical analysis is based on the assumption that the S-N relationship can be approximated by a straight line for a specific interval of stress. The following line equation was used:

$$Y = A + BX$$

in which:

$$Y = \log N$$
$$X = \Delta\sigma$$

The coefficients A and B of this linear model can be calculated according to:

$$\hat{A} = \bar{Y} - \hat{B}\bar{X}$$

$$\hat{B} = \frac{\sum_{i=1}^{k} (X_i - \bar{X})(Y_i - \bar{Y})}{\sum_{i=1}^{k} (X_i - \bar{X})^2}$$

$$\bar{X} = \frac{\sum_{i=1}^{k} X_i}{k} \quad \text{(average } X_i \text{ value)}$$

$$\bar{Y} = \frac{\sum_{i=1}^{k} Y_i}{k} \quad \text{(average } Y_i \text{ value)}$$

k = total number of test specimens.

$\hat{A}$ and $\hat{B}$ are called the maximum likelihood estimators of A and B.
(The symbol "caret" (^) denotes estimate: the symbol "overbar" (–) denotes average).

Variance

To estimate the variance of the normal distribution for log N the following expression is recommended:

$$\hat{\sigma}^2 = \frac{\sum_{i=1}^{k} (Y_i - \hat{Y}_i)^2}{k - 2}$$

in which:

$$\hat{Y}_i = \hat{A}_i + \hat{B}X_i$$

The term k-2 is used instead of k to make $\hat{\sigma}^2$ an unbiased estimator of the normal population variance σ^2.

Confidence intervals for A and B

The confidence intervals for A and B are given by:

$$\hat{A} \pm t_p \hat{\sigma} \left[\frac{1}{k} + \frac{\bar{X}^2}{\sum_{i=1}^{k} (X_i - \bar{X})^2} \right]^{1/2}$$

$$\hat{B} \pm t_p \hat{\sigma} \left[\sum_{i=1}^{k} (X_i - \bar{X})^2 \right]^{-1/2}$$

The value of t_p is read from the t-distribution using the desired value of the confidence level P associated with the confidence interval (see Table A1). The entry parameter n (the degrees of freedom of t) equals k - 2 for the two above equations.

TABLE A1
Values of t_p

n (k - 2)	P, %	
	90	95
4	2.1318	2.7764
5	2.0150	2.5706
6	1.9432	2.4469
7	1.8946	2.3646
8	1.8595	2.3060
9	1.8331	2.2622
10	1.8125	2.2281
11	1.7959	2.2010
12	1.7823	2.1788
13	1.7709	2.1604
14	1.7613	2.1448
15	1.7530	2.1315
16	1.7459	2.1199
17	1.7396	2.1098
18	1.7341	2.1009
19	1.7291	2.0930
20	1.7247	2.0860
21	1.7207	2.0796
22	1.7171	2.0739

Note: P is the probability in percent that the random variable t lies in the interval from $-t_p$ to $+t_p$.
n is not sample size, but the degrees of freedom of t, that is n = k - 2

Confidence band for the entire median S-N curve

The confidence band for the entire log N - $\Delta\sigma$ curve is calculated using the following equation:

$$Y = \hat{A} + \hat{B}X \pm \sqrt{2F_p}\,\hat{\sigma} \left[\frac{1}{k} + \frac{(X - \bar{X})^2}{\sum_{i=1}^{k} (X_i - \bar{X})^2} \right]^{1/2}$$

in which F_p is given in Table A2. This table contains two entry parameters n_1 and n_2, which are the statistical degrees of freedom for F. For the above equation n_1 = 2 and n_2 = k-2.

TABLE A2
Values of F_p for a 95 % probability

		Degrees of freedom $n_1 = \ell - 2$			
		1	2	3	4
Degrees of freedom, n_2 $n_2 = k - \ell$	1	161.45	199.50	215.71	224.58
	2	18.513	19.000	19.164	19.247
	3	10.128	9.5521	9.2766	9.1172
	4	7.7086	6.9443	6.5914	6.3883
	5	6.6079	5.7861	5.4095	5.1922
	6	5.9874	5.1433	4.7571	4.5337
	7	5.5914	4.7374	4.3468	4.1203
	8	5.3177	4.4590	4.0662	3.8378
	9	5.1174	4.2565	3.8626	3.6331
	10	4.9646	4.1028	3.7083	3.4780
	11	4.8443	3.9823	3.5874	3.3567
	12	4.7472	3.8853	3.4903	3.2592
	13	4.6672	3.8056	3.4105	3.1791
	14	4.6001	3.7389	3.3439	3.1122
	15	4.5431	3.6823	3.2874	3.0556

APPENDIX B

A summary of the Ti-6Al-4V low cycle fatigue test results generated in the core programme is presented below. A more detailed description of these test results is given in AGARD Report No. 766: "AGARD Engine disc cooperative test programme" (1988).

TABLE B1
Fatigue life test results on LCF specimens (R=0.1)

DISC AGARD 1113

laboratory	specimen no.	stress range $\Delta\sigma$ MPa	cycles to failure N_f	laboratory	specimen no.	stress range $\Delta\sigma$ MPa	cycles to failure N_f
UT	LCF 2	800	2850	RR	LCF 33	878	3
	LCF 6	800	2340		LCF 35	828	437
	LCF 4	775	4790		LCF 36	788	5067
	LCF 5	775	5150		LCF 34	788	5687
	LCF 1	750	13540		LCF 38	742	21217
	LCF 3	-	-		LCF 37	742	14515
QE	LCF 19	800	3509	NL	LCF 23	875	<1
	LCF 16	775	5665		LCF 21	800	3151
	LCF 18	775	7050		LCF 25	775	8605
	LCF 17	750	8851		LCF 22	775	7264
	LCF 14	750	12484		LCF 20	750	9457
	LCF 15	700	40341		LCF 24	750	19426
NR	LCF 12	800	1800	RA	LCF 31	880	<1
	LCF 7	800	1900		LCF 27	790	5982
	LCF 9	750	12100		LCF 28	750	8545
	LCF 8	750	8800		LCF 32	750	13284
	LCF 10	725	18500		LCF 29	720	22474
	LCF 11	700	42000		LCF 30	720	15209

DISC AGARD 7200

laboratory	specimen no.	stress range $\Delta\sigma$ MPa	cycles to failure N_f	laboratory	specimen no.	stress range $\Delta\sigma$ MPa	cycles to failure N_f
AF	LCF 19	800	3928	CE	LCF 33	878	40
	LCF 18	775	4672		LCF 35	832	3136
	LCF 16	775	5632		LCF 36	788	8508
	LCF 14	750	16143		LCF 34	788	5440
	LCF 17	750	25933		LCF 38	742	>16262
	LCF 15	-	-		LCF 37	742	23076
ND	LCF 5	825	3831	IA	LCF 27	878	1158
	LCF 2	800	6235		LCF 29	878	348
	LCF 3	775	8174		LCF 30	810	3298
	LCF 6	750	21709		LCF 32	810	4466
	LCF 4	725	41222		LCF 28	742	12805
	LCF 1	-	-		LCF 31	742	14656
NS	LCF 9	809	2679	PI	LCF 22	800	3071
	LCF 8	809	2350		LCF 23	800	2472
	LCF 7	779	5510		LCF 24	775	6874
	LCF 12	766	11016		LCF 25	775	4724
	LCF 10	751	8156		LCF 20	750	9964
	LCF 11	747	11327		LCF 21	750	7540

TABLE B2

Fatigue life test results on K_t=2.2 specimens (R=0.1)

DISC 1113

laboratory	specimen no.	stress range $\Delta\sigma$ MPa	cycle to "1% crack initiation" N_i	cycles to failure N_f	laboratory	specimen no.	stress range $\Delta\sigma$ MPa	cycles to "1% crack initiation" N_i	cycles to failure N_f
UT	K_t 5	775	3420	3476	RR	K_t 36	700	5950	6700
	K_t 1	775	4202	4247		K_t 40	562	6700	7900
	K_t 4	625	8484	8920		K_t 35	562	13000	14200
	K_t 2	625	10630	10999		K_t 39	562	17500	19500
	K_t 6	475	22764	23856		K_t 37	486	20500	23500
	K_t 3	475	31717	33026		K_t 38	486	34000	36500
QE	K_t 17	775	3501	3701	NL	K_t 25	775	3026	3557
	K_t 14	775	3301	3726		K_t 26	775	3301	3714
	K_t 15	625	-	10952		K_t 23	625	16941	18584
	K_t 13	625	7701	8826		K_t 24	625	10207	11436
	K_t 18	475	41680	43730		K_t 27	475	27101	29352
	K_t 16	475	36601	38826		K_t 28	475	21501	24118
NR	K_t 10	775	2707	2771	RA	K_t 31	775	2832	3288
	K_t 9	775	2750	2841		K_t 32	775	3023	3810
	K_t 11	625	10090	11191		K_t 29	625	11357	12342
	K_t 8	625	8875	8921		K_t 33	625	11349	12176
	K_t 7	475	29500	30061		K_t 30	475	48748	51337
	K_t 12	475	38500	39551		K_t 34	475	>56511	>56511

DISC 7200

laboratory	specimen no.	stress range $\Delta\sigma$ MPa	cycle to "1% crack initiation" N_i	cycles to failure N_f	laboratory	specimen no.	stress range $\Delta\sigma$ MPa	cycles to "1% crack initiation" N_i	cycles to failure N_f
AF	K_t 14	775	2037	2334	CE	K_t 38	698	4691	5230
	K_t 13	775	2704	3039		K_t 35	562	19832	20599
	K_t 17	625	8131	9254		K_t 37	562	13811	14953
	K_t 16	625	9043	9768		K_t 39	428	201594	211330
	K_t 18	475	21775	23053		K_t 40	428	36500	40190
	K_t 15	475	59499	61568		K_t 36	-	-	-
ND	K_t 1	775	2150	2765	IA	K_t 32	780	2040	2466
	K_t 5	625	5850	6038		K_t 33	776	2510	3039
	K_t 4	625	9200	10258		K_t 34	627	6550	7317
	K_t 6	475	46950	48995		K_t 31	626	7340	9040
	K_t 2	475	27300	29800		K_t 30	528	12300	13180
	K_t 3	-	-	-		K_t 29	475	>63750	>63750
KS	K_t 9	775	4050	4340	PI	K_t 26	1091	28	38
	K_t 12	775	2575	2890		K_t 23	775	3010	3182
	K_t 7	625	9200	9660		K_t 27	625	5964	6800
	K_t 8	625	8950	9810		K_t 28	625	7888	8855
	K_t 11	500	27000	29350		K_t 24	550	17024	17933
	K_t 10	500	25100	27120		K_t 25	475	>55197	>55197

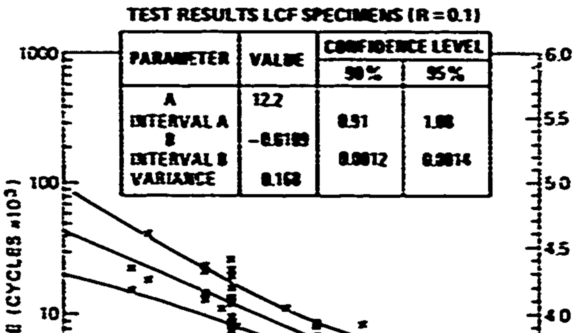

Fig. B1 Fitted relationship between fatigue life and stress range for the LCF data

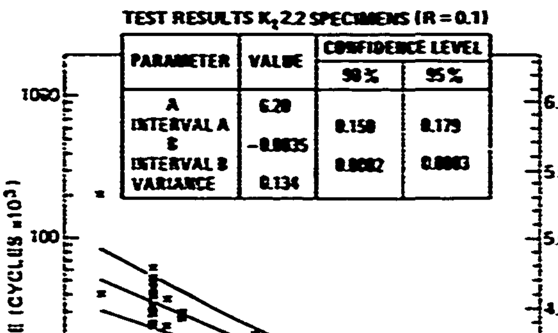

Fig. B2 Fitted relationship between fatigue life and stress range for the K_t2.2 data

FATIGUE CRACK GROWTH RESULTS FOR Ti-6Al-4V, IMI 685 and Ti-17

M.D. Raizenne
Institute for Aerospace Research
National Research Council of Canada
Ottawa, Ontario
K1A 0R6

SUMMARY

This chapter presents the fatigue crack growth results for the titanium alloys IMI 685, Ti-6Al-4V and Ti-17 that were tested in the Supplemental phase of the AGARD SC.33 Engine Disc Cooperative Test Programme. The fatigue crack growth work was carried out under load control using compact tension and corner crack specimen geometries. Tests were conducted under the following loading conditions: constant amplitude (R = 0.1 and R = 0.7), constant amplitude (R=0) with minor cycles, an R=1.7 single overload sequence and the cold TURBISTAN variable amplitude sequence. The data is presented using a point to point or secant method. The constant amplitude and single overload data base was subsequently used by five participating laboratories to predict a series of 60 load cases using their respective crack growth prediction models.

Nomenclature:

a	-	Crack Length (mm)
B	-	Specimen thickness (mm)
CC	-	Corner Crack Specimen
CT	-	Compact Tension Specimen
da/dN	-	Meters / Cycle or Meters/Flight
ΔK	-	Change in crack tip stress intensity during a single load cycle (MPa $\sqrt{m}$)
Kmax	-	Maximum crack tip stress intensity (MPa$\sqrt{m}$)
N	-	Cycles
P	-	Applied load (kN)
R-ratio	-	Minimum load/maximum load
W	-	Specimen width (mm)
σ	-	Applied stress (MPa)

1.0 INTRODUCTION

The AGARD Structures and Materials Subcommittee 33 - AGARD Engine Disc Cooperative Test Programme was carried out in two phases: an initial Core phase and a follow-on Supplemental phase. In the Core phase twelve laboratories from seven NATO countries generated a single R-ratio (0.1) database of fatigue crack growth data for titanium Ti-6Al-4V. The Ti-6Al-4V material was supplied by Rolls Royce from RB-211 compressor fan forgings. The Core phase succeeded in calibrating the twelve participating laboratories using standardized test specimens and test procedures. The results, reported in Reference 1, show a narrow scatter band of between two and three for the crack growth rate data between 20 and 35 MPa$\sqrt{m}$.

In the Supplemental phase the single alloy/load case was expanded to sixty different alloy/load case combinations. The expanded test matrix included:

- one $\alpha + \beta$ processed alloy (Ti-6Al-4V) and two β processed alloys (IMI 685 and Ti-17)
- two constant amplitude sequences (R = 0.1 and 0.7)
- one overload sequence (R = 1.7)
- three constant amplitude sequences with varying levels of minor cycles
- cold TURBISTAN and three modified versions, and
- two specimen geometries, the compact tension and the corner crack.

The sixty alloy/load cases were also modelled using five different fatigue crack growth models currently in use at NASA Langley, CEAT, FFA, NLR and Rolls Royce. The objective of the modelling was to compare predicted and experimental results. Model descriptions and results are presented in Chapters Five and Six.

The purpose of this chapter is to present the experimentally derived fatigue crack growth results in graphical format.
The data base can also be made available in

numerical format by contacting:

Donald Raizenne,
National Research Council Canada
Institute for Aerospace Research
Building M-14
Ottawa, Ontario
Canada K1A 0R6

2.0 PARTICIPANTS

The participating laboratories in the generation of the fatigue crack growth data were the following:

AF Air Force Materials Laboratory (AFML), WPAFB, Dayton, Ohio, USA
CE Centre d'Essais Aéronautique de Toulouse (CEAT), France
IA Industrieanlagen - Betriebsgesellschaft (IABG), Ottobrunn, Germany
NL National Aerospace Laboratory (NLR), Amsterdam, The Netherlands
PI University of Pisa, Pisa, Italy
QE Quality Engineering Test Establishment (QETE), Ottawa, Canada
RA Royal Aerospace Establishment (RAE), Farnborough, United Kingdom
RR Rolls Royce, Derby, United Kingdom
UT University of Toronto, Toronto, Canada

The IAR coordinated the test programme by preparing the detailed test procedures [2], collecting the crack growth data, providing selected data to the five modelling laboratories [3] and presenting the experimental results.

3.0 MATERIALS AND SPECIMEN GEOMETRIES

The specimen material used in the Supplemental phase was provided in the form of solution treated and aged compressor disc forgings by Rolls Royce (Ti-6Al-4V and IMI 685) and General Electric (Ti-17). Typical mechanical properties for the three alloys are provided in Table 1.

There is a distinct difference in grain size between the conventionally $\alpha + \beta$ processed Ti-6Al-4V and the β processed IMI 685 and Ti-17 alloys. Ti-6Al-4V has a typical grain size of 25 µm while IMI 685 and Ti-17 have typical grain sizes in the range of 400 µm. One objective of the Supplemental phase was to determine the grain size sensitivity of the potential drop technique in measuring crack size. A second objective was to compare the scatter in the fatigue crack growth results between the two alloy groups.

Two specimen geometries were used for the fatigue crack propagation testing. The ASTM compact tension specimen (designated CT) was used for crack lengths in the long crack regime which are typically two-dimensional through-the-thickness flaws. The second specimen, developed by Rolls Royce [4], is the corner crack specimen (designated CC). Rolls Royce developed this specimen to simulate corner crack flaw geometries with three-dimensional stress fields typically found in the disc bore locations and fastener holes. Both the CT and CC specimen geometries are shown in Figure 1.

The specimen blanks were cut from various locations in the disc forgings. The disc cut-up drawings are shown in Figures 2, 3 and 4. The orientation of the specimen crack planes to the forging directions were specified so that they would be representative of those encountered in service. Rolls Royce machined the Ti-6Al-4V and IMI 685 specimens and IAR machined the Ti-17 specimens.

The thickness of the compact tension blanks cut from the Ti-17 forging (Figure 4) were less than the specified 25 mm in Figure 1. A lack of available material necessitated specimen thicknesses in the range of 7 mm to 18 mm.

In order to simplify specimen identification, the supplemental test programme specimens were coded as follows:

RR	CT	18
Laboratory	Specimen Geometry	Specimen #

A detailed specimen cross reference, including material, disc location and sequence is provided in Tables 2, 3 and 4.

4.0 LOADING SEQUENCES

4.1 Constant Amplitude

Two constant amplitude sequences, R = 0.1 and R = 0.7 were selected for the test programme. The wave shape was trapezoidal with a frequency of 0.25 Hz. The R = 0.1 load

sequence as shown in Figure 5.

4.2 Simple Sequences

Three simple sequences were selected to study the effect of minor cycles on a single major cycle. The sequences designated SS1, SS2 and SS3 are shown in Figure 6. The dwell time at peak load in the constant amplitude trapezoidal cycle (Figure 5) is replaced with 10 minor cycles. Minor cycle amplitudes of 10, 30 and 50 percent of peak load were investigated. All major and minor cycle loading rates were constant and the R-ratio was set at zero. The cycle period, defined as the time for one major cycle, increased from four seconds for the constant amplitude cycle (Figure 5) to 13 seconds for the SS3 cycle.

The fourth simple sequence (designated SS4) was selected to investigate the retardation effect of a single overload on 1000 constant amplitude cycles. An overload ratio of 1.7 was chosen. The wave shape used for this sequence is a simple triangular shape. The SS4 sequence is shown in Figure 7.

4.3 Complex Sequences

The four complex sequences used in the test programme were the complete Cold TURBISTAN sequence [5] and three modified versions. TURBISTAN is a variable amplitude loading standard that was developed for 'cold' compressor parts using combat jet aircraft engine data from four NATO airforces and five aircraft types. The basic Cold Turbistan sequence is comprised of 100 individual flights with an average of 154 end points per flight. The loading points are expressed in percent values of the maximum load. The maximum loads for the supplemental test programme were selected to provide approximately 30,000 TURBISTAN flights to specimen failure.

One of the programme objectives was to investigate the influence of minor cycle omission on fatigue life. Four Turbistan sequences (designated TURB100, TURB10, TURB30 and TURB50) were tested with minor cycle omission levels of 0%, 10%, 30% and 50%. The number of end points per sequence are listed in Table 5. As the small cycles have small amplitudes and varying mean stresses, the omission algorithm was not based on range filtering, but on damage filtering.[5]

An illustration of the effects of the three omission levels on a TURBISTAN flight is presented in Figure 8.

5.0 CRACK LENGTH MEASUREMENT PROCEDURE

Crack lengths were measured using a direct current (DC) potential drop technique. The details of the technique are provided in the core programme report, Reference 1. For the supplemental work, the DC potential drop technique was modified to accommodate the simple and complex sequences as illustrated in Figures 9 and 10. Typically a one second hold time is applied to the maximum load level during which both current off and current on measurements are taken.

The detailed test procedures for the supplemental phase are provided in Reference 2.

6.0 RESULTS

The fatigue crack growth results for the three titanium alloys are presented in:

Figures 11 to 20 -	Ti-6Al-4V
Figures 21 to 31 -	IMI 685
Figures 32 to 41 -	Ti-17

The fatigue crack growth rates were calculated from the incremental crack length measurements:

$$da/dN = (a_{i+1} - a_i) / (N_{i+1} - N_i)$$

The crack tip stress intensity solutions used in the analysis for the two specimen geometries are the following:

<u>**Compact Tension**</u>

$$K_I = \frac{P}{B\sqrt{W}} \frac{2 + a/w}{(1-a/w)^{1.5}} (0.886 + 4.64\ (a/w) - 13.32$$

$$(a/w)^2 + 14.72\ (a/w)^3 - 5.6\ (a/w)^4)$$

<u>**Corner Crack or Quarter Circular Crack**</u>
(potential drop crack length measurement) [1],[6]

The crack tip stress intensity equations for the average circular crack length are:

$$K_I = (0.97 - 0.09\ (a/w)^2)\ 1.16\ \frac{2}{\pi} \sigma \sqrt{\pi a}$$
for $a/w < 0.2$

$$K_I = (0.97 - 0.09\,(a/w)^2)\,(1.12 - 0.13\,(a/w) + 1.84\,(a/w)^2 - 0.11(a/w)^3 + 0.8\,(a/w)^4)\,\frac{2}{\pi}\,\sigma\sqrt{\pi a}$$

for $a/w \geq 0.2$

Ti-6AL-4V

The results in Table 6 indicate:

- For the simple sequence data, using R=0.1 as baseline, the addition of minor cycles does not influence the crack growth rate until the magnitude of the minor cycle reaches 50% (SS3) of the major cycle.
- For the complex sequences, using the full TURBISTAN sequence (TURB100) as baseline, minor cycle omission levels of 10 and 30% do not significantly alter the TURB100 data. When the omission level reaches 50% (TURB50) the crack growth data is reduced by a factor of two at 30 MPa√m
- The crack growth rate for the full TURBISTAN sequence, TURB100 is four times more severe than the R = 0.1 data at K_{MAX} = 30 MPa√m
- The overload sequence, SS4, compared to the R = 0.1 data retards the crack growth rate by a factor of eight at 10 Mpa√m and four at 30 MPa√m.

IMI 685

The results in Table 7 indicate:

- For the simple sequence data, using R = 0.1 as baseline, the minor cycles increase the crack growth rate when the minor cylces reach 30% (SS2) of the major cycle and increase further at 50% (SS3).
- For the complex sequences, the omission levels of 10, 30 and 50% do not significantly alter the baseline (TURB100) data.
- The crack growth rate for the full TURBISTAN sequence, TURB100 is approximately three times more severe than the R = 0.1 data at K_{MAX} = 30 MPa√m
- The overload sequence, SS4 compared to the R = 0.1 data retards the crack growth rate by a factor of four at 30 MPa√m.

Ti-17

The result in Table 8 indicates:

- For the simple sequence data, using R = 0.1 as baseline, the addition of minor cycles of 30 and 50% (SS2 and SS3) of the major cycle increases the baseline crack growth rate.
- For the complex sequences, the crack growth rate is reduced by a factor of two for the 50% omission level (TRUB50) at 30 MPa√m.
- The full TURBISTAN sequence, TURB100, is approximately four times more severe than the R = 0.1 data at Kmax - 30 MPa√m.
- The overload sequence, SS4, compared to the R = 0.1 data retards the crack growth rate by a factor of four at 30 MPa√m.

A comparison of the different alloys indicates:

- Minor cycles of 10 to 30% of the major cycle do not significantly alter the constant amplitude or TURBISTAN baseline data for Ti-6Al-4V or Ti-17.
- For IMI 685 the data is conflicting as the minor cycle effect starts at 30% of the major cycle for the constant amplitude data while omission levels of 10, 30 and 50% did not reduce the crack growth rates for the baseline TURBISTAN data.
- The full TURBISTAN sequence produces crack growth rates three to four times higher than the simple R = 0.1 trapezoidal baseline data for the three alloys.
- The retardation effect in SS4 is greater in the fine grained Ti-6Al-4V (x10) than the two coarse grained alloys, IMI 685 and Ti-17 (x4).
- The DC potential drop technique proved successful in measuring crack lengths in the two coarse grained Titanium alloys.
- In comparing the scatter in the data, Ti-17 produced the narrowest range of data for all of the test sequences. The different CT specimen thicknesses (7 to 25 mm) for the Ti-17 specimens did not influence the crack growth rate results.

7.0 DISCUSSION & CONCLUSIONS

The major objectives of the fatigue crack growth part of the Supplmental Programme were:

- build on the testing expertise developed during the Core Programme.
- expand the test matrix to investigate the effects of minor cycles, retardation and variable amplitude loading on fatigue crack growth.
- investigate the crack growth rate

properties of coarse grained titanium alloys, and
- evaluate the DC potential drop technique for crack length measurements in coarse grained titanium alloys.

In all aspects the programme objectives were met. One hundred and eighty-five tests were carried out by the nine participating laboratories. Sixty different alloy/load case combinations were studied. The DC potential drop technique developed in the Core Phase was successfully used for all tests.

The test results indicate that the use of test sequences other than simple constant amplitude can greatly affect the crack growth rate properties of a material. Loading sequences for rotating gas turbine components have traditionally been reduced to a single major cycle. Minor cycle effects have largely been ignored or viewed as non-damaging. The data produced in the test programme indicates that minor cycle effects must be viewed in the context of the material microstructure. Ti-6Al-4V with a grain size in the range of 25 µm is less sensitive to the 30% minor cycle range than the two coarser grained (400 µm) alloys where the 30% minor cycle range noticeably accelerated the crack growth rate. However, when minor cycle effects are combined in a variable amplitude sequence such as TURBISTAN the results show a different ranking. The Ti-6Al-4V and Ti-17 show emission level effects at the 50% level while IMI 685 shows only a minor effect. The reason for the different material responses to the loading sequences is difficult to explain. A more detailed statistical approach would be useful in quantifying the effects. A conclusion however is that generalizing sequence effects can result in a non-conservative estimate of fatigue life.

The use of a specific loading standard such as TURBISTAN is very useful for comparative purpose. At present TURBISTAN is the only accepted loading standard for gas turbine applications. The TURBISTAN crack growth results indicate that using a single cycle to simulate a flight is a non-conservative approach by two to three times when compared to the TURBISTAN data. Conversely the TURBISTAN sequence and the load selected load levels may be too severe. The crack growth modelling results in Chapter six address the TURBISTAN load levels and the rate of damage accumulation.

The retardation effect again points to material microstructure as an influence. The retardation in Ti-6Al-4V was two to three times more severe than Ti-17 and IMI685.

8.0 REFERENCES

1. Mom, A.J.A. and Raizenne, M.D. 'AGARD Engine Disc Cooperative Test Programme, AGARD Report No. 766, August 1988.

2. Raizenne, M.D., 'AGARD TX114 Test Procedures for Supplemental Engine Disc Test Programme', National Research Council of Canada, LTR-ST-1617, June 1988.

3. Raizenne, M.D., 'AGARD SMP SC.33 Engine Disc Test Programme Fatigue Crack Growth Rate Data and Modelling Cases for Ti-6Al-4V, IMI 685 and Ti-17', National Research Council of Canada, LTR-ST-1785, November 1990.

4. Pickard, A.C., Brown, C.W. and Hicks M.A., 'The Development of Advanced Specimen Testing and Analysis Techniques Applied to Fracture Mechanics Lifing of Gas Turbine Components', ASME International Conference on Advances in Life Prediction Methods, Edited by D.A. Woodford and J.R. Whitehead, Published by ASME, 1983.

5. ten Have, A.A. 'Cold TURBISTAN. Final Definition of a Standardized Fatigue Test Loading Sequence for Tactical Aircraft Cold Section Engine Discs', Combined Report of the MTU, IABG, LBF, RWTH Aachen, Rolls-Royce, RAE, SNECMA, CEAT, ONERA, NLR, University of Utah and NRC, National Aerospace Laboratory TR87054L, The Netherlands, March 1987.

6. Pickard, A.C., 'Stress Intensity Factors for Cracks with Circular and Elliptic Crack Fronts, Determined by 3D Finite Element Methods', 2nd International Conference on Numerical Methods on Fracture Mechanics, Swansea, 1980.

TABLE 1
MECHANICAL PROPERTIES AT ROOM TEMPERATURE FOR TITANIUM ALLOYS

	UTS (MPa)	0.2% YS (MPa)	Elongation (%)	Reduction in Area (%)	Fracture Toughness $MPa\sqrt{m}$
Ti-6Al-4V	970	870	11	27	70
IMI 685	1029	903	6*	15*	70
Ti-17	1175	1035	10	19	70

* Minimum Specified

TABLE 2

FATIGUE CRACK GROWTH SPECIMEN IDENTIFICATION

Ti-6Al-4V

SPECIMEN#	LOCATION	SEQUENCE
AFCT07	DISC 1, 21	SS TYPE 1, R=0.0
" 08	" 22	SS TYPE 1, R=0.0
" 09	" 24	SS TYPE 2, R=0.0
" 10	" 25	SS TYPE 3, R=0.0
" 11	" 26	SS TYPE 3, R=0.0
" 12	" 27	SS TYPE 4, R=0.1
" 13	" 28	SS TYPE 4, R=0.1
" 14	" 37	10% TURBISTAN
" 15	" 41	10% "
" 16	" 30	30% "
" 17	" 40	30% "
" 18	" 39	50% "
" 19	" 38	FULL "
CECC07	" 1	CST AMP, R=0.7
" 08	" 3	SS TYPE 1, R=0.0
" 09	" 4	SS TYPE 2, R=0.0
" 10	" 2	CST AMP, R=0.1
CECT11	" 10	CST AMP, R=0.1
" 12	" 8	CST AMP, R=0.7
" 13	" 6	SS TYPE 1, R=0.0
CECC14	" 5	SS TYPE 3, R=0.0
" 15	" 10	SS TYPE 3, R=0.0
" 16	" 6	SS TYPE 4, R=0.1
CECT17	" 31	SS TYPE 4, R=0.1
" 18	" 35	10% TURBISTAN
" 19	" 7	FULL TURBISTAN
CECC20	" 7	10% "
" 21	" 13	10% "
" 22	" 12	30% "
" 23	" 8	30% "
" 24	" 9	50% "
PICC07	" 20	10% "
" 08	" 23	10% "
" 09	" 21	30% "
" 10	" 24	30% "
" 11	" 22	50% "
" 12	" 17	FULL "
" 13	" 19	FULL "
PICT14	" 15	10% "
" 15	" 16	30% "
" 16	" 18	30% "
" 17	" 13	50% "
" 18	" 14	FULL "
" 19	" 17	FULL "
RRCT28	" 19	CST AMP, R=0.1

TABLE 3

FATIGUE CRACK GROWTH SPECIMEN IDENTIFICATION

IMI 685 (5 discs)

SPECIMEN #	LOCATION	SEQUENCE
IACC07	DISC 2,2	CST AMP, R=0.1
" 08	" 4*	CA(SINE), R=0.1
" 09	" 4*	CST AMP, R=0.1
" 10	DISC 4,4*	CST AMP, R=0.7
" 11	" 4*	CST AMP, R=0.7
IACT12	DISC 2,10	CA(SINE), R=0.1
" 13	" 7*	CST AMP, R=0.1
" 14	" 7*	CST AMP, R=0.1
" 15	" 5	CST AMP, R=0.1
" 16	" 2*	CA(SINE), R=0.74
" 17	" 2*	CST AMP, R=0.74
IACC18	" 1	FULL TURBISTAN
" 19	" 3	FULL "
" 20	" 5*	10% "
" 21	" 5*	10% "
" 22	" 6	10% "
" 23	" 7	30% "
" 24	DISC 4,6	30% "
" 25	DISC 2,8	50% "
" 26	DISC 4,5	50% "
IACT27	DISC 2,1	FULL "
" 28	" 1	FULL "
" 29	" 4	FUL "
" 30	" 4	FULL "
" 31	" 9	10% "
" 32	" 11	30% "
" 33	" 8	30% "
" 34	" 3	50% "
" 35	" 6	50% "
NLCC07	DISC 1,1	CST AMP, R=0.1
" 08	" 3	CST AMP, R=0.7
" 09	" 5	CST AMP, R=0.0
NLCT10	" 7	CST AMP, R=0.1
" 11	" 8	CST AMP, R=0.7
" 12	" 9	CST AMP, R=0.1
" 13	" 11	CST AMP, R=0.1
NLCC14	" 7	10% TURBISTAN
" 15	" 2	30% "
" 16	DISC 4, 3	50% "
" 17	DISC 1, 6	FULL "
" 18	DISC 4, 2	FULL "
NLCT19	DISC 1, 3	10% "
" 20	" 2	30% "
" 21	" 4	50% "
" 22	" 1	FULL "
" 23	" 5	FULL "
" 24	" 6	FULL "

*two tests from one specimen

TABLE 3 (Continued)

SPECIMEN #	LOCATION	SEQUENCE
RACT07	DISC 5, 1	SS TYPE 3, R=0.05
" 08	" 2	SS TYPE 2, R=0.02
" 09	DISC 2,16	SS TYPE 3, R=0.04
" 10	DISC 3, 1	SS TYPE 1, R=0.06
" 11	DISC 2, 14	SS TYPE 4, R=0.11
RACC12	DISC 4, 10	SS TYPE 1, R=0.05
" 13	" 22	SS TYPE 2, R=0.06
RACT14	DISC 2, 17	SS TYPE 2, R=0.05
" 15	" 18	SS TYPE 1, R=0.06
" 16	DISC 3, 2	SS TYPE 3, R=0.02
RACC17	DISC 4, 13	SS TYPE 3, R=0.06
" 18	" 17	SS TYPE 1, R=0.05
" 19	" 14	SS TYPE 2, R=0.06
" 20	" 20	SS TYPE 4, R=0.12
RACT21	DISC 2, 22	FULL TURBISTAN
RACT22	" 21	FULL "
RACC23	" 4, 15	FULL "
RACC24	" 11	FULL "
RRCC07	DISC 3, 1	CST AMP, R=0.1
" 08	" 2	CST AMP , R=0.7
" 09	" 3	CST AMP, R=0.7
" 10	" 5	SS TYPE 1, R=0.0
" 11	" 4	SS TYPE 1, R=0.0
" 12	" 6	SS TYPE 2, R=0.0
" 13	" 7	SS TYPE 2, R=0.0
" 14	" 8	SS TYPE 3, R=0.0
" 15	" 9	SS TYPE 3, R=0.0
" 16	" 11	SS TYPE 4, R=0.0
" 17	" 10	SS TYPE 4, R=0.0
RRCT18	DISC 1,17	CST AMP, R=0.7
" 19	DISC 3, 6	CST AMP, R=0.1
" 20	DISC 1,13	CST AMP, R=0.1
" 21	DISC 3,10	SS TYPE 1, R=0.0
" 22	" 9	SS TYPE 1, R=0.0
" 23	" 5	SS TYPE 2, R=0.0
" 24	" 7	SS TYPE 3, R=0.0
" 25	" 11	SS TYPE 3, R=0.0
" 26	DISC 1,12	SS TYPE 4, R=0.1
" 27	" 15	SS TYPE 4, R=0.1
" 29	" 14	10% TURBISTAN
" 30	" 18	10% "
" 31	" 21	30% "
" 32	" 22	30% "
" 33	" 19	50% "
" 34	" 20	50% "
" 35	DISC 3,12	FULL "
" 36	DISC 1,16	FULL "
RRCC37	DISC 5, 3	10% "
" 38	" 2	10% "
" 39	" 8	30% "
" 40	" 5	30% "
" 41	" 6	50% "
" 42	DISC 3, 12	FULL "
" 43	DISC 5, 1	FULL "

TABLE 4

FATIGUE CRACK GROWTH SPECIMEN IDENTIFICATION

TI-17

SPECIMEN #	LOCATION	SEQUENCE
QECT07	DISC 1, 5	CST AMP, R=0.1
" 08	" 6	CST AMP, R=0.1
" 09	" 21	CST AMP, R=0.1
" 10	" 6B	CST AMP, R=0.7
" 11	" 1	SS TYPE 1, R=0.01
" 12	" 14	SS TYPE 1, R=0.01
" 13	" 10B	SS TYPE 2, R=0.01
" 14	" 12	SS TYPE 2, R=0.01
" 15	" 7	SS TYPE 3, R=0.01
" 16	" 2	SS TYPE 4, R=0.1
" 17	" 4	SS TYPE 4, R=0.1
" 18	" 20	FULL TURBISTAN
" 19	" 19	10% "
" 20	" 13	30% "
" 21	" 18	50% "
" 22	" 10A	FULL "
" 23	" 24	10% "
" 24	" 16	30% "
" 25	" 5B	50% "
UTCC07	DISC 1,1	CST AMP, R=0.1
" 08	" 2	CST AMP, R=0.1
" 09	" 3	CST AMP, R=0.7
" 10	" 8	CST AMP, R=0.7
" 11	" 11	SS TYPE 1, R=0.01
" 12	" 21	SS TYPE 1, R=0.01
" 13	" 22	SS TYPE 2, R=0.01
" 14	" 23	SS TYPE 2, R=0.01
" 15	" 15	SS TYPE 3, R=0.01
" 16	" 16	SS TYPE 3, R=0.01
" 17	" 17	SS TYPE 4, R=0.1
" 18	" 18	SS TYPE 4, R=0.1
" 19	" 19	10% TURBISTAN
" 20	" 10	10% "
" 21	" 4	30% "
" 22	" 5	30% "
" 23	" 9	50% "
" 24	" 20	50% "
" 25	" 10	FULL "
" 26	" 13	FULL "

TABLE 5
COLD TURBISTAN SEQUENCES

SEQUENCE	DESIGNATION	END POINTS
TURBISTAN	TURB100	15452
10% OMISSION	TURB10	6298
30% OMISSION	TURB30	1924
50% OMISSION	TURB50	962

TABLE 6
CRACK GROWTH RATE RATE DATA FOR TI-6AL-4V

SEQUENCE	FIGURE#	da/dN (m / Cycle)	
		$\Delta k = 10$ (MPa$\sqrt{m}$)	$\Delta K = 30$
R=0.1	11	$8x10^{-9}$	$8x10^{-7}$
R=0.7	12	$4x10^{-8}$	-
SS1	13	$8x10^{-9}$	$5x10^{-}$
SS2	14	$8x10^{-9}$	$8x10^{-7}$
SS3	15	$4x10^{-8}$	$2x10^{-6}$
SS4	16	$1x10^{-9}$	$2x10^{-7}$
TURB10	17	$1x10^{-8}$	$2x10^{-6}$
TURB30	18	-	$2x10^{-6}$
TURB50	19	$1x10^{-8}$	$1.5x10^{-6}$
TURB100	20	$1x10^{-8}$	$3x10^{-6}$

TABLE 7
CRACK GROWTH RATE DATA FOR IMI 685

SEQUENCE	FIGURE#	da/dN (m / Cycle)	
		$\Delta k = 15$ (MPa$\sqrt{m}$)	$\Delta k = 40$
R=0.1	21	$1x10^{-8}$	$2.5x10^{-7}$
R=0.7	22	$5x10^{-8}$	-
SS1	23	$2x10^{-8}$	$2x10^{-7}$
SS2	24	$1x10^{-8}$	$4 x10^{-7}$
SS3	25	-	$8x10^{-7}$
SS4	26	$5x10^{-9}$	$5x10^{-8}$
TURB10	27	$6x10^{-8}$	$7x10^{-7}$
TURB30	28	$6x10^{-8}$	$7x10^{-7}$
TURB50	29	$3x10^{-8}$	$6x10^{-7}$
TURB100	30, 31	$5x10^{-8}$	$7x10^{-7}$

TABLE 8
CRACK GROWTH RATE DATA FOR TI-17

SEQUENCE	FIGURE #	da/dN (m / Cycle)	
		$\Delta k = 10$ (MPa$\sqrt{m}$)	$\Delta k = 30$
R=0.1	32	$3x10^{-8}$	$6x10^{-7}$
R=0.7	33	$6x10^{-8}$	-
SS1	34	$3x10^{-8}$	$6x10^{-7}$
SS2	35	$3.5x10^{-8}$	$9x10^{-7}$
SS3	36	$7x10^{-8}$	$1.5x10^{-6}$
SS4	37	$6x10^{-9}$	$1.5x10^{-7}$
TURB10	38	$1x10^{-7}$	$2.5x10^{-6}$
TURB30	39	$8x10^{-8}$	$2x10^{-6}$
TURB50	40	$5x10^{-8}$	$1x10^{-6}$
TURB100	41	$9x10^{-8}$	$2x10^{-6}$

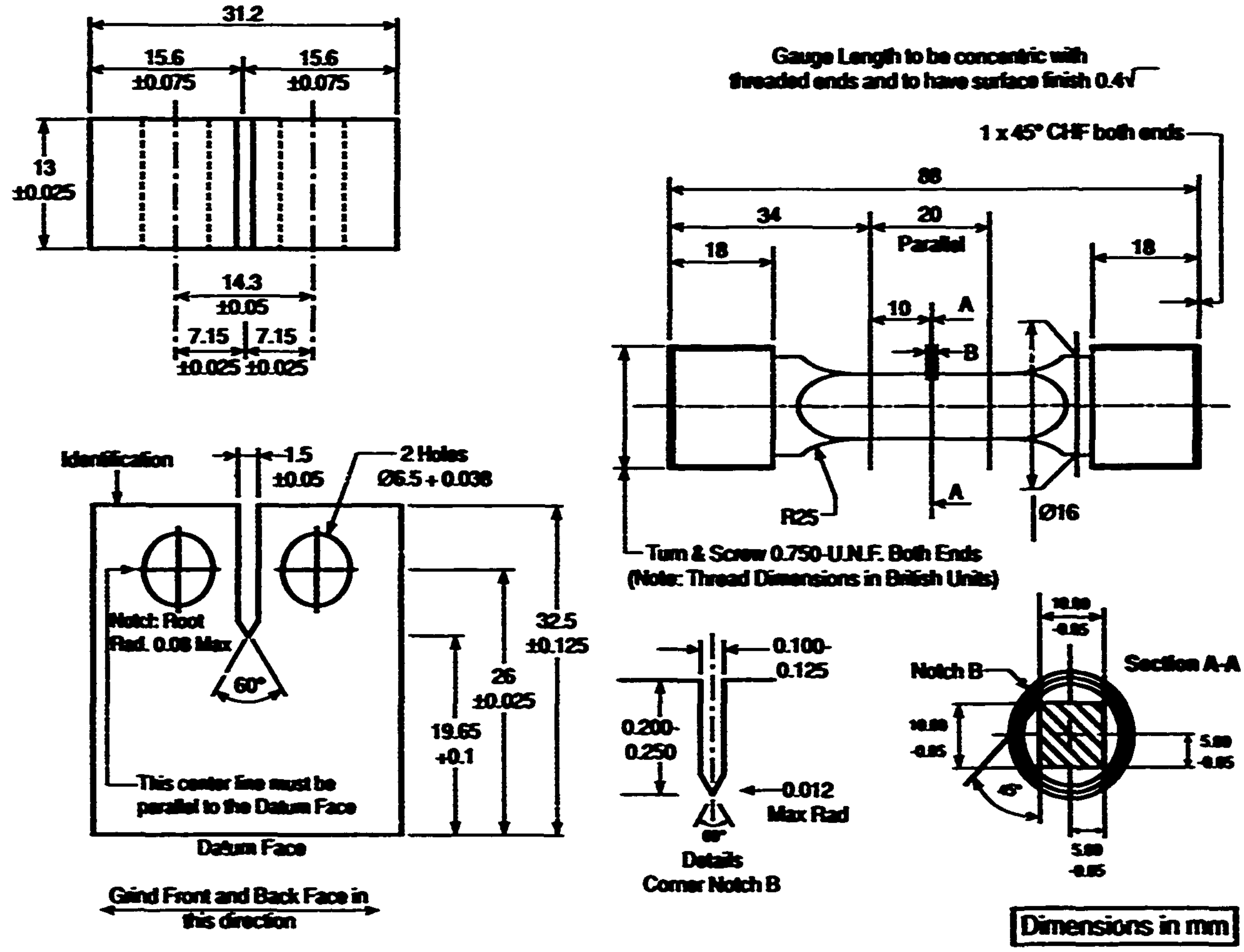

a) Compact tension (CT) specimen

a) Corner crack (CC) specimen

Fig. 1: Specimens used in the programme[1]

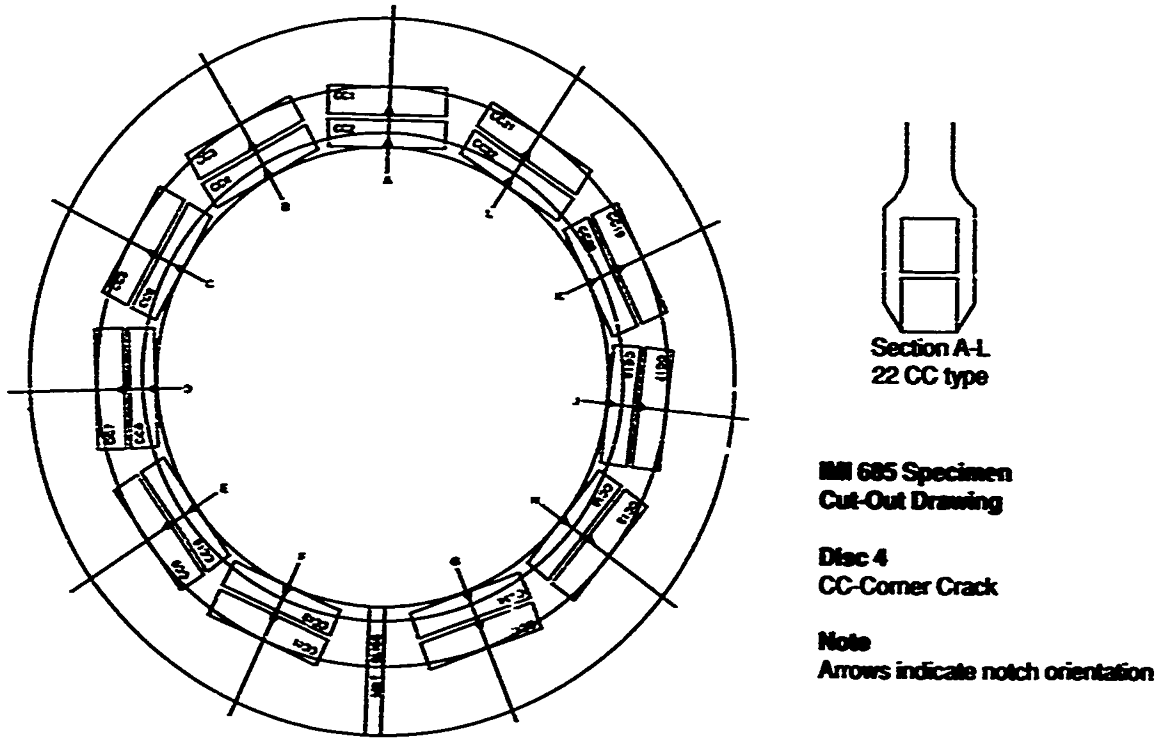

Fig. 2: Disc Cut-Up Drawing for IMI 685

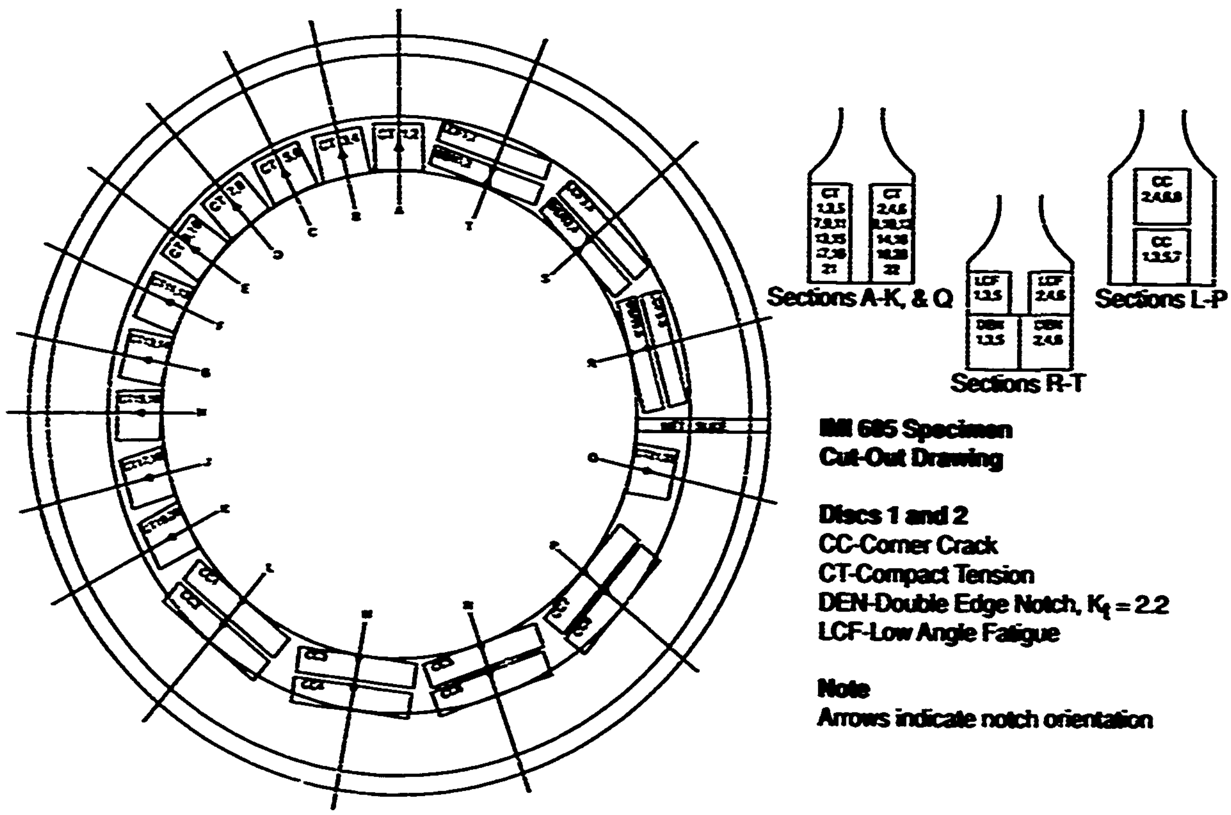

Fig. 3: Disk Cut-Up Drawing for IMI 685

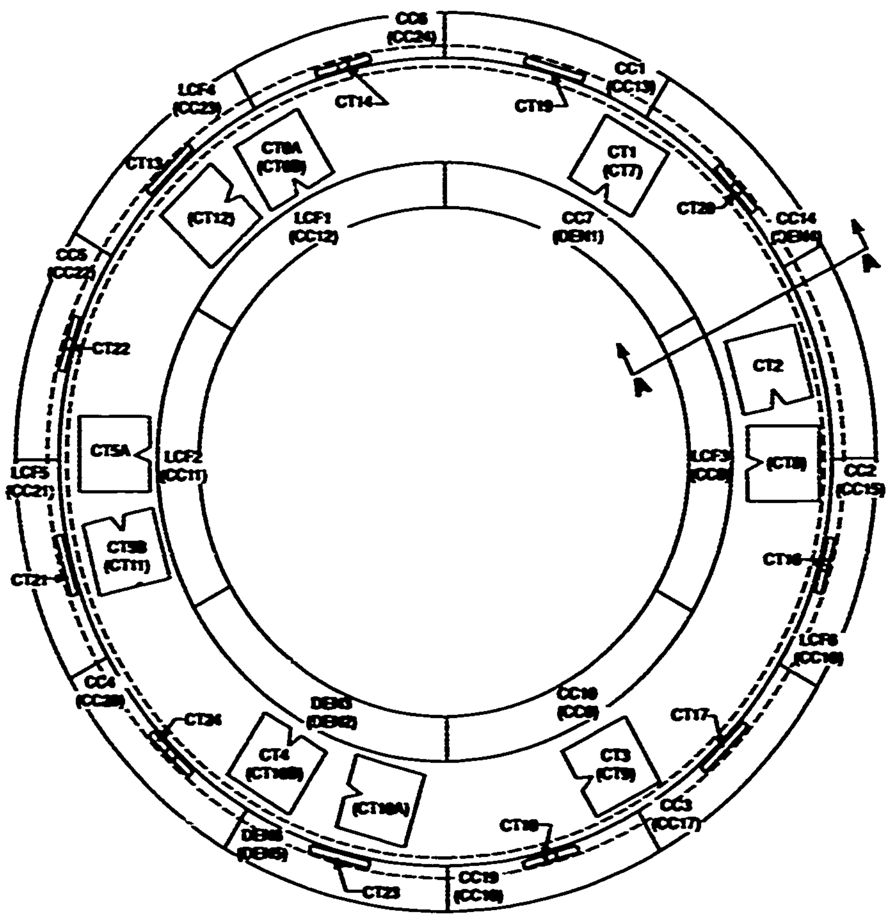

Section A-A

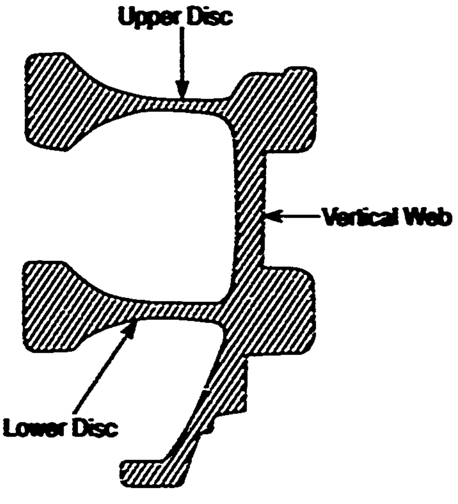

AGARD SC 33 Engine Disc
Cooperative Test Programme
Ti-17 F404 Compressor Disc
Specimen Cut-Out Drawing:

CC-Corner Crack Specimen
CT-Compact Tension Specimen
DEN-Double Edge Notch Specimen
LCF-Low Cycle Fatigue Specimen

Notes:
1. Specimen #'s in parentheses indicate specimens removed from bottom disc
2. CT specimens removed from vertical with crack direction vertical
3. CT specimens removed from vertical with crack direction horizontal or circumferential

Fig. 4: Disc cut-up drawing for Ti-17

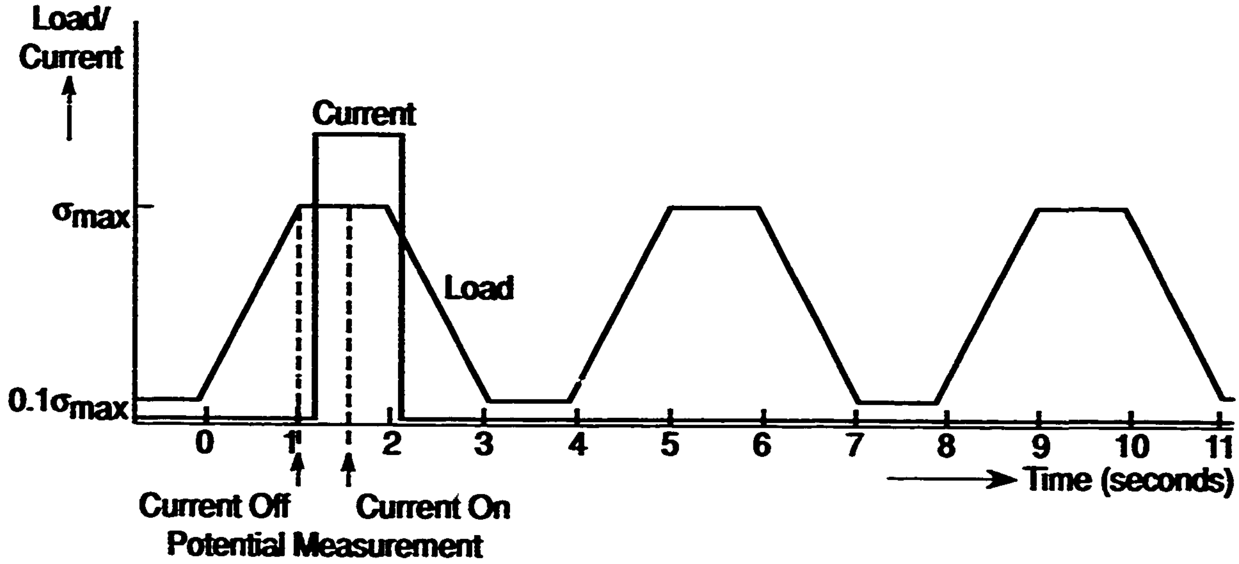

Fig. 5: Trapezoidal waveshape used for constant amplitude tests.

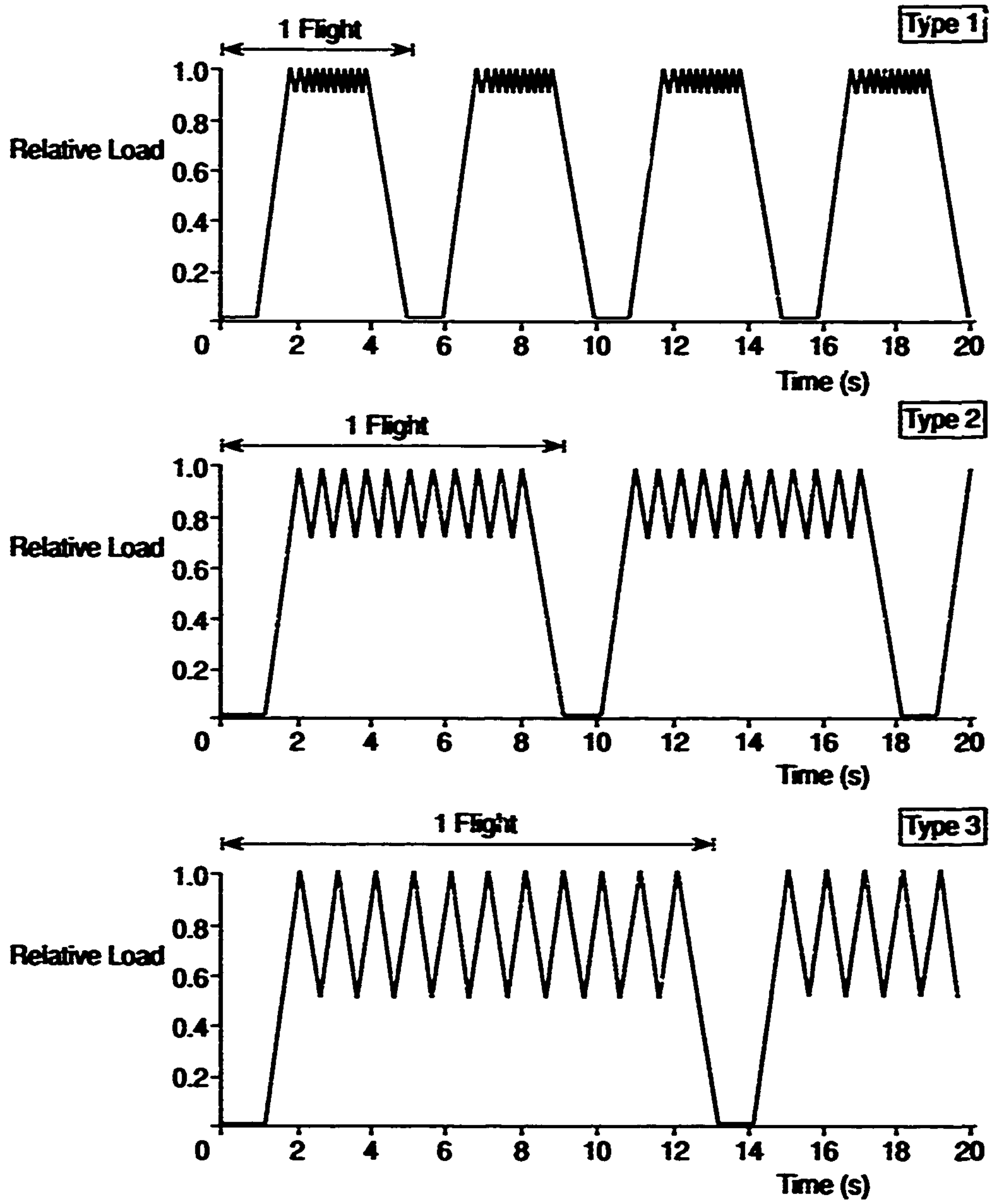

Fig. 6: Graphical presentation of simple sequences, SS1, SS2, and SS3.

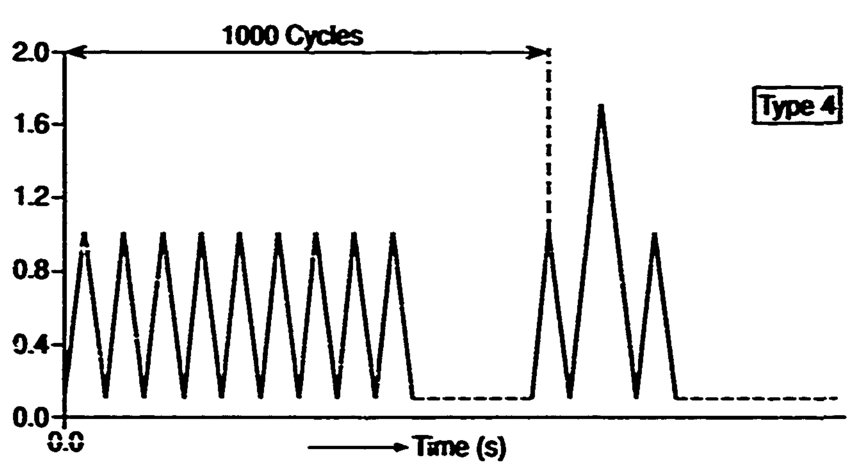

Fig. 7: Graphical presentation of overload sequence SS4

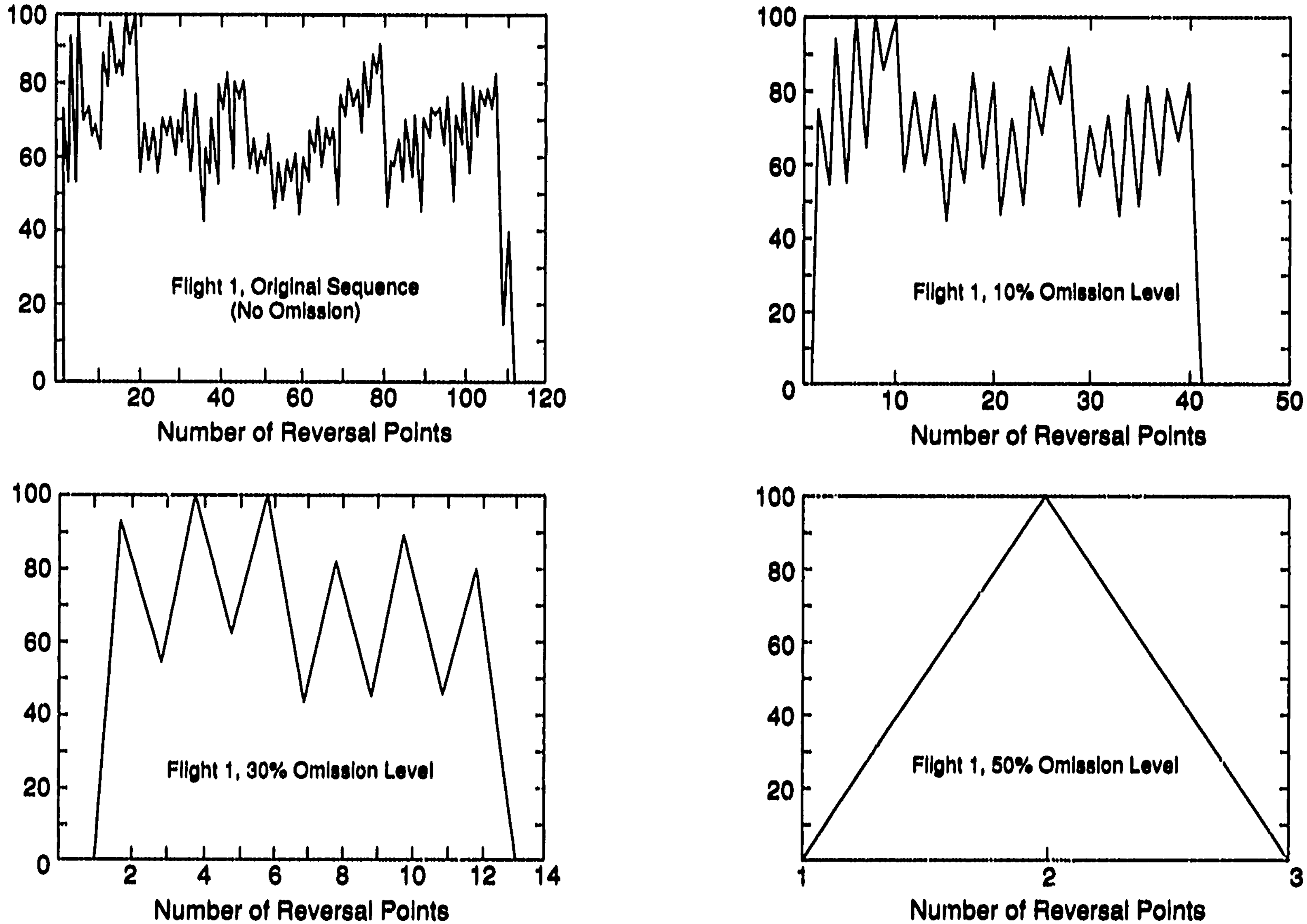

**Fig. 8: Example of TURBISTAN simplification:
Figures show flight number 1 of Turbistan
sequence with various omittance levels**

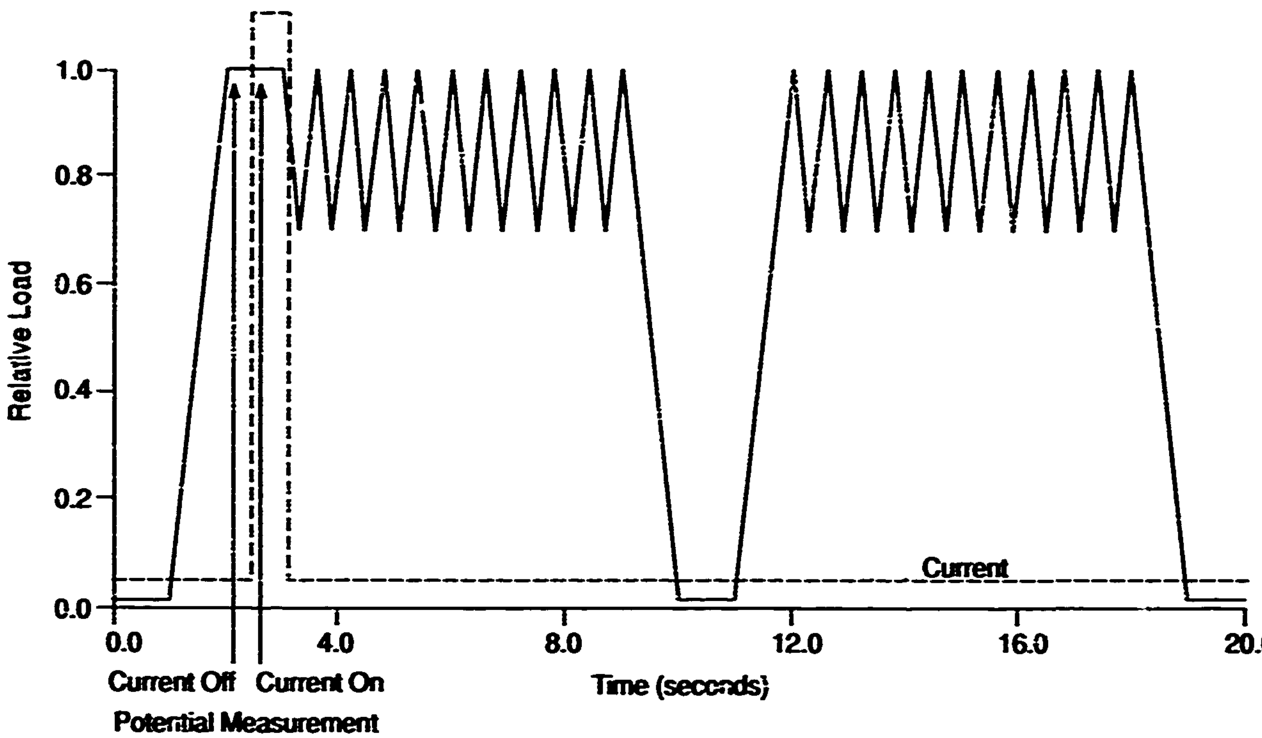

Fig. 9: Suggested PD measurement procedure for SS2 sequence. Note the addition of the one second dwell time 100% relative load.

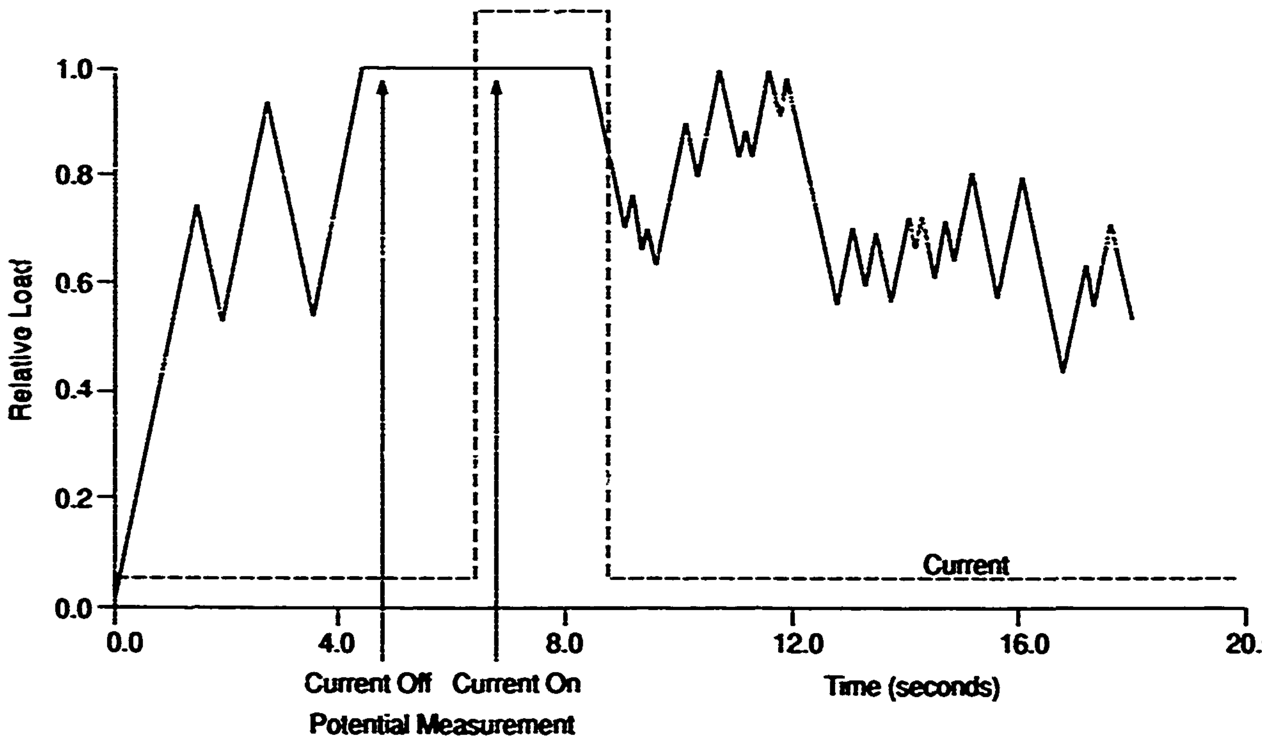

Fig. 10: Suggested PD measurement procedure in flight #1 of TURBISTAN sequence. Note the addition of the one second dwell time at 100% relative load.

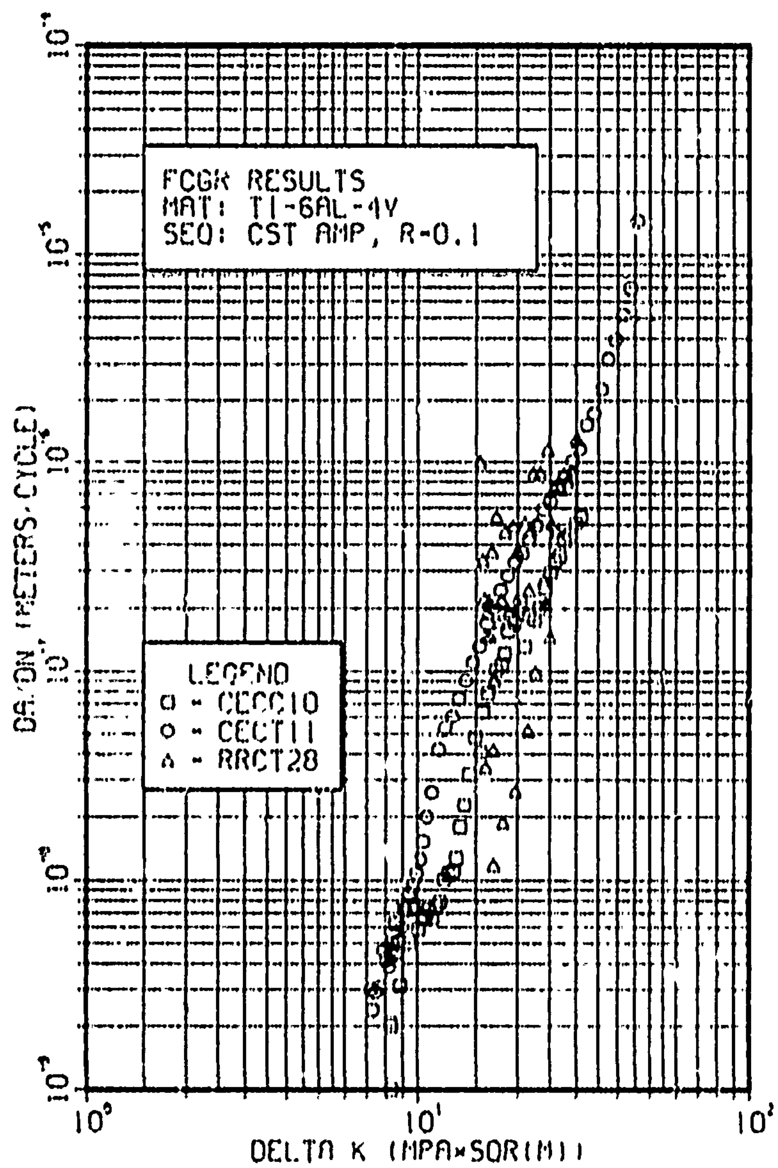
FCGR RESULTS
MAT: TI-6AL-4V
SEQ: CST AMP, R-0.1
LEGEND
□ - CECC10
○ - CECT11
△ - RRCT28
DA/DN (METERS/CYCLE)
DELTA K (MPA×SQR(M))
10^-4
10^-5
10^-6
10^-7
10^-8
10^-9
10^0
10^1
10^2

Fig. 11

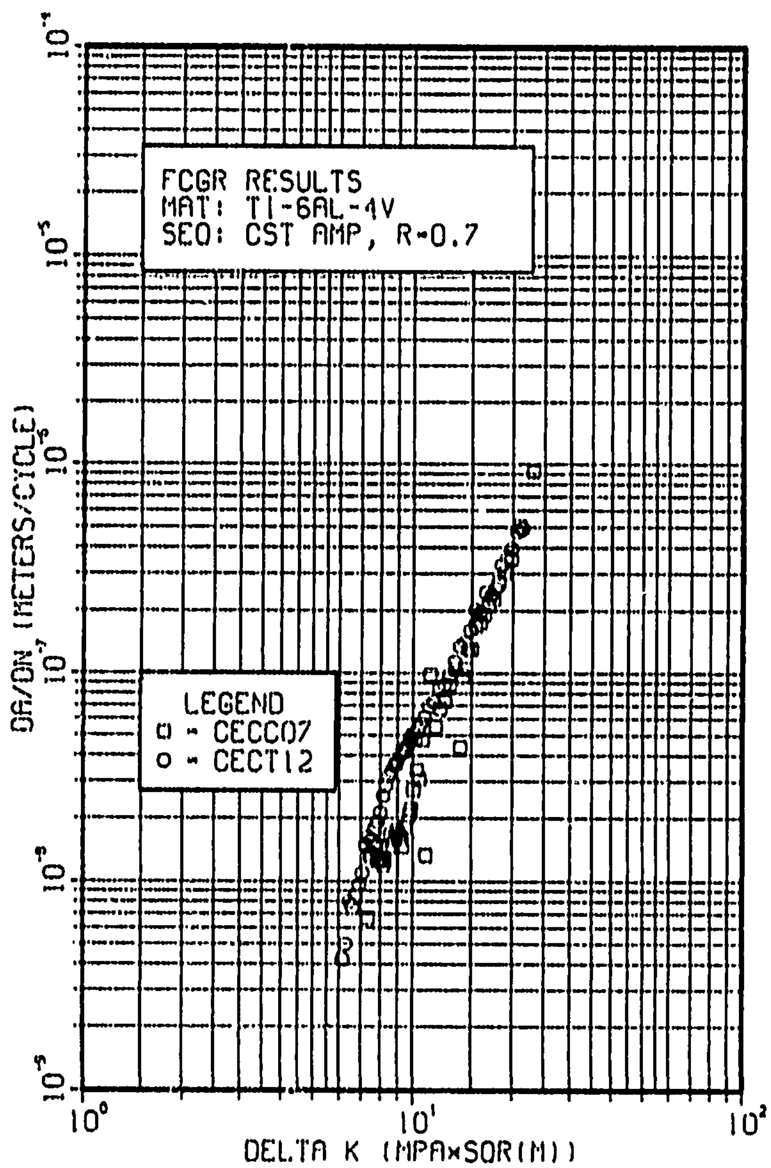
FCGR RESULTS
MAT: TI-6AL-4V
SEQ: CST AMP, R-0.7
LEGEND
□ - CECC07
○ - CECT12
DA/DN (METERS/CYCLE)
DELTA K (MPA×SQR(M))
10^-4
10^-5
10^-6
10^-7
10^-8
10^-9
10^0
10^1
10^2

Fig. 12

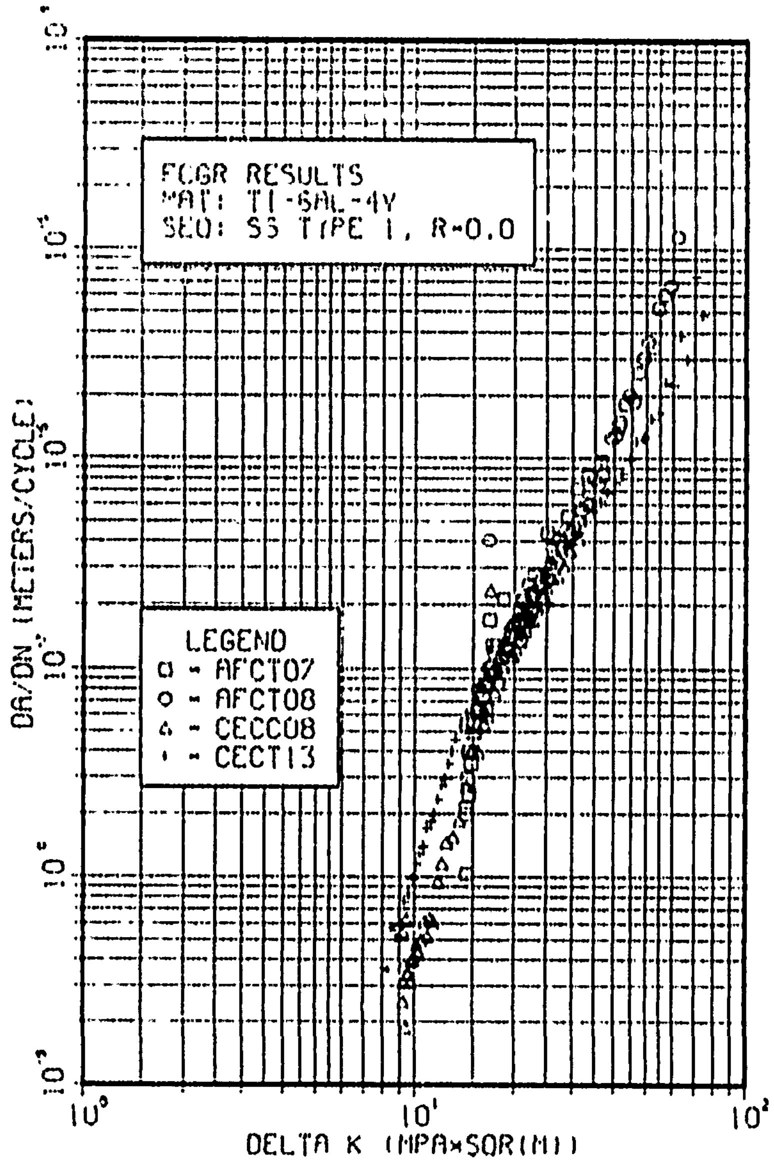
FCGR RESULTS
MAT: TI-6AL-4V
SEQ: SS TYPE 1, R=0.0
LEGEND
□ = AFCT07
○ = AFCT08
△ = CECC08
+ = CECT13
DA/DN (METERS/CYCLE)
DELTA K (MPA*SQR(M))

Fig. 13

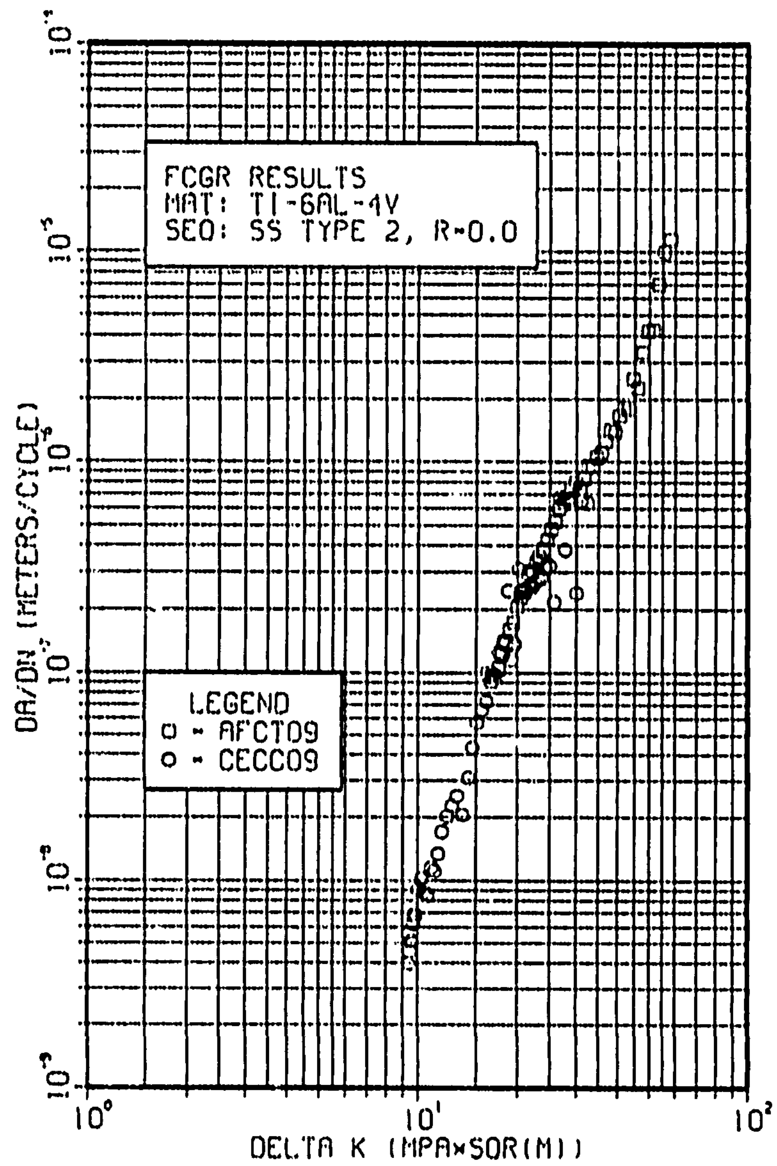
FCGR RESULTS
MAT: TI-6AL-4V
SEQ: SS TYPE 2, R=0.0
LEGEND
□ = AFCT09
○ = CECC09
DA/DN (METERS/CYCLE)
DELTA K (MPA*SQR(M))

Fig. 14

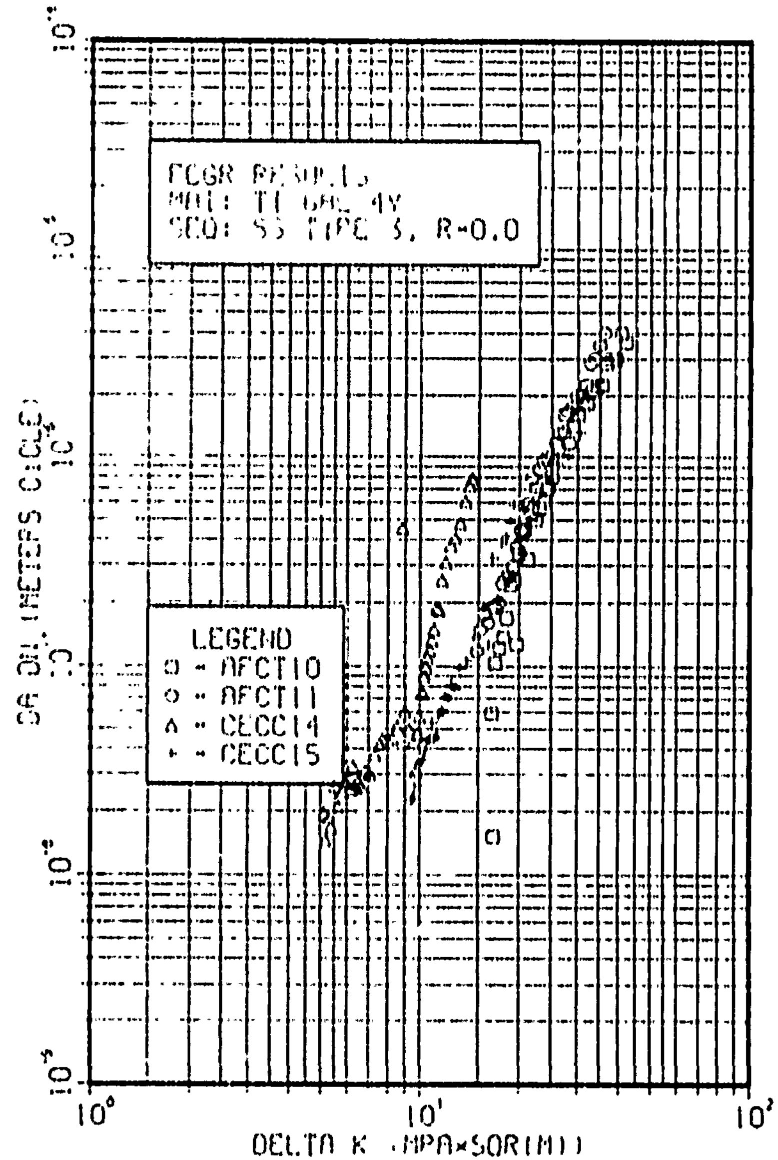
LEGEND
□ = AFCT10
○ = AFCT11
△ = CECC14
+ = CECC15
DELTA K (MPA×SQR(M))
10⁰
10¹
10²
10⁻⁹
10⁻⁸
10⁻⁴

Fig. 15

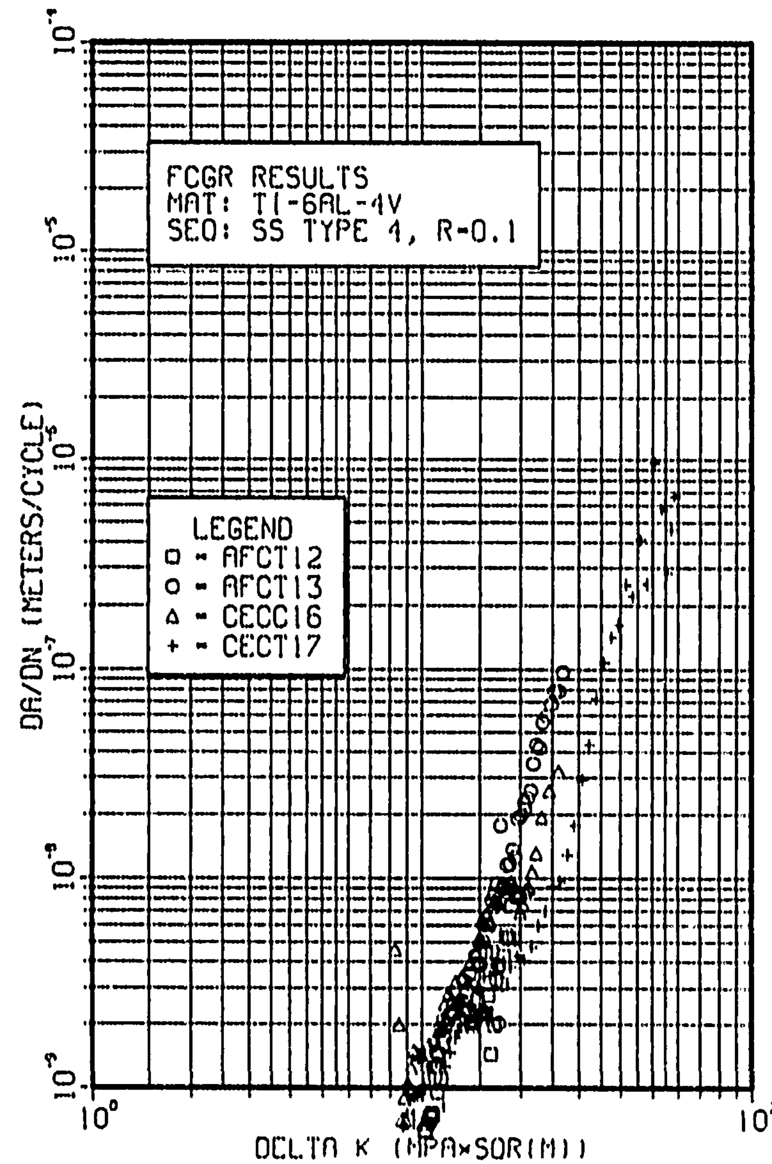
FCGR RESULTS
MAT: TI-6AL-4V
SEQ: SS TYPE 4, R=0.1
LEGEND
□ = AFCT12
○ = AFCT13
△ = CECC16
+ = CECT17
DA/DN (METERS/CYCLE)
DELTA K (MPA×SQR(M))
10⁰
10²
10⁻⁹
10⁻⁸
10⁻⁷
10⁻⁶
10⁻⁵
10⁻⁴

Fig. 16

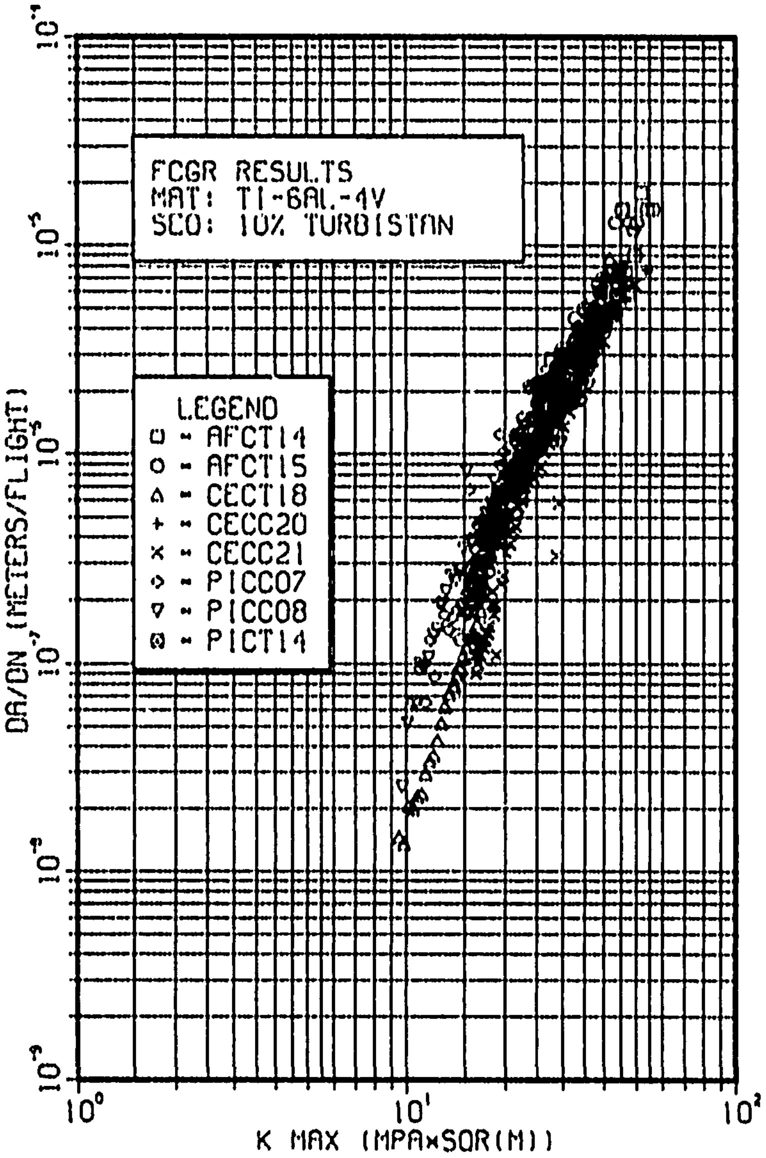
FCGR RESULTS
MAT: TI-6AL-4V
SEQ: 10% TURBISTAN
LEGEND
□ - AFCT14
○ - AFCT15
△ - CECT18
+ - CECC20
× - CECC21
◇ - PICC07
▽ - PICC08
⊠ - PICT14
DA/DN (METERS/FLIGHT)
K MAX (MPA×SQR(M))
10⁻⁴
10⁻⁵
10⁻⁶
10⁻⁷
10⁻⁸
10⁻⁹
10⁰
10¹
10²

Fig. 17

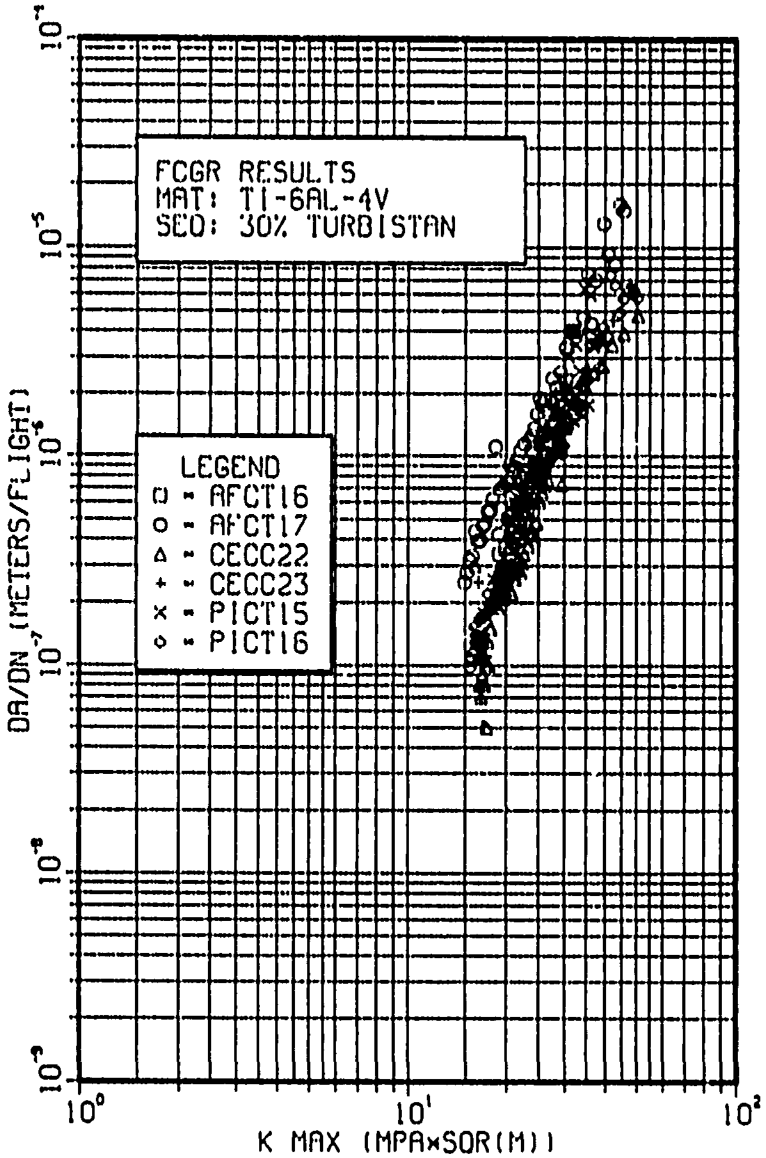
FCGR RESULTS
MAT: TI-6AL-4V
SEQ: 30% TURBISTAN
LEGEND
□ - AFCT16
○ - AFCT17
△ - CECC22
+ - CECC23
× - PICT15
◇ - PICT16
DA/DN (METERS/FLIGHT)
K MAX (MPA×SQR(M))
10⁻⁴
10⁻⁵
10⁻⁶
10⁻⁷
10⁻⁸
10⁻⁹
10⁰
10¹
10²

Fig. 18

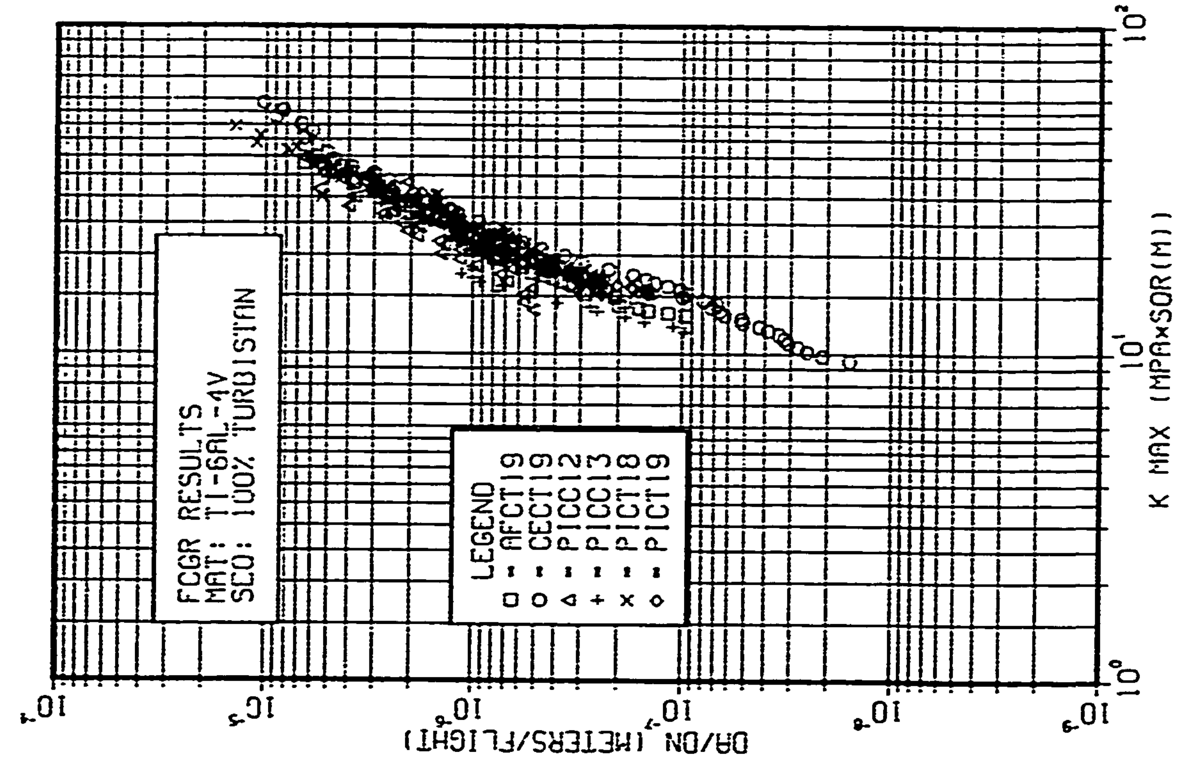

FCGR RESULTS
MAT: TI-6AL-4V
SCO: 100% TURBISTAN
LEGEND
□ = AFCT19
○ = CECT19
△ = PICC12
+ = PICC13
× = PICT18
◇ = PICT19
DA/DN (METERS/FLIGHT)
K MAX (MPA×SQR(M))

Fig. 20

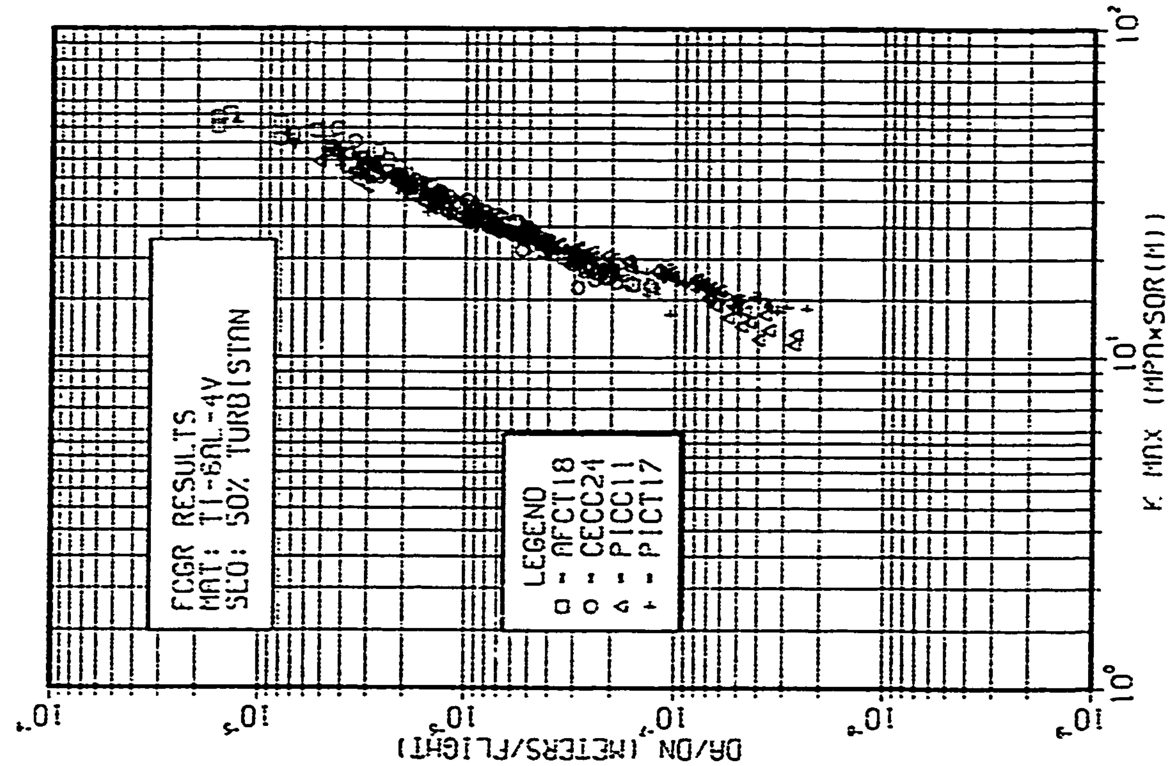

FCGR RESULTS
MAT: TI-6AL-4V
SCO: 50% TURBISTAN
LEGEND
□ = AFCT18
○ = CECC21
△ = PICC11
+ = PICT17
DA/DN (METERS/FLIGHT)
K MAX (MPA×SQR(M))

Fig. 19

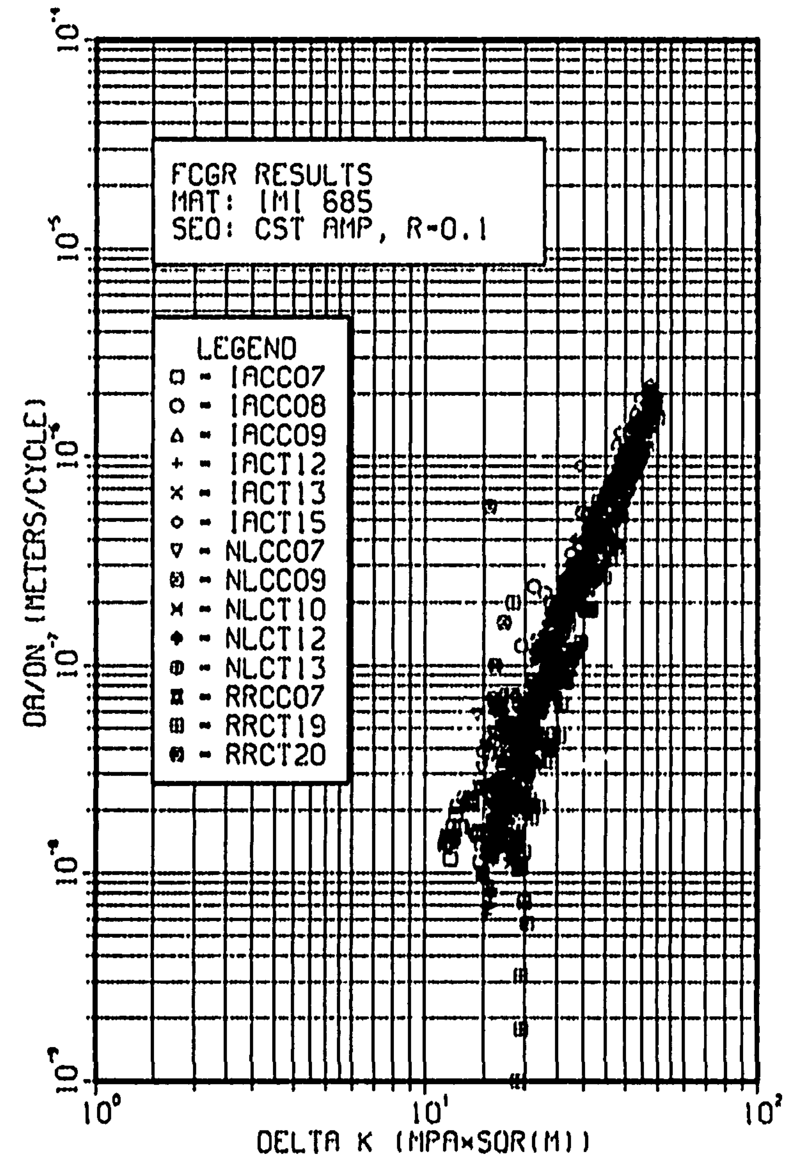
FCGR RESULTS
MAT: IMI 685
SEQ: CST AMP, R=0.1
LEGEND
IACC07
IACC08
IACC09
IACT12
IACT13
IACT15
NLCC07
NLCC09
NLCT10
NLCT12
NLCT13
RRCC07
RRCT19
RRCT20
DA/DN (METERS/CYCLE)
DELTA K (MPA×SQR(M))

Fig. 21

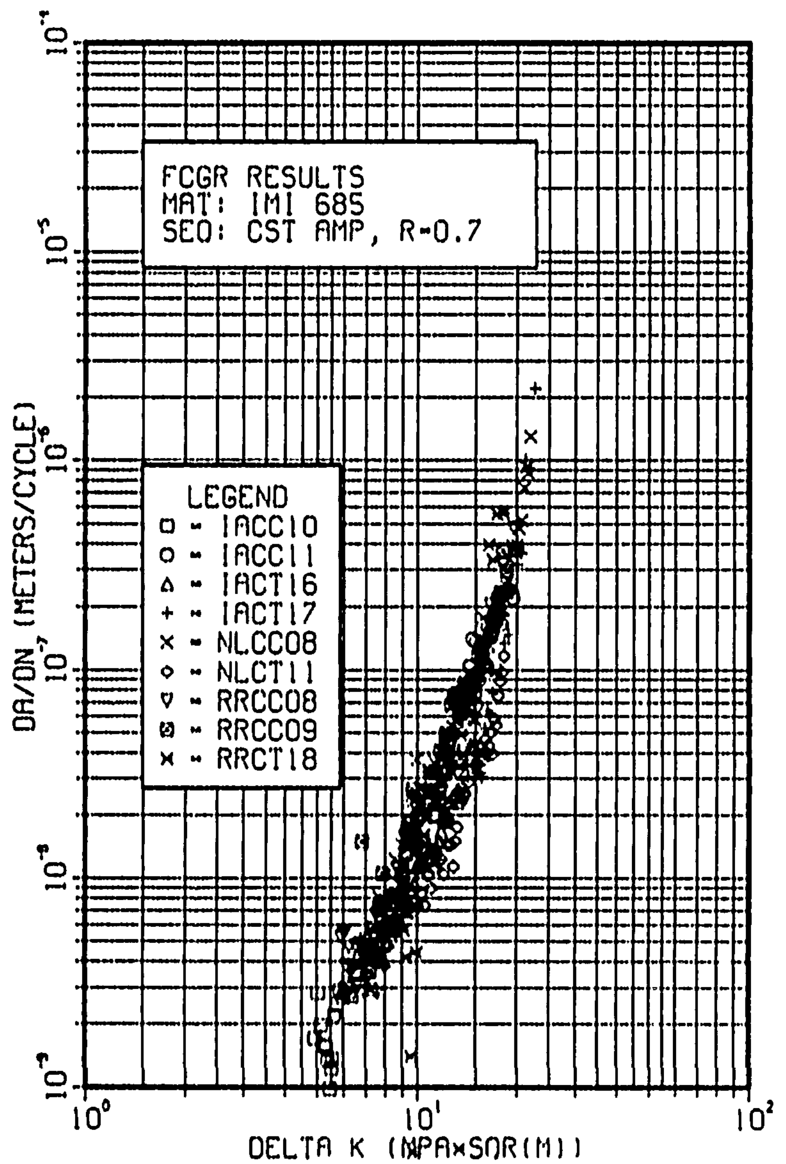
FCGR RESULTS
MAT: IMI 685
SEQ: CST AMP, R=0.7
LEGEND
IACC10
IACC11
IACT16
IACT17
NLCC08
NLCT11
RRCC08
RRCC09
RRCT18
DA/DN (METERS/CYCLE)
DELTA K (MPA×SQR(M))

Fig. 22

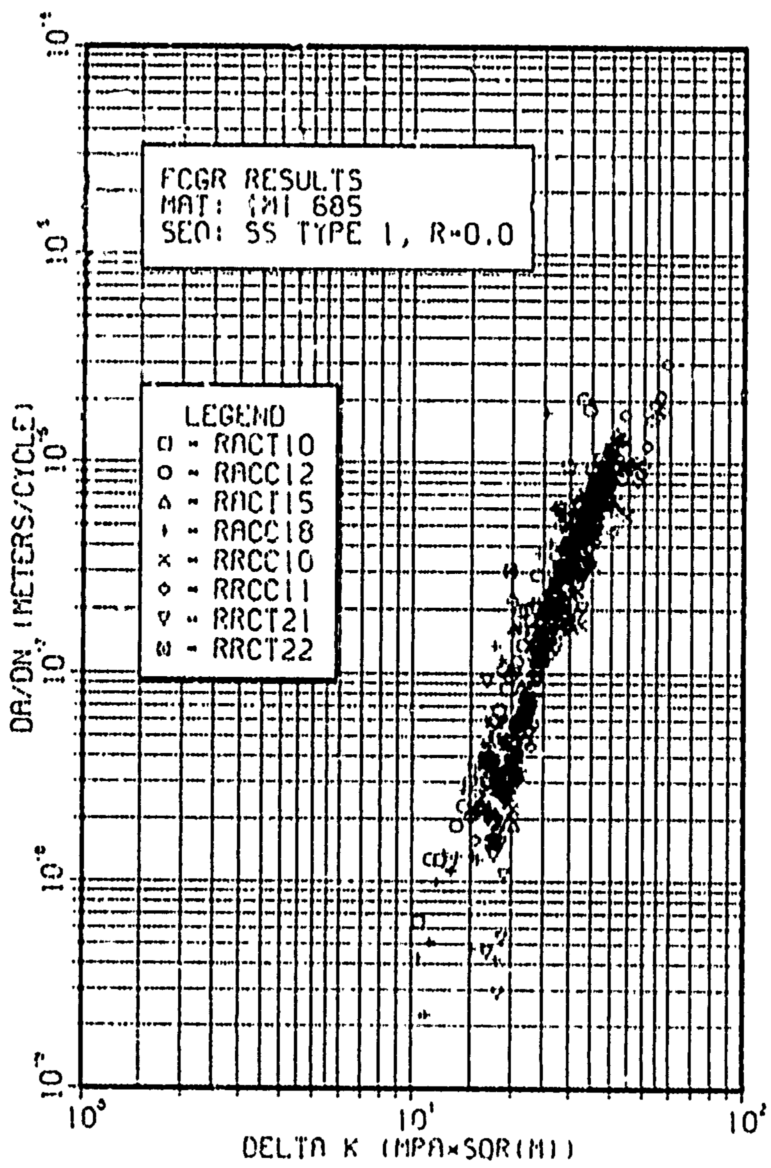
FCGR RESULTS
MAT: IMI 685
SEQ: SS TYPE 1, R=0.0
LEGEND
□ - RACT10
○ - RACC12
△ - RACT15
+ - RACC18
× - RRCC10
◇ - RRCC11
▽ - RRCT21
ω - RRCT22
DA/DN (METERS/CYCLE)
DELTA K (MPA×SQR(M))

Fig. 23

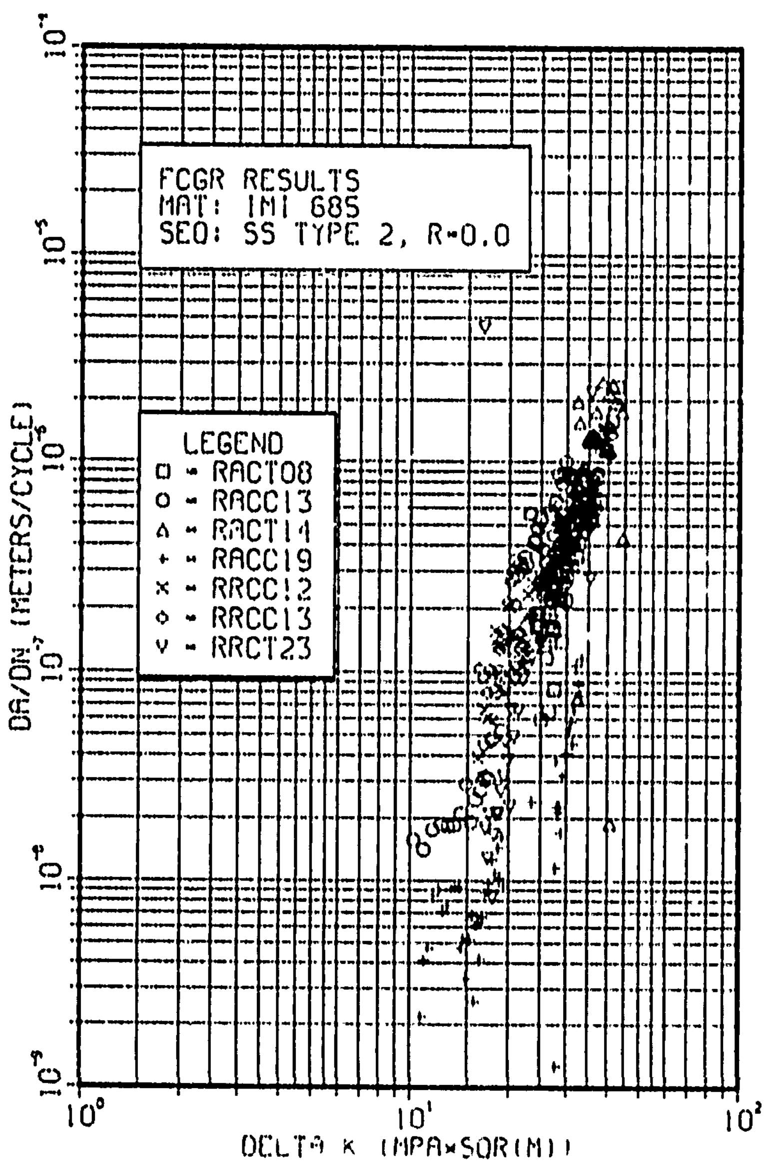
FCGR RESULTS
MAT: IMI 685
SEQ: SS TYPE 2, R=0.0
LEGEND
□ - RACT08
○ - RACC13
△ - RACT14
+ - RACC19
× - RRCC12
◇ - RRCC13
▽ - RRCT23
DA/DN (METERS/CYCLE)
DELTA K (MPA×SQR(M))

Fig. 24

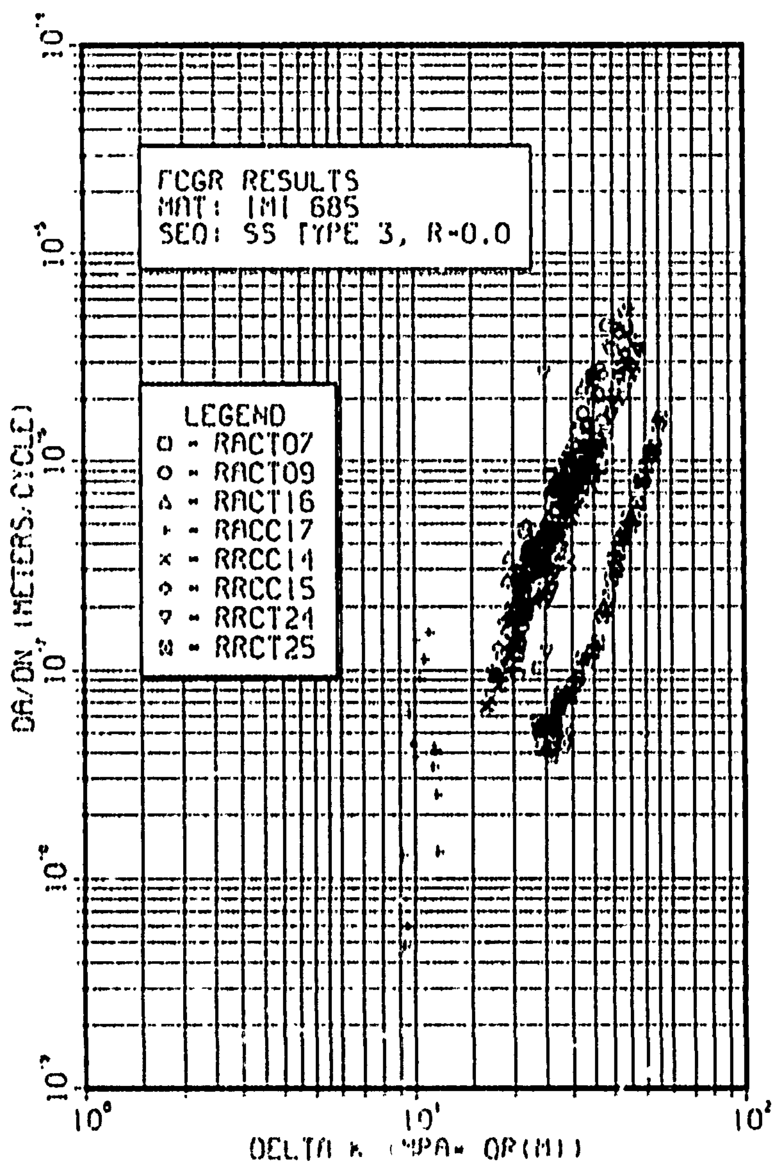
FCGR RESULTS
MAT: IMI 685
SEQ: SS TYPE 3, R=0.0
LEGEND
□ - RACT07
○ - RACT09
△ - RACT16
+ - RACC17
× - RRCC14
◇ - RRCC15
▽ - RRCT24
⊠ - RRCT25
DA/DN (METERS/CYCLE)
DELTA K (MPA* QR(M))
10^{-4}
10^{-5}
10^{-6}
10^{-7}
10^{-8}
10^{-9}
10^{0}
10^{1}
10^{2}

Fig. 25

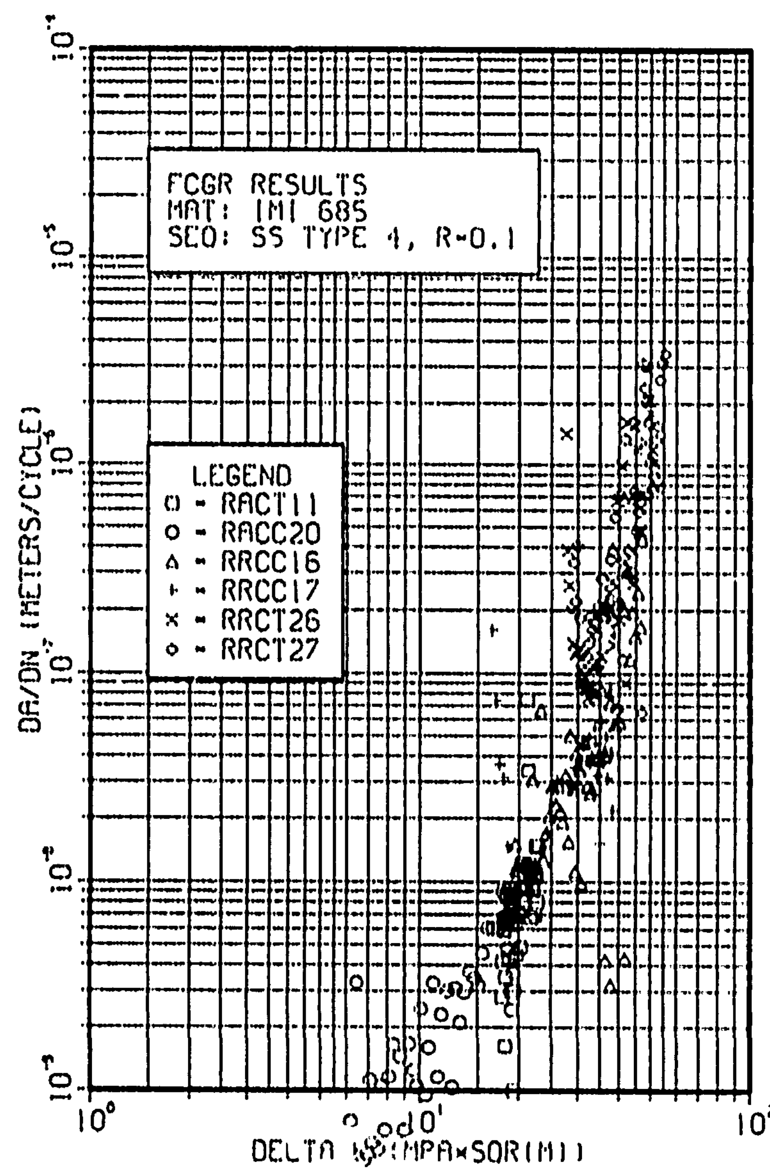
FCGR RESULTS
MAT: IMI 685
SEQ: SS TYPE 4, R=0.1
LEGEND
□ - RACT11
○ - RACC20
△ - RRCC16
+ - RRCC17
× - RRCT26
◇ - RRCT27
DA/DN (METERS/CYCLE)
DELTA K (MPA*SQR(M))
10^{-4}
10^{-5}
10^{-6}
10^{-7}
10^{-8}
10^{-9}
10^{0}
10^{1}
10^{2}

Fig. 26

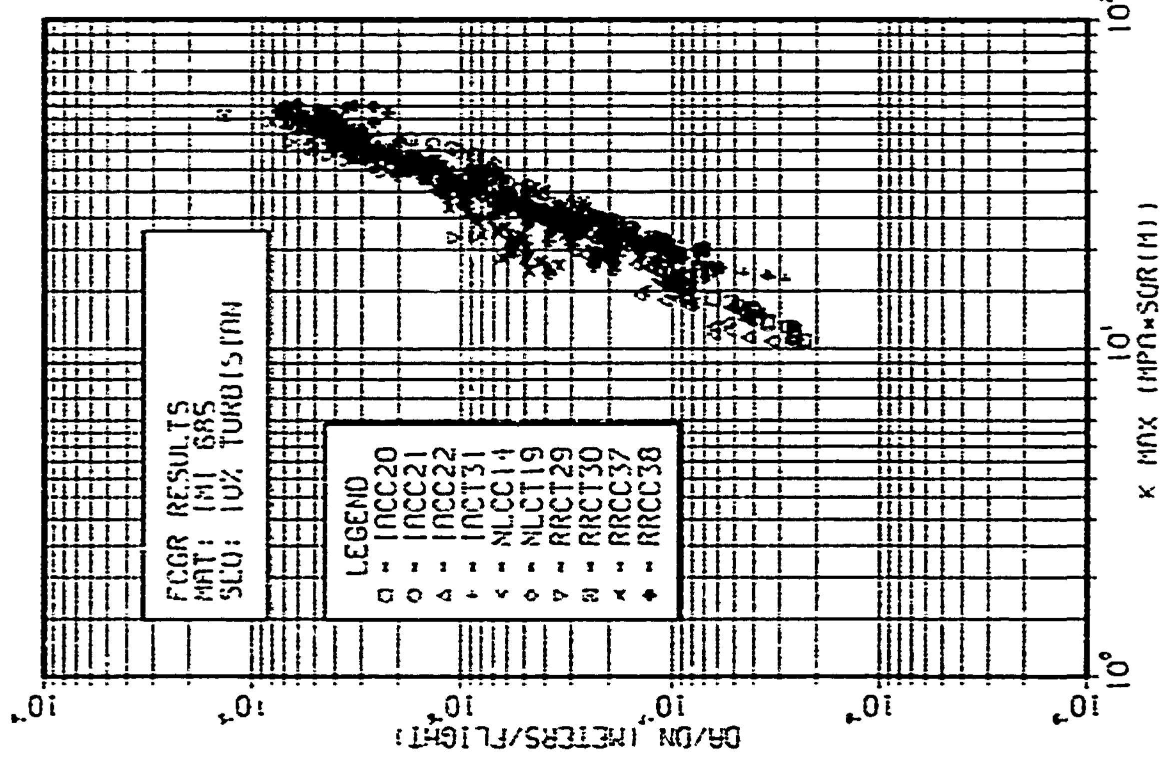
FCGR RESULTS
MAT: IMI 685
SCO: 10% TURBISTAN
LEGEND
IACC20
IACC21
IACC22
IACT31
NLCC14
NLCT19
RRCT29
RRCT30
RRCC37
RRCC38
DA/DN (METERS/FLIGHT)
K MAX (MPA×SQR(M))

Fig. 27

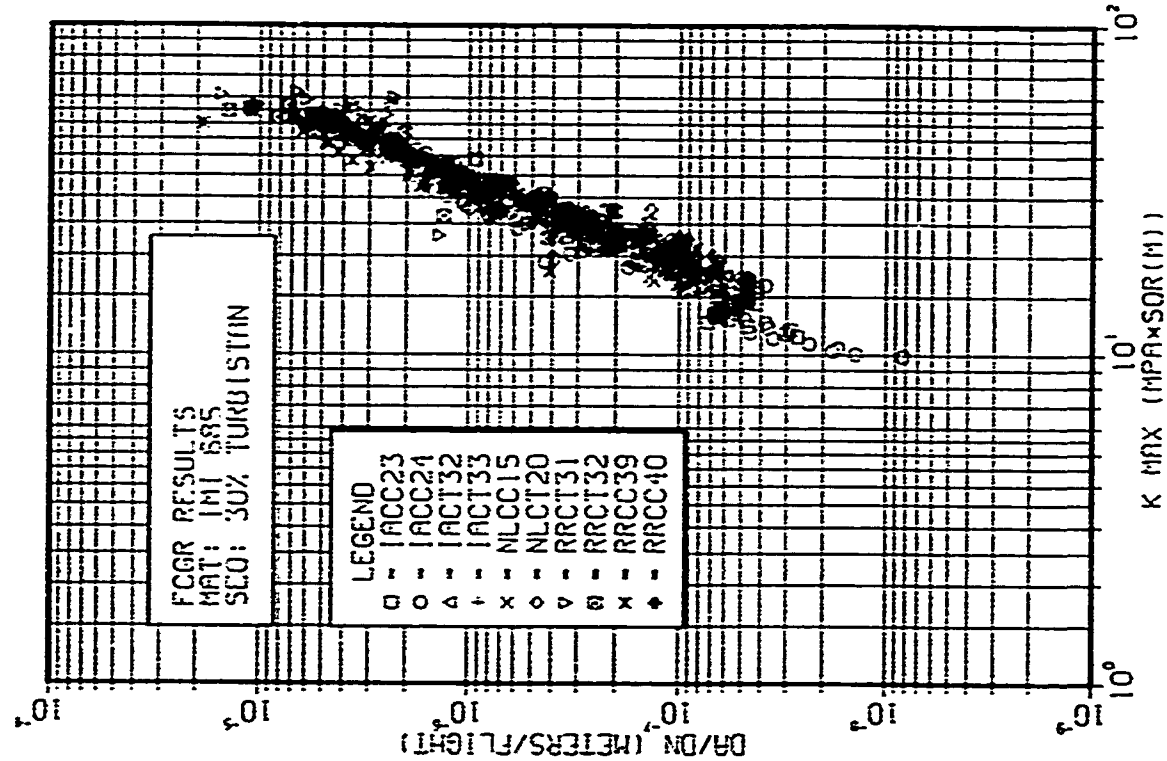
FCGR RESULTS
MAT: IMI 685
SCO: 30% TURBISTAN
LEGEND
IACC23
IACC24
IACT32
IACT33
NLCC15
NLCT20
RRCT31
RRCT32
RRCC39
RRCC40
DA/DN (METERS/FLIGHT)
K MAX (MPA×SQR(M))

Fig. 28

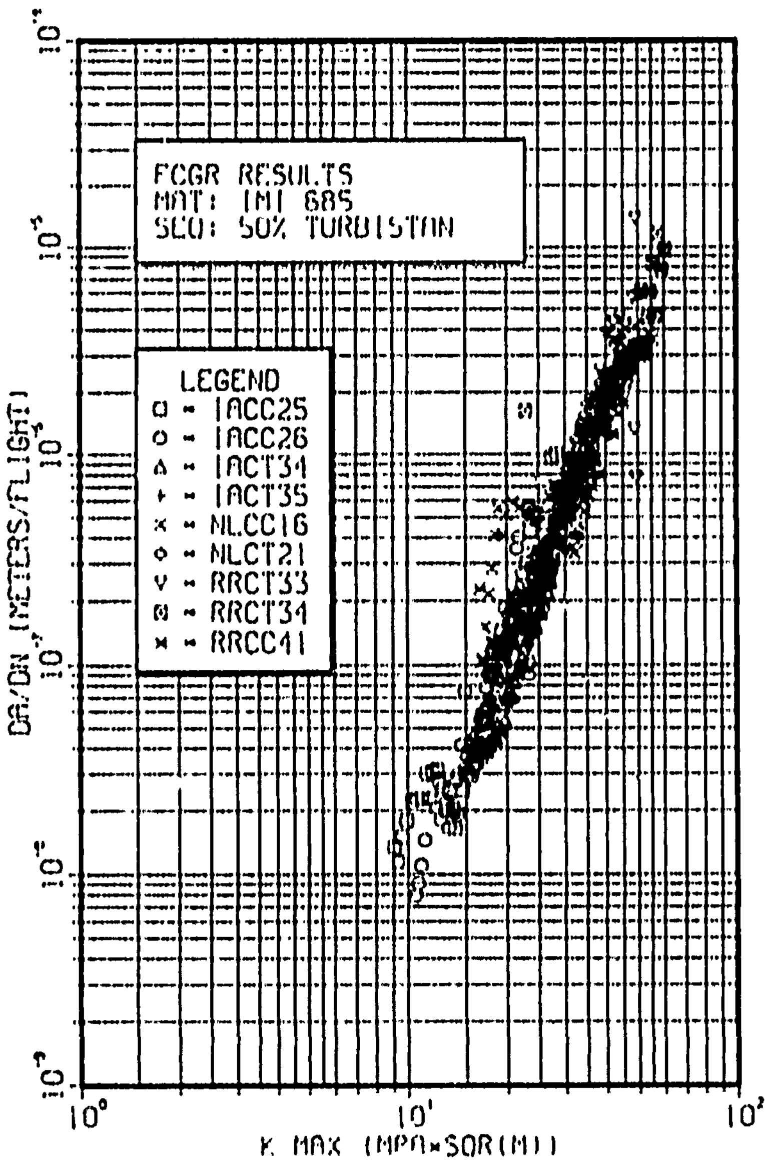
FCGR RESULTS
MAT: IMI 685
SEQ: 50% TURBISTAN
LEGEND
IACC25
IACC26
IACT34
IACT35
NLCC16
NLCT21
RRCT33
RRCT34
RRCC41
DA/DN (METERS/FLIGHT)
K MAX (MPA*SQR(M))
10^0
10^1
10^2
10^{-9}
10^{-8}
10^{-7}
10^{-6}
10^{-5}
10^{-4}

Fig. 29

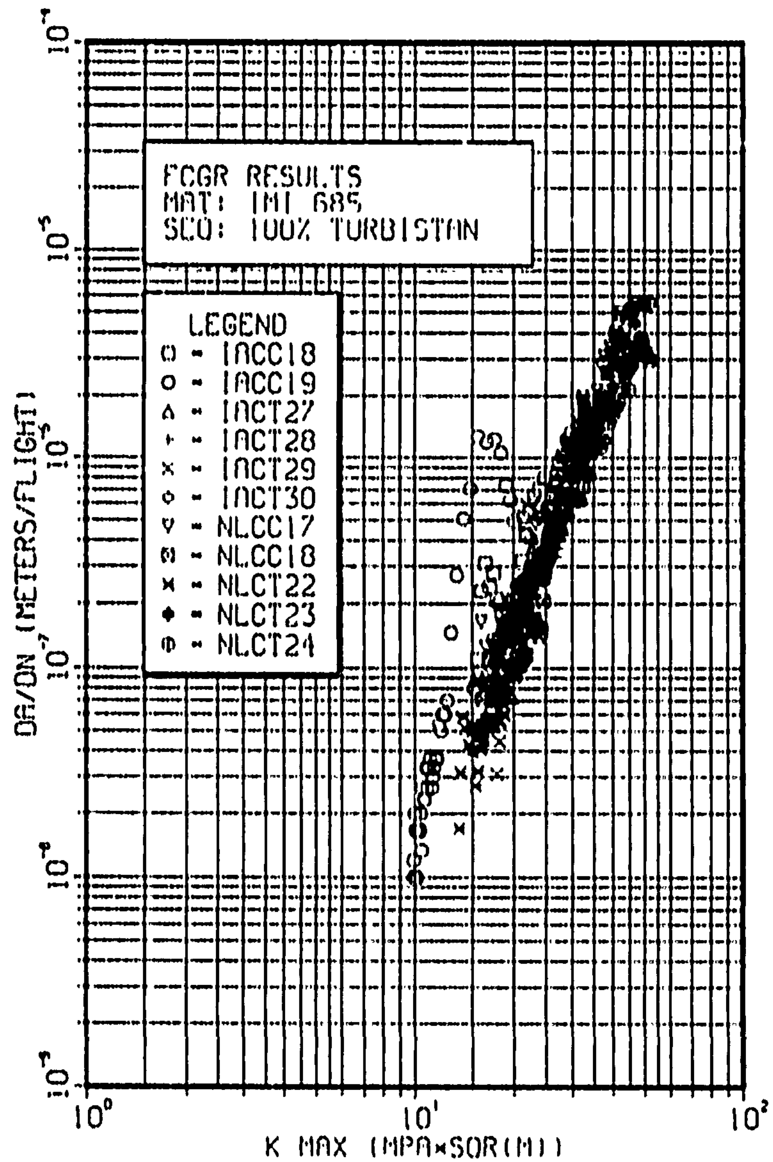
FCGR RESULTS
MAT: IMI 685
SEQ: 100% TURBISTAN
LEGEND
IACC18
IACC19
IACT27
IACT28
IACT29
IACT30
NLCC17
NLCC18
NLCT22
NLCT23
NLCT24
DA/DN (METERS/FLIGHT)
K MAX (MPA*SQR(M))
10^0
10^1
10^2
10^{-9}
10^{-8}
10^{-7}
10^{-6}
10^{-5}
10^{-4}

Fig. 30

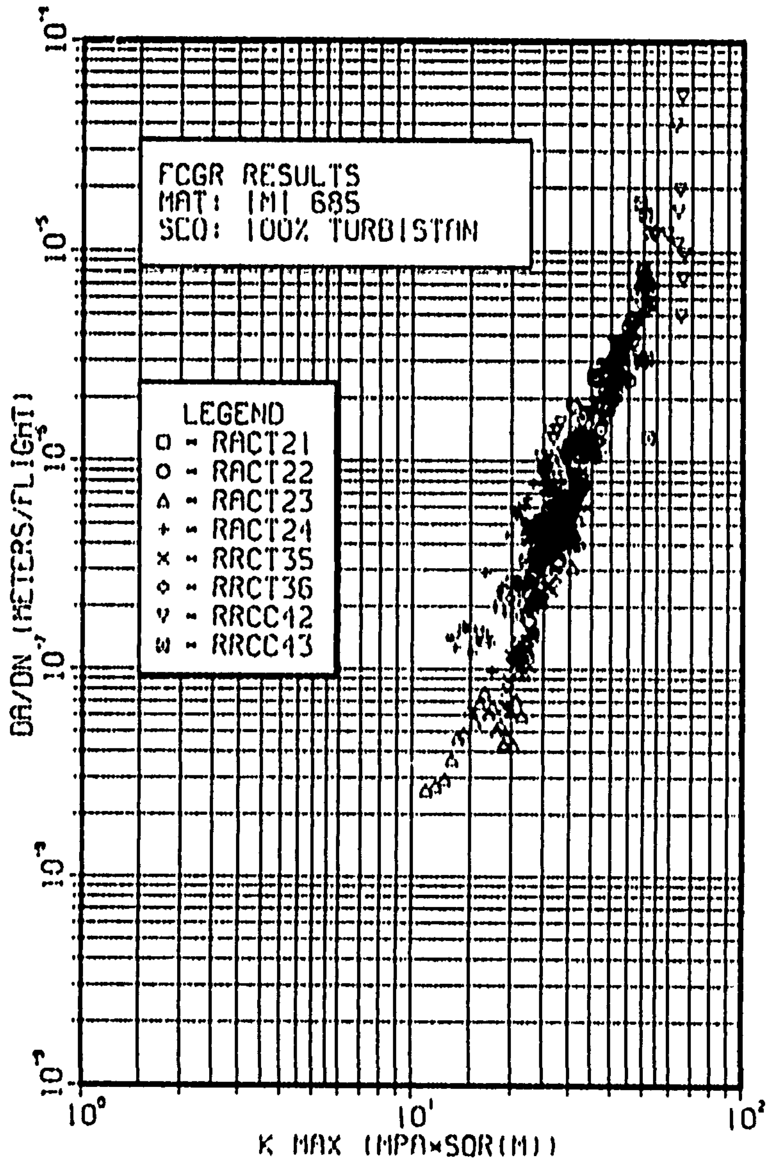
FCGR RESULTS
MAT: IMI 685
SEQ: 100% TURBISTAN
LEGEND
□ - RACT21
○ - RACT22
△ - RACT23
+ - RACT24
× - RRCT35
◇ - RRCT36
▽ - RRCC42
ω - RRCC43
DA/DN (METERS/FLIGHT)
10^{-4}
10^{-5}
10^{-6}
10^{-7}
10^{-8}
10^{-9}
10^{0}
10^{1}
10^{2}
K MAX (MPA×SQR(M))

Fig. 31

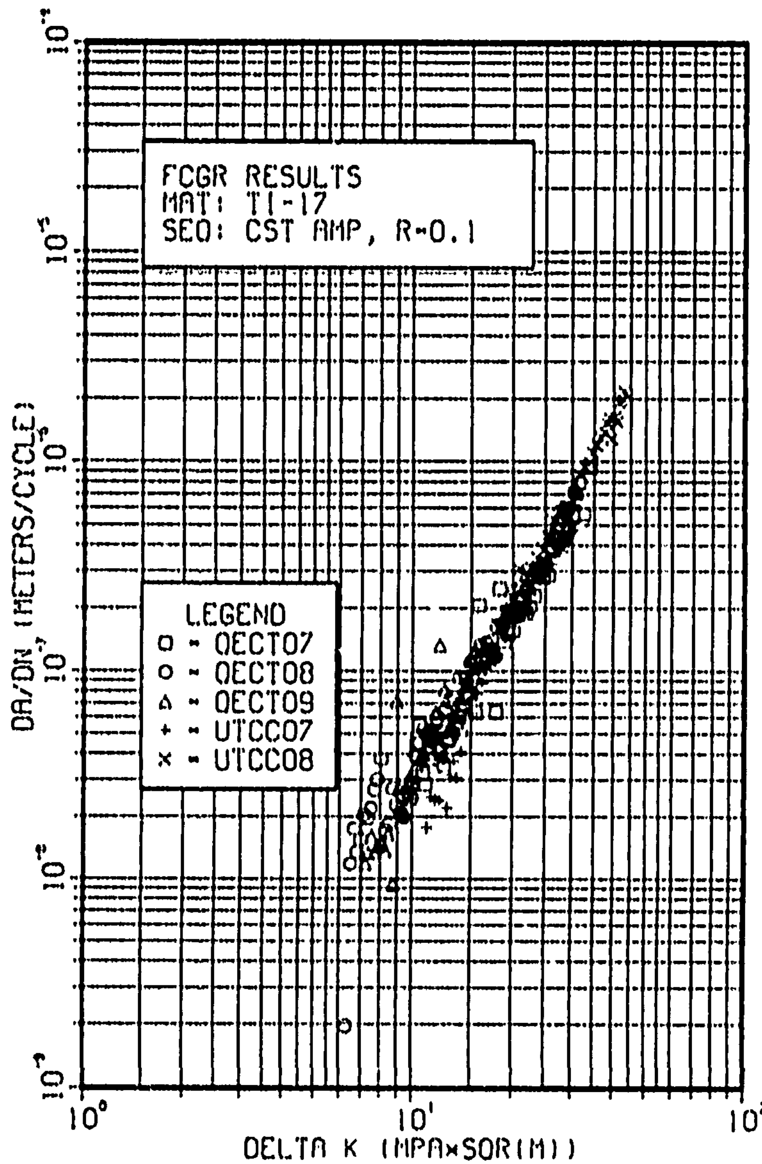
FCGR RESULTS
MAT: TI-17
SEQ: CST AMP, R=0.1
LEGEND
□ - QECT07
○ - QECT08
△ - QECT09
+ - UTCC07
× - UTCC08
DA/DN (METERS/CYCLE)
10^{-4}
10^{-5}
10^{-6}
10^{-7}
10^{-8}
10^{-9}
10^{0}
10^{1}
10^{2}
DELTA K (MPA×SQR(M))

Fig. 32

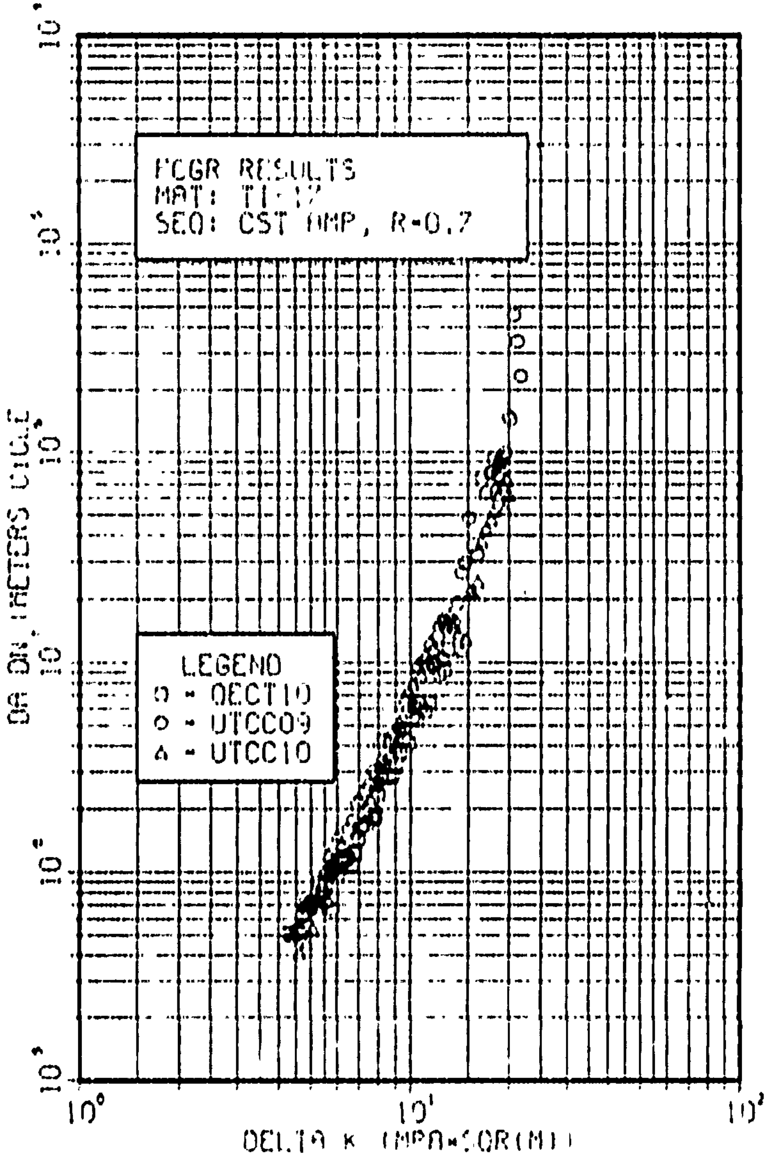
FCGR RESULTS
MAT: TI-17
SEQ: CST AMP, R=0.7
LEGEND
□ = QECT10
○ = UTCC09
△ = UTCC10
DA/DN (METERS/CYCLE)
DELTA K (MPA*SQR(M))

Fig. 33

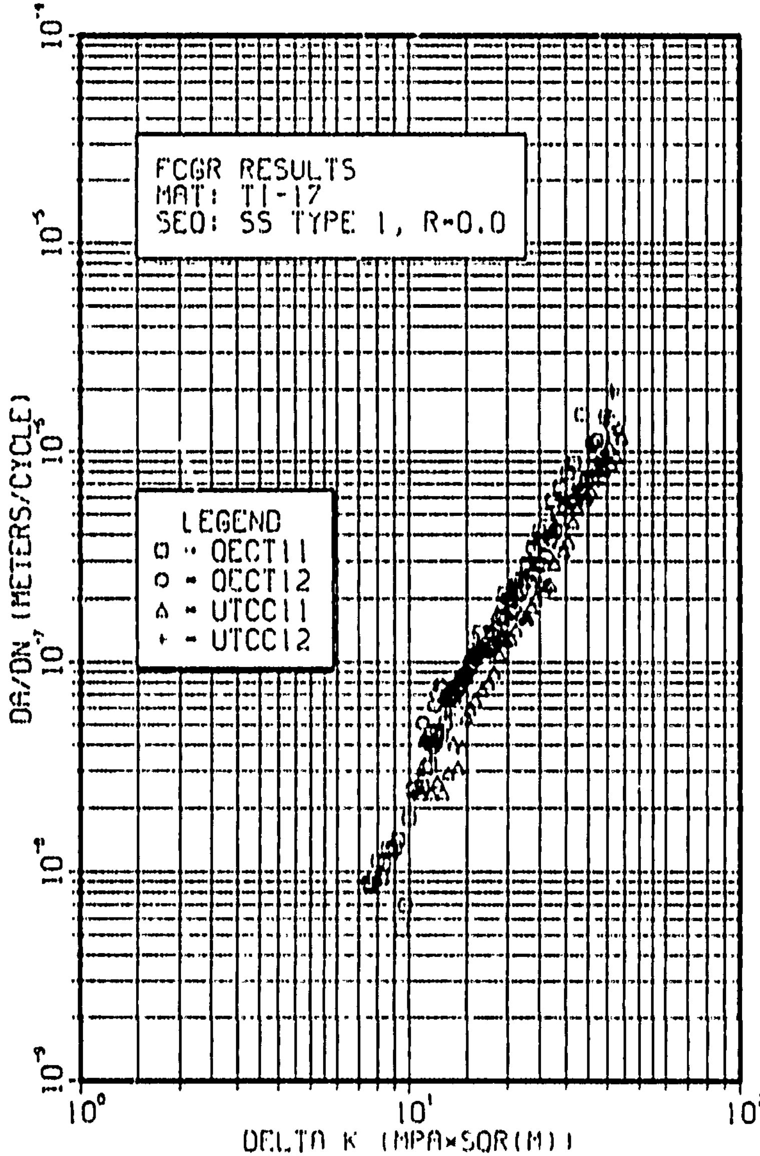
FCGR RESULTS
MAT: TI-17
SEQ: SS TYPE 1, R=0.0
LEGEND
□ = QECT11
○ = QECT12
△ = UTCC11
+ = UTCC12
DA/DN (METERS/CYCLE)
DELTA K (MPA*SQR(M))

Fig. 34

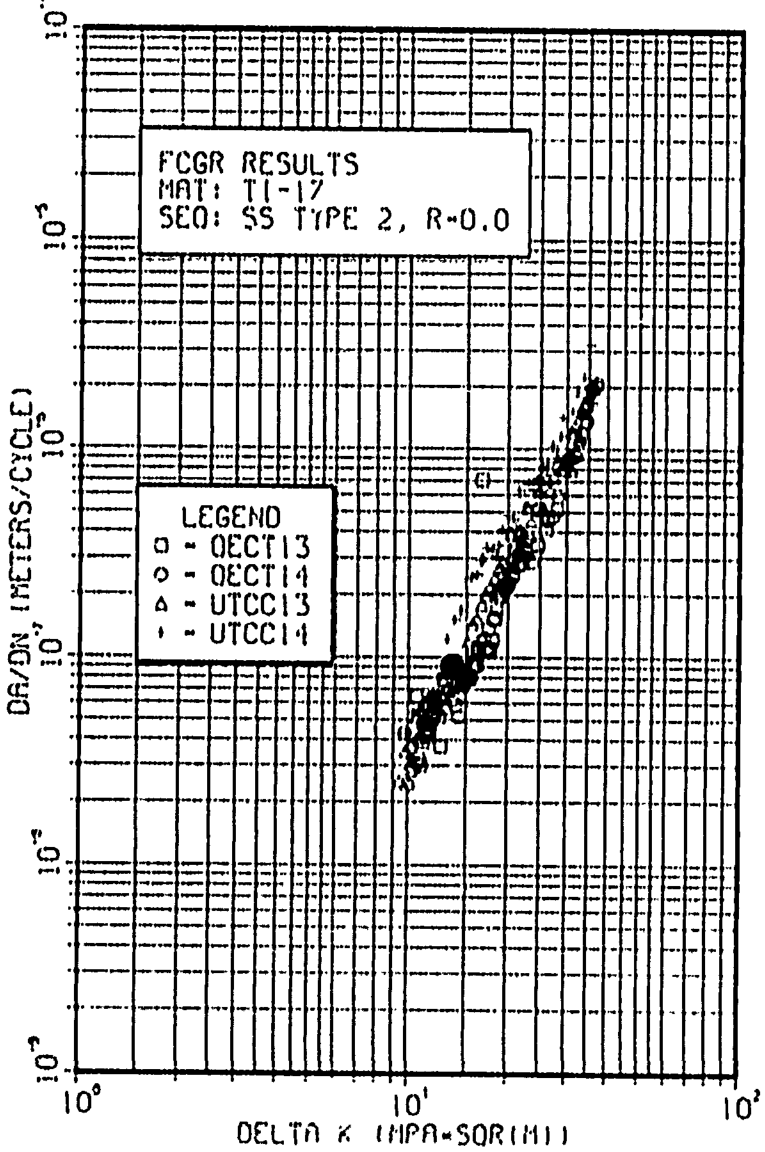
FCGR RESULTS
MAT: TI-17
SEQ: SS TYPE 2, R=0.0
LEGEND
□ = QECT13
○ = QECT14
△ = UTCC13
+ = UTCC14
DA/DN (METERS/CYCLE)
DELTA K (MPA*SQR(M))
10^{-4}
10^{-5}
10^{-6}
10^{-7}
10^{-8}
10^{-9}
10^{0}
10^{1}
10^{2}

Fig. 35

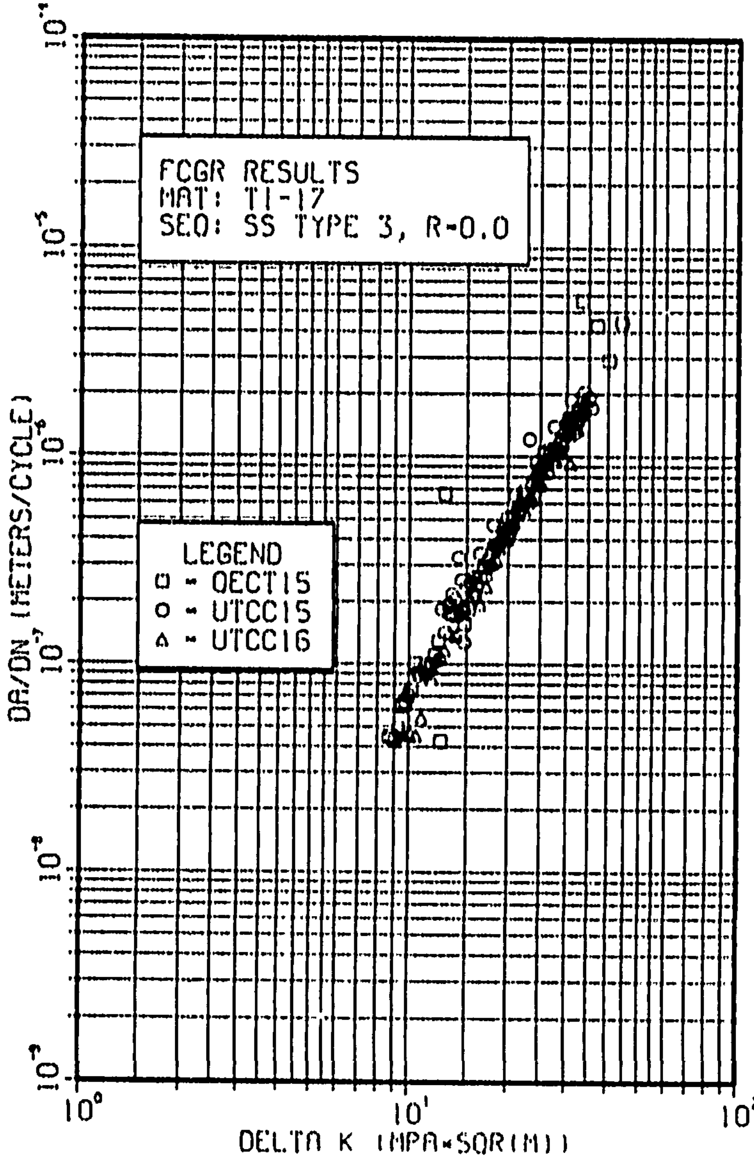
FCGR RESULTS
MAT: TI-17
SEQ: SS TYPE 3, R=0.0
LEGEND
□ = QECT15
○ = UTCC15
△ = UTCC16
DA/DN (METERS/CYCLE)
DELTA K (MPA*SQR(M))
10^{-4}
10^{-5}
10^{-6}
10^{-7}
10^{-8}
10^{-9}
10^{0}
10^{1}
10^{2}

Fig. 36

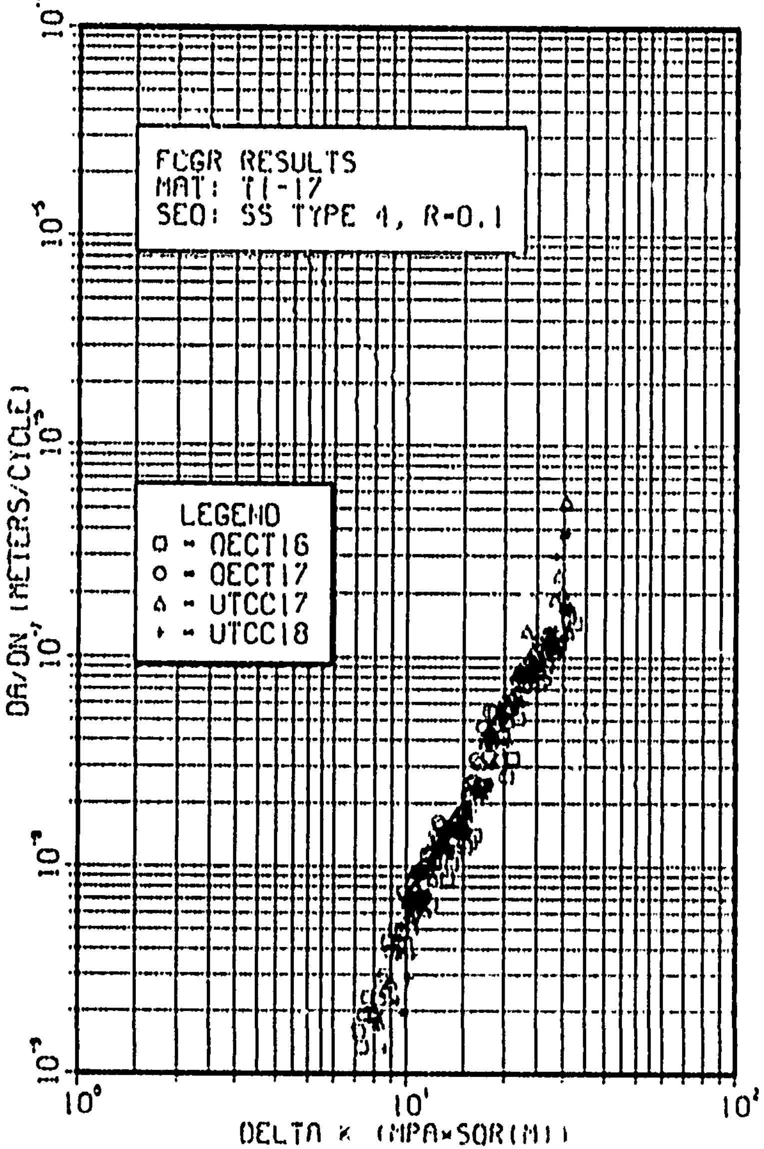
FCGR RESULTS
MAT: TI-17
SEQ: SS TYPE 4, R=0.1
LEGEND
□ - OECT16
○ - OECT17
Δ - UTCC17
+ - UTCC18
DA/DN (METERS/CYCLE)
DELTA K (MPA*SQR(M))
10^0
10^1
10^2
10^-4
10^-5
10^-6
10^-7
10^-8
10^-9

Fig. 37

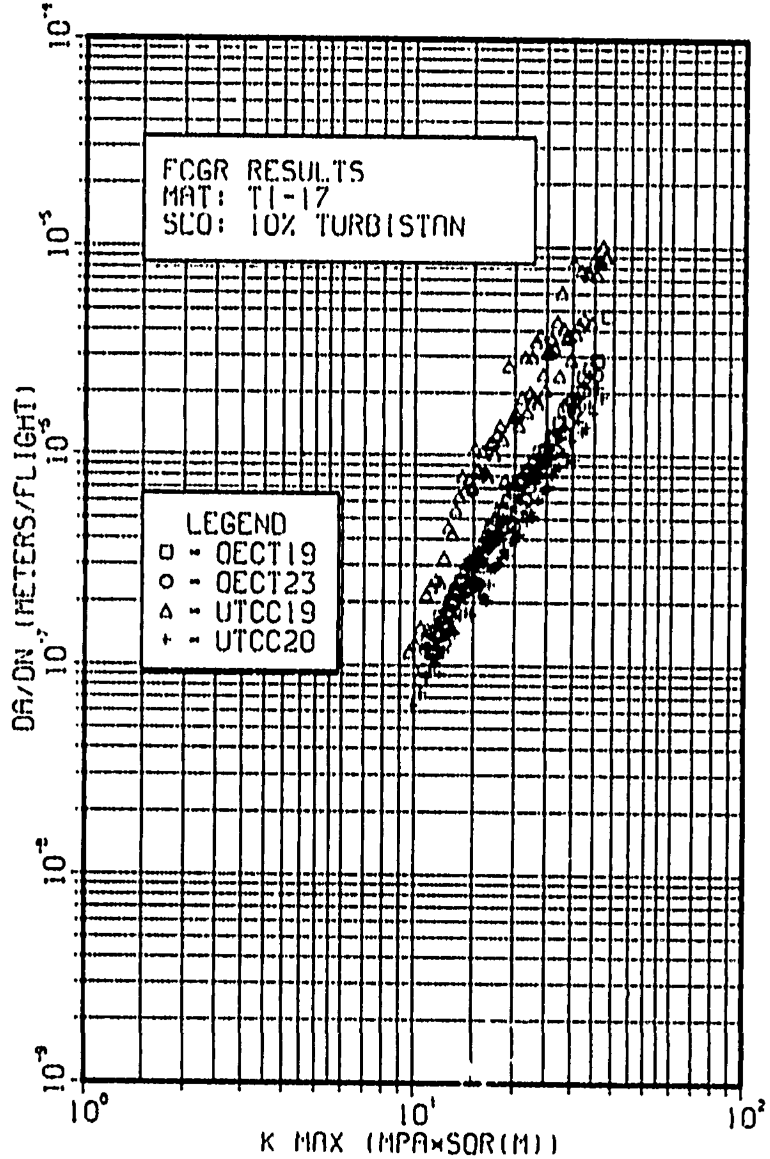
FCGR RESULTS
MAT: TI-17
SEQ: 10% TURBISTAN
LEGEND
□ - OECT19
○ - OECT23
Δ - UTCC19
+ - UTCC20
DA/DN (METERS/FLIGHT)
K MAX (MPA*SQR(M))
10^0
10^1
10^2
10^-4
10^-5
10^-6
10^-7
10^-8
10^-9

Fig. 38

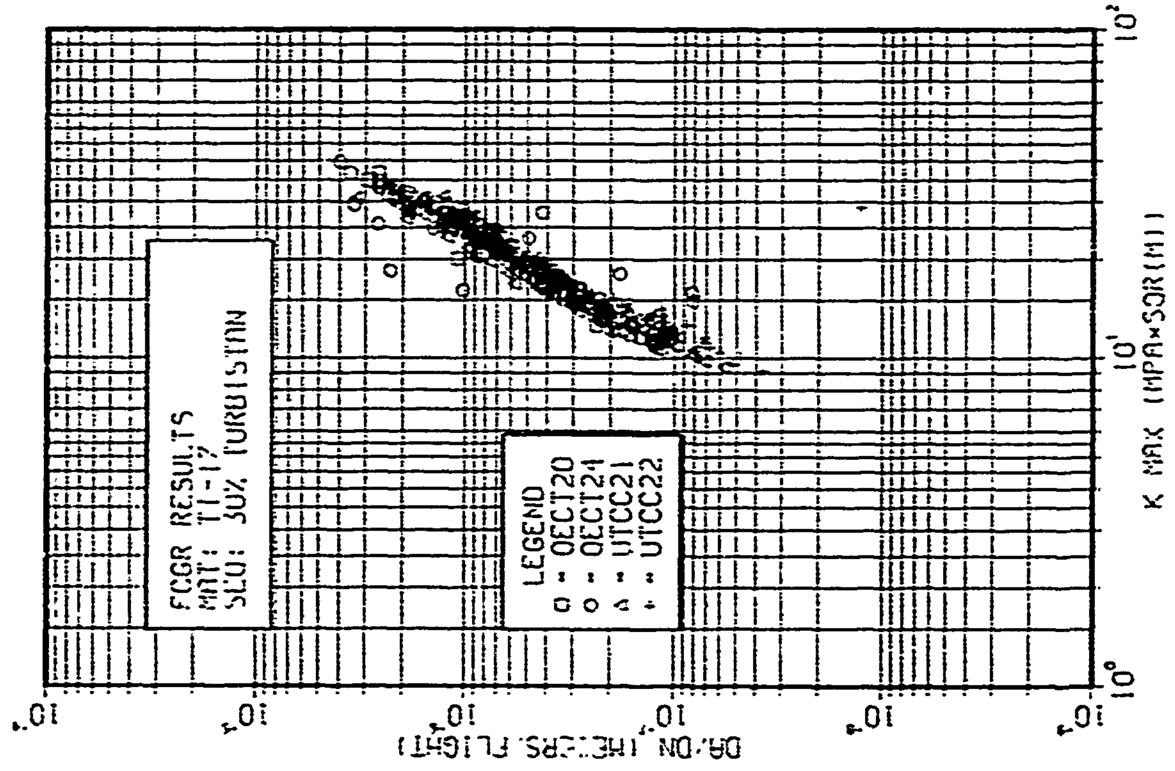

FCGR RESULTS
MAT: TI-17
SEQ: 50% TURBISTAN
LEGEND
□ = OECT20
○ = OECT24
△ = UTCC21
+ = UTCC22
DA/DN (METERS/FLIGHT)
K MAX (MPA×SQR(M))

Fig. 39

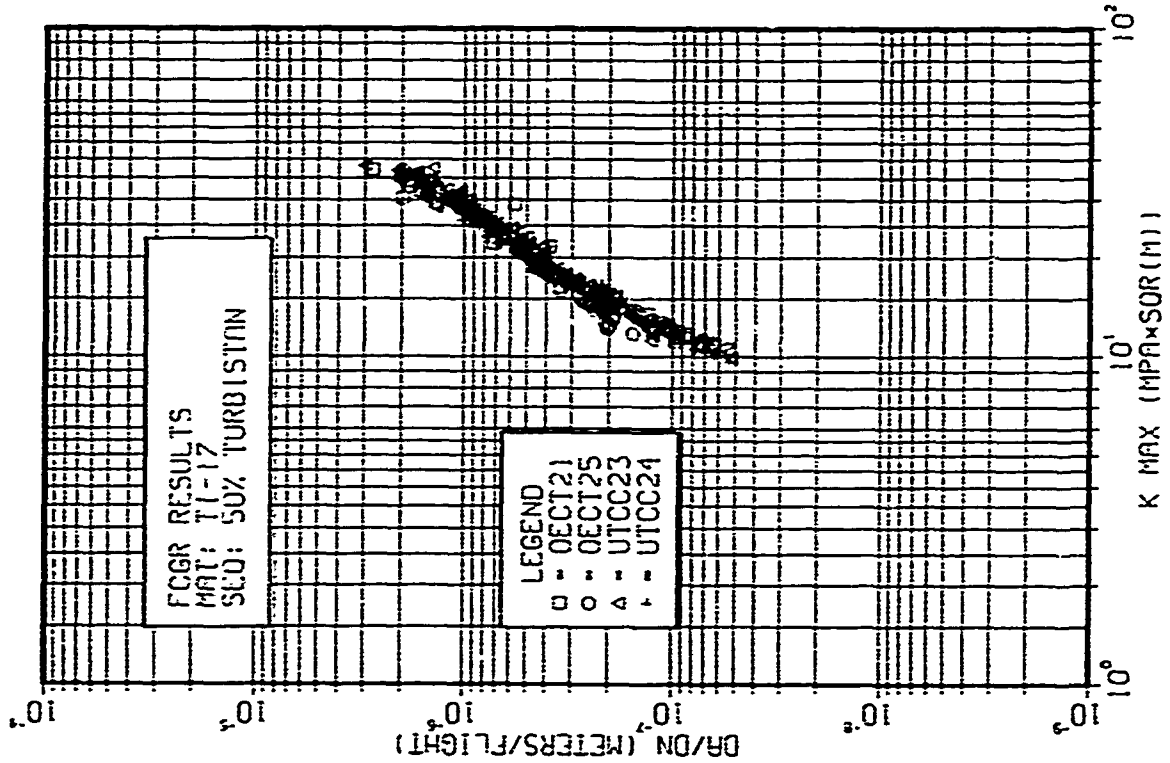

FCGR RESULTS
MAT: TI-17
SEQ: 50% TURBISTAN
LEGEND
□ = OECT21
○ = OECT25
△ = UTCC23
+ = UTCC24
DA/DN (METERS/FLIGHT)
K MAX (MPA×SQR(M))

Fig. 40

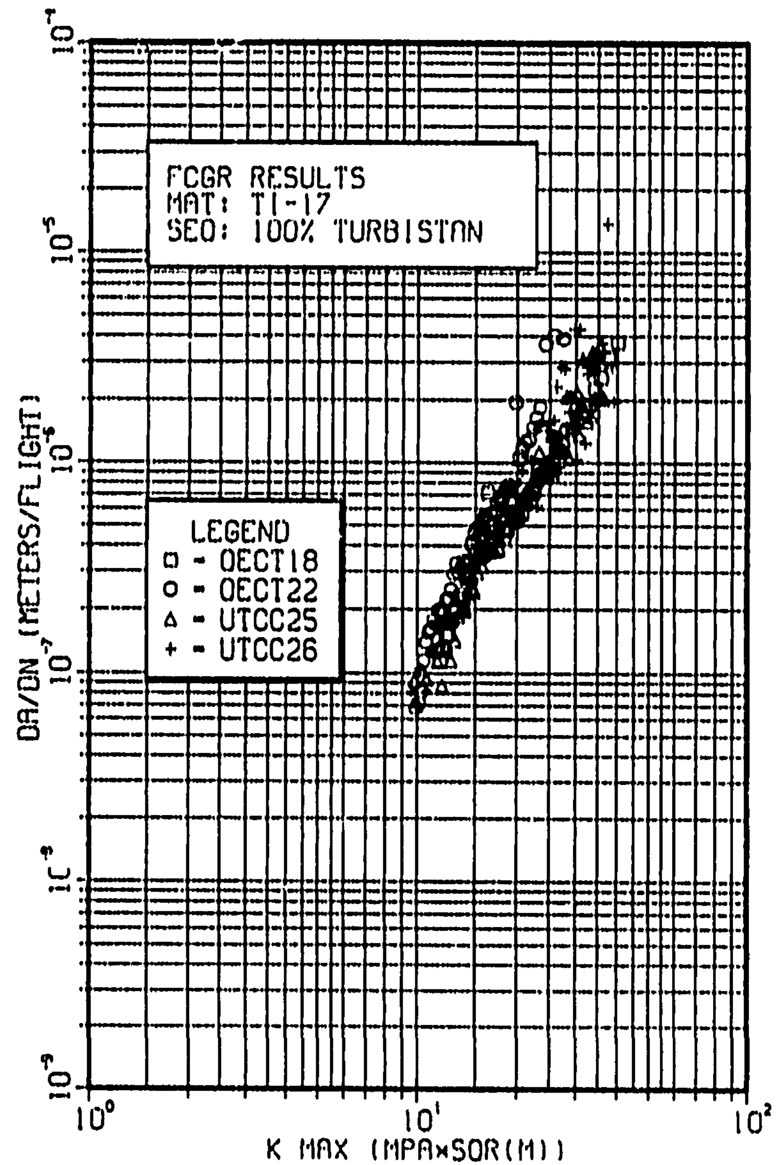
FCGR RESULTS
MAT: TI-17
SEQ: 100% TURBISTAN
LEGEND
□ - OECT18
○ - OECT22
△ - UTCC25
+ - UTCC26
DA/DN (METERS/FLIGHT)
K MAX (MPA×SQR(M))
10^0
10^1
10^2
10^-4
10^-5
10^-6
10^-7
10^-8
10^-9

Fig. 41

CHAPTER 5
CRACK GROWTH PREDICTION MODELS

by

Eric Jany
Centre d'Essais Aéronautique de Toulouse
23, Av. Henri Guillaumet
31056 Toulouse Cedex
France

Paul Heuler
IABG mbH
Abt. TAB
Einsteinstrasse 20
8012 Ottobrunn
Germany

1. INTRODUCTION

Seven companies or laboratories initially entered the exercise: CEAT, FFA, GE, NASA, NLR, Pratt & Whitney, Rolls-Royce. Two of them withdrew (GE, Pratt & Whitney). The following paragraphs present a short description of the models and some information on how the data base was handled in order to carry out the predictions. A list of references on each model is given.

2. CEAT MODEL

2.1 Model Description

CEAT used the PREFFAS (1, 2, 3) model for crack growth predictions. This model was developed by Aérospatiale typically for application on aluminum alloy components under spectra typical for aircraft. It is based on the crack closure phenomena and on the corresponding effective stress intensity factor range. It considers $da/dN = C\,\Delta K_{eff}^{n}$.

In order to account for small cycles - large cycles interaction, the sequence is decomposed in elementary cycles by an algorithm which takes into account the rainflow effect. The model requires a short block size during which the crack length is held constant. The effective stress intensity factor is determined for each cycle of the sequence using the Elber's concept as $\Delta K_{eff} = (AR+B)\,\Delta K$ (with A+B=1). It then calculates, on a cycle by cycle basis, the growth during one block and the so-called block efficiency $(EF = \sum_{i=1}^{N} \Delta P_{eff}^{\,n})$. The crack growth rate per block can then be determined as $da/dN = D.EF\,K_{max}^{n}$. The identification of the model involves determining the values of A, B, C and n. For aircraft loading conditions, the authors recommend the use of crack growth results for R=0.1 and of a 1.7 ratio overload (every 100 cycle) sequence. However, the model can be identified from any two sets of data under different loading conditions.

2.2 Data Handling

The values of A, B, C and n are determined by a best fit method applied to the R=0.1, R=0.7 and Type 4 (1.7 overload sequence) data.

For the three alloys, the following sets of parameters were chosen:

	n	A	B
Ti-6Al-4V/CT	4.36	0.439	0.561
Ti-6Al-4V/CC	3.75	0.353	0.647
IMI685/CT	4.43	0.190	0.810
IMI685/CC	3.80	0.377	0.623
Ti17/CT	2.72	0.405	0.595
Ti17/CC	3.55	0.287	0.713

3. NASA MODEL

3.1 Model Description

The NASA crack growth predictions were made using the life prediction code FASTRAN II (4, 5, 6). FASTRAN II is a life prediction code based on Elber's plasticity-induced closure concept and the effective stress-intensity factor range ΔK_{eff}.

The analytical crack closure model is based on the Dugdale model modified to leave plastically deformed material in the wake of the crack. At the cycle peak stress (in tension only), the effect of state of stress on plastic zone size and displacements are approximately accounted for by using a constraint factor α. The effective flow stress is taken as $\alpha \sigma_o$, with α=1 for plane stress and α=3 for plain strain conditions. σ_0 is the average between the yield stress and the ultimate stress. The physical crack growth is operated independently of the analytical closure model. It is calculated essentially cycle by cycle from the growth rate relation. The opening stress is held constant until a certain amount of crack extension, Δa^*, has been reached (Δa^* is a fraction of the cyclic plastic zone size) or until the applied stress exceeds one third of the maximum stress to be applied to the cracked specimen. After that phase, the crack opening level is updated involving the relevant max and min stress levels of the previous phase.

3.2 Data Handling

The constraint factor α has been determined by a trial and error method as the value which fits the R=-0.1 and R=0.7 data. For the three alloy a similar α values were taken for both CT and CC geometries.

	α
Ti-6Al-4V	1.9
IMI685	1.8
Ti17	2.0

The baseline crack growth rate vs. ΔK_{eff} relation was determined for each alloy-geometry case as an assembly of linear segments in order to account for the transitional behaviours. Fracture toughness and flow stress (σ_0) values were determined from the literature.

4. FFA MODEL

4.1 Model Description

FFA used a linear crack growth prediction code LIFE (7, 8) since non-linear load interaction effects were not expected to prevail to a significant amount. R ratio effects were taken into account by use of Newsman's formula for crack opening stress level depending on the material flow stress, σ_0, a constraint factor, α and the maximum stress of the cycle. Newman's formula which had been derived from analytical and numerical studies was applied to establish the basic crack growth curves in terms of ΔK_{eff}. For variable amplitude loading, this formula was applied to derive effective stress intensity ranges for individual reversals and corresponding crack increments from the basic curve. Crack increments were accumulated linearly.

4.2 Data Handling

All experimental results from the two constant amplitude load test series have been used. In a log-log da/dN vs. ΔK diagram, a curve composed of several linear segments was visually fitted for each R value. Points on this curve were then given as a table in the prediction programme.

Similar to the NASA approach, the R=0.1 and R=0.7 data were used to determine the constraint factor, α. The threshold value ΔK_{th} and K_{Ic} were set to the following values.

	ΔK_{th} (MPa$\sqrt{m}$)	K_{Ic} (MPa$\sqrt{m}$)
Ti-6Al-4V	5.0	75.0
IMI685	7.5	70.0
Ti17	6.0	70.0

5.0 NLR MODEL

5.1 Model Description

The NLR predictions were made using the CRACKS 2000 software. It is based on the NASA/FLAGRO programme which provides the framework for calculation and was extended by the NLR/CORPUS crack opening model (9-11). Crack growth is analysed not on a cycle-by-cycle basis, but by integrating crack increments resulting from the rainflow counted load steps of the spectrum histogram under consideration of effective stress ranges. Each load step of the histogram consists of a number of constant amplitude load cycles where the opening load and the stress intensity factor as well as the opening level are updated.

For crack opening level calculation the CORPUS module is activated. It consists of a set of rules which control the opening level dependent on previous mas and min stress levels and their mutual interaction. Previous peak loads loose their influence on crack opening as soon as the crack and its current plastic zone have grown through the plastic zone caused by the respective peak load. For calculation of opening levels caused by single load cycles empirically or analytically (via a strip yield model) derived functions are implemented.

The physical background of the opening model is explained by the introduction of plastic deformation caused by peak loads which will be visible as ridges or humps on the fracture surfaces and will increase the crack opening stress. Subsequent underload may flatten the ridges and therefore decrease the opening stress to some extent. Multiple overload effects can be handled by consideration of the interaction of several peak loads.

Thickness effects, or the state of stress at the crack tip, are accounted for through a constraint factor, α, which influences the opening level. It is determined by fitting material parameters to overload test results i.e. to simple sequence Type 4 data.

5.2 Input Data Handling

The input data od CRACKS 2000 consist of:

- Material properties, e.g., K_{Ic}, ΔK_{th}, $\sigma_{0.2}$, E
- Material properties
- Specimen geometry
- Load Spectrum (rainflow counted).

The material parameters are determined by fits of da/dN-ΔK data for R=0.1, R=0.7 and simple sequence Type 4 using the software module CRAFIT. Material parameters are generated for each of the materials not differentiating between specimen geometries. These material. parameters account for threshold, C and n similar to the Paris-Elber law, primary plastic flow and constraint of yielding.

6. ROLLS-ROYCE MODEL

6.1 Model Description

Stress ratio effects are taken into account by use of the Walker model $da/dN = (\Delta K \cdot (1-R)^m)^n$. The simple sequence cases were predicted by linear accumulation of crack increments. For the TURBISTAN cases a so-called "Modified Trend Analysis" is applied which consists of a linear accumulation rule including rainflow count procedures modified by an overload parameter. Paris constant C and n derived from overload tests Type 4 are therefore additionally introduced as basic input data for spectrum crack growth predictions. Further details of the model were not disclosed within the present exercise.

6.2 Input Data Handling

The crack growth data base results (R = 0.1 and 0.7, Type 4 sequence) have been regression analysed to provide the Paris law coefficients C and n as well as the Walker exponent m. CC and CT specimen results were analysed separately which means that constants and co-efficients were assumed to be not only material dependent. The following set of coefficients have been used by Rolls Royce.

	CONSTANT AMPLITUDE		TYPE 4 SEQUENCE		
	C	n	C	n	m
Ti6Al4V/CT	0.7214E-12	4.238	0.3239E-13	4.225	0.767
Ti6Al4V/CC	0.2455E-12	4.327	0.6829E-12	3.256	0.691
IMI685/CT	0.1745E-13	4.822	0.4435E-16	6.192	0.670
IMI685/CC	0.2349E-12	4.109	0.2570E-12	3.487	0.628
Ti-17/CT	0.4543E-10	2.800	0.3900E-11	3.109	0.858
Ti-17/CC	0.2153E-11	3.700	0.6323E-12	3.697	0.577

7.0 REFERENCES

(1) Aliaga, D., "Prévision de la fissuration en fatigue sous chargement d'amplitude variable - modèle PREFFAS", rapport no 47904, Aerospatiale, 1985.

(2) Bleuzen, C. and T. Pardessus, "Crack propagation life predictions for engine materials under variable amplitude loading conditions", Third International SFM Spring Meeting, Vol. II, 1988.

(3) Aliaga, D., A. Davy and H. Schaff, "A simple crack closure model for predicting fatigue crack growth under flight simulation loading", in: Durability and Damage Tolerance in Aircraft Design (Proc. 13th ICAF Symp.), EMAS, 1985, pp. 605-630.

(4) Newman, J.C., Jr., "A crack closure model for predicting fatigue crack growth under aircraft spectrum loading", Methods and models for predicting fatigue crack growth under random loading, ASTM STP 748, 1981, pp. 53-84.

(5) Newman, J.C., Jr., "Prediction of fatigue crack growth under variable amplitude and spectrum loading", Design of fatigue and fracture resistant structures, ASTM STP 761, 1982, pp. 255-277.

(6) Newman, J.C., Jr., M.H. Swain and E.P. Phillips, "An assessment of the small crack effect for 2024-T3 aluminum alloy", Small Fatigue Cracks, 1986, pp. 427-452.

(7) Palmberg. B., "Life Crack Growth Prediction and Evaluation Program LIFE version VAX/APOLLO 04". FFAP-H-1000. The Aeronautical Research Institute of Sweden. Bromma. 1989.

(8) Palmberg. B., "Automated Analysis of Crack Growth Rate for Obtaining da/dN versus ΔK Relation". FFA TN 1987-70. The Aeronautical Research Institute of Sweden. Bromma 1987.

(9) DeKoning. A.U., "Prediction of fatigue crack growth rates under variable loading using a simple crack closure model". NLR MP 81023 U. 1981.

(10) DeKoning. A.U., "User manual for the NLR/CORPUS module in the ESACRACK computer programme". ESA Contract Report CR89290L. 1989.

(11) DeKoning. A.U., "The architecture and detail design of the NLR/CORPUS crack opening module in the ESACRACK software for damage tolerance analysis. ESA Contract Report CR89292L. 1989.

CHAPTER 6

CRACK GROWTH PREDICTION RESULTS

by

Eric Jany & Olivier Renne
Centre d'Essais Aéronautique de Toulouse (DGA/CEAT)
31056 Toulouse - France

and

Paul Heuler
Industrienanlagen Betriebgesellschaft mbH (IABG)
D-8012 Ottobrunn, Germany

1. Introduction

In the following, prediction results for the 60 test cases described in Chapter 4 are presented and discussed. The predictions were made by CEAT, NASA, FFA, NLR and RR (who carried out only a limited number of cases) using the respective models described in Chapter 5. This chapter starts with a short consideration of criteria for the assessment of model predictions, presents an overview of the whole body of results followed by a discussion of aspects relevant to modelling of crack growth and application within the design process.

2. Criteria for the assessment of prediction models

The assessment of the prediction capabilities of models is not straightforward because durability and crack growth considerations represent only one part of the design and lifing process among many others. It is not reasonable to ask for a high precision of prediction models if important input variables such as the loading environment or the influence of corrosive media can only be specified with a relatively high degree of uncertainty. According to Schijve (1) results of prediction models can be judged based on different criteria:

- crack growth life from an initial to a specified crack length or to failure

- crack growth rate within the range of crack lengths considered

- crack increments due to individual segments, e.g. flights or even individual cycles.

From a practical point of view, the first criterion would be sufficient. As Schijve points out, however, a more detailed assessment is recommended in order to check the physical basis of a prediction model which, in case of a positive judgement, would give more confidence for general application. This consideration brings about the requirement that models should predict empirical trends in simple variable amplitude (e.g. overload) tests with a sufficient quantitative accuracy (1). The definition of an acceptable quantitative overall prediction accuracy depends again on many aspects. Schijve proposes, as a personal view, to consider a prediction to be good if the ratio of predicted versus actual lives is within the range of 0.67 to 1.5 and as an acceptable quality if the range is 0.5 to 2. The latter definition is identical to that suggested in (2), whereas Gassner (3) proposed (mainly with regard to Miner type life predictions) that 90 percent of the predictions should fall into a range of 1:2 on the safe side.

3. Prediction results

In the following an overview of the prediction results is done for each material and each specimen geometry. This covers general comments on the data base and its utilisation by the modellers and an overall comparison of the predicted and experimental results.
Experimental results on Ti-6Al-4V, IMI685 and Ti17 taken into account for the comparison are listed respectively in Table 1,2 and 3.

For each (material, specimen) couple, the following data are provided:

- an overall result table

This gives the number of cycles predicted by each model, the cycle number measured during the test and the N prediction / N test ratio. If the prediction or the test was performed for non valid load conditions (resp. non valid crack length range), the table reads NV1 (resp. NV2) (non valid meaning different from the prescribed one).

- a N prediction / N test ratio chart

- a vs. N curves for each test condition

These curves enable for each test condition a comparison between the test result and the prediction.

-da/dN vs. ΔK curves for the different tests or for each modelled result test

These curves enable a more complete analysis of the model performance. In these charts, ΔK is the stress intensity factor variation during one elementary cycle (R=0.1 and 0.7 , Type 4 sequence without considering the overload cycle), during each periodical sequence (for Type 1 to 3 sequences) during each flight (for Turbistan sequences). da/dN is the crack extension during each of the cycle or flight as defined above.

Nota:

i) The crack length ranges considered in the analysis differ for some cases from the original ones presented in the NRC report (ref.: LTR-ST-1785). These modifications have been done in order to take into account predictions which have been done with crack length ranges different from the prescribed ones.

ii) For some predictions the crack length range was still too different from the standard one. In these cases, a Nprediction / Ntest ratio was calculated on the basis of the longest common crack length range.

iii) It should be noted that the thickness of the Ti17 CT specimens varied to some extent. This might introduce some differences with regard to the constraint prevailing at the crack tip.

3.1 Ti-6Al-4V, CT specimens

Prediction overall results: Table 4
Nprediction / Ntest charts: Fig.1
a vs. N plots: Fig.4 to 13
da/dN vs. ΔK plots: Fig.64 to 73

The data base is composed of only a very limited number of tests, since it has been decided to restrict the data base to the results created within the present programme. Thus results from the Core programme were not considered. The test results appear to be consistent except for the R=0 1 case where specimen CT11 seems more valid than CT28. CT11 specimen has been used by all modellers and is used for prediction analysis as well. Comparison test for Type 3, Turbistan 30 and 50 do not exist. Other comparison tests do not show any specific feature.

Prediction results show a good agreement for Type 1 and Type 2 cases and for Turbistan 00 and 10. Predictions for Type 4 sequence are very scattered; only NASA provides a good prediction. Predictions on Turbistan sequences are conservative. For type 1 and 2 conditions NLR and NASA's predictions are not conservative.

All da/dN vs. ΔK prediction, except FFA's exhibit a linear behaviour. FFA models a slope change similar to the actual test behaviour.

3.2 Ti-6Al-4V, CC specimens

Prediction overall results: Table 4
Nprediction / Ntest charts: Fig.1
a vs. N plots: Fig.14 to 23
da/dN vs. ΔK plots: Fig.74 to 85

There is no peculiar feature in the data base. All comparison tests exist. There is a high discrepancy between the Turbistan00 and 10 on one side and the Turbistan 30 and 50 on the other side as shown on Fig.75.

Prediction results are in good agreement with tests and conservative for Turbistan 30 and 50. They are not for Turbistan 10 and especially Turbistan 00 where the N prediction / N test ratio is higher than 2 for all models. For type 1 and 2 conditions the predictions are good. They are conservative for all modellers except NASA. No prediction is conservative for type 3 condition and the N prediction / N test ratio reaches a value of 2 for FAA and Rolls-Royce predictions. Type 4 prediction is poor for FFA.

All predicted da/dN vs. ΔK curves exhibit a linear behaviour except NLR and FFA for R=0.7 condition.

3.3 IMI 685, CT specimens

Prediction overall results: Table 5
Nprediction / Ntest charts: Fig.2
a vs. N plots: Fig.24 to 33
da/dN vs. ΔK plots: Fig.86 to 95

In this case, the data base is very rich but shows very little scattering. The da/dN vs. K curves are mostly linear with a slope of about 4.5. All comparison tests, except Type 3, exist.
Prediction results are generally in good agreement with the tests sometimes conservative sometimes not. Type 4 prediction is poor for FFA and CEAT.
da/dN vs. ΔK prediction curves show a linear behaviour except FFA and NASA 's

3.4 IMI 685, CC specimens

Prediction overall results: Table 5
Nprediction / Ntest charts: Fig.2
a vs. N plots: Fig.34 to 43
da/dN vs. ΔK plots: Fig.96 to 105

The data base is also very rich and equivalent to the CT data base. All comparison tests exist. Type 2 test shows high crack growth rates compared with Type 1 and Type 3 (Fig.96). Turbistan 50 test also shows a complex behaviour in its first part (Fig.97).
Prediction results are in good agreement with the tests except for Type 2 conditions. NASA and NLR predictions remain conservative in most cases.
da/dN vs. ΔK prediction curves show a linear behaviour except for FFA.

3.5 Ti 17, CT specimens

Prediction overall results: Table 6
Nprediction / Ntest charts: Fig.3
a vs. N plots: Fig.44 to 53
da/dN vs. ΔK plots: Fig.106 to 115

The data base is very consistent and shows a linear behaviour with a 2.7 slope. All comparison tests exist. No specific feature is to be noticed.
The prediction results are in good agreement with the tests except for FFA's Type 4. The prediction/test ratios are around unity.
Only FFA da/dN vs. ΔK prediction curves do not show a linear behaviour.

3.6 Ti 17, CC specimens

Prediction overall results: Table 6
Nprediction / Ntest charts: Fig.3
a vs. N plots: Fig.54 to 63
da/dN vs. ΔK plots: Fig.116 to 125

The data base is also very consistent and similar to the CT specimen data base. All comparison tests exist. Type 2 crack growth rate is a bit high compared with type 1 and Type 3 results.
The prediction results are in good agreement with the tests except for CEAT's Type 2 and FFA's Type 4. They are sometimes conservative sometimes not.
Only FFA da/dN vs. ΔK prediction curves show a non linear behaviour.

4. Discussion

4.1 General comments

For an assessment of the results presented above, the basis for the comparison of tests and predictions should be reconsidered. In most cases, two or more sets of data for each material/geometry/loading condition were available to the modellers to derive average base-line da/dN versus ΔK curves. Contrary to that, the variable amplitude (simple sequences) and Turbistan test load cases consist of one individual test result each. Therefore no smoothening or averaging effect prevents the direct influence of possible singular

phenomena on test life. Such singular events, maybe due to microstructural peculiarities or some unknown problems with testing itself, are normally not covered by base-line mean curves which means that the respective predictions might erroneously be termed as non acceptable. This should be kept in mind for the following discussions. Examples for the above mentioned problem are the cases of Ti-6Al-4V CC Turbistan00 and IMI 685 CC Type 2 where all models reveal non conservative predictions, see Figs. 1 and 2.

4.2 Crack growth lives

With regard to the above statements, it can be said that, with the exception of the overload Type 4 sequence, all predictions are in most cases in good agreement with the test results. Significant differences between the five models do not occur which is somewhat surprising at first glance with regard to the differences of the models, ranging from rather simple linear algorithms to quite complex interaction models.

Most predictions of the present exercise are in the 0.5 to 2 range which can be designated as acceptable in accordance with Schijve's criterion.

For a more detailed analysis, the life ratios given in Tables 4 to 6 have been statistically evaluated to determine a mean life ratio and the standard deviation assuming a log-normal distribution of life ratios. Results for CT and CC specimens and all three materials have been combined, but individual consideration is made for the type of loading sequence, i.e. constant amplitude loading, Type 1 to 3 sequences, Turbistan and Type 4 sequence (Table 10). For the sake of completeness, the statistical evaluation has been made for all predictions (see first group Table 10). For the following discussion, however, two test cases have been excluded for the reason mentioned above (see paragraph 4.1).

Predictions of the constant amplitude tests (R=0.1 and R=0.7) are good. However it must be noticed that the results are not significantly better than those obtained for complex sequences.

Combining Turbistan and Type 1 to 3 results, i.e. loading sequences which represent actual disc loads, all models provide very good predictions. Some small differences between the models can be observed with regard to scatter. The lowest scatter is found with the NLR model, but FFA linear prediction also delivers good results.

With regard to the overload Type 4 sequence, the linear prediction (FFA) turns out to be very conservative due to the retardation effects which are not taken into account. Here, NLR and CEAT predictions are rather scattered, though Type 4 test results have been used as input data to identify the model. It can be assumed that predictions for this type of loading strongly depend on the weight which is given to overload data for determination of the basic coefficients and factors of the respective models. The overload Type 4 results are well predicted by the NASA model which uses only constant amplitude data as basic input.

4.3 Crack growth rates da/dN vs. ΔK

<u>Constant amplitude loading (R=0.1 and R=0.7)</u>

These data provide the basis for predictions and it is , therefore, interesting to note how the input data were handled by each participant.
Most of the actual crack growth rate data present a more or less linear behaviour in a log-log plot. Some exceptions are test data for Ti-6Al-4V and IMI685 CT and CC at R=0.7 where a slope change of the crack growth curves exists. Slight irregularities of the test data are of course not reflected in great detail by the mean curves produced by the modellers. In most cases, the predicted da/dN vs. ΔK are linear and parallel for both R ratios. Again, exceptions can be found for FFA and NLR predictions for Ti-6Al-4V CC, NASA predictions for IMI685 CT with a slope decrease at ΔK levels of 13 (R=0 7) and 24 (R=0.1) $MPa\sqrt{m}$ respectively. Contrary to that, the FFA prediction reveals a slope increase for the IMI685 CC data at R=0.1 around $\Delta K=16\ MPa\sqrt{m}$.

As an example of how modelling the input data controls the prediction for variable amplitude loading, the CEAT predictions for Ti17 Type 2 cases will be considered. For the CT specimen, the R=0.7 crack growth life is underpredicted (Fig.3). The Type 2 sequence where the R ratio of the small cycles is also 0.7 is then also underpredicted. A similar dependency, but this time on the non-conservative side, can be found for the respective lives of the CC specimens.

Tables 7, 8 and 9 provide the values of the da/dN vs. ΔK slopes of each prediction. The scatter in the slope appreciation is of the order of 0 4 around the mean value.

Variable amplitude loading

In most cases, the predicted curves are linear where the R=0.1 and R=0.7 curves were considered linear. Transitions in the constant amplitude curves are reflected in the predicted variable amplitude curves. There are, however, some exception for Ti-6Al-4V FFA CT and CC and NLR CC specimens where a knee in the R=0.7 curve is not reflected in the variable amplitude predictions.

The comparison of R=0.1 and Type 1 cases shows for all materials and specimens lower crack growth rates for Type 1 than for R=0.1 except for FFA predictions where in most cases the two results are equivalent. Obviously, the minor cycles with 10% of the maximum load range were not effective, i.e. below threshold. Furthermore it can be assumed that this finding is a consequence of crack closure which gives slightly higher ΔK_{eff} values for R=0.1 than for R=0 Type 1 sequence.

4.4 Contribution of small cycle

An important feature of the models is their accounting of small cycles for crack growth propagation growth. If a model gives less weight to the small cycles than experimental tests, it is likely that this model will provide non conservative predictions.
In order to study this point, an analysis is done by comparing Turbistan test results and predictions as shown on Fig.126 to 137. From Turbistan 50 to Turbistan 00 small cycles of progressively lower amplitude are added to the sequence. Each plot presents the relative life reduction due to the addition of this small cycles, for the test results and for the prediction results as well. A similar analysis is done with the Type 1, 2 and 3 conditions by plotting the relative life reduction due to the increase of the small cycle amplitude from 10% (Type 1) to 30 (Type 2) and then 50% (Type 3).

This shows:

- the difficulty to compare small cycle influence between tests and predictions due to the scatter in experimental results. This is true for both, the overall life data and the da/dN vs. ΔK plots.

for Type 1, 2 and 3 sequences:
- the life reduction due to the increase of small cycle amplitude is different from one model to another, but it seems that NASA always predicts the higher reduction and FFA generally predicts the lower reduction.
- the analysis of the da/dN vs. ΔK plots shows that in almost all cases and for the ΔK range considered, the three curves are linear and parallel. This can be considered as an indication that the small amplitude cycles of respectively 10, 30 and 50% are totally effective over the whole stress intensity factor range. The NASA IMI 685 CT cases are special in the sense that the predictions for the three sequences exhibit a double slope behaviour, reflecting the R=0.7 data, but the slopes are still parallel. The only real exception to this behaviour is for FFA Ti17 CT cases where there is a typical "threshold" effect. The small cycles start to be crack growth effective only above a threshold value. This appears clearly on the Type 2 and Type 3 predictions.

for Turbistan sequences:
- the difference between models. For all (material, specimen) couples, the models predict a saturation in life reduction. The life decreases from Turbistan 50 to Turbistan 30 and from Turbistan 30 to Turbistan 10 but stays constant between Turbistan 10 to Turbistan 00. Surprising results are obtained with FFA and NASA who both predict a life increase due to the addition of the lowest amplitude cycle (between Turbistan 10 to Turbistan 00).
- for each model the effect of small cycle is similar for both specimen geometries but differs with the material.

4.5 Material related aspects

Some features of the crack propagation behaviour and of the predictions differ from one alloy to another.
Ti-6Al-4V and Ti17 exhibit overall results quite equivalent although it appears (Table 11) that the efficiency of a Turbistan flight is higher for Ti17 than for Ti-6Al-4V. IMI 685 exhibit results which are in all cases lower than for the two other alloys. The Turbistan efficiency is similar (slightly lower) than Ti-6Al-4V.
A comparison between both β-processed alloys can be tried to explain the difference in Turbistan efficiency. With Ti17, in the low K range the small cycles are more efficient than for IMI 685. Due to the coarser microstructure of IMI 685, higher crack opening levels and hence lower effective stress ranges are expected which means that under spectrum loading, Ti17 would exhibit a lower crack growth resistance to small cycles than IMI 685.

For Ti-6Al-4V it is difficult to carry out such an analysis because the results are not as consistent as those of the β-processed alloys (maybe due to the more complex microstructure).

5 Conclusion

The different crack growth prediction models which have been used here generally give satisfactory results That is specially true for Type 1 to 3 sequences (superposition of small amplitude cycle on low cycle fatigue cycles) and the Turbistan sequences (representative of actual disc solicitations). The predictions are not as accurate for Type 4 sequence (representative of an overload effect). This tends to show that, for Turbistan like sequences, the important point to take into account is the stress ratio effect, which is done by all models. The integration of other effects, like overload or underload effects, is not necessary for such sequences. The "equivalence" of the different models which has been demonstrated here can not be "a priori" extended for any other load sequence.

It should be noted, too, that three of the participants (CEAT, NASA, RR) used individual base-line data sets for the two different specimen geometries (CT and CC). This means that uncertainties and inaccuracies which might arise due to possible errors of the K solutions and related factors such as the constraint present in more complex real components have been totally excluded from the present exercise.

6.References

(1) Schijve, J.:
Fatigue crack growth predictions for variable amplitude and spectrum loading.
Proc. Int. Conf. Fatigue 87, Charlottesville, USA, 1987.
EMAS, Warley U.K., Vol. III, pp. 1685-1721

(2) Buch, A.:
Verification of Fatigue Crack Initiation Life Prediction Results.
Tech. Israel inst. of Techn. , Haifa, RAE N). 400, 1980

(3) Gasner, E.:
U0- Verfahren zur treffsicheren Vorhersage von Betriebfestigkeits-Kennwerten nach Wöhler-Versuchen.
Materialprüfung 22 (1980), Nr. 4, pp. 155-159

LIST OF TABLES AND FIGURES

	Page
Tables	
Prediction cases	
Ti-6Al-4V (Table 1)	6-8
IMI 685 (Table 2)	6-8
Ti17 (Table 3)	6-9
Prediction overall results	
Ti-6Al-4V (Table 4)	6-10
IMI 685 (Table 5)	6-11
Ti17 (Table 6)	6-12
da/dN vs ΔK slopes	
Ti-6Al-4V (Table 7)	6-13
IMI 685 (Table 8)	6-13
Ti17 (Table 9)	6-14
Turbistan flight efficiency (Table 10)	6-14
Figures	
Nprediction/Ntest charts	
Ti-6Al-4V (Fig. 1)	6-15
IMI 685 (Fig. 2)	6-15
Ti17 (Fig. 3)	6-16
a vs N plots (tests, predictions)	
Ti-6Al-4V - CT specimens - cases 01, 03, . . . 19 (Fig. 4 to 13)	6-17 to 6-21
Ti-6Al-4V - CC specimens - cases 02, 04, . . . 20 (Fig. 14 to 23)	6-22 to 6-26
IMI 685 - CT specimens - cases 21, 23, . . . 39 (Fig. 24 to 33)	6-27 to 6-31
IMI 685 - CC specimens - cases 22, 24, . . . 40 (Fig. 34 to 43)	6-32 to 6-36
Ti17 - CT specimens - cases 41, 43, . . . 59 (Fig. 44 to 53)	6-37 to 6-41
Ti17 - CC specimens - cases 42, 44, . . . 60 (Fig. 54 to 63)	6-42 to 6-46
da/dN vs ΔK plots (tests, predictions)	
Ti-6Al-4V - CT spec. - tests, FFA, NLR, NASA, CEAT (Fig. 64 to 73)	6-47 to 6-51
Ti-6Al-4V - CC spec. - tests, FFA, NLR, NASA, CEAT, RR (Fig. 74 to 85)	6-52 to 6-57
IMI 685 - CT spec. - tests, FFA, NLR, NASA, CEAT (Fig. 86 to 95)	6-58 to 6-62
IMI 685 - CC spec. - tests, FFA, NLR, NASA, CEAT (Fig. 96 to 105)	6-63 to 6-67
Ti17 - CT spec. - tests, FFA, NLR, NASA, CEAT (Fig. 106 to 115)	6-68 to 6-72
Ti17 - CC spec. - tests, FFA, NLR, NASA, CEAT (Fig. 116 to 125)	6-73 to 6-77
Small amplitude cycle sensitivity charts	
Ti-6Al-4V (Fig. 126 to 129)	6-78 to 6-79
IMI 685 (Fig. 130 to 133)	6-80 to 6-81
Ti17 (Fig. 134 to 137)	6-82 to 6-83

Table 1 - Ti-6Al-4V prediction cases

Ti-6Al-4V

CT specimens

	case n°	a initial (mm)	a final (mm)	ΔP (kN)	specimen reference
R=0.1	1	9.5	16.9	2.25	CE CT 11
R=0.7	3	8.1	13.7	2.25	CE CT 12
Type1	5	8	17	5.34	AF CT 07
Type2	7	9	17	5.34	AF CT 09
Type3	9	10	17	5.34	none
Turbistan00	19	7.5	17.3	3.6	CE CT 19
Turbistan10	13	7.5	15.5	3.6	CE CT 18
Turbistan30	15	7.5	14.7	3.6	none
Turbistan50	17	7.5	17.5	3.6	none
Type4	11	11	17	2.25	CE CT 17

CC specimens

R=0.1	2	0.6	5	27	CE CC 10
R=0.7	4	0.6	4.5	24	CE CC 07
Type1	6	0.6	4.8	30	CE CC 08
Type2	8	0.6	3.8	30	CE CC 09
Type3	10	0.5	5	30	CE CC 15
Turbistan00	20	0.4	3.55	45	PI CC 13
Turbistan10	14	0.4	4	45	PI CC 07
Turbistan30	16	0.4	4	45	PI CC 09
Turbistan50	18	0.4	4.2	45	PI CC 11
Type4	12	0.6	5	27	CE CC 16

Table 2 - IMI 685 prediction cases

IMI 685

CT specimens

	case n°	a initial (mm)	a final (mm)	ΔP (kN)	specimen reference
R=0.1	21	7.5	16.9	6.3	NL CT 12
R=0.7	23	7.5	15.2	3	NL CT 11
Type1	25	8.7	16.1	5.34	RR CT 22
Type2	27	8.5	15.6	5.34	RR CT 23
Type3	29	8.5	16.9	5.34	none
Turbistan00	39	7.5	16.9	7	NL CT 23
Turbistan10	33	7.5	16.9	7	NL CT 19
Turbistan30	35	7.5	16.9	7	NL CT 20
Turbistan50	37	7.5	16	7	NL CT 21
Type4	31	8.5	15	6	RA CT 11

CC specimens

R=0.1	22	0.9	5	30.6	IA CC 07
R=0.7	24	0.5	5	18	IA CC 10
Type1	26	1	5	37.5	RR CC 11
Type2	28	1	4.52	37.5	RR CC 13
Type3	30	1	4.3	37.5	RR CC 14
Turbistan00	40	0.5	5	50	NL CC 18
Turbistan10	34	0.5	4.42	50	NL CC 14
Turbistan30	36	0.5	4.62	50	NL CC 15
Turbistan50	38	0.5	5	50	NL CC 16
Type4	32	0.5	5	33	RA CC 20

Table 3 - Ti 17prediction cases

Ti 17

CT specimens

	case n°	a initial (mm)	a final (mm)	B (mm)	W (mm)	ΔP (kN)	specimen reference
R=0.1	41	7.5	18.9	4.2	25.39	0.66	QE CT 09
R=0.7	43	7.5	16.9	2.41	25.37	0.3	QE CT 10
Type1	45	7.6	16.9	2.41	25.5	0.745	QE CT 12
Type2	47	7.7	16.9	3.1	25.5	0.845	QE CT 14
Type3	49	7.5	16.9	3.17	25.45	0.792	QE CT 15
Turbistan00	59	7.5	16.9	2.16	25.47	0.7	QE CT 18
Turbistan10	53	7.5	16.9	2.55	25.42	0.75	QE CT 23
Turbistan30	55	7.9	16.2	4.125	25.45	1.2	QE CT 20
Turbistan50	57	7.5	16.9	2.4	25.4	0.7	QE CT 21
Type4	51	7.5	16.9	2.55	25.33	0.72	QE CT 17

CC specimens

R=0.1	42	0.5	5			37.5	UT CC 07
R=0.7	44	0.6	5			17.5	UT CC 09
Type1	45	0.6	5			34.7	UT CC 12
Type2	48	0.6	5			31	UT CC 14
Type3	50	0.6	5			29.7	UT CC 16
Turbistan00	60	0.6	5			31.5	UT CC 26
Turbistan10	54	0.6	5			31.5	UT CC 20
Turbistan30	56	0.6	5			31.5	UT CC 22
Turbistan50	58	0.6	5			31.5	UT CC 24
Type4	52	0.5	5			29.3	UT CC 17

Table 4 - Ti-6Al-4V prediction overall results

Ti-6Al-4V: Prediction of the TURBISTAN sequences for CT specimen

Sequence	Npred	Npred/Ntest	Sequence	Npred	Npred/Ntest	Sequence	Npred	Npred/Ntest	Sequence	Npred	Npred/Ntest	Sequence	Npred	Npred/Ntest	Sequence	N
		FFA			NLR			RR			NASA			CEAT		TEST
C.A (R=0.1)	889010	1,112	C.A (R=0.1)	1010000	1,264	C.A (R=0.1)			C.A (R=0.1)	1029354	1,288	C.A (R=0.1)	696804	0,872	C.A (R=0.1)	799151
TURB10	133800	0,778	TURB10	132000	0,767	TURB10			TURB10	113358	0,659	TURB10	97259	0,565	TURB10	172000
TURB30	125100		TURB30	140000		TURB30			TURB30	111364		TURB30	101679		TURB30	
TURB50	133900		TURB50	168000		TURB50			TURB50	123831		TURB50	119585		TURB50	
TURB00	152750	1,015	TURB00	128000	0,850	TURB00			TURB00	121146	0,805	TURB00	98025	0,651	TURB00	150500

Ti-6Al-4V: Prediction of the simple sequences for CT specimen

Sequence	Npred	Npred/Ntest	Sequence	Npred	Npred/Ntest	Sequence	Npred.	Npred/Ntest	Sequence		Npred/Ntest	Sequence	Npred	Npred/Ntest	Sequence	N
		FFA			NLR			RR			NASA			CEAT		TEST
C.A (R=0.7)	525000	1,678	C.A (R=0.7)	440000	1,407	C.A (R=0.7)			C.A (R=0.7)	408352	1,305	C.A (R=0.7)	264704	0,846	C.A (R=0.7)	312799
TYPE 1	34212	0,699	TYPE 1	69000	1,410	TYPE 1			TYPE 1	66432	1,357	TYPE 1	44827	0,916	TYPE 1	48950
TYPE 2	18982	0,655	TYPE 2	33000	1,138	TYPE 2			TYPE 2	35846	1,236	TYPE 2	20980	0,723	TYPE 2	29000
TYPE 3	6794		TYPE 3	8800		TYPE 3			TYPE 3	5677		TYPE 3	5746		TYPE 3	NV1
TYPE 4	395	0,097	TYPE 4	750	0,185	TYPE 4			TYPE 4	3541	0,873	TYPE 4	8517	2,099	TYPE 4	4057

Ti-6Al-4V: Prediction of the TURBISTAN sequences for CC specimen

Sequence	Npred	Npred/Ntest	Sequence	Npred	Npred/Ntest	Sequence	Npred	Npred/Ntest	Sequence	Npred	Npred/Ntest	Sequence	Npred	Npred/Ntest	Sequence	N
		FFA			NLR			RR			NASA			CEAT		TEST
C.A (R=0.1)	87577	0,568	C.A (R=0.1)	NV2	0,675	C.A (R=0.1)	140180	0,909	C.A (R=0.1)	118596	0,770	C.A (R=0.1)	113043	0,734	C.A (R=0.1)	154070
TURB10	7400	1,622	TURB10	7100	1,556	TURB10	10900	2,380	TURB10	6948	1,523	TURB10	9518	2,086	TURB10	4563
TURB30	6850	0,715	TURB30	NV2	0,804	TURB30	11700	1,220	TURB30	6978	0,728	TURB30	10244	1,069	TURB30	9582
TURB50	7200	0,480	TURB50	NV2	0,610	TURB50	13550	0,906	TURB50	7989	0,533	TURB50	12139	0,809	TURB50	15000
TURB00	8100	2,455	TURB00	7200	2,182	TURB00	10750	3,200	TURB00	7165	2,171	TURB00	9378	2,842	TURB00	3300

Ti-6Al-4V: Prediction of the simple sequences for CC specimen

Sequence	Npred	Npred/Ntest	Sequence	Npred	Npred/Ntest	Sequence	Npred	Npred/Ntest	Sequence	Npred	Npred/Ntest	Sequence	Npred	Npred/Ntest	Sequence	N
		FFA			NLR			RR			NASA			CEAT		TEST
C.A (R=0.7)	48500	0,858	C.A (R=0.7)	NV2	0,746	C.A (R=0.7)	53356	0,944	C.A (R=0.7)	49213	0,871	C.A (R=0.7)	63335	1,121	C.A (R=0.7)	56500
TYPE 1	53250	0,427	TYPE 1	88000	0,706	TYPE 1	99536	0,798	TYPE 1	130746	1,049	TYPE 1	89479	0,718	TYPE 1	124677
TYPE 2	48200	0,599	TYPE 2	68000	0,845	TYPE 2	80119	0,996	TYPE 2	103467	1,286	TYPE 2	67818	0,843	TYPE 2	80450
TYPE 3	28616	1,373	TYPE 3	29000	1,391	TYPE 3	44584	2,139	TYPE 3	27339	1,312	TYPE 3	31922	1,532	TYPE 3	20842
TYPE 4	86	0,100	TYPE 4	NV2	0,820	TYPE 4	1507	1,754	TYPE 4	751	0,874	TYPE 4	728	0,847	TYPE 4	859

Table 5 - IMI 685 prediction overall results

IMI 685: Prediction of the TURBISTAN sequences for CT specimen

Sequence	Npred.	Npred/Ntest	Sequence	Npred	Npred/Ntest	Sequence	Npred.	Npred/Ntest	Sequence	Npred.	Npred/Ntest	Sequence	Npred.	Npred/Ntest	Sequence	N
		FFA			NLR			RR			NASA			CEAT		TEST
C.A (R=0.1)	134250	1,462	C.A (R=0.1)	NV2	0,980	C.A (R=0 1)			C.A (R=0.1)	136013	1,482	C.A (R=0.1)	123181	1,342	C.A (R=0.1)	91800
TURB10	23000	0,951	TURB10	20000	0,827	TURB10			TURB10	24784	1,025	TURB10	36783	1,521	TURB10	24177
TURB30	22800	0,780	TURB30	22500	0,770	TURB30			TURB30	26956	0,922	TURB30	37925	1,297	TURB30	29237
TURB50	25800	0,928	TURB50	28000	1,007	TURB50			TURB50	32550	1,171	TURB50	41550	1,495	TURB50	27800
TURB00	24500	1,043	TURB00	20000	0 851	TURB00			TURB00	26623	1,133	TURB00	36754	1 564	TURB00	23500

IMI 685: Prediction of the simple sequences for CT specimen

Sequence	Npred	Npred/Ntest	Sequence	Npred	Npred/Ntest	Sequence	Npred	Npred/Ntest	Sequence	Npred	Npred/Ntest	Sequence	Npred	Npred/Ntest	Sequence	N
		FFA			NLR			RR			NASA			CEAT		TEST
C A (R=0 7)	450970	0,603	C.A (R=0.7)	520000	0,696	C.A (R=0 7)			C A (R=0.7)	555000	0,743	C.A (R=0.7)	1842500	2,465	C.A (R=0 7)	747400
TYPE 1	74149	0,655	TYPE 1	99000	0,875	TYPE 1			TYPE 1	197984	1,749	TYPE 1	108699	0,960	TYPE 1	113170
TYPE 2	62633	0,542	TYPE 2	68000	0,588	TYPE 2			TYPE 2	106700	0,923	TYPE 2	108700	0,940	TYPE 2	115577
TYPE 3	31700		TYPE 3	29000		TYPE 3			TYPE 3	34350		TYPE 3	71200		TYPE 3	NV1
TYPE 4	NV2	0 130	TYPE 4	580	1 170	TYPE 4			TYPE 4	443	0 940	TYPE 4	193	0 430	TYPE 4	NV2

IMI 685: Prediction of the TURBISTAN sequences for CC specimen

Sequence	Npred	Npred/Ntest	Sequence	Npred	Npred/Ntest	Sequence	Npred	Npred/Ntest	Sequence	Npred	Npred/Ntest	Sequence	Npred	Npred/Ntest	Sequence	N
		FFA			NLR			RR			NASA			CEAT		TEST
C.A (R=0 1)	104810	1,557	C.A (R=0.1)	84000	1,248	C.A (R=0 1)			C.A (R=0.1)	86296	1,282	C.A (R=0.1)	96445	1,433	C.A (R=0 1)	67300
TURB10	9100	0,956	TURB10	6900	0,725	TURB10			TURB10	5535	0,581	TURB10	9013	0,947	TURB10	9522
TURB30	9000	1,121	TURB30	7800	0,971	TURB30			TURB30	5845	0,728	TURB30	9738	1,213	TURB30	8029
TURB50	10200	1,259	TURB50	9800	1,209	TURB50			TURB50	7030	0,867	TURB50	11599	1,431	TURB50	8104
TURB00	9700	0 941	TURB00	7000	0 679	TURB00	NV2	0 690	TURB00	5947	0 577	TURB00	9071	0 880	TURB00	10310

IMI 685: Prediction of the simple sequences for CC specimen

Sequence	Npred	Npred/Ntest	Sequence	Npred	Npred/Ntest	Sequence	Npred	Npred/Ntest	Sequence	Npred	Npred/Ntest	Sequence	Npred	Npred/Ntest	Sequence	N
		FFA			NLR			RR			NASA			CEAT		TEST
C.A (R=0.7)	474830	1,320	C.A (R=0.7)	NV2	0,990	C.A (R=0.7)			C.A (R=0.7)	304987	0,822	C.A (R=0.7)	467211	1,270	C.A (R=0.7)	NV2
TYPE 1	39517	0,918	TYPE 1	46000	1,069	TYPE 1			TYPE 1	54200	1,259	TYPE 1	48306	1,122	TYPE 1	43046
TYPE 2	30500	2,368	TYPE 2	29500	2,291	TYPE 2			TYPE 2	32872	2,552	TYPE 2	34446	2,675	TYPE 2	12879
TYPE 3	15568	1,116	TYPE 3	12500	0,896	TYPE 3			TYPE 3	9961	0,714	TYPE 3	16139	1,157	TYPE 3	13949
TYPE 4	166	0,280	TYPE 4	NV2	1 820	TYPE 4			TYPE 4	479	0,787	TYPE 4	1214	2 020	TYPE 4	NV2

Table 6 - Ti 17 prediction overall results

Ti 17: Prediction of the TURBISTAN sequences for CT specimen

Sequence	Npred.	Npred /Ntest	Sequence	Npred	Npred /Ntest	Sequence	Npred	Npred /Ntest	Sequence	Npred	Npred /Ntest	Sequence	Npred	Npred /Ntest	Sequence	N
		FFA			NLR			RR			NASA			CEAT		TEST
C.A (R=0.1)	416870	1,418	C.A (R=0.1)	440000	1,497	C.A (R=0 1)			C.A (R=0.1)	354669	1,206	C.A (R=0.1)	264704	0,900	C.A (R=0.1)	294000
TURB10	42500	1,232	TURB10	29500	0,855	TURB10			TURB10	27630	0,801	TURB10	24500	0,710	TURB10	34500
TURB30	37500	1,330	TURB30	30000	1,064	TURB30			TURB30	27743	0,984	TURB30	26612	0,944	TURB30	28200
TURB50	49800	1,073	TURB50	44000	0,948	TURB50			TURB50	40089	0,864	TURB50	39279	0,847	TURB50	46400
TURB00	32800	1,355	TURB00	21500	0,888	TURB00			TURB00	21525	0,889	TURB00	18655	0,771	TURB00	24200

Ti17: Prediction of the simple sequences for CT specimen

Sequence	Npred	Npred /Ntest	Sequence	Npred	Npred /Ntest	Sequence	Npred	Npred /Ntest	Sequence	Npred	Npred /Ntest	Sequence	Npred	Npred /Ntest	Sequence	N
		FFA			NLR			RR			NASA			CEAT		TEST
C.A (R=0 7)	786310	1,156	C.A (R=0 7)	720000	1,059	C.A (R=0 7)			C.A (R=0 7)	617971	0,909	C.A (R=0.7)	418528	0,615	C.A (R=0 7)	680000
TYPE 1	103000	1,242	TYPE 1	112000	1,351	TYPE 1			TYPE 1	137273	1,656	TYPE 1	94192	1,136	TYPE 1	82900
TYPE 2	121932	1,035	TYPE 2	96000	0,815	TYPE 2			TYPE 2	104768	0,889	TYPE 2	66635	0,566	TYPE 2	117800
TYPE 3	82896	1,148	TYPE 3	60000	0,831	TYPE 3			TYPE 3	49051	0,679	TYPE 3	42685	0,591	TYPE 3	72213
TYPE 4	138	0,297	TYPE 4	520	1 118	TYPE 4			TYPE 4	464	0 998	TYPE 4	680	1 462	TYPE 4	465

Ti 17: Prediction of the TURBISTAN sequences for CC specimen

Sequence	Npred	Npred /Ntest	Sequence	Npred	Npred /Ntest	Sequence	Npred	Npred /Ntest	Sequence	Npred	Npred /Ntest	Sequence	Npred	Npred /Ntest	Sequence	N
		FFA			NLR			RR			NASA			CEAT		TEST
C.A (R=0 1)	23495	0,783	C.A (R=0 1)	18500	0,615	C.A (R=0.1)			C.A (R=0.1)	23489	0,791	C.A (R=0.1)	30032	1,010	C.A (R=0.1)	NV2
TURB10	11500	0,838	TURB10	7400	0,539	TURB10			TURB10	9270	0,675	TURB10	16840	1,227	TURB10	13730
TURB30	11500	0,839	TURB30	8600	0,627	TURB30			TURB30	9960	0,726	TURB30	18210	1,328	TURB30	13710
TURB50	13500	0,993	TURB50	11000	0,809	TURB50			TURB50	12195	0,897	TURB50	21501	1,581	TURB50	13600
TURB00	12700	1 503	TURB00	7400	0 876	TURB00	12200	1 444	TURB00	9711	1,149	TURB00	16771	1 985	TURB00	8450

Ti17: Prediction of the simple sequences for CC specimen

Sequence	Npred	Npred /Ntest	Sequence	Npred	Npred /Ntest	Sequence	Npred	Npred /Ntest	Sequence	Npred	Npred /Ntest	Sequence	Npred	Npred /Ntest	Sequence	N
		FFA			NLR			RR			NASA			CEAT		TEST
C.A (R=0.7)	81504	1,030	C.A (R=0.7)	NV2		C.A (R=0 7)			C.A (R=0.7)	94726	1,197	C.A (R=0.7)	178305	2,253	C.A (R=0.7)	79140
TYPE 1	25694	1,127	TYPE 1	25000	1,097	TYPE 1			TYPE 1	37846	1,661	TYPE 1	37569	1,649	TYPE 1	22789
TYPE 2	27492	1,470	TYPE 2	22000	1,177	TYPE 2			TYPE 2	33459	1,790	TYPE 2	42376	2,267	TYPE 2	18696
TYPE 3	14559	0,179	TYPE 3	10800	0,578	TYPE 3			TYPE 3	12483	0,668	TYPE 3	24974	1,336	TYPE 3	18689
TYPE 4	56	0,207	TYPE 4	NV2	0,650	TYPE 4			TYPE 4	233	0,863	TYPE 4	282	1,044	TYPE 4	270

Table 7 - Ti-6Al-4V da/dN vs ΔK slopes

da/dN vs ΔK slopes

Nota
for predictions which do not exhibit a linear behaviour, the initial and final slopes are given
test slopes are given only if the results are fairly linear
non existing test results or predictions are indicated by X

Ti-6Al-4V

		R=0.1	R=0.7	Type1	Type2	Type3	Turb00	Turb10	Turb30	Turb50
CT	FFA	4.6	4.6	4.6	4.6	4.6	4.6	4.6	4.6	4.6
	NLR	4.0	4.2	4.4	4.4	4.4	4.4	4.4	4.4	4.4
	NASA	4.6	4.4	4.2	4.2	4.0	4.6	4.6	4.6	4.6
	CEAT	4.4	4.4	4.4	4.4	4.4	4.4	4.4	4.4	4.4
	TEST	*4.6-3.4*	*5.2-3.4*	*10-3.4*	*3.4*	*3.4*	*4.2*	*4.6*	*X*	*X*
CC	FFA	5.0	4.6-3.0	4.6	4.6	4.6	4.6	4.6	4.6	4.6
	NLR	4.6	4.6-2.4	4.6	4.6	4.6	4.4	4.4	4.4	4.4
	NASA	4.2	4.2	4.2	4.2	4.2	4.2	4.2	4.2	4.2
	RR	4.4	4.4	4.4	4.4	4.4	4.4	4.4	4.4	4.4
	CEAT	3.8	3.8	3.8	3.8	3.8	3.8	3.8	3.8	3.8
	TEST	*4.2*	*4.0*	*4.8*	*4.0*	*3.8*	*3.8*	*4.0*	*4.2*	*4.0*

Table 8 - IMI 685 da/dN vs ΔK slopes

da/dN vs ΔK slopes

Nota
for predictions which do not exhibit a linear behaviour, the initial and final slopes are given
test slopes are given only if the results are fairly linear
non existing test results or predictions are indicated by X

IMI 685

		R=0.1	R=0.7	Type1	Type2	Type3	Turb00	Turb10	Turb30	Turb50
CT	FFA	4.8	4.0-5.0	4.2	4.2	4.2	5.0	5.0	5.0	5.0
	NLR	3.2	3.4	3.2	3.2	3.2	3.4	3.4	3.4	3.4
	NASA	4.8	2.8-4.6	3.0-4.6	3.0-4.0	3.0-4.6	4.4	4.4	4.4	4.4
	CEAT	4.4	4.4	4.4	4.4	4.4	4.4	4.4	4.4	4.4
	TEST	*5.2-3.2*	*2.0-5.0*	*4.4*	*4.4*	*4.4*	*4.2*	*4.2*	*4.2*	*4.2*
CC	FFA	4.0	4.2	4.2	4.2	4.2	4.2	4.2	4.2	4.2
	NLR	3.4	3.4	3.4	3.4	3.4	3.4	3.4	3.4	3.4
	NASA	3.8	3.8	3.8	3.8	3.8	3.8	3.8	3.8	3.8
	CEAT	3.8	3.8	3.8	3.8	3.8	3.8	3.8	3.8	3.8
	TEST	*3.5*	*3.8*	*3.8*	*3.5*	*3.5*	*3.8*	*3.8*	*3.8*	*3.5*

Table 9 - Ti 17 da/dN vs ΔK slopes

da/dN vs ΔK slopes

Nota
for predictions which do not exhibit a linear behaviour, the initial and final slopes are given
test slopes are given only if the results are fairly linear
non existing test results or predictions are indicated by X

			R=0.1	R=0.7	Type1	Type2	Type3	Turb00	Turb10	Turb30	Turb50
Ti17		FFA	4.4-3.0	3.4	3.0	3.2	3.4	3.4	3.4	3.4	3.2
		NLR	3.2	3.2	3.2	3.2	3.2	3.2	3.2	3.2	3.2
	CT	NASA	3.0	2.8	2.8	2.8	2.8	3.0	3.0	3.0	3.0
		CEAT	2.8	2.8	2.8	2.8	2.8	2.8	2.8	2.8	2.8
		TEST	*2.8*	*2.5*	*2.5*	*2.8*	*2.5*	*2.8*	*2.5*	*2.8*	*2.6*
		FFA	3.0	3.2	3.0	3.2	3.2	3.2	3.2	3.2	3.2
		NLR	3.2	3.2	3.2	3.2	3.2	3.2	3.2	3.2	3.2
	CC	NASA	3.2	3.2	3.2	3.2	3.2	3.2	3.2	3.2	3.2
		CEAT	3.6	3.6	3.6	3.6	3.6	3.6	3.6	3.6	3.6
		TEST	*4.4-2.4*	*3.8*	*2.8*	*2.5*	*2.6*	*3.0*	*3.0*	*3.0*	*3.0*

Table 10: Accuracy and reliability of predictions of fatigue crack growth (combining CT and CC geometries and three materials Ti-6Al-4V, IMI 685 and Ti17)

		No. of predictions	FFA		NLR		NASA		CEAT	
			$\bar{x}$	s	$\bar{x}$	s	$\bar{x}$	s	$\bar{x}$	s
1	Type 1-3 (all results)	16	0.92	0.20	1.0	0.16	1.21	0.17	1.08	0.20
	Turbistan (all results)	22	1.04	0.15	0.88	0.13	0.88	0.14	1.16	0.18
2	Const. Ampl. (R = 0.1, R = 0.7)	12	1.07	0.16	0.97	0.14	1.03	0.11	1.14	0.19
	Type 1 - 3 1)	15	0.86	0.17	0.95	0.13	1.15	0.15	1.02	0.175
	Turbistan 2)	21	1.0	0.12	0.84	0.105	0.84	0.12	1.12	0.16
	Type 4	6	0.17	0.23	0.79	0.36	0.89	0.04	1.15	0.28
3	Type 1 - 3 + Turbistan 1) 2)	36	0.94	0.14	0.89	0.115	0.96	0.15	1.08	0.165
4	Type 1 - 4 + Turbistan 1) 2)	42	0.74	0.29	0.87	0.15	0.95	0.14	1.09	0.18

1) IMI 685 CC Type 2 excluded
2) Ti-6Al-4V CC Turbistan 00 excluded

$\bar{x}$ = ratio of N_{pred}/N_{test}, s = standard deviation (log. norm. distr.)

Ti-6Al-4V

CT specimens — N prediction / N test

	inf	0.5	0.6	0.7	0.8	0.9	1	1.2	1.4	1.6	1.8	2	sup
R=0.1						CEAT		FFA NLR NASA					
R=0.7					CEAT				NASA NLR	FFA			
Type1				FFA		CEAT			NASA NLR				
Type2				FFA CEAT				NLR NASA					
Type3													
Turbostan00				CEAT	NASA	NLR	FFA						
Turbostan10			CEAT	NASA	NLR FFA								
Turbostan30													
Turbostan50													
Type4	FFA NLR					NASA							CEAT

CC specimens

	inf	0.5	0.6	0.7	0.8	0.9	1	1.2	1.4	1.6	1.8	2	sup
R=0.1			FFA	NLR CEAT	NASA	RR							
R=0.7				NLR		FFA NASA RR		CEAT					
Type1	FFA			NLR CEAT	RR		NASA						
Type2			FFA		CEAT NLR		RR	NASA					
Type3									NASA FFA NLR CEAT				RR
Turbostan00												NASA NLR	FFA CEAT RR
Turbostan10										NASA NLR FFA			CEAT RR
Turbostan30				FFA NASA	NLR		CEAT	RR					
Turbostan50	FFA	NASA	NLR		CEAT	RR							
Type4	FFA				NLR CEAT	NASA					RR		

Fig.1 - Ti-6Al-4V N prediction / N test chart

IMI 685

CT specimens — N prediction / N test

	inf	0.5	0.6	0.7	0.8	0.9	1	1.2	1.4	1.6	1.8	2	sup
R=0.1							NLR		CEAT FFA NASA				
R=0.7			FFA	NLR NASA									CEAT
Type1				FFA		NLR	CEAT				NASA		
Type2		FFA	NLR			NASA CEAT							
Type3													
Turbostan00						NLR	FFA	NASA		CEAT			
Turbostan10					NLR		FFA NASA			CEAT			
Turbostan30					NLR FFA	NASA		CEAT					
Turbostan50						FFA	NLR	NASA	CEAT				
Type4	FFA CEAT					NASA		NLR					

CC specimens

	inf	0.5	0.6	0.7	0.8	0.9	1	1.2	1.4	1.6	1.8	2	sup
R=0.1								NLR NASA	CEAT	FFA			
R=0.7					NASA		NLR	CEAT	FFA				
Type1						FFA	NLR	CEAT NASA					
Type2												NLR FFA	NASA CEAT
Type3				NASA		NLR		FFA CEAT					
Turbostan00			NASA	NLR		CEAT FFA							
Turbostan10			NASA	NLR		CEAT	FFA						
Turbostan30				NASA			NLR	FFA CEAT					
Turbostan50						NASA		NLR FFA	CEAT				
Type4	FFA				NASA						NLR	CEAT	

Fig.2 - IMI 685 prediction / N test chart -

Ti 17

CT specimens

N prediction / N test

	inf	0.5	0.6	0.7	0.8	0.9	1	1.2	1.4	1.6	1.8	2	sup
R=0.1						CEAT		NASA	FFA NLR				
R=0.7			CEAT			NASA	NLR	FFA					
Type1								CEAT FFA	NLR	NASA			
Type2			CEAT		NLR	NASA	FFA						
Type3			CEAT	NASA	NLR			FFA					
Turbostan00					CEAT	NLR NASA			FFA				
Turbostan10				CEAT	NASA	NLR		FFA					
Turbostan30						CEAT	NASA NLR		FFA				
Turbostan50					CEAT	NASA NLR	FFA						
Type4	FFA						NASA	NLR	CEAT				

CC specimens

	inf	0.5	0.6	0.7	0.8	0.9	1	1.2	1.4	1.6	1.8	2	sup
R=0.1			NLR		FFA NASA		CEAT						
R=0.7							FFA	NASA					CEAT
Type1							NLR	FFA		CEAT NASA			
Type2								NLR	FFA		NASA		CEAT
Type3			NLR	NASA	FFA				CEAT				
Turbostan00						NLR		NASA	RR	FFA		CEAT	
Turbostan10		NLR		NASA	FFA			CEAT					
Turbostan30			NLR	NASA	FFA				CEAT				
Turbostan50					NLR	NASA	FFA			CEAT			
Type4	FFA			NLR		NASA	CEAT						

Fig.3 - Ti17 prediction / N test chart

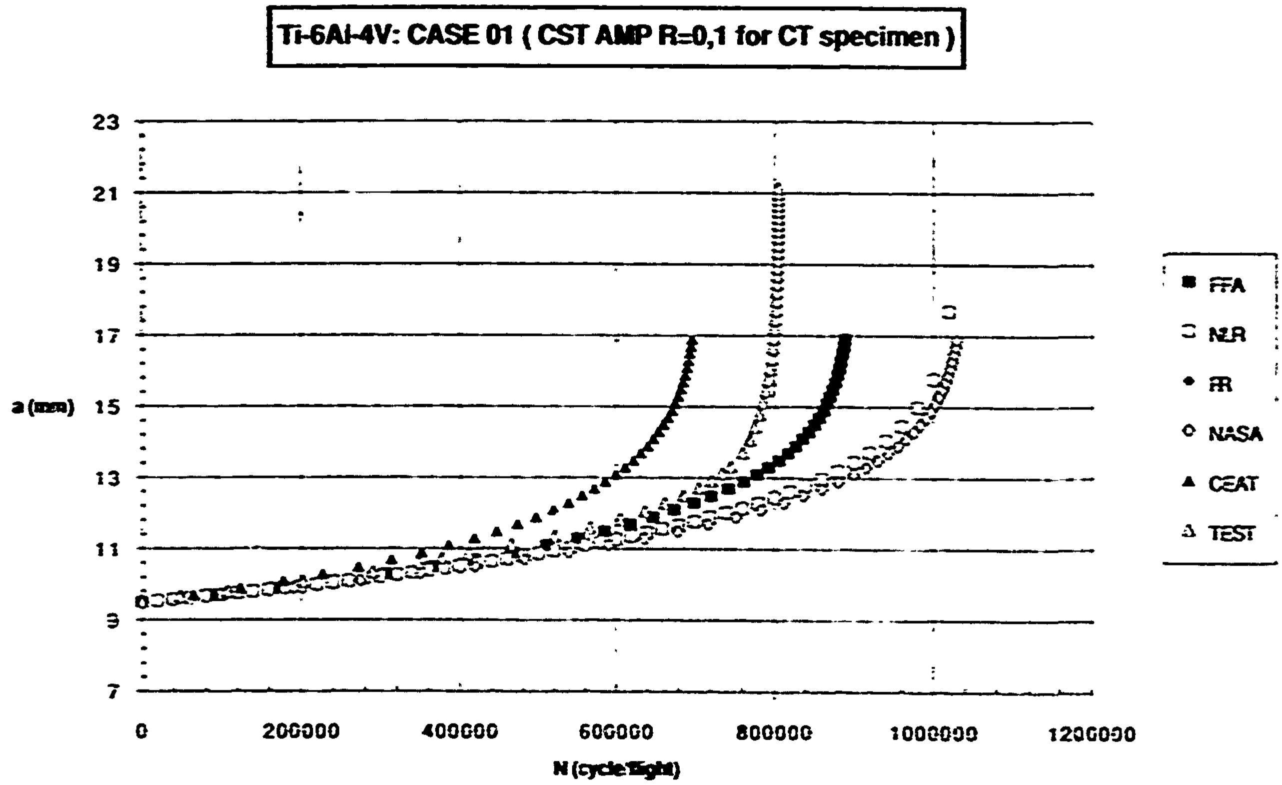

Fig.4 - Ti-6Al-4V Case 01

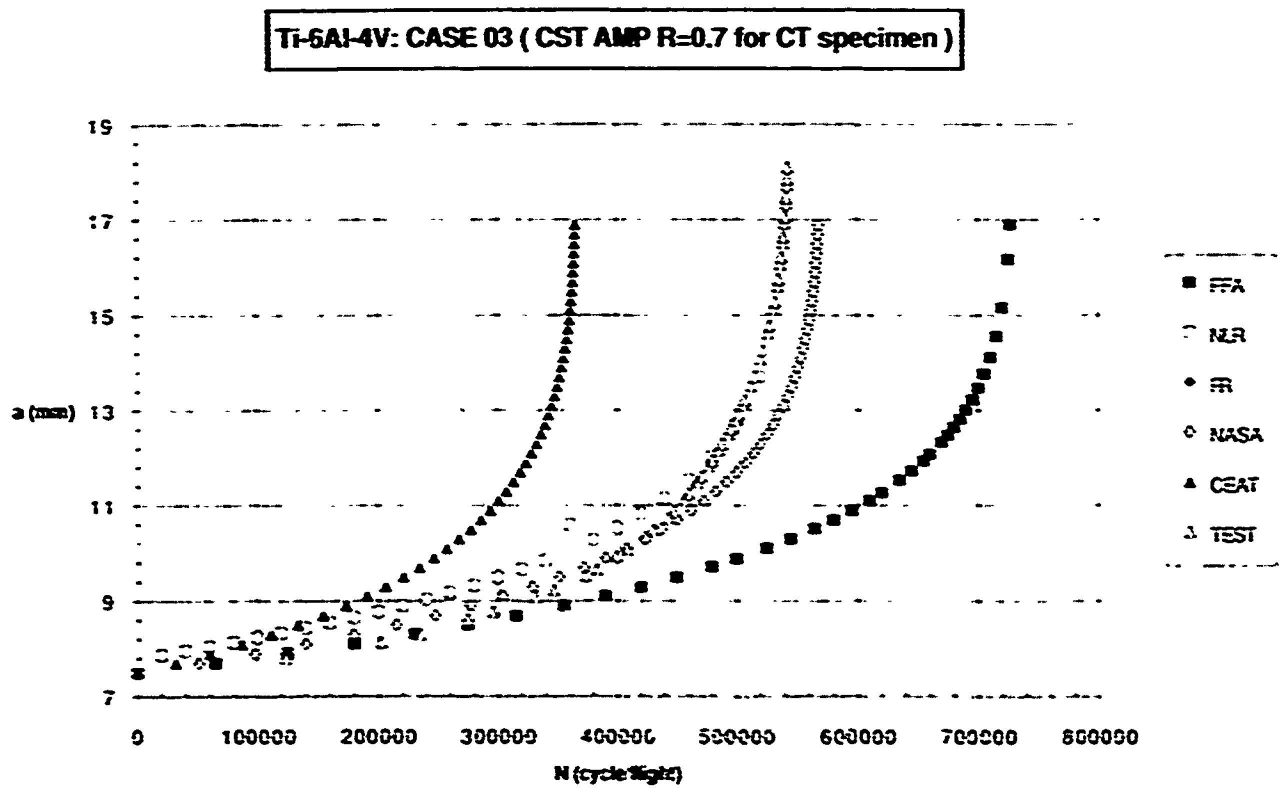

Fig.5 - Ti-6Al-4V Case 03

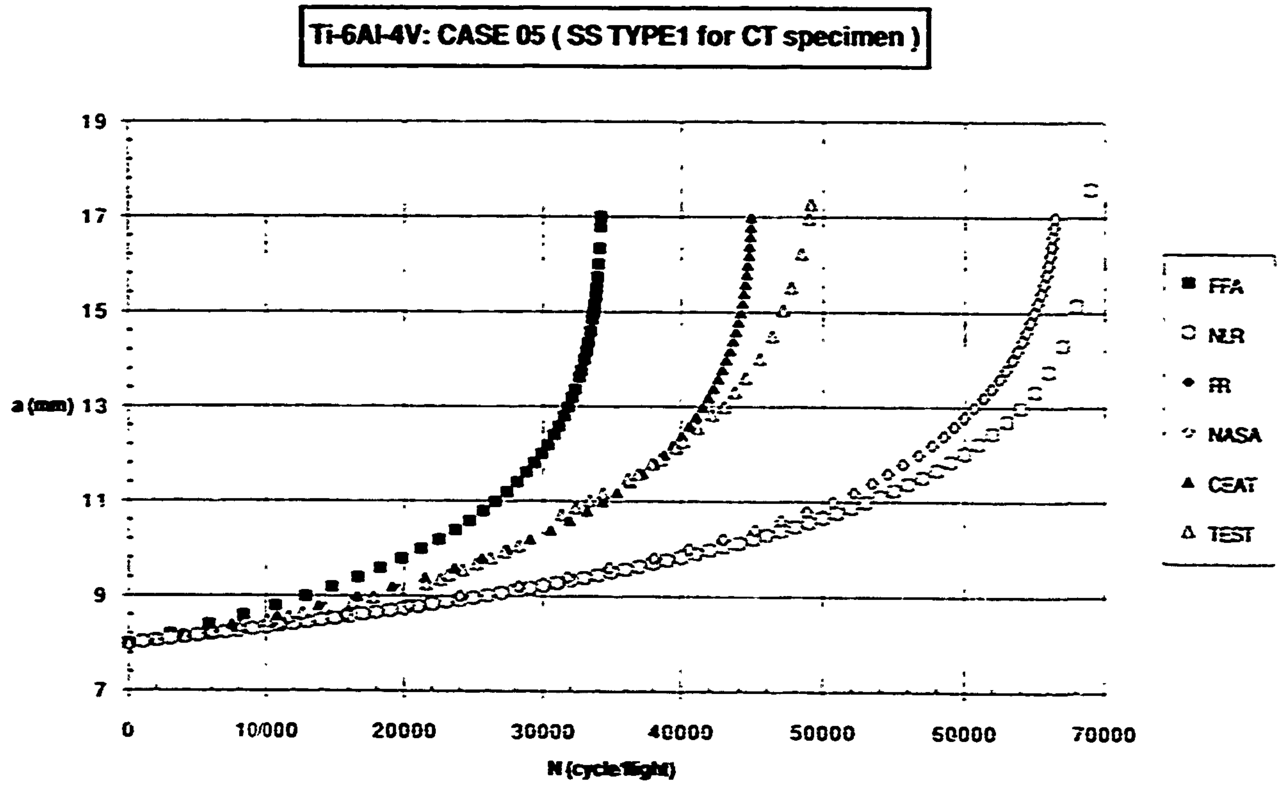

Fig.6 - Ti-6Al-4V Case 05

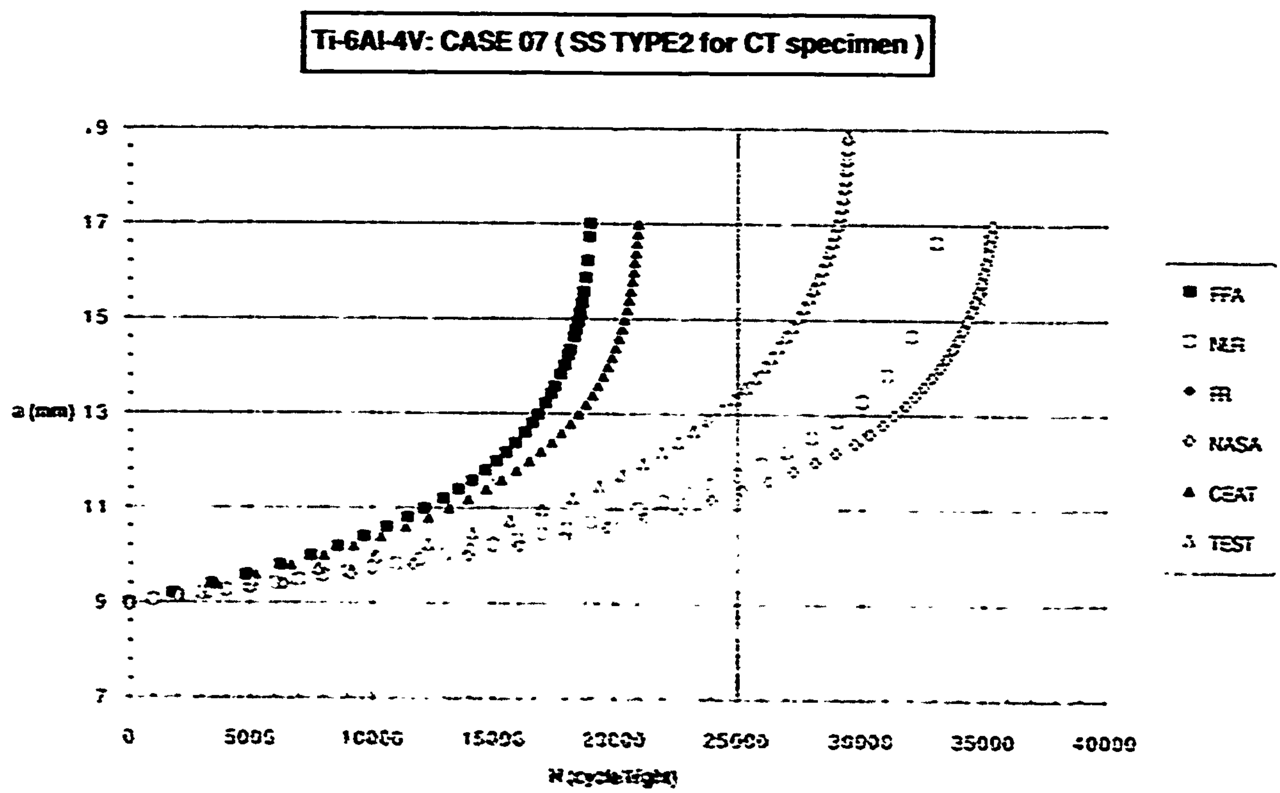

Fig 7 - Ti-6Al-4V Case 07

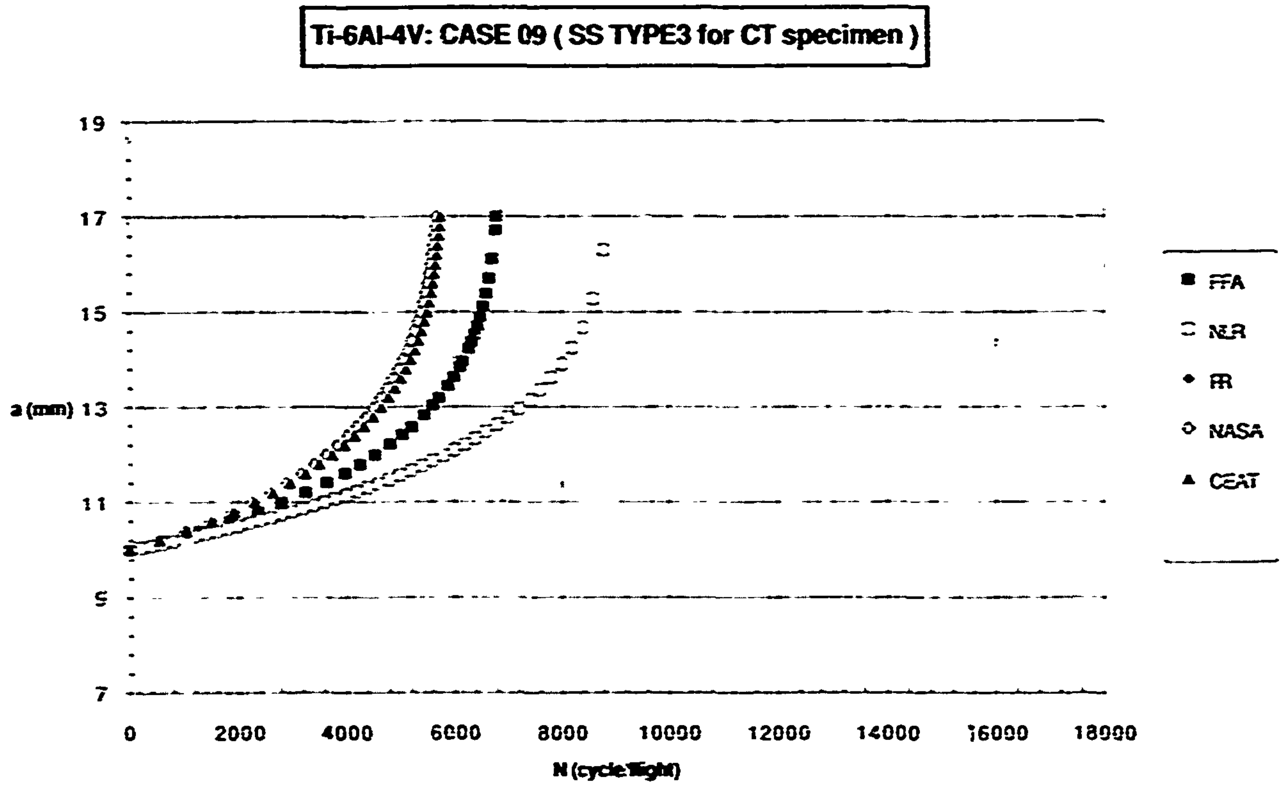

Fig.8 - Ti-6Al-4V Case 09

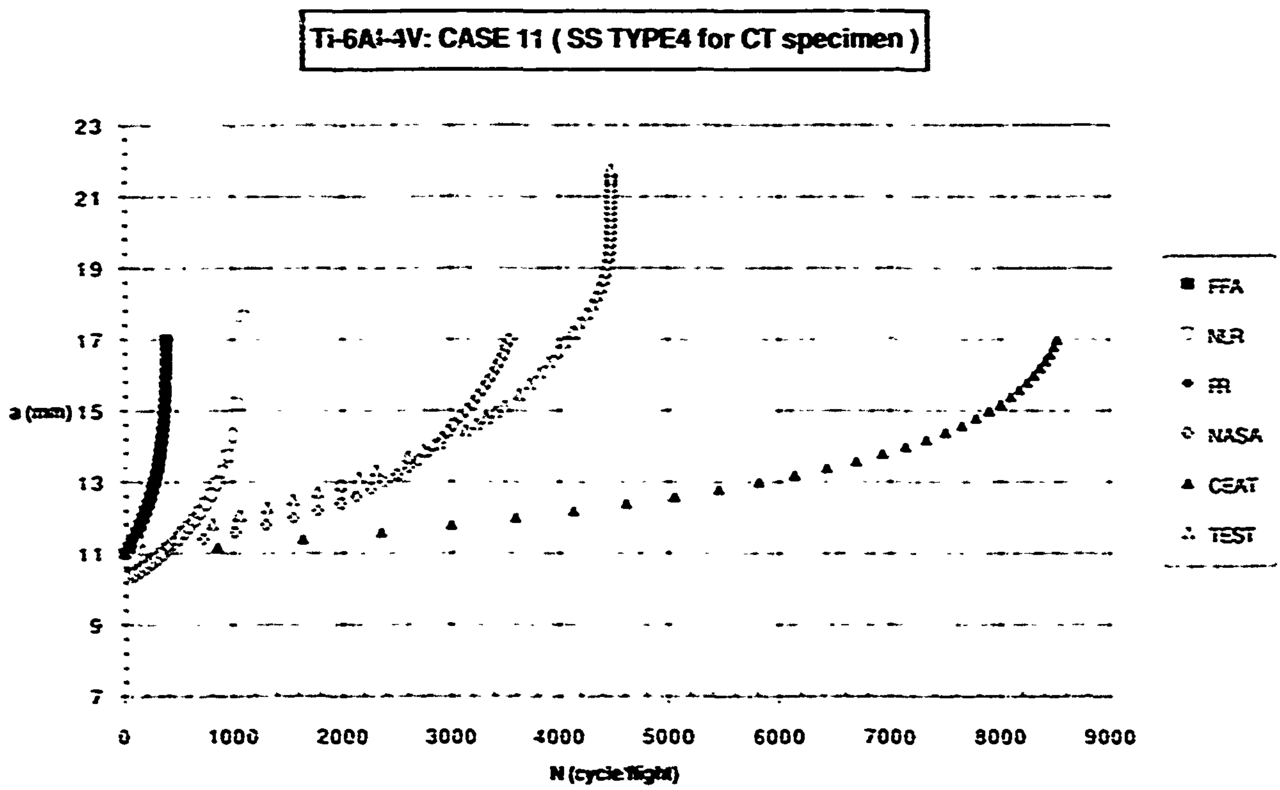

Fig.9 - Ti-6Al-4V Case 11

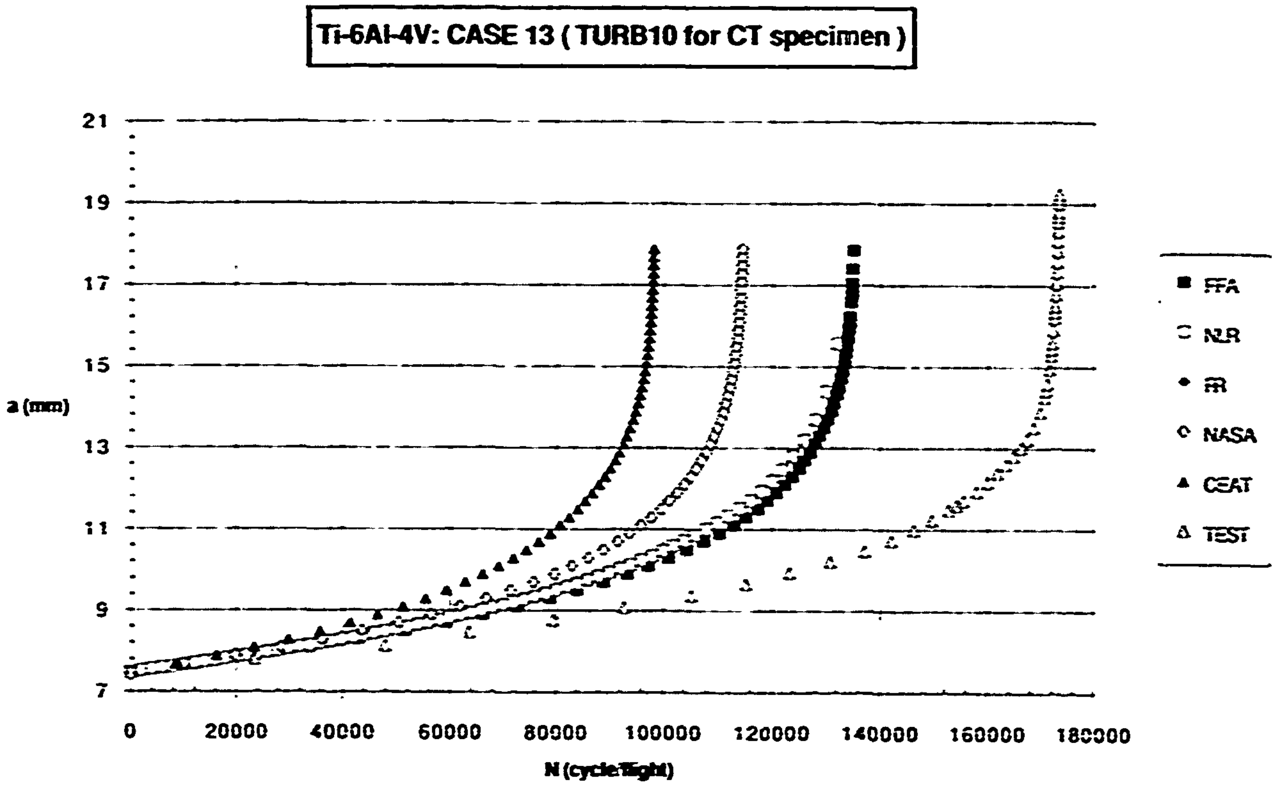

Fig.10 - Ti-6Al-4V Case 13

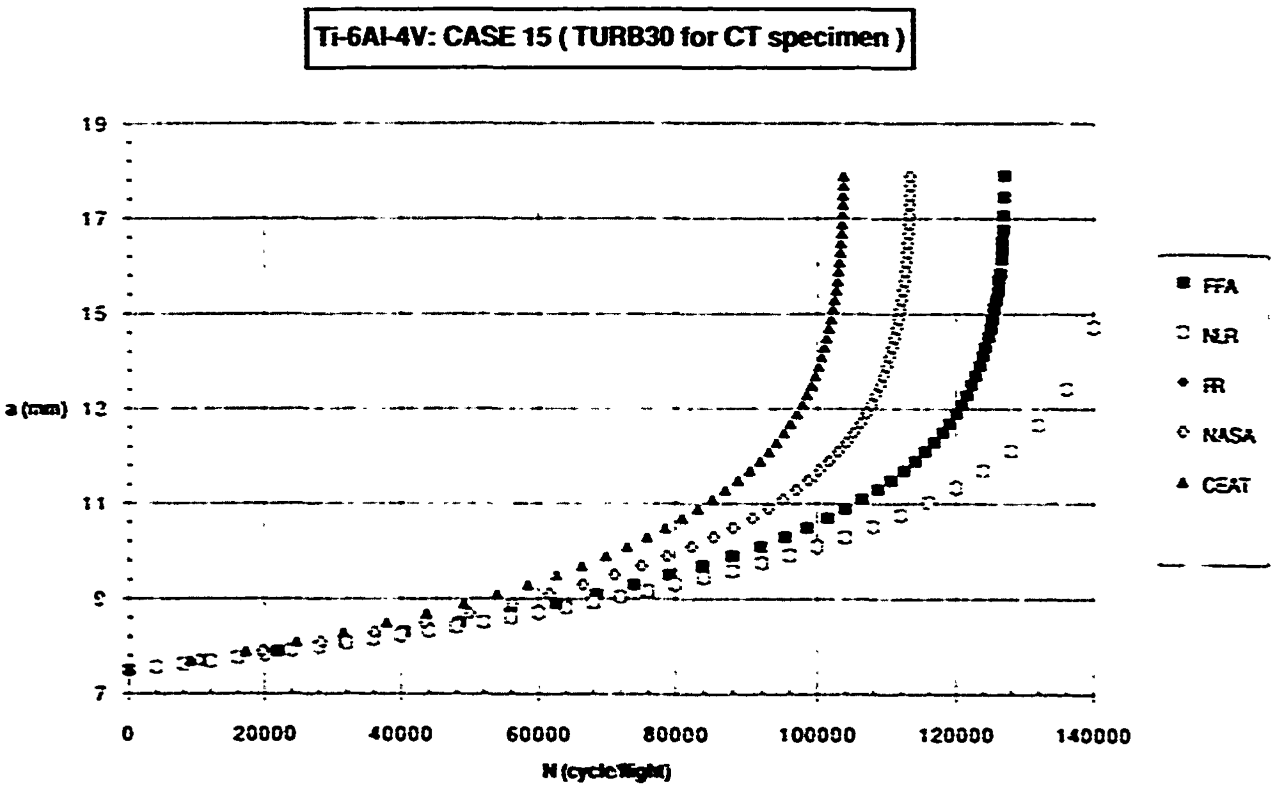

Fig.11 - Ti-6Al-4V Case 15

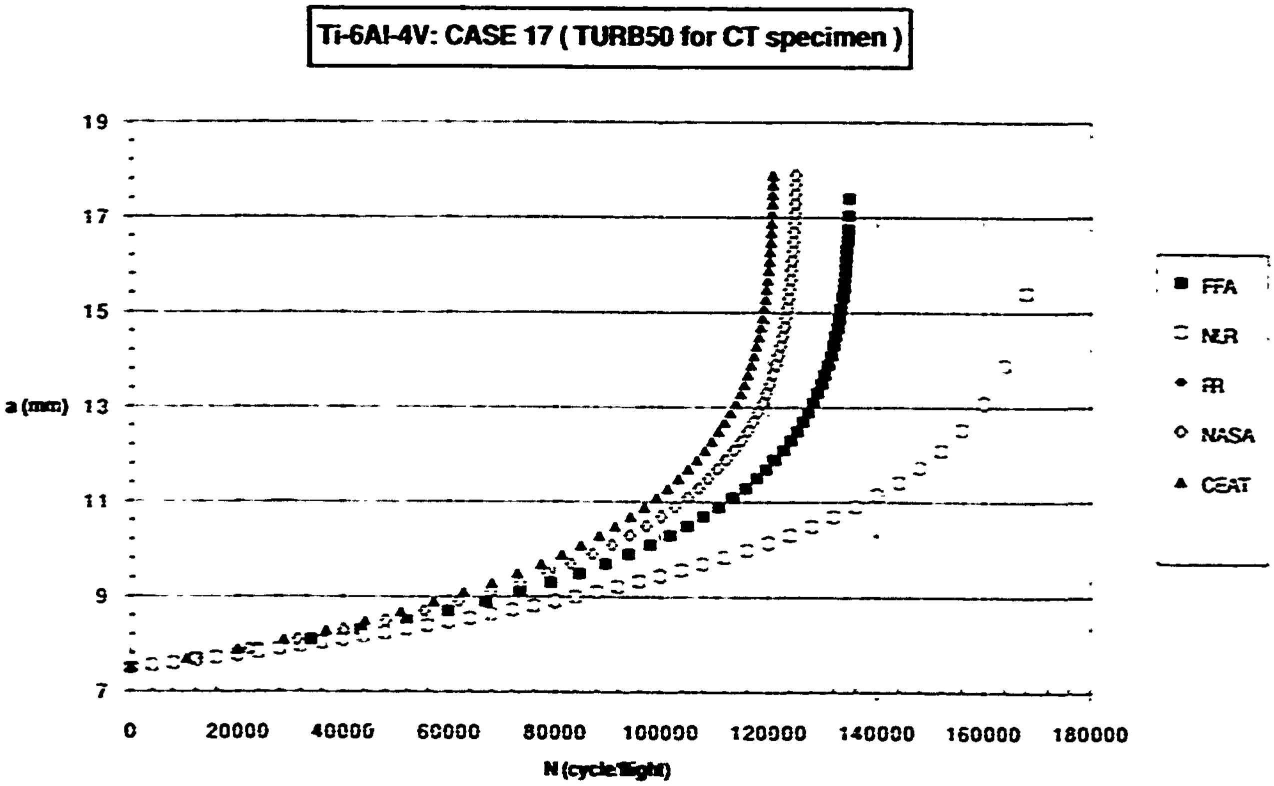

Fig.12 - Ti-6Al-4V Case 17

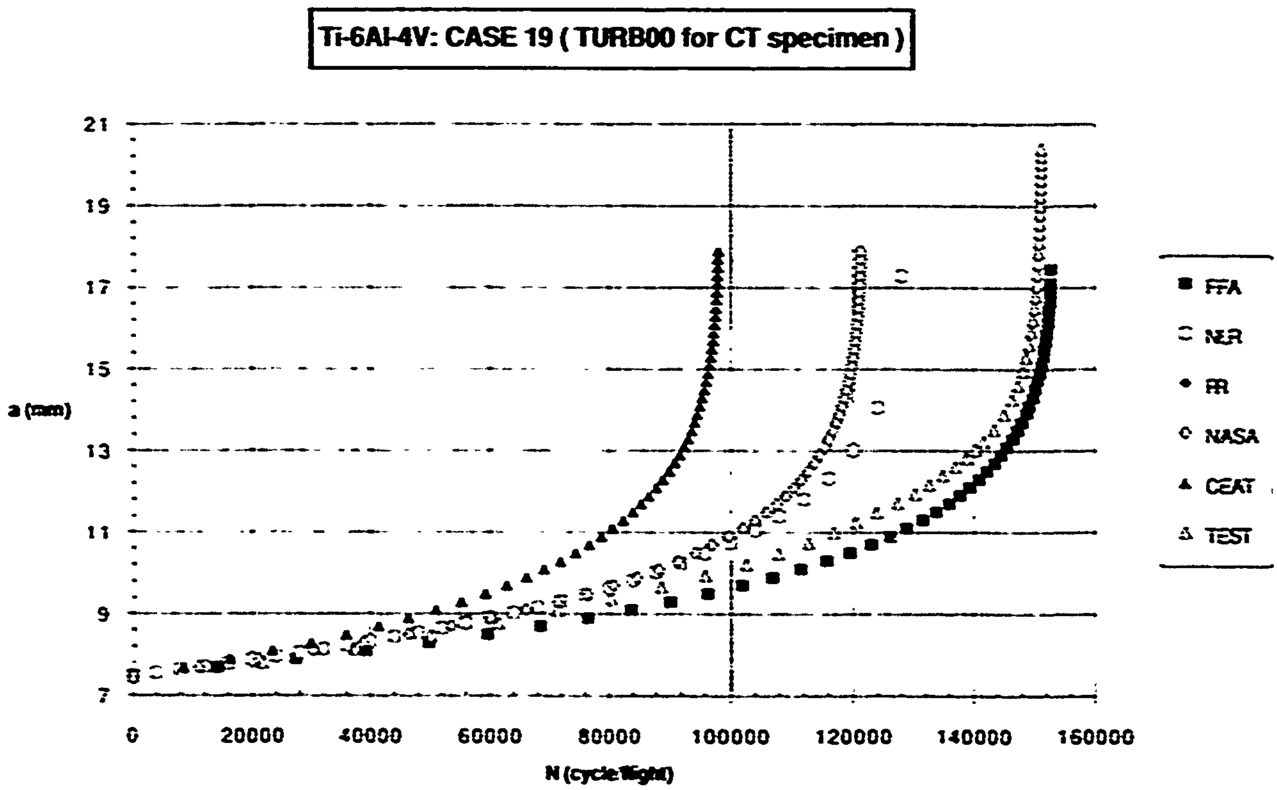

Fig.13 - Ti-6Al-4V Case 19

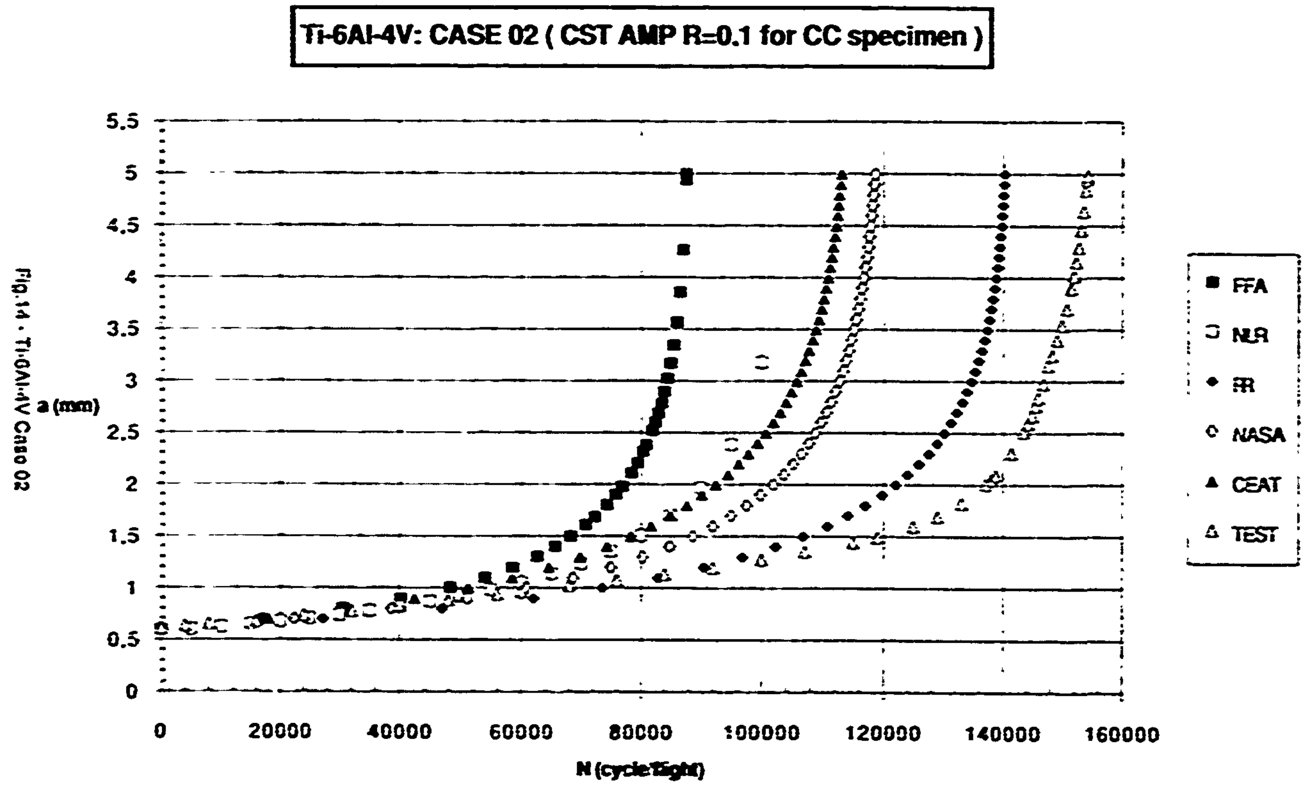

Fig.14 - Ti-6Al-4V Case 02

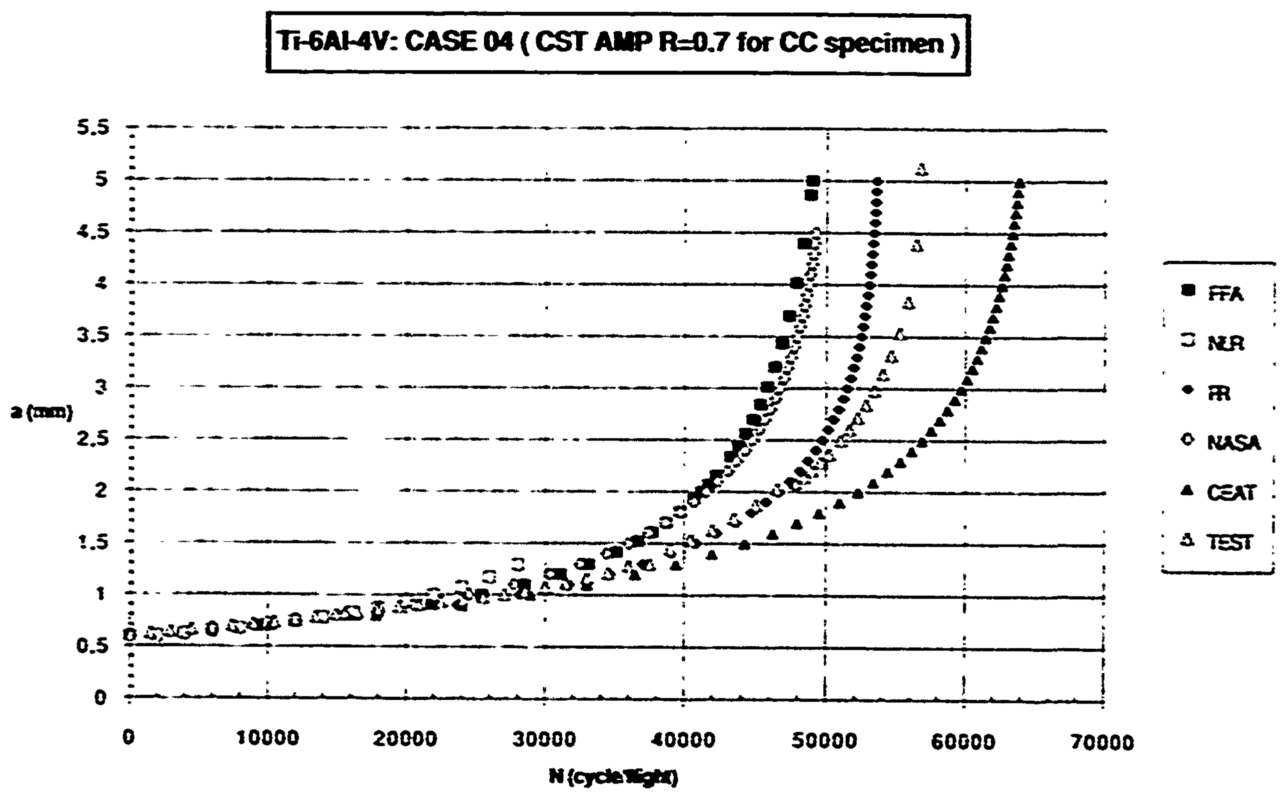

Fig.15 - Ti-6Al-4V Case 04

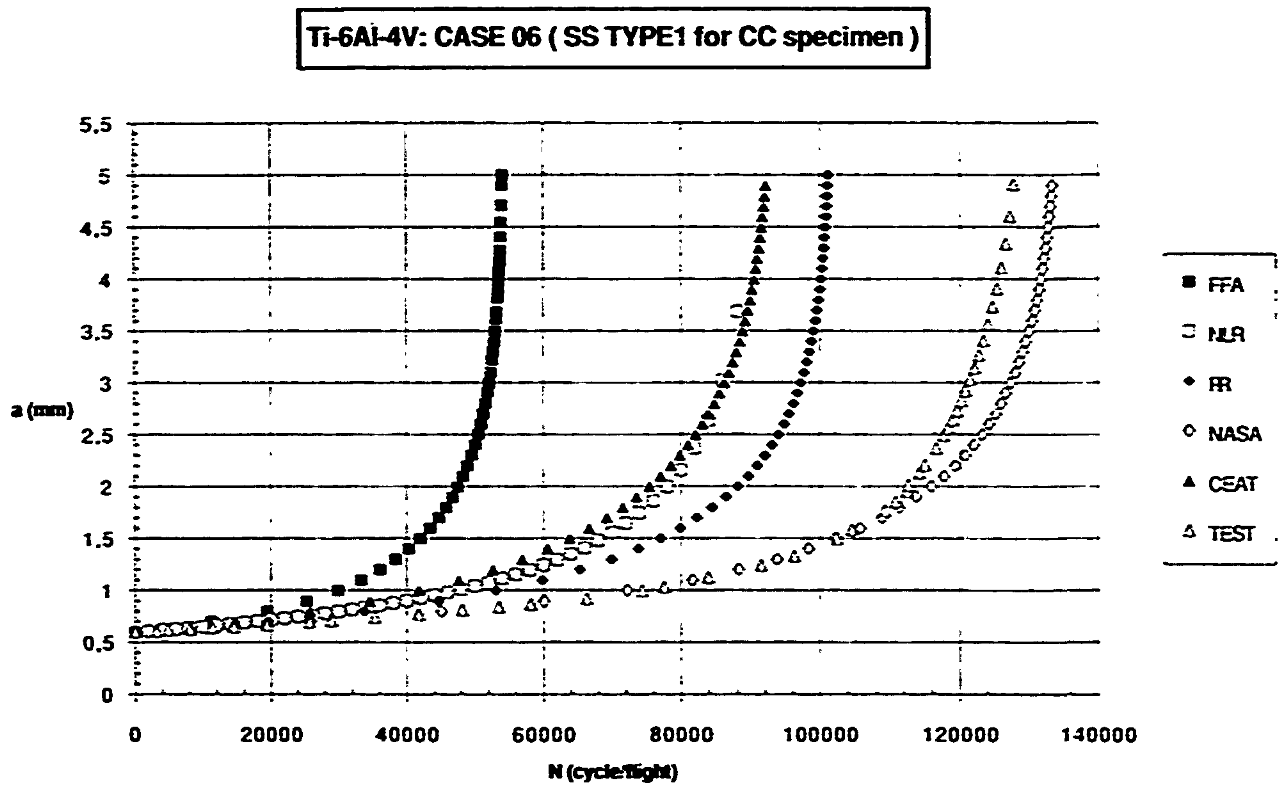

Fig.16 - Ti-6Al-4V Case 06

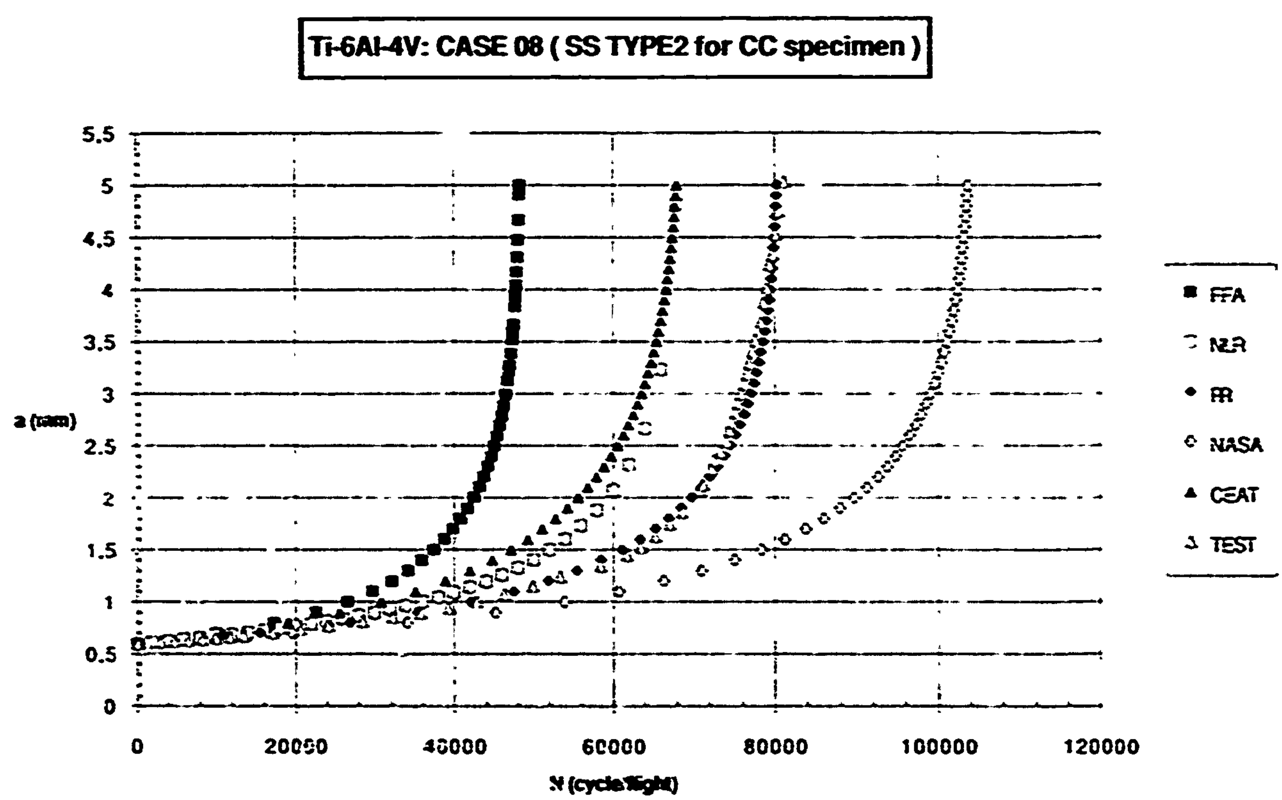

Fig.17 - Ti-6Al-4V Case 08

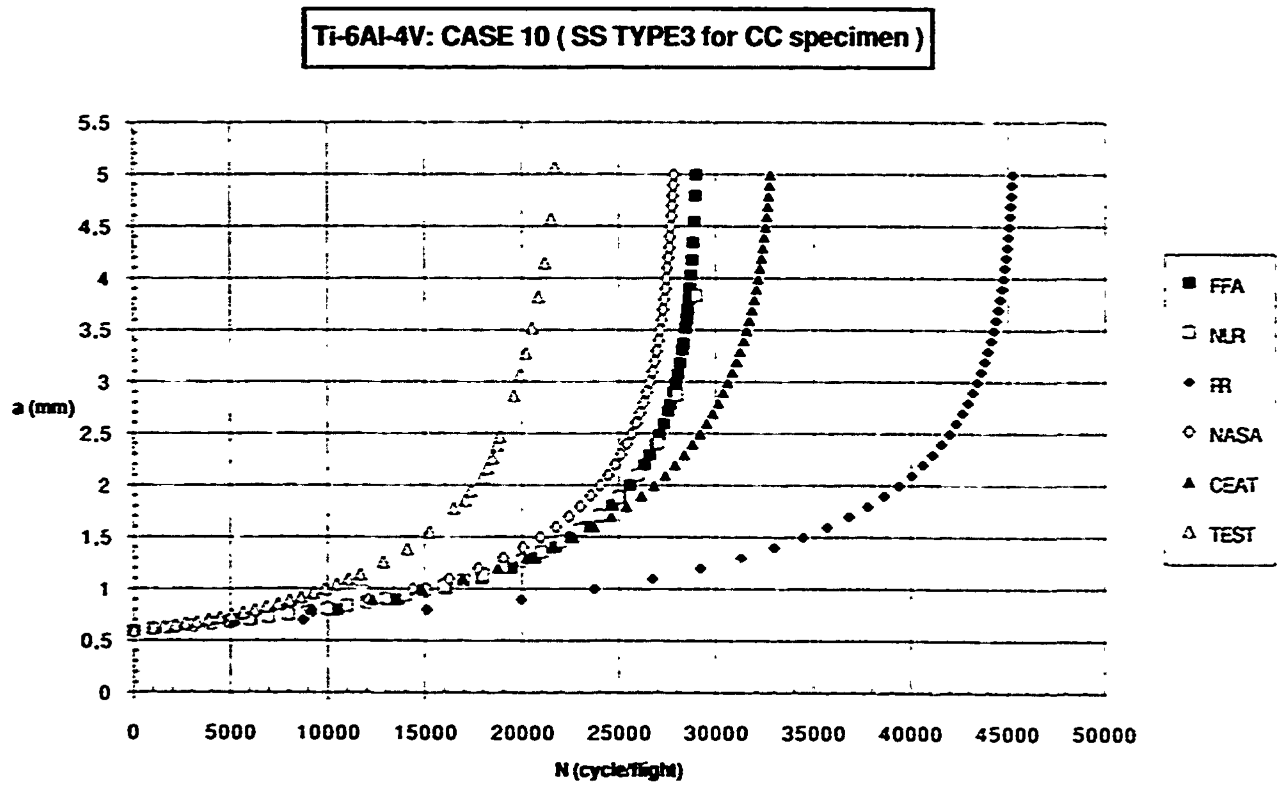

Fig.18 - Ti-6Al-4V Case 10

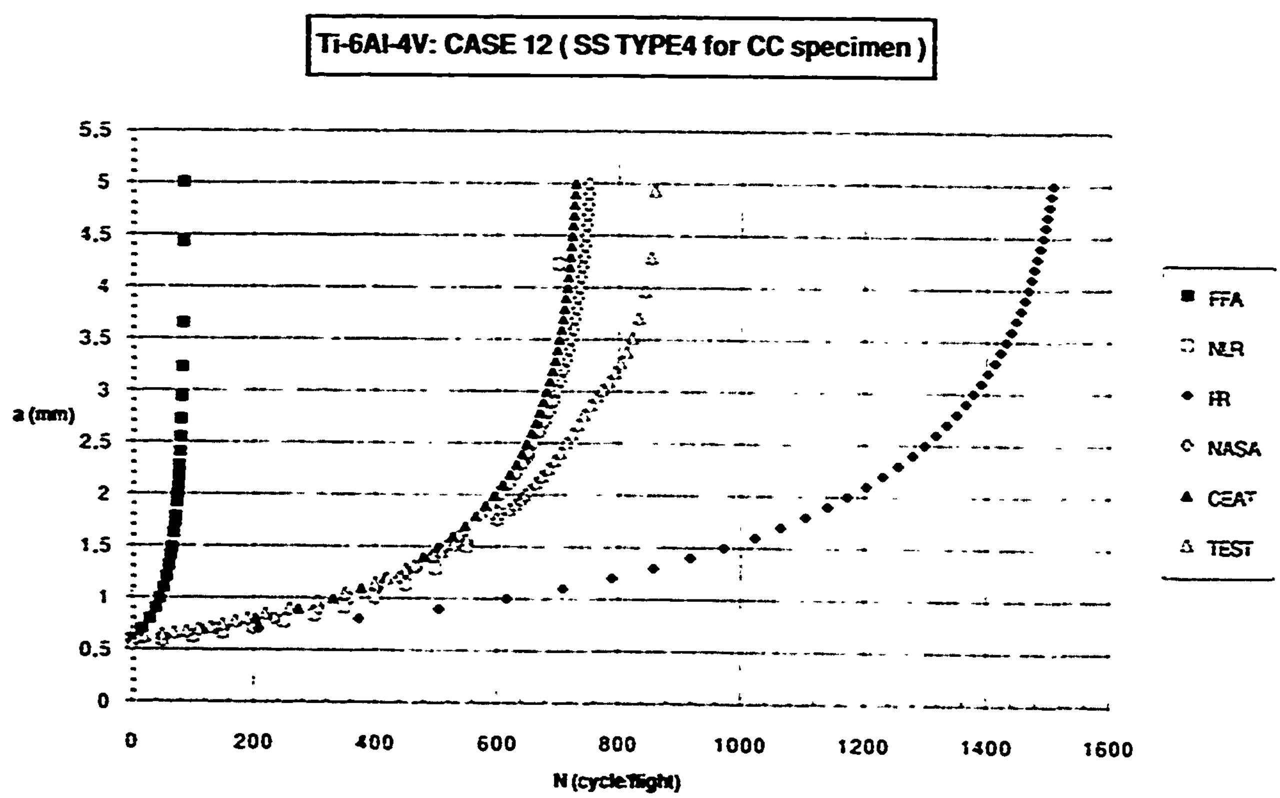

Fig.19 - Ti-6Al-4V Case 12

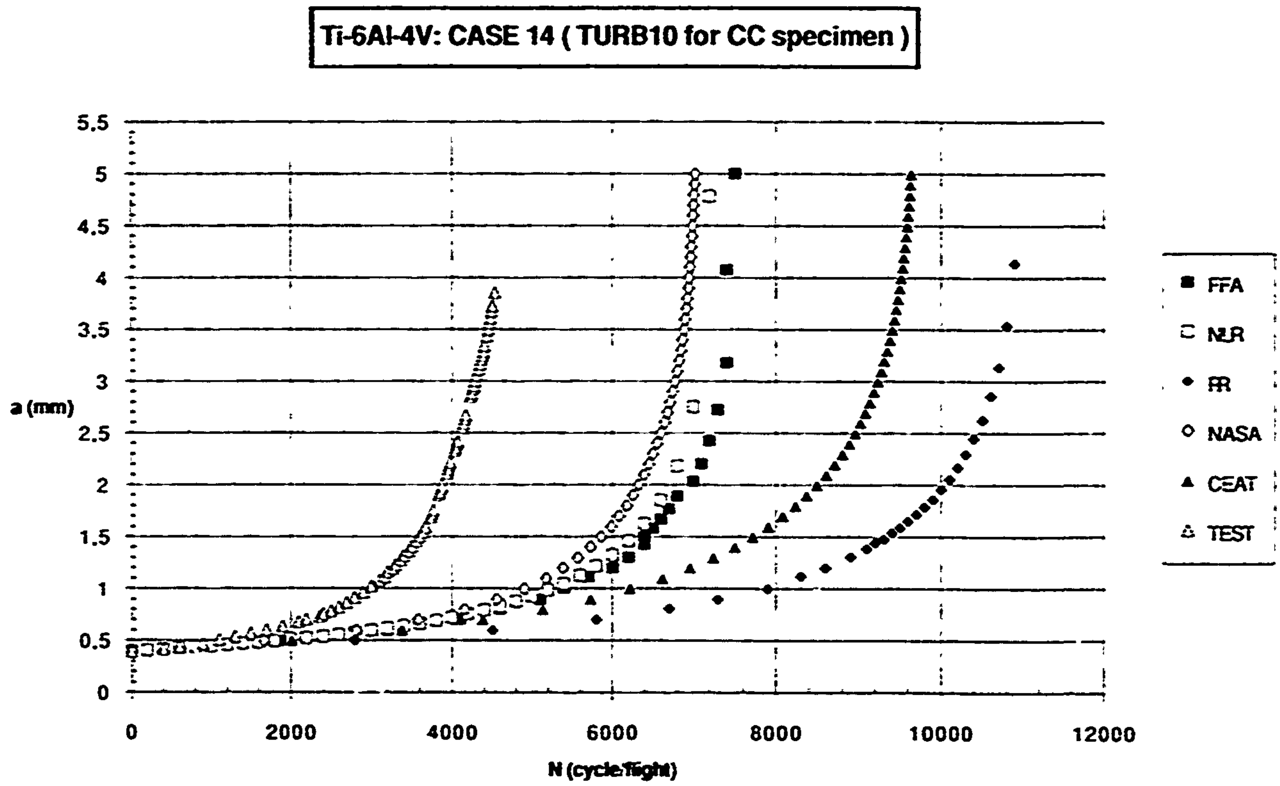

Fig.20 - Ti-6Al-4V Case 14

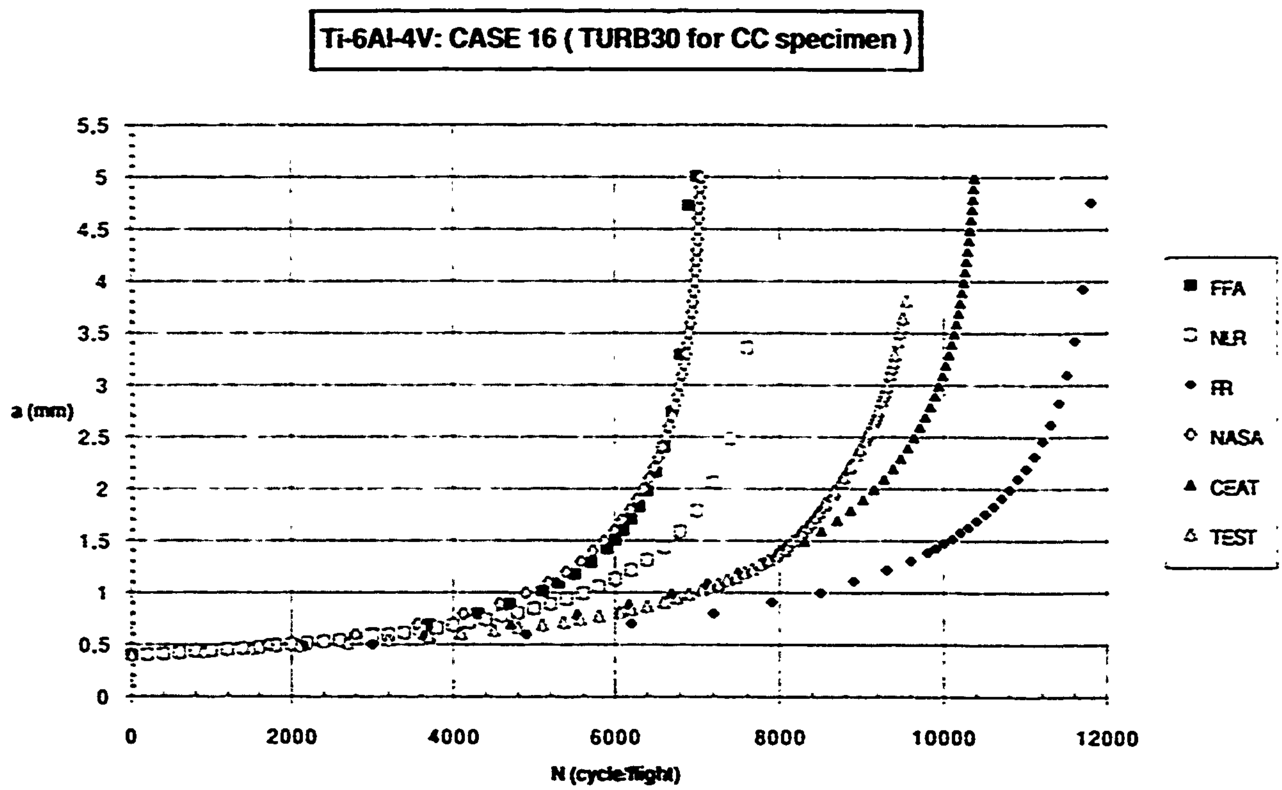

Fig.21 - Ti-6Al-4V Case 16

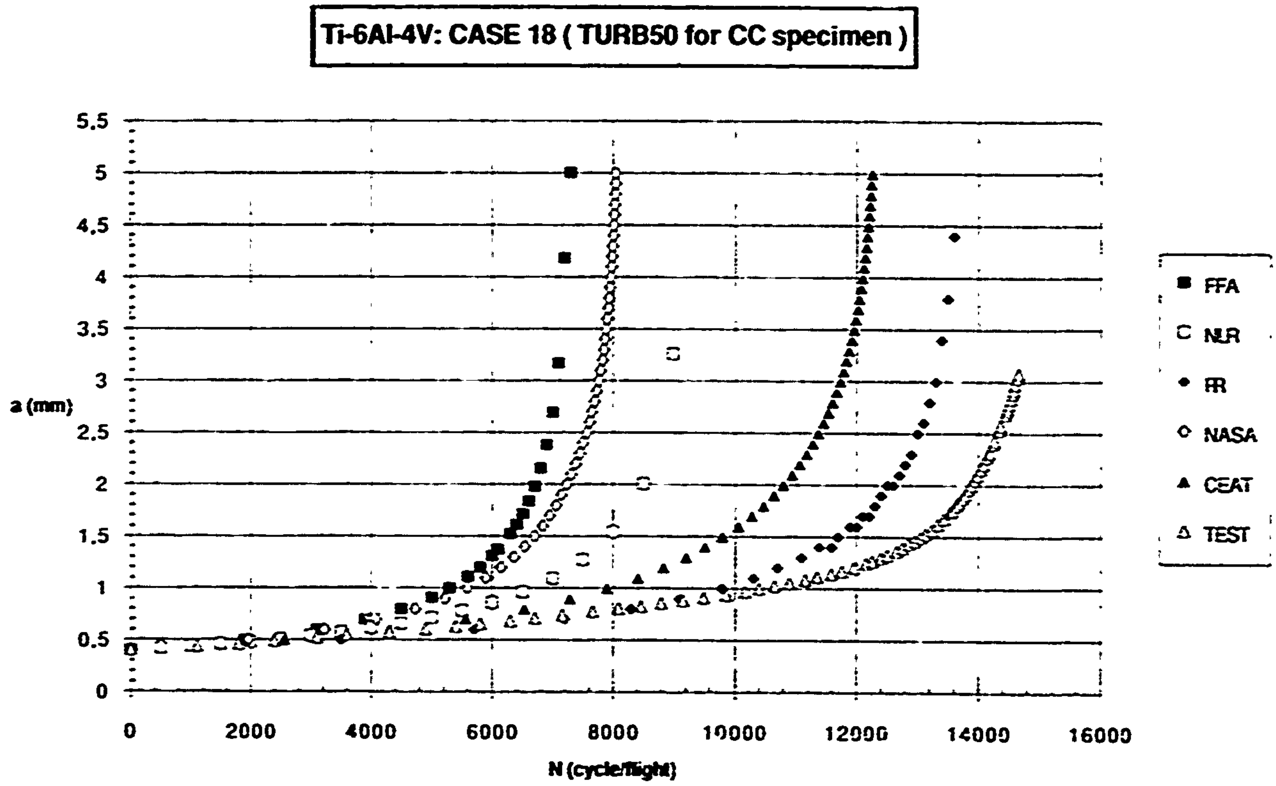

Fig.22 - Ti-6Al-4V Case 18

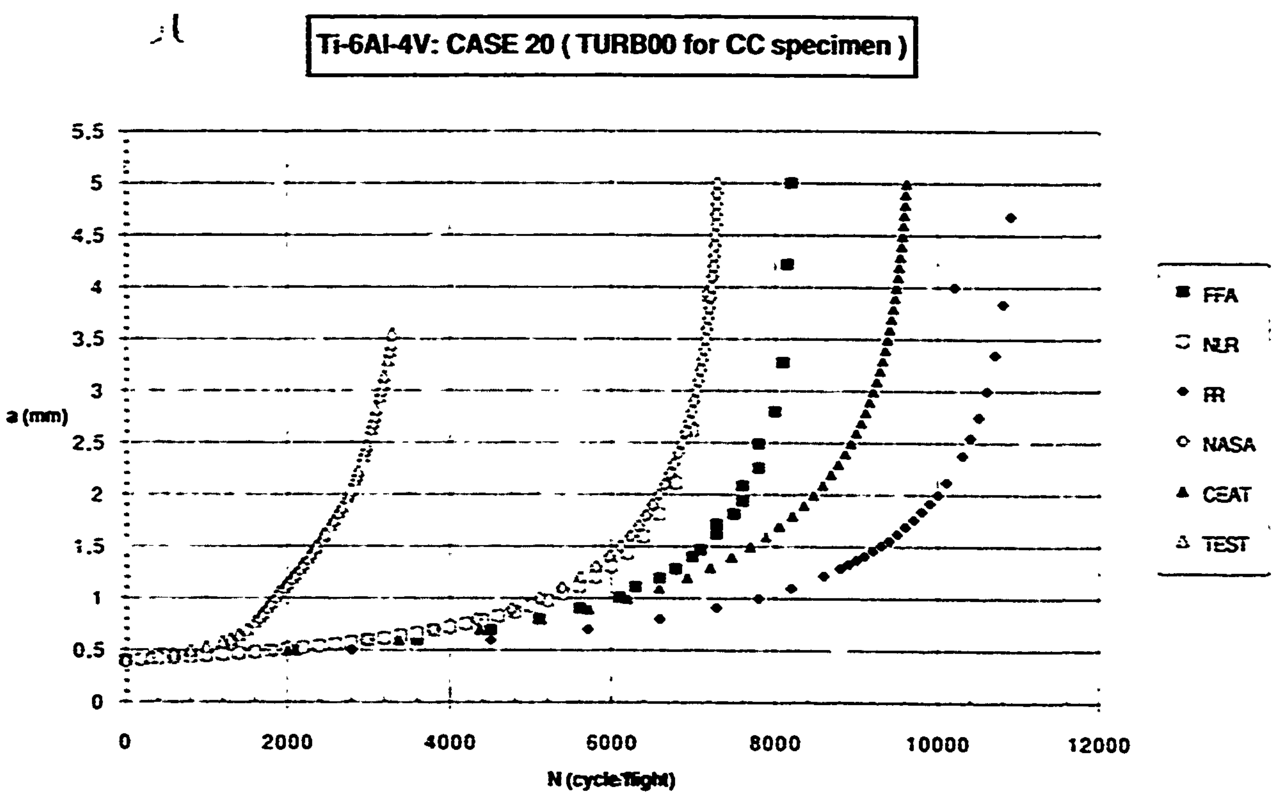

Fig.23 - Ti-6Al-4V Case 20

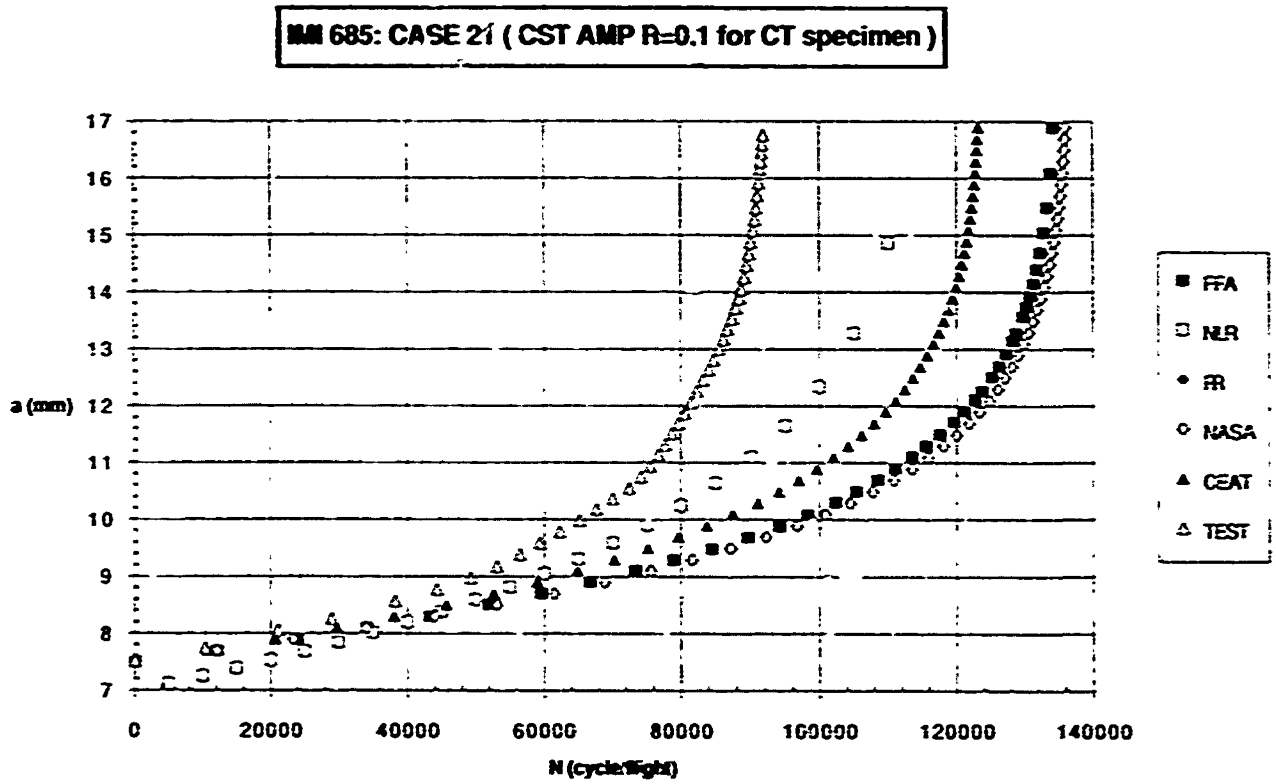

Fig.24 - IMI685 Case 21

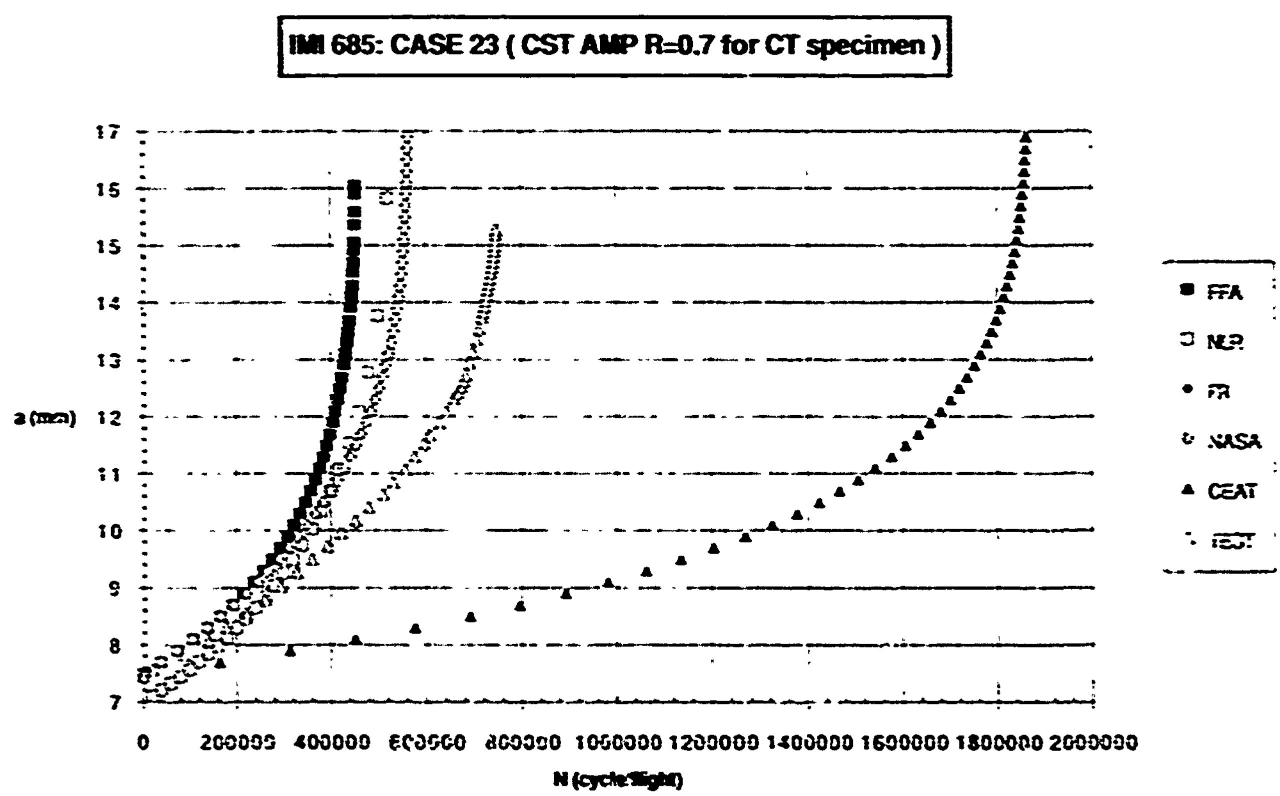

Fig.25 - IMI685 Case 23

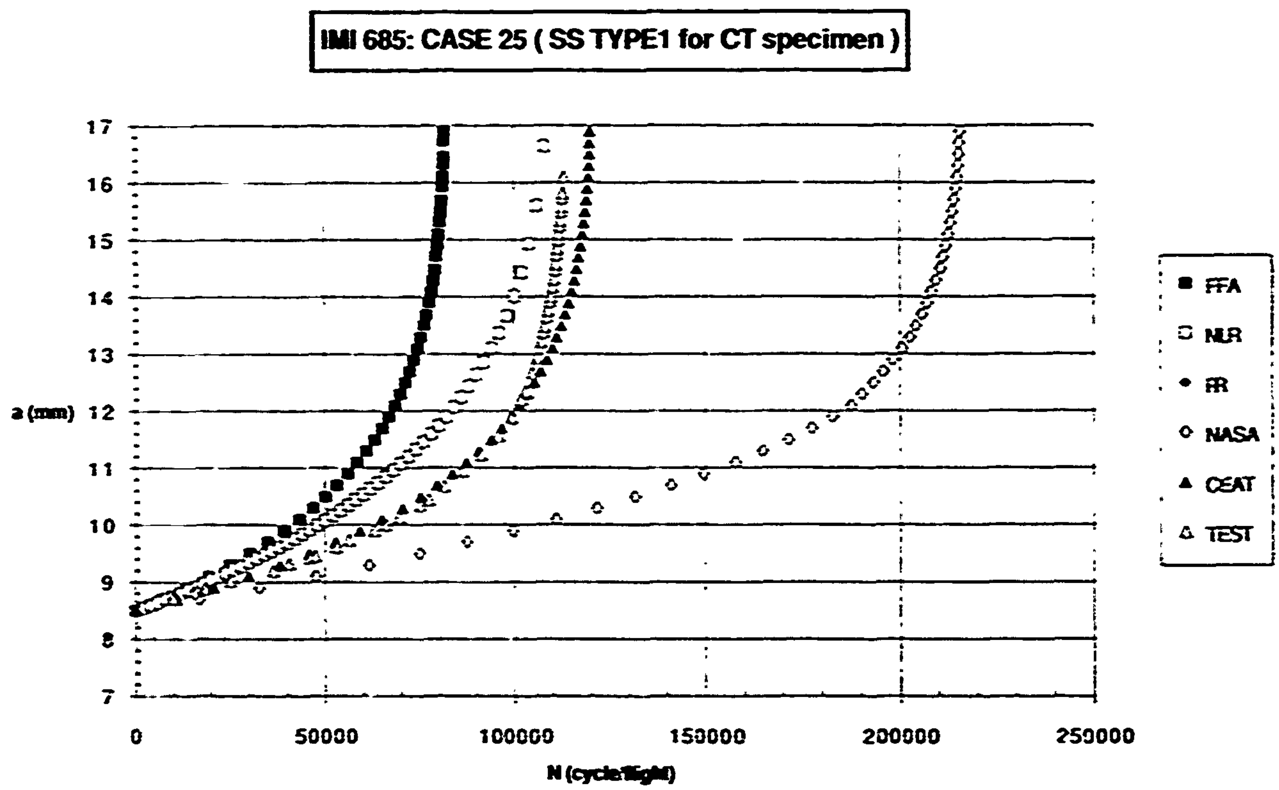

Fig.26 - IMI685 Case 25

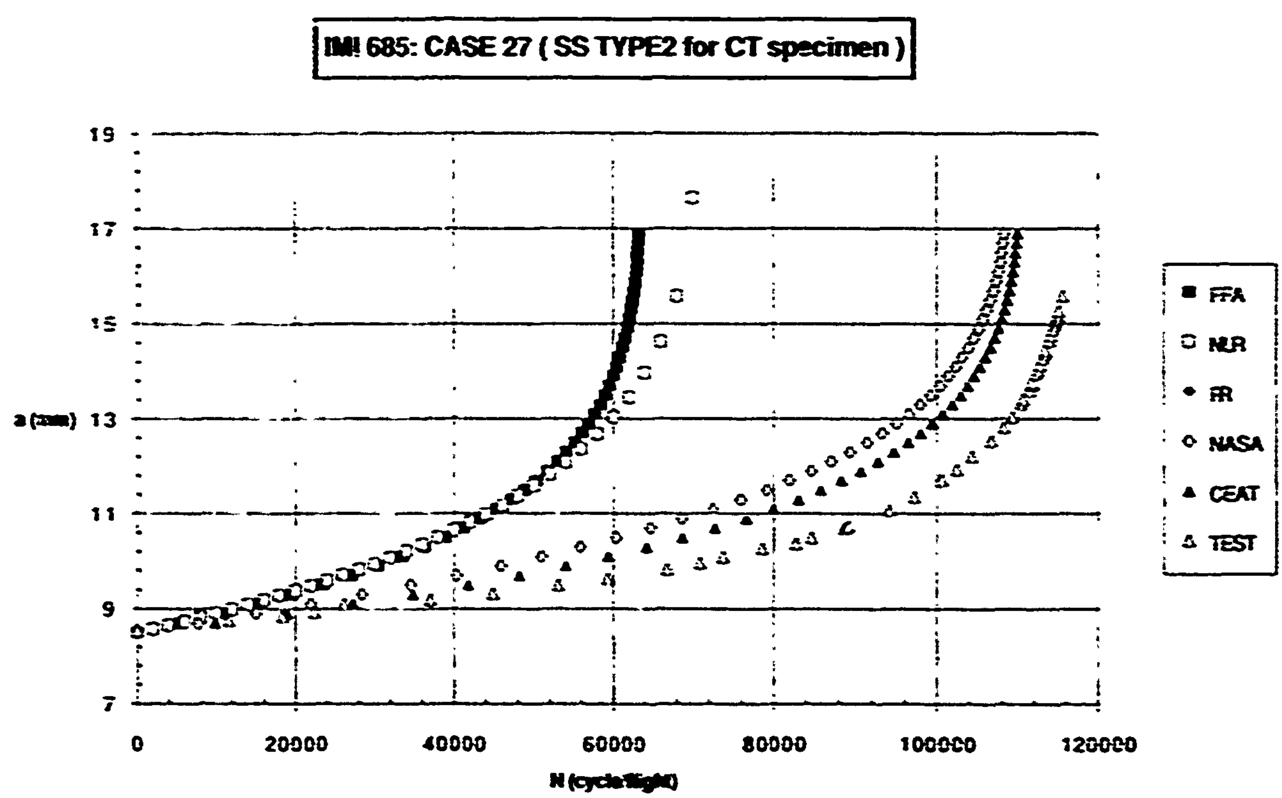

Fig.27 - IMI685 Case 27

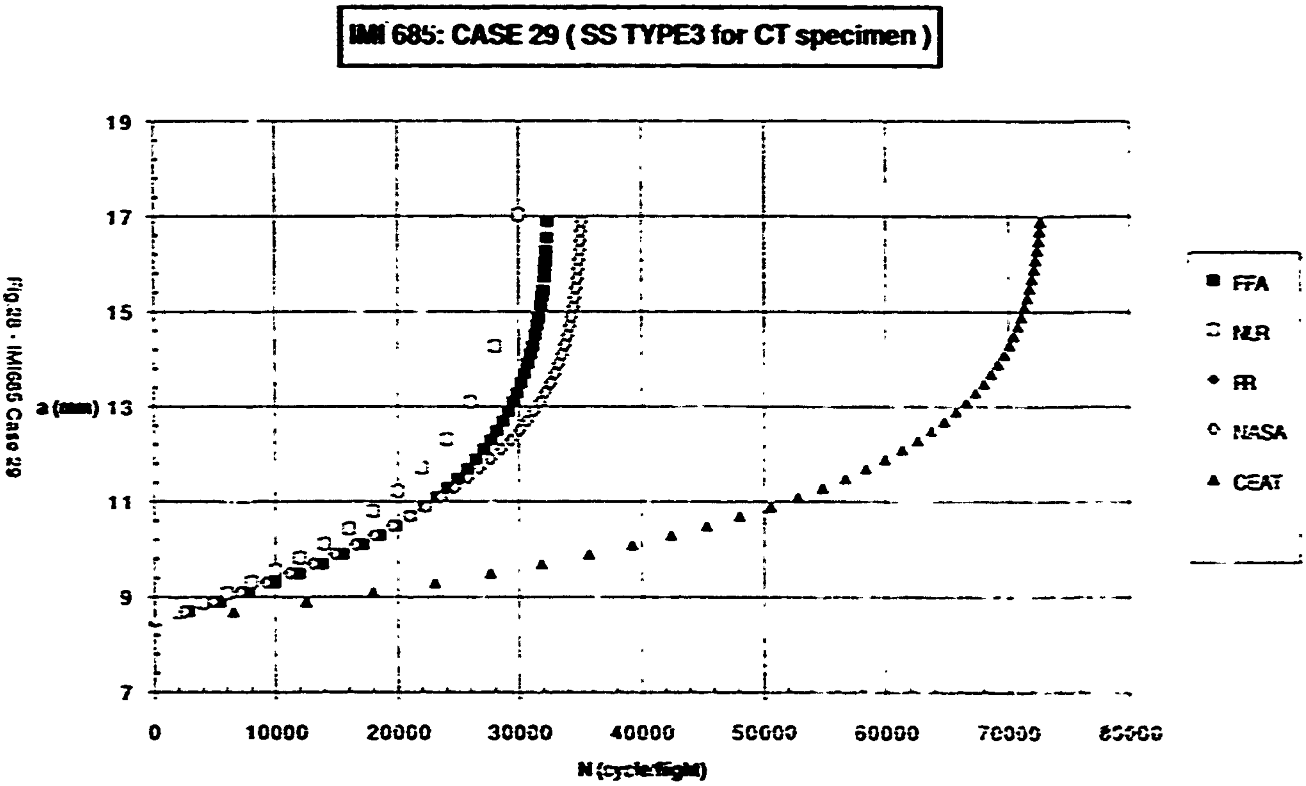

Fig.28 - IMI685 Case 29

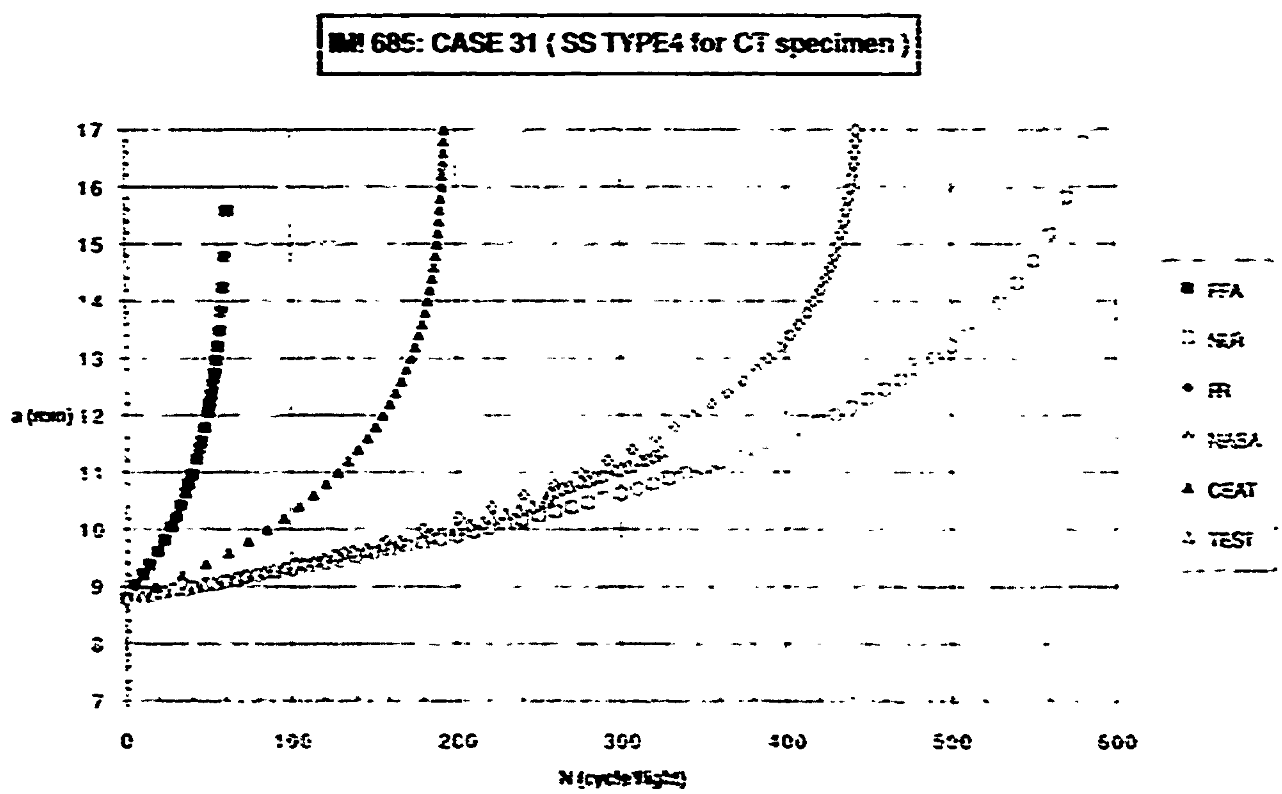

Fig.29 - IMI685 Case 31

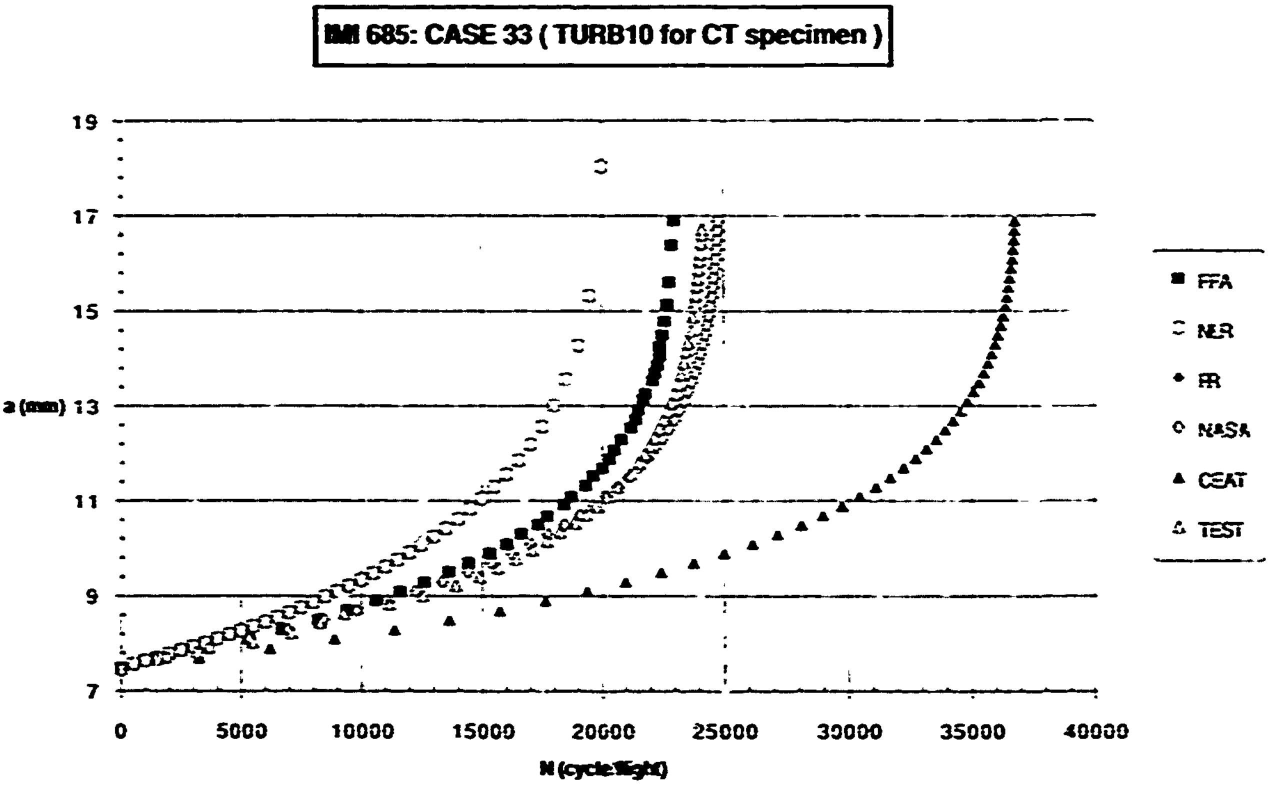

Fig.30 - IMI685 Case 33

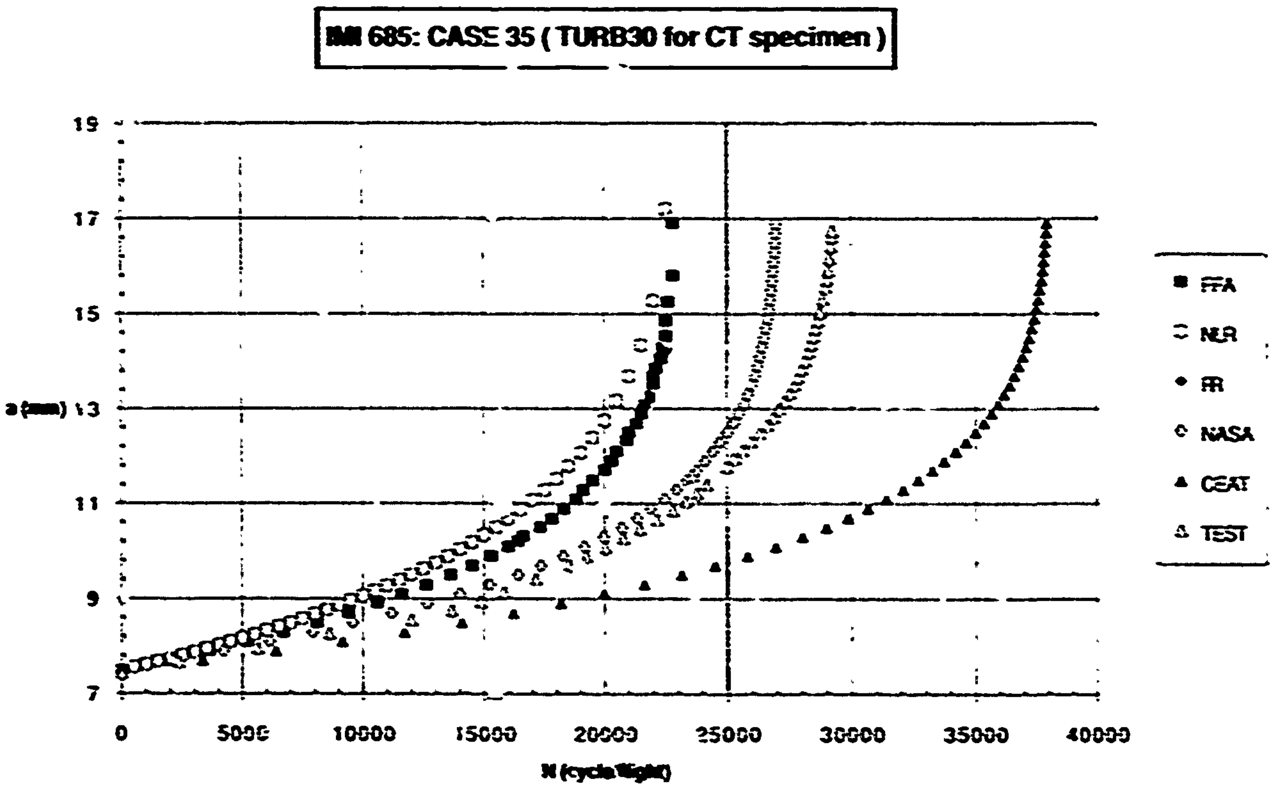

Fig.31 - IMI685 Case 35

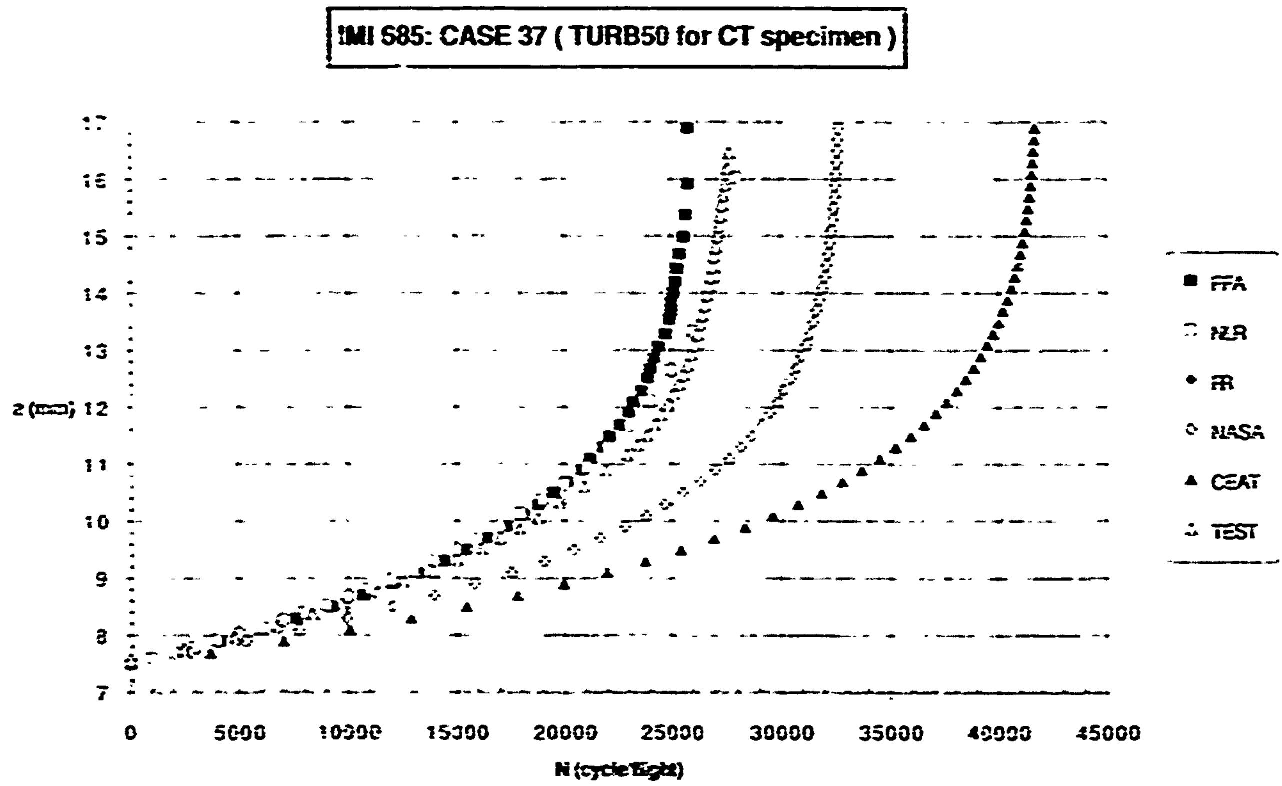

Fig.32 - IMI685 Case 37

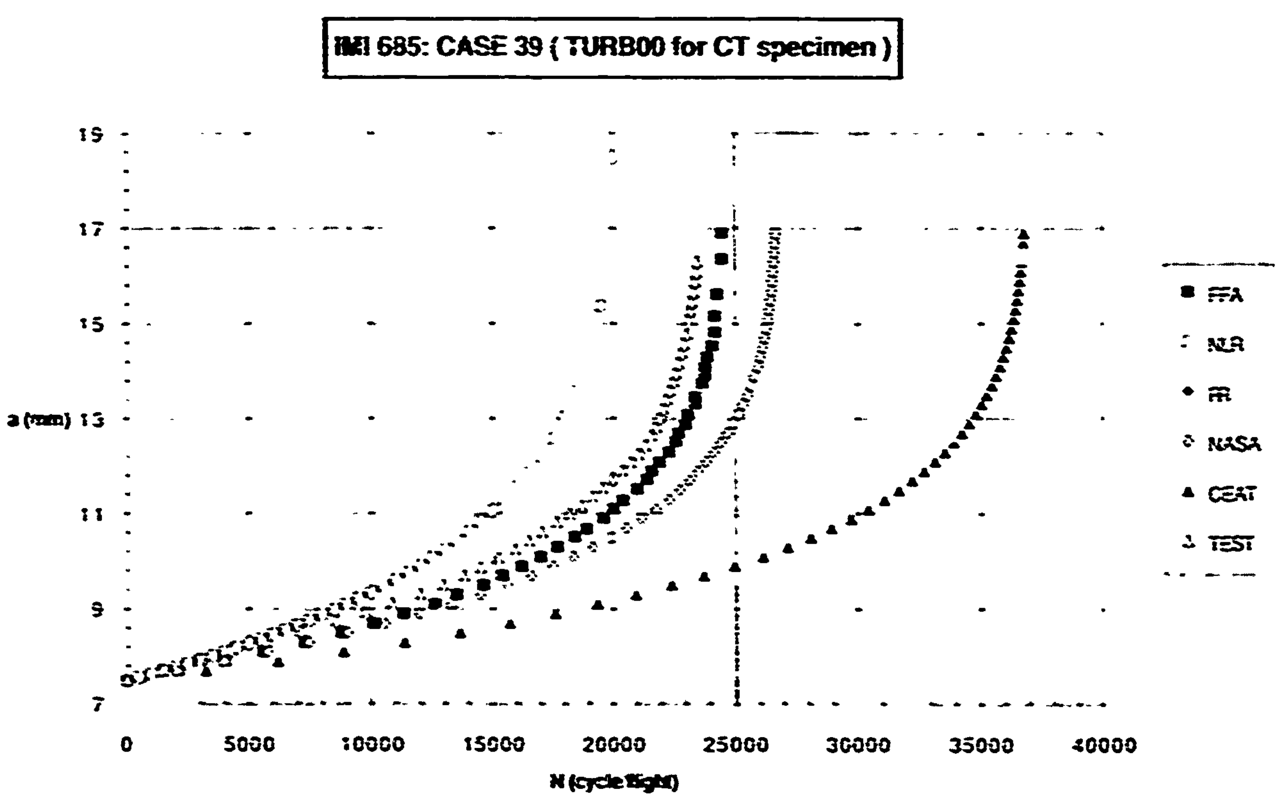

Fig.33 - IMI685 Case 39

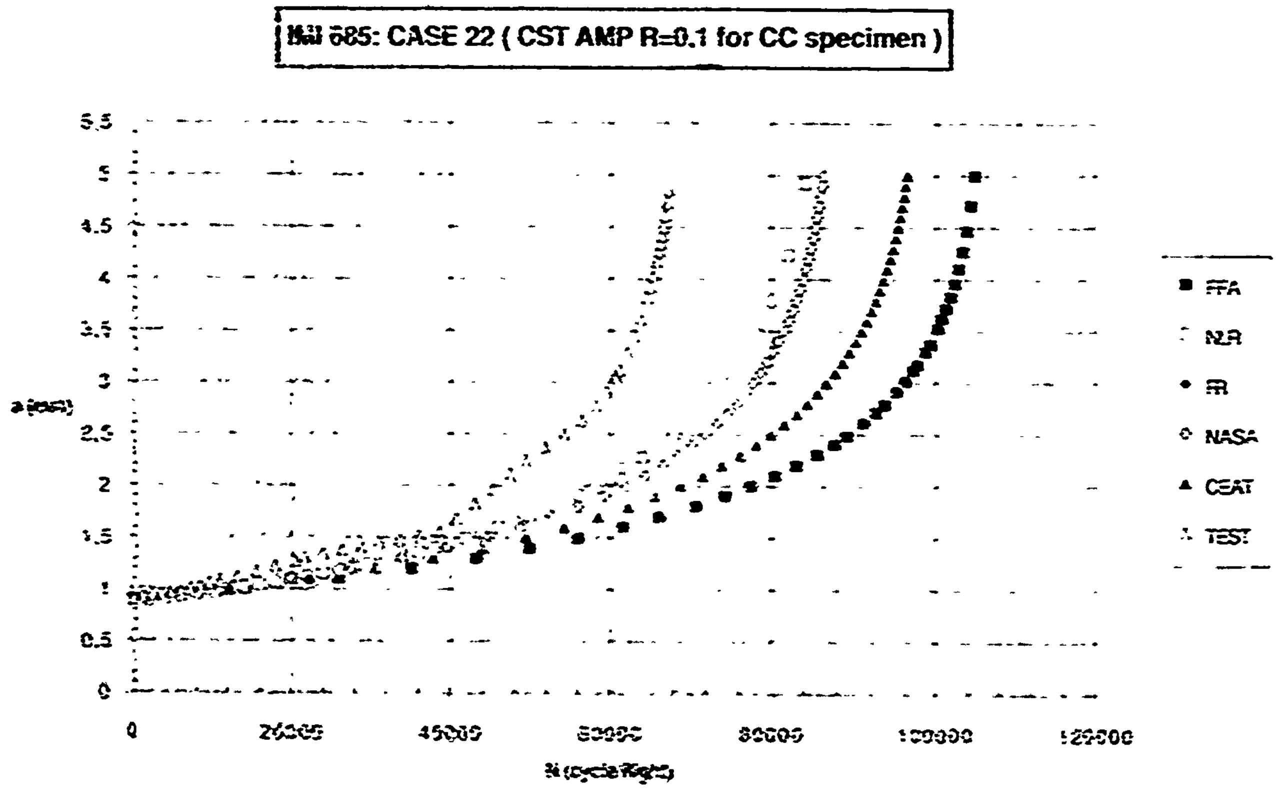

Fig.34 - IMI685 Case 22

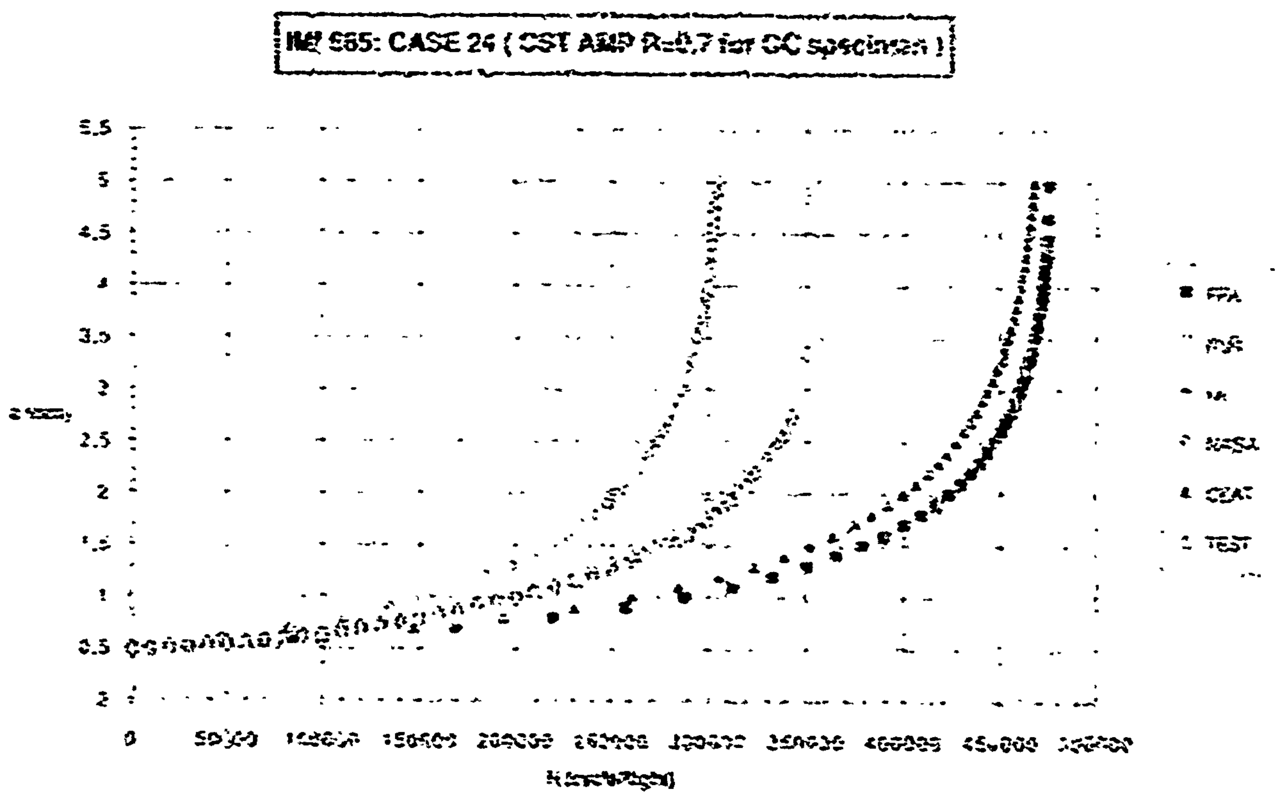

Fig.35 - IMI685 Case 24

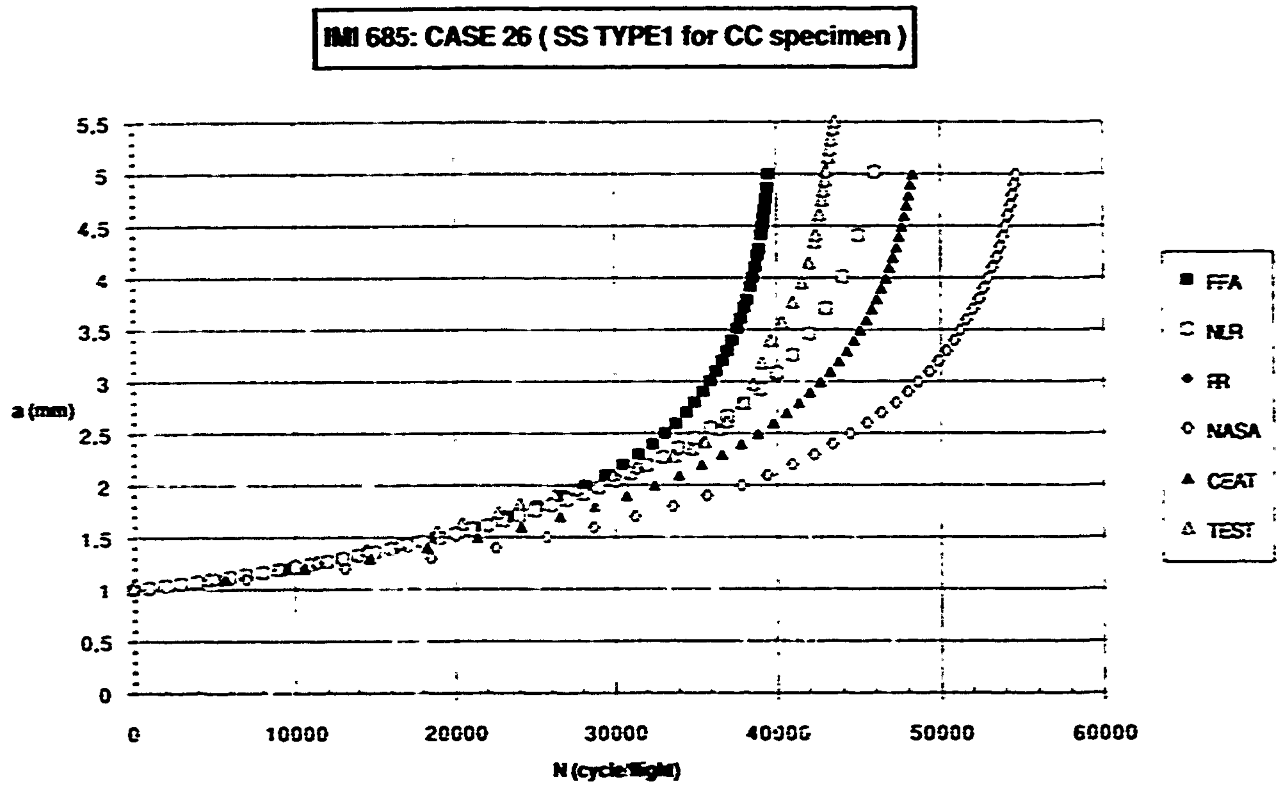

Fig.36 - IMI685 Case 36

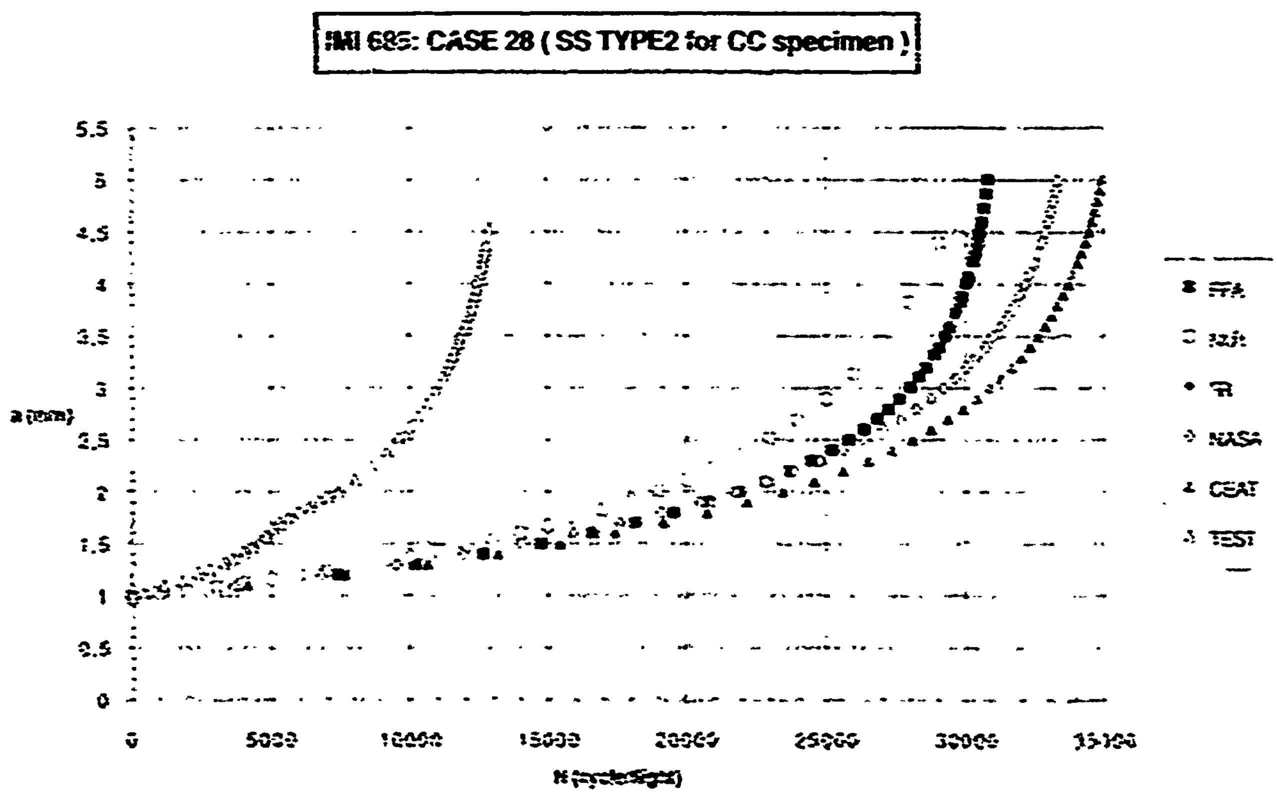

Fig.37 - IMI685 Case 28

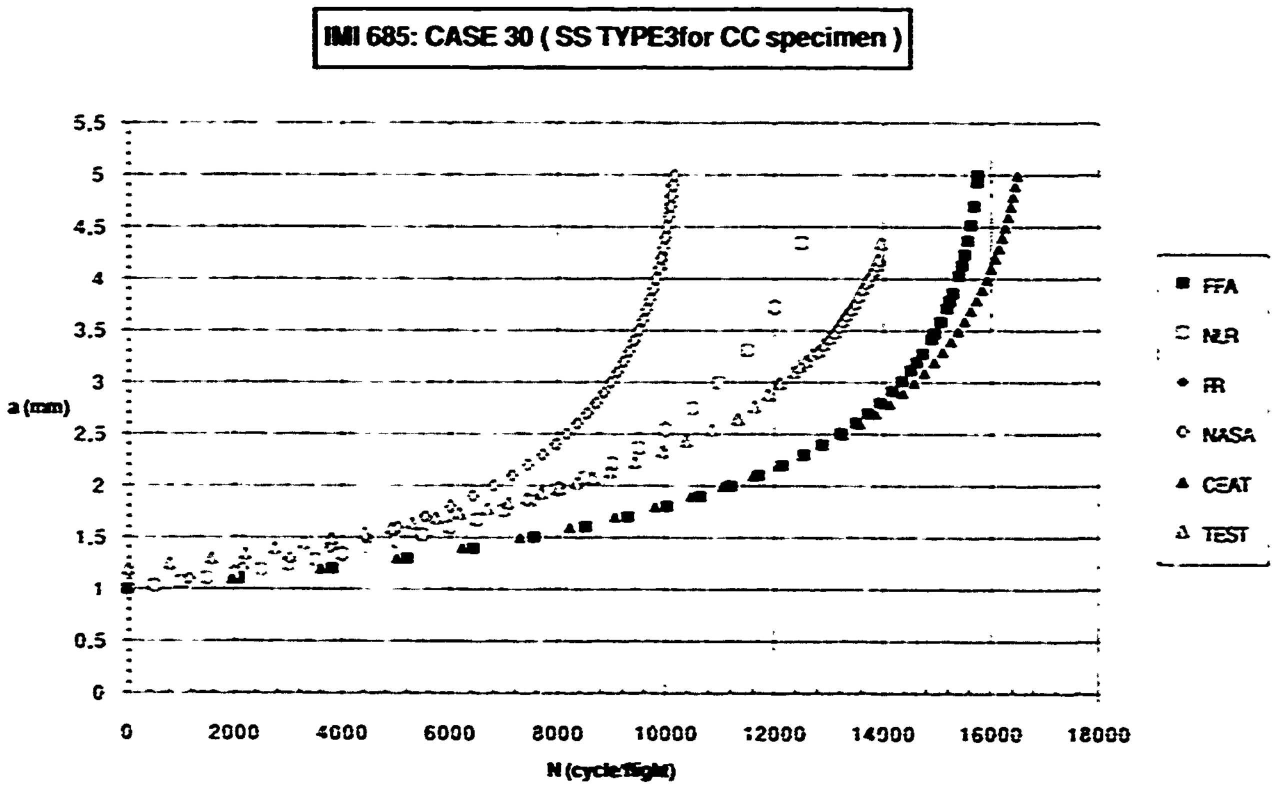

Fig.38 - IMI685 Case 30

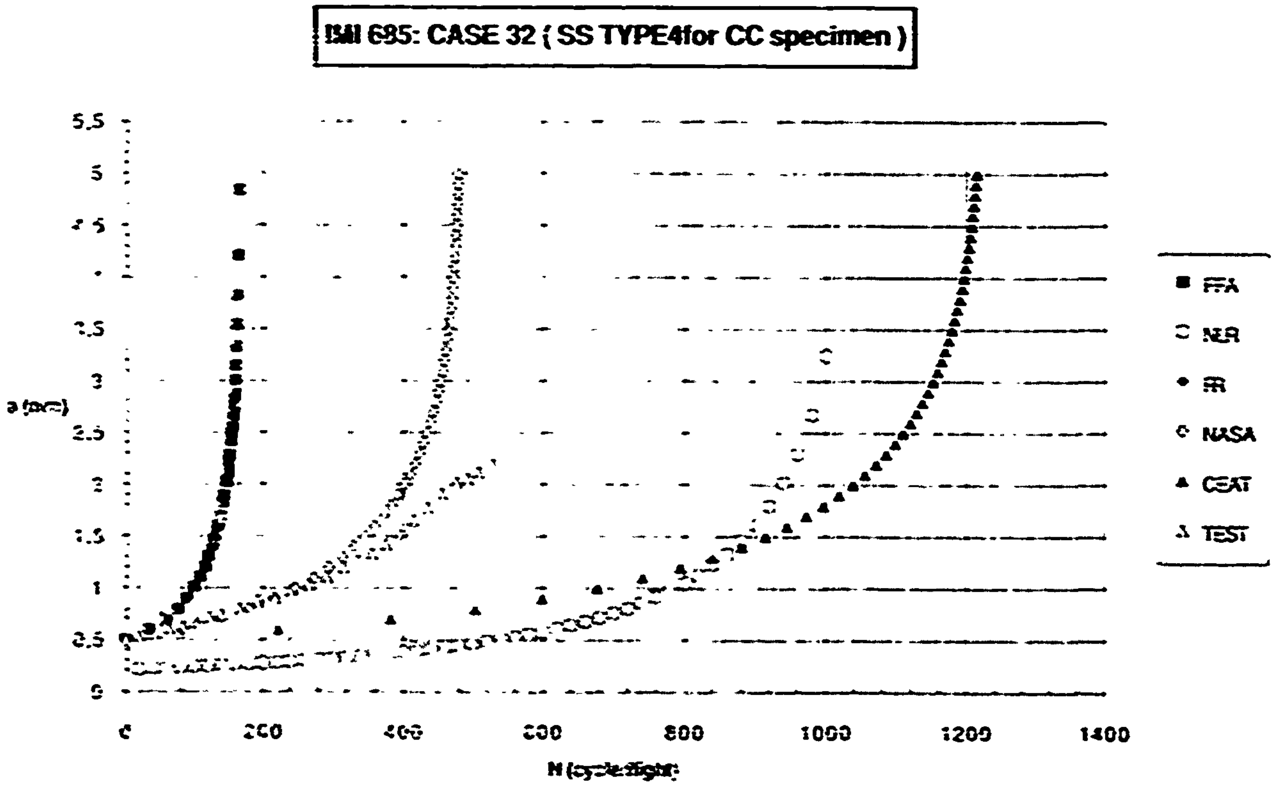

Fig.39 - IMI685 Case 32

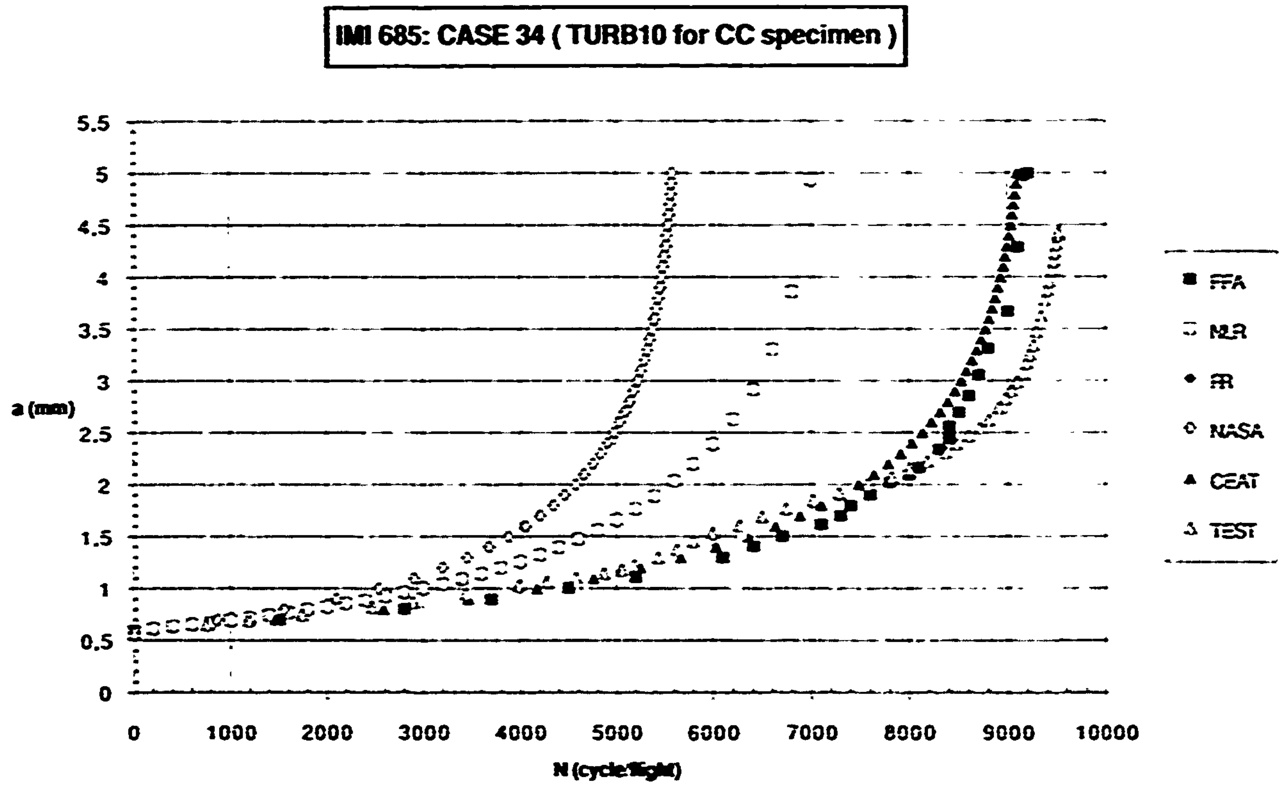

Fig.40 - IMI685 Case 34

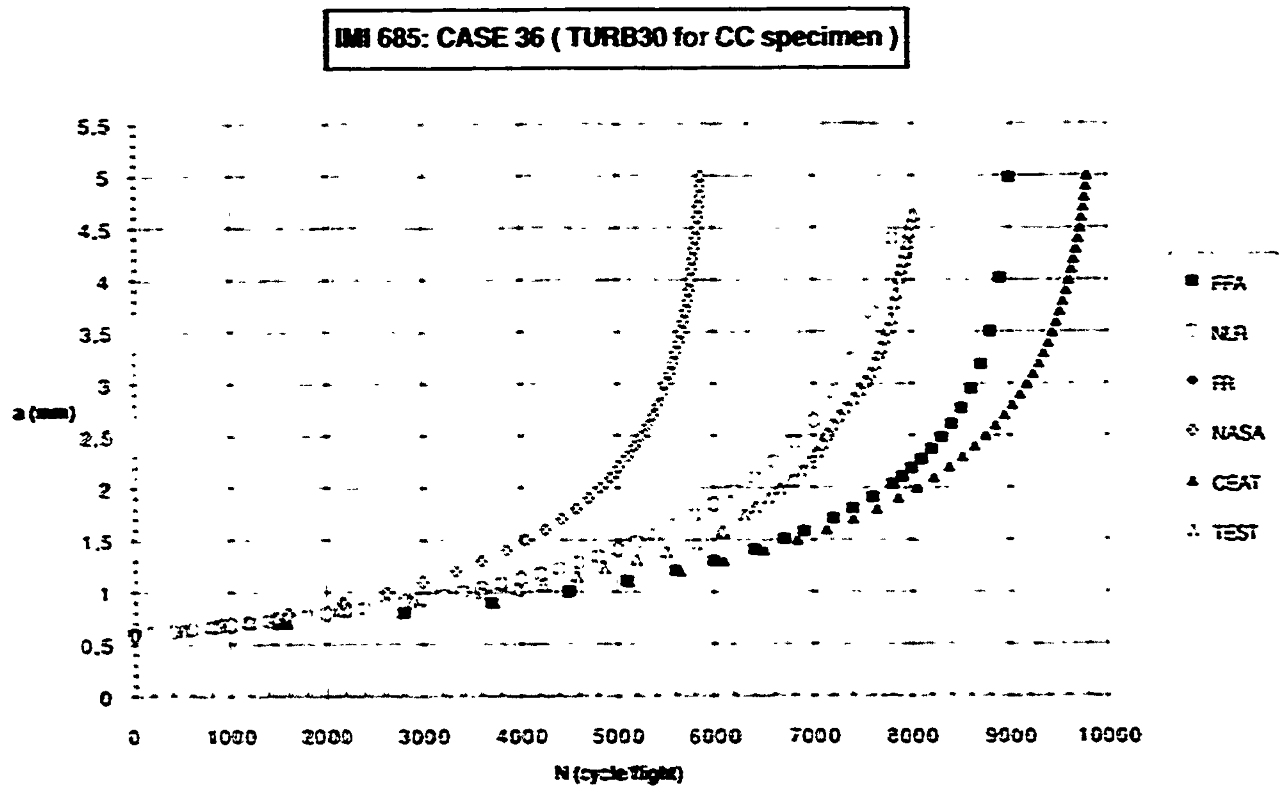

Fig.41 - IMI685 Case 36

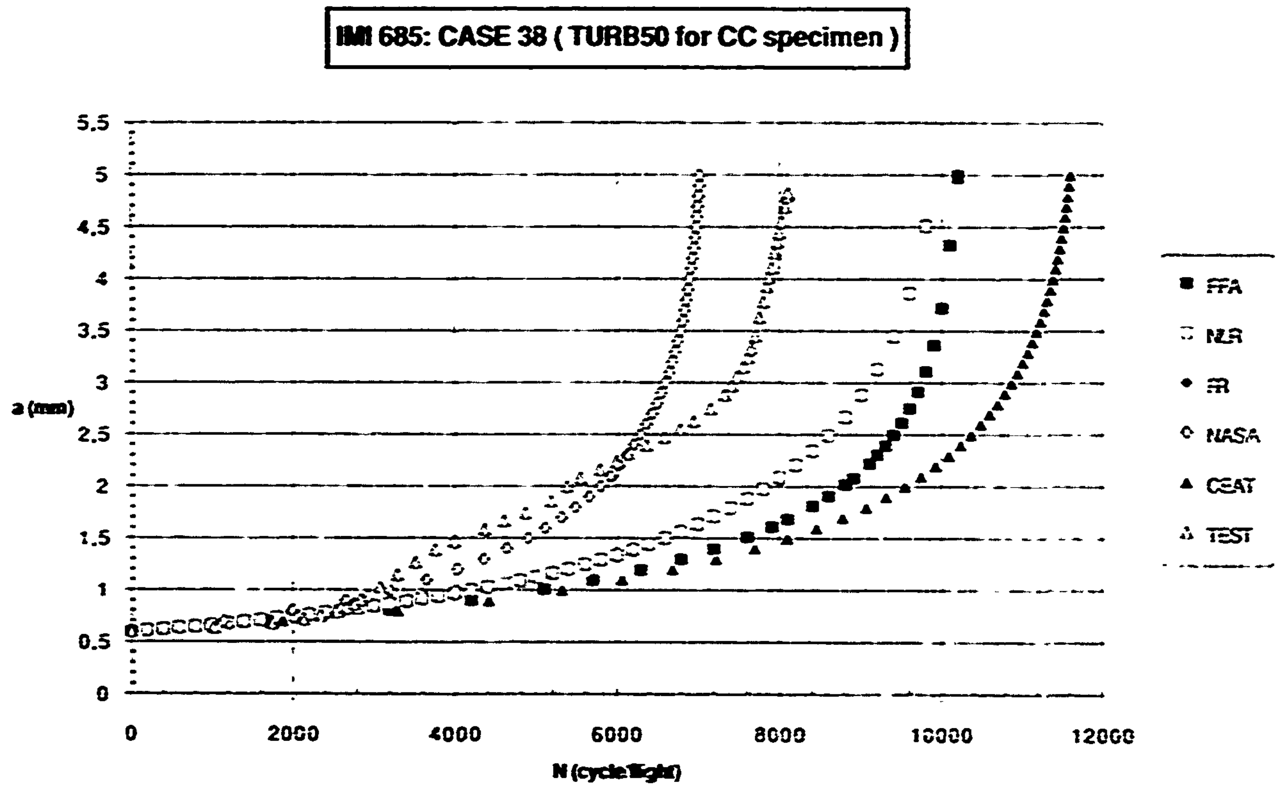

Fig.42 - IMI685 Case 38

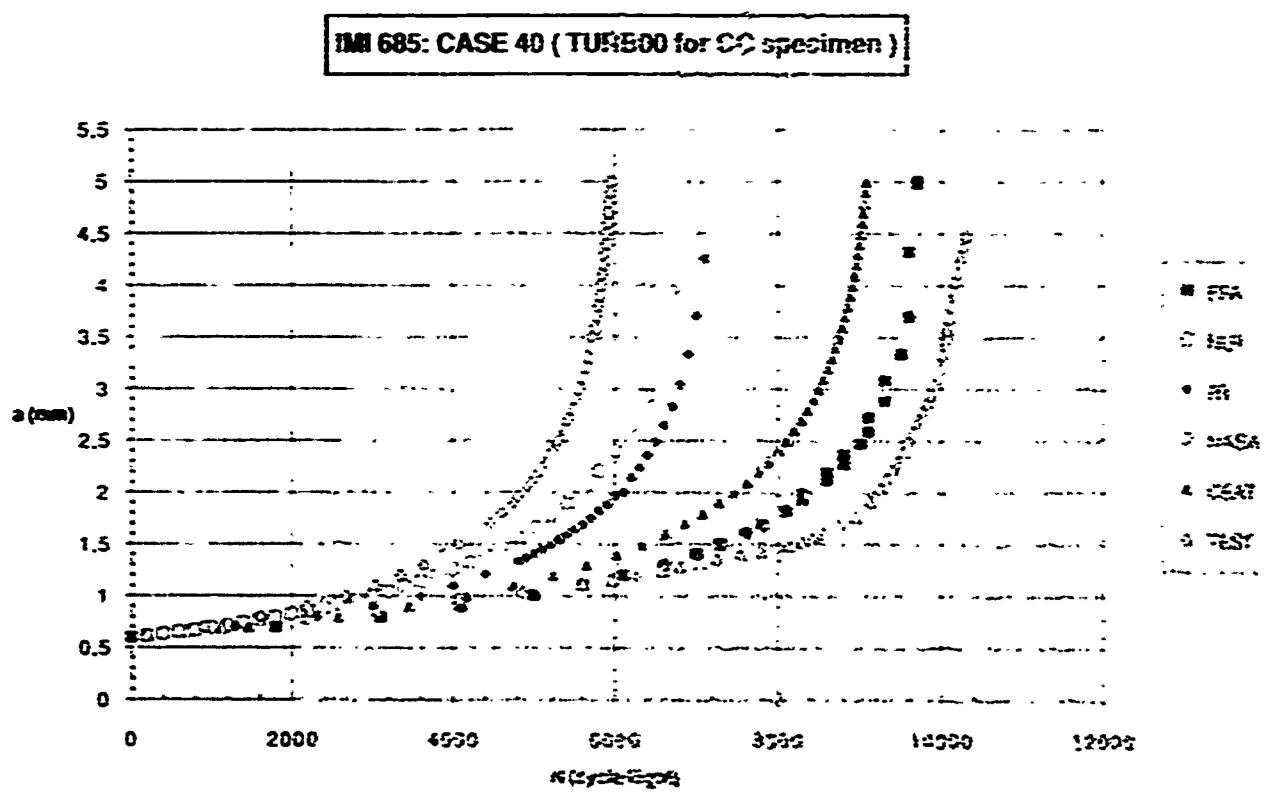

Fig.43 - IMI685 Case 40

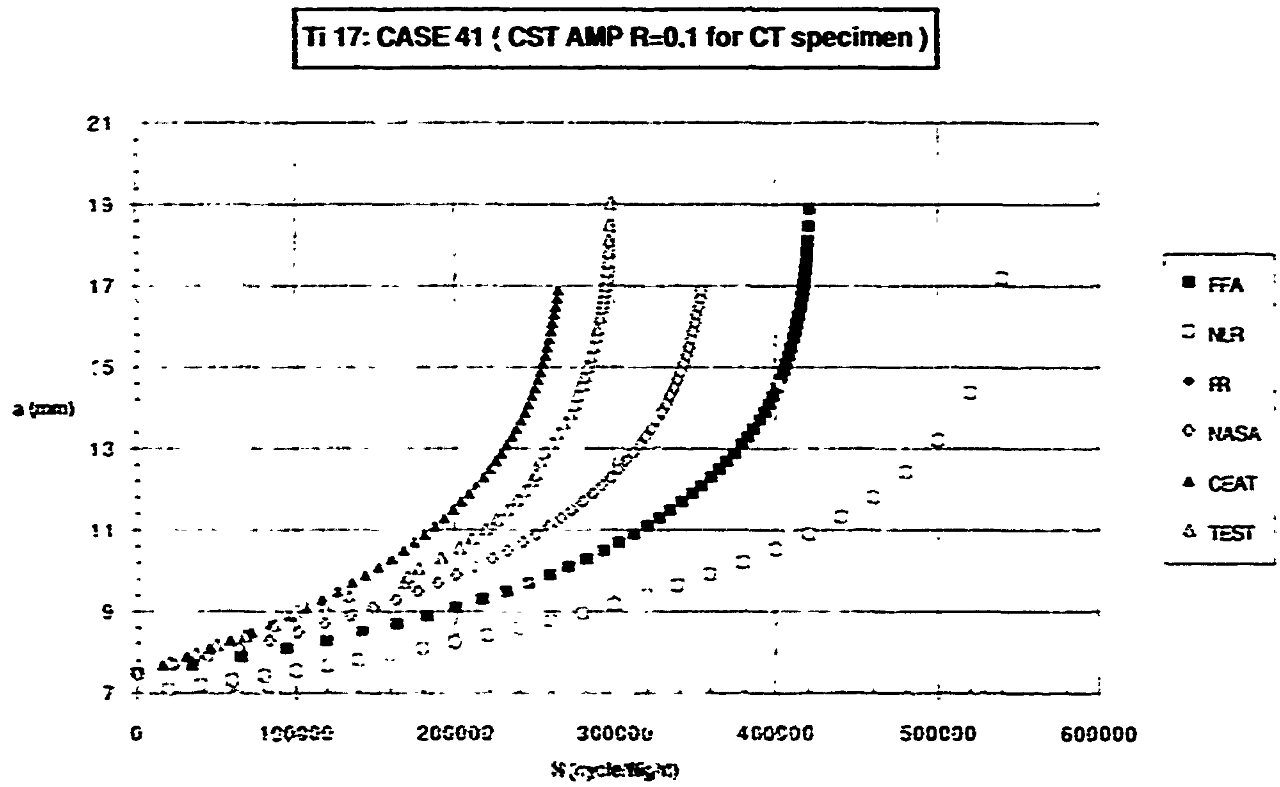

Fig.44 - Ti17 Case 41

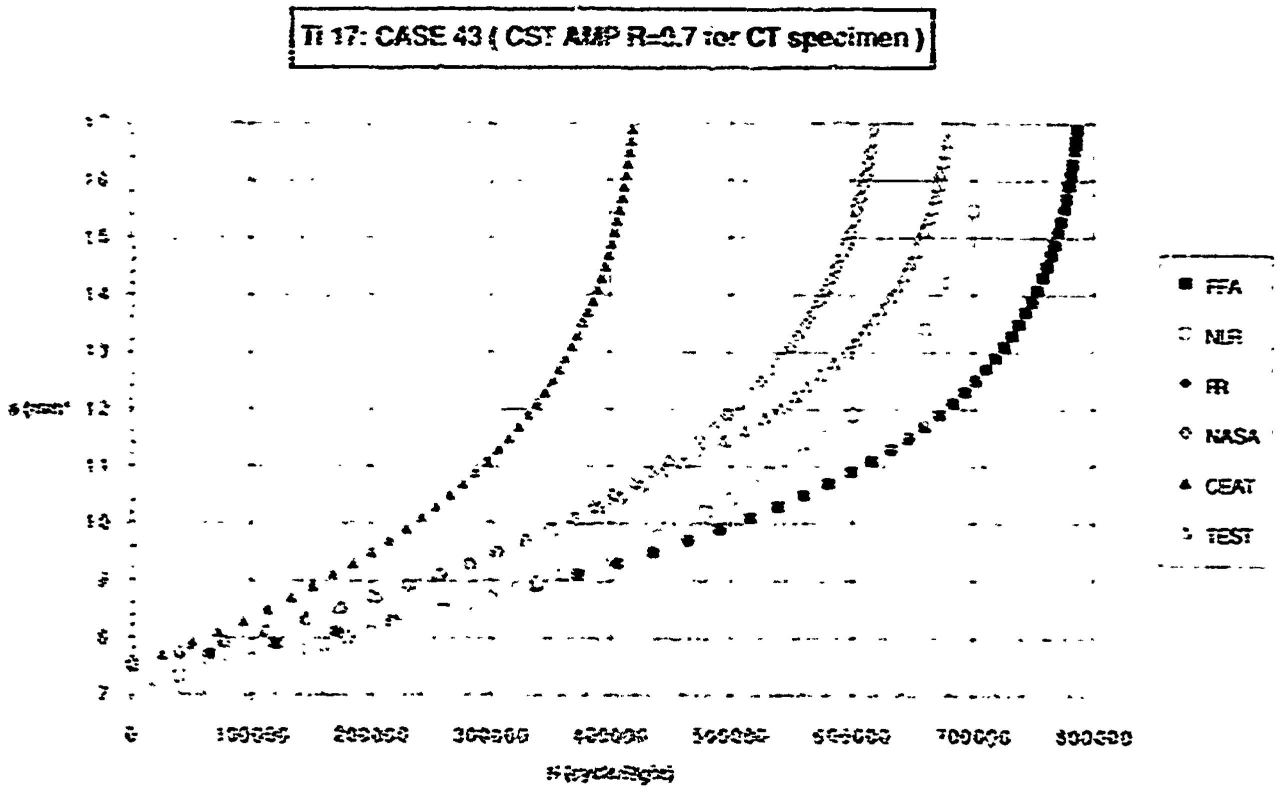

Fig.45 - Ti17 Case 43

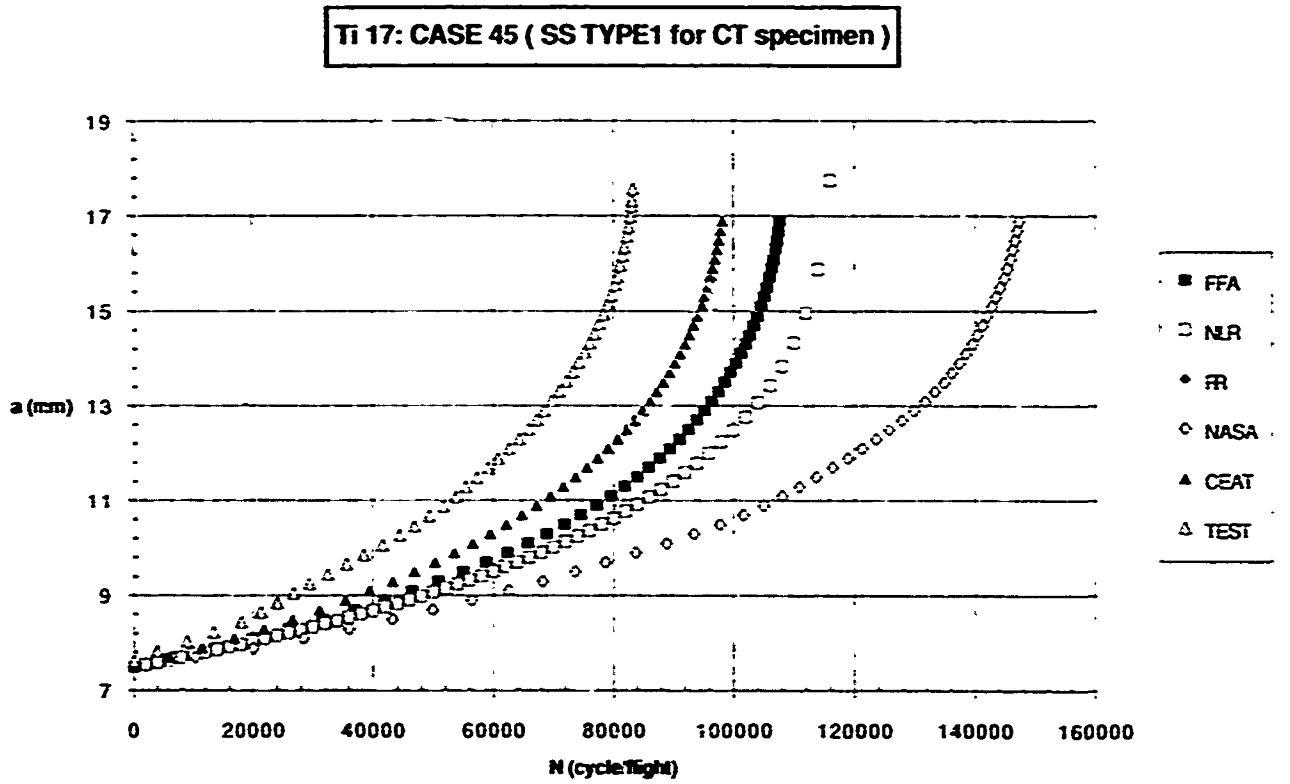

Fig.46 - Ti17 Case 45

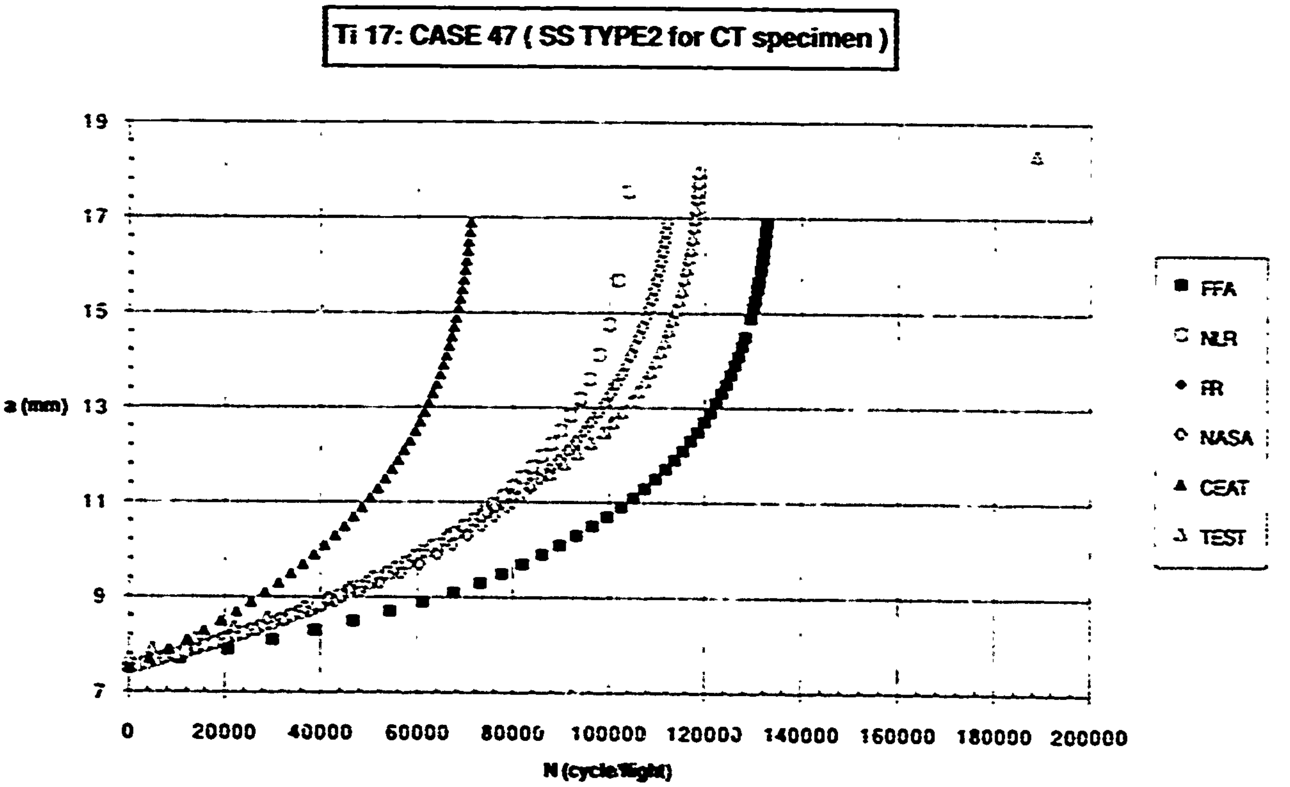

Fig.47 - Ti17 Case 47

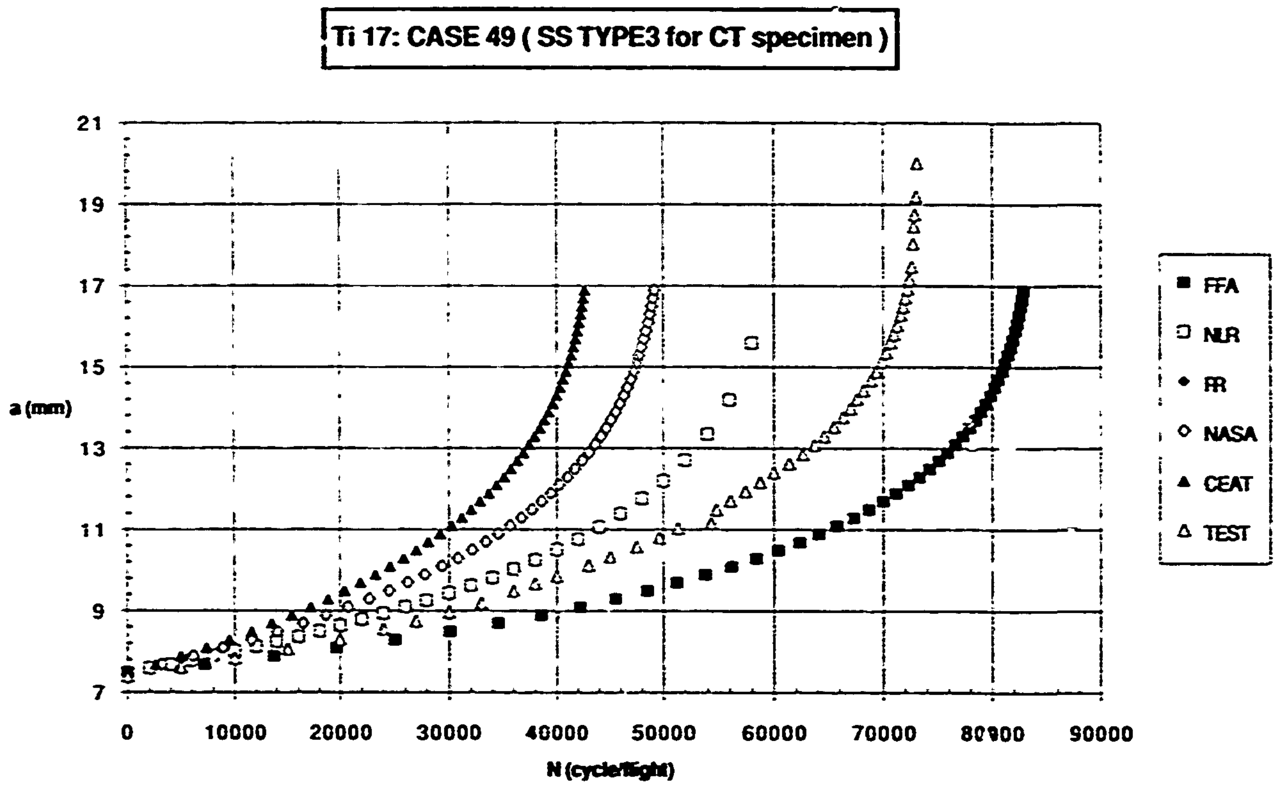

Fig.48 - Ti17 Case 49

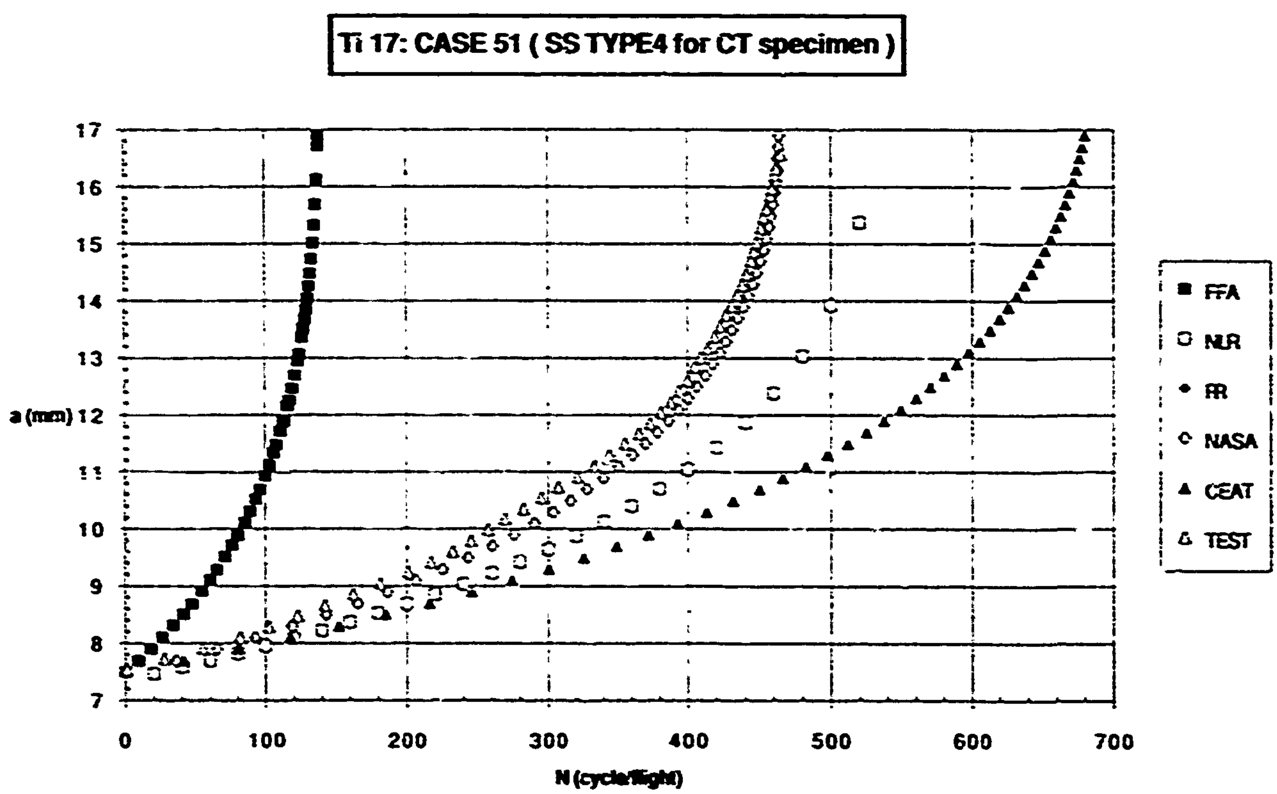

Fig.49 - Ti17 Case 51

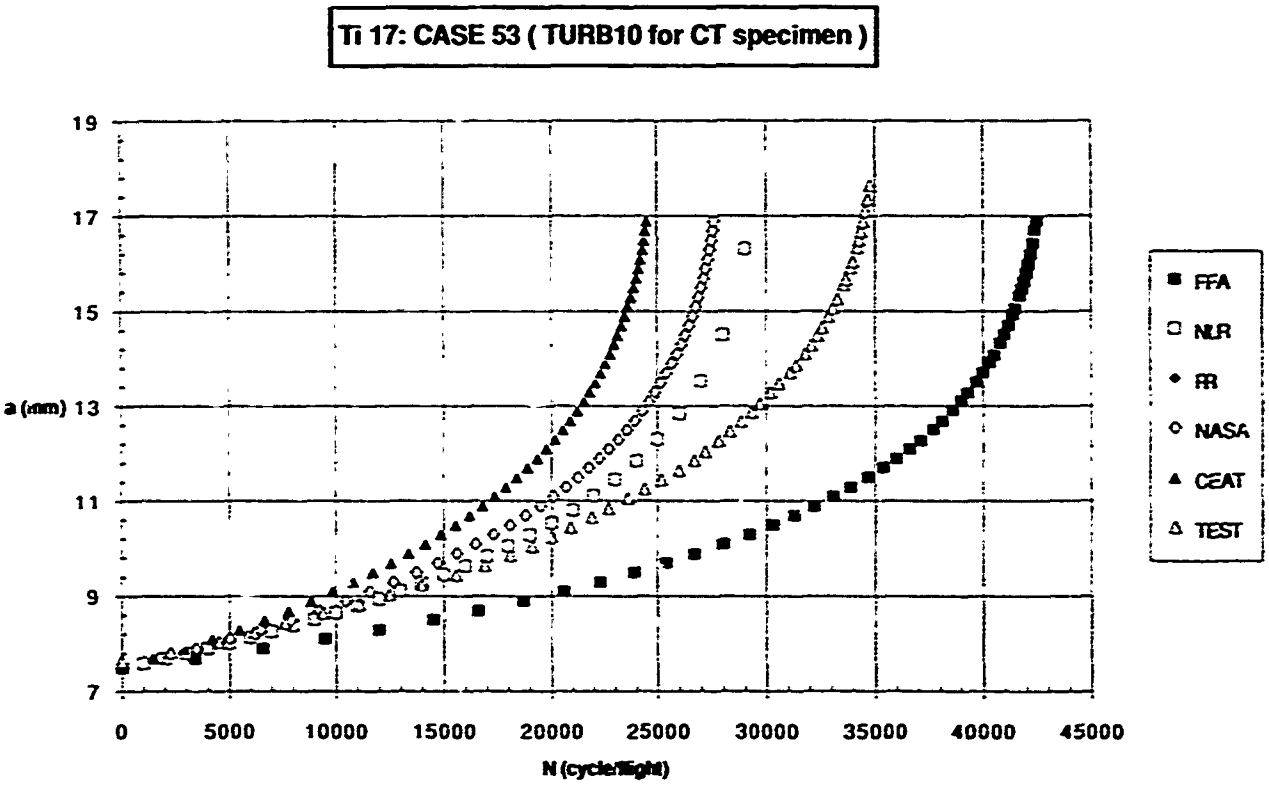

Fig.50 - Ti17 Case 53

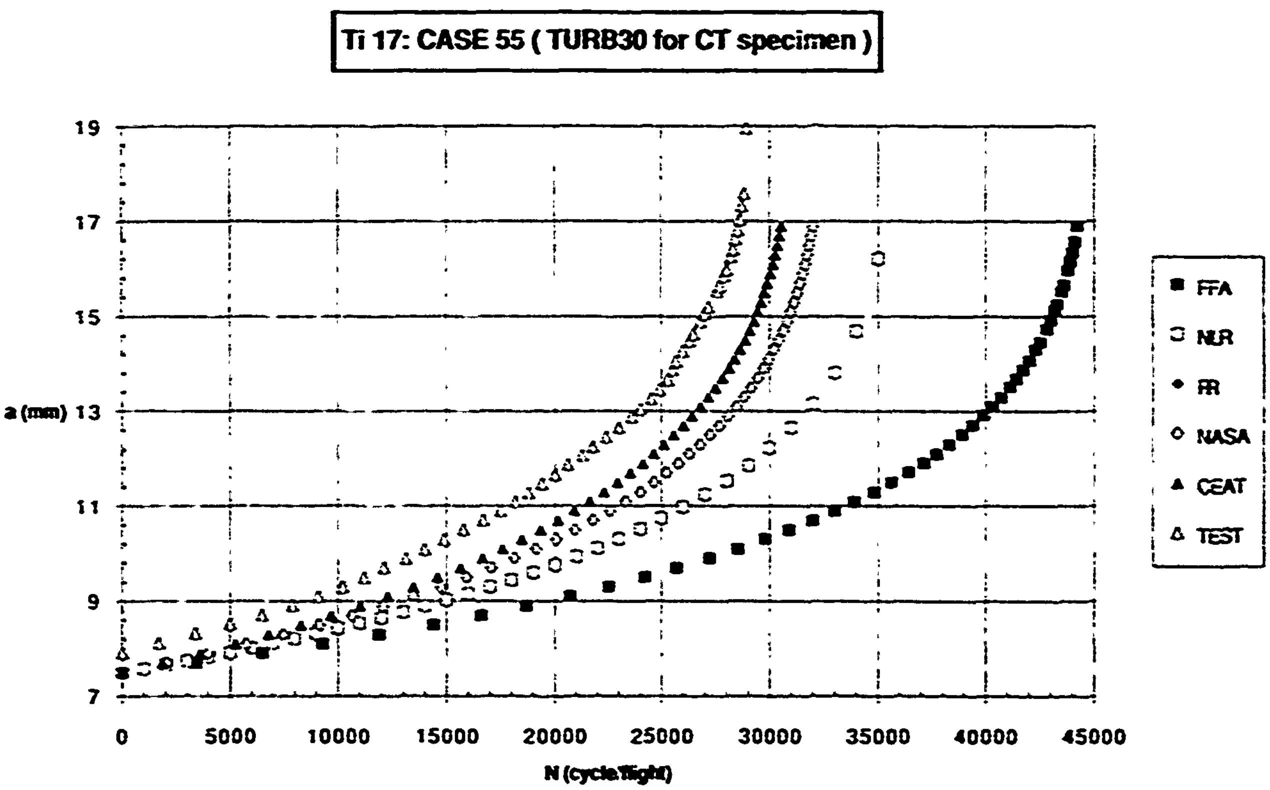

Fig.51 - Ti17 Case 55

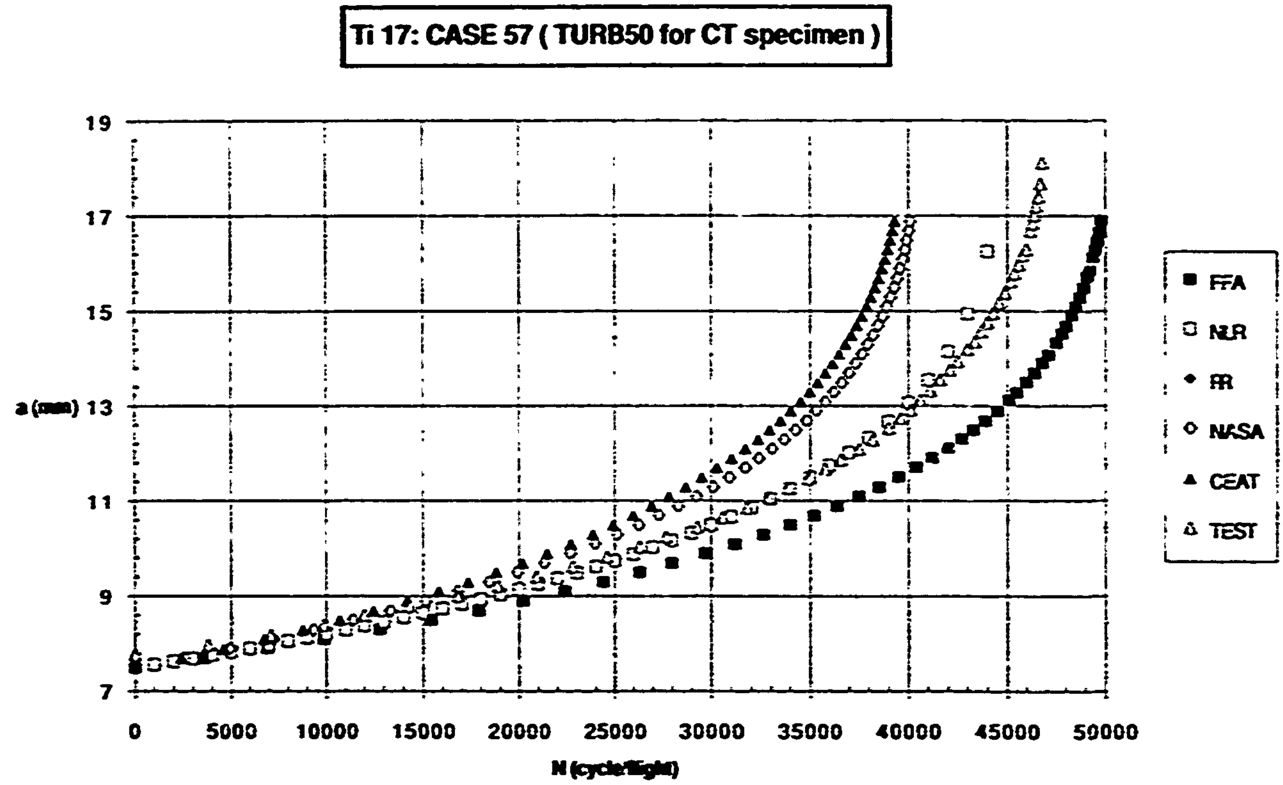

Fig.52 - Ti17 Case 57

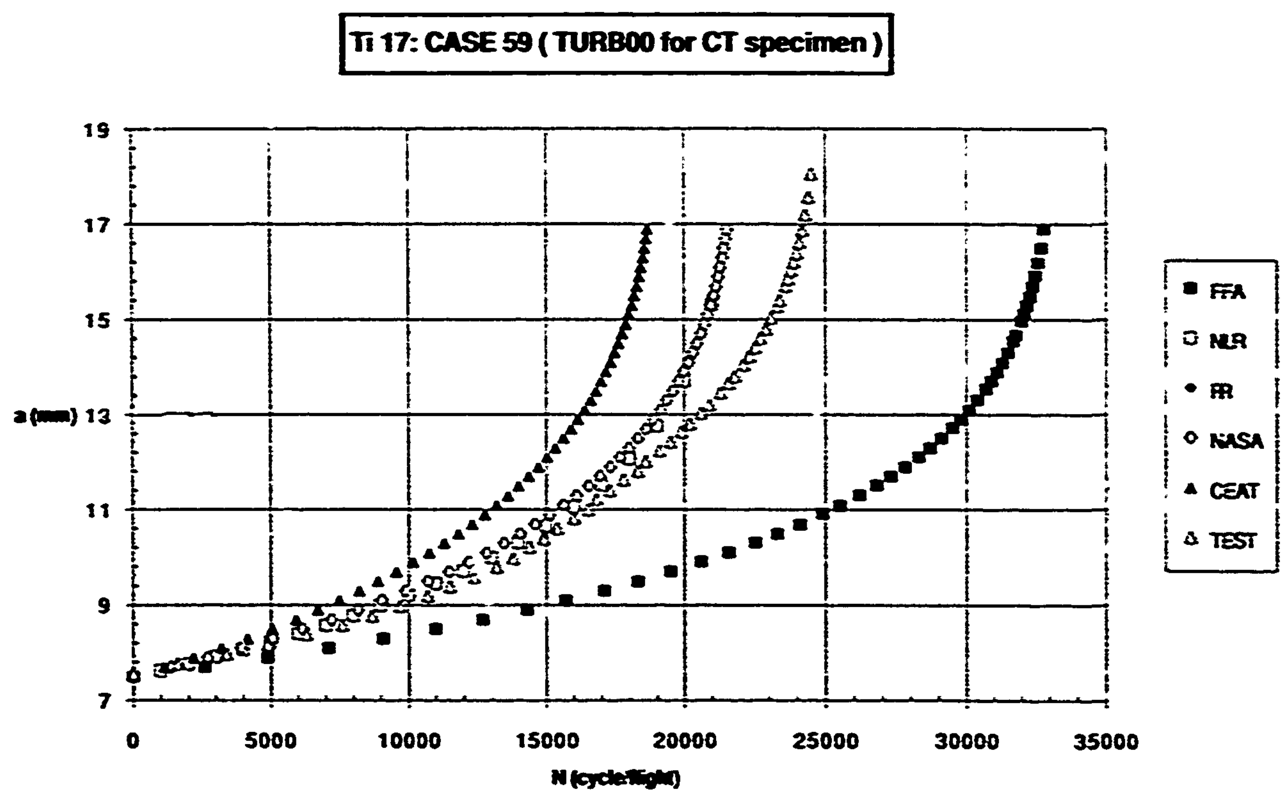

Fig.53 - Ti17 Case 59

Ti 17: CASE 42(CST AMP R=0,1 for CC specimen)

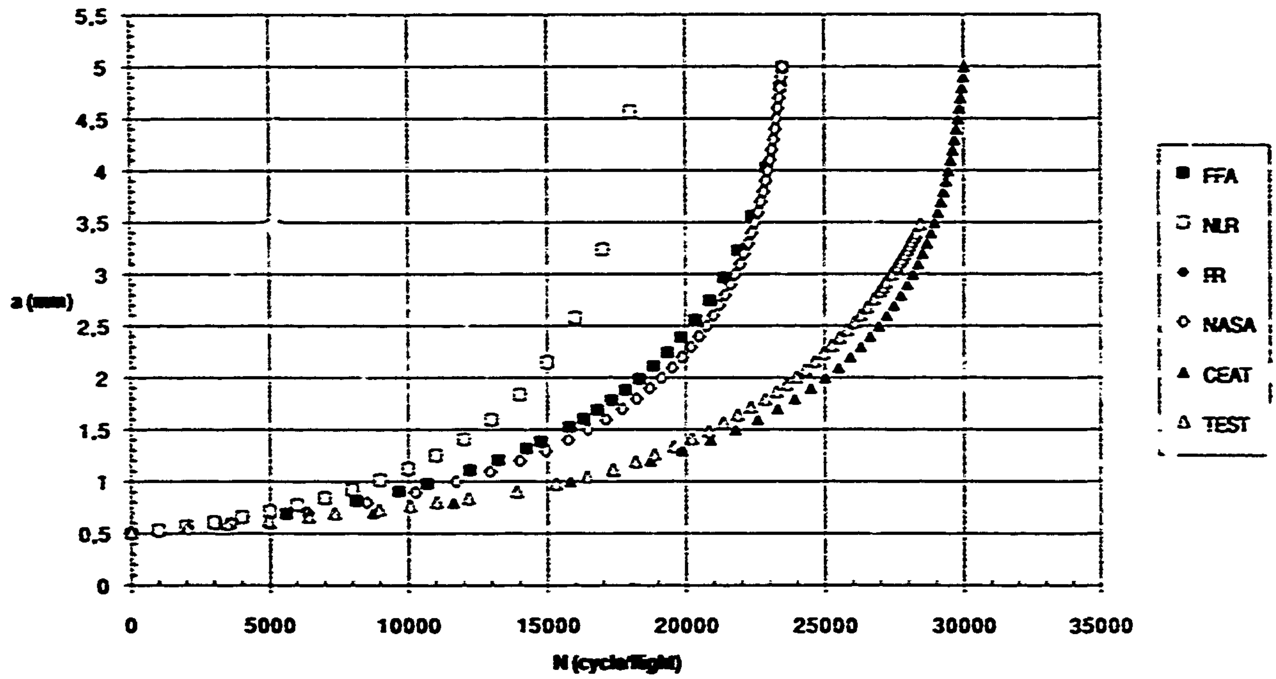

Fig.54 - Ti17 Case 42

Ti 17: CASE 44(CST AMP R=0.7 for CC specimen)

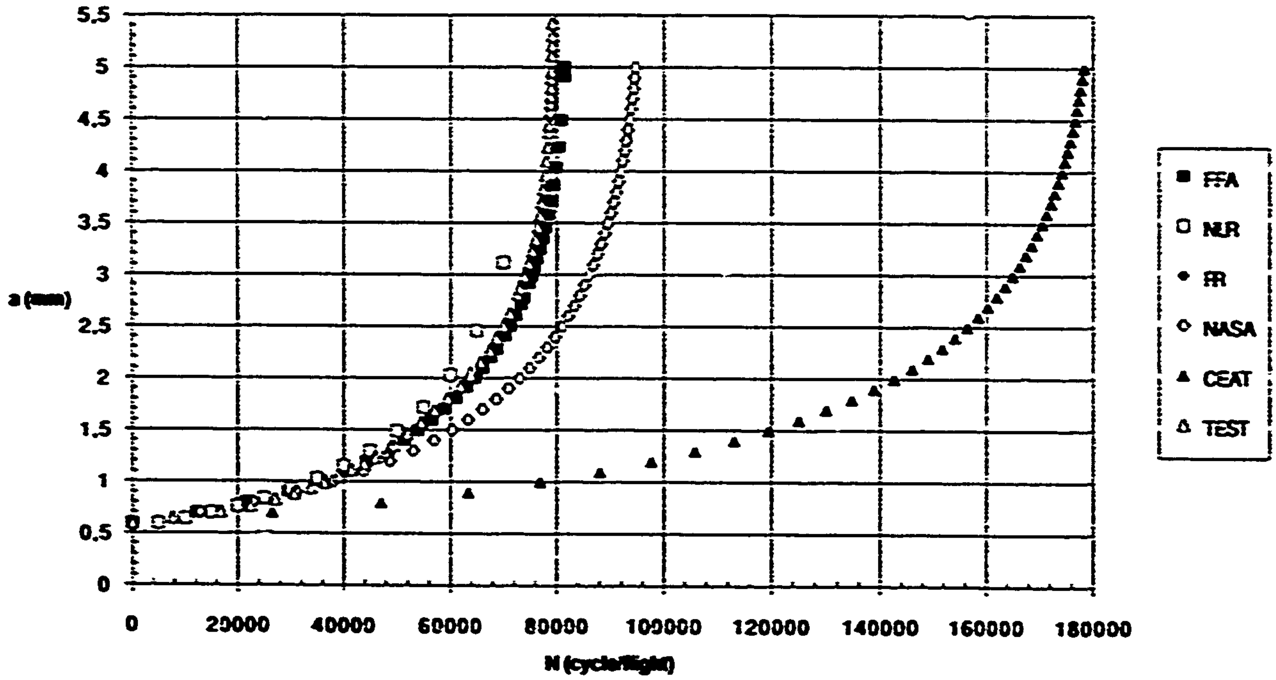

Fig.55 - Ti17 Case 44

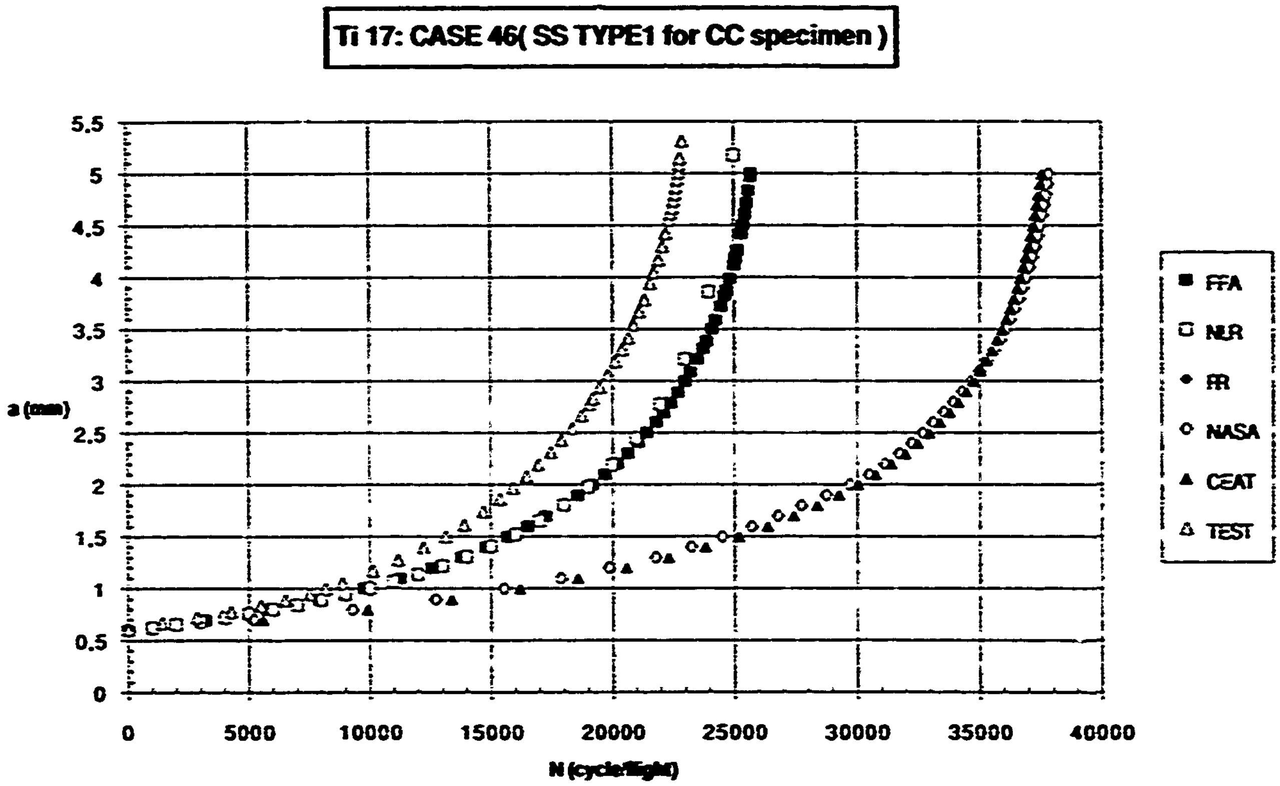

Fig.56 - Ti17 Case 46

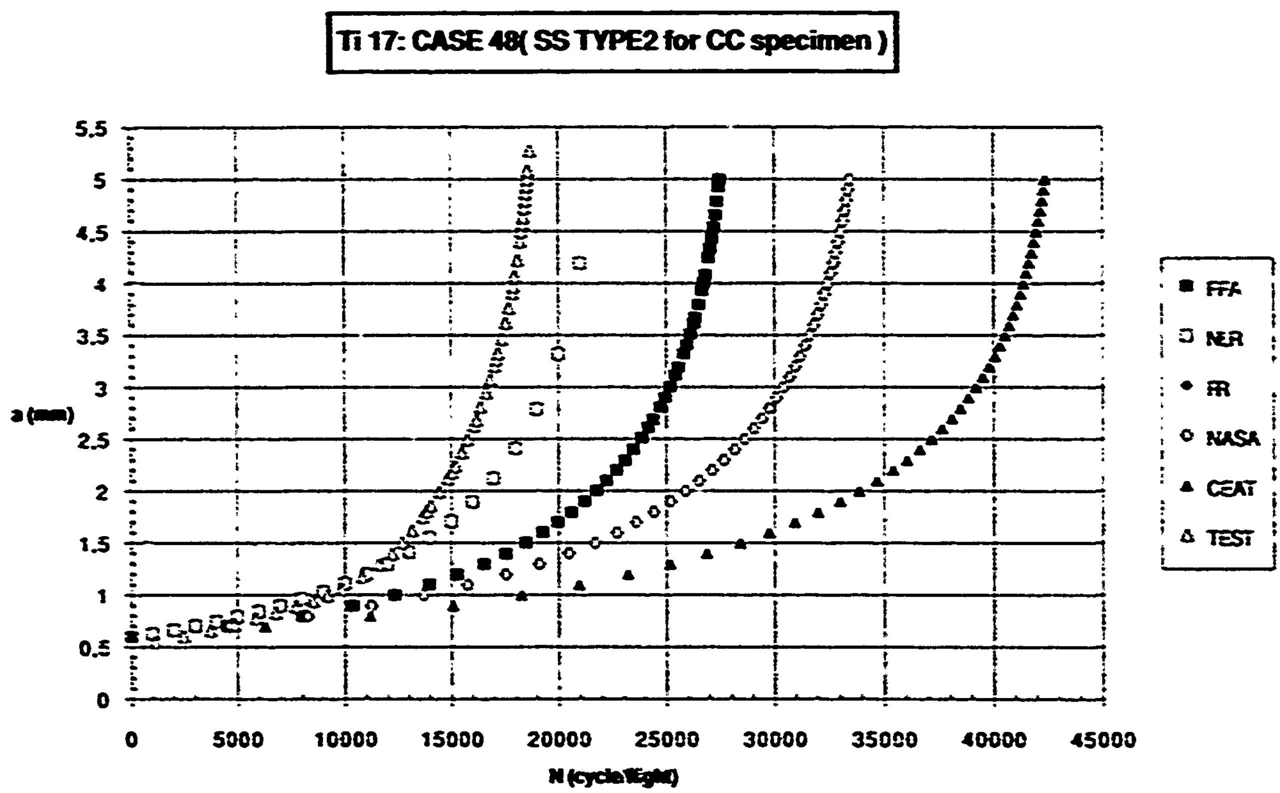

Fig.57 - Ti17 Case 48

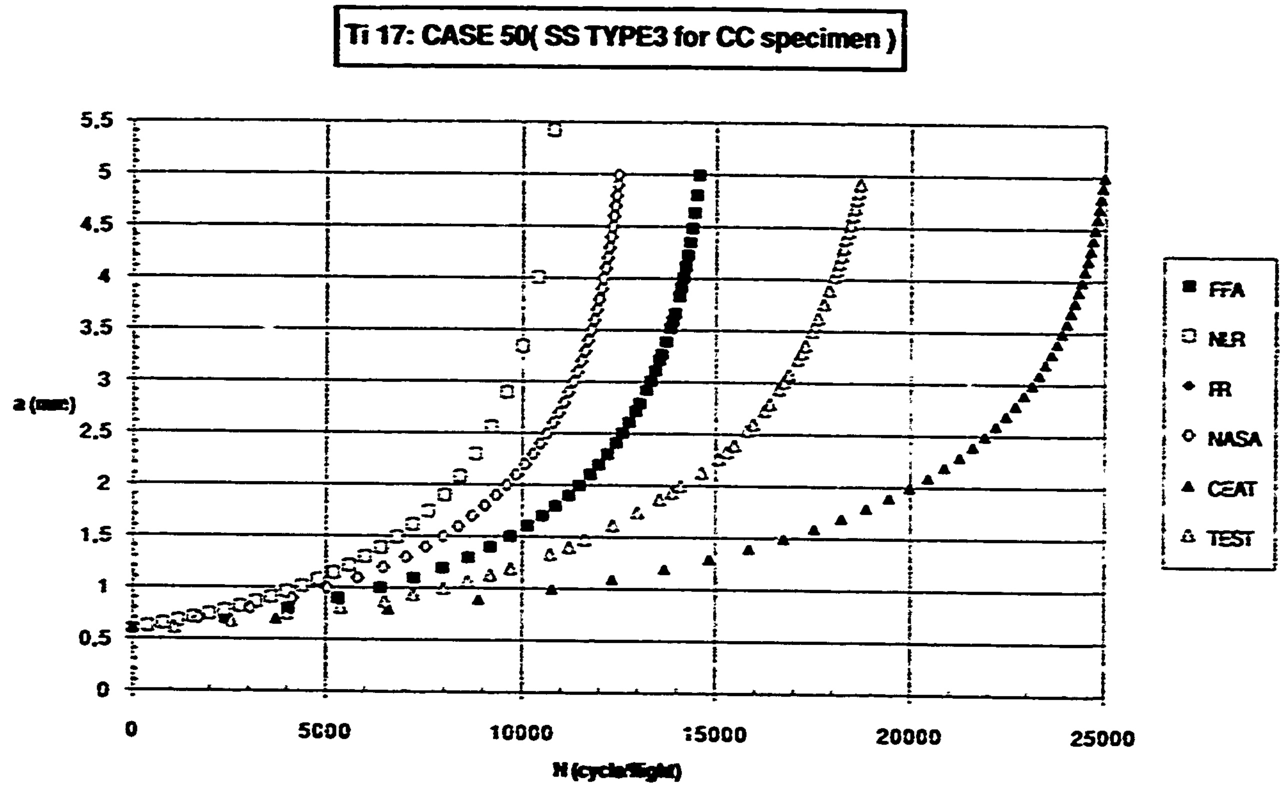

Fig.58 - Ti17 Case 50

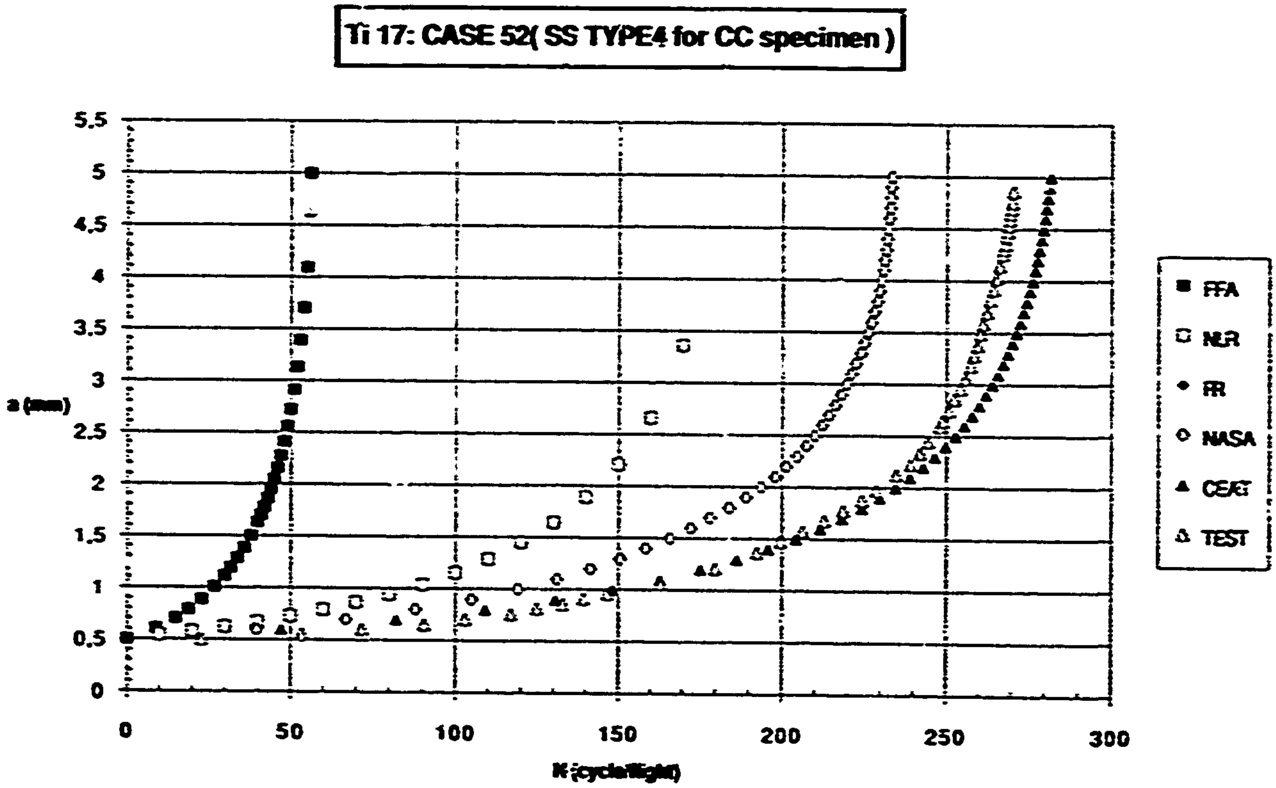

Fig.59 - Ti17 Case 52

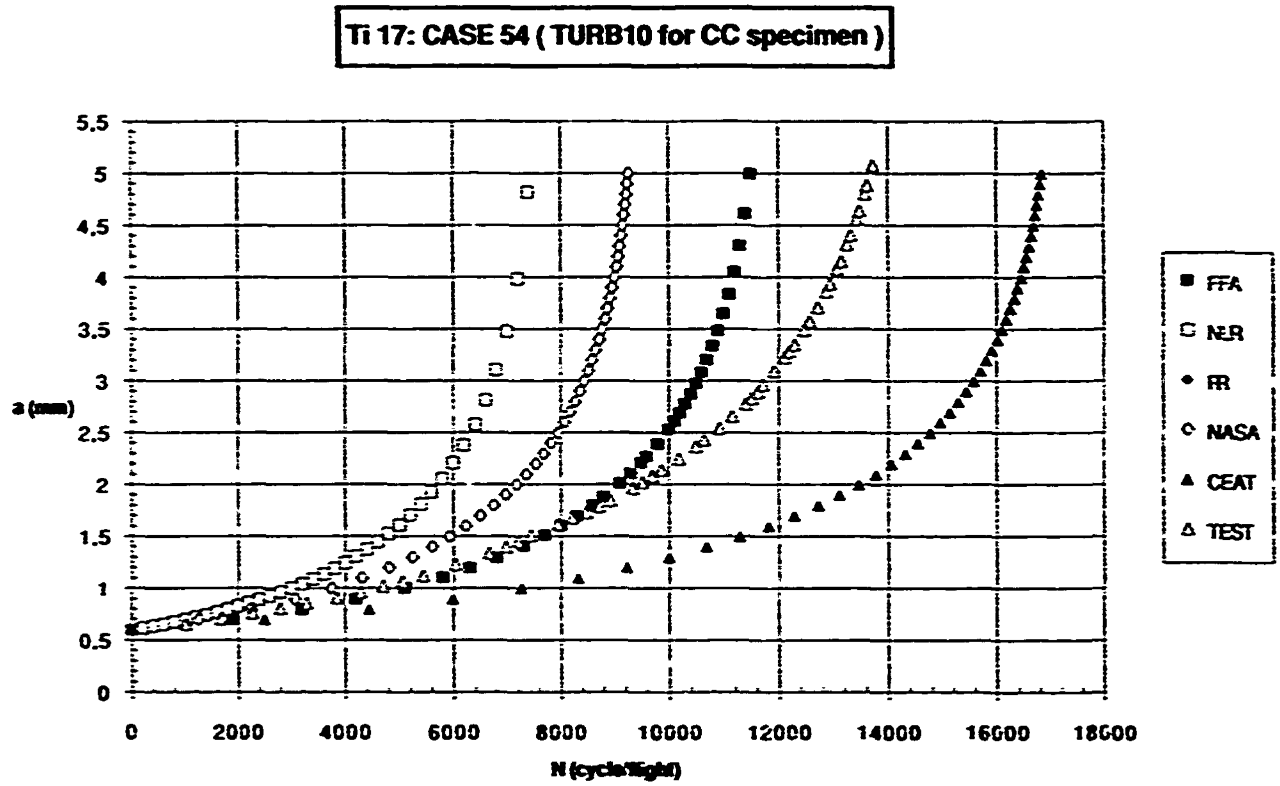

Fig.60 - Ti17 Case 54

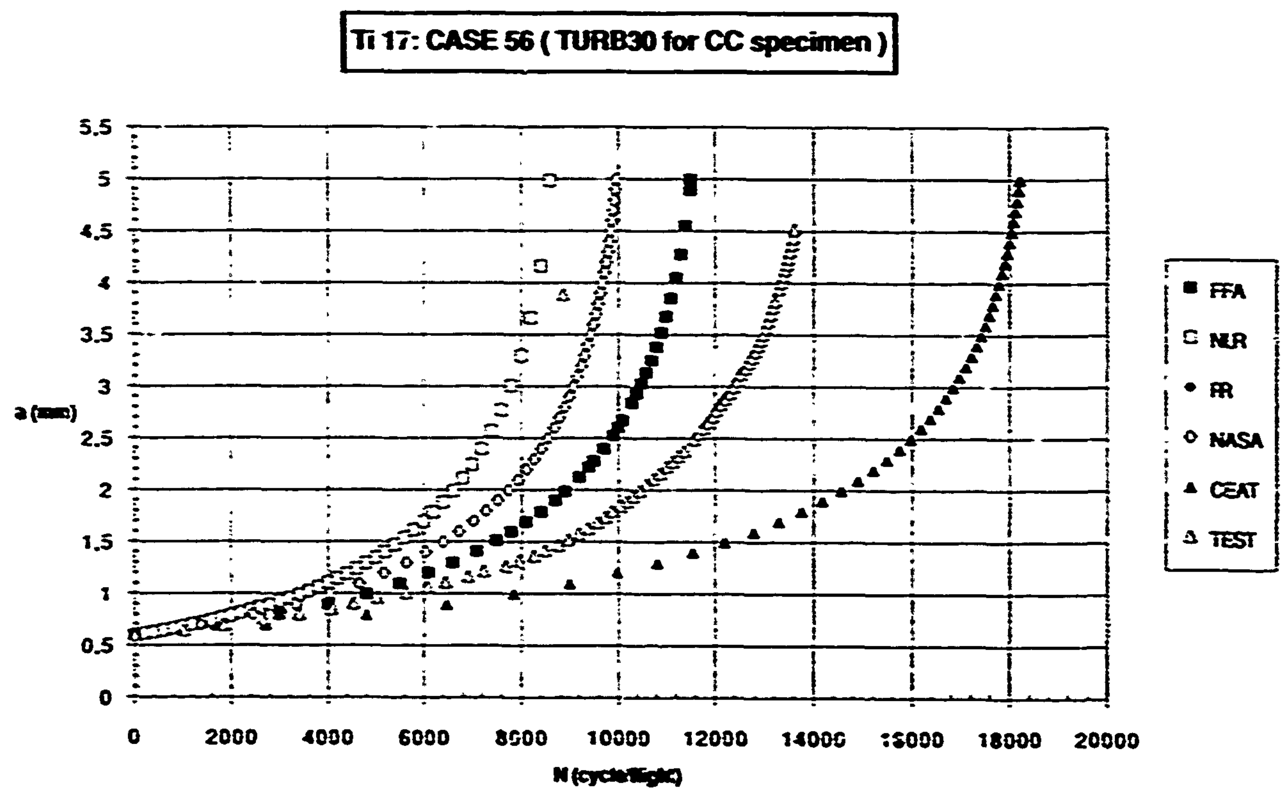

Fig.61 - Ti17 Case 56

Ti 17: CASE 58 (TURB50 for CC specimen)

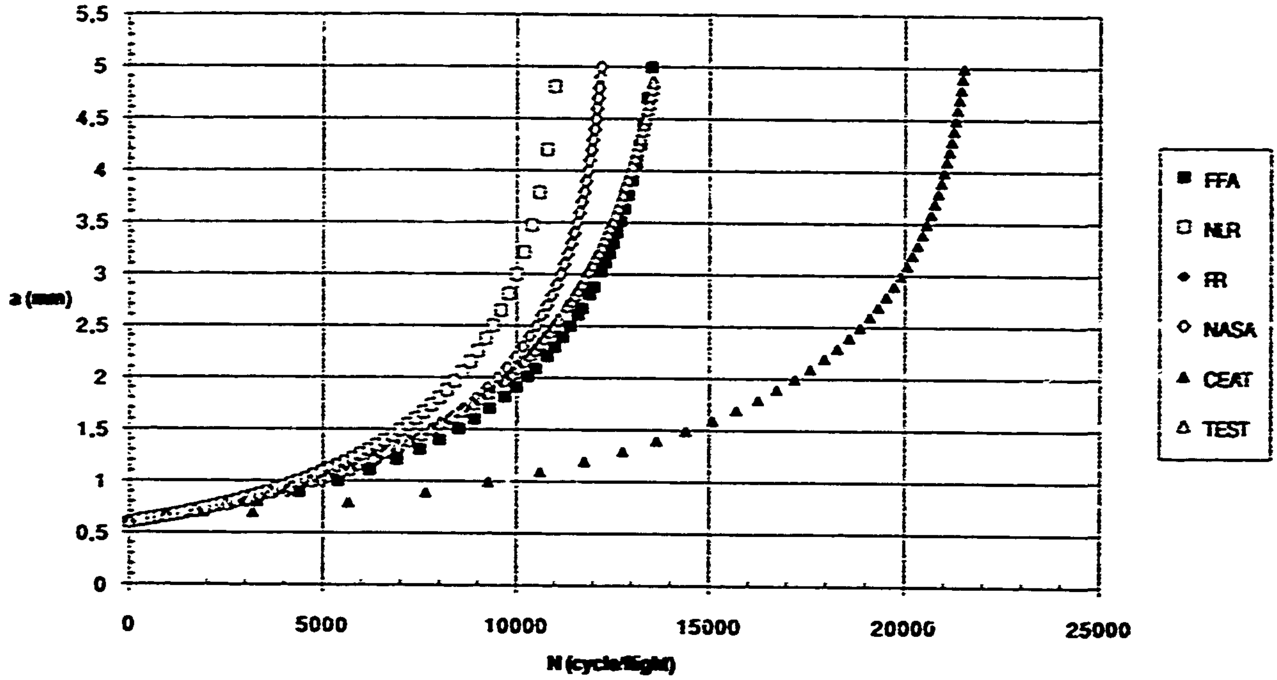

Fig.62 - Ti17 Case 58

Ti 17: CASE 60 (TURB00 for CC specimen)

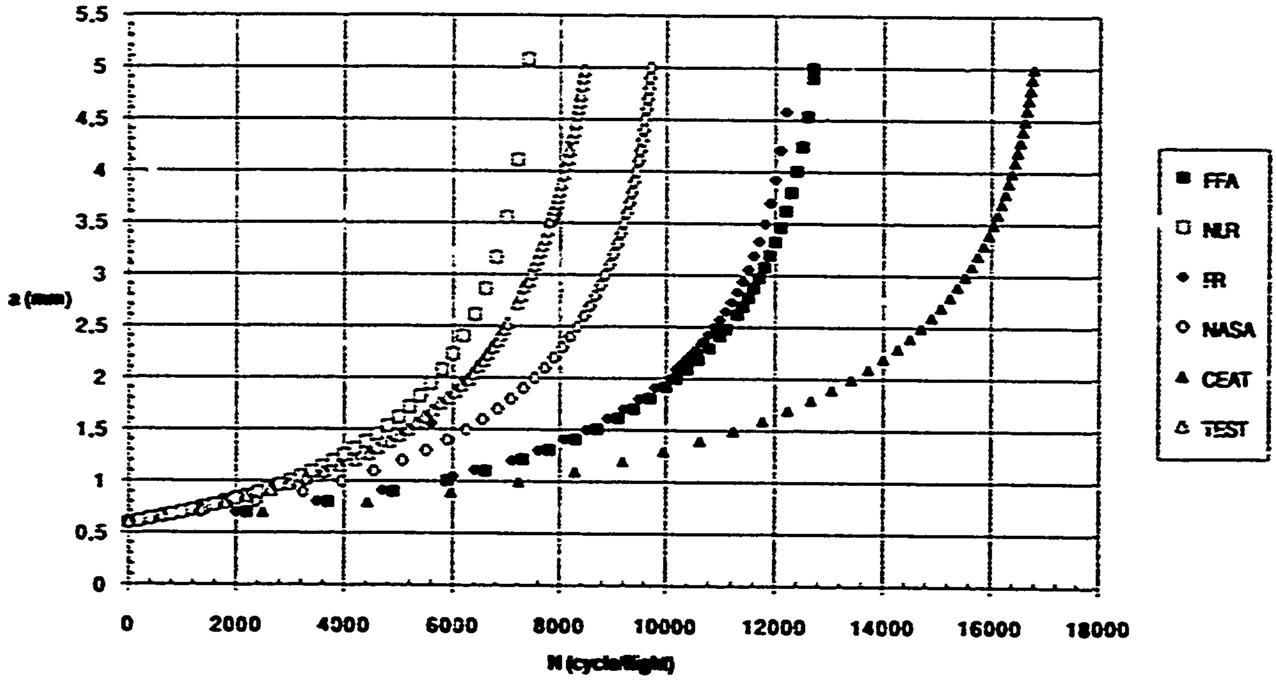

Fig.63 - Ti17 Case 60

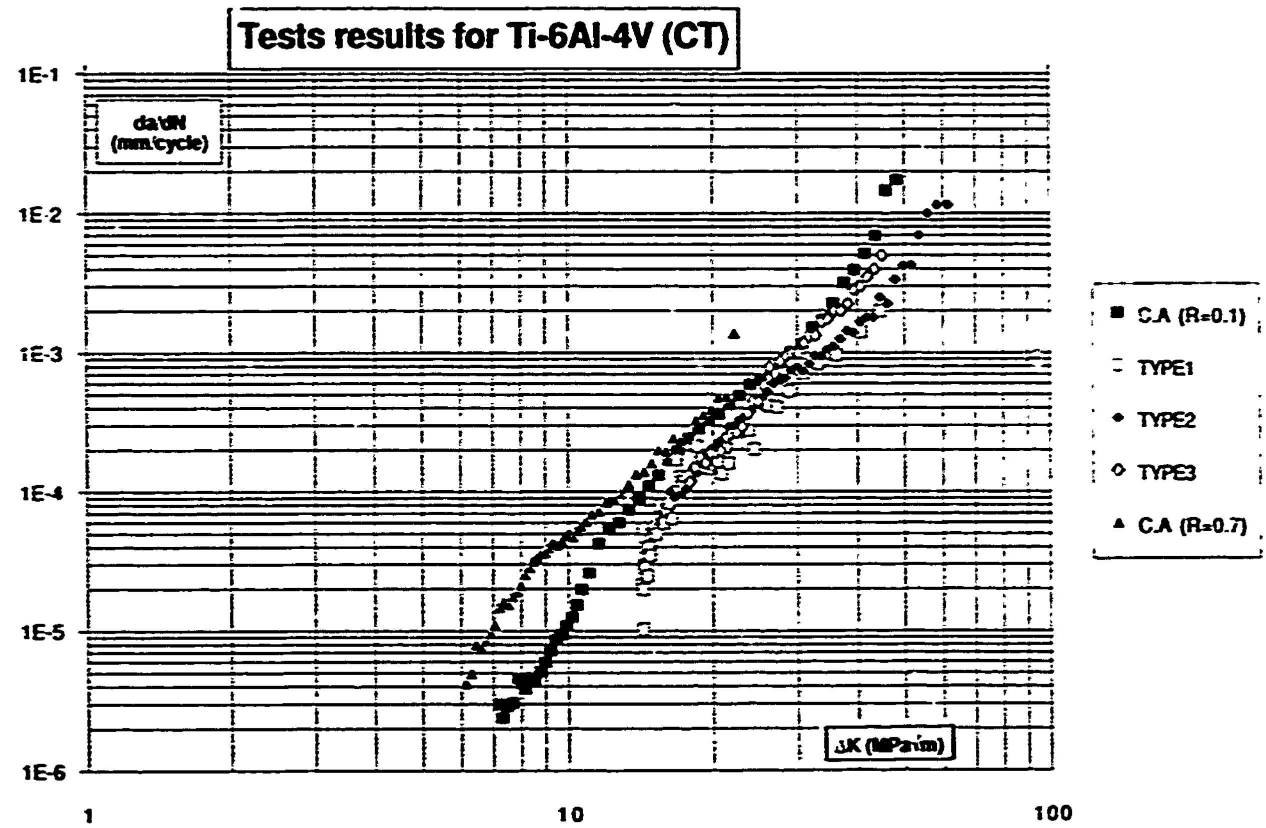

Fig.64 - da/dN vs ΔK Ti-6Al-4V / CT test results

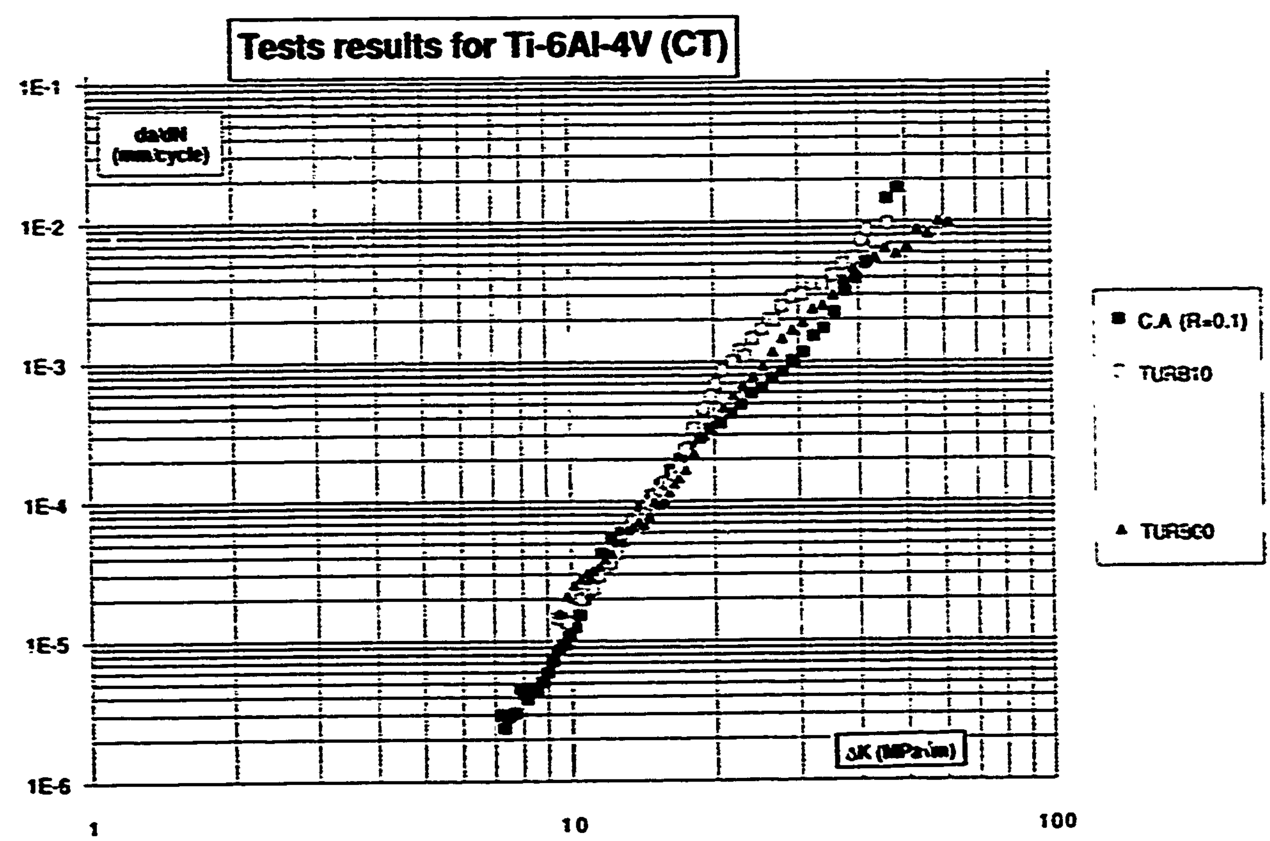

Fig.65 - da/dN vs ΔK Ti-6Al-4V / CT test results

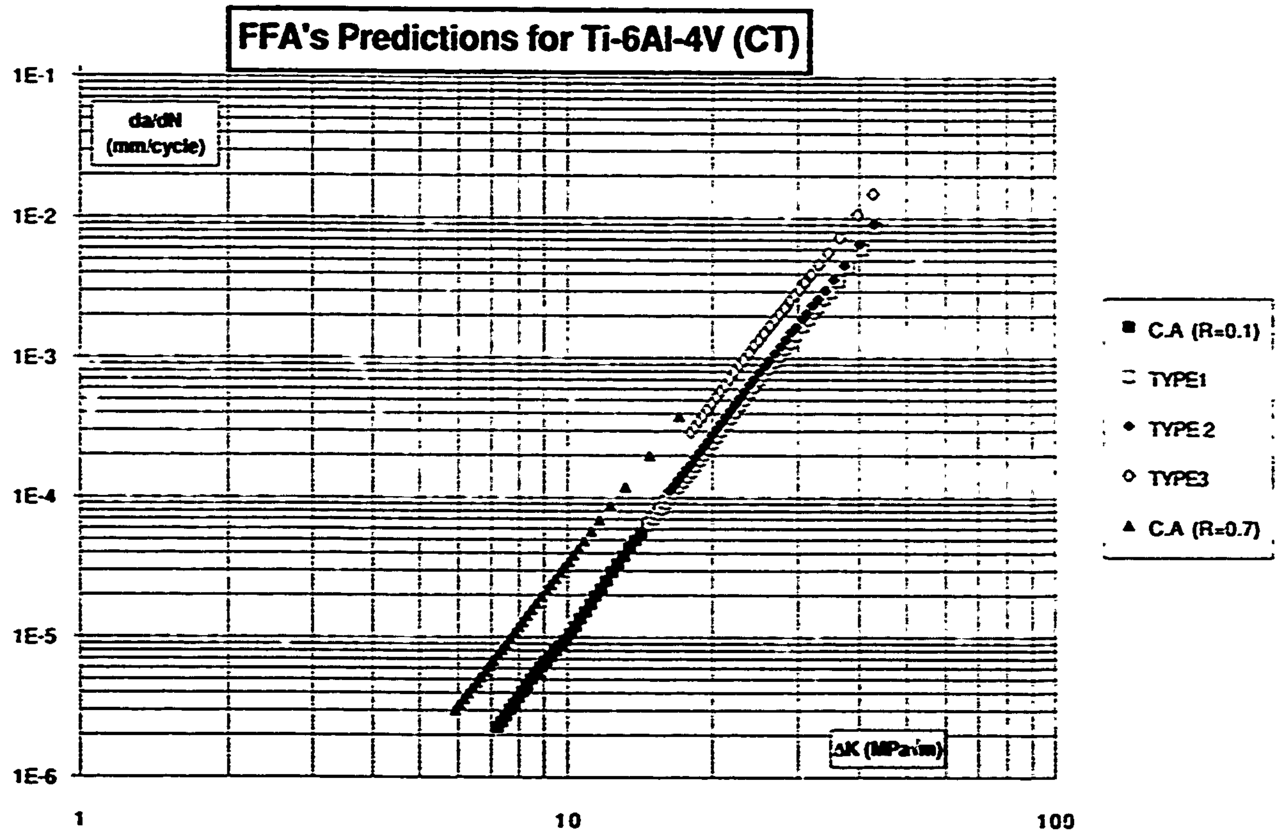

Fig.66 - da/dN vs ΔK Ti-6Al-4V / CT FFA predictions

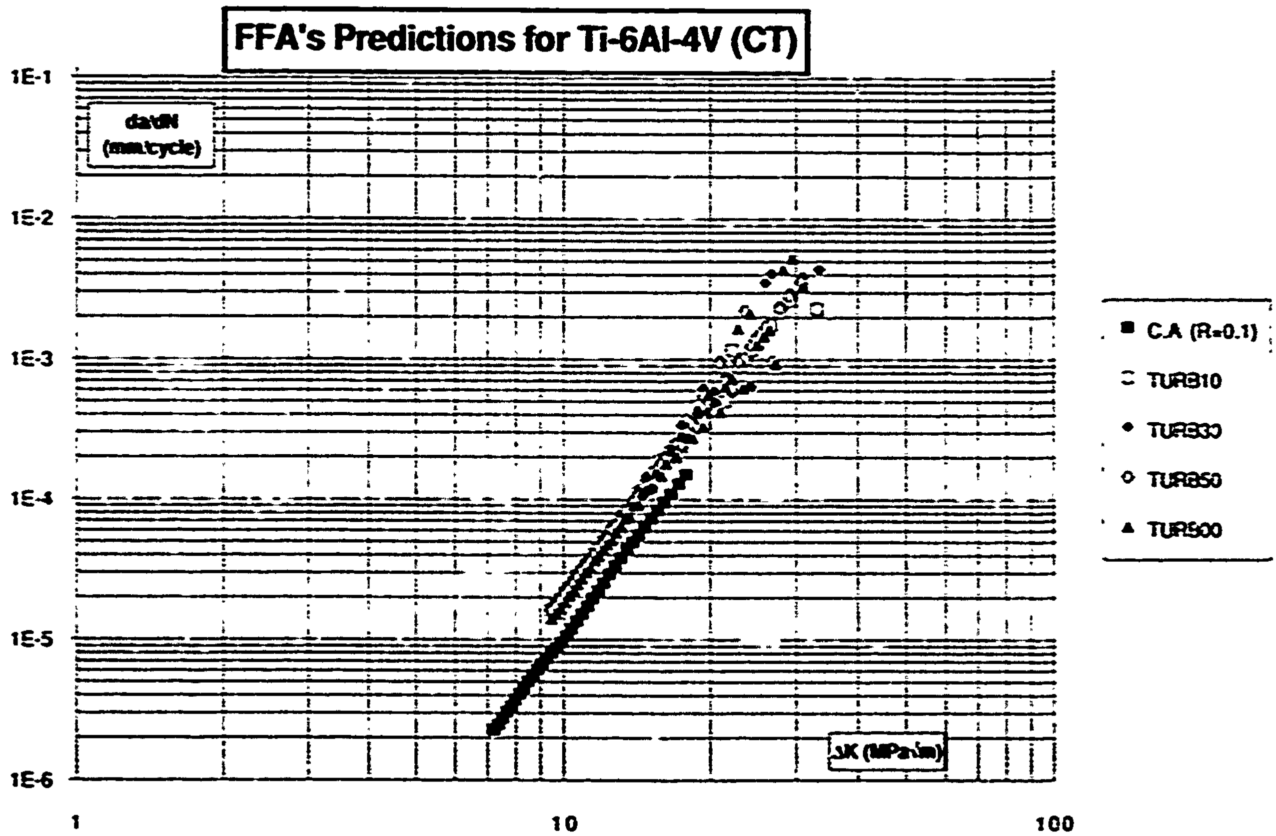

Fig.67 - da/dN vs ΔK Ti-6Al-4V / CT FFA predictions

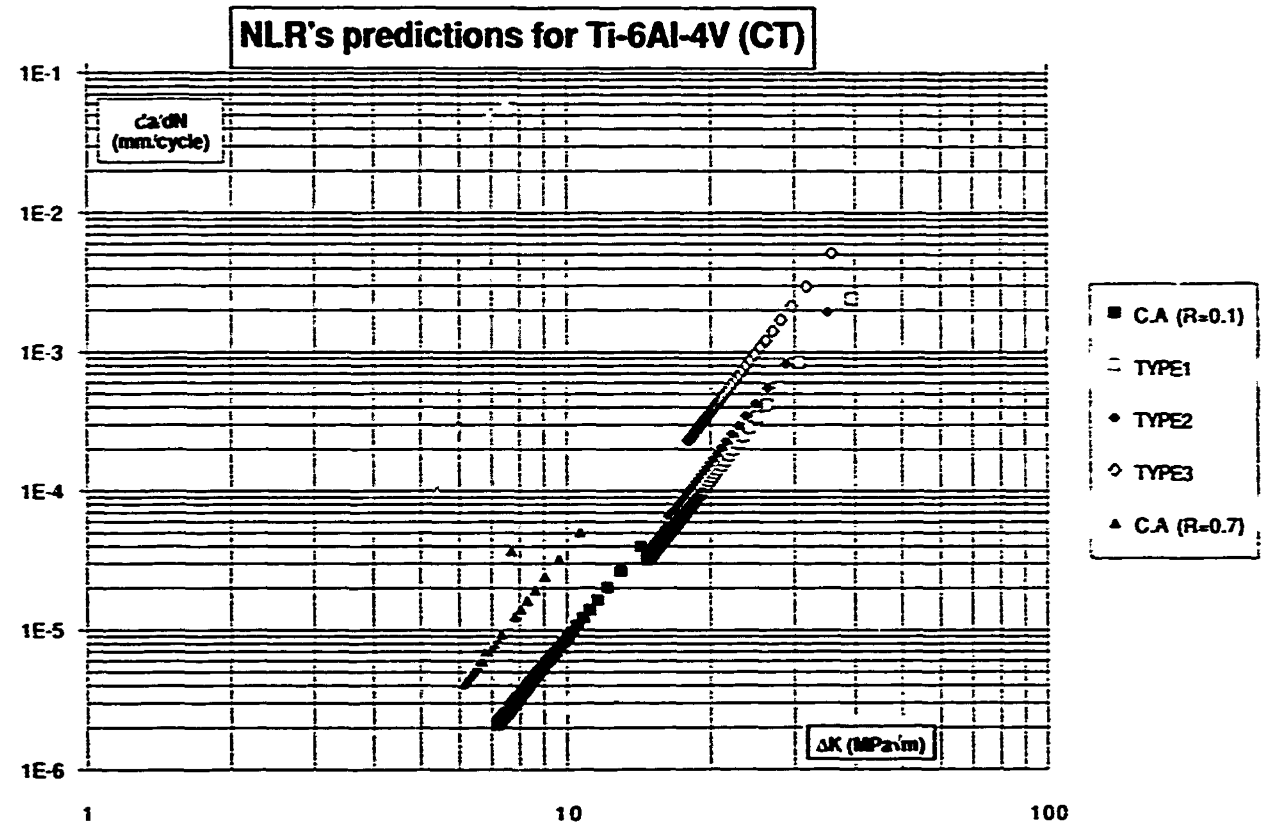

Fig.68 - da/dN vs ΔK Ti-6Al-4V / CT NLR predictions

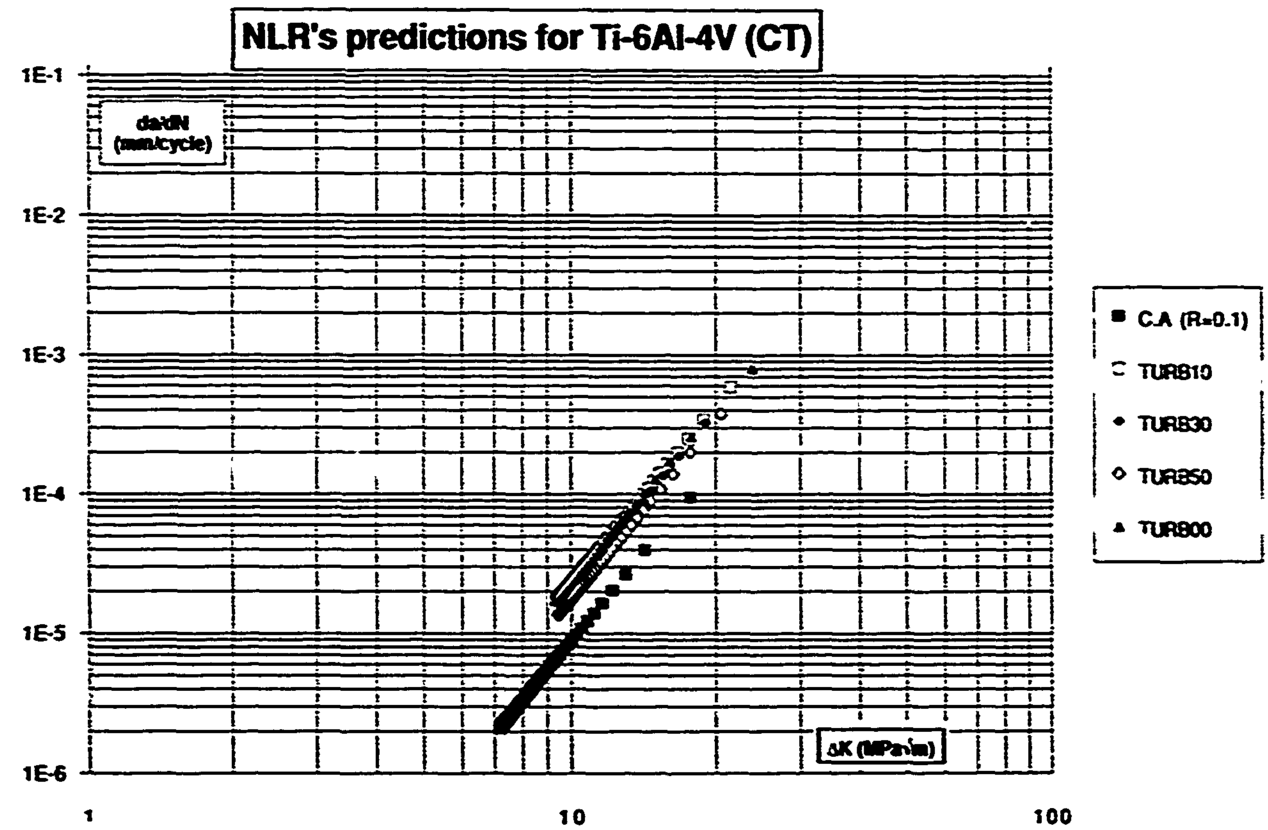

Fig.69 - da/dN vs ΔK Ti-6Al-4V / CT NLR predictions

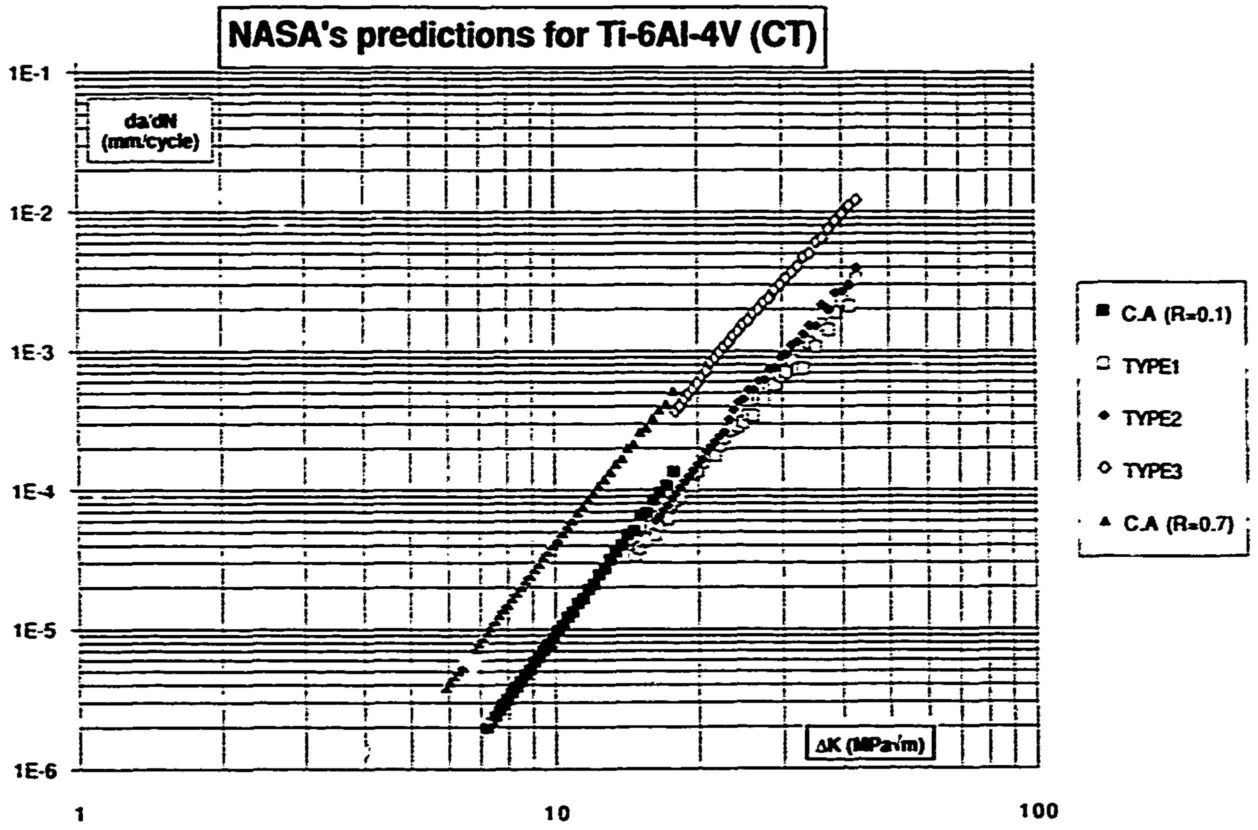

Fig.70 - da/dN vs ΔK Ti-6Al-4V / CT NASA predictions

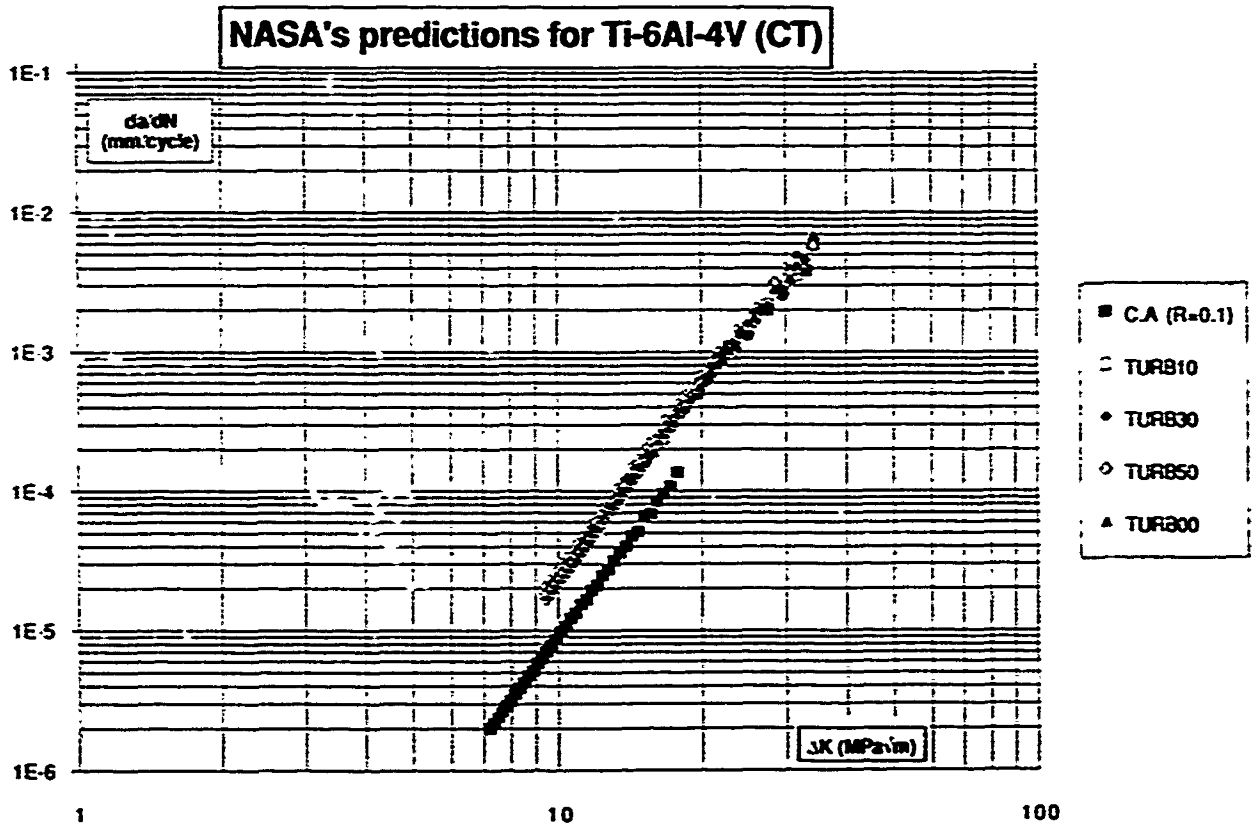

Fig.71 - da/dN vs ΔK Ti-6Al-4V / CT NASA predictions

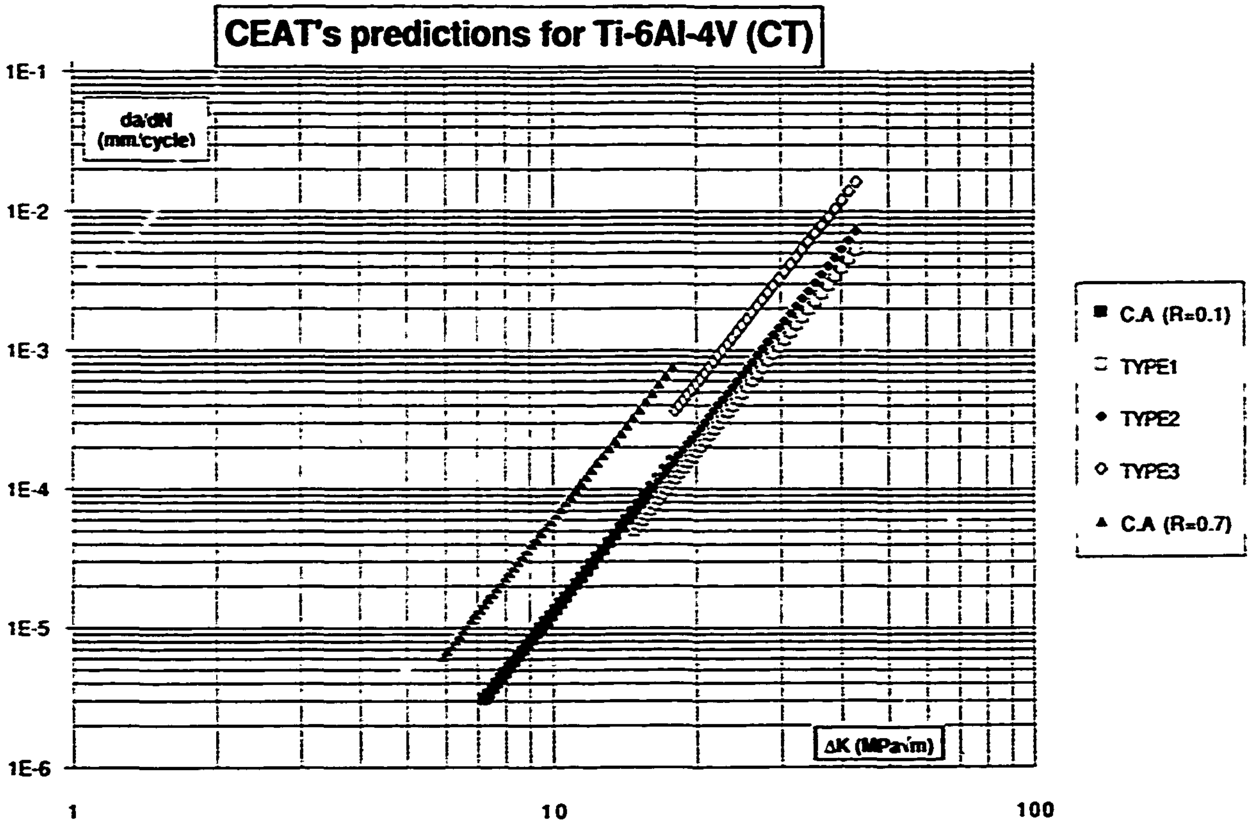

Fig.72 - da/dN vs ΔK Ti-6Al-4V / CT CEAT predictions

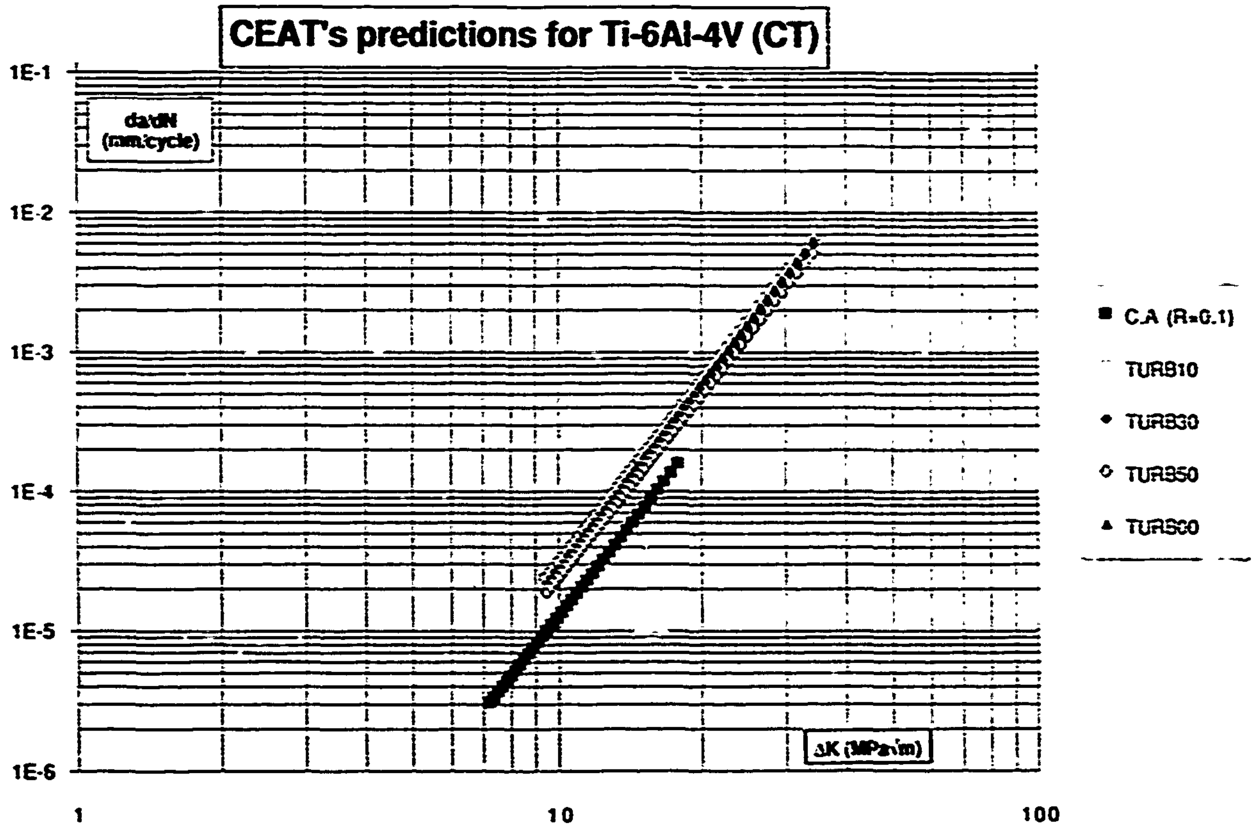

Fig.73 - da/dN vs ΔK Ti-6Al-4V / CT CEAT predictions

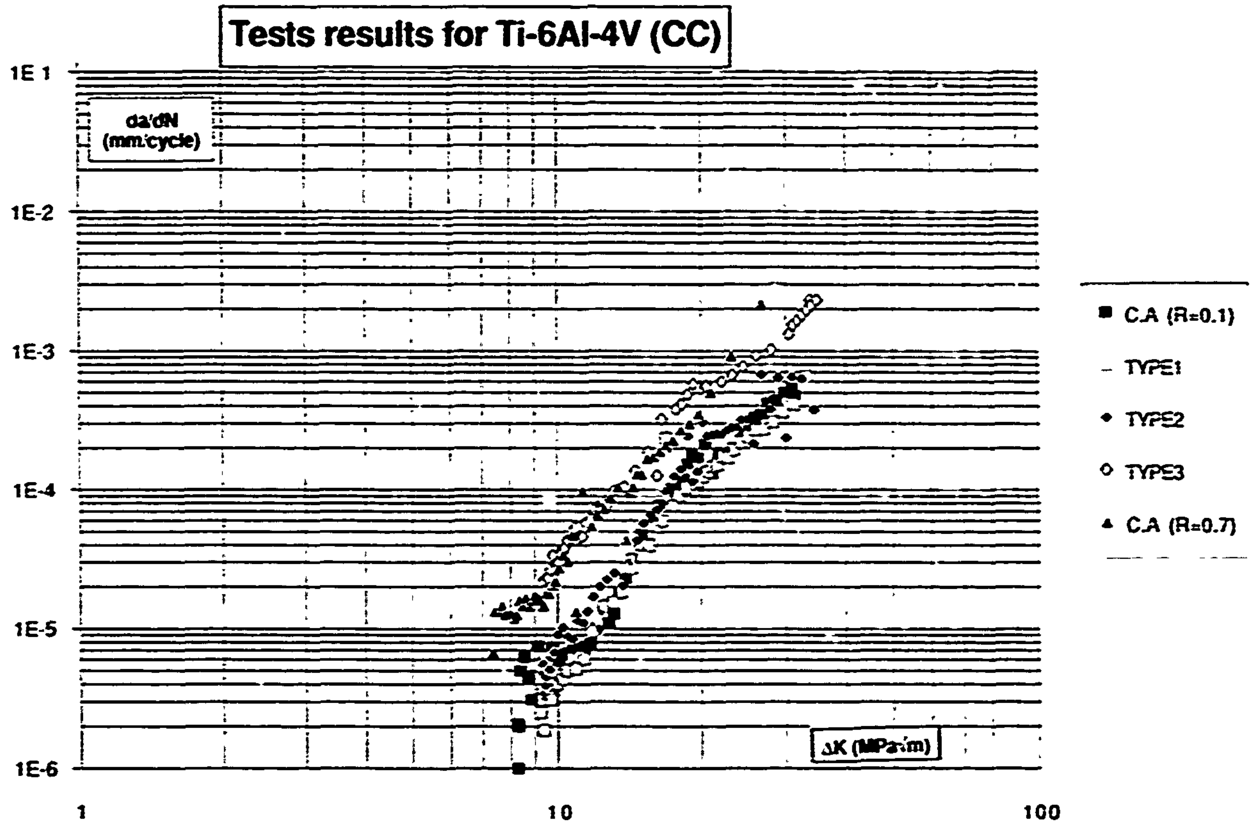

Fig.74 - da/dN vs ΔK Ti-6Al-4V / CC test results

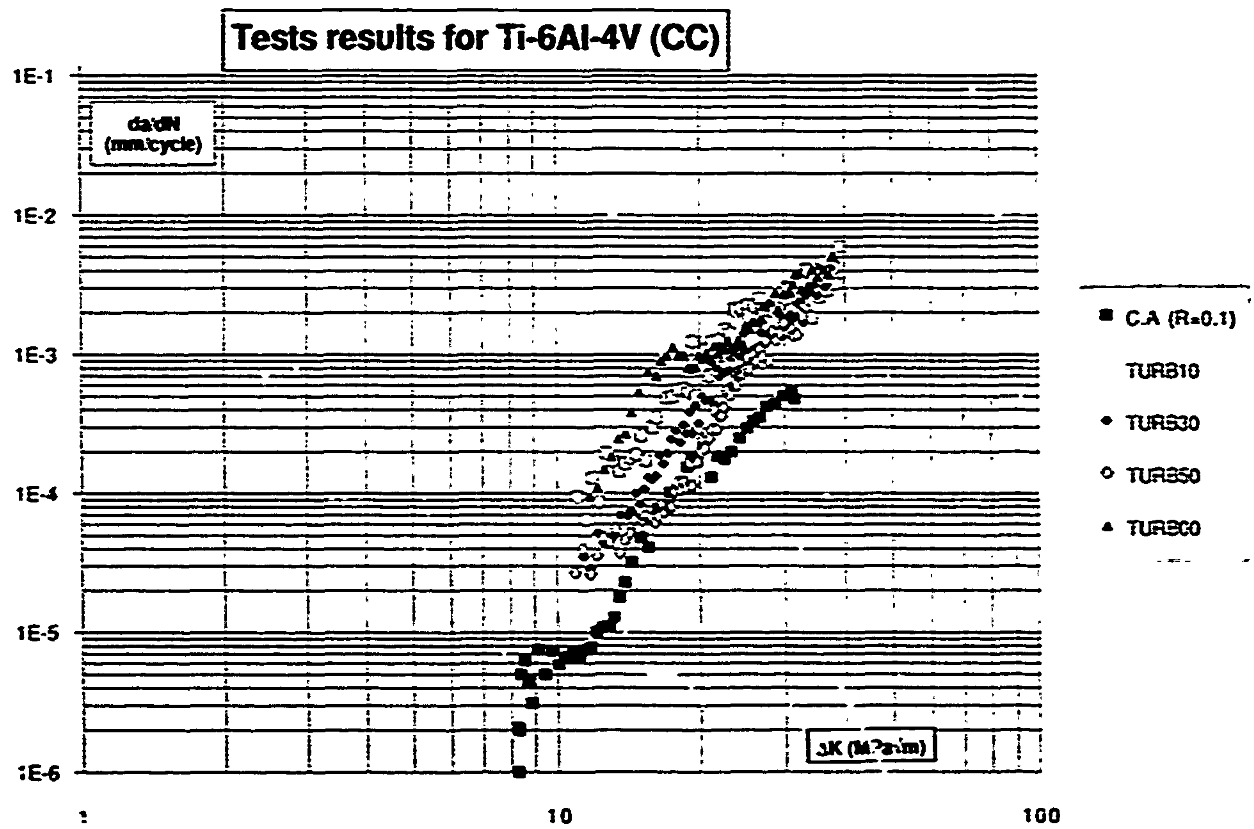

Fig.75 - da/dN vs ΔK Ti-6Al-4V / CC test results

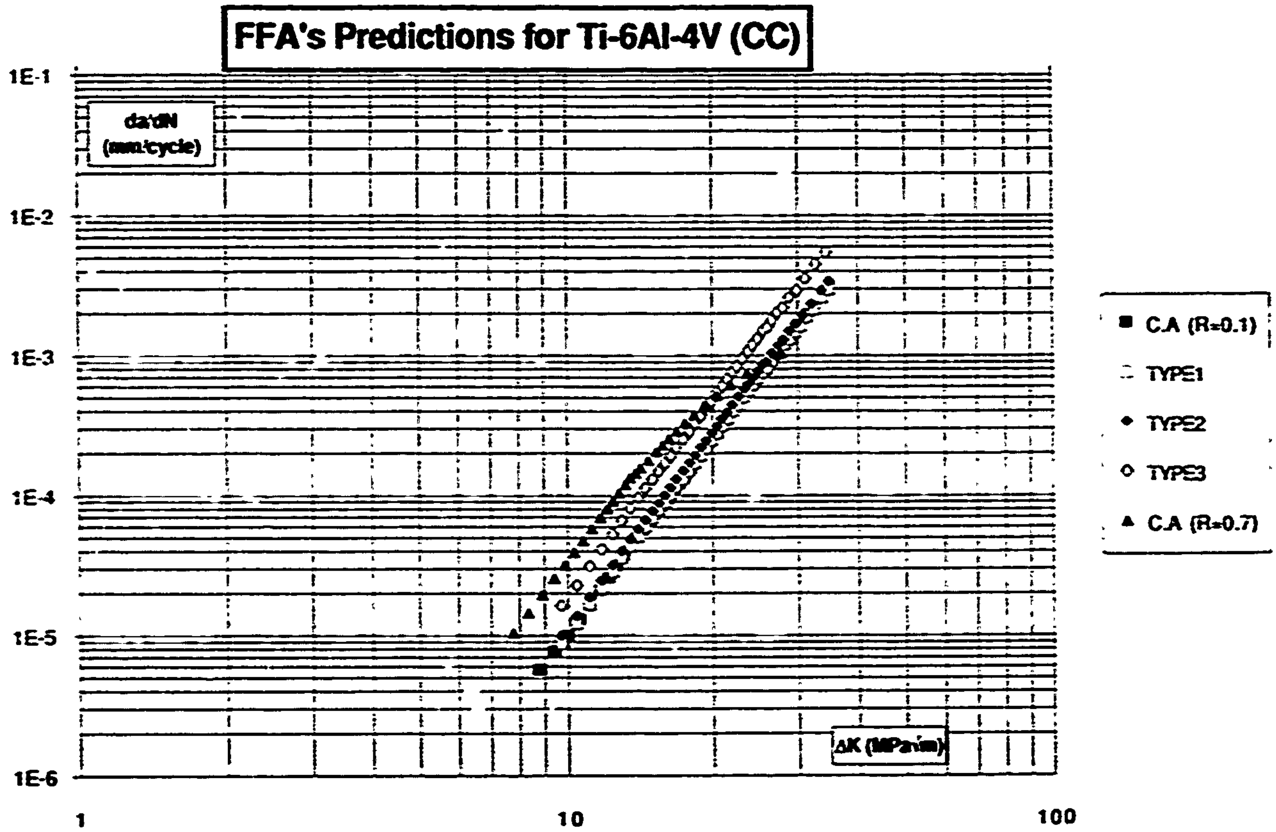

Fig.76 - da/dN vs ΔK Ti-6Al-4V / CC FFA predictions

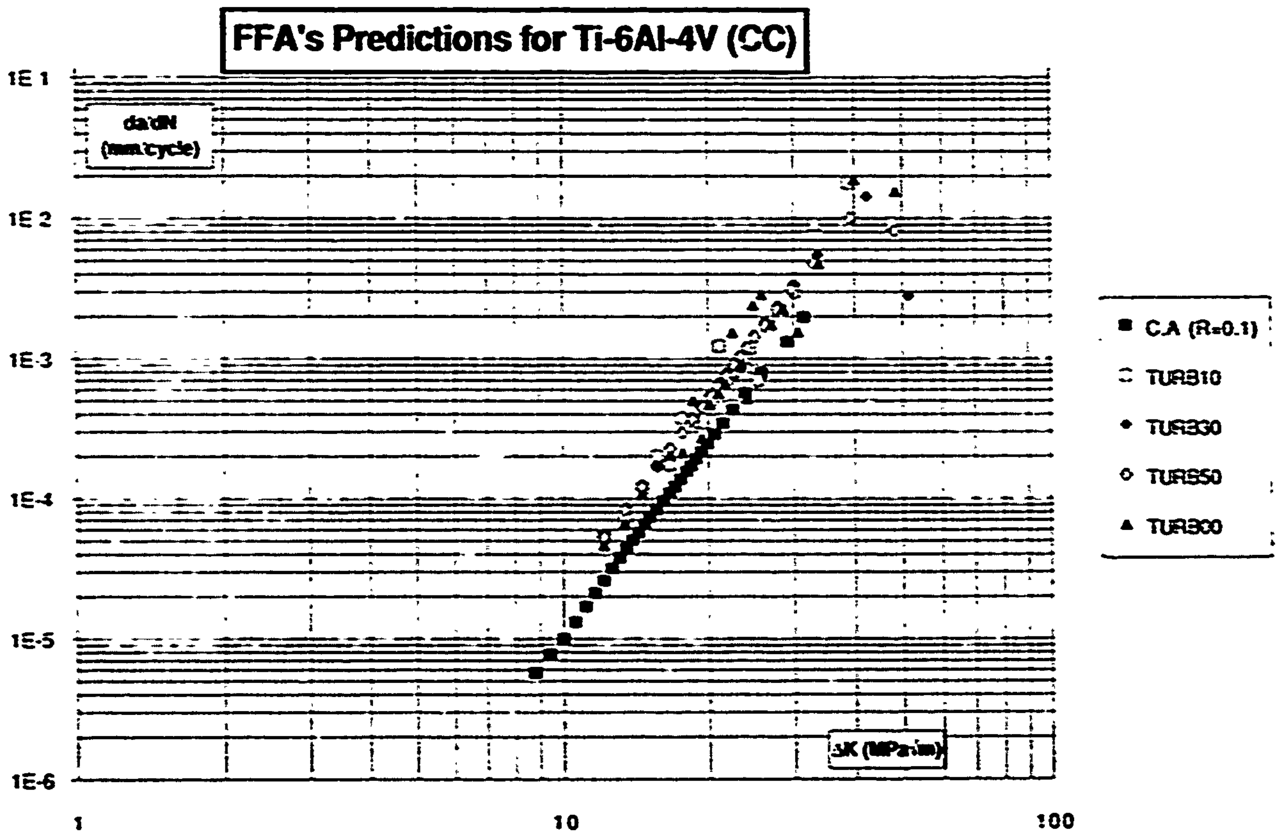

Fig.77 - da/dN vs ΔK Ti-6Al-4V / CC FFA predictions

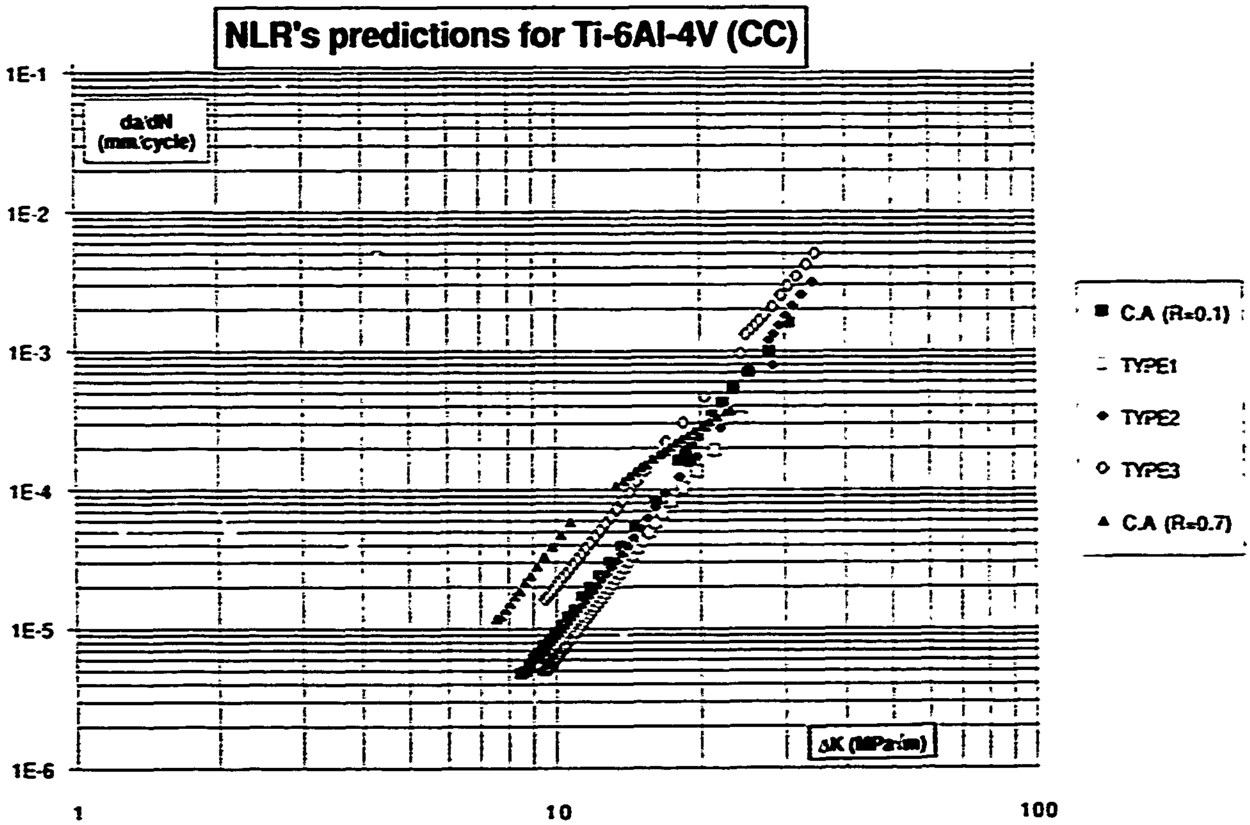

Fig.78 - da/dN vs ΔK Ti-6Al-4V / CC NLR predictions

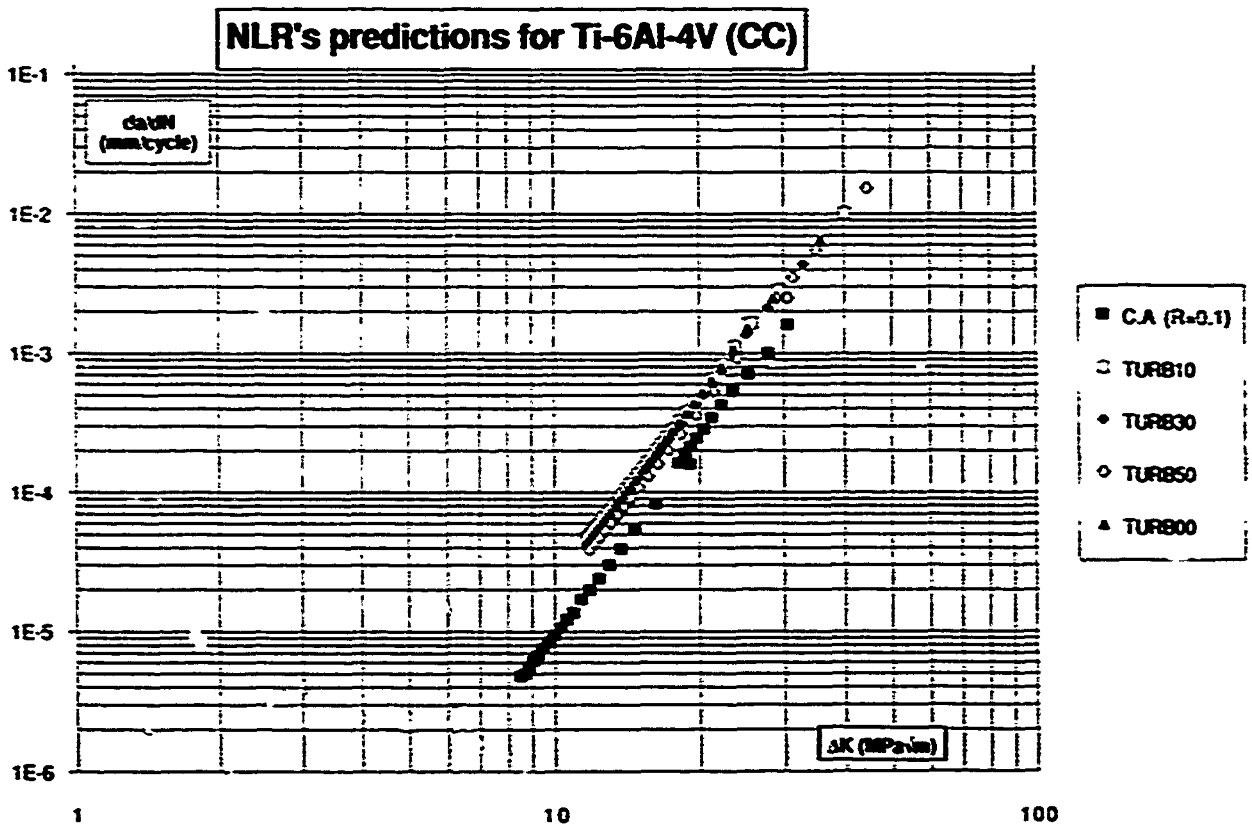

Fig.79 - da/dN vs ΔK Ti-6Al-4V / CC NLR predictions

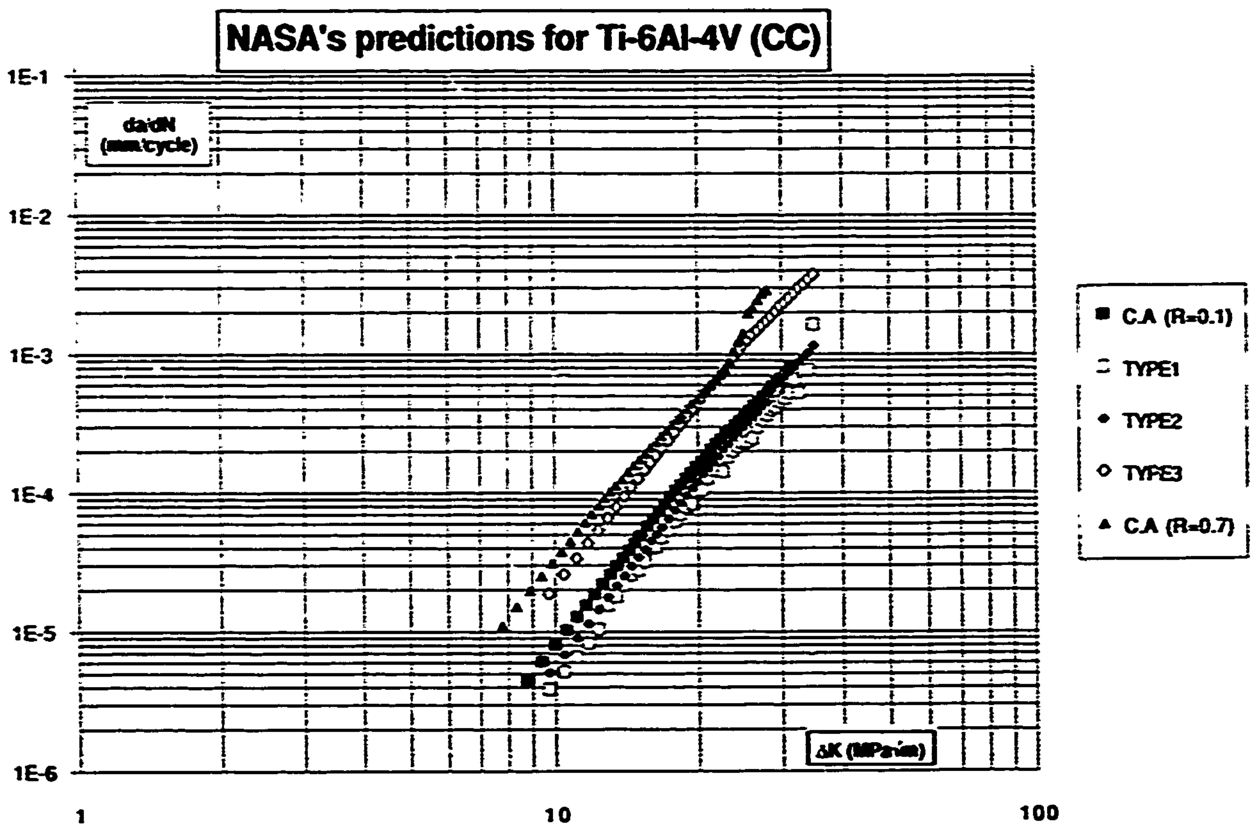

Fig.80 - da/dN vs ΔK Ti-6Al-4V / CC NASA predictions

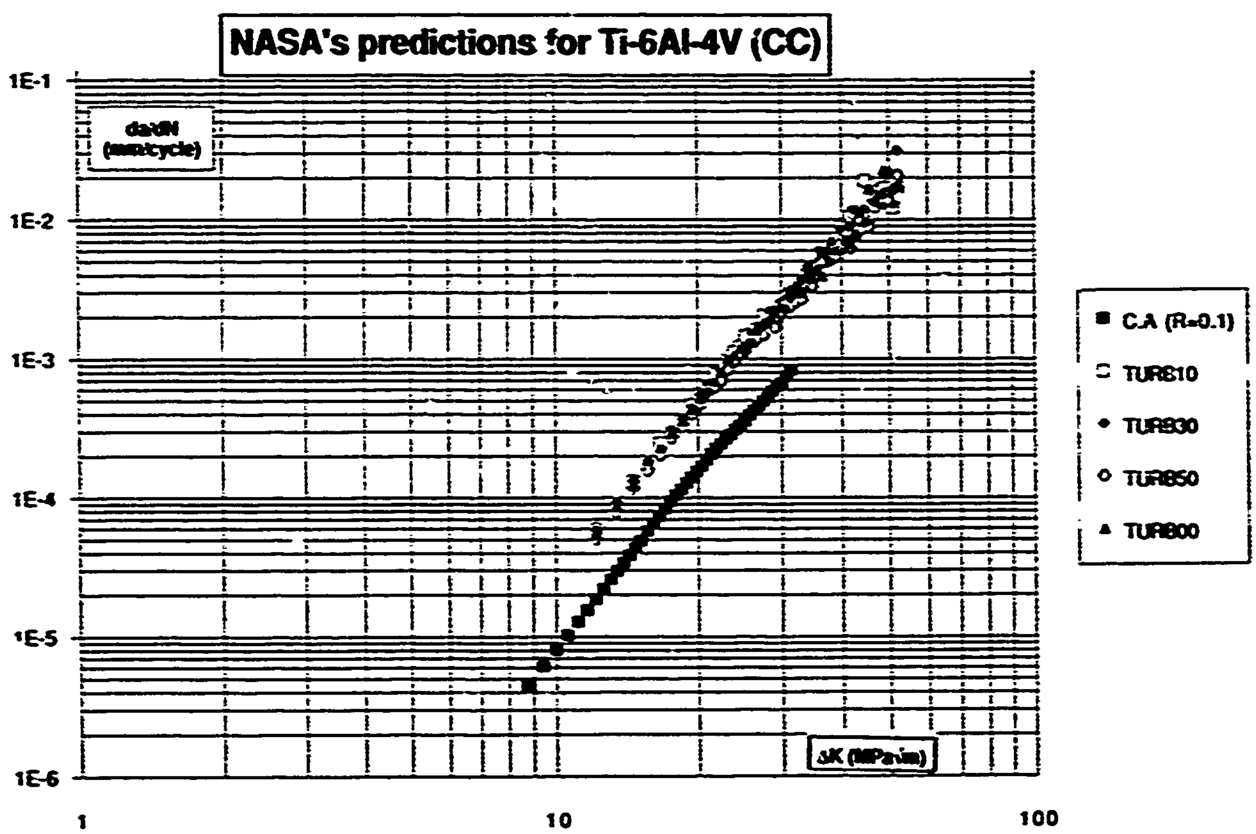

Fig.81 - da/dN vs ΔK Ti-6Al-4V / CC NASA predictions

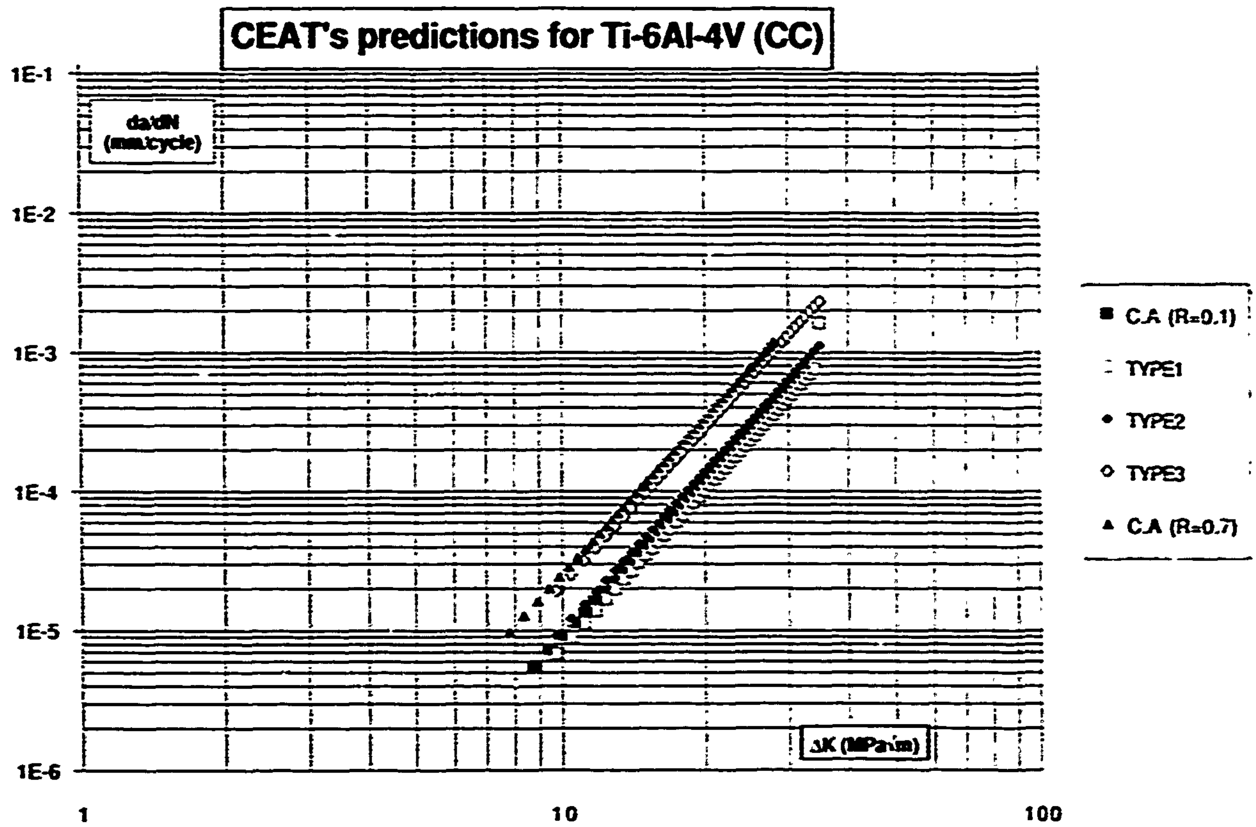

Fig.82 - da/dN vs ΔK Ti-6Al-4V / CC CEAT predictions

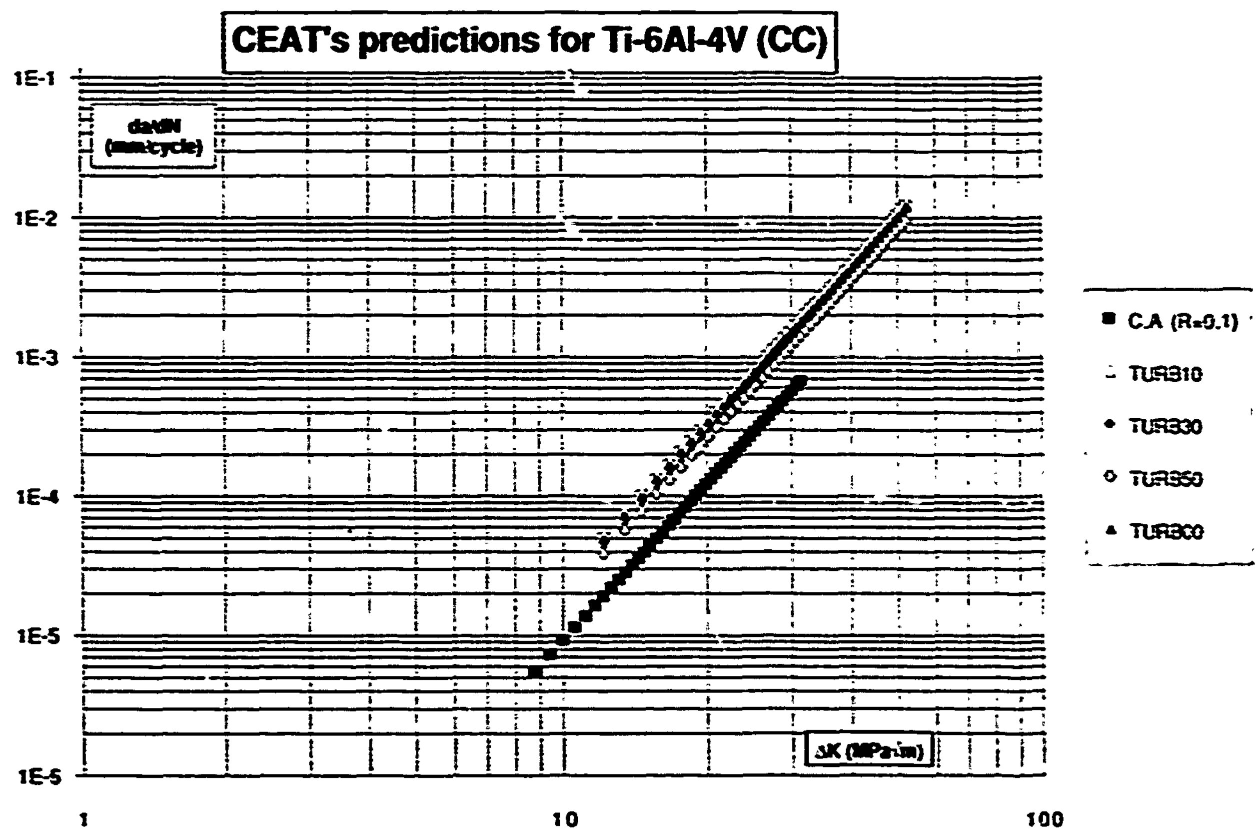

Fig.83 - da/dN vs ΔK Ti-6Al-4V / CC CEAT predictions

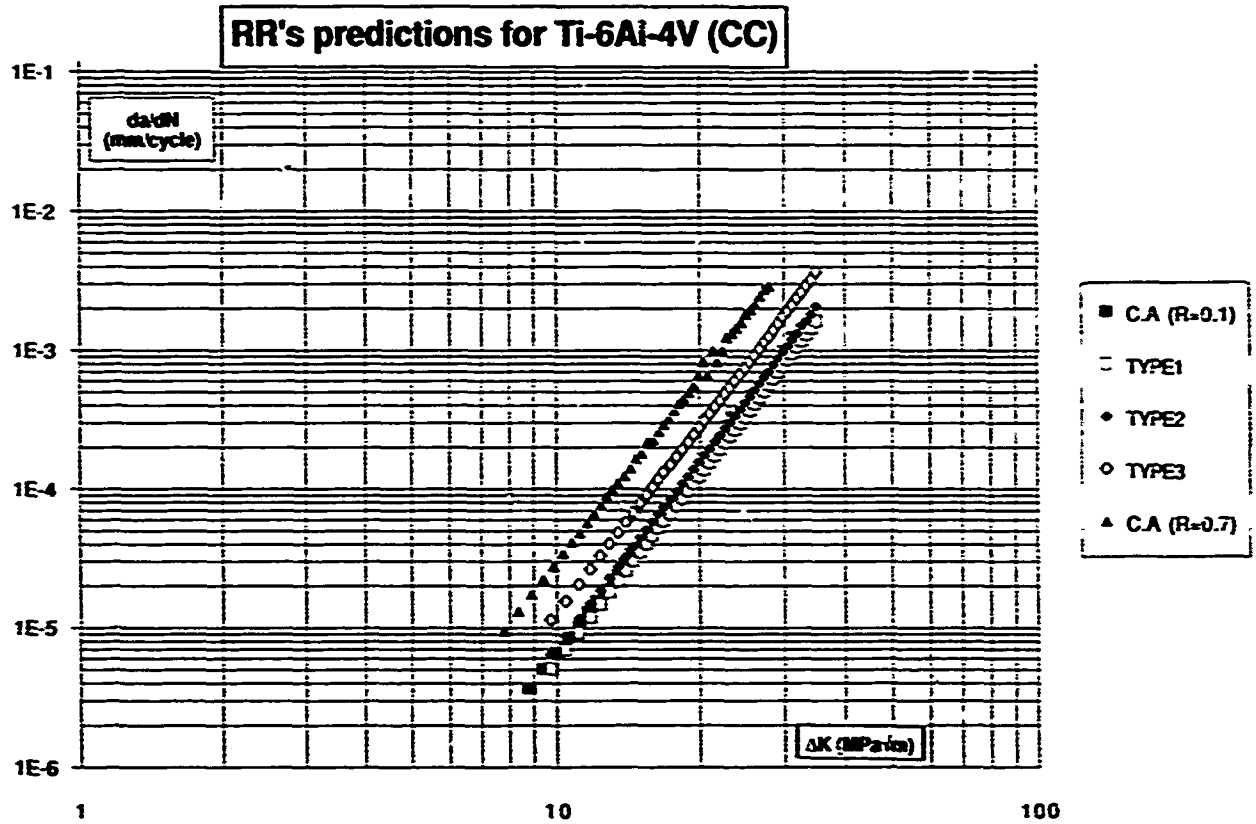

Fig.84 - da/dN vs ΔK Ti-6Al-4V / CC RR predictions

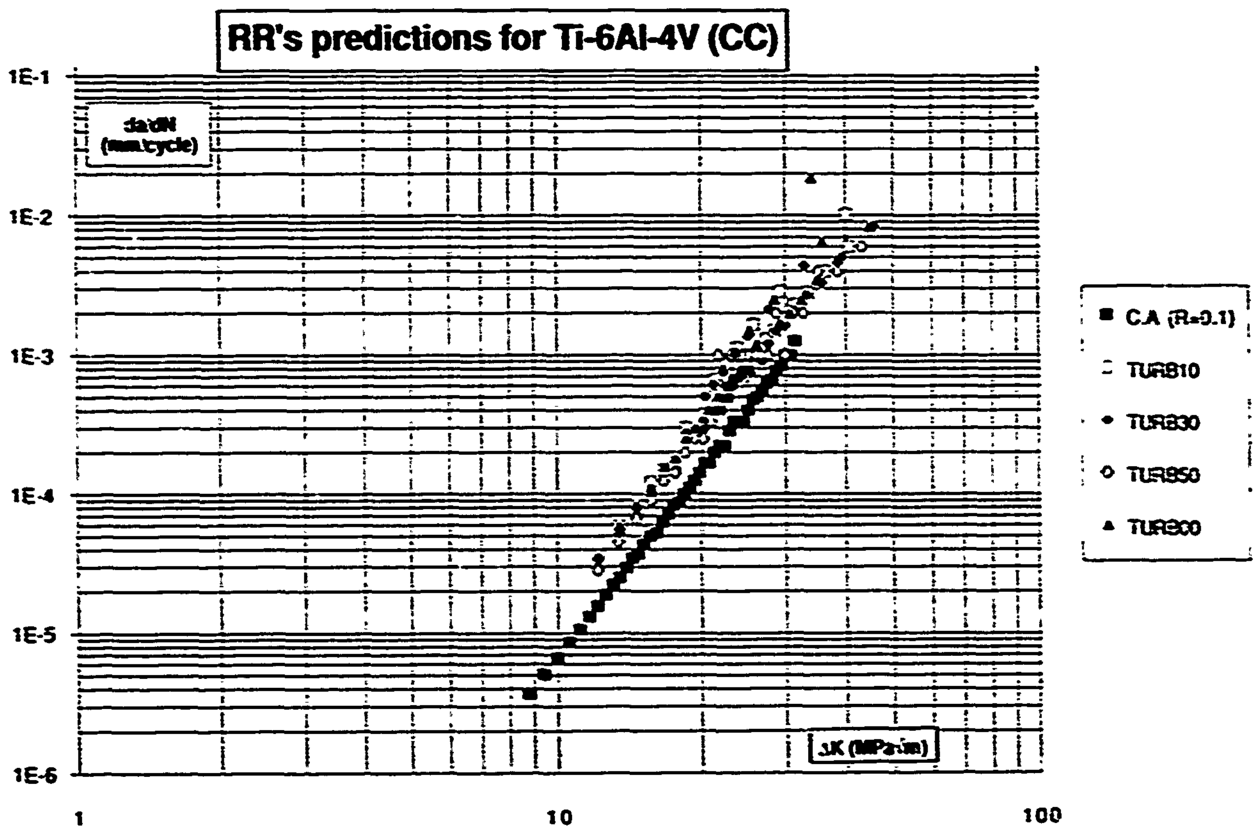

Fig.85 - da/dN vs ΔK Ti-6Al-4V / CC RR predictions

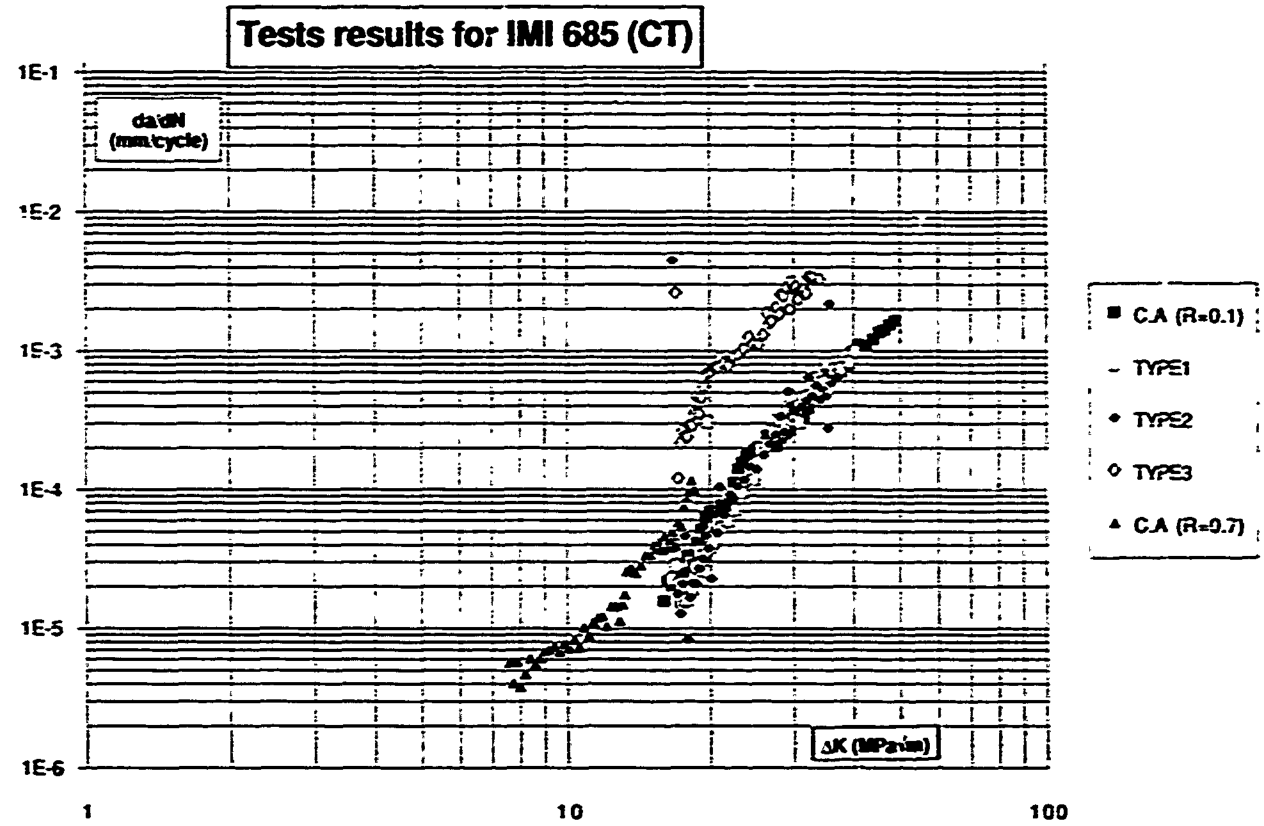

Fig.86 - da/dN vs ΔK IMI685 / CT test results

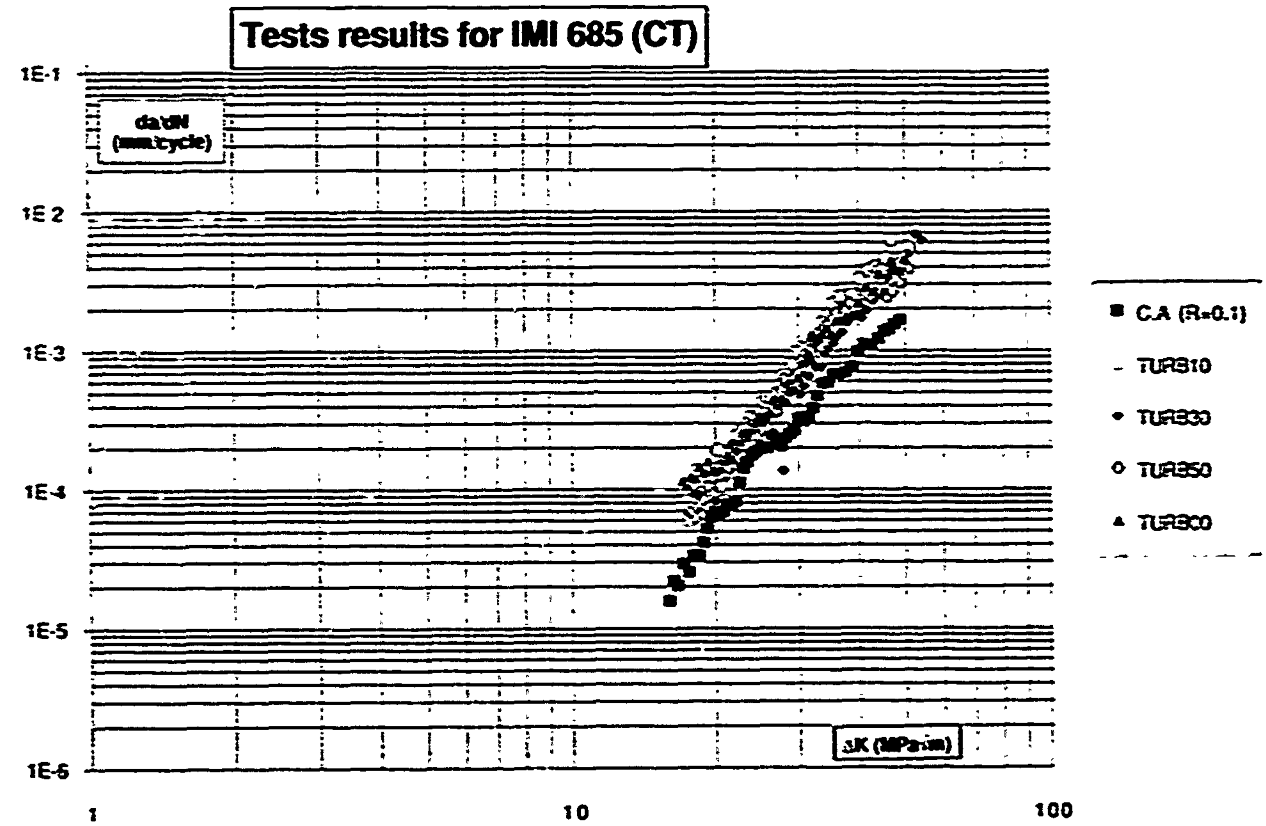

Fig.87 - da/dN vs ΔK IMI685 / CT test results

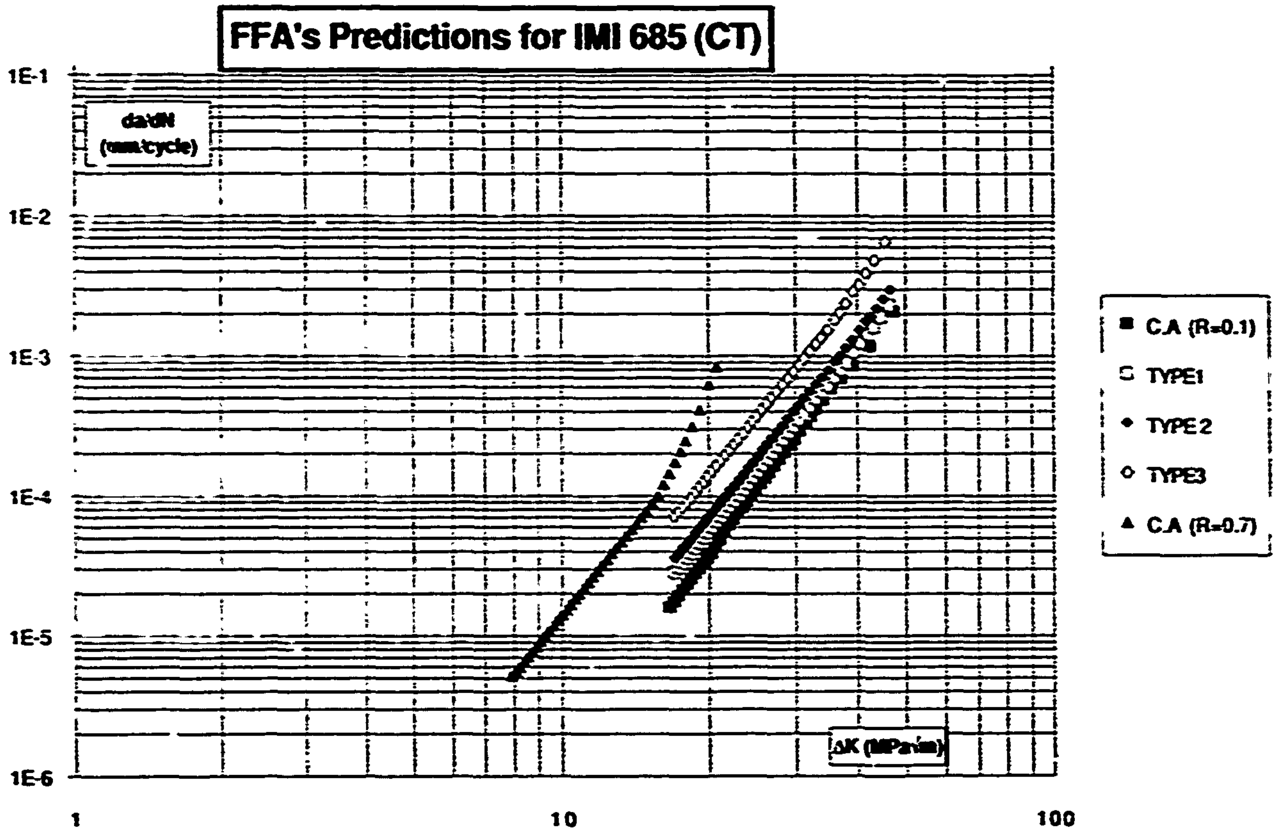

Fig.88 - da/dN vs ΔK IMI685 / CT FFA predictions

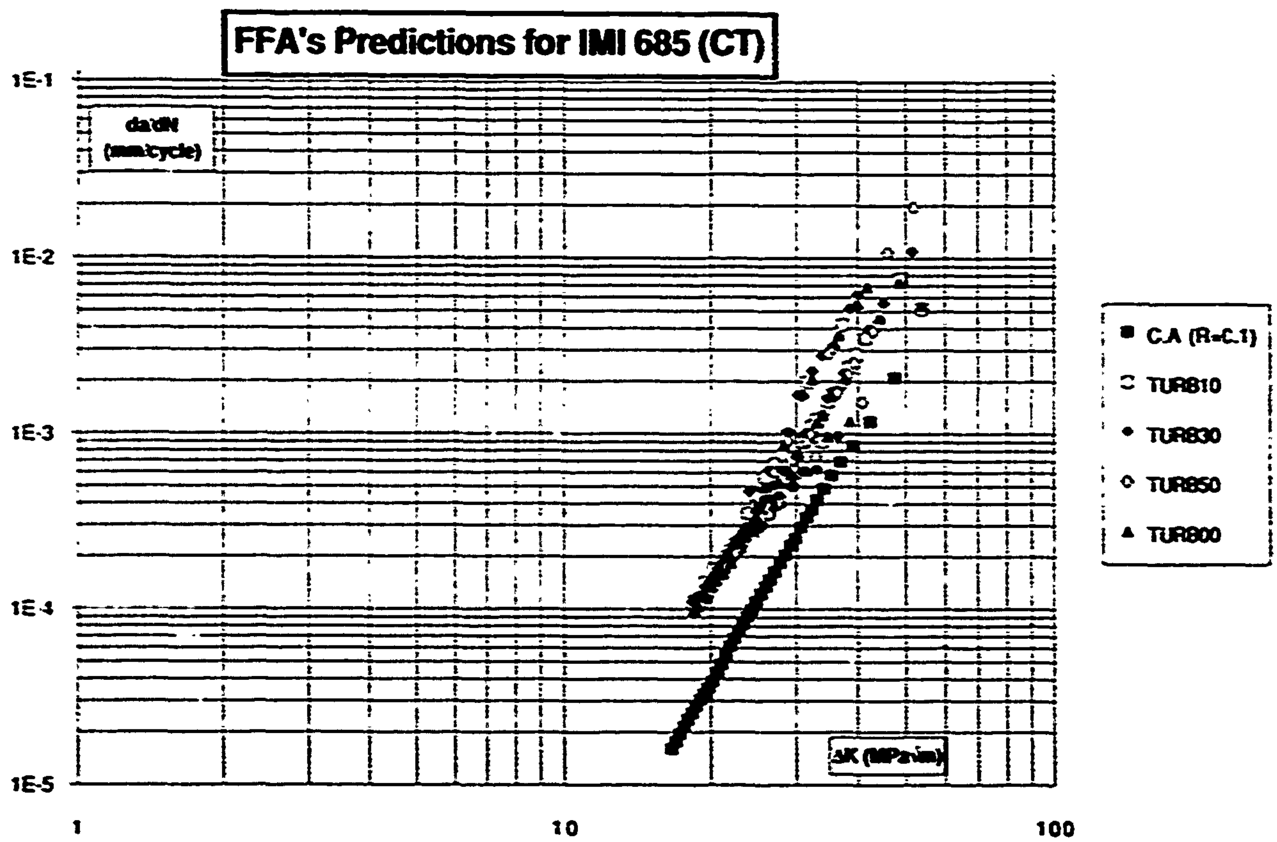

Fig.89 - da/dN vs ΔK IMI685 / CT FFA predictions

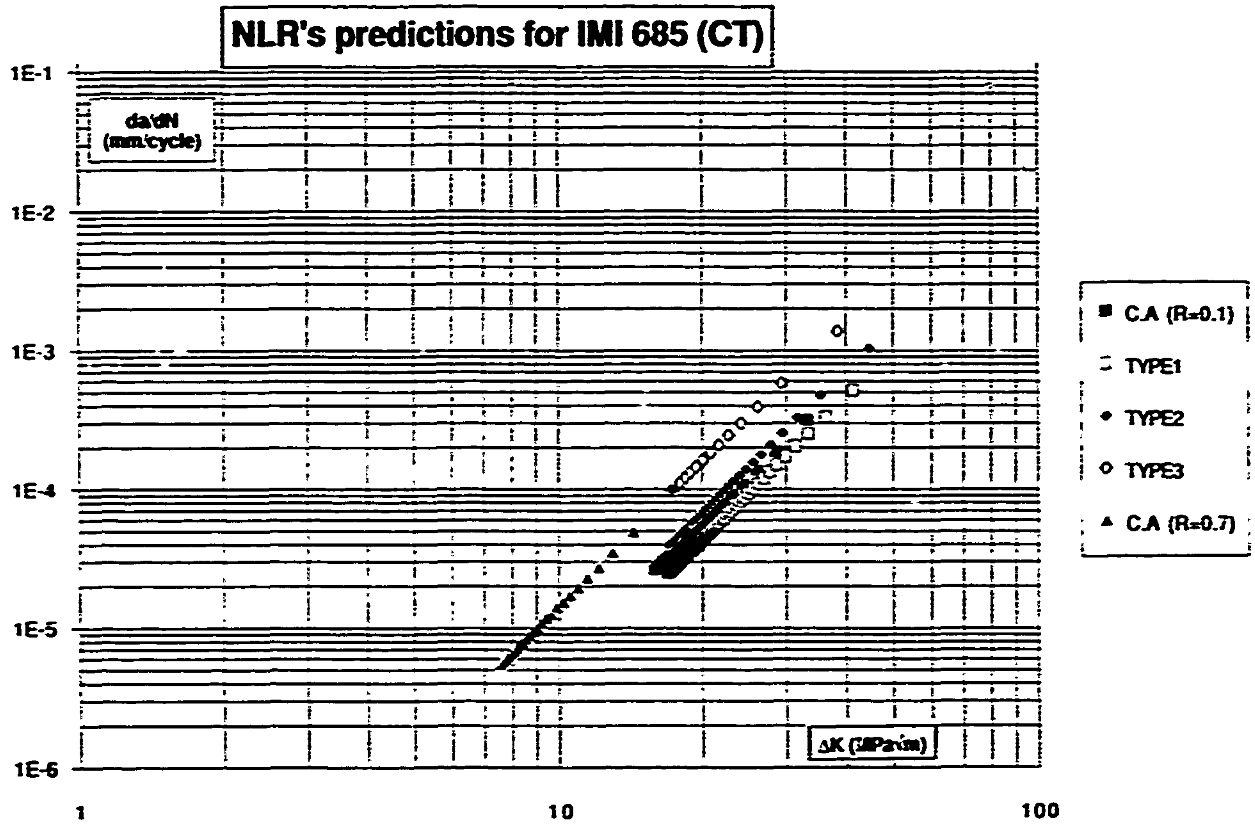

Fig.90 - da/dN vs ΔK IMI685 / CT NLR predictions

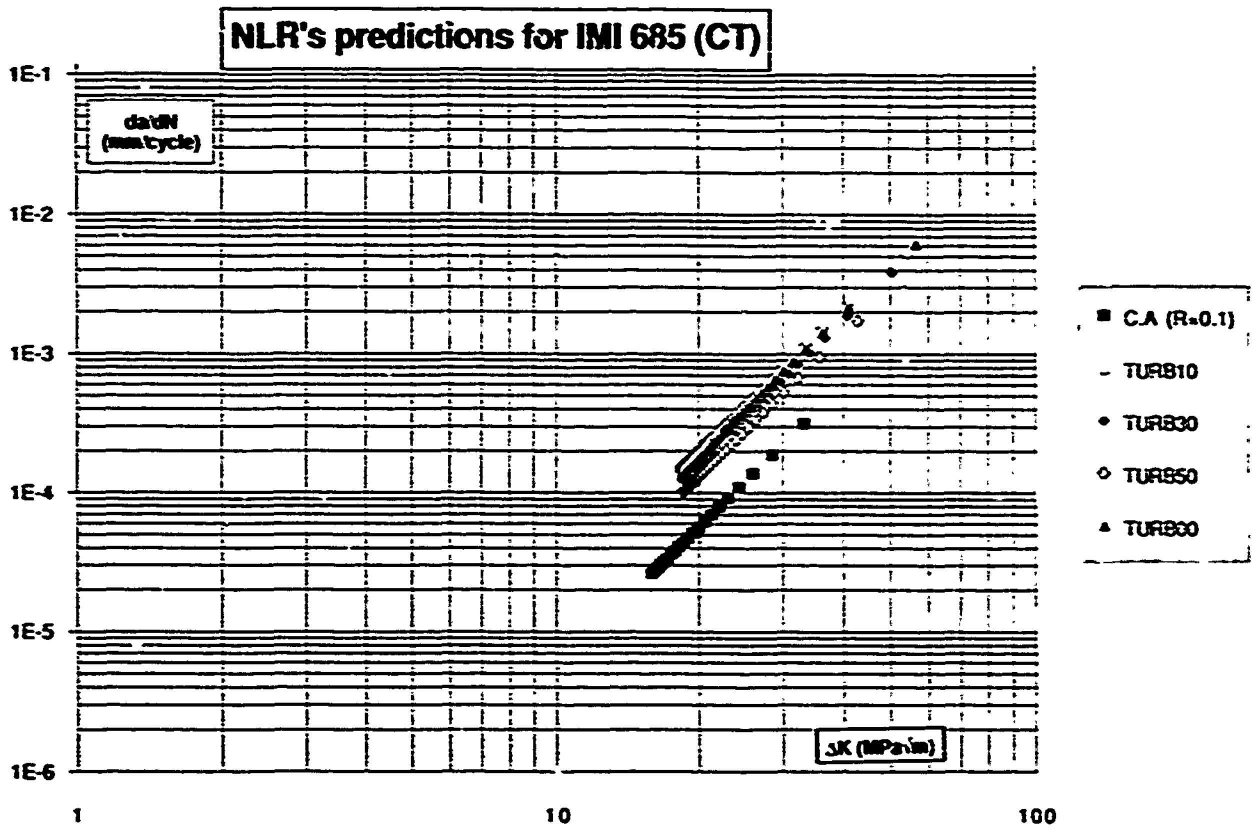

Fig.91 - da/dN vs ΔK IMI685 / CT NLR predictions

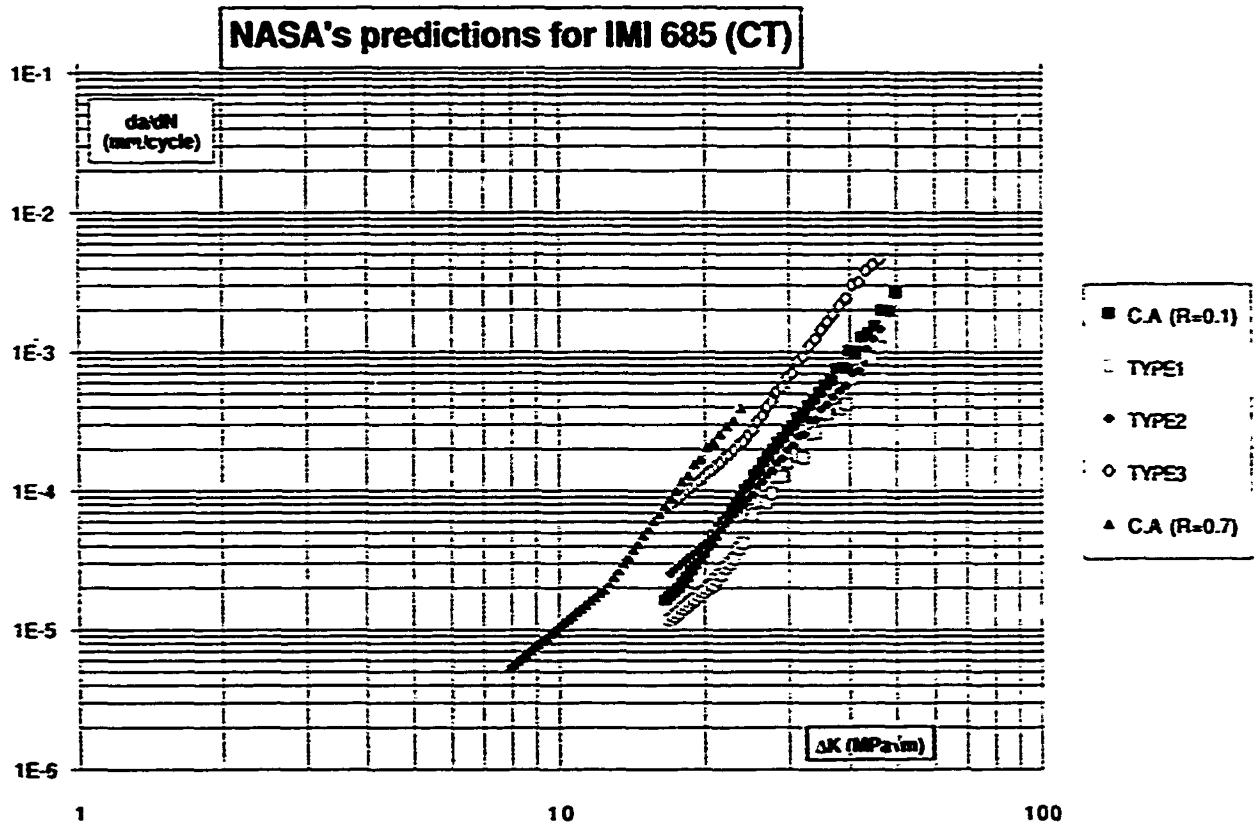

Fig.92 - da/dN vs ΔK IMI685 / CT NASA predictions

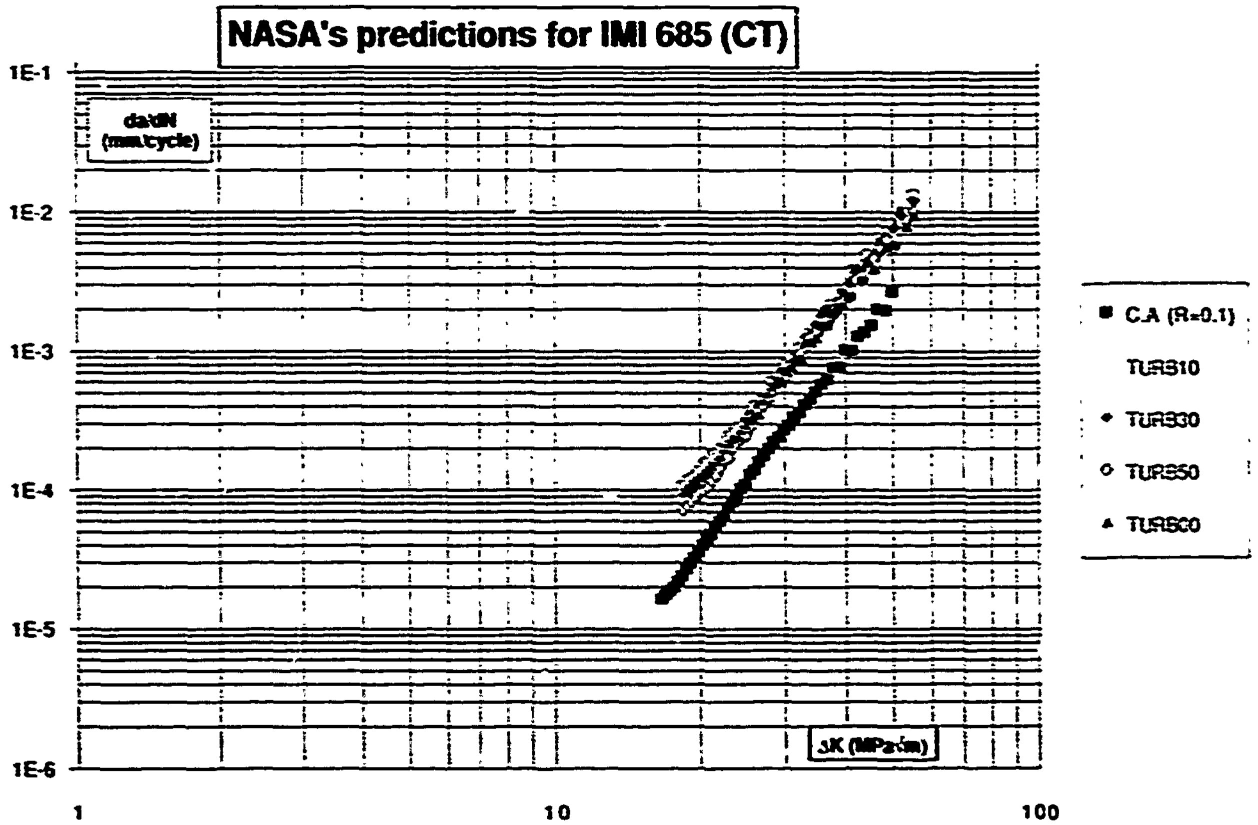

Fig.93 - da/dN vs ΔK IMI685 / CT NASA predictions

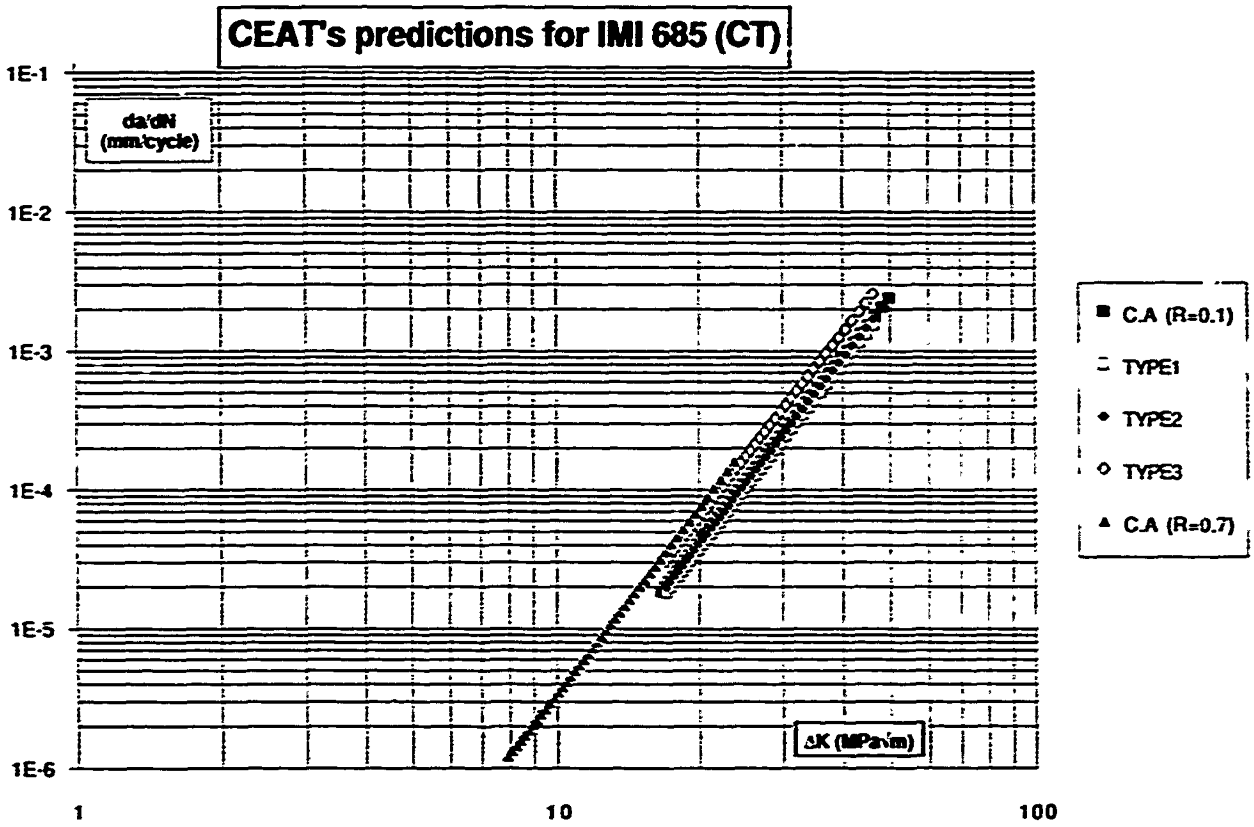

Fig.94 - da/dN vs ΔK IMI685 / CT CEAT predictions

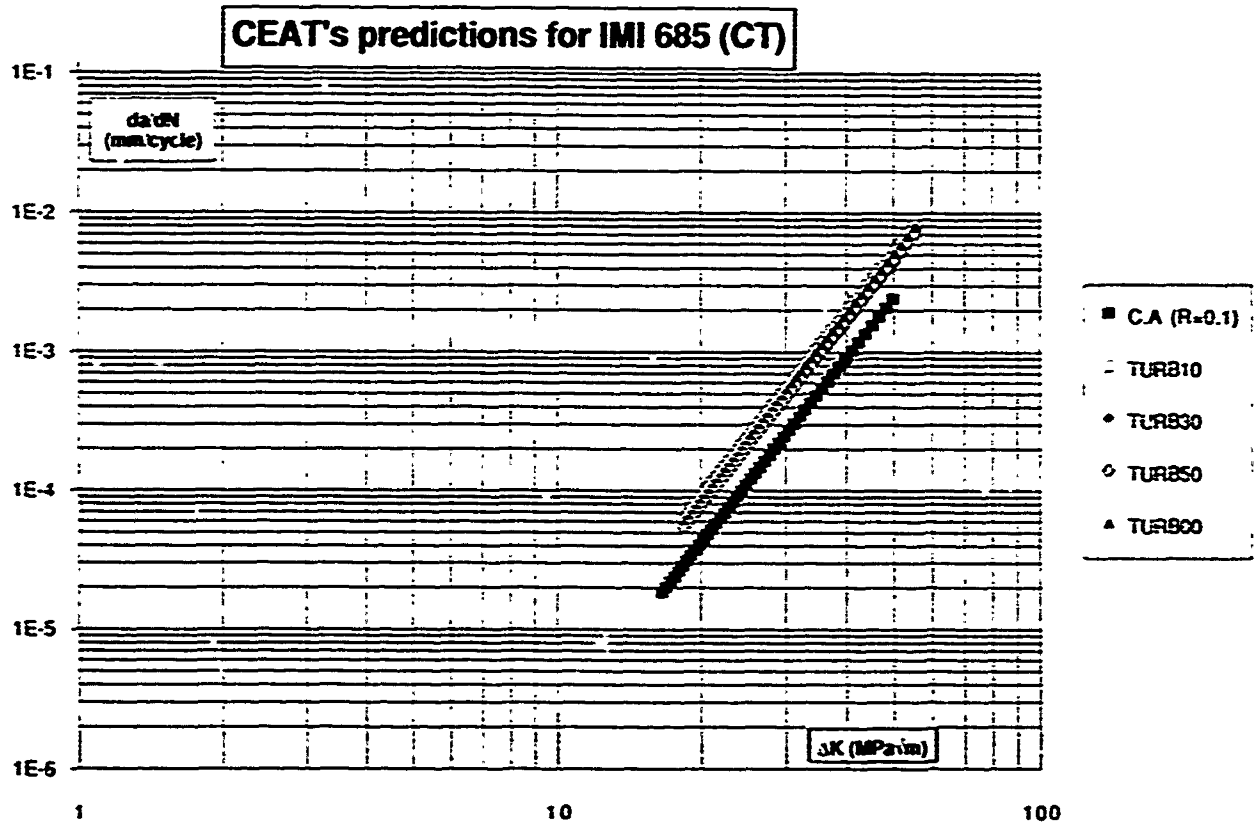

Fig.95 - da/dN vs ΔK IMI685 / CT CEAT predictions

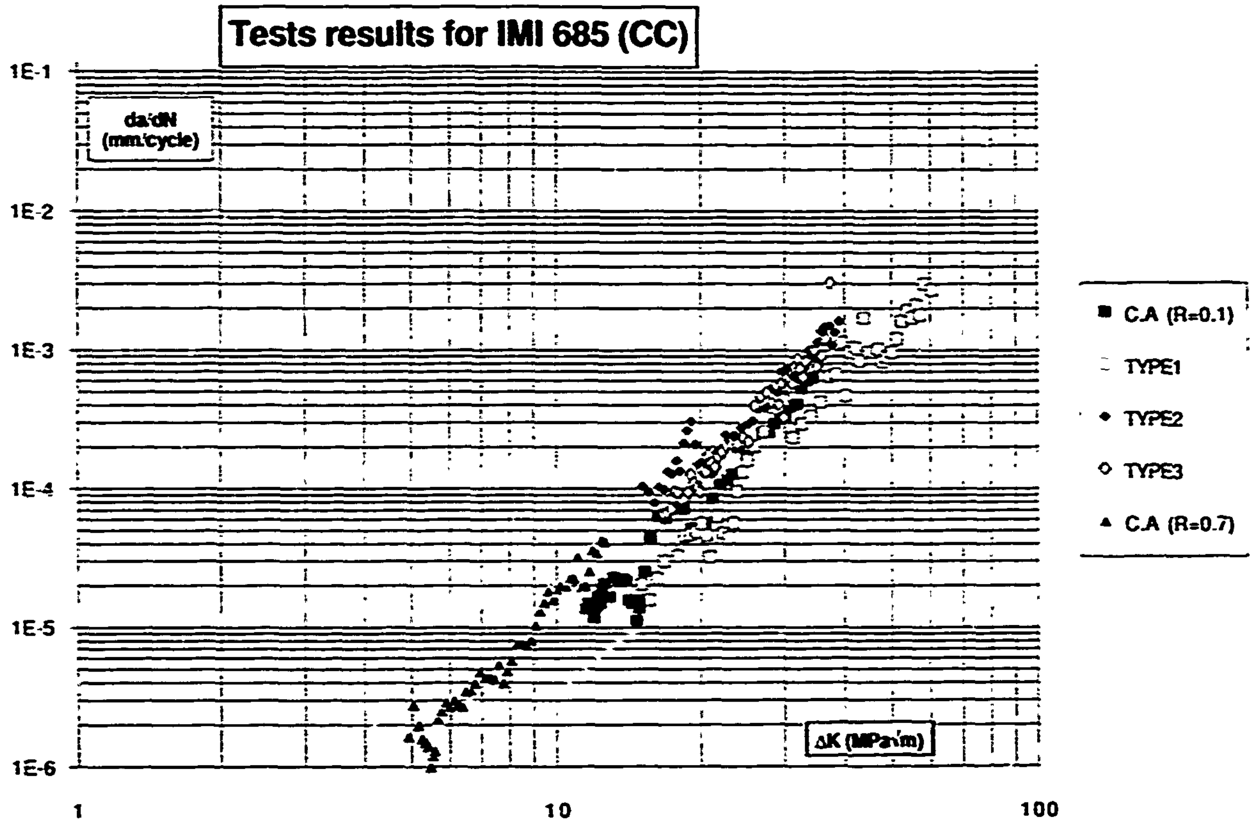

Fig.96 - da/dN vs ΔK IMI685 / CC test results

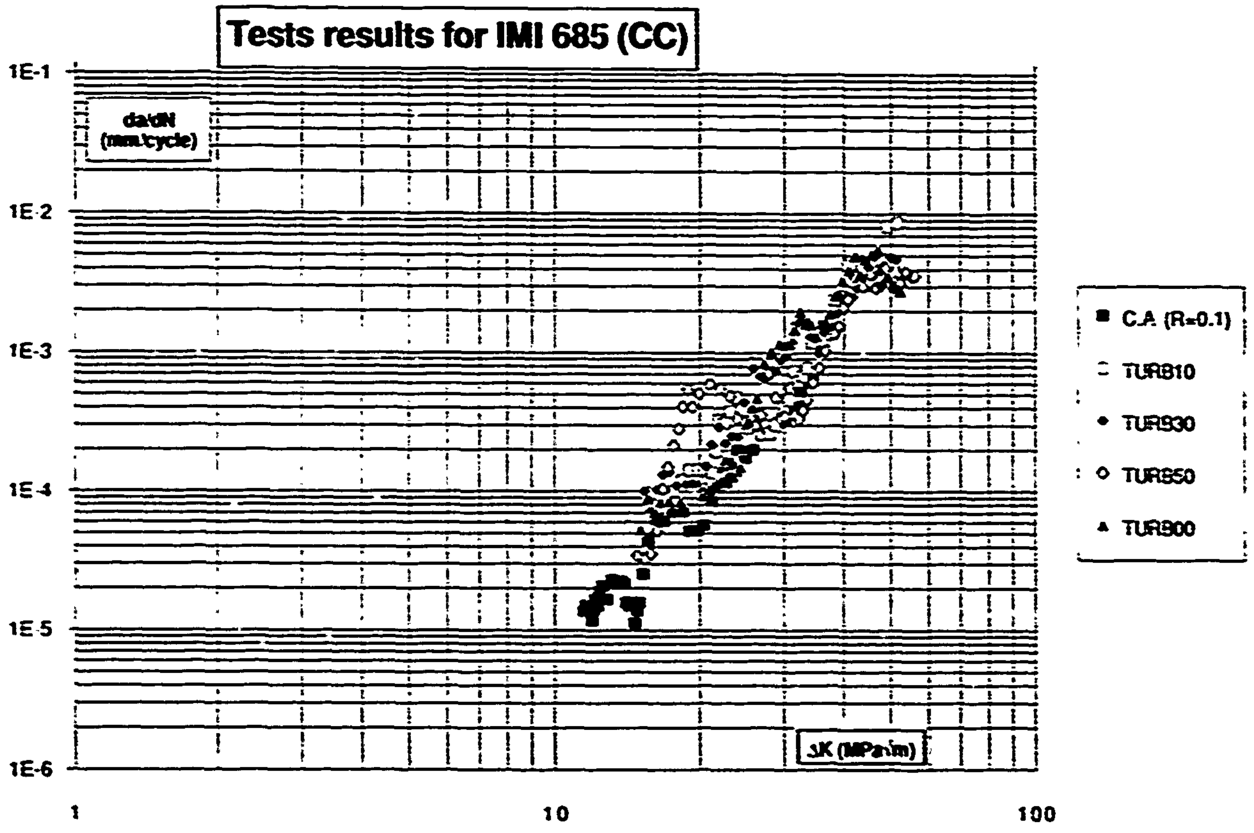

Fig.97 - da/dN vs ΔK IMI685 / CC test results

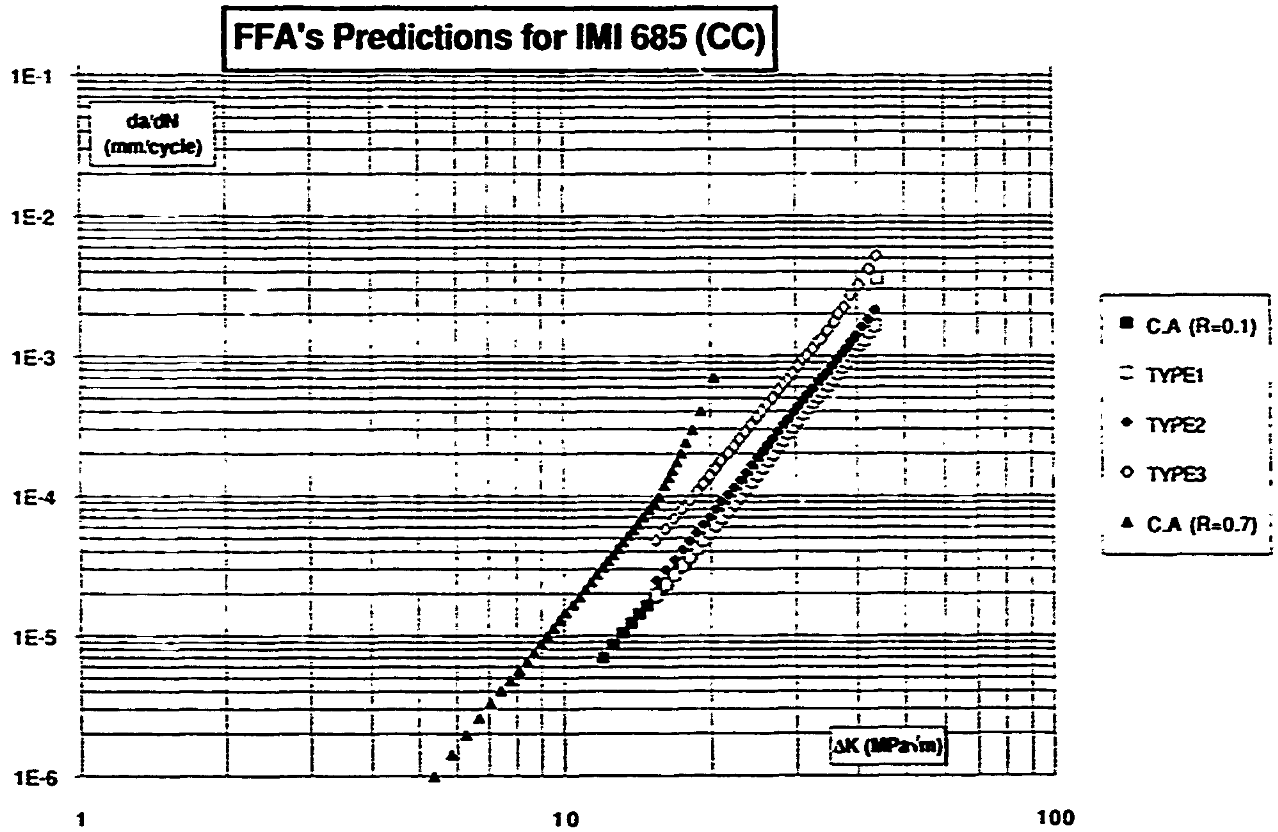

Fig.98 - da/dN vs ΔK IMI685 / CC FFA predictions

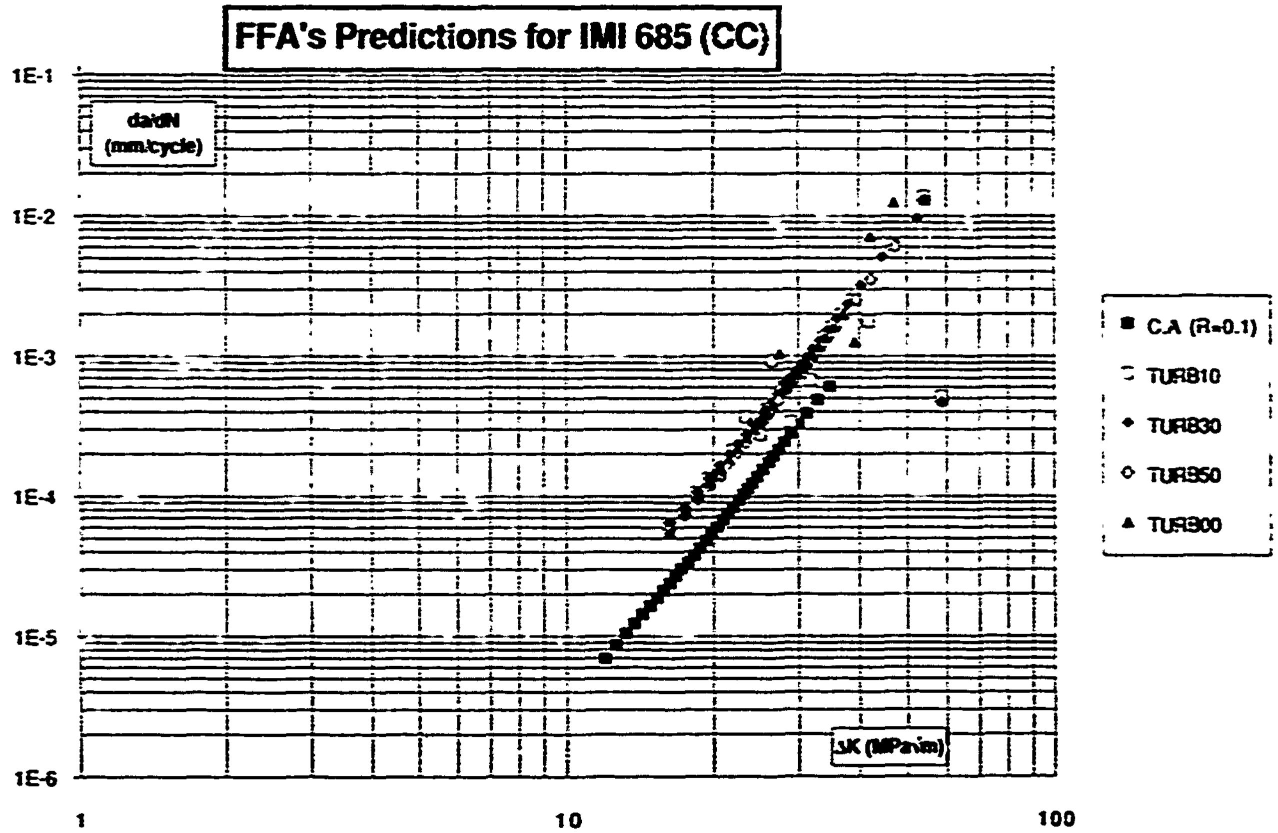

Fig.99 - da/dN vs ΔK IMI685 / CC FFA predictions

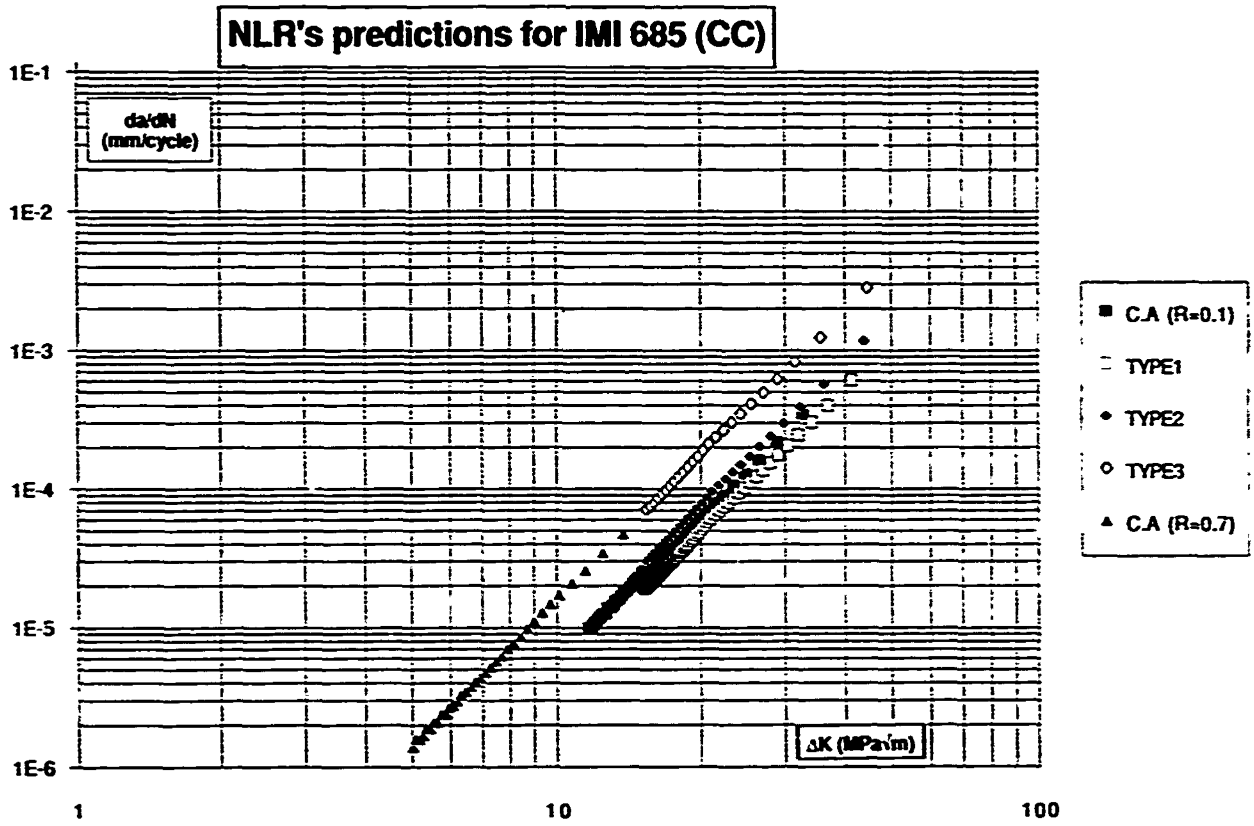

Fig.100 - da/dN vs ΔK IMI685 / CC NLR predictions

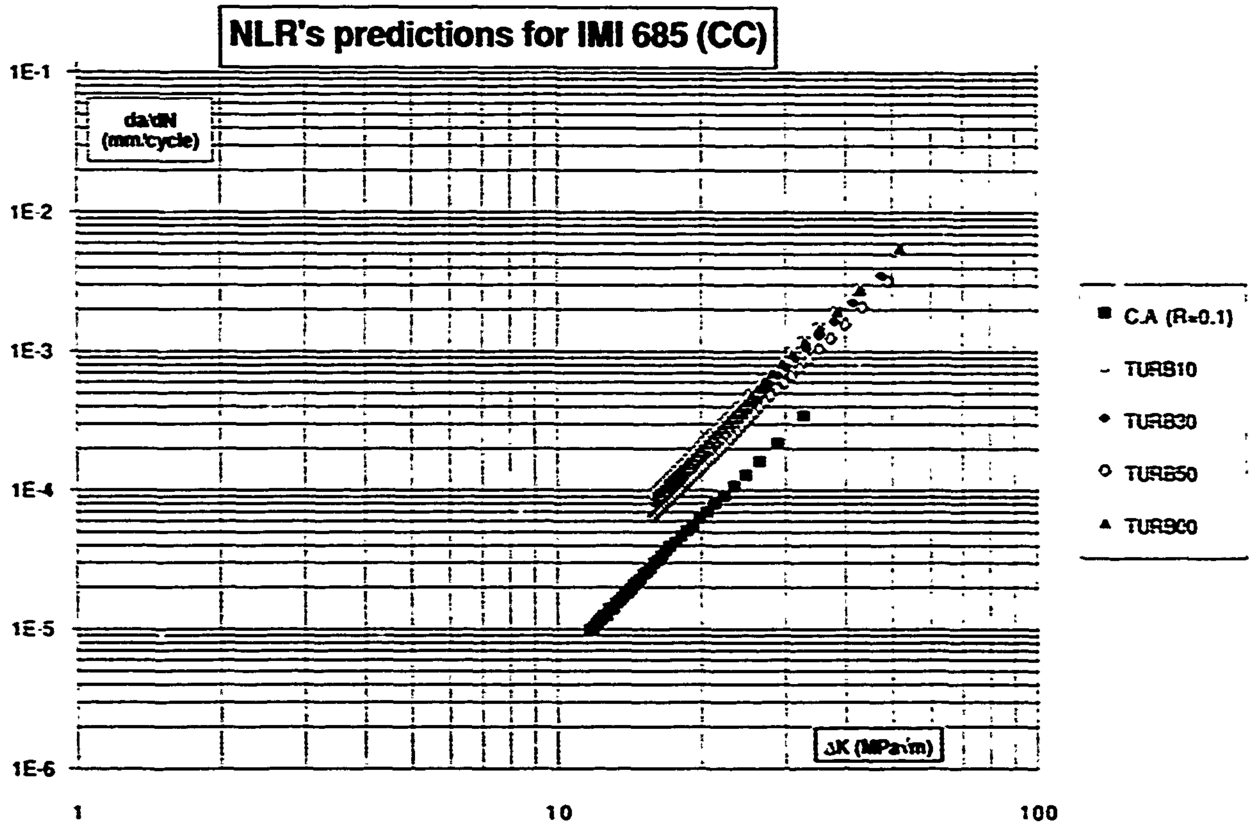

Fig.101 - da/dN vs ΔK IMI685 / CC NLR predictions

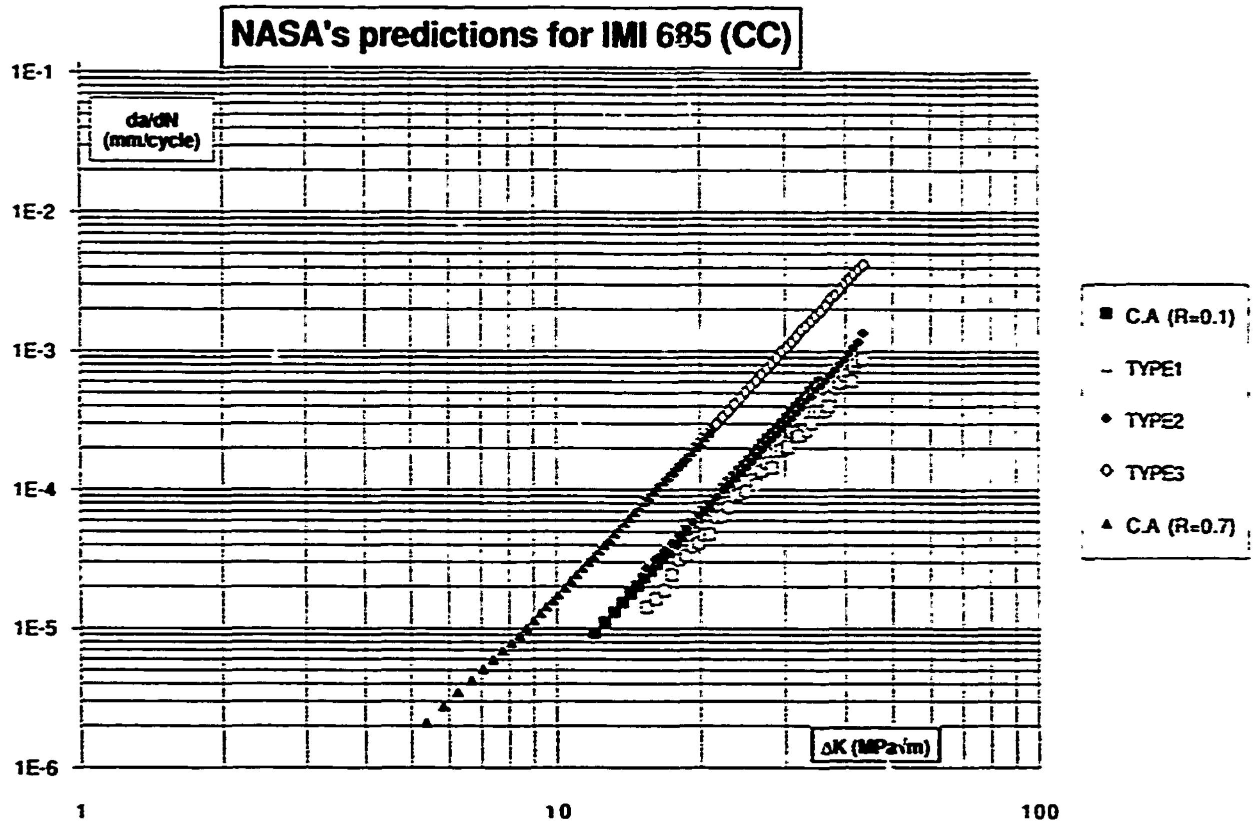

Fig.102 - da/dN vs ΔK IMI685 / CC NASA predictions

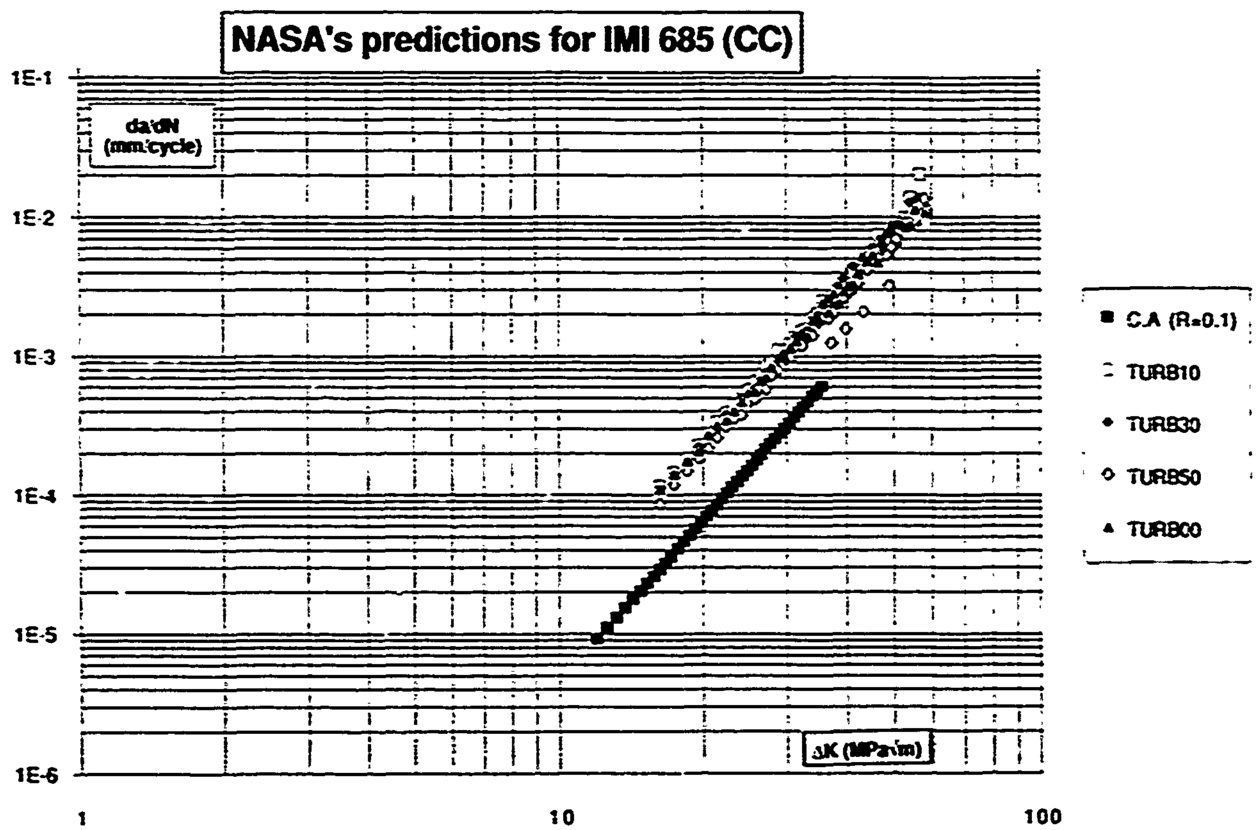

Fig.103 - da/dN vs ΔK IMI685 / CC NASA predictions

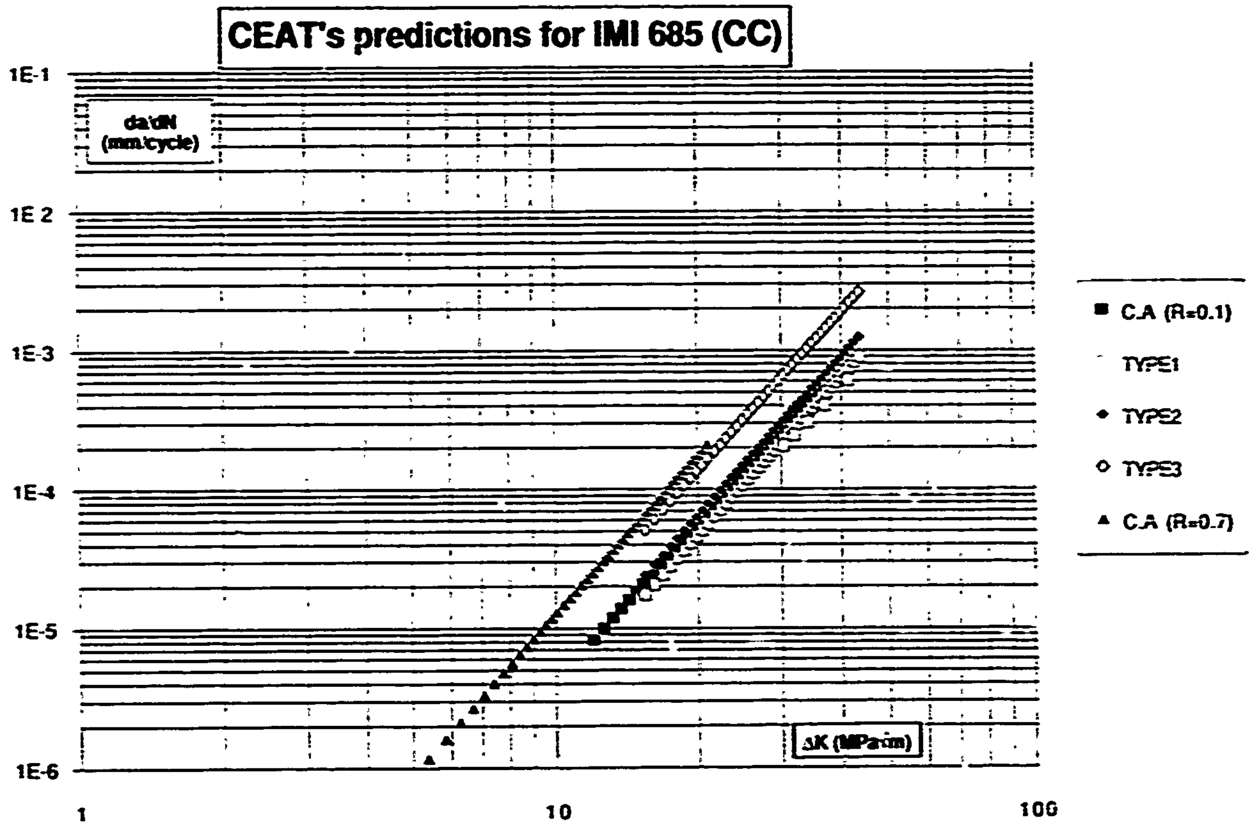

Fig.104 - da/dN vs ΔK IMI685 / CC CEAT predictions

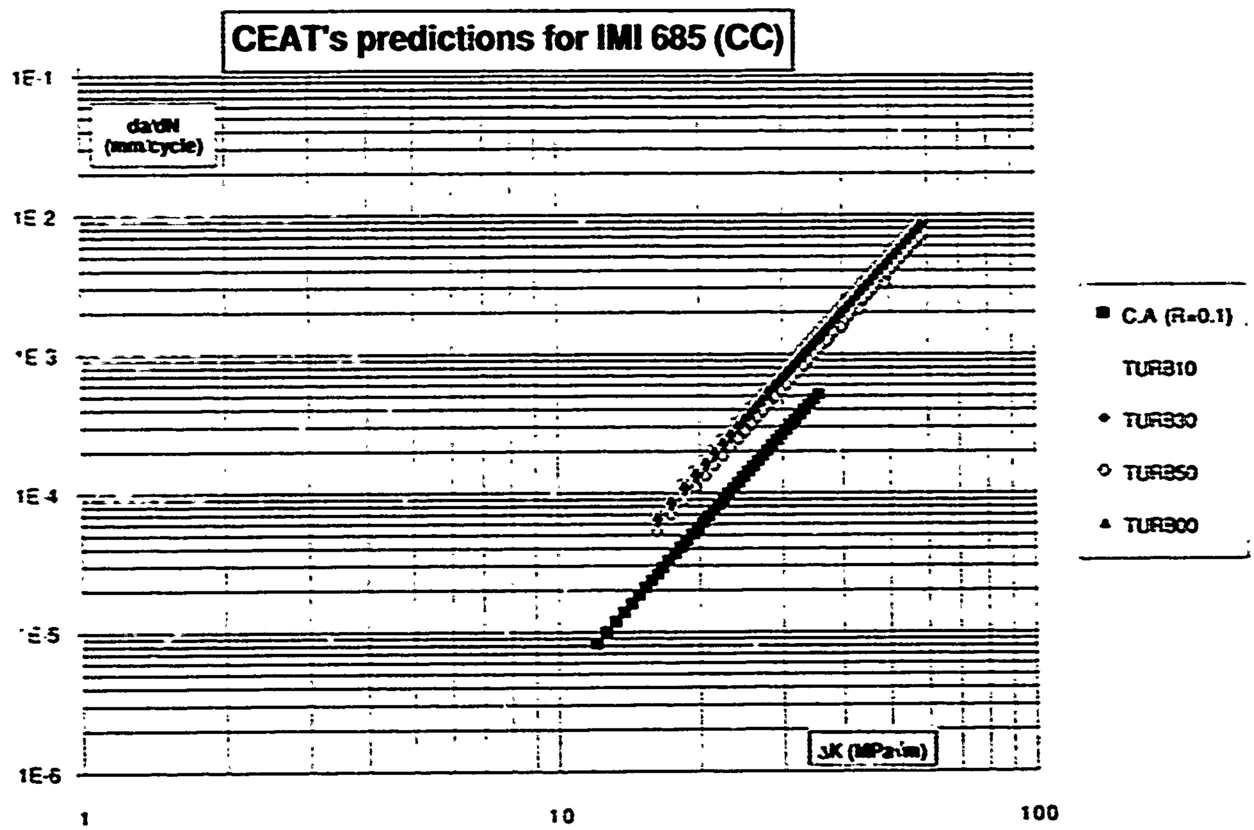

Fig.105 - da/dN vs ΔK IMI685 / CC CEAT predictions

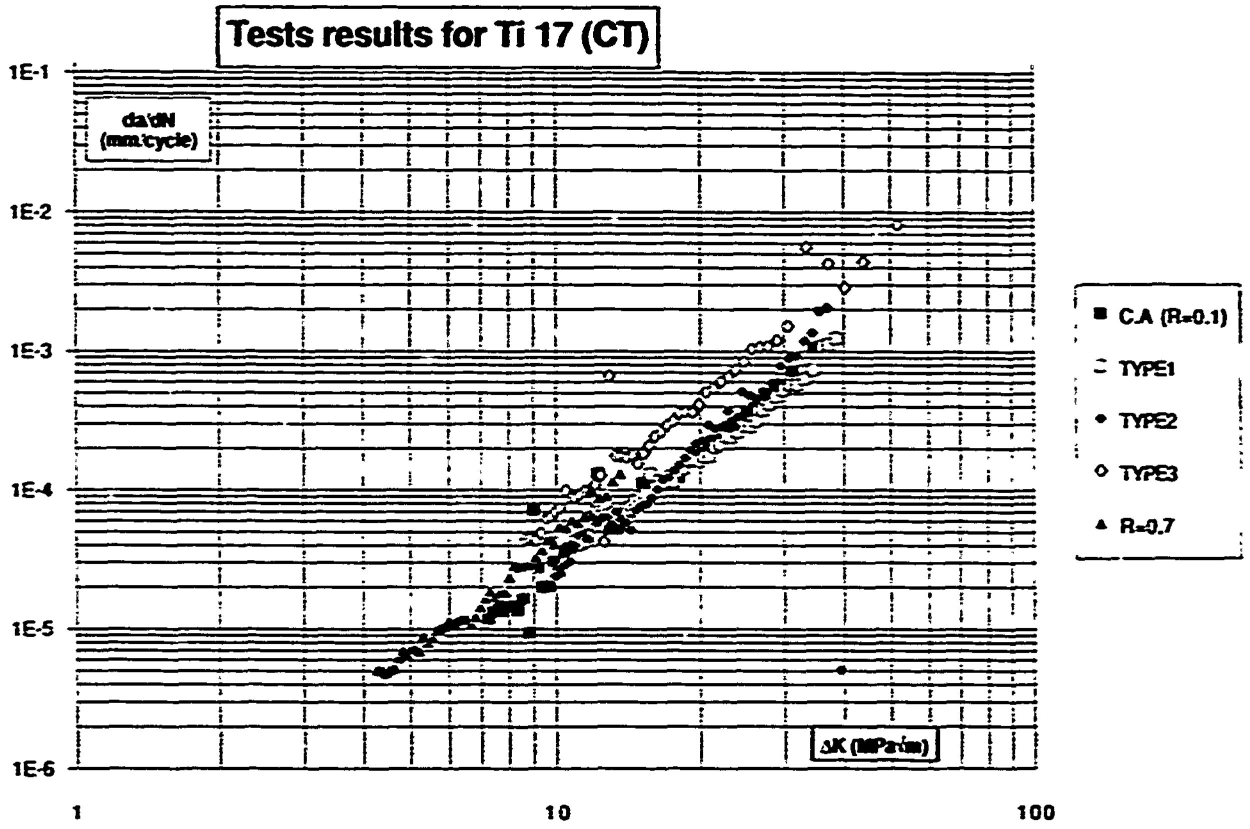

Fig.106 - da/dN vs ΔK Ti17 / CT test results

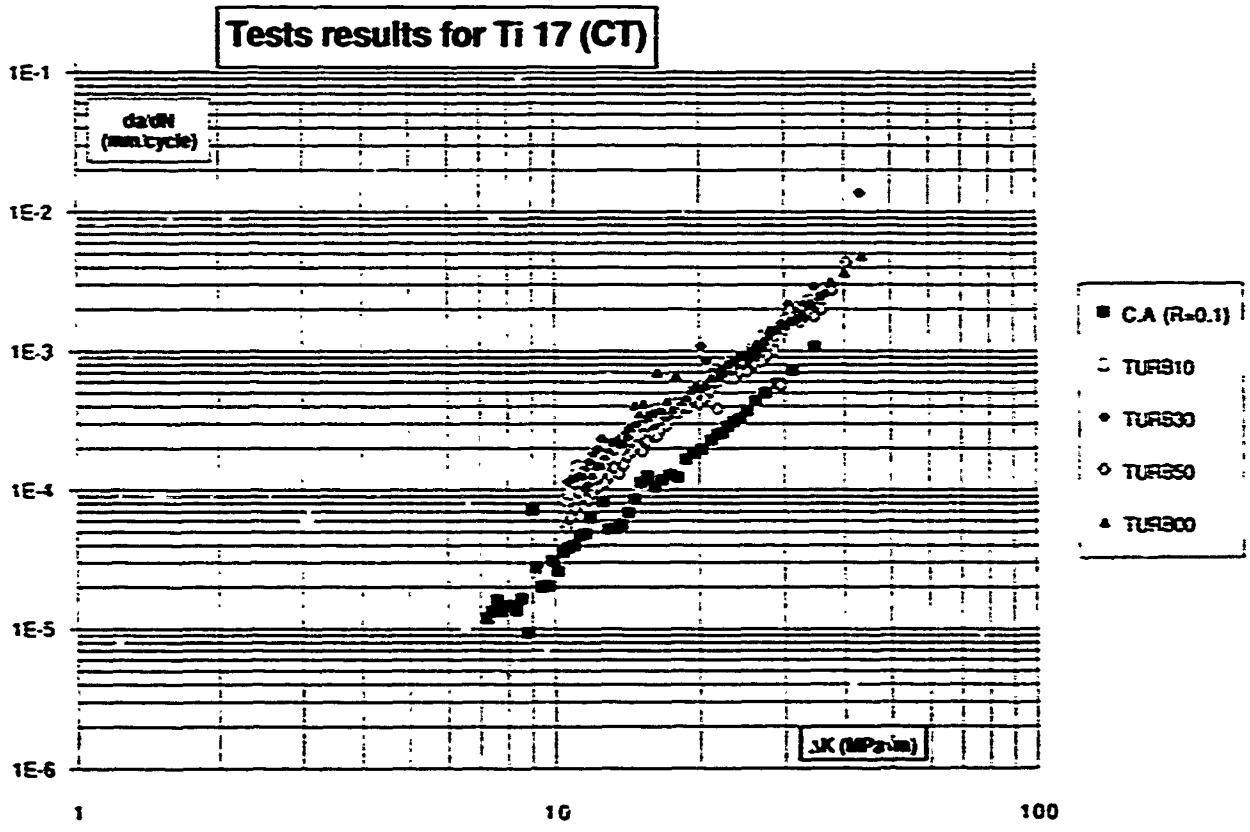

Fig.107 - da/dN vs ΔK Ti17/ CT test results

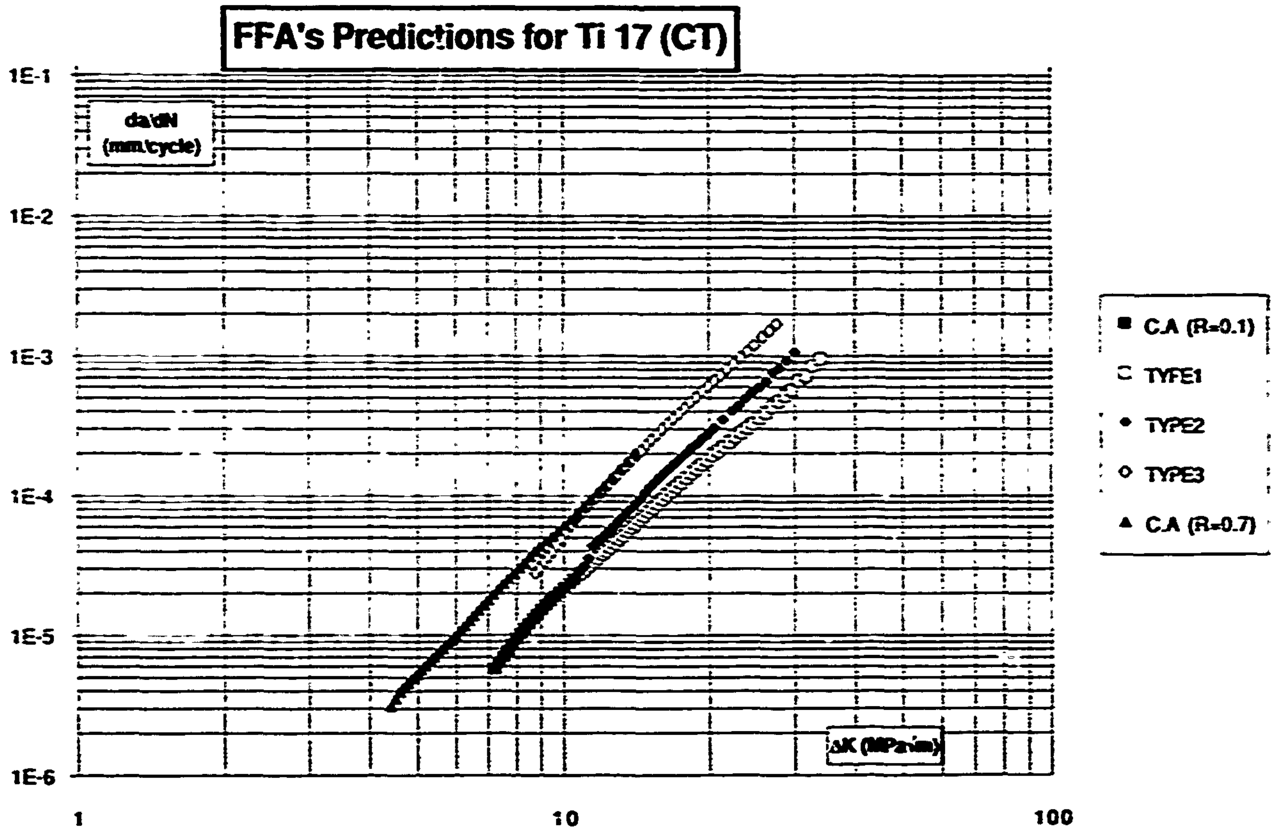

Fig.108 - da/dN vs ΔK Ti17/ CT FFA predictions

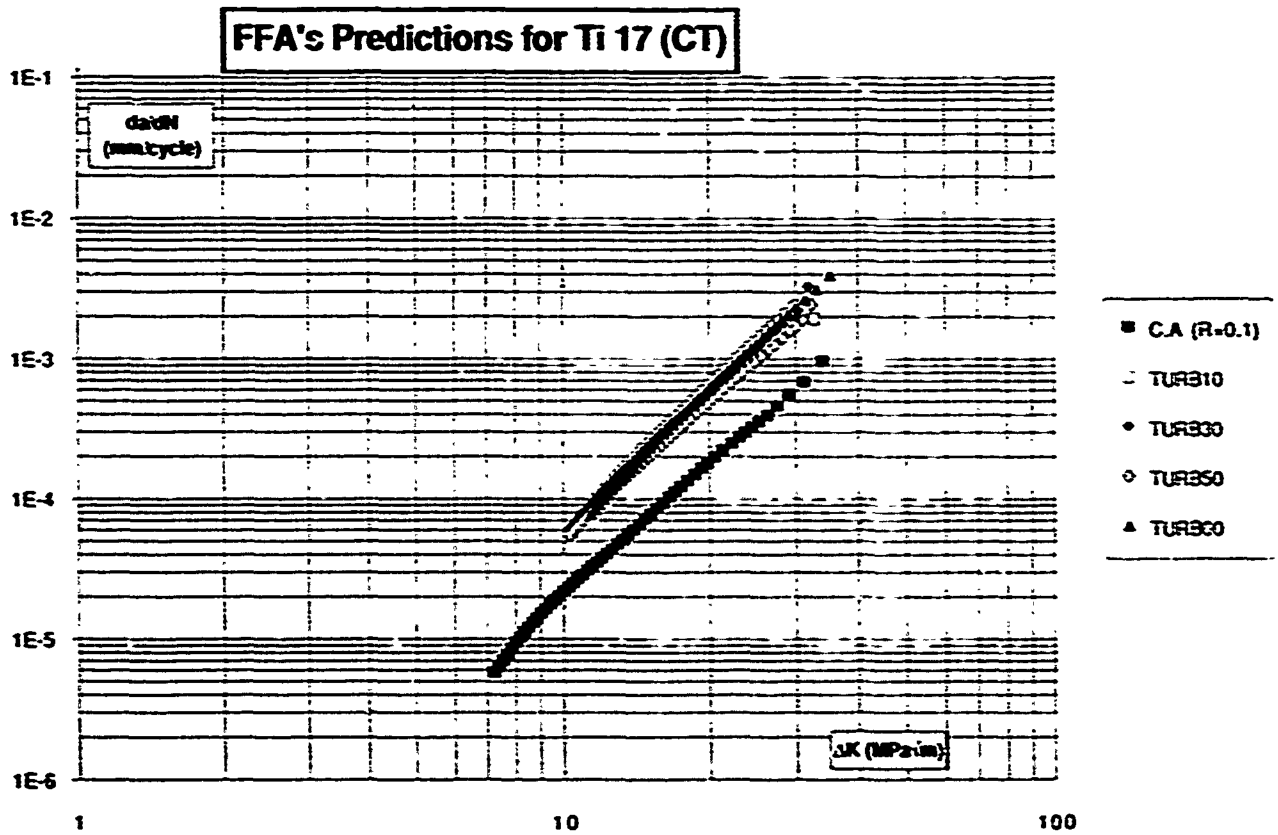

Fig.109 - da/dN vs ΔK Ti17/ CT FFA predictions

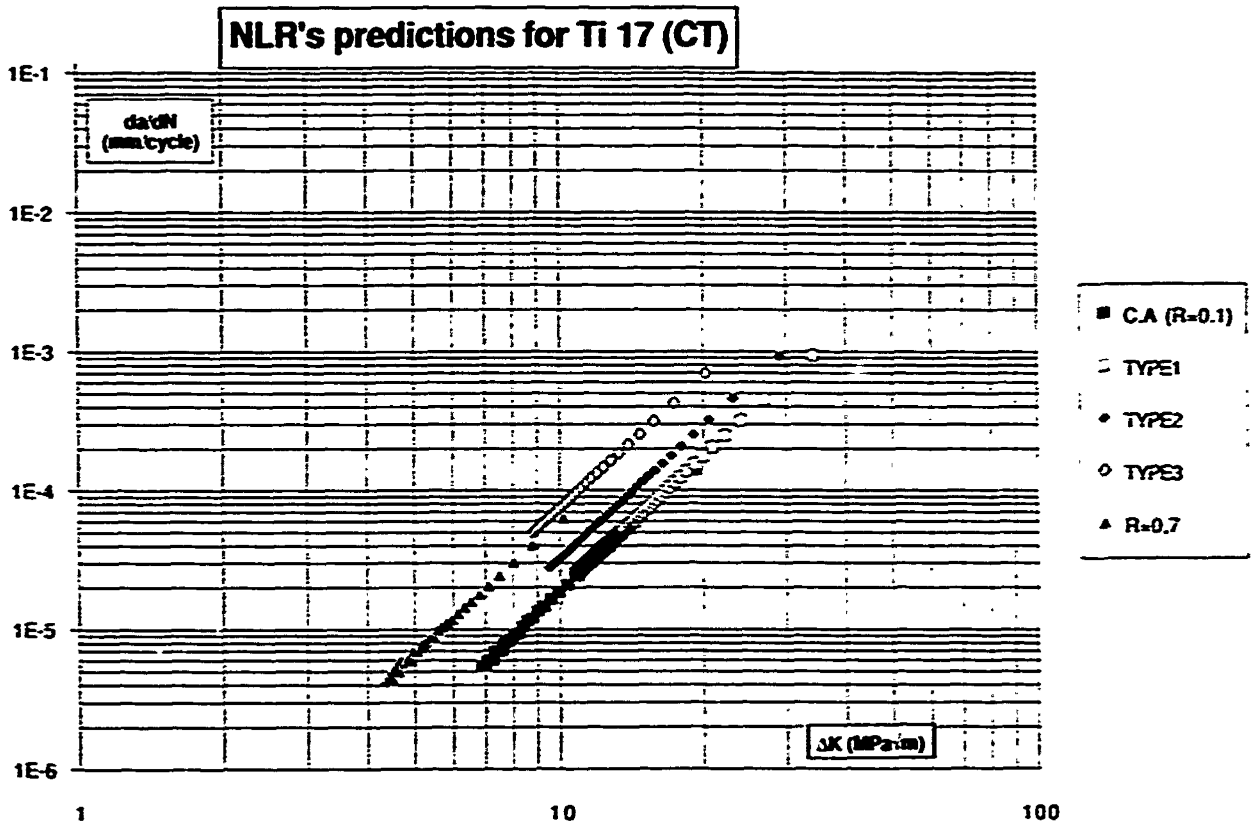

Fig.110 - da/dN vs ΔK Ti17/ CT NLR predictions

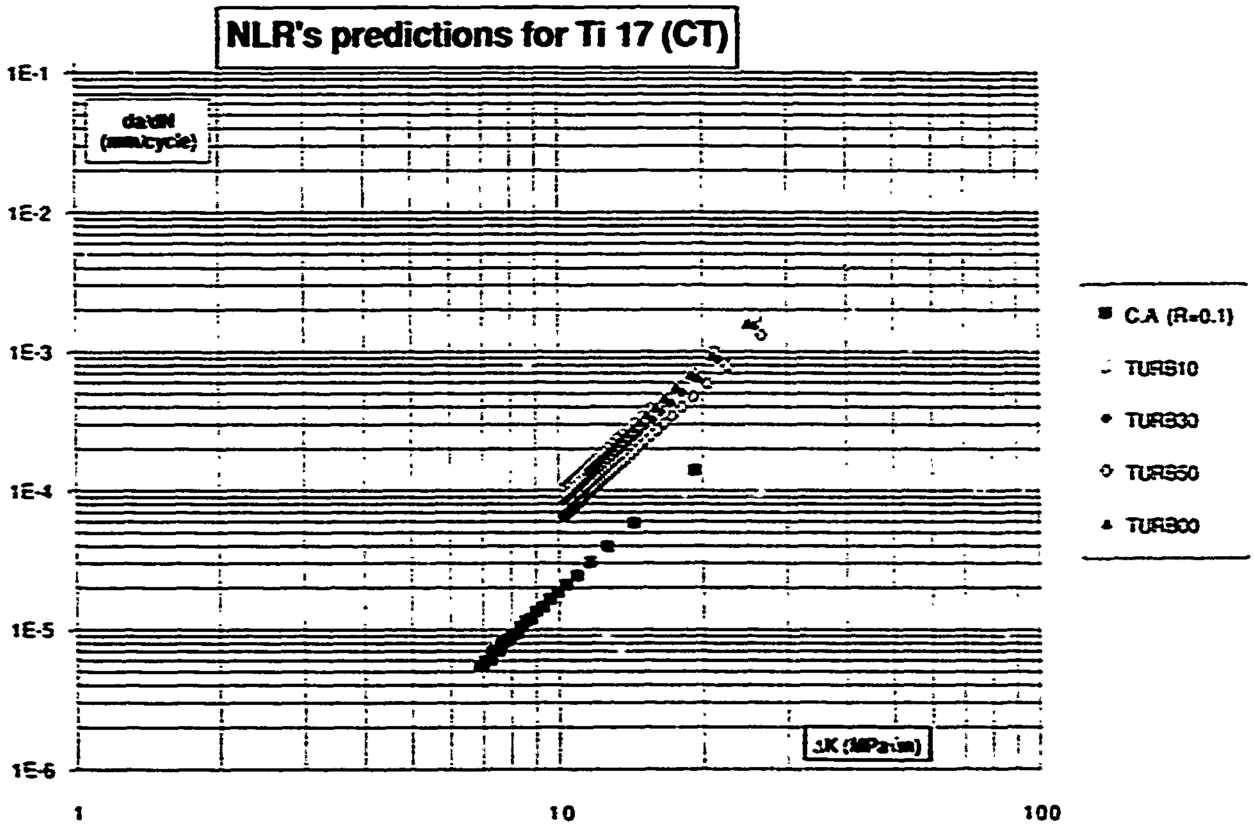

Fig.111 - da/dN vs ΔK Ti17/ CT NLR predictions

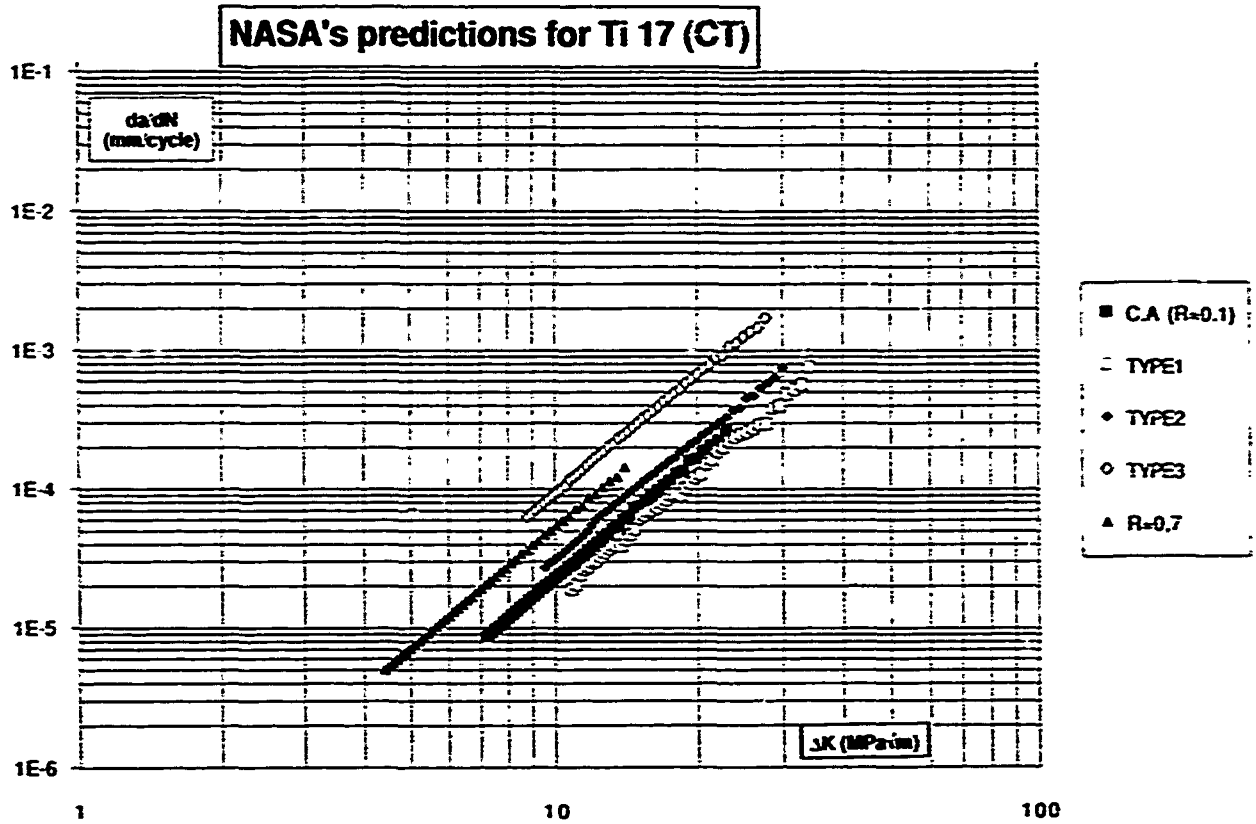

Fig.112 - da/dN vs ΔK Ti17/ CT NASA predictions

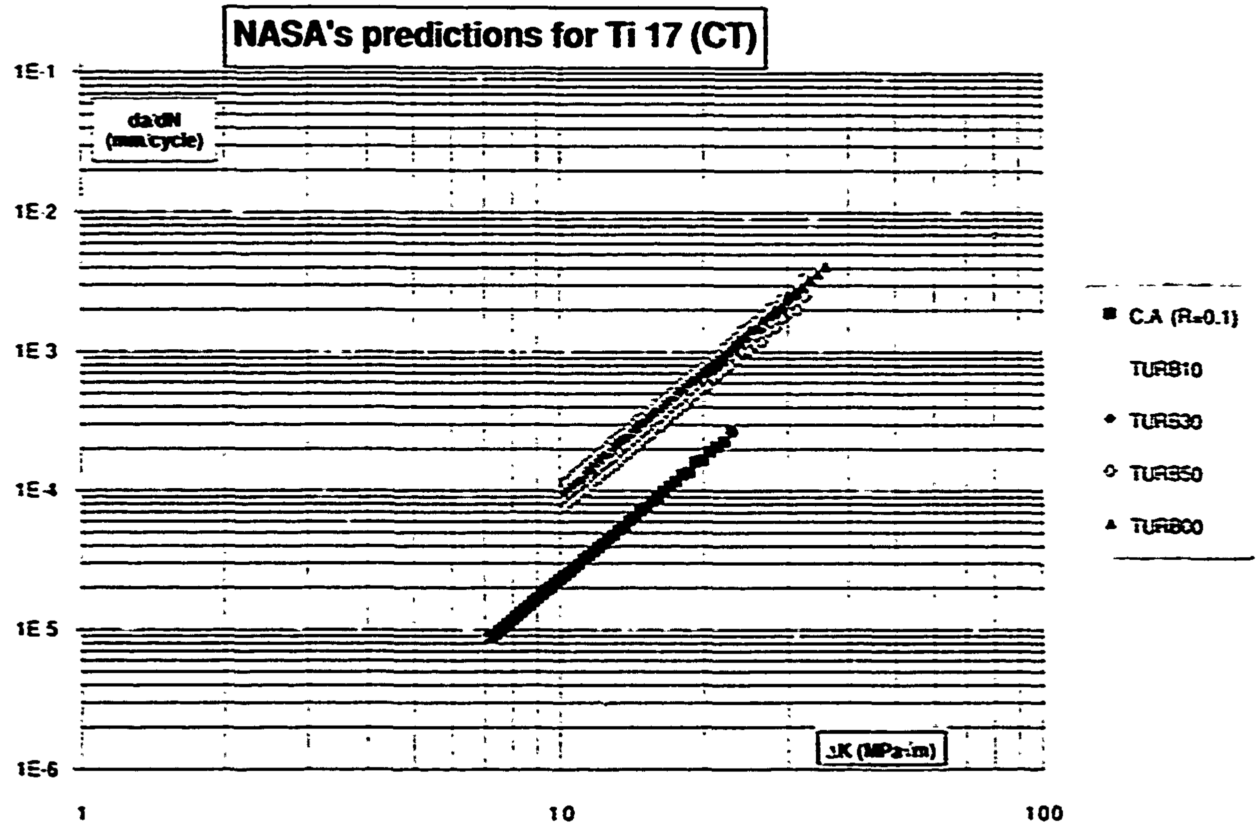

Fig.113 - da/dN vs ΔK Ti17/ CT NASA predictions

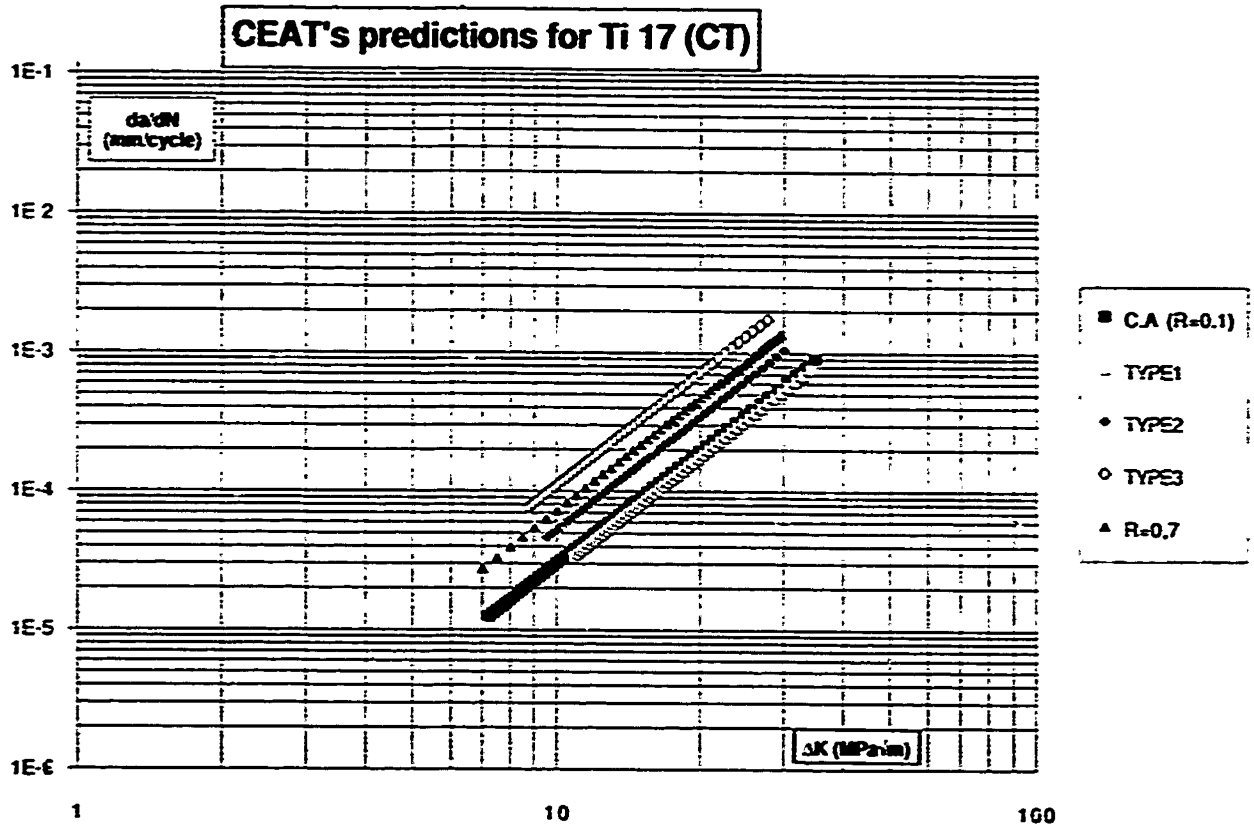

Fig.114 - da/dN vs ΔK Ti17/ CT CEAT predictions

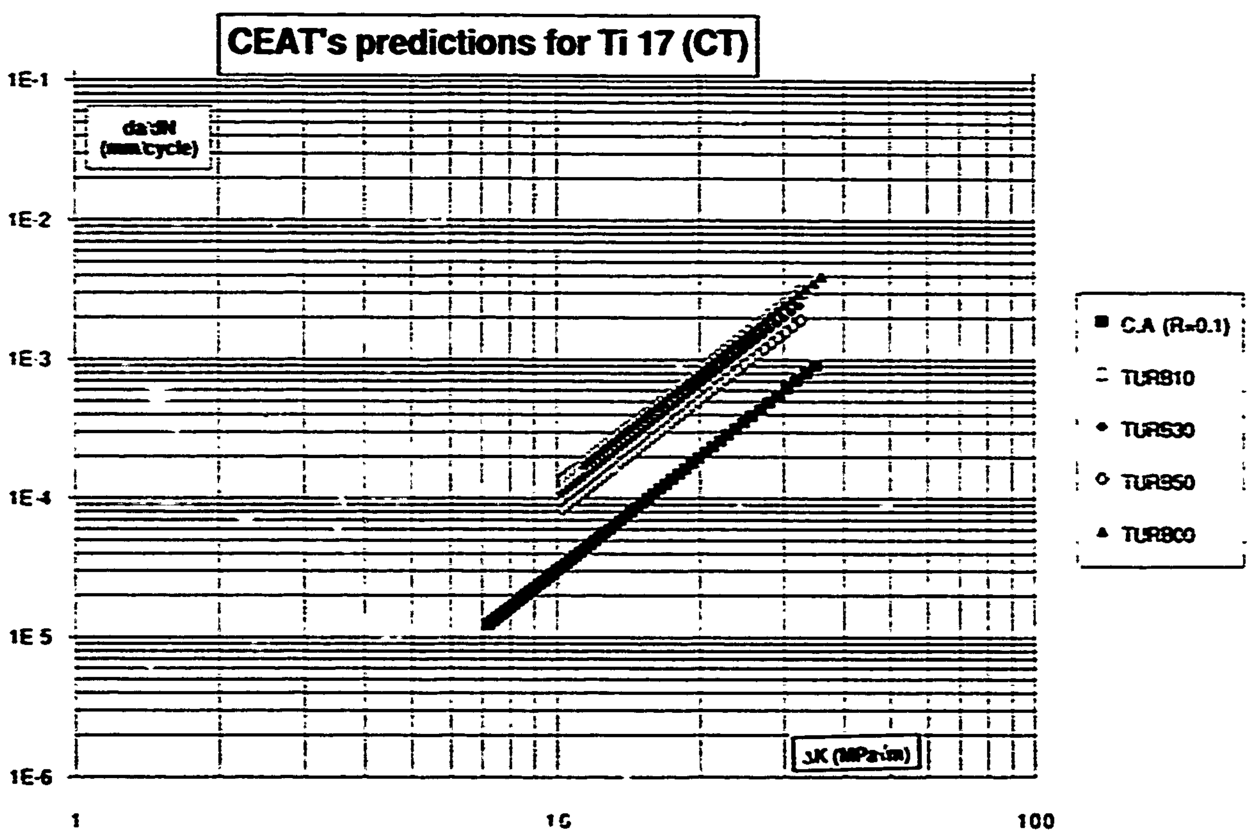

Fig.115 - da/dN vs ΔK Ti17/ CT CEAT predictions

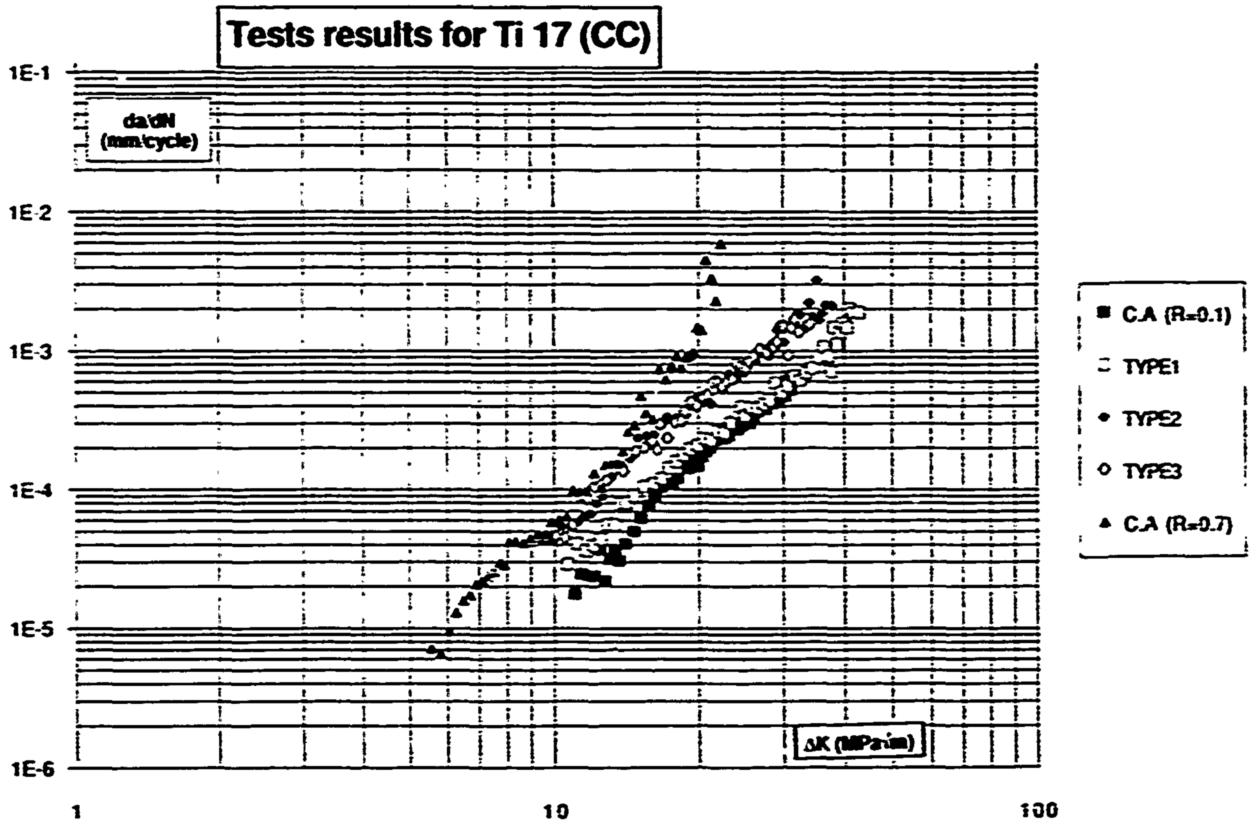

Fig.116 - da/dN vs ΔK Ti17/ CC test results

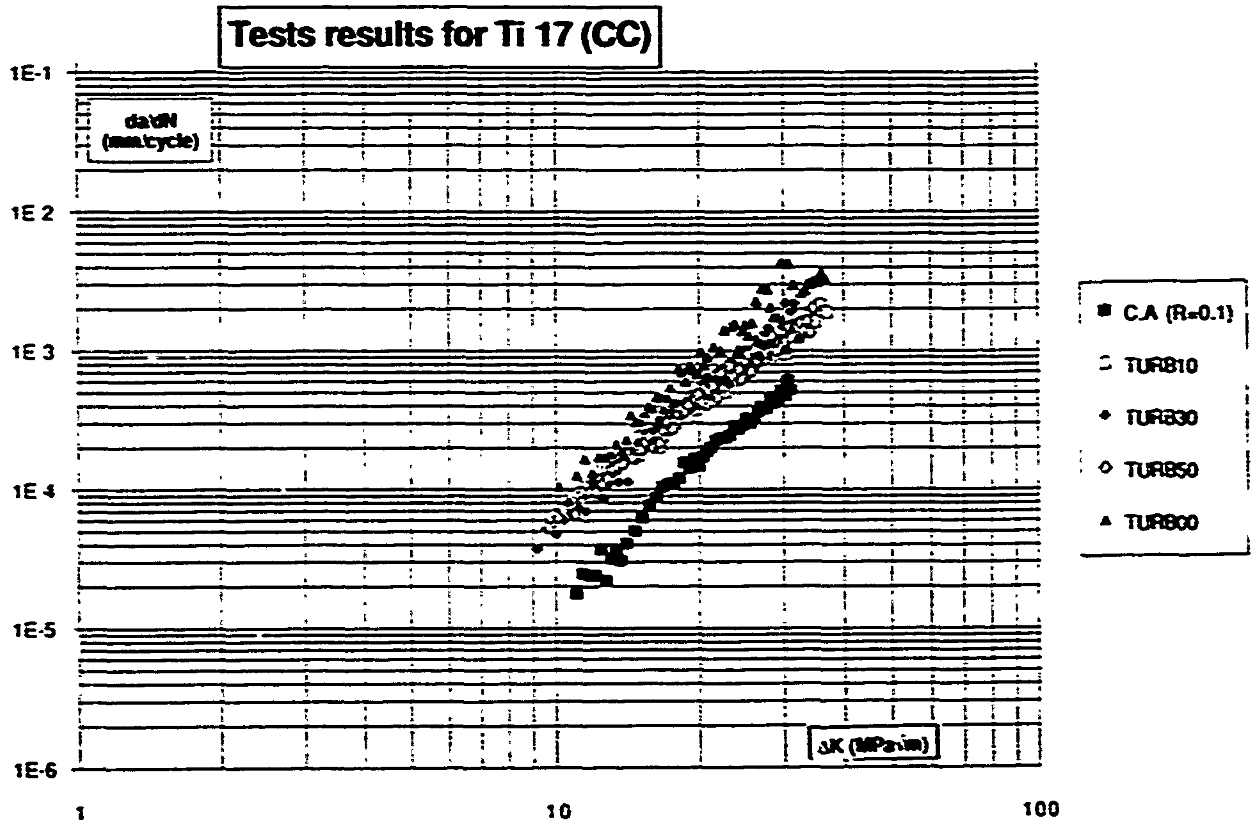

Fig.117 - da/dN vs ΔK Ti17/ CC test results

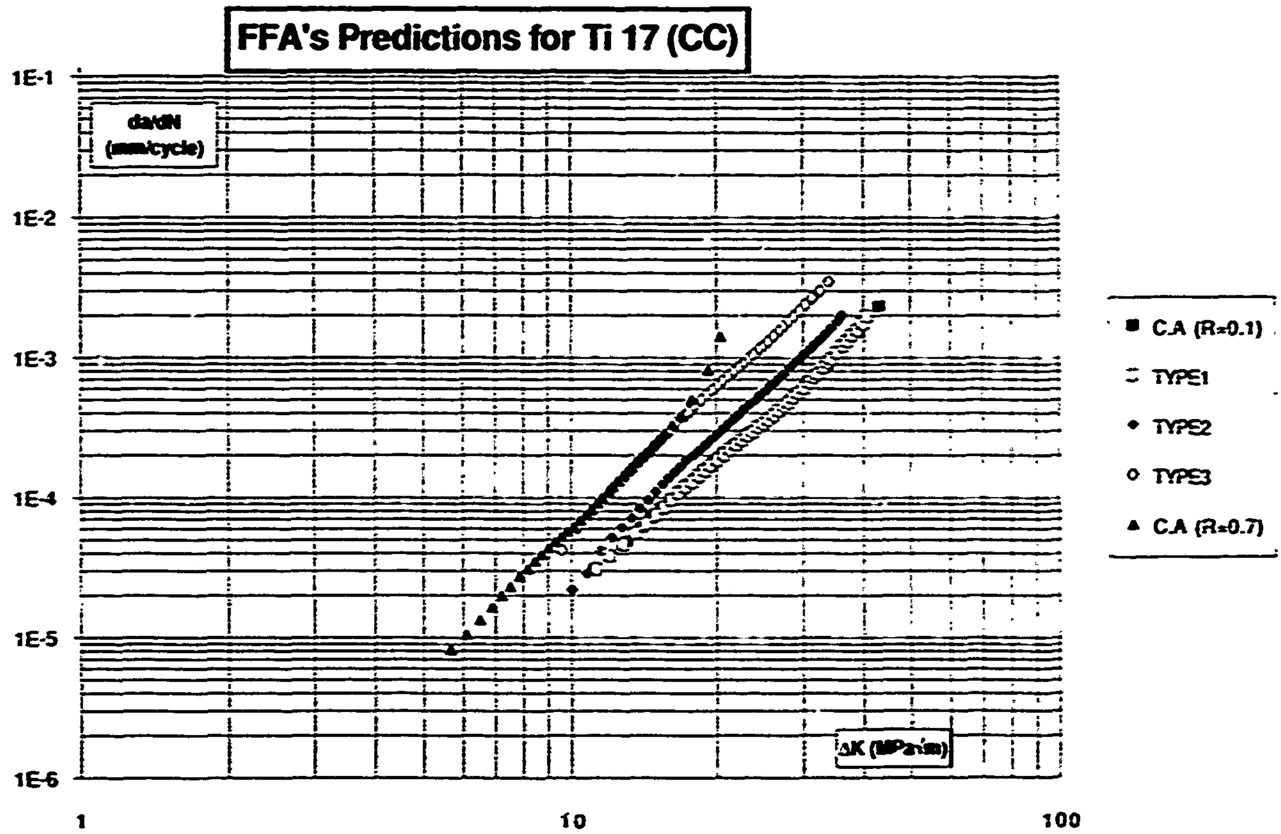

Fig.118 - da/dN vs ΔK Ti17/ CC FFA predictions

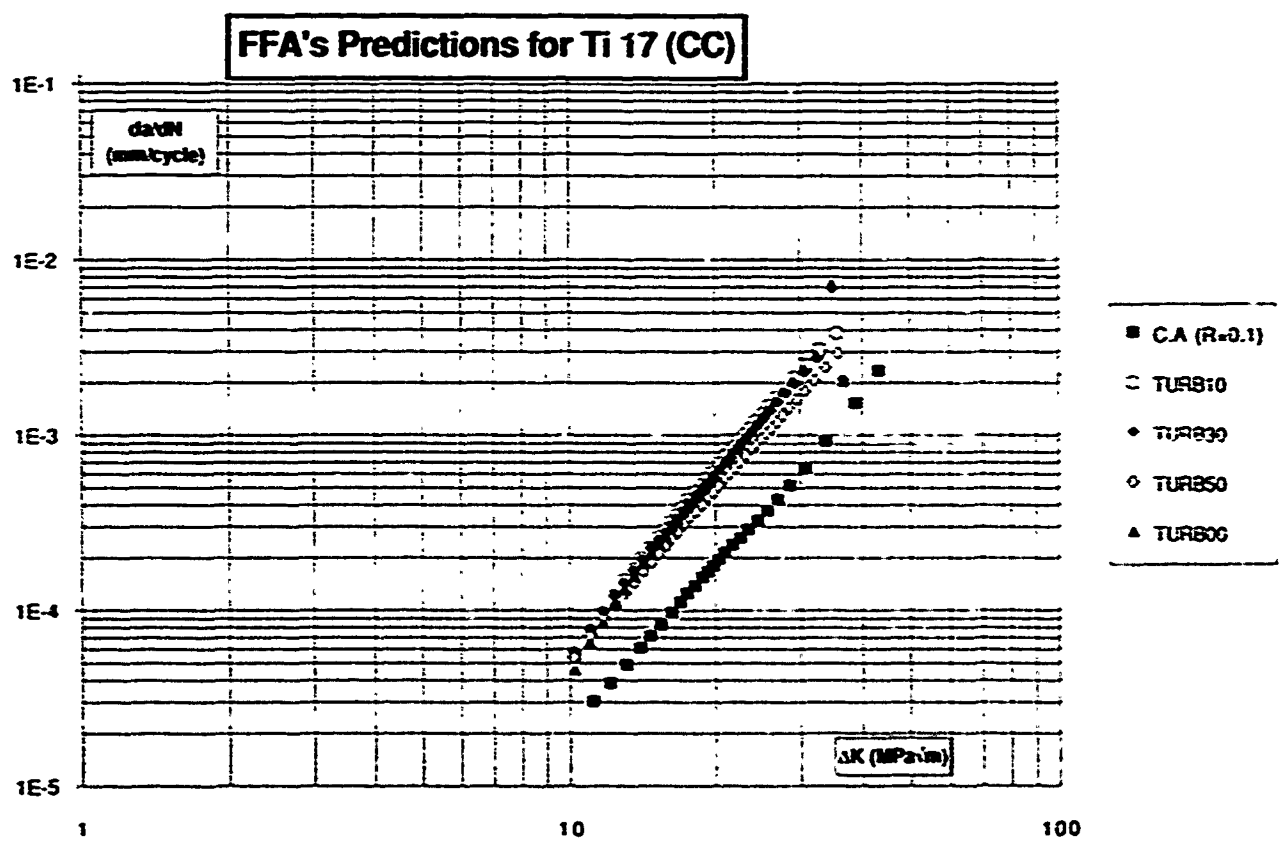

Fig.119 - da/dN vs ΔK Ti17/ CC FFA predictions

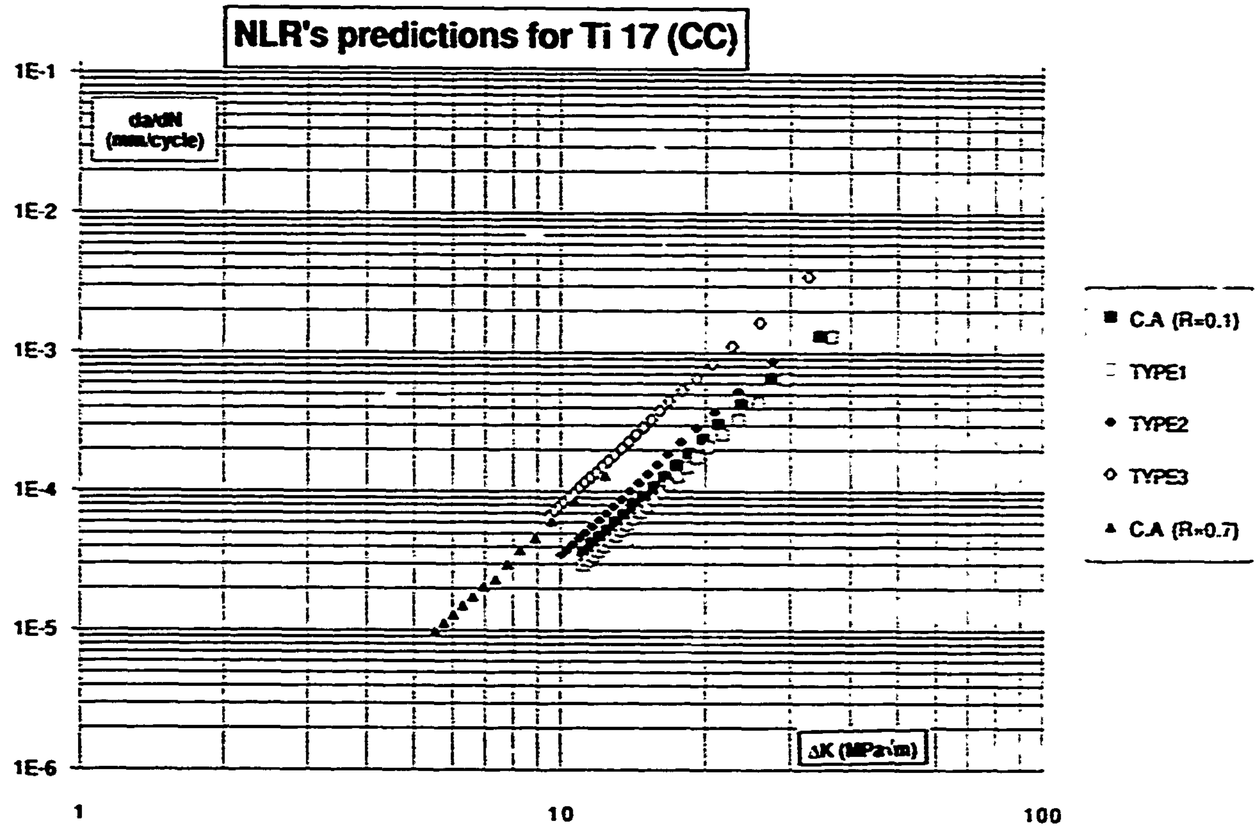

Fig.120 - da/dN vs ΔK Ti17/ CC NLR predictions

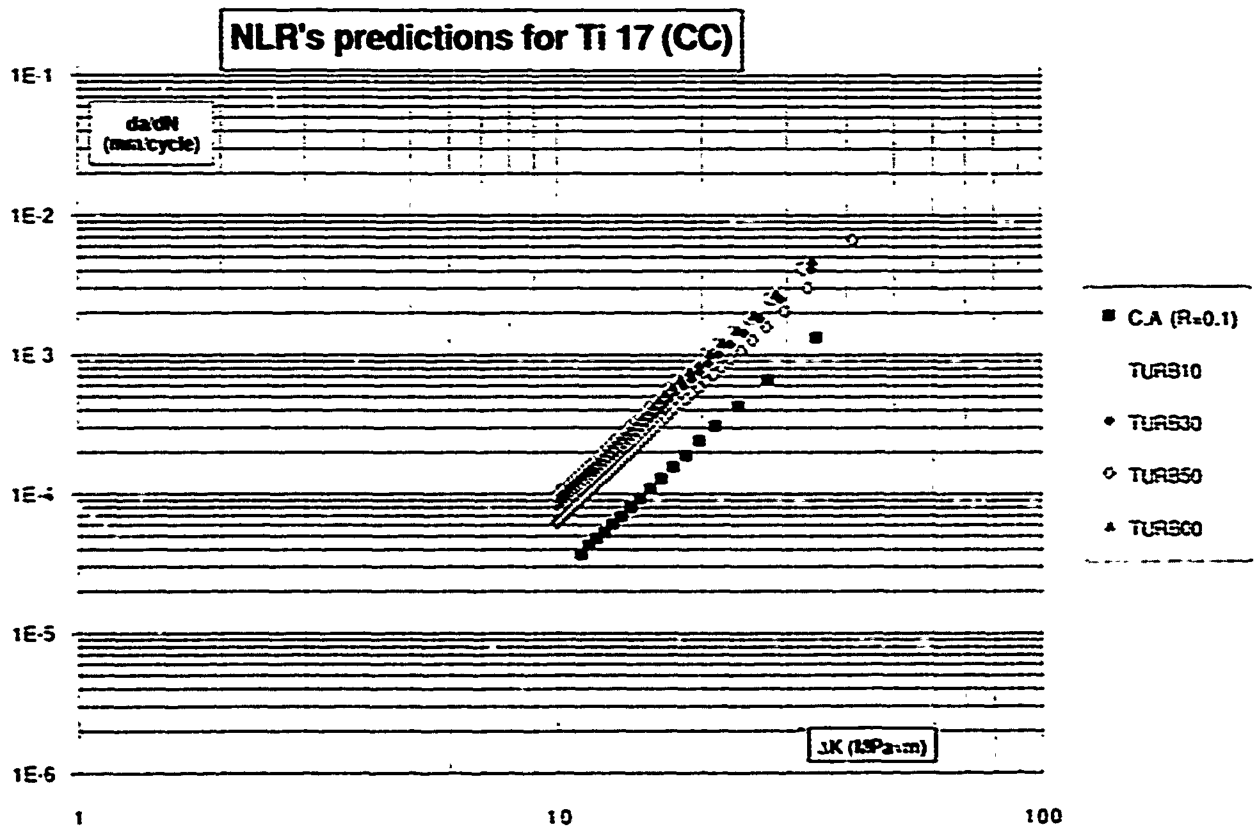

Fig.121 - da/dN vs ΔK Ti17/ CC NLR predictions

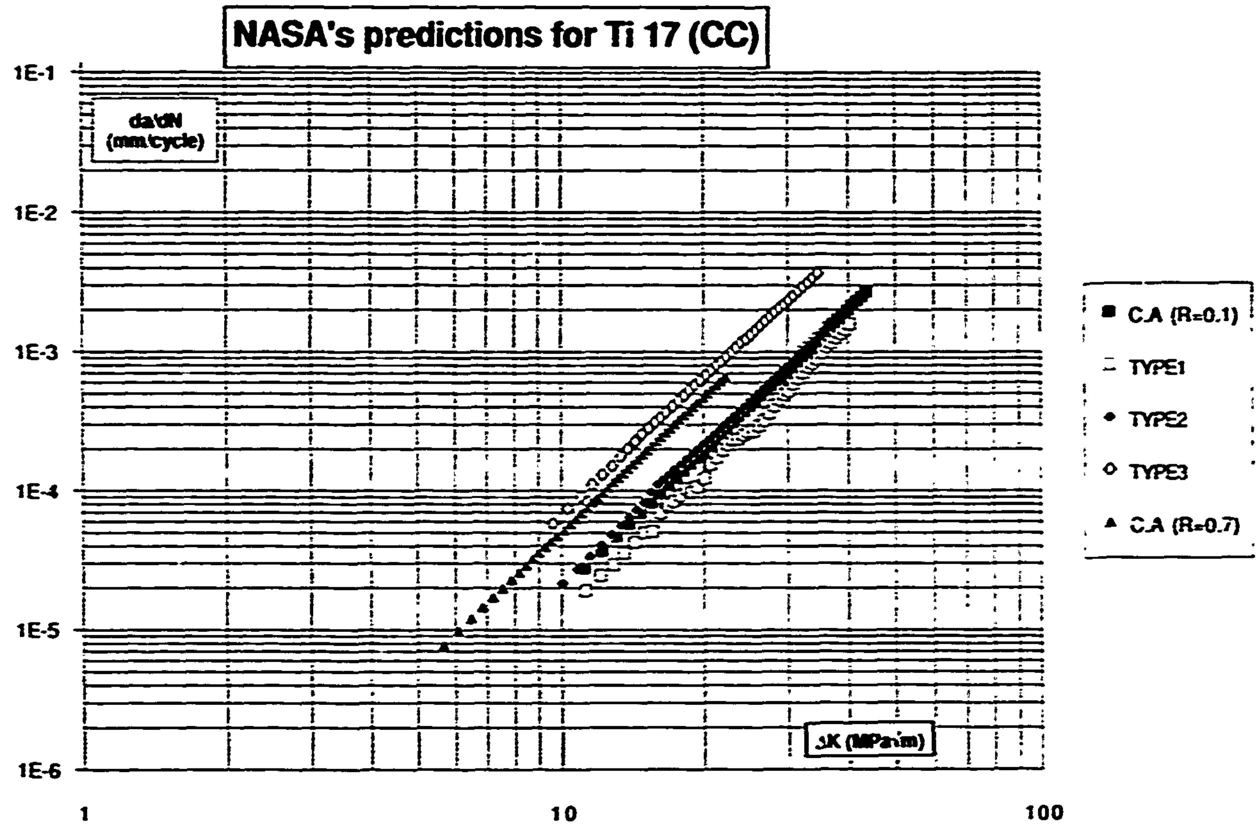

Fig.122 - da/dN vs ΔK Ti17/ CC NASA predictions

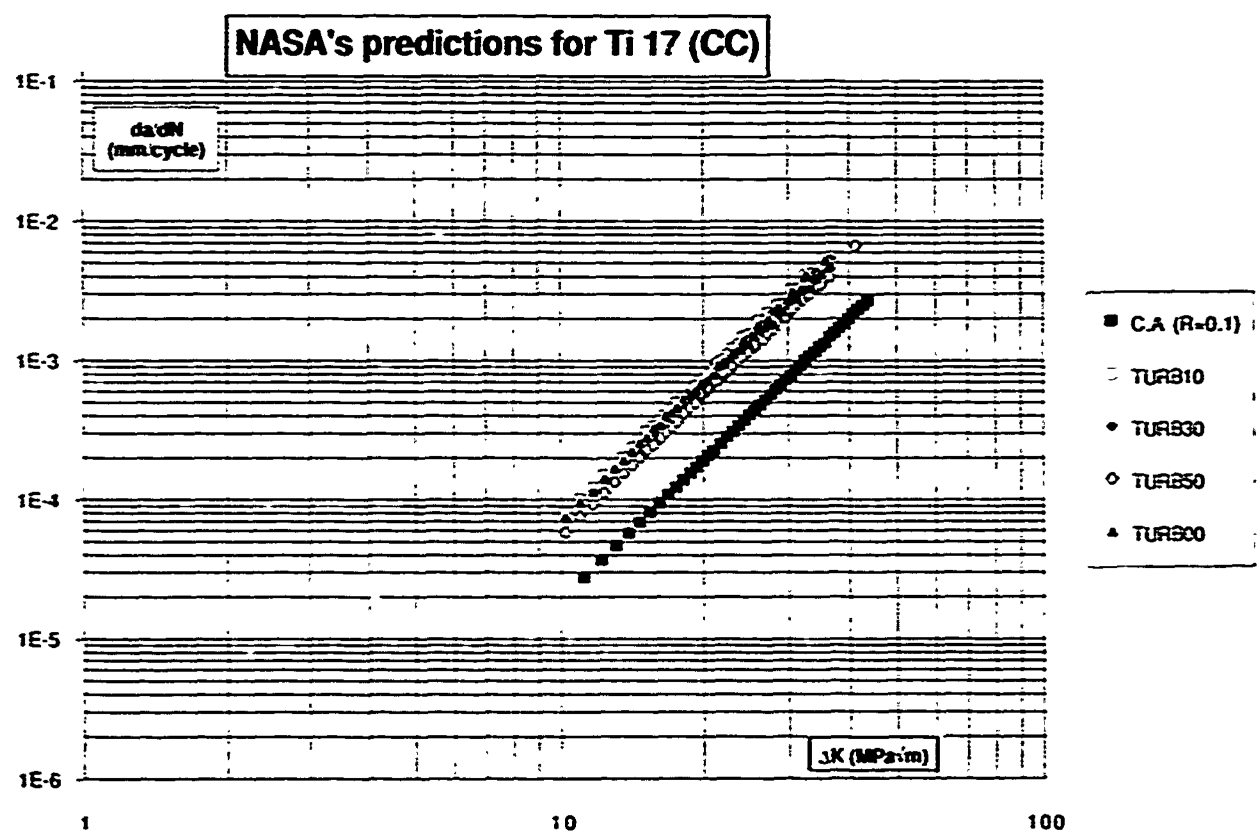

Fig.123 - da/dN vs ΔK Ti17/ CC NASA predictions

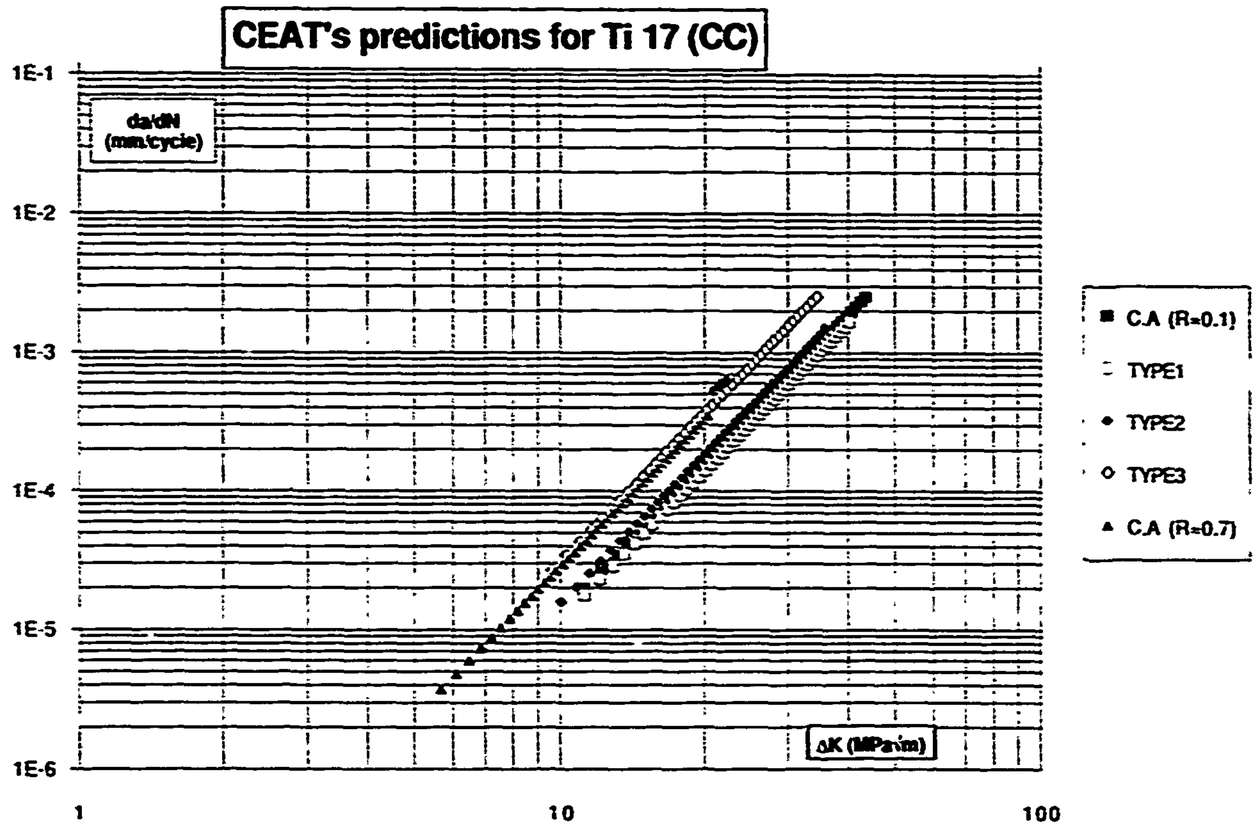

Fig.124 - da/dN vs ΔK Ti17/ CC CEAT predictions

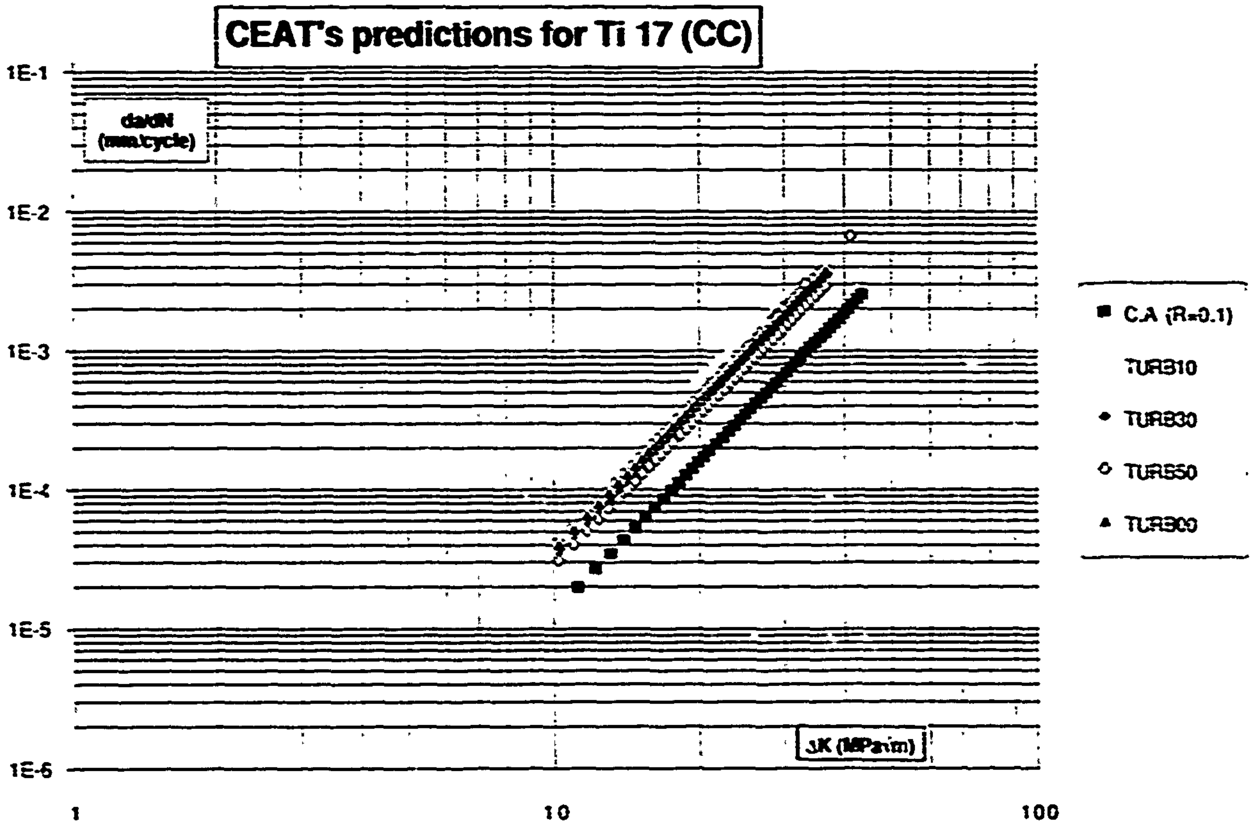

Fig.125 - da/dN vs ΔK Ti17/ CC CEAT predictions

Ti-6Al-4V: CT specimen

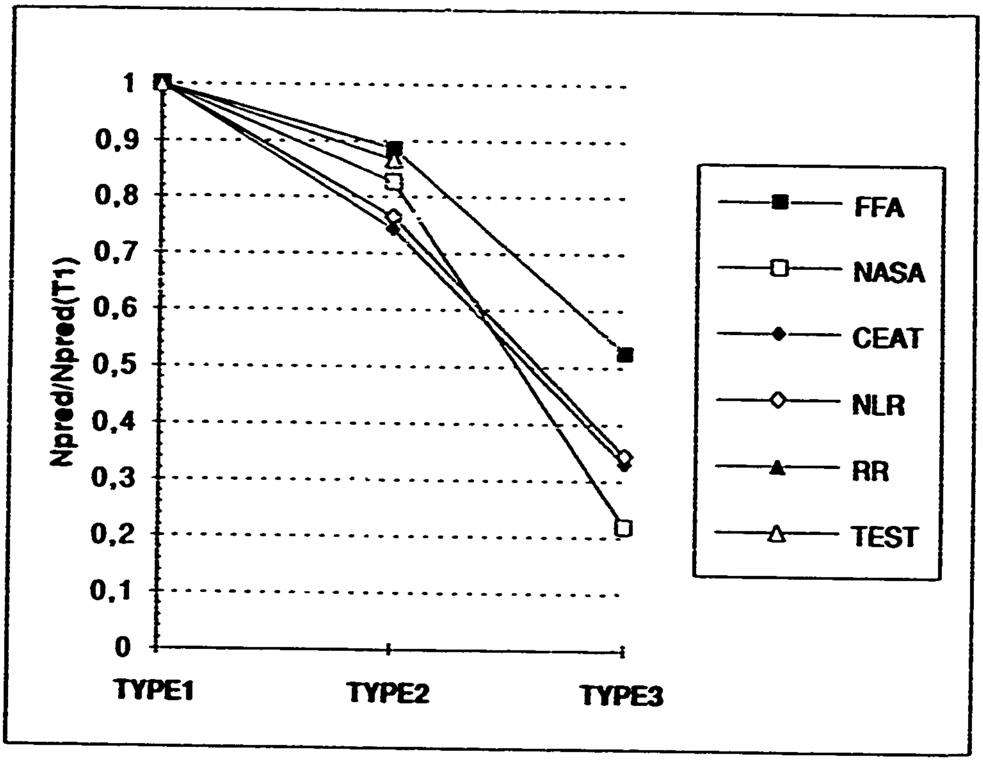

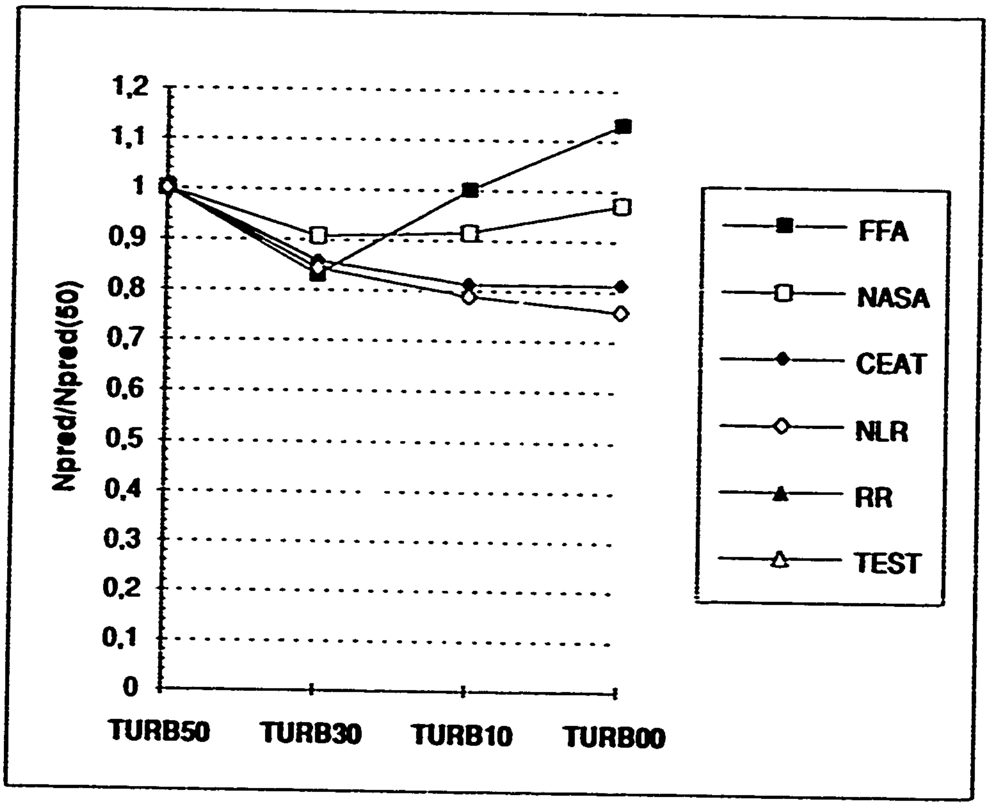

Fig.126 & 127 - Small amplitude cycle sensitivity chart Ti-6Al-4V / CT

Ti-6Al-4V: CC specimen

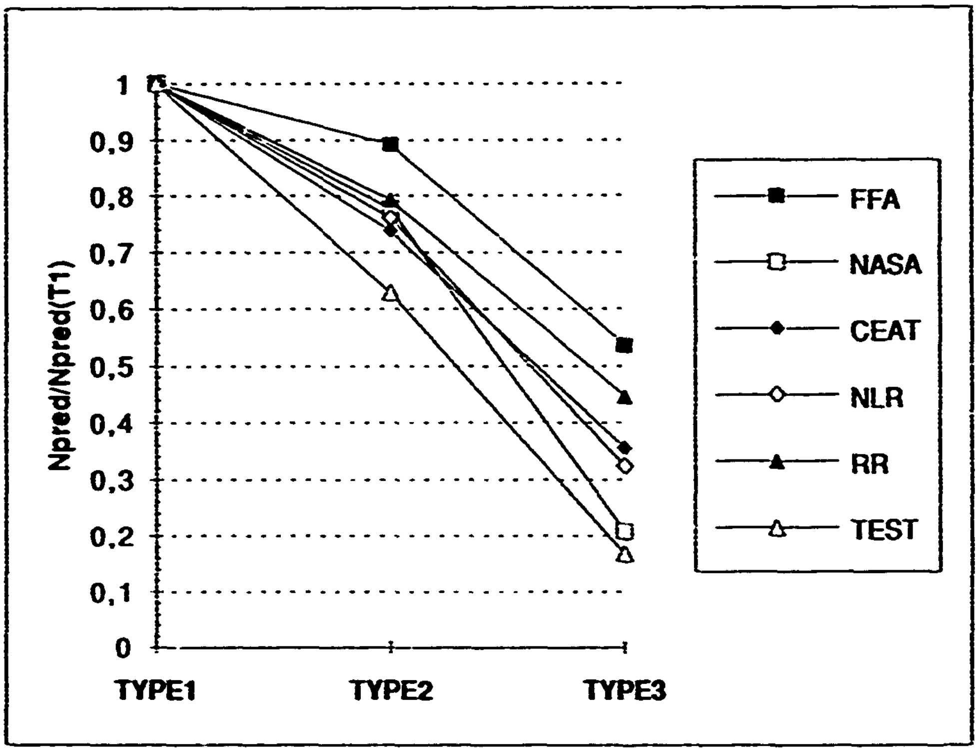

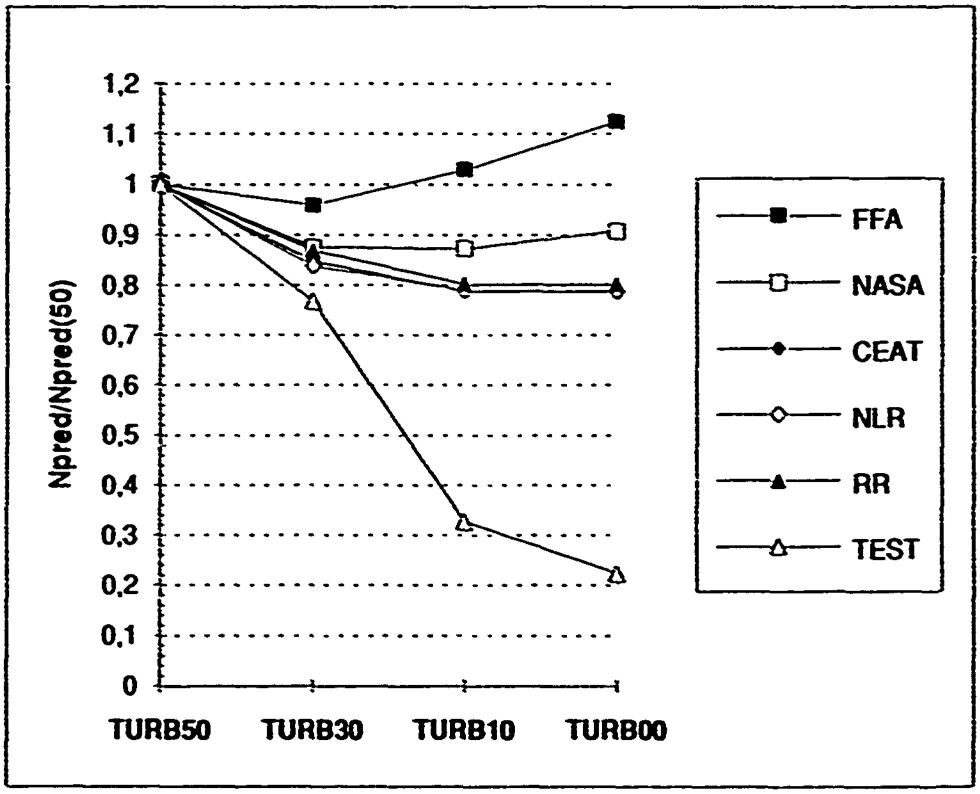

Fig.128 & 129 - Small amplitude cycle sensitivity chart Ti-6Al-4V / CC

IMI 685: CT specimen

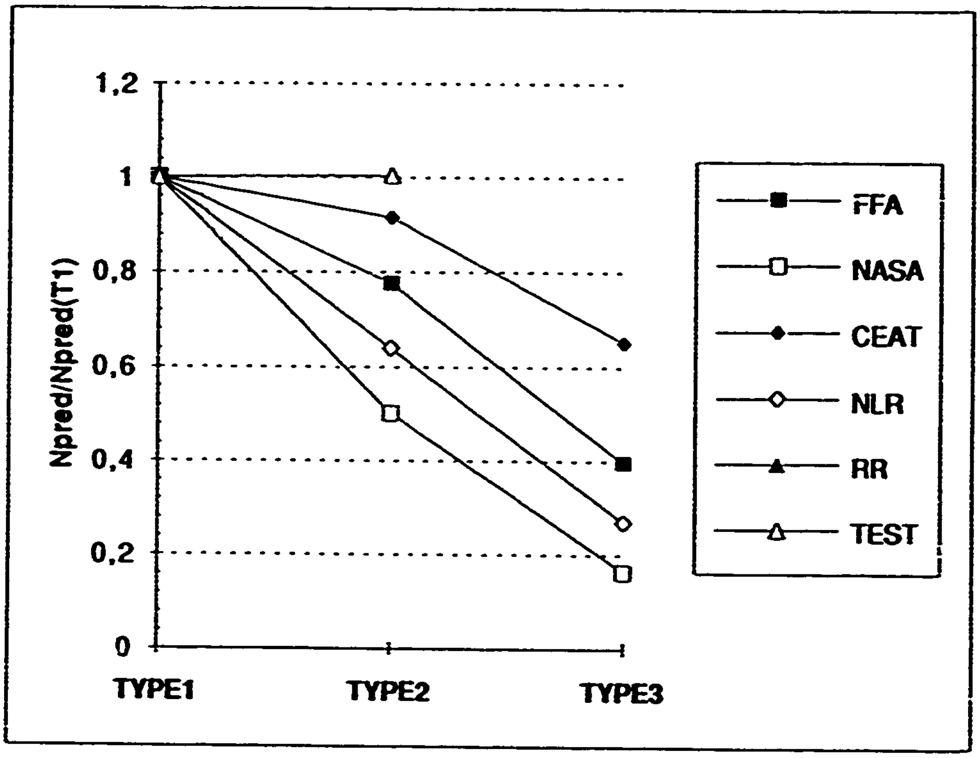

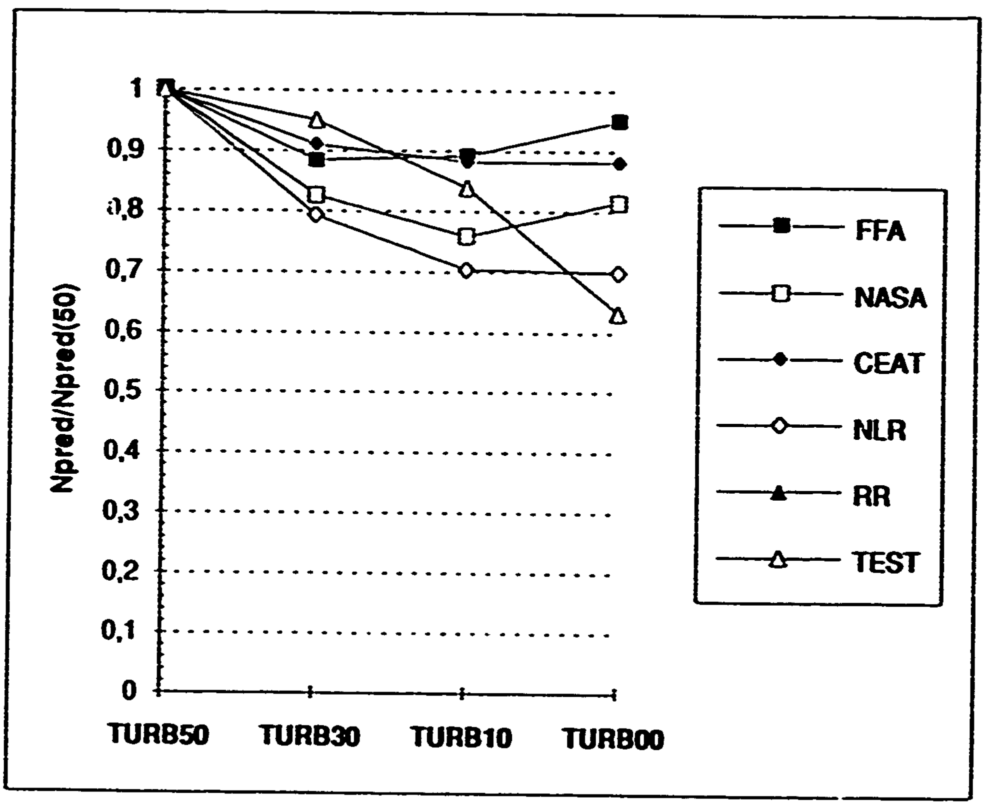

Fig.130 & 131 - Small amplitude cycle sensitivity chart IMI685 / CT

IMI 685: CC specimen

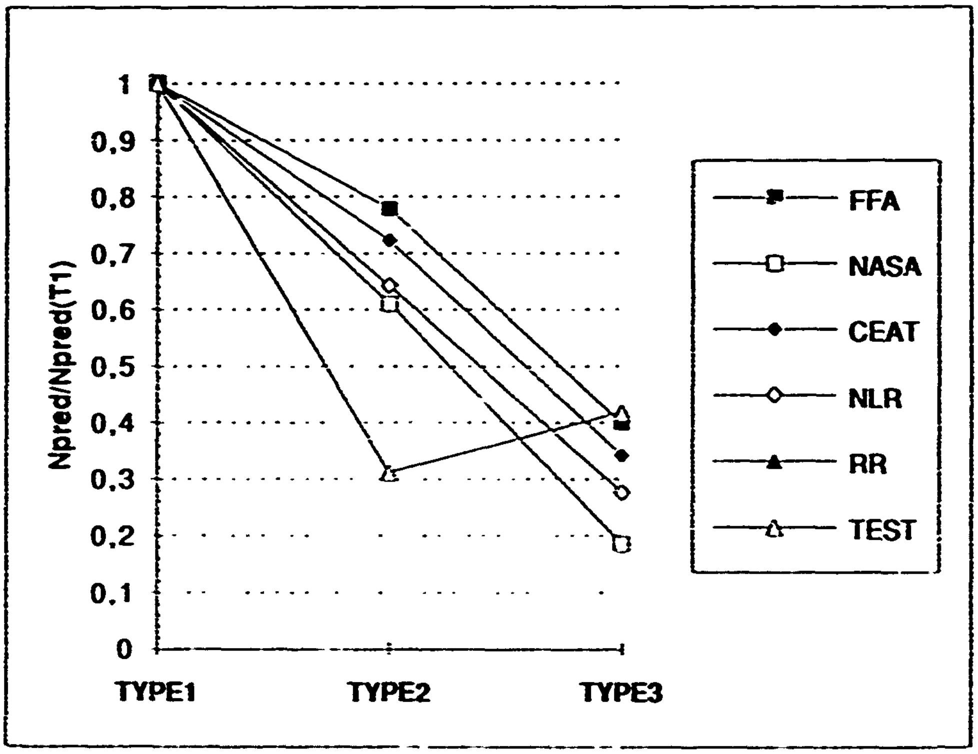

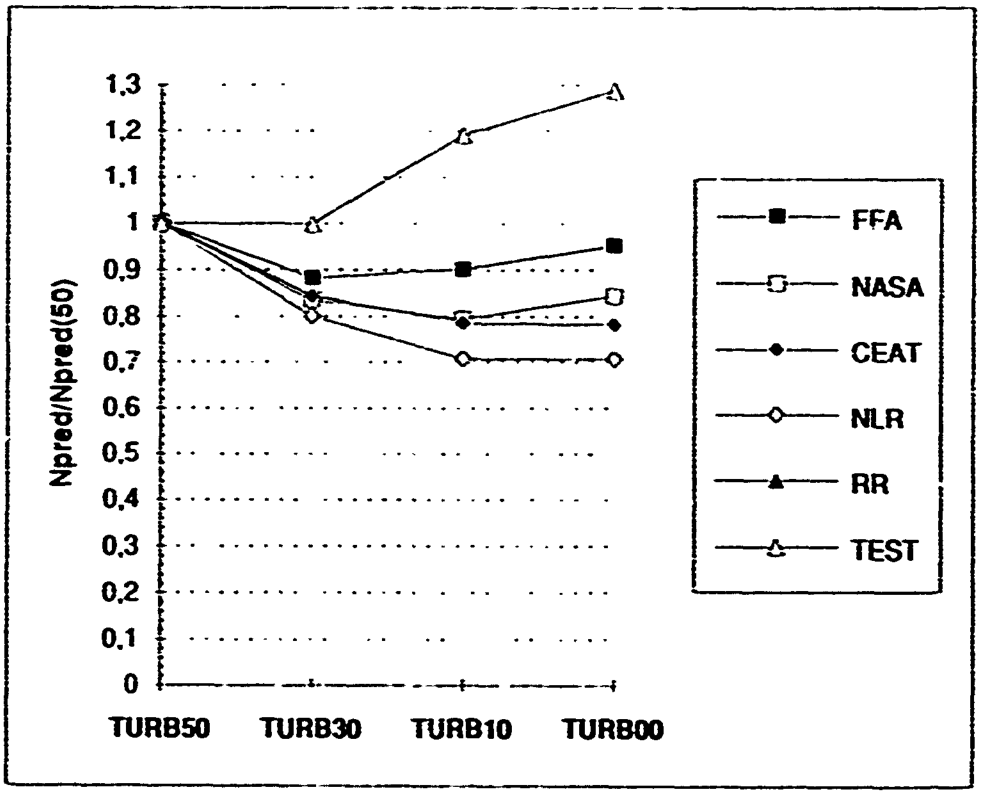

Fig.132 & 133 - Small amplitude cycle sensitivity chart IMI685 / CC

Ti 17: CT specimen

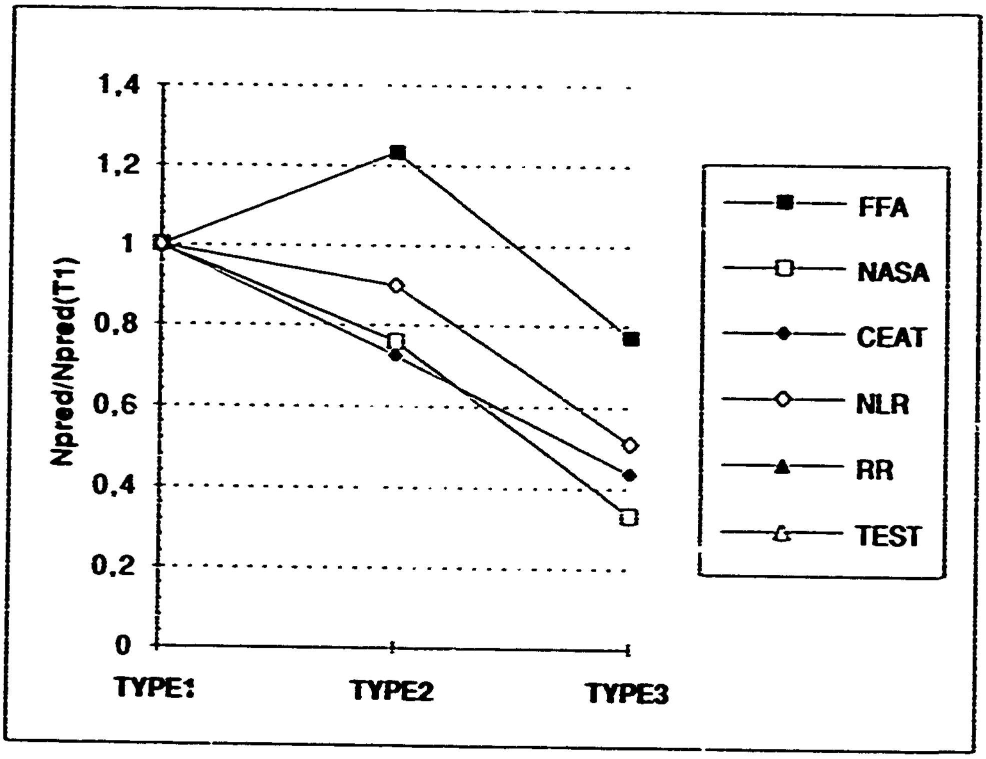

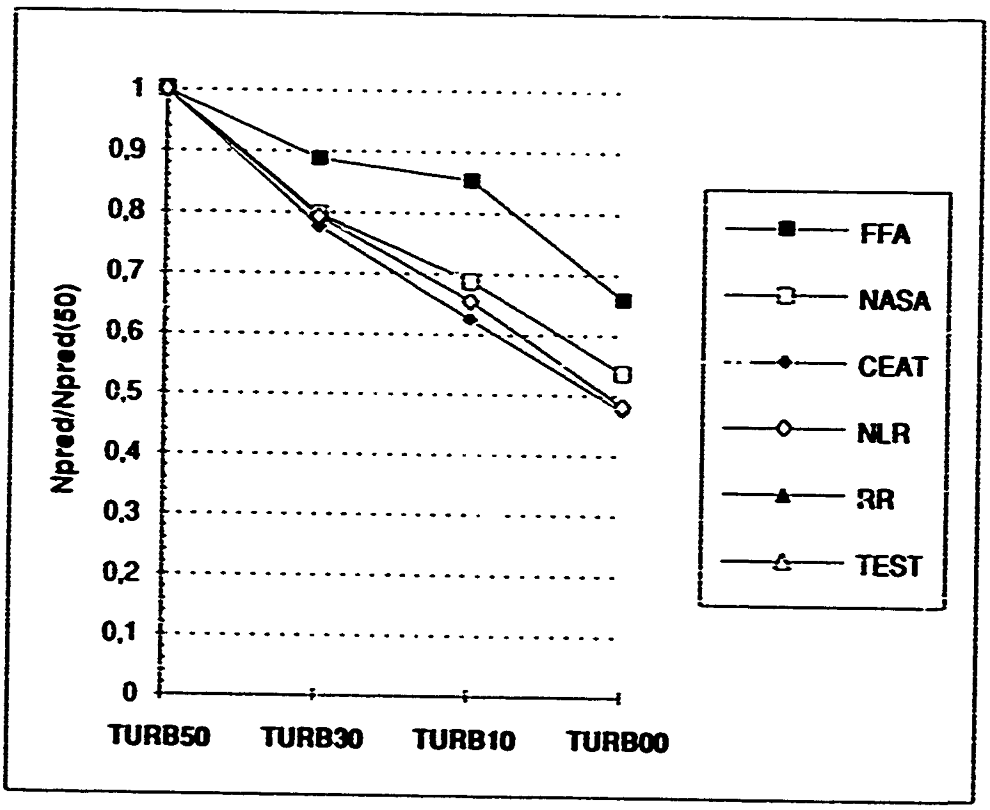

Fig.134 & 135 - Small amplitude cycle sensitivity chart Ti17 / CT

Ti 17: CC specimen

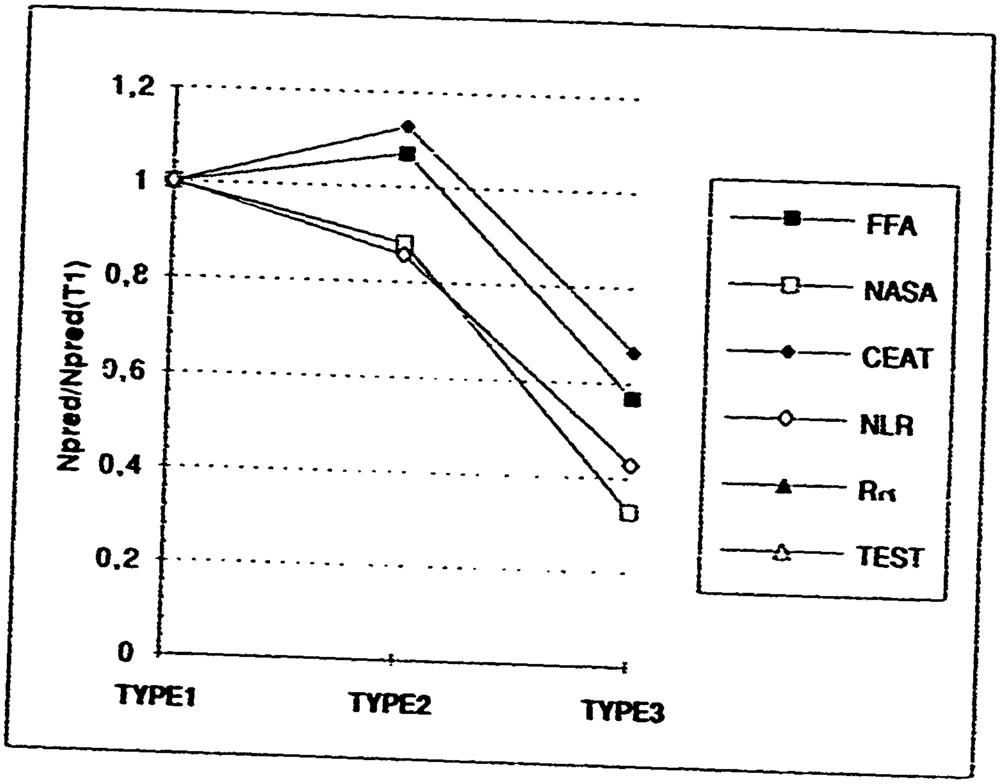

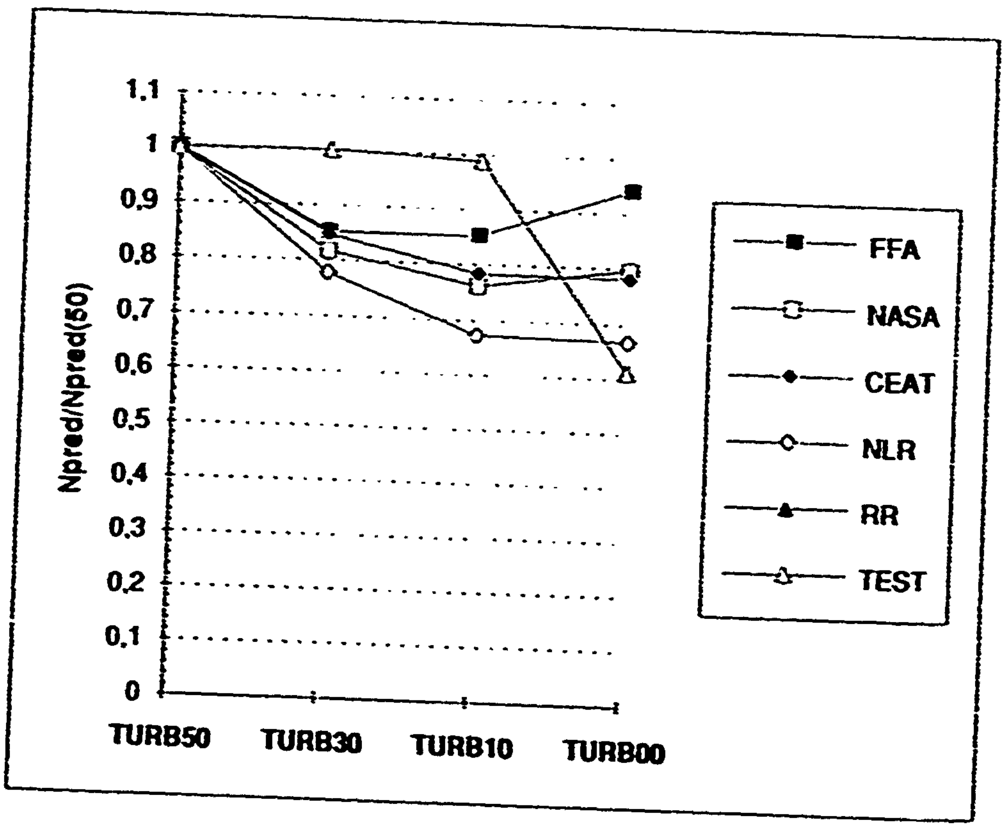

Fig.136 & 137 - Small amplitude cycle sensitivity chart Ti17 / CC

CHAPTER 7

CONCLUSIONS AND RECOMMENDATIONS

by
Paul Heuler and Walter Schütz
Industrieanlagen-Betriebsgesellschaft (IABG)
8012 Ottobrunn
Germany

and

Eric Jany
Centre d'Essais Aeronautique de Toulouse (CEAT)
31056 Toulouse
France

1 Introduction

The preceding chapters have presented and discussed the objectives related to this large collaborative effort as well as relevant test techniques, modelling details and results in great detail. In 1988 an AGARD report had been published on the results obtained within the Core Programme [1] which represents the first of two parts of the AGARD Engine Disc Cooperative Test Programme. The major issues treated within the present Supplemental Programme were:

- To expand the initial Ti-6Al-4V data base to other titanium materials such as the β-processed IMI 685 and Ti-17. Here again load controlled LCF tests were carried out on smooth and notched specimens as well as crack growth tests on compact tension (CT) and corner crack (CC) specimens under constant amplitude loading.

- To consider variable amplitude and spectrum load sequences that would be typical of compressor disc loading conditions. Aspects related to both the experimental techniques as well as to materials' response to non-constant amplitude loading are being discussed.

- To apply and evaluate fatigue crack growth modelling techniques based on the material/load cases of the Cooperative Test Programme as mentioned above.

Additionally microstructural and fractographic analyses have been undertaken in order to relate macro crack growth behaviour to microstructural features and intrinsic material properties. In this final chapter, some main aspects and results are summarized. Conclusions and recommendations for future work are given.

2 Testing

LCF Smooth and Notched Specimens

These tests were carried only under constant amplitude loading applying a trapezoidal wave form with R = 0.1 and a nominal frequency of 0.25 Hz. Both types of specimens were tested under load control. For smooth specimens this control mode might turn out to be questionable because of the extensive cyclic creep occurring at higher stress levels. Tests under strain control, however, were beyond the scope of the present programme; they are considered within a successive AGARD test programme [2]. Despite of the inherent cyclic creep effect, the data produced were very consistent. Scatter of the IMI 685 data is reduced as compared to the Ti-6Al-4V data created within the Core Programme [1] although this might be - in part - a consequence of the higher number of test results and laboratories involved in the Ti-6Al-4V excercise.

Crack Growth Tests - Constant Amplitude Loading

Similar to the LCF tests, constant amplitude tests were conducted to expand the data base under identical conditions as in the Core Programme. The results again turned out to be very consistent for the vast majority of tests.

For Ti-6Al-4V it had been found in the Core Programme that the average CC crack growth data were between 30 and 50 percent slower than the respective CT data for given ΔK values between 15 and 35 $MPa\sqrt{m}$ [1]. The reason for this difference could not be resolved. Within the Supplemental Programme, trends with respect to the effect of specimen geometry were not as clear. For Ti-17 no significant influence of the specimen geometry was observed, whereas for Ti-6Al-4V again lower growth rates were found for the CC geometry. For IMI 685, higher rates could be observed for CC specimens at low ΔK levels whereas both CC and CT rate data merged at higher ΔK levels. This can be rationalized based on the coarse microstructure of that material where the CC crack is - at least in the initial stage - shorter than microstructural dimensions. Considering the increasing coarseness of the microstructures of Ti-6Al-4V, Ti-17, and IMI 685, respectively, it might be speculated whether the above ranking is connected in some way to microstuctural effects. However, the different (and limited) amount of individual test data for the three materials should be noted which prevents final conclusions.

Crack Growth Tests - Variable Amplitude and Spectrum Loading

Consideration of variable amplitude and spectrum loading was one of the major steps beyond the scope of the Core Programme. It consisted of an overload sequence which was required for the identificaion of basic input data for some of the models, three "underload" sequences and four TURBISTAN sequences where small cycles were successively omitted from the full spectrum. The underload sequences (high R-ratio constant amplitude cycles interrupted by large zero-max

cycles) represent further simplifications of the complex TURBISTAN cycle which is typical for disc loading environment.

The results obtained for the complex loading sequences were again very consistant providing a sound basis for the following modelling excercise. In some cases where large deviations from the major data trend were observed, fractographic analyses provided insight into the mechanisms responsible for those findings. An excellent analysis has been provided for Ti-6Al-4V by Wanhill and Looije (see Chapter 2) who showed characteristic microstructural phenomena to control macroscopic fatigue crack growth which may be different for constant amplitude and spectrum loading in particular at low ΔK levels. This type of information may be relevant for the applicability of basic constant amplitude data for spectrum crack growth prediction.

With respect to the number and complexity of tests conducted by many participants within the whole programme, the quality and consistency of the data base created should again be emphasized. This is certainly a consequence of the efforts of the laboratories involved, but also confirms the quality and significance of the detailed Working Documents [3 - 6] providing a common basis for all participants. Thus the persons involved in the preparation of these documents provided a valuable input to the whole exercise.

3 Modelling and Crack Growth Prediction

Lifing of aero-engine components increasingly requires, or totally relies on, fatigue crack crack growth assessment under consideration of near-service conditions. Therefore, crack growth modelling represents one of the essential parts of the Cooperative Test Programme. As described in great detail in Chapters 5 and 6, prediction of crack growth was rather accurate for the bulk of test cases. It should be noted that in most cases the modellers were not aware of the experimental results i.e. "blind" predictions were to be made.

Some major conclusions from Chapter 6 are repeated here:

- Both complex models taking load-interaction into account as well as more simple non-interaction models produced acceptable results for spectrum loading with a slight superiority of the more complex models.

- This can be rationalized by the nature of the TURBISTAN and underload sequences where the major contribution to damage accumulation, i.e. crack growth, is provided by the frequent zero-max cycles. This is supported by the relative insensitivity of fatigue test lives to severe omission of small cycles.

- The overload sequence tests are appropriately modelled only by the complex models.

- Using individual base-line data sets for each of the two specimen geometries excludes all possible uncertainties and inaccuracies which might result from K calibrations and other factors such as the constraint present in real components.

Without intending to detract from the success of the modelling exercise, it should be pointed out (what is self-evident, but repeated here again) that for an application many further aspects have to be considered such as the definition of initial crack or flaw sizes, the effect of temperature and corrosion, the consideration of scatter etc.

4 General Remarks

As already mentioned, the success of a collaborative effort such as the AGARD Engine Disc Cooperative Test Programme is dependent to a large extent on the quality and significance of guidelines prepared to share experimental and theoretical studies between several participants. These guidelines have been discussed within the working group, but prepared as Working Documents by individuals who therefore significantly contributed to the final result. It is recommended for future activities similar to the present one to devote sufficient time and energy to the preparation of guidelines or working documents.

With regard to the topic of the present programme, it is unfortunate that only one engine manufacturer took part (with a reduced set of predictions) in the modelling excercise. This may be understandable from a competition point of view, but nevertheless a more active role would have been desirable in particular with regard to real application problems. Manufacturers have supported the programme through delivery of materials and specimens which is very much appreciated.

Finally it should be emphasized that projects like the present one are only possible as collaborative programmes due to obvious reasons of cost, but an equally important aspect can be seen in bringing together experts from different areas and countries and encouraging exchange of ideas and expertise. Therefore, this type of effort should be continued in the future.

5 References

[1] Mom, A.J.A. and M.D. Raizenne:
AGARD Engine Disc Cooperative Test Programme.
AGARD Report No. R-766, August 1988.

[2] Gostelow, C.R. and C. Wilkinson:
High Temperature Cyclic Behaviour of Aerospace Materials - Part I.
AGARD Report No. R-778, 1992.

[3] Mom, A.J.A.:
Revised Working Document for the AGARD Cooperative Test Programme on Titanium Alloy Engine Disc Materials.
NLR TR 86019 L, 1986.

[4] Raizenne, M.D.:
AGARD TX 114 Test Procedures for Supplemental Engine Disc Test Programme.
NRC Laboratory Techn. Report ST-1617, Ottawa, June 1988.

[5] Raizenne, M.D.:
AGARD SMP Sub-Committee 33 Engine Disk Test Programme Fatigue Crack Growth Rate Data and Modelling Cases for Ti-6Al-4V, IMI 685 and Ti-17.
NRC Laboratory Techn. Report ST-1785, Ottawa, August 1990.

[6] Jany, E.:
AGARD SC 33 - Crack Growth Prediction Model - Description Form.
CEAT, Toulouse, July 1990.

REPORT DOCUMENTATION PAGE

1. Recipient's Reference	2. Originator's Reference	3. Further Reference	4. Security Classification of Document
	AGARD-R-766 (Addendum)	ISBN 92-835-0709-6	UNCLASSIFIED/ UNLIMITED

5. Originator Advisory Group for Aerospace Research and Development
North Atlantic Treaty Organization
7 rue Ancelle, 92200 Neuilly sur Seine, France

6. Title AGARD ENGINE DISC COOPERATIVE TEST PROGRAMME

7. Presented on

8. Author(s)/Editor(s)	9. Date
Various	April 1993

10. Author's/Editor's Address	11. Pages
Various	244

12. Distribution Statement There are no restrictions on the distribution of this document. Information about the availability of this and other AGARD unclassified publications is given on the back cover.

13. Keywords/Descriptors

Fatigue tests	Crack initiation
Fatigue (materials)	Crack propagation
Cracking (fracturing)	Aircraft engines

14. Abstract

The Report describes fatigue and crack growth tests of Ti-Al6-4V, IMI 685 and Ti-17 specimens under constant amplitude and under variable amplitude TURBISTAN loading sequences at room temperature. Five crack growth models are evaluated and compared against experimental data. Microstructure and fractography data for the tested materials are also presented.

This publication was sponsored by the Structures and Materials Panel of AGARD.

AGARD Report 766 (Addendum)
Advisory Group for Aerospace Research and Development, NATO
AGARD ENGINE DISC COOPERATIVE TEST PROGRAMME
Published April 1993
244 pages

The Report describes fatigue and crack growth tests of Ti-Al6-4V, IMI 685 and Ti-17 specimens under constant amplitude and under variable amplitude TURBISTAN loading sequences at room temperature. Five crack growth models are evaluated and compared against experimental data. Microstructure and fractography data for the tested materials are also presented.

This publication was sponsored by the Structures and Materials Panel of AGARD.

ISBN 92-835-0709-6

AGARD-R-766
(Addendum)

Fatigue tests
Fatigue (materials)
Cracking (fracturing)
Crack initiation
Crack propagation
Aircraft engines

AGARD Report 766 (Addendum)
Advisory Group for Aerospace Research and Development, NATO
AGARD ENGINE DISC COOPERATIVE TEST PROGRAMME
Published April 1993
244 pages

The Report describes fatigue and crack growth tests of Ti-Al6-4V, IMI 685 and Ti-17 specimens under constant amplitude and under variable amplitude TURBISTAN loading sequences at room temperature. Five crack growth models are evaluated and compared against experimental data. Microstructure and fractography data for the tested materials are also presented.

This publication was sponsored by the Structures and Materials Panel of AGARD.

ISBN 92-835-0709-6

AGARD-R-766
(Addendum)

Fatigue tests
Fatigue (materials)
Cracking (fracturing)
Crack initiation
Crack propagation
Aircraft engines

AGARD Report 766 (Addendum)
Advisory Group for Aerospace Research and Development, NATO
AGARD ENGINE DISC COOPERATIVE TEST PROGRAMME
Published April 1993
244 pages

The Report describes fatigue and crack growth tests of Ti-Al6-4V, IMI 685 and Ti-17 specimens under constant amplitude and under variable amplitude TURBISTAN loading sequences at room temperature. Five crack growth models are evaluated and compared against experimental data. Microstructure and fractography data for the tested materials are also presented.

This publication was sponsored by the Structures and Materials Panel of AGARD.

ISBN 92-835-0709-6

AGARD-R-766
(Addendum)

Fatigue tests
Fatigue (materials)
Cracking (fracturing)
Crack initiation
Crack propagation
Aircraft engines

AGARD Report 766 (Addendum)
Advisory Group for Aerospace Research and Development, NATO
AGARD ENGINE DISC COOPERATIVE TEST PROGRAMME
Published April 1993
244 pages

The Report describes fatigue and crack growth tests of Ti-Al6-4V, IMI 685 and Ti-17 specimens under constant amplitude and under variable amplitude TURBISTAN loading sequences at room temperature. Five crack growth models are evaluated and compared against experimental data. Microstructure and fractography data for the tested materials are also presented.

This publication was sponsored by the Structures and Materials Panel of AGARD.

ISBN 92-835-0709-6

AGARD-R-766
(Addendum)

Fatigue tests
Fatigue (materials)
Cracking (fracturing)
Crack initiation
Crack propagation
Aircraft engines